Unconventional Phase Field Simulations of Transforming Materials with Evolving Microstructures

Chi Hou Lei

A dissertation[†]
submitted in partial fulfillment of the
requirements for the degree of

Doctor of Philosophy

University of Washington

2015

Reading Committee:

Jiangyu Li, Chair

Lucien Brush

Marco Rolandi

Mark Tuttle

Junlan Wang

Program Authorized to Offer Degree:
Mechanical Engineering

[†]an egocentric imitation, actually

University of Washington

Abstract

Unconventional Phase Field Simulations of Transforming Materials with Evolving Microstructures

Chi Hou Lei

Chair of the Supervisory Committee:
Professor of Mechanical Engineering: Jiangyu Li
Department of Mechanical Engineering

Transforming materials are a class of multi-functional materials that couples multiple physical couplings, such as, mechanical and thermal in shape memory alloy (SMA), mechanical and electrical in ferroelectrics, mechanical and magnetic in ferromagnetic shape memory (FSMA), mechanical and chemical with electrical as in ion battery. These materials exhibit their characteristic properties because of their underlying microstructures. In this thesis, we would like to address to the fundamental question: Why do materials form microstructures, and how do microstructures evolve?

The thesis starts with an introduction to phase field simulation for modeling and simulating microstructures in material systems with multiple phases or variants, as a literature review. In order to simulate Austenite-Marteniste interfaces in shape memory alloys that appears in different physical length scales and temperature range, a two-level phase field approach is developed, which enables us to further simulate special two dimensional structures such as tunnels and tents, as well as possible interfaces in shape memory alloys. The new approach also allows us to study thermal hysteresis and to numerically verify the critical dependence of the hysteresis length on the crystal symmetry of the participating Austenite and Martensitic phases. Rigorous analysis in one dimension is also carried out to study domain formation and switching, which serves as foundation for the methodology of phase field simulation and the choices of parameters.

Conventional phase field simulation assumes strong periodicity in all physical dimensions, which makes it inconvenient to study the simulations related to experiments such as functional materials being probed in various atomic force microcopy (AFM). To extend the possibilities for simulations,

we release the periodicity, first along the out-of-plane direction and then along all directions. Numerical schemes for solving Maxwell equations (for electrical and magnetic orderings), elasticity equations (for mechanical ordering) and phase field equations (as a diffusion-type PDE) are formulated in these geometric configuration, utilizing eigen-expansion, finite difference and Chebyshev spectral method. These approaches are then used to simulate electromechanical responses in piezoelectric and ferroelectric materials, as well as domain formations in multi-functional materials, for instance, shape memory alloys and ferroelectrics. As a remark, Chebyshev spectral method for general geometry without any periodicity also works for inhomogeneous materials and arbitrary boundary conditions, which becomes an ideal candidate for investigating problems in the most general contexts and configurations.

Modeling, numerical solution and quantitative analysis in lithium ion electrode are also considered. A simplified model (as differential equation) for the dynamics of lithium ions due to externally applied voltage is set up and solved. Method of line (MOL) is adopted to solve the solution numerically to maintain conservative system, resulting in simulation of ion dynamics and corresponding deformation as deflection as detected by Electrochemical Strain Microscopy (ESM). Harmonic analysis is carried out semi-analytically to the system subjected to sinusoidal voltage (AC). Ion dynamics and deformation due to combined DC-AC bias are simulated and further compared with existing experimental data to estimate diffusivity and local concentration of ions in the electrode.

TABLE OF CONTENTS

Page

List of Figures iv

List of Tables xv

Chapter 1: Introduction and Overview 1

Chapter 2: Unconventional Phase Field Simulation in Shape Memory Alloys 4
- 2.1 The Phase Field Model 6
- 2.2 Numerical Implementation 11
- 2.3 Simulations and Results 11
- 2.4 Discussion and conclusion 20

Chapter 3: Austenite-Martensite Interfaces in Shape Memory Alloys 21
- 3.1 Background and Theory 23
- 3.2 Austenite-Martesite interfaces in Thin Films 26
- 3.3 The Two-Scale Phase Field Simulation 34
- 3.4 Implementation of Two-Scale Phase Field Simulation 36
- 3.5 Simulation in two dimensions (Plane-Strain Configurations) 40
- 3.6 Further exposures to the Austenite-Martensite interfaces in Cubic-to-Orthorhombic system 42
- 3.7 Simulation in three dimensions 51
- 3.8 Hysteresis 56
- 3.9 Austenite-Martensite interfaces in real crystal systems 61
- 3.10 Discussion and Conclusion 63

Chapter 4: Martensitic Tents and Tunnels in Shape Memory Alloy Thin Films by Phase Field Simulation 65

Chapter 5: Electromechanical Fields in Thin Films (3D-configuration) 73
- 5.1 Introduction and Background 73

5.2 Simulation in piezoelectric materials and SPM of ferroelectric materials 76
5.3 Discussions and Conclusions 92

Chapter 6: Phase Field Simulation in Finite Geometries 93
6.1 Unconventional Phase Field Simulation of Shape Memory Alloys in Finite Geometry 93
6.2 Unconventional Phase Field Simulation of Ferroelectric in Finite Geometry 105

Chapter 7: Lithium Ion Battery and Electro-chemical Strain Microscopy 109
7.1 Model of Lithium Ion Battery 110
7.2 One-dimensional study 112
7.3 Harmonic Analysis in ESM 133
7.4 Resolving Diffusivity and Local Concentration by Relaxation of ESM 144
7.5 Formulation in higher dimensions 156

Chapter 8: Spectral methods in Electro-mechanics and Phase Field Simulations 170
8.1 Preparation 171
8.2 Solving Maxwell's Equation with x-periodicity using Spectral Method 174
8.3 Solving General Maxwell's Equation using Spectral Method 180
8.4 Solving Elasticity Equation using Spectral Method 192
8.5 Fully Coupled Model for Piezoelectric Materials and Solution using Spectral Method 203
8.6 Piezoelectric Response of Ferroelectric with Spectral Method 212
8.7 Phase Field Simulations of Multi-variant Multi-functional Materials using Spectral Method 219

Chapter 9: Summary and Conclusions 226
9.1 Phase Field Simulations in Periodic Geometry 226
9.2 Phase Field Simulation in Thin Film 227
9.3 Phase Field Simulations in Finite Geometry 227
9.4 Lithium Ion Battery and Electrochemical Strain Microscopy 228
9.5 Spectral method 228

Bibliography 229

Appendix A: Theoretical Development in One-dimension 237
A.1 Microstructure under the effect of External Strain - One dimensional study 237
A.2 Microstructure under the effect of External Stress - One dimensional study 252
A.3 Effect of External Strain on 'Uniform' Volume Fraction 268

A.4 Summary and Conclusion 272

Appendix B: Austenite-Martensite Interfaces of Shape Memory Alloys in real Crystal Systems 273

B.1 Cubic-to-Tetragonal System 273

B.2 Cubic-to-Orthorhombic System 283

B.3 Cubic-to-Monoclinic-I System 299

B.4 Summary and Conclusion 313

Appendix C: Other forms of Characteristic Functions in Phase Field Simulation 314

Appendix D: Numerical solutions of Maxwell's and elasticity equations in Thin Films (3D-configuration) 318

D.1 Maxwell's equation by eigen-expansion 318

D.2 Maxwell's equation by finite differences 330

D.3 Elasticity equation by eigen-expansion 336

D.4 Elasticity equation by finite differences 364

D.5 Convention of elastic stiffness 380

Appendix E: Some background of ESM 383

E.1 Normalization of the ESM equation 383

E.2 SPM tip 384

E.3 Plane-Sphere Model 385

E.4 Parameters used in simulations 386

E.5 Second Harmonic 387

E.6 Numerical scheme for ESM equation in 2D 390

LIST OF FIGURES

Figure Number Page

2.1 The crystal lattices of variants in the cubic-to-tetragonal system. The high-temperature Austenite phase is cubic, while the low-temperature may appear in three possible lattice structures, due to loss of symmetry. [1] 5

2.2 (Clamped boundary condition) (a) The simulated pattern is shown in (a) with 4 variants denoted by (1), (2), (3) and (4). (b) Since (1) and (4) are considered as equal, as well as (2) and (3), the simulated pattern is re-visualized with two distinct variants. 14

2.3 (Clamped boundary condition) With a different parameter: (a) The simulated pattern is shown in (a) with 4 variants denoted by (1), (2), (3) and (4). (b) Since (1) and (4) are considered as equal, as well as (2) and (3), the simulated pattern is re-visualized with two distinct variants. 15

2.4 (External strain with $r = 0.5$) (a) The simulated pattern is shown in (a) with 4 variants denoted by (1), (2), (3) and (4). (b) Since (1) and (4) are considered as equal, as well as (2) and (3), the simulated pattern is re-visualized with two distinct variants. Equal volume fractions of variant 1 and variant 2 are observed. 16

2.5 (External strain with $r = 0.7$) (a) The simulated pattern is shown in (a) with 4 variants denoted by (1), (2), (3) and (4). (b) Since (1) and (4) are considered as equal, as well as (2) and (3), the simulated pattern is re-visualized with two distinct variants. The ratio of the volume fractions between variant 1 and variant 2 is 70% to 30%. . 17

2.6 (External stress with $a = 1000000000$) (a) The simulated pattern is shown in (a) with 4 variants denoted by (1), (2), (3) and (4). (b) Since (1) and (4) are considered as equal, as well as (2) and (3), the simulated pattern is re-visualized. This stress favours variant 1. The whole domain is occupied by variant 1 only. 17

2.7 (External stress with $a = -1000000000$) (a) The simulated pattern is shown in (a) with 4 variants denoted by (1), (2), (3) and (4). (b) Since (1) and (4) are considered as equal, as well as (2) and (3), the simulated pattern is re-visualized. This stress favours variant 2. The whole domain is occupied by variant 2 only. 18

2.8 Effect of external stress in domain switching. The snapshots (a) to (f) show how variant 1 is evolving to variant 2. 19

3.1 Experimental observation of microstructure that involves a Austenite-Martensite interface (Chu and James). 22

3.2 Simulation of microstructure in thin film configuration for Cubic-to-Trigonal system. The Martensitic ratio is 60% to 40%. (a) The simulated pattern is shown in (a) with 4 variants denoted by (1), (2), (3) and (4). (b) Since (3) and (4) represent the Austenite phase, the simulated pattern is re-visualized with three distinct variants. (c) Four identical patterns in (b) are packed together to obtain a better image. . . . 31

3.3 Simulation of microstructure in thin film configuration for Cubic-to-Trigonal system. The Martensitic ratio is 70% to 30%. (a) The simulated pattern is shown in (a) with 4 variants denoted by (1), (2), (3) and (4). (b) Since (3) and (4) represent the Austenite phase, the simulated pattern is re-visualized with three distinct variants. (c) Four identical patterns in (b) are packed together to obtain a better image. . . . 32

3.4 Another Simulation of microstructure in thin film configuration for Cubic-to-Trigonal system. The Martensitc ratio is 70% to 30%. (a) The simulated pattern is shown in (a) with 4 variants denoted by (1), (2), (3) and (4). (b) Since (3) and (4) represent the Austenite phase, the simulated pattern is re-visualized with three distinct variants. (c) Four identical patterns in (b) are packed together to obtain a better image. . . . 33

3.5 The schematics of an inexact interface between Austenite (A) and Martensitic twin M_1 and M_2. 35

3.6 The schematics of the two scale algorithm. In the upper level where the Austenite twins with the twinned Martensities, only μ_1 evolves. The upper level passes the average total strain to the lower level, which serves as the external strain for the mechanical equilibrium in the lower level. In the lower level where the Martensitic variants twin, only μ_2 evolves while μ_1 is fixed. After both μ_1 and μ_2 converge, the two levels are then superposed to give the microstructure. 37

3.7 Procedures of two scale algorithm. Starting from random initial μ_1^0 and μ_2^0, subprogram 1 is used to iterate μ_1^1 in the upper level. Average total strain is obtained at this level and is passed into the lower level. Subprogram 2 uses μ_1^1 and μ_2^0 to generate μ_2^1. This completes one iteration. The procedures continue until both μ_1^i and μ_2^i meet the convergence criteria. 39

3.8 AusteniteMartensite interfaces by phase field simulation; (a) compatible interface when the middle eigenvalue of the transformation strain is 0 and (b) inexact interface when the middle eigenvalue of the transformation strain is not 0; (c) and (d) the corresponding distribution of elastic energy in the structure, with the scale bar indicating the elastic energy density. 41

3.9 The elastic energy as function of middle eigenvalue of the transformation strain for volume-preserving transformation. 42

3.10 Simulation of Austenite-Martensite interface in plane strain configuration when the Martensitic ratio r is 0.6 = 60%. The volume fraction of Austenite in (a), (b), (c), (d) and (e) are respectively 0%, 20%, 40%, 50% and 70%. 45

3.11 Simulation of Austenite-Martensite interface in plane strain configuration when the Martensitic ratio r is 0.66 = 66%. The volume fraction of Austenite in (a), (b), (c), (d) and (e) are respectively 0%, 20%, 40%, 50% and 70%. 46

3.12 Simulation of Austenite-Martensite interface in plane strain configuration when the Martensitic ratio r is 0.7 = 70%. The volume fraction of Austenite in (a), (b), (c), (d) and (e) are respectively 0%, 20%, 40%, 50% and 70%. 47

3.13 Simulation of Austenite-Martensite interface in plane strain configuration when the Martensitic ratio r is 0.75 = 75%. The volume fraction of Austenite in (a), (b), (c), (d) and (e) are respectively 0%, 20%, 40%, 50% and 70%. 48

3.14 Simulation of Austenite-Martensite interface in plane strain configuration when the Martensitic ratio r is 0.8 = 80%. The volume fraction of Austenite in (a), (b), (c), (d) and (e) are respectively 0%, 20%, 40%, 50% and 70%. 49

3.15 Simulation of Austenite-Martensite interface in plane strain configuration when the Martensitic ratio r is 1 = 100%. The volume fraction of Austenite in (a), (b), (c), (d) and (e) are respectively 0%, 20%, 40%, 50% and 70%. Only one martebsitic variant is present and sharp compatible interface is observed. The (common) middle eigenvalue of the Martensitic variant is zero. 50

3.16 Simulation of Austenite-Martensite interface in three dimensions when the Martensitic ratio r is 0.6 = 60%, with various orientations of the Austenite-Martensite interfaces. 52

3.17 Simulation of Austenite-Martensite interface in three dimensions when the Martensitic ratio r is 0.66 = 66%, with various orientations of the Austenite-Martensite interfaces. 53

3.18 Simulation of Austenite-Martensite interface in three dimensions when the Martensitic ratio r is 0.7 = 70%, with various orientations of the Austenite-Martensite interfaces. 54

3.19 Simulation of Austenite-Martensite interface in three dimensions when the Martensitic ratio r is 0.75 = 75%, with various orientations of the Austenite-Martensite interfaces. 55

3.20 Simulation of Austenite-Martensite interface in three dimensions when the Martensitic ratio r is 0.8 = 80%, with various orientations of the Austenite-Martensite interfaces. Unfortunately, simulations with some direction of interface are not successful. 56

3.21 Sum of anisotropy energy and thermal energy. (a) At transformation temperature $T = T_c$, the energy is minimized and stable at either Austenite or Martensite, thus both phases have equal priorities to exist. (b) Below transformation temperature $T < T_c$, the energy is minimized at field variable corresponding to Martensites, thus Martensite is more likely to form. (c) Above transformation temperature $T < T_c$, the energy is minimized at field variable corresponding to Austenite, thus Austenite is more likely to form. 58

3.22 Hysteresis loop and snapshots showing the evolution of the microstructure for $r = 0.6$ . . . 59

3.23 Hysteresis loop and snapshots showing the evolution of the microstructure for $r = 0.7$ . . . 60

3.24 Schematic showing how the eight possible of micro-structures are generated. . . . 63

4.1 Schematic showing (a) shape-memory alloy deposited on a substrate; (b) shape-memory alloy released in a suitable region and remains at in the austenite; (c) bulges out in Martensite below transformation temperature; (d) various interfaces in tent; (e) various interfaces in tunnel. In fig. (d) and (e), the notions (0), (1) and (2) represent the regions occupied by the austenite phase and the two Martensitic phase respectively. Also $\mathbf{n}_{01}$ denotes the interface between austenite and Martensitic variant 1, $\mathbf{n}_{02}$ denotes the interface between austenite and Martensitic variant 2, and $\mathbf{n}_{12}$ denotes the interface between austenite and Martensitic variant 2. . . . 67

4.2 Simulation of patterns of tunnel and tent and the corresponding three-dimensional views; (a) Pattern of tunnel; (b) Three-Dimensional view of tunnel; (c) Pattern of tent; (d) Three-Dimensional view of tent; (e) experimentally observed formation of tent (Bhattacharya and James) for comparison. . . . 70

4.3 Thermal hysteresis of tunnel; (a) $\sim$ (i): patterns of intermediate structures; Patterns along cooling on the curve are marked by circles, patterns along heating are marked by square diamonds. . . . 71

4.4 Thermal hysteresis of tent; (a) $\sim$ (i): patterns of intermediate structures; Patterns along cooling on the curve are marked by circles, patterns along heating are marked by square diamonds. . . . 72

5.1 Configurations for solving (a) the Maxwell's equation and (b) the mechanical equilibrium equation. . . . 74

5.2 Configurations for solving electromechanical responses of piezoelectric materials. 76

5.3 (Electromechanical responses of piezoelectric materials) Electric potential and fields: (a) electric potential ϕ, (b) field component E_1, (c) field component E_2 and (d) field component E_3. . . . 79

5.4 (Electromechanical responses of piezoelectric materials) displacement components or deformation: (a) u_1, (b) u_2 and (c) u_3. . . . 80

5.5 (Electromechanical responses of piezoelectric materials) strains: (a) ε_{11}, (b) ε_{22}, (c) ε_{33}, (d) ε_{23}, (e) ε_{13} and (f) ε_{12}. . . . 81

5.6 (Electromechanical responses of piezoelectric materials) stresses: (a) σ_{11}, (b) σ_{22}, (c) σ_{33}, (d) σ_{23}, (e) σ_{13} and (f) σ_{12}. . . . 82

5.7 (Electromechanical responses of piezoelectric materials) displacement for non-zero polarization with $P_0 = 10^2$: (a) u_1, (b) u_2 and (c) u_3. . . . 83

5.8 (Electromechanical responses of piezoelectric materials) displacement for non-zero polarization with $P_0 = 10^4$: (a) u_1, (b) u_2 and (c) u_3. 84

5.9 (Electromechanical responses of piezoelectric materials) displacement for non-zero polarization with $P_0 = 10^6$: (a) u_1, (b) u_2 and (c) u_3. 85

5.10 Configuration of SPM experiment 87

5.11 (SPM) distribution of displacements on probed surface. (a) u_1; (b) u_2; (c) u_3; (d) magnitude of u_3 as 3D plot 89

5.12 (SPM) Distribution of displacements on probed specimen in three-dimensions. (a) u_1; (b) u_2; (c) u_3; 90

5.13 (SPM) Distribution of displacements on probed specimen in three-dimensions, zoomed near the SPM tip, to explore the local responses. (a) u_1; (b) u_2; (c) u_3; 91

6.1 Configuration of computational domain for elasticity. 98

6.2 Schematic showing how the elasticity equation is solved by decomposing into two parts. The first part represents a macroscopic / homogeneous solution. The second part is a perturbed solution that considers realistic boundary conditions 100

6.3 Shape memory alloys with varying thickness of substrate underneath. 103

6.4 Shape memory alloys with varying misfit strain of substrate underneath. 104

6.5 Simulated domain pattern of ferroelectric with four variants. Arrows indicate the polarizations. 108

7.1 Schematic of working principle of lithium ion battery 109

7.2 Physical configurations for one-dimensional PNP equation: (a) Three dimensional box whose length and width are longer than height. (b) Nanowire or nanotube. . . 114

7.3 Grid for one-dimensional simulation. The length of the sample is divided into N cells with $N+1$ subdivision points denoted by x_i, at which electric fields or potentials are discretized. The midpoints of the cells are denoted by x_j, at which the ion concentrations are discretized. 119

7.4 Simulation results for linear applied potential: (a) spatial distribution of electric potential. (b) spatial distribution of electric field. (c) spatial distribution of ion at initial and steady state. (d) spatial distribution of strain at initial and steady state. (e) spatial distribution of displacement at initial and steady state. 123

7.5 Simulation results for linear applied potential: Ion concentration and deflection at the top surface measured from initial to steady states. 124

7.6 Simulation results for ESM: (a) spatial distribution of electric potential. (b) spatial distribution of electric field. (c) variation of total ion over time, showing that the system is conserved. (d) spatial distribution of ion at initial and steady state. (e) spatial distribution of strain at initial and steady state. (f) spatial distribution of displacement at initial and steady state. 127

7.7 Simulation results for ESM: Ion concentration and deflection at the top surface measured from initial to steady states. 128

7.8 Simulation results for ESM due to sinusoidal voltage: (a) Temporal profile of applied voltage of ESM tip. (b) Resulting sinusoidal profile of ion concentration at top surface. (c) Resulting sinusoidal profile of deflection at top surface. 130

7.9 Simulation results for ESM due to sinusoidal voltage: Snapshots of displacement of the probed sample over one cycle. x-axis presents the length and y-axis shows the value of the displacement. Notice that x = 0 corresponds to the top surface. 131

7.10 Simulation results for ESM due to sinusoidal voltage: Relationship between the operating frequency and the corresponding maximum deflection at the top surface, as measured by the ESM tip. 132

7.11 Real and imaginary parts, and magnitude, of first harmonic of ion due to SPM with sinusoidal input voltage. 142

7.12 Effect of domain thickness on first harmonic of (a) ion concentration and (b) deflection on top surface. Notice that for (b), the magnitude of the deflection is with respect to the tip radius R. 142

7.13 Contour showing ion concentration at steady state for domain subjected to SPM tip with positive voltage. Notice that lithium ion are attracted towards the site of SPM tip. 143

7.14 Profile of applied voltage $V(t)$ during a charging / relaxation process to probe diffusivity and local ion concentration. 147

7.15 Simulation results of relaxation study of lithium ion. The top graph shows the profile of applied voltage $V(t)$. The middle graph shows the resulting ion concentration at the top surface of the electrode, $c(x = H,t)$. The bottom graph shows the deformation, $u(x = H,t)$. 150

7.16 Experimental results of relaxation study of lithium ion. Deflection detected by the SPM tip is shown. Profile of DC voltage for manipulating ions is also shown. . . . 151

7.17 Simulation results of relaxation study of lithium ion. Deflection detected by the SPM tip is shown. The data is also fitted with functions in exponential form. The magnitude of the deflection is normalized with respect to the radius of SPM tip. . . 152

7.18 Grid for one-dimensional simulation. The length of the sample is divided into N cells with $N+1$ subdivision points denoted by x_i, at which electric fields or potentials are discretized. The midpoints of the cells are denoted by x_j, at which the ion concentrations are discretized. 159

7.19 The explicit forms of the differential equations for concentration at (x_i,y_j), that is the differential equation for $c_{ij}(t)$, depends on which section of the two-dimensional domain within which (x_i,y_j) lies. There are nine possible cases that refer to interior points (denoted by A), four boundaries (denoted by $B1,B2,B3,B4$) and four corners (denoted by $C1,C2,C3,C4$). 160

7.20 Boundary conditions for (a) ESM equation and (b) Elasticity equation. For ESM equation, all four boundaries assume zero flux so as not to allow ion to flow out. For elasticity equation, the top surface is traction-free while the bottom is displacement-free. The left and right boundaries are periodic. 162

7.21 Contour showing ion concentration at steady state for domain subjected to SPM tip with positive voltage. Notice that lithium ion are attracted towards the site of SPM tip. 163

7.22 Displacement components of domain of Lithium ions in steady state due to SPM tip with positive voltage. 164

7.23 Schematic showing positive voltage induces attraction of ion towards SPM tip and the resulting deformation. 164

7.24 Contour showing ion concentration at steady state for domain subjected to SPM tip with negative voltage. Notice that lithium ion are attracted towards the site of SPM tip. 165

7.25 Displacement components of domain of Lithium ions in steady state due to SPM tip with negative voltage. 165

7.26 Schematic showing negative voltage induces attraction of ion towards SPM tip and the resulting deformation. 166

7.27 Region of influence of ion distribution and displacement on top surface as detected by SPM tip in 2D model. The top graph shows the initial and steady state ion distribution over the center line of the two-dimensional domain. The bottom graph shows the displacements. 167

7.28 First harmonic deflection in two dimensional model. 168

7.29 169

8.1 Chebyshev points (n = 16) 172

8.2 Schematic of computational domain for Maxwell's equation with boundary condition. Periodicity is assumed in x-direction. 175

8.3 Periodic Maxwell's equation; grounded on bottom surface, potential on top surface $\cos(2\pi x)$. (a) Schematic, (b) Simulation: potential. 178

8.4 Periodic Maxwell's equation; grounded on bottom surface, electric field (y-component) on top surface $E_y = \sin(\pi x)$. (a) Schematic, (b) Simulation: potential. 179

8.5 Periodic Maxwell's equation; grounded on bottom surface, zero electric flux on top surface. Spontaneous polarization exists. (a) Schematic, (b) Simulation: potential. 180

8.6 Schematic of computational domain for Maxwell's equation with boundary condition. Physical boundary condition can be imposed on each boundary. 181

8.7 Schematic illustrating equivalence between two dimensional data and one dimensional vector 182

8.8 Non-periodic Maxwell's equation; four different conditions on four boundaries. (a) Schematic, (b) Simulation: potential. 189

8.9 Schematic of computational domain for Maxwell's equation with boundary condition. Periodicity is assumed in x-direction. 190

8.10 Spital distribution of permittivity κ (homogeneous) and resulting potential ϕ. It is used as a control set. 191

8.11 Spital distribution of permittivity κ (non-homogeneous) and resulting potential ϕ. . 191

8.12 Schematic of instantaneous polarization and resulting potential ϕ. 192

8.13 Schematic of computational domain for Maxwell's equation with boundary condition. Periodicity is assumed in x-direction. 193

8.14 Displacement components u and v of solid subjected to traction on top surface and zero displacement on bottom, left and right surface. No periodicity is assumed. . . 199

8.15 Displacement components u and v of solid subjected to traction on top surface and zero displacement on bottom. Periodicity is assumed in x-direction. 200

8.16 Displacement components u and v of solid subjected to traction on top boundary and zero displacement on bottom boundary. The left and right boundaries are traction-free. No periodicity is assumed. 201

8.17 Displacement components u and v of solid with laminated eigenstrain ε^*_{12} subjected to traction on top surface and zero displacement on bottom, left and right surface. No periodicity is assumed. 202

8.18 Boundary conditions for coupled piezo-electric model. 207

8.19 Simulation of electromechanical response in piezoelectric material with artificial applied potential on top surface and natural boundary conditions on other boundaries. (a) Potential, (b) x-displacement, (c) y-displacement. Notice that due to normalization, the displacements are in the unit of 10^{10} (m), while the unit of the potential is Volt (V). 208

8.20 Simulation of electromechanical response in piezoelectric material with artificial applied potential on top surface and natural boundary conditions on other boundaries. (a) Potential, (b) x-displacement, (c) y-displacement. Notice that due to normalization, the displacements are in the unit of 10^{10} (m), while the unit of the potential is Volt (V). 210

8.21 Simulation of electromechanical response of piezoelectric material as in PFM. The top surface is subjected to a potential induced by PFM tip. All other boundaries are natural. (a) Potential, (b) x-displacement, (c) y-displacement. Notice that due to normalization, the displacements are in the unit of 10^{10} (m), while the unit of the potential is Volt (V). 211

8.22 SPM of ferroelectric with single domain. 213

8.23 Distribution of (a) potential, (b) electric field component E_1 and (c) electric field component E_2 induced by PFM tip whose tip radius is 25 (nm) and applied voltage is 1 (Volt). 214

8.24 Distribution of the displacement components induced from the electric field (a) u, (b) v 216

8.25 SPM of ferroelectric with single domain. 217

8.26 Snapshots of vertical displacements for PFM scanning of ferroelectric with two domains 218

8.27 Relation between the PFM response as vertical displacement versus distance from the domain wall at center line 219

8.28 Schematic showing how Neumann boundaries are treated in the conventional methods when solving heat equation. Problems occur at the four corners. 223

8.29 Schematic showing how Neumann boundaries are treated during the two stages of the ADI scheme. 224

A.1 One-dimensional simulated patterns for $\gamma = 0.3$. The value of μ is plotted along the x-axis. $\mu = 1$ presents that the domain is occupied by variant 1, while $\mu = 0$ presents that the domain is occupied by variant 2. If K is too small, the pattern is uniform and homogeneous. As K increases, the patterns become laminated. But if K gets too large, the alternating patterns become too rapid and do not reflect the reality. There is a range of K on which the desired patterns can be generated. Notice that the average values of μ is equal to $\gamma = 0.3$. 248

A.2 One-dimensional simulated patterns for $\gamma = 0.5$. The value of μ is plotted along the x-axis. $\mu = 1$ presents that the domain is occupied by variant 1, while $\mu = 0$ presents that the domain is occupied by variant 2. If K is too small, the pattern is uniform and homogeneous. As K increases, the patterns become laminated. But if K gets too large, the alternating patterns become too rapid and do not reflect the reality. There is a range of K on which the desired patterns can be generated. Notice that the average values of μ is equal to $\gamma = 0.5$. 249

A.3 One-dimensional simulated patterns for $\gamma = 0.8$. The value of μ is plotted along the x-axis. $\mu = 1$ presents that the domain is occupied by variant 1, while $\mu = 0$ presents that the domain is occupied by variant 2. If K is too small, the pattern is uniform and homogeneous. As K increases, the patterns become laminated. But if K gets too large, the alternating patterns become too rapid and do not reflect the reality. There is a range of K on which the desired patterns can be generated. Notice that the average values of μ is equal to $\gamma = 0.8$. 250

A.4 One-dimensional simulated patterns for $\gamma = 0$. The value of μ is plotted along the x-axis. $\mu = 1$ presents that the domain is occupied by variant 1, while $\mu = 0$ presents that the domain is occupied by variant 2. Over a wide range of K, the patterns remain uniform as 0. 251

A.5 One-dimensional simulated patterns for $\gamma = 1$. The value of μ is plotted along the x-axis. $\mu = 1$ presents that the domain is occupied by variant 1, while $\mu = 0$ presents that the domain is occupied by variant 2. Over a wide range of K, the patterns remain uniform as 1. But if K gets too large, at some points of the patterns, there are rapid switching between 0 and 1. The average value of μ is approximately 1. . 251

A.6 One-dimensional simulated patterns by external stress that favours variant 1 with $S = s_1 < 0$. The value of μ is plotted along the x-axis. $\mu = 1$ presents that the domain is occupied by variant 1, while $\mu = 0$ presents that the domain is occupied by variant 2. (a) Initial random pattern. (b) and (c) Intermediate patterns. (d) Final pattern. The microstructure evolves to variant 1 with $\mu = 1$. 260

A.7 One-dimensional simulated patterns by external stress that favours variant 2 with $S = s_2 > 0$. The value of μ is plotted along the x-axis. $\mu = 1$ presents that the domain is occupied by variant 1, while $\mu = 0$ presents that the domain is occupied by variant 2. (a) Initial random pattern. (b) and (c) Intermediate patterns. (d) Final pattern. The microstructure evolves to variant 2 with $\mu = 0$. 261

A.8 (One dimensional) Illustration of domain switching by stress from variant 1 to variant 2. The value of μ is plotted along the x-axis. $\mu = 1$ presents that the domain is occupied by variant 1, while $\mu = 0$ presents that the domain is occupied by variant 2. (a) Initial pattern: Domain occupied by variant 1 but a narrow nucleation of variant 2. (b) (c) (d) (e) Intermediate patterns. (d) Final pattern. The microstructure evolves to variant 2 with $\mu = 0$, growing from the nucleation. 267

A.9 Relation between the imposed external strains in terms of transformation strains of Martensitc variants in the ratio γ and the resulting volume fraction between the two variants μ. Here $\lambda = 1$ 271

A.10 Relation between the imposed external strains in terms of transformation strains of Martensitc variants in the ratio γ and the resulting volume fraction between the two variants μ. Here $\lambda = 1$ 272

B.1 Simulated micro-structures in tetragonal system: Cases (1) - (4). 281

B.2 Simulated micro-structures in tetragonal system: Cases (5) - (8). 282

B.3 Simulated micro-structures in orthorhombic system involving variants 1 and 2: Cases (1) - (4). 290

B.4 Simulated micro-structures in orthorhombic system involving variants 1 and 2: Cases (5) - (8). 291

B.5 Simulated micro-structures in orthorhombic system involving variants 1 an 3: Cases (1) - (4). 297

B.6 Simulated micro-structures in orthorhombic system involving variants 1 an 3: Cases (5) - (8). 298

B.7 Simulated micro-structures in monoclinic-I system involving variants 1 an 2: Cases (3) (6) (8). 305

B.8 Simulated micro-structures in monoclinic-I system involving variants 1 an 5: Cases (1) - (4). 312
B.9 Simulated micro-structures in monoclinic-I system involving variants 1 an 5: Cases (6) and (7). 313
C.1 Shape memory alloys with varying misfit strain of substrate underneath, using θ as characteristic functions. 317
D.1 Configurations for solving (a) the Maxwell's equation and (b) the mechanical equilibrium equation. 342
D.2 Configurations for solving (a) the Maxwell's equation and (b) the mechanical equilibrium equation. 346

LIST OF TABLES

Table Number Page

3.1 (Cubic-to-Orthorhombic system) In order to obtain Austenite-Martensite interface between Austenite and twinned Martensites in predicted volume ratio r of Martensitic variants $\varepsilon^{(1)}$ and $\varepsilon^{(2)}$, the lattice parameters α and γ have to be in certain derived ratio. Recall that $\beta = -2\alpha$. The three (common) eigenvalues of the participating Martensitic variants are given. The middle eigenvalue (printed in bold face) is critically related to the appropriate shape of the interface (stereotype). If the middle eigenavlue is 0, a compatible sharp interface is expected. On the other hand, non-zero eigenvalues induce incompatible (rough) interfaces. 44

6.1 Two choices of elements on top and bottom rows of the second order differentiation matrix with Neumann boundary conditions at end points 97

ACKNOWLEDGMENTS

I would like to gratefully acknowledge the guidance, support and encouragement of my doctoral advisor, Prof Jiangyu Li, and the members of my committee, Prof. Lucien Brush, Prof. Marco Rolandi, Prof. Junlan Wand and Prof Mark Tuttle, during my time at the University of Washington. Moreover, I thank Prof. Li for being patient for my slow progress due to various technical issues and allowing me to develop my own philosophy without pressure.

I thank my lab mates and visiting scholars of the lab. They have been helping and encouraging me in various aspects in my research. I have enjoyed wonderful group activities with them. They are: Dr. Liangjun Li, Dr. Yuanming Liu, Dr. Yang Yang, Dr. Feiyue Ma, Prof. Shuhong Xie, Prof. Yunya Liu, Mr. Yang Lu, Dr. Nataly Chen, Dr. Yun Ou, Dr. Kai Pun, Ms. Peiqi Wang, Mr. Ahmad Eshghinejad, Mr. I-Le Peng, Mr. Peng Jiang and Ehsan Nasr Esfahani.

I am fortunate to have the opportunity to teach with Prof. Martin Berg, Prof. Joseph Garbini and Prof. Steve Shen in System Dynamics for eight quarters. System dynamics is not related to my primary academic area in computational material sciences. Yet they have inspired me and extended my knowledge in the areas of Control and System, which also have broadened my possibility to become well-prepared for teaching a wider spectrum of courses. Interacting and learning with my beloved students in these courses is the most rewarding experience. I will never forget the time studying with them for exams and having pizzas. Without their supports though nominations and recommendations, I would not be able to be awarded with the teaching awards at both college level and university level.

Finally, I would like to thank Prof. Yi-Chung Shu of National Taiwan University for bringing me academically to the exciting field of computational material sciences, by showing me the fascinating pictures of twinned microstructures observed by Prof. Richard James of the University of Minnesota, and explaining to me the beautiful mathematics behind.

DEDICATION

I dedicate this thesis to my family,
my father, Mr Weng Kei Lee,
my mother, Ms Sok I Lou, and
my sister, Ms Si Hang Lei,
for their constant support and unconditional love.
I love you all dearly.

Chapter 1

INTRODUCTION AND OVERVIEW

Transforming materials with evolving microstructures is one of the most important classes of smart materials that have many potential technological applications in sensing, actuation, transduction, data storage, and energy harvesting. They include shape memory alloys (SMAs) [2, 3, 4], ferroelectrics [5], ferromagnetic shape memory alloys (FSMAs) [6, 7, 8, 9, 10], and multiferroic magnetoelectric materials [11, 12, 13, 14, 15, 16, 17], among others, which have been extensively investigated for a variety of structure and device applications. One of the key characteristics of these materials is the phase transformation from a higher temperature phase to a lower temperature one at a critical transition temperature, upon which the material symmetry is often reduced, resulting in coexistence of multiple transforming variants that are symmetry-related and energetically equivalent in lower temperature phase. In order to minimize the overall energy of the materials, fascinating yet characteristic microstructures involving multiple transforming variants are often observed [2, 18, 19, 20, 21], and the configurations and evolutions of such microstructures have profound influences on the macroscopic behaviors of transforming materials under external loading, especially in the nonlinear regime. Understanding the formation and evolution of such microstructures thus is actively pursued in materials science, solid mechanics, as well as applied mathematics.

It is generally understood that the formation and evolution of microstructures in transforming materials are driven by minimization of potential energy of the system, and rigorous energy minimization theories based on relaxation or homogenization have been developed to analyze such phenomena [19, 22, 23, 24, 25]. Various computational techniques have also been developed to simulate the configuration and evolution of the microstructures, including first-principles modeling [26] and sharp interface model by level set method [27, 28, 29], among others. In the past decade or so, phase field simulations have become increasingly popular [30], wherein the microstructures are represented by a set of continuous field variables, eliminating the need to track the interfaces explicitly. While the conventional phase field simulations are based on phenomenological theory

of phase transformation and use order parameters as field variables [30], unconventional phase field approaches based on characteristic functions of transforming variants have recently been developed, and have been applied successfully to simulate a wide range of microstructures in SMAs [31, 32, 33], ferroelectrics [34], FSMAs [35, 36, 37], and multiferroic magnetoelectric materials [38, 39, 40, 41] with varying degrees of couplings.

Practically the microstructures of materials are imaged and characterized by scanning probe microscopy (SPM) and its variants, piezoelectric force microscopy (PFM) (for piezoelectric and ferroelectric) and electrochemical strain microscopy (ESM) (for lithium ion battery) [42, 43, 44]. They have been applied to study a wide range of phenomena, such as static and dynamic imaging [45], domain switching and fatigue [46, 47], and domain-defect interactions [48]. The development of SPM has promoted the investigation of elctromechanical response at nanoscale. However, the quantitative interpretations of the SPM are difficult. For example, while ferroelectric domain structures can be inferred from the PFM scanning, the correlation between PFM mappings and the underlying ferroelectric structure is nontrivial, which requires careful analysis and interpretation. This technical difficulty comes from the fact that the tip induced displacement is influenced by the three-dimensional polarization in the full specimen, which results from the long-range electro-elastic interactions. Overcoming these difficulties, our goal is to accurately reconstruct the underlying domain structure from SPM measurements. As a first step, simulations thus serve as an alternative tool to predict the SPM response from any given domain.

The first half of this thesis is devoted to unconventional phase field simulation of shape memory alloys. In chapter one, unconventional phase field simulations are introduced and are applied to shape memory alloys in thin film configurations. Microstructures generated from various mechanical conditions are also studied. In chapter two, we carry out one-dimensional analyses of the phase field models. This study gives us some insight on the choices of parameters in the phase field models that yield reasonable patterns. In chapter three, the unconventional phase field is extended to a two-scale version for the simulation of Austenite-Martensite interfaces, where two different length scales are involved. In chapter four, special thin film structures, called tunnels and tents, are simulated.

The second half of this thesis starts with the numerical solutions of the Maxwell's and the elasticity equations in a more realistic physical configuration for simulations in experiments, where

the samples possess no periodicity in the x_3 direction. Boundary conditions can be imposed to the top and the bottom surfaces, which resembles experimental set-ups. As a remark, unlike other researchers who adopted sophisticated level of mechanics like the Stroh's formulation, our approaches are simply based on eigen-expansion and finite difference, which make it easier to understand and implement. In the chapters that follow, we utilize the solutions of the Maxwell's and the elasticity equations to study electromechanical responses in piezoelectric and ferroelectric materials during SPM, and electrochemical response of lithium ion cell during ESM.

Ongoing and future works are presented at the end.

Chapter 2

UNCONVENTIONAL PHASE FIELD SIMULATION IN SHAPE MEMORY ALLOYS

Shape memory alloys (SMAs) exhibit a first-order, diffusion-less, solid-to-solid phase transformation during which there is a sudden change in the crystal structure at a certain temperature [32]. The microstructure undergoes phase transformation and evolves as the temperature changes. Above the transformation temperature T_c, the crystal structure is cubic and is referred as the Austenite phase. Below the transformation temperature T_c, the crystal structure loses cubic symmetry which gives rises to several equivalent Martensite phases. The Martensite phases are symmetry-related variants that are identical crystal lattices with different orientations. At the transformation temperature T_c, both the Austenite phase and the various Martensite phases may co-exist. As an example, the variants in the cubic-to-tetragonal crystal system is illustrated in figure (2.1) [1].

The microstructure can take a specific shape (and resulting pattern) by forming a fine-scaled mixture of different variants, which can be controlled by applying external mechanical condition. The proportions of these variants and how they mix in the overall structure are not arbitrary. Between any two variants is an interface that is well orientated. The variants thus form highly intricate and very characteristic patterns at a length scale much smaller than the size of the sample.

The evolution of microstructure in SMA can be described by the time-dependent Ginburg-Landau (TDGL) model [30], where a suitable set of order parameters and special polynomial expansions of these parameters. In the conventional models [30, 49], the order parameters are usually the physical characteristics of the materials. In SMA, transformation strains or eigenstrains of the participating variants are chosen as parameters, whereas in ferroelectric materials, spontaneous polarizations are chosen as the order parameters.

In the unconventional modal, a new set of field variables is introduced to represent each participating variants. This approach is motivated by the hierarchical structure of multi-rank laminates structure by Bhattacharya for establishing the rule of mixtures. Under this circumstance, the poly-

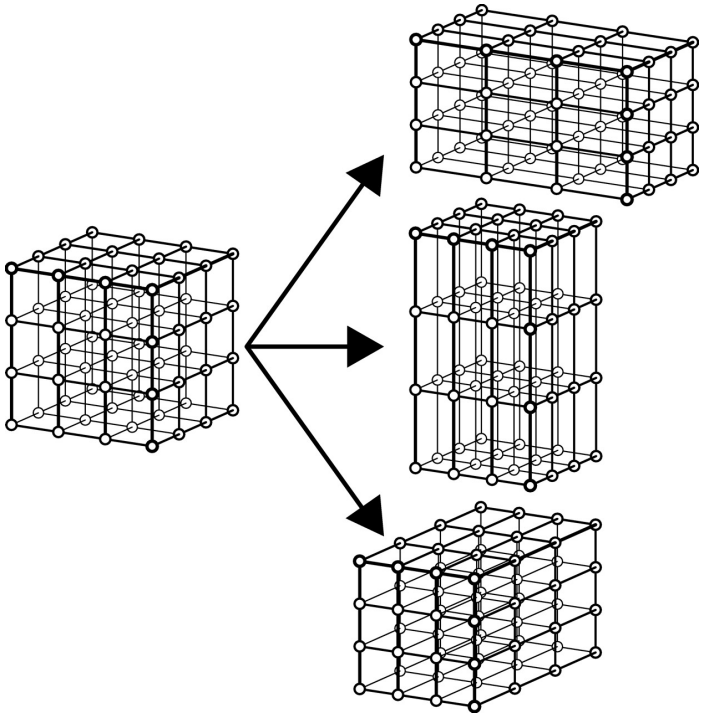

Figure 2.1: The crystal lattices of variants in the cubic-to-tetragonal system. The high-temperature Austenite phase is cubic, while the low-temperature may appear in three possible lattice structures, due to loss of symmetry. [1]

nomial describing the energy-well structure appears to be simpler, which require less parameters to fix.

This chapter is devoted to unconventional phase field modal for microstructure in shape memory alloy below transformation temperature (T_c) where the Martensitic variants are participating. The framework of the unconventional phase field model is briefly introduced, followed by numerical simulation for cubic-to-tetragonal crystal system. One-dimensional analysis is then studied which provides information on the relationship between the model parameters and the resulting patterns. We also propose a way to modify the mathematical expression of the order parameters and the characteristic functions so as to speed up the simulation and enhance the effects on texture and visualization.

2.1 The Phase Field Model

In this section we give a brief introduction to the phase field model for micro-structures.

The high-temperature phase, Austenite, induces no deformation in the lattice crystal structure, due to cubic symmetry. It is considered as the reference configuration. As the temperature drops below the transformation temperature T_c, the crystal structure transforms to Martensites. The lattice crystal structure is of lower symmetry. The common ones are tetragonal, trigonal, orthorhombic or monoclinic symmetry. Thus there exists several symmetry-related martesitic variants. All variants can be described mathematically by the transformation (Bian) strains $\varepsilon^{(i)}$ as the way their crystal lattices deform with respect to the reference configuration. The number of Austeniteic variants and their transformation strains in each crystal systems are different. Notice that the Austenite has stress-free strain $\varepsilon^{(0)} = \mathbf{0}$.

Assume the domain Ω of the sample is occupied by N variants. Each variant occupies a sub-domain $\Omega_i \in \Omega$ for $i = 1,2,...,N$. Since each point of the sample can only be occupied by only one variant, no two variants can overlap, that is, $\Omega_i \bigcap \Omega_j, i \neq j$. The existences of Martensitic variants induce a locally inhomogeneous transformation strain field, that is, $\varepsilon^*(\mathbf{x}) = \varepsilon^{(i)}$ if $\mathbf{x} \in \Omega_i$. With the uses of the characteristic functions $\gamma_i(\mathbf{x})$ over each sub-domain Ω_i, the inhomogeneous

transformation strain can be re-expressed as:

$$\varepsilon^*(\mathbf{x}) = \sum_{i=1}^{N} \gamma_i(\mathbf{x})\varepsilon^{(i)}, \tag{2.1}$$

where $\gamma_i(\mathbf{x}) = 1$ if $x \in \Omega_i$ and $\gamma_i(\mathbf{x}) = 0$ otherwise. Furthermore the constraint $\sum_{i=1}^{N} \gamma_i(\mathbf{x}) = 1 \forall \mathbf{x} \in \Omega$ motivates us to propose another set of field variables $\mu_1, \mu_2, ..., \mu_{N-1}$ to describe the laminated structures of the variants.

$$\begin{aligned}
\gamma_1 &= \mu_1 \\
\gamma_2 &= (1-\mu_1)\mu_2 \\
\gamma_3 &= (1-\mu_1)(1-\mu_2)\mu_3 \\
&\vdots \\
\gamma_{N-1} &= (1-\mu_1)(1-\mu_2)\cdots(1-\mu_{N-2})\mu_{N-1} \\
\gamma_N &= (1-\mu_1)(1-\mu_2)\cdots(1-\mu_{N-2})(1-\mu_{N-1})
\end{aligned} \tag{2.2}$$

From the construction of μ_i from γ_i, the values of μ_i also take 0 or 1. Two advantages of this setting are: First, the N original characteristic functions are reduced to $N-1$ laminated characteristic functions. Secondly, the introduction of the laminated characteristic functions have inherited the constraint that the sum of all characteristic functions to be one. These two aspects will speed up the simulation and eliminate the use of the energy functional for the sum of the characteristic functions. As a remark, the new laminated characteristic functions are motivated by the rule of mixtures proposed by Bhattacharya [50] and have been implemented successfully in the theories for ferroelectrics by Shu and Li [34, 19].

Between two variants is an interface whose normal direction can be predicted by the twinning equation or the strain compatibility. Suppose two variants, i-th and j-th, are twinned, the following equation must hold:

$$\varepsilon^{(i)} - \varepsilon^{(j)} = \frac{1}{2}(\mathbf{a} \otimes \mathbf{n}\mathbf{n} \otimes \mathbf{a}), \tag{2.3}$$

where $\mathbf{n}$ is the normal to the interface and $\mathbf{a}$ is the shear vector of the interface. This condition

implies that a laminate microstructure can be constructed by alternating layers of these two variants with an overall strain:

$$\lambda\varepsilon^{(i)} + (1-\lambda)\varepsilon^{(j)}, \tag{2.4}$$

where $0 \leq \lambda \leq 1$ is the volume fraction of the *i*-th variant.

The twining equation (2.3) seems to be hard to verify in practice. An alternative way to verify is outlined as follow. Assume that the eigenvalues and eigenvectors of $\varepsilon^{(i)} - \varepsilon^{(j)}$ are respectively $\{e_1 \leq e_2 \leq e_3\}$ and $\{\mathbf{v}_1, \mathbf{v}_2, \mathbf{v}_3\}$. The following (general) conditions ensure the existence of interfaces:

$$e_1 \leq 0, e_2 = 0, e_3 \geq 0 \tag{2.5}$$

Furthermore, the normal of the interface can be evaluated by:

$$\mathbf{n} = \frac{1}{\sqrt{e_3 - e_1}} \left(-\kappa\sqrt{-e_1}\mathbf{v}_1 + \sqrt{e_3}\mathbf{v}_3 \right), \tag{2.6}$$

where $\kappa = \pm 1$. Thus there are at most two possible interfaces and associated normals.

As a remark, if the crystal system is restricted to two dimensions, where the transformation strains are two-by-two matrices, with two eigenvalues $\{e_1 \leq e_3\}$ and eigenvectors $\{\mathbf{v}_1, \mathbf{v}_3\}$, the above condition can be relaxed to:

$$e_1 \leq 0, e_3 \geq 0, \tag{2.7}$$

where the formula to evaluate the normal $\mathbf{n}$ remains the same. The middle eigenvalue e_2 does not need to be zero for forming patterns.

We are now in a position to set up the evolution equation for the microstructure by considering several free energies.

Elastic energy

With the inhomogeneous transformation strain ε^*, the elastic energy density is:

$$W^{elas}(\mu) = \frac{1}{2}\left[\varepsilon - \varepsilon^*(\mu)\right] \cdot \mathbf{C}\left[\varepsilon - \varepsilon^*(\mu)\right], \tag{2.8}$$

where $\mathbf{C}$ is the (isotropic) elastic modulus, $\mu = \{\mu_1, \mu_2, ..., \mu_{N-1}\}$ and ε is the compatible strain, which depends implicitly on μ and can be solved from the mechanical equilibrium equation:

$$\begin{cases} \nabla \cdot \sigma = 0 \\ \sigma = \mathbf{C}\left(\varepsilon - \varepsilon^*(\mu)\right) \end{cases}, \tag{2.9}$$

subjected to suitable boundary conditions.

Anisotropy energy

The laminated characteristic functions μ_i are supposed to take on either 0 or 1 such that the eigen-strain $\varepsilon^*(\mu)$ represents the transformation strain of the variant occupying the sample. Anisotropy energy is introduced to enforce the supposed values:

$$W^{ani}(\mu) = \sum_{i=1}^{N-1} K_i \mu_i^2 (1-\mu_i)^2, \tag{2.10}$$

where $K_i > 0$ are the anisotropy constants. This energy serves as the energetic cost (as penalty) when the field variable μ deviates from 0 or 1. Since all the Martensitic variants are equivalent up to a rotation in the symmetry group in the specific crystal system, we may assume that the anisotropy constants to be identical, that is, $K_i = K \forall i$.

Interfacial energy

Interfacial energy is introduced for the sharp interface separating different variants:

$$W^{int}(\mu) = A|\nabla \mu|^2, \tag{2.11}$$

where $A > 0$ is the exchange or gradient coefficient. This constant should be small. This energetic term ensures the field variables μ_i to vary continuously across the boundaries of the variants and serves as the energy for forming interfaces.

Total energy

The pattern of microstructure at fixed temperature below the critical transformation temperature T_c is obtained by minimizing the functional:

$$\mathscr{I}(\mu) = \int_{\Omega} \left\{ W^{int}(\mu) + W^{ani}(\mu) + W^{elas}(\mu) - \sigma \cdot \varepsilon \right\} d\mathbf{x}, \tag{2.12}$$

subjected to the mechanical equilibrium equation (2.9).

Evolution of microstructure under driving force

Taking the variational derivatives of (2.12) with respect to the field variables μ leads to the evolution equation:

$$\frac{\partial \mu}{\partial t} = -M \frac{\delta \mathscr{I}}{\delta \mu} = M\mathbf{F}, \tag{2.13}$$

where $M > 0$ is the mobility constant, $\mathbf{F}$ is the total thermodynamic driving force defined by the negative of the variational derivative of the free energy with respect to the field variables μ:

$$\mathbf{F}(\mu) = -\frac{\delta \mathscr{I}}{\delta \mu} = \mathbf{F}^{int} + \mathbf{F}^{ani} + \mathbf{F}^{elas}. \tag{2.14}$$

Physically, $\mathbf{F}^{int}$ is the driving force for coarsening the microstructure, $\mathbf{F}^{ani}$ is the driving force for selecting the variants and $\mathbf{F}^{elas}$ is the driving force for refining the microstructure to accommodate the specified boundary condition and applied mechanical loadings. These driving forces are obtained by taking the variational derivatives of the component energies with respect to the field variable μ:

$$\begin{aligned} \mathbf{F}^{int} &= -\frac{\delta W^{int}(\mu)}{\delta \mu} = 2A\nabla^2 \mu \\ \mathbf{F}^{ani} &= -\frac{\delta W^{ani}(\mu)}{\delta \mu} \\ \mathbf{F}^{elas} &= -\frac{\delta W^{elas}(\mu)}{\delta \mu} = \sigma \cdot \frac{\partial \varepsilon^*(\mu)}{\partial \mu} \end{aligned} \tag{2.15}$$

2.2 Numerical Implementation

The evolution equation for the microstructure is re-organized into the form:

$$\frac{\partial \mu}{\partial t} = M\left(2A\nabla^2\mu + \mathbf{F}^{ani} + \mathbf{F}^{elas}\right), \mathbf{x} = (x_1, x_2) \in (0, l_0)^2. \tag{2.16}$$

The length and time scales can be normalized by setting:

$$\widetilde{x_1} = \frac{x_1}{l_0}, \widetilde{x_2} = \frac{x_2}{l_0}, \widetilde{t} = 2MKt. \tag{2.17}$$

The normalized equation becomes:

$$\frac{\partial \mu}{\partial \widetilde{t}} = D\widetilde{\nabla}^2\mu + \frac{1}{2K}\left[\mathbf{F}^{ani} + \mathbf{F}^{elas}\right], \widetilde{\mathbf{x}} = (\widetilde{x_1}, \widetilde{x_2}) \in (0,1)^2, \tag{2.18}$$

where $\widetilde{\nabla}^2 = \frac{\partial^2}{\partial \widetilde{x_1}} + \frac{\partial^2}{\partial \widetilde{x_1}}$ and $D = \frac{A/K}{l_0^2}$.

Following the semi-implicit method proposed by Chen and Shen [51], let $\Delta\widetilde{t}$ be the time step, $\mu^n = \mu(\widetilde{x_1}, \widetilde{x_2}, n\Delta\widetilde{t})$ and $\mu^{n+1} = \mu(\widetilde{x_1}, \widetilde{x_2}, (n+1)\Delta\widetilde{t})$. Under the periodic boundary condition, Fourier transform is applied in both directions. The resulting numerical scheme is obtained as:

$$\overline{\mu^{n+1}} = \frac{\overline{\mu^n} + \frac{\Delta\widetilde{t}}{2K}\left[\overline{\mathbf{F}^{ani}(\mu^n)} + \overline{\mathbf{F}^{elas}(\mu^n)}\right]}{1 + D(\xi_1^2 + \xi_2^2)\Delta\widetilde{t}}, \tag{2.19}$$

where ξ_1 and xi_2 are the Fourier coordinates, $\overline{\mu^{n+1}} = \mathfrak{F}[\mu^{n+1}]$, $\overline{\mu^n} = \mathfrak{F}[\mu^n]$, $\overline{\mathbf{F}^{ani}(\mu)} = \mathfrak{F}[\mathbf{F}^{ani}(\mu)]$, $\overline{\mathbf{F}^{elas}(\mu)} = \mathfrak{F}[\mathbf{F}^{elas}(\mu)]$ and $\mathfrak{F}[\cdot]$ represents the Fourier transform. The formulation in three dimensions is straight forward.

2.3 Simulations and Results

As an example to illustrate the numerical scheme for the microstrcuture, we choose Ti-Ni at the trigonal R-phase, as the material to be simulated. The number of equivalent Austeniteic variants is

$N = 4$. Their transformation strains are given by:

$$\varepsilon^{(1)} = \begin{pmatrix} \alpha & \delta & \delta \\ \delta & \alpha & \delta \\ \delta & \delta & \alpha \end{pmatrix}, \varepsilon^{(2)} = \begin{pmatrix} \alpha & -\delta & -\delta \\ -\delta & \alpha & \delta \\ -\delta & \delta & \alpha \end{pmatrix},$$
$$\varepsilon^{(3)} = \begin{pmatrix} \alpha & -\delta & \delta \\ -\delta & \alpha & -\delta \\ \delta & -\delta & \alpha \end{pmatrix}, \varepsilon^{(4)} = \begin{pmatrix} \alpha & \delta & -\delta \\ \delta & \alpha & -\delta \\ -\delta & -\delta & \alpha \end{pmatrix}, \tag{2.20}$$

where $\alpha = 0$ and $\delta = 0.0047$.

To simulate the patterns in two dimensions, the above transformation strains have to be re-orientiated and projected into two dimensions (as in the thin film). For the simplest configuration, we consider the thin film in the (001) direction. The transformation strains $\varepsilon^{(i)}$ are rotated through the rotation matrix:

$$\mathbf{R}_{(001)} = \begin{pmatrix} \frac{1}{\sqrt{2}} & \frac{1}{\sqrt{2}} & 0 \\ -\frac{1}{\sqrt{2}} & \frac{1}{\sqrt{2}} & 0 \\ 0 & 0 & 1 \end{pmatrix}. \tag{2.21}$$

The in-plane components of the resulting transformation strains are then given by:

$$\varepsilon^{(1)} = \varepsilon^{(4)} = \begin{pmatrix} \alpha+\delta & 0 \\ 0 & \alpha-\delta \end{pmatrix} = \begin{pmatrix} 0.0047 & 0 \\ 0 & -0.0047 \end{pmatrix}$$
$$\varepsilon^{(2)} = \varepsilon^{(3)} = \begin{pmatrix} \alpha-\delta & 0 \\ 0 & \alpha+\delta \end{pmatrix} = \begin{pmatrix} -0.0047 & 0 \\ 0 & 0.0047 \end{pmatrix}. \tag{2.22}$$

Notice that there are only two distinct variants in the (001) film. The resulting simulated patterns are controlled by applying different mechanical loadings (stresses or strains), as illustrated and discussed in the following subsections.

Throughout the simulations, without otherwise stated, we assume the following parameters:

$$\begin{aligned} \widetilde{t} &= 0.005 \\ K &= K_i = 2650800 \\ D &= D_i = 0.00001 \\ \mathbf{C} &= \begin{pmatrix} c_1 & c_3 & 0 \\ c_3 & c_1 & 0 \\ 0 & 0 & c_2 \end{pmatrix}, \end{aligned} \tag{2.23}$$

where $c_1 = 80$ GPa, $c_2 = 20$ GPa and $c_3 = 30$ GPa. The simulations are taken over a 128×128 grid.

2.3.1 Clamped boundary condition

Suppose the film is unstressed as deposited and then attached to the substrate, the film is subjected to the clamped boundary condition, that is, zero strain, or $\langle \varepsilon \rangle = \varepsilon^0 = 0$. The simulation is shown in figure (2.2) (a), where the microstructure is self-accommodating to the laminated pattern with overall zero strain. Different variants, denoted by (1), (2), (3) and (4), are represented in different colors. But since (1) and (4) actually represent the same variant, while (2) and (3) represent the other variant. The pattern can be re-visualized with variant 1 (which is composed of the region occupied by (1) and (4)) and variant 2 (which is composed of the region occupied by (2) and (3)) as shown in figure (2.2) (b). The normal to the interface in the simulated pattern is exactly what we can predict from the geometric compatibility condition. More specifically, $\mathbf{n}_1 = \frac{1}{\sqrt{2}} \begin{pmatrix} 1 \\ 1 \end{pmatrix}$ and $\mathbf{n}_2 = \frac{1}{\sqrt{2}} \begin{pmatrix} 1 \\ -1 \end{pmatrix}$. It can be seen in the figure that the volume fractions of these two distinct variants are approximately one-half, when the applied strain or the average strain is zero. This is expected from theory, since the average of the transformation strain is zero, or, $\frac{1}{2} \left\langle \varepsilon^{(1)} \right\rangle + \frac{1}{2} \left\langle \varepsilon^{(2)} \right\rangle = 0 = \left\langle \varepsilon^0 \right\rangle$.

The simulated patterns are not unique. They depend on the random initial patterns and the parameters chosen. If we increase the anisotropy constant and employ a different random initial condition, we obtain a different pattern, as shown in figure (2.3).

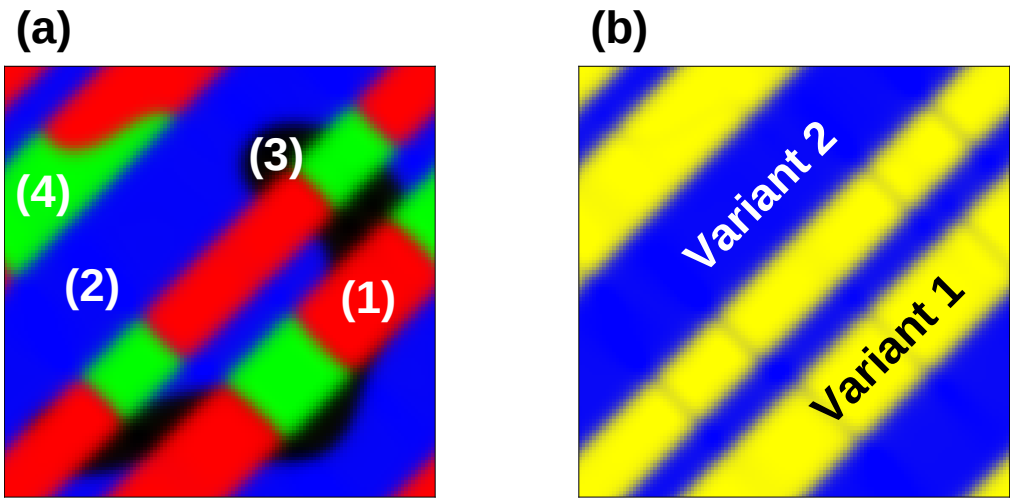

Figure 2.2: (Clamped boundary condition) (a) The simulated pattern is shown in (a) with 4 variants denoted by (1), (2), (3) and (4). (b) Since (1) and (4) are considered as equal, as well as (2) and (3), the simulated pattern is re-visualized with two distinct variants.

2.3.2 Imposed strains and self-accommodating structures

We have seen that, if we impose zero strain to the sample, equal volume fractions of both variants are generated. A question arises if different volume fractions of variants can form. In fact, this can be achieved by applying a suitable external strain. If the desired volume fractions between the two distinct variants are r and $1-r$, then setting the imposed strain as the linear combination of the transformation strains of these variants in the same ratio will do the work.

$$\varepsilon^0 = r\varepsilon^{(1)} + (1-r)\varepsilon^{(2)} \tag{2.24}$$

Two examples of simulations with $r = 0.5$ and $r = 0.7$ are illustrated respectively in figure (2.4) and figure (2.5). The volume fractions of variants in the simulated patterns are expected for both cases.

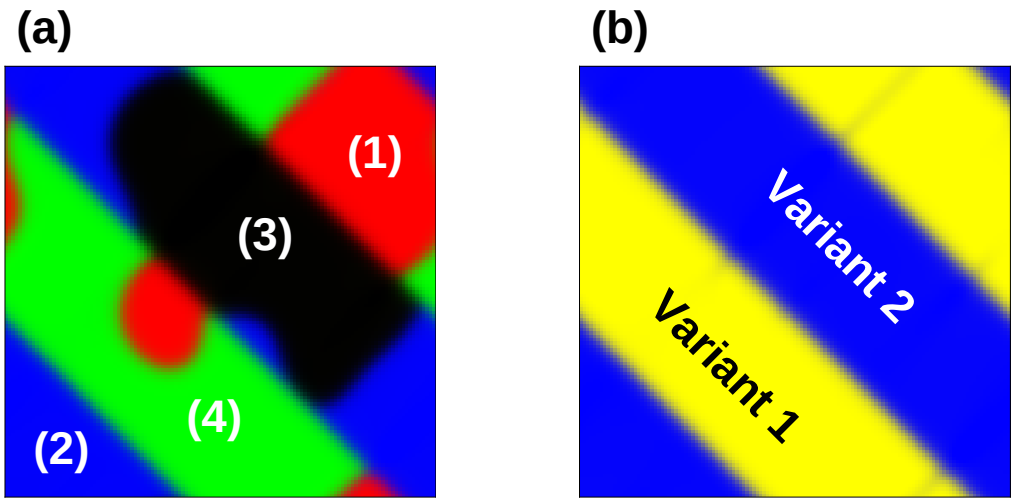

Figure 2.3: (Clamped boundary condition) With a different parameter: (a) The simulated pattern is shown in (a) with 4 variants denoted by (1), (2), (3) and (4). (b) Since (1) and (4) are considered as equal, as well as (2) and (3), the simulated pattern is re-visualized with two distinct variants.

2.3.3 Imposed stress and domain switching

We may also apply external stress in the form $\sigma^0 = \begin{pmatrix} a & 0 \\ 0 & 0 \end{pmatrix}, a \neq 0$ to the sample. If $a > 0$, only one variant is generated. On the other hand, if $a < 0$, another variant is generated. This is due to the part of the total energy functional attributable to the external stress in the minimization problem, that is, $-\sigma^0 \cdot \varepsilon$.

If the stress σ^0 is such that $-\sigma^0 \cdot \varepsilon^{(1)} < -\sigma^0 \cdot \varepsilon^{(2)}$, then variant 1, whose transformation strain is $\varepsilon^{(1)}$, possesses lower work done than variant 2 does. It turns out that variant 1 is more preferable to form than variant 2 and the whole domain will be occupied by variant 1 eventually.

To illustrate this, two simulations are run. In the first case, $a = 1000000000$, this stress favours variant 1 as the work done with its transformation strain is lower, thus the whole domain is occupied by variant 1, as shown in figure (2.6). In the second case, $a = -1000000000$, this stress will induce variant 2 to occupy the whole domain, as shown in figure (2.7).

The effect of external mechanical stresses on the domain microstructure provides the mechanism

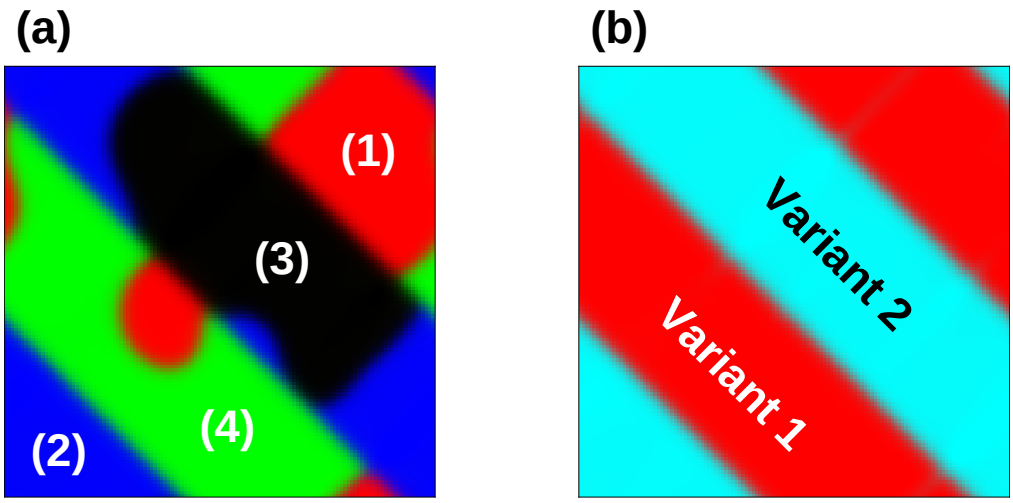

Figure 2.4: (External strain with $r = 0.5$) (a) The simulated pattern is shown in (a) with 4 variants denoted by (1), (2), (3) and (4). (b) Since (1) and (4) are considered as equal, as well as (2) and (3), the simulated pattern is re-visualized with two distinct variants. Equal volume fractions of variant 1 and variant 2 are observed.

of domain switching in shape memory alloys.

Assume that initially the domain is almost occupied by variant 1 with a small layer of variant 2 as nucleation. A stress that is favorable to variant 2 is applied to the sample. It is seen that the island of variant 2 is growing to the whole domain. The snapshots showing the evolution of variant 2 are shown in figure 2.8.

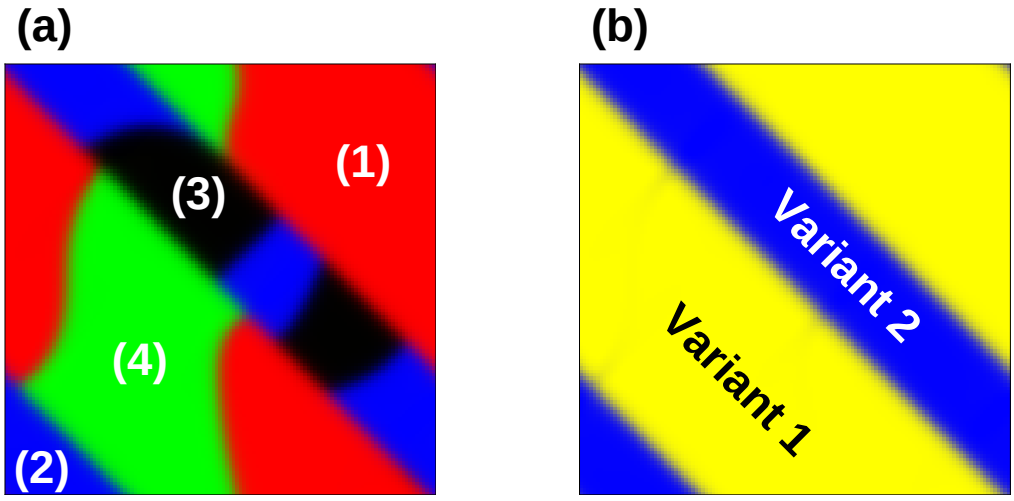

Figure 2.5: (External strain with $r = 0.7$) (a) The simulated pattern is shown in (a) with 4 variants denoted by (1), (2), (3) and (4). (b) Since (1) and (4) are considered as equal, as well as (2) and (3), the simulated pattern is re-visualized with two distinct variants. The ratio of the volume fractions between variant 1 and variant 2 is 70% to 30%.

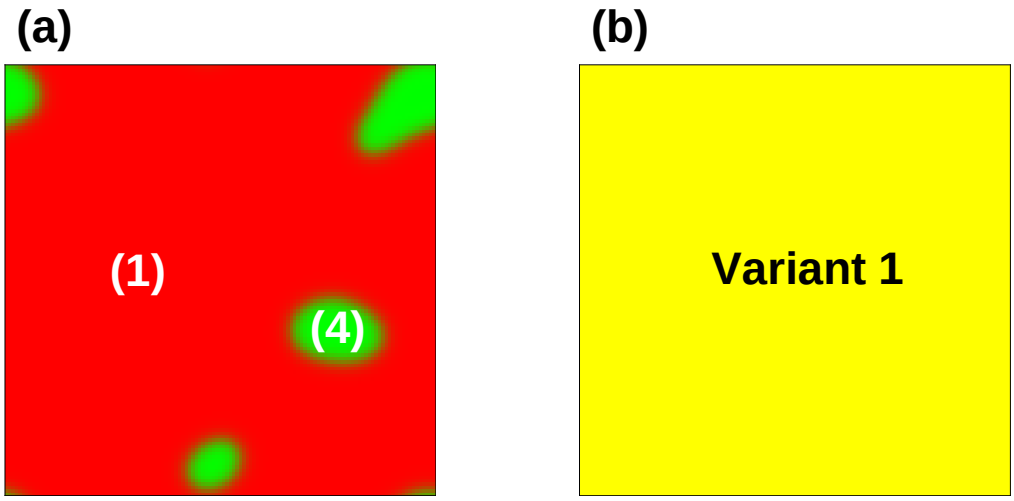

Figure 2.6: (External stress with $a = 1000000000$) (a) The simulated pattern is shown in (a) with 4 variants denoted by (1), (2), (3) and (4). (b) Since (1) and (4) are considered as equal, as well as (2) and (3), the simulated pattern is re-visualized. This stress favours variant 1. The whole domain is occupied by variant 1 only.

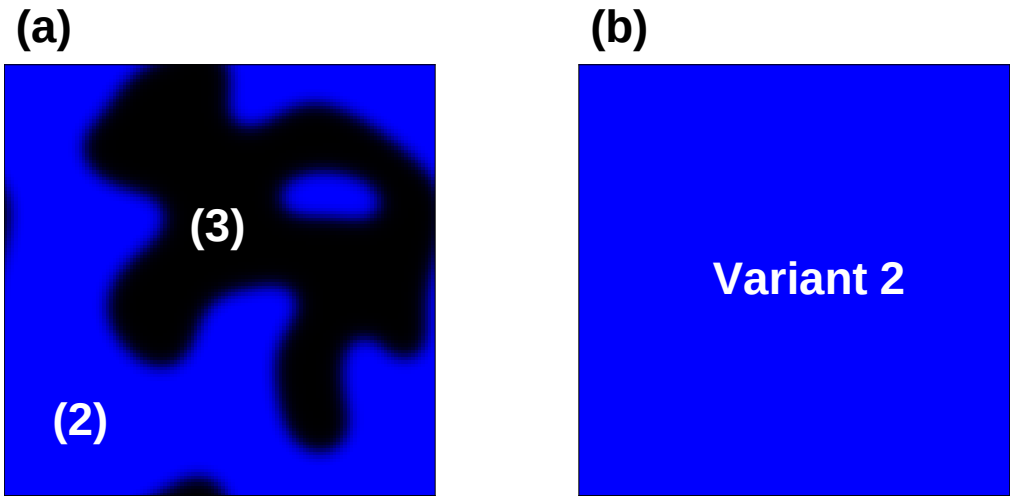

Figure 2.7: (External stress with $a = -1000000000$) (a) The simulated pattern is shown in (a) with 4 variants denoted by (1), (2), (3) and (4). (b) Since (1) and (4) are considered as equal, as well as (2) and (3), the simulated pattern is re-visualized. This stress favours variant 2. The whole domain is occupied by variant 2 only.

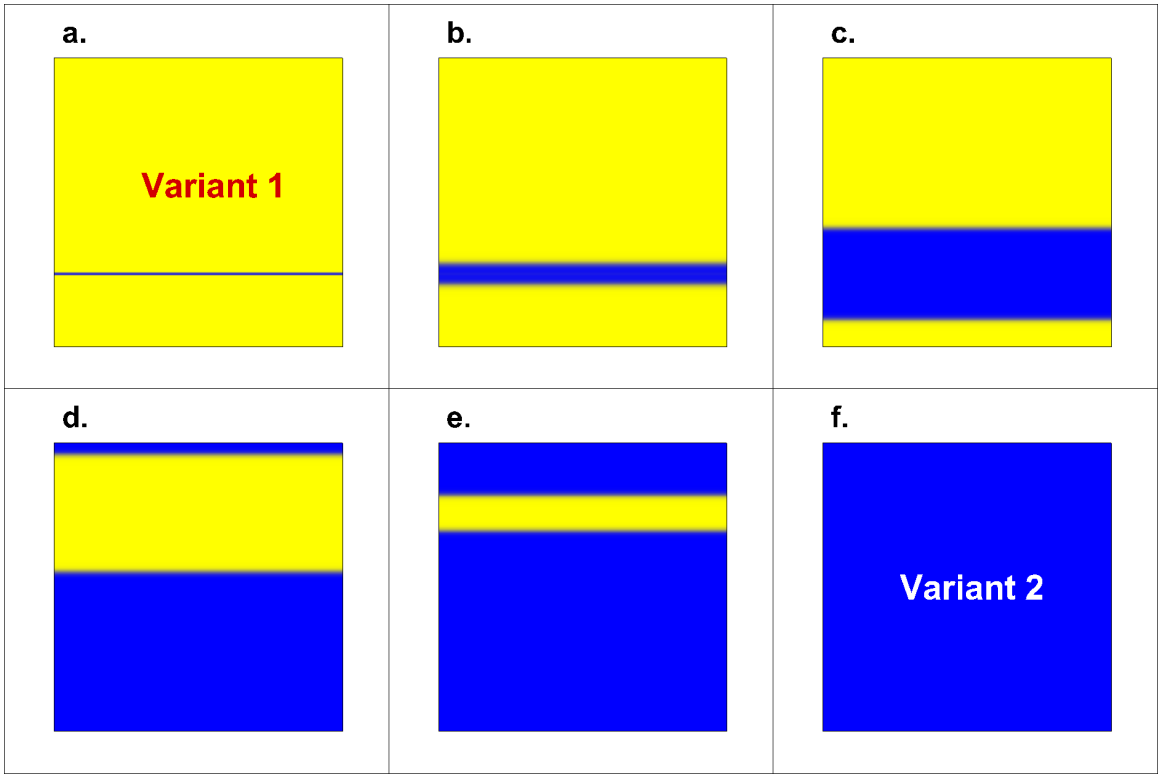

Figure 2.8: Effect of external stress in domain switching. The snapshots (a) to (f) show how variant 1 is evolving to variant 2.

2.4 Discussion and conclusion

In this preliminary chapter, we introduce the method of unconventional phase field model and implement this approach to simulate micro-structures in shape memory alloys. Various micro-structures can form depending on the applied mechanical conditions. External strain can be used to control the volume ratios of the participating variants. External stress is used for domain switching. So far this method is restricted to micro-structures that involve Martensitic variants only. If Austenite is included, the current phase field modal has to be ungraded to a two-scale version. We also found that the parameters (anisotropy constants) play a critical role in the formation of microstructure. In the simulations in two dimensions, if the parameters are badly chosen, no expected patterns will form.

We also carry out one dimensional analyses of the model where we study how these parameters affect the micro-strictures that can be formed. The detail is found in appendix (A).

Chapter 3

AUSTENITE-MARTENSITE INTERFACES IN SHAPE MEMORY ALLOYS

Unconventional phase field was successfully employed to simulate microstructure of variants of Martensitic phases below the transformation temperature, where Martensitic variants twinning with interfaces are observed. One natural and possible direction on research is potentially an attempt to simulate microstructure that involves also the Austenite phrase and that works with a wider range of temperature. However, it turns out that the original formulation and numerical scheme by considering trivial addition of the Austenite phase does not generate any desired pattern, due to the fact that the length scales are no longer comparable and that the formulation did not take into account the effect of temperature above and below transformation temperature.

From the experimental observation of microstructure that involves both Austenite and Martenites by James and Chu [52, 53] as shown in figure (3.1), at approximately the transformation temperature where all phases can co-exist, two Martenitic variants are twinned together before the resulting twinned Martensites generate pattern with the Austenite phase with an see-saw shaped interface, which we refer as the Austenite-Martensite interface. It can also be seen that the length scale for the Austenite-Martenite twinning is larger than that for the Martenite-Martenite twinning. This serves as an evidence of why the current formulation does not work since it assumes all variants to be in the same scale for twinning.

Another issue for including Austenite phase in the simulation arises in the possibility of forming the Austenite-Martensite twin with interfaces based on the theory of crystallography, or more specifically, the crystalline symmetry and the geometric compatibilities of the Austenite and the Martensite phases [54]. Several outcomes can happen for the twinning between the Austenite and the Martensite phases: no interface, sharp AM interface, see-saw shaped AM interface or interface in any other possible configurations. Interfaces in various shapes possess different levels of energies. The energy inherited in the interfaces is proposed to be related to the hysteresis, or the switching between phases due to cycling temperature change, as a characteristic of the reversibility

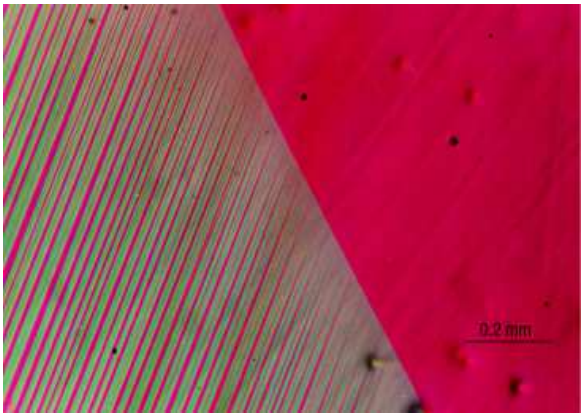

Figure 3.1: Experimental observation of microstructure that involves a Austenite-Martensite interface (Chu and James).

of structural phase transformations. On the other hand, this energy is considered as a barrier for the initiation of hysteresis and switching between phases, on which many applications and designs are based, ranging from fatigue life of shape memory alloys to magnetoelectric coupling in multiferroic oxides.

Thus understanding how the underlying crystal symmetry of the variants determine the type of Austenite-Martensite interface and the associated energy content will give us insights on the syntheses of alloys that require minimal energy and minimal temperature range for domain switching, inferring narrower hysteresis loops and faster structural phase transformation [55].

To resolve the difficulty that deals with the two different length scales between the Austenite-Martensite twinning and Martinsite-Martensite twinning, a two-scale phase field simulation is developed for Austenite-Martensite interface to understand the effects of crystalline symmetry and geometric compatibilities on the reversibility of structural phase transformations in shape memory alloys [33, 56].

We will briefly outline the theory of Austenite-Martensite interfaces based on the crystallography and the associated linear geometric compatibility. Simulations of microstructure involving Austenite-Martensite interfaces are illustrated for Cubic-to-Trigonal crystals in thin film configuration. It will be shown that in thin film, individual Martensitic variants are twinned with Austenite but these Martensitic variants do not generally twin with each others. In other words, all variants

are the in the same length scale and the original algorithm of phase field simulation suffices for thin film configuration. However in three dimensions (plane strain and general configurations), Austenite and Martensitic variants are not in the same length scales, the original algorithm can no longer result the expected microstructure. Thus separation of length scales is the key. A two-scale phase field approach is developed and adopted to simulate Austenite-Martensite interfaces. Examples are illustrated with the the Cubic-to-Orthorhombic crystal system, which associates with more lattice parameters, to explore the Austenite-Martensite interfaces. Several related problems are also discussed, such as the relation between the energy content and the middle eigenvalues of the participating Martensites, and thermal hysteresis. Simulations will also be extended to general three dimensions.

3.1 Background and Theory

Recall from previous chapter that the crystalline lattice structures in shape memory alloys are described by their transformation strains or transformation matrices. The transformation strain of Austenite is zero while those of the Martensites are equivalent up to rotation matrices related to the symmetry of the participating crystal system. For example, in Cubic-to-Trigonal system, the transformation strain of Austenite is $\varepsilon^{(0)} = \mathbf{0}$ while there are three equivalent Martensitic variants whose transformation strains are:

$$\varepsilon^{(1)} = \begin{pmatrix} \beta & 0 & 0 \\ 0 & \alpha & 0 \\ 0 & 0 & \alpha \end{pmatrix}, \varepsilon^{(2)} = \begin{pmatrix} \alpha & 0 & 0 \\ 0 & \beta & 0 \\ 0 & 0 & \alpha \end{pmatrix}, \varepsilon^{(3)} = \begin{pmatrix} \alpha & 0 & 0 \\ 0 & \alpha & 0 \\ 0 & 0 & \beta \end{pmatrix}, \tag{3.1}$$

where α and β are the lattice parameters. It should be pointed out that all Martensitic variants are of the same rank. They exhibit the same level of symmetry as a geometric characteristic of crystal system they belong to. The transformation strains of any two Martenitic variants are related through a rotation in the symmetry group of the crystal system. They have the same set of eigenvalues [2].

The eigenvalues of the these transformation strains play an important role in the formation of interfaces [54, 57]. When the (common) middle eigenvalue of the transformation matrix of the Martensite lattice with respect to the Austenite structure equals 0, a compatible interface between

these two phases can be formed, and it was suggested that the corresponding thermal hysteresis of shape memory alloys will be minimized. This principle has been used to guide the search for shape memory alloys with extremely low hysteresis, and a clear relationship between the thermal hysteresis and the middle eigenvalue as expected from the theory has been observed.

When the middle eigenvalue of the transformation matrix is different from 0, a compatible Austenite-Martensite interface is no longer possible. Instead, interfaces between Austenite phase and twined Martensites are observed, which satisfy the compatibility condition on average. This leads to increased elastic energy due to the incompatibility between the Austenite and the Martensite phases, resulting in higher energy barrier for phase transformation and thus higher thermal hysteresis. Indeed, an analytic model based on an inexact interface with an assumed transition layer between Austenite and twined Martensites yield a relationship between thermal hysteresis and middle eigenvalue that resembles experimental observations [54]. The analysis, however, depends on the transition layer assumed. To understand the detailed structure of Austenite-Martensite interface and its implication on thermal hysteresis of shape memory alloys, especially when the middle eigenvalue of transformation matrix deviates from 0, direct numerical simulation without making any prior assumption on the underlying microstructure is highly desirable, which we seek to develop using phase field approach.

We consider two Martensitic variants with transformation strains $\varepsilon^{(i)}$ and $\varepsilon^{(j)}$, which are assumed to be compatible with each other, satisfying

$$\varepsilon^{(i)} - \varepsilon^{(j)} = \frac{1}{2}(\mathbf{a}\otimes\mathbf{n} + \mathbf{n}\otimes\mathbf{a}), \tag{3.2}$$

making it possible to form a Martensitic twin with these two variants, where $\mathbf{n}$ is the normal of twin interface, and $\mathbf{a}$ is related to the shear of the twin structure.

Equivalently, the above condition can be interpreted in terms of eigenvalues. The normal to the interface between the two Martensitic variants can also be found using the eigenvalues and eigenvectors. For instance, let the eigenvalues (in ascending order) and the corresponding eigenvectors of $\varepsilon^{(i)} - \varepsilon^{(j)}$ be $\{\varepsilon_1 \le \varepsilon_2 \le \varepsilon_3\}$ and $\{\mathbf{v}_1, \mathbf{v}_2, \mathbf{v}_3\}$. If the middle eigenvalue ε_2 is zero, an interface between the two Martensitic variants can be formed. Moreover, the normal $\mathbf{n}$ to the interface is

given by:

$$\mathbf{n} = -\kappa \mathbf{v}_1 + \mathbf{v}_3, \tag{3.3}$$

where $\kappa = \pm 1$. Notice that the above condition and formula imply that the smallest eigenvalue ε_1 must be nagnative or zero, while the largest eigenvalue ε_3 must be positive or zero.

Twinned Martensites can further form an interface with the Austenite phase, where the two Martensitic variants have to be in certain ratio r. Assume that the effective transformation strains of the twinned Martensites is expressed as $r\varepsilon^{(i)} + (1-r)\varepsilon^{(j)}$. The transformation strain of Austenite is 0. For the twinned Martensite and the Austenite to be compatible with each other by forming an interface, the following geometric compatibility condition has to be satisfied:

$$r\varepsilon^{(i)} + (1-r)\varepsilon^{(j)} - 0 = \frac{1}{2}(\mathbf{b} \otimes \mathbf{m} + \mathbf{m} \otimes \mathbf{b}), \tag{3.4}$$

where **m** is the normal to the Austenite-Martensite interface and **b** is the shear vector for the interface.

Equivalently the condition can also be checked using eigenvalues. Briefly, let the eigenvalues (in ascending order) and the corresponding eigenvectors of $r\varepsilon^{(i)} + (1-r)\varepsilon^{(j)} - 0$ be $\{\Sigma_1 \leq \Sigma_2 \leq \Sigma_3\}$ and $\{\mathbf{V}_1, \mathbf{V}_2, \mathbf{V}_3\}$. If the middle eigenvalue Σ_2 is zero, the Austenite-Martensite interface between Austenite and twinned Martensites can be formed. The normal **m** to the interface is given by:

$$\mathbf{m} = -\kappa \mathbf{V}_1 + \mathbf{V}_3, \tag{3.5}$$

where $\kappa = \pm 1$. Notice that the above condition and formula imply that the smallest eigenvalue Σ_1 must be negative or zero, while the largest eigenvalue Σ_3 must be positive or zero.

As a remark to the theory applied to thin film configurations, all quantities are expressed in two dimensions. Thus the transformation strains taken for simulations are 2-tensors. The original 3×3-matrices have to be re-oriented and projected onto two dimensions as thin film. The geometric compatibility condition in terms of eigenvalues for forming interfaces are also weakened so that the requirement of the middle eigenvalue being zero is removed. We only require that the smallest eigenvalues be negative or zero while the largest eigenvalues be positive or zero. The formulae for

finding the normals remain unchanged since they originally involve no middle eigenvalues.

3.2 Austenite-Martesite interfaces in Thin Films

We implement the above theory to simulate the micro-structures in thin films that involve Austenite and Martensites, in the Cubic-to-Trigonal systems. The first two variants in the system are adopted:

$$\varepsilon^{(1)} = \begin{pmatrix} \beta & 0 & 0 \\ 0 & \alpha & 0 \\ 0 & 0 & \alpha \end{pmatrix}, \varepsilon^{(2)} = \begin{pmatrix} \alpha & 0 & 0 \\ 0 & \beta & 0 \\ 0 & 0 & \alpha \end{pmatrix}, \tag{3.6}$$

where α and β are the lattice parameters. Without loss of generality, we further assume that $\beta > \alpha$.

For the twinned Martensites, the eigenvalues and eigenvetors of $\varepsilon^{(1)} - \varepsilon^{(2)}$ are $\{\varepsilon_1 \leq \varepsilon_2 \leq \varepsilon_3\} = \{\alpha - \beta \leq 0 \leq \beta - \alpha\}$ and $\left\{ \mathbf{v}_1 = \begin{pmatrix} 0 \\ 1 \\ 0 \end{pmatrix}, \mathbf{v}_2 = \begin{pmatrix} 0 \\ 0 \\ 1 \end{pmatrix}, \mathbf{v}_3 = \begin{pmatrix} 1 \\ 0 \\ 0 \end{pmatrix} \right\}$. The normal to the Martensite-Martensite interface is:

$$\mathbf{n} = -\kappa \begin{pmatrix} 0 \\ 1 \\ 0 \end{pmatrix} + \begin{pmatrix} 1 \\ 0 \\ 0 \end{pmatrix} = \begin{pmatrix} 1 \\ \pm 1 \\ 0 \end{pmatrix}, \tag{3.7}$$

where $\kappa = \pm 1$.

For the twinned Martensites and Austenite to a further twin, the ratio r of the Martensitic variants can not be arbitrary. We consider the effective transformation strains of the microstructure:

$$r\varepsilon^{(1)} + (1-r)\varepsilon^{(2)} - \mathbf{0} = \begin{pmatrix} r\beta + (1-r)\alpha & 0 & 0 \\ 0 & r\alpha + (1-r)\beta & 0 \\ 0 & 0 & \alpha \end{pmatrix}. \tag{3.8}$$

A further assumption is made on the signs of the lattice parameters α and β to ensure geometrical compatibility condition: $\beta > 0 > \alpha$. The eigenvalues are $\{r\beta + (1-r)\alpha, r\alpha + (1-r)\beta, \alpha\}$. Since $\alpha < 0$, the other two eigenvalues must be positive and zero. Without loss of generality, as-

sume $r\alpha+(1-r)\beta=0$, which implies $r=\frac{\beta}{\beta-\alpha}$ or $\beta=-\frac{r}{1-r}\alpha$. One may check that the remained eigenvalue $(\beta+\alpha)$ is positive. Thus the geometric compatibility condition is valid.

To summarize, the eigenvalues and eigenvectors are $\{\varepsilon_1\leq\varepsilon_2\leq\varepsilon_3\}=\{\alpha<0<\beta+\alpha\}$ and $\left\{\mathbf{v}_1=\begin{pmatrix}0\\0\\1\end{pmatrix},\mathbf{v}_2=\begin{pmatrix}0\\1\\0\end{pmatrix},\mathbf{v}_3=\begin{pmatrix}1\\0\\0\end{pmatrix}\right\}$.

The normal to the Austenite-Martensite interface is thus

$$\mathbf{m}=-\kappa\sqrt{-\alpha}\begin{pmatrix}0\\0\\1\end{pmatrix}+\sqrt{\alpha+\alpha}\begin{pmatrix}1\\0\\0\end{pmatrix}=\begin{pmatrix}\sqrt{\beta+\alpha}\\0\\\pm\sqrt{-\alpha}\end{pmatrix}. \tag{3.9}$$

Given the desired ratio r of the Martensitic variants, one may relate the the lattice parameters α and β for the compatible eigenstrains that will yield a microstricture with Austenite-Martensite interface. Three examples of simulation in thin film (two dimensions) will be shown with $r=0.6$ and $r=0.7$ with two possible outcomes. The plots are shown in figures (3.2), (3.3) and (3.4).

As an example, if $r=0.6$, the lattice parameters α and β are related by $\beta=-\frac{r}{1-r}\alpha=-1.5\alpha$. The transformation strains now become

$$\varepsilon^{(1)}=\alpha\begin{pmatrix}1.5&0&0\\0&1&0\\0&0&1\end{pmatrix},\varepsilon^{(2)}=\alpha\begin{pmatrix}1&0&0\\0&1.5&0\\0&0&1\end{pmatrix}, \tag{3.10}$$

where α can be adjusted.

We briefly outline the procedures to re-orientate the transformation strains of the Martensitic variants. For the sake of simplicity, we assume that $\alpha=-0.04$, then with $r=0.6$, $\beta=0.06$. By the formulae derived for the normals to the two interfaces, we have:

$$\mathbf{n}=\begin{pmatrix}1\\1\\0\end{pmatrix},\mathbf{m}=\begin{pmatrix}\sqrt{\beta+\alpha}\\0\\\sqrt{-\alpha}\end{pmatrix}=\begin{pmatrix}\sqrt{-0.5\alpha}\\0\\\sqrt{-\alpha}\end{pmatrix} \tag{3.11}$$

We are interested in the direction of these normal. We may normalize these vectors by dividing

by some suitable constants. In fact, we may take:

$$\mathbf{m} = \begin{pmatrix} 1 \\ 0 \\ \sqrt{2} \end{pmatrix} \tag{3.12}$$

We want to project the three dimensional transformation strains to the two-dimensional plane spanned by these two normal vectors, that is, **n** and **m**. Let the normal to that plane be **N**. It is clearly the cross product of **n** and **m**:

$$\mathbf{N} = \mathbf{n} \times \mathbf{m} = \begin{pmatrix} \sqrt{2} \\ -\sqrt{2} \\ -1 \end{pmatrix} \tag{3.13}$$

However one may check that these three vectors $(\mathbf{n}, \mathbf{m}, \mathbf{N})$ are not mutually orthogonal, due to the fact that **n** and **m** are not orthogonal. **n** and **N** are orthogonal. We may resolve this problem by replacing **m** by the cross product of **N** and **n**. Denote the resulting vector by $\mathbf{m}'$.

$$\mathbf{m}' = \mathbf{N} \times \mathbf{n} = \begin{pmatrix} 1 \\ -1 \\ 2\sqrt{2} \end{pmatrix} \tag{3.14}$$

Notice that by now the vectors $(\mathbf{n}, \mathbf{m}', \mathbf{N})$ are orthogonal to each others. However these vectors are not of unit length. They have to be normalized to form an orthogonal basis analogue to **i**, **j** and **k**. We denote the normalized vectors by the same symbols.

$$\mathbf{n} = \begin{pmatrix} \frac{1}{\sqrt{2}} \\ \frac{1}{\sqrt{2}} \\ 0 \end{pmatrix}, \mathbf{m}' = \begin{pmatrix} \frac{1}{\sqrt{10}} \\ -\frac{1}{\sqrt{10}} \\ \frac{2}{\sqrt{5}} \end{pmatrix}, \mathbf{N} = \begin{pmatrix} \sqrt{\frac{2}{5}} \\ -\sqrt{\frac{2}{5}} \\ -\frac{1}{\sqrt{5}} \end{pmatrix}. \tag{3.15}$$

The transformation matrix from the canonical orthogonal Cartesian bases (coordinates) $\{\mathbf{i}, \mathbf{j}, \mathbf{k}\}$

to the orthogonal bases $\{\mathbf{n}, \mathbf{m}', \mathbf{N}\}$ is:

$$\mathbf{S} = \begin{pmatrix} \mathbf{n} & \mathbf{m}' & \mathbf{N} \end{pmatrix} = \begin{pmatrix} \frac{1}{\sqrt{2}} & \frac{1}{\sqrt{10}} & \sqrt{\frac{2}{5}} \\ \frac{1}{\sqrt{2}} & -\frac{1}{\sqrt{10}} & -\sqrt{\frac{2}{5}} \\ 0 & \frac{2}{\sqrt{5}} & -\frac{1}{\sqrt{5}} \end{pmatrix}. \tag{3.16}$$

One may check that $\det(\mathbf{S}) = 1$ from orthogonality. Its inverse matrix $\mathbf{T}$ then implies the transformation from orthonormal bases $\{\mathbf{n}, \mathbf{m}', \mathbf{N}\}$ back to the canonical orthogonal Cartesian bases $\{\mathbf{i}, \mathbf{j}, \mathbf{k}\}$.

$$\mathbf{T} = \mathbf{S}^{-1} = \mathbf{S}^T = \begin{pmatrix} \frac{1}{\sqrt{2}} & \frac{1}{\sqrt{2}} & 0 \\ \frac{1}{\sqrt{10}} & -\frac{1}{\sqrt{10}} & \frac{2}{\sqrt{5}} \\ \sqrt{\frac{2}{5}} & -\sqrt{\frac{2}{5}} & -\frac{1}{\sqrt{5}} \end{pmatrix}. \tag{3.17}$$

Now we will transform the transformation strains of the two Martensites to the canonical bases $\{\mathbf{i}, \mathbf{j}, \mathbf{k}\}$ and then project to the two-dimensional plane spanned by $\{\mathbf{i}, \mathbf{j}\}$. This enables us to stimulate the microstructure in two dimensions. After the transformation, the transformation strain $\boldsymbol{\varepsilon}^{(1)}$ and $\boldsymbol{\varepsilon}^{(2)}$ become respectively,

$$\begin{aligned} \boldsymbol{\varepsilon}^{(1)'} &= \mathbf{T}\boldsymbol{\varepsilon}^{(1)}\mathbf{T}^T = \begin{pmatrix} 0.001 & 0.002236 & ? \\ 0.002236 & -0.003 & ? \\ ? & ? & ? \end{pmatrix}, \\ \boldsymbol{\varepsilon}^{(2)'} &= \mathbf{T}\boldsymbol{\varepsilon}^{(2)}\mathbf{T}^T = \begin{pmatrix} 0.001 & -0.002236 & ? \\ -0.002236 & -0.003 & ? \\ ? & ? & ? \end{pmatrix}, \end{aligned} \tag{3.18}$$

where the elements marked as ? are not important as they will be dropped out in the next step.

We can further project the transformation strains onto an equivalent $\{\mathbf{i}, \mathbf{j}\}$-plane by pre-multiplying

and post-multiplying by the projection matrix $\mathbf{P} = \begin{pmatrix} 1 & 0 & 0 \\ 0 & 1 & 0 \end{pmatrix}$ and its transpose, that is,

$$\begin{aligned} \varepsilon^{(1)''} &= \mathbf{P}\varepsilon^{(1)'}\mathbf{P}^T = \begin{pmatrix} 0.001 & 0.002236 \\ 0.002236 & -0.003 \end{pmatrix} \\ \varepsilon^{(2)''} &= \mathbf{P}\varepsilon^{(2)'}\mathbf{P}^T = \begin{pmatrix} 0.001 & -0.002236 \\ -0.002236 & -0.003 \end{pmatrix} \end{aligned} \tag{3.19}$$

Similarly, for the case $r = 0.7$, by the same procedure, the transformation strains of the participating Martensitic variants become:

$$\begin{aligned} \varepsilon^{(1)''} &= \begin{pmatrix} 0.002 & 0.00316227766017 \\ 0.00316227766017 & -0.001 \end{pmatrix} \\ \varepsilon^{(2)''} &= \begin{pmatrix} 0.002 & -0.00316227766017 \\ -0.00316227766017 & -0.001 \end{pmatrix} \end{aligned} \tag{3.20}$$

For the mechanical condition, we apply strain as a linear combination of eigen-strains in certain proportions that correspond to the volume ratios of each such variant in the simulated pattern. For instance, if the desired ratio of Austenite and twinned Martensites is 50 % to 50 %, and the volume ratio between the Martensitic variants is r to $1-r$, with $r = 0.5$, which is assigned at the beginning, then the external strain is expressed as:

$$\begin{aligned} \varepsilon^0 &= 0.5\varepsilon^0 + 0.5\varepsilon^{Martensites} \\ &= \underbrace{\varepsilon^0}_{=0} + 0.5\left(r\varepsilon^{(1)} + (1-r)\varepsilon^{(2)}\right) \end{aligned} \tag{3.21}$$

In two dimensional thin films, since the transformation strains are reduced to 2×2-matrices and the requirement of middle eigenvalues being zero are removed, Austenite and individual Martensitic variants twin as a physical outcome. Sharp interfaces are observed and are expected to carry low levels of energies. They are not of great interest. We can not verify the relation between the energy and the magnitude of the (common) middle eigenvalues of the participating Martensitic variants. In

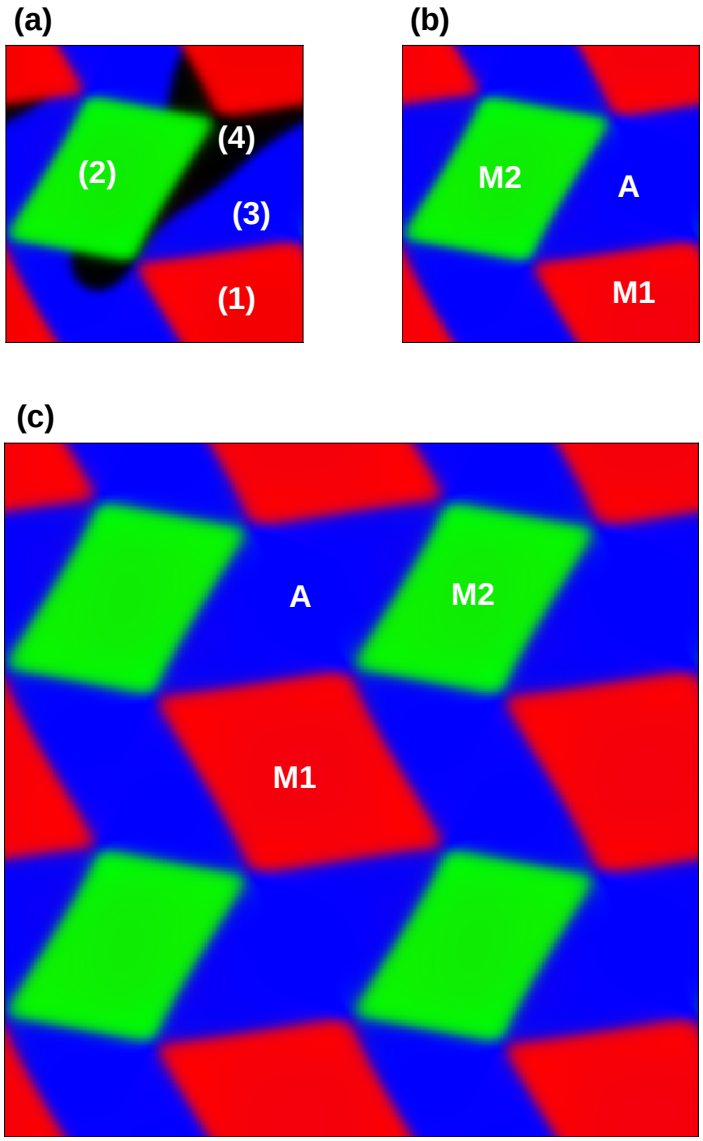

Figure 3.2: Simulation of microstructure in thin film configuration for Cubic-to-Trigonal system. The Martensitic ratio is 60% to 40%. (a) The simulated pattern is shown in (a) with 4 variants denoted by (1), (2), (3) and (4). (b) Since (3) and (4) represent the Austenite phase, the simulated pattern is re-visualized with three distinct variants. (c) Four identical patterns in (b) are packed together to obtain a better image.

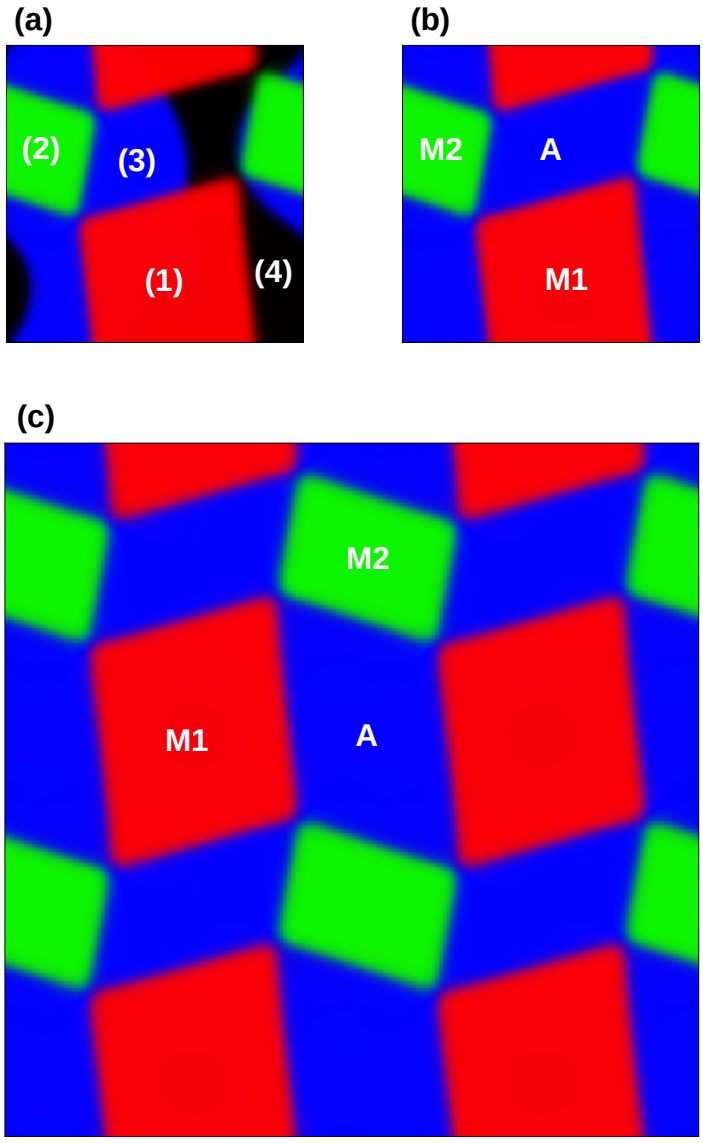

Figure 3.3: Simulation of microstructure in thin film configuration for Cubic-to-Trigonal system. The Martensitic ratio is 70% to 30%. (a) The simulated pattern is shown in (a) with 4 variants denoted by (1), (2), (3) and (4). (b) Since (3) and (4) represent the Austenite phase, the simulated pattern is re-visualized with three distinct variants. (c) Four identical patterns in (b) are packed together to obtain a better image.

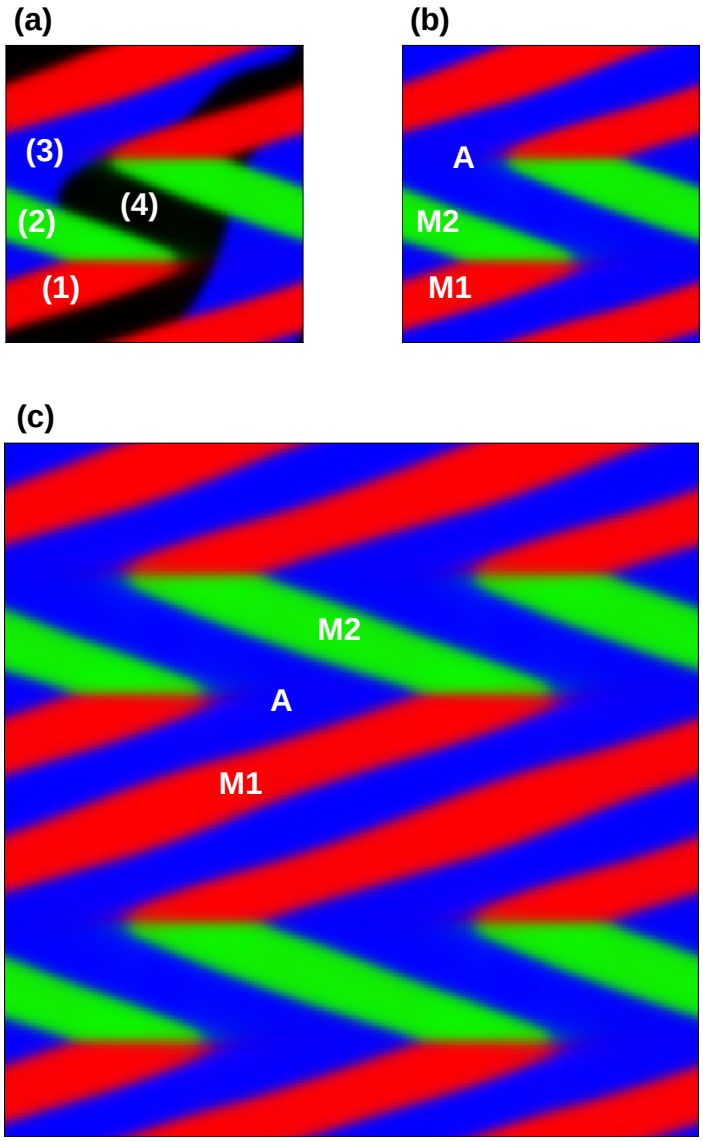

Figure 3.4: Another Simulation of microstructure in thin film configuration for Cubic-to-Trigonal system. The Martensitc ratio is 70% to 30%. (a) The simulated pattern is shown in (a) with 4 variants denoted by (1), (2), (3) and (4). (b) Since (3) and (4) represent the Austenite phase, the simulated pattern is re-visualized with three distinct variants. (c) Four identical patterns in (b) are packed together to obtain a better image.

two dimensions, there is no concept related to the middle eigenvalue.

Starting from the next section, we will extend our approach to three dimensions, where the participating Martensitic variants twin before the resulting twinned martesites twin with the Austenite. Separation of length scales are critical here and two scale simulations are developed.

3.3 The Two-Scale Phase Field Simulation

By definition, the transformation strain of the Austenite phase is 0, and in order for a compatible Austenite-Martensite interface to form, the middle eigenvalue of the transformation strain $\varepsilon^{(i)}$ or $\varepsilon^{(j)}$ of Martensitic variant has to be 0. This turns out to be a very restrictive condition, and is not satisfied in general. Instead, the averaging transformation strain $\mu_2\varepsilon^{(i)}+(1-\mu_2)\varepsilon^{(j)}$ of a Martensitic twin structure can have zero middle eigenvalue when appropriate volume fraction μ_2 is chosen, suggesting an inexact interface between Austenite and Martensitic twin, such that

$$\mu_2\varepsilon^{(i)}+(1-\mu_2)\varepsilon^{(j)}=\frac{1}{2}(\mathbf{b}\otimes\mathbf{m}+\mathbf{m}\otimes\mathbf{b}), \tag{3.22}$$

where **m** is the normal of the inexact interface, and **b** is the corresponding shear, as schematically shown in figure (3.5). In general, two sets of solutions for Eq. (3.22) exist, corresponding to two possible interfaces with specific normal and volume fractions of the Martensitic twins.

To confirm that an inexact interface between Austenite and twined Martensite can indeed be formed as schematically shown in figure (3.5), an unconventional phase field approach is developed. Two characteristic functions μ_1 and μ_2 are introduced as the field variables to define the structure, such that μ_1 takes value of 1 if **x** is occupied by Austenite phase and 0 if it is occupied by either of the Martensitic variants, whose specification is governed by μ_1, which takes the value of 1 if **x** is occupied by variant 1 and 0 if it is occupied by variant 2. As a result, the transformation strain at **x** is given by

$$\begin{aligned}\varepsilon^*[\mu]&=\mu_1\varepsilon^{(0)}+(1-\mu_1)\mu_2\varepsilon^{(i)}+(1-\mu_1)(1-\mu_2)\varepsilon^{(j)}\\&=(1-\mu_1)\mu_2\varepsilon^{(i)}+(1-\mu_1)(1-\mu_2)\varepsilon^{(j)},\end{aligned} \tag{3.23}$$

where $\mu=[\mu_1,\mu_2]$. Note that while μ_2 is governed by Eq. 3.22, μ_1 is generally determined by

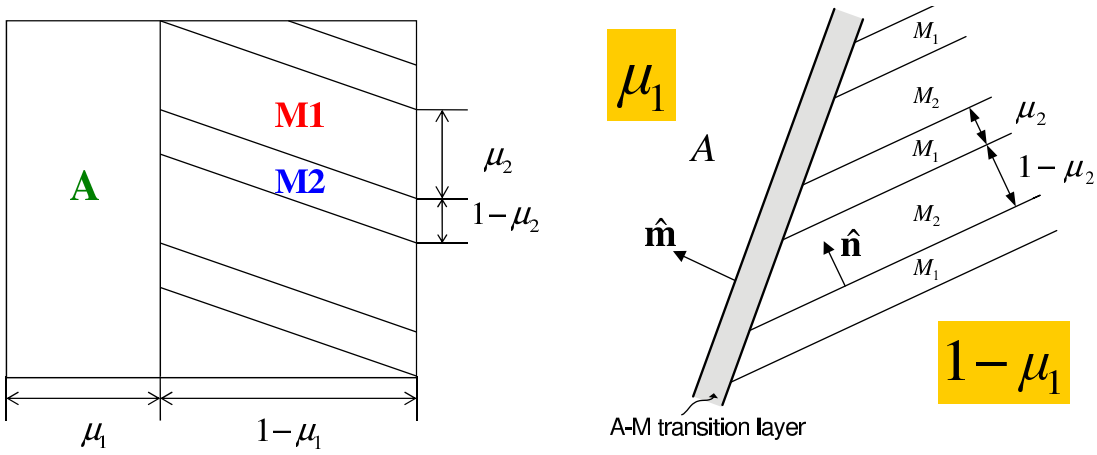

Figure 3.5: The schematics of an inexact interface between Austenite (A) and Martensitic twin M_1 and M_2.

the mechanical boundary condition. For an arbitrary distribution of $\mu(\mathbf{x})$, this transformation strain might not be compatible, and an elastic field will be induced, resulting in elastic energy in the structure,

$$W^{elas}(\mu) = \frac{1}{2}(\varepsilon - \varepsilon^*[\mu]) \cdot \mathbf{C}(\varepsilon - \varepsilon^*[\mu]), \tag{3.24}$$

where ε is the total strain that can be solved from mechanical equilibrium equation, consisting of elastic strain and transformation strain, and $\mathbf{C}$ is the elastic stiffness tensor.

To ensure that μ_1 and μ_2 take either 1 or 0, an anisotropy energy is introduced,

$$W^{ani}(\mu) = K_1\mu_1^2(1-\mu_1)^2 + K_2\mu_2^2(1-\mu_2)^2, \tag{3.25}$$

where K_1 and K_2 are the anisotropy constants. Since the length scales in μ_1 and μ_2 are not equal, K_1 and K_2 do not need to be identical.

In addition, interfacial energy is introduced to penalize gradients in the characteristic functions,

such that

$$W^{int}(\mu) = A_1 |\nabla \mu_1|^2 + A_2 |\nabla \mu_2|^2, \tag{3.26}$$

where A_1 and A_2 are the penalty constants for the interfaces.

The potential energy of the system is then given by:

$$\mathscr{I}(\mu) = \int_\Omega \left[W^{elas}(\mu) + W^{ani}(\mu) + W^{int}(\mu) - \sigma^0 \cdot \varepsilon \right] d\mathbf{x}, \tag{3.27}$$

where Ω is the domain occupied by the shape memory alloy, and σ^0 is the stress arising from the traction applied at the boundary. The variation in potential energy with respect to μ results in the driving force for the evolution of μ,

$$\mathbf{F}(\mu) = -\frac{\delta \mathscr{I}(\mu)}{\delta(\mu)} = \mathbf{F}^{elas}(\mu) + \mathbf{F}^{ani}(\mu) + \mathbf{F}^{int}(\mu) \tag{3.28}$$

and under a linear kinetic approximation, the evolution equation for μ is derived as

$$\frac{\partial \mu}{\partial t} = M \left[\mathbf{F}^{elas}(\mu) + \mathbf{F}^{ani}(\mu) + \mathbf{F}^{int}(\mu) \right], \tag{3.29}$$

where M is the linear evolution coefficient.

In fact, all the governing equations are the same as those explained in the previous chapter.

3.4 Implementation of Two-Scale Phase Field Simulation

The theory is implemented into a numerical simulation on a x_1-x_2 plane whose normal is defined by $\mathbf{m} \times \mathbf{n}$, and all the field variables are assumed to be independent of x_3. Thus a two-dimensional simulation will be sufficient, though all the tensorial variables are three-dimensional in nature. From the definition of μ_1 and μ_2, it is clear that μ_1 represents Austenite-Martensite structure, while μ_2 represents Martensitic twin within the Austenite-Martensite structure. As a result, the length scales involved in μ_1 and μ_2 are clearly different. A two-scale simulation scheme is adopted to reflect such difference, where μ_1 and μ_2 are simulated at two distinct length scales, yet are coupled together through boundary condition and distribution of transformation strain, as schematically shown in

figure (3.6).

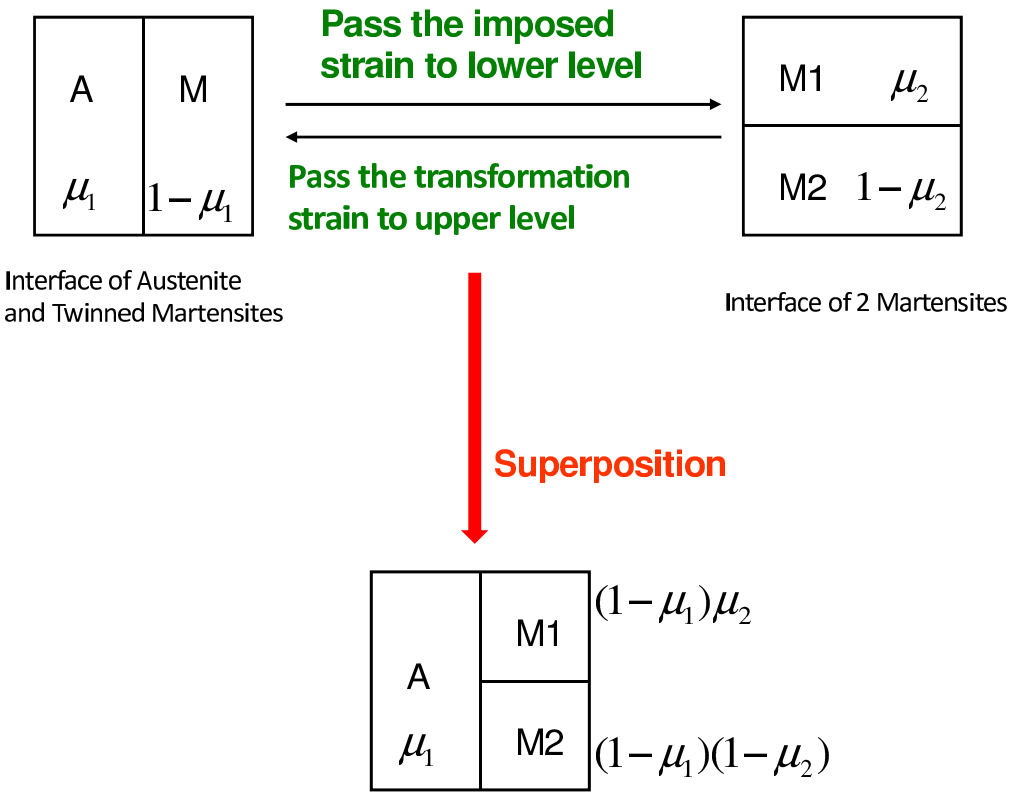

Figure 3.6: The schematics of the two scale algorithm. In the upper level where the Austenite twins with the twinned Martensities, only μ_1 evolves. The upper level passes the average total strain to the lower level, which serves as the external strain for the mechanical equilibrium in the lower level. In the lower level where the Martensitic variants twin, only μ_2 evolves while μ_1 is fixed. After both μ_1 and μ_2 converge, the two levels are then superposed to give the microstructure.

At upper scale where μ_1 is evolved, μ_2 is assumed to be fixed, and it specifies the transformation strain of the Martensite through Eq. 3.23. On the other hand, at lower scale where μ_2 is evolved, μ_1 is assumed to be fixed, and the boundary condition on the lower scale simulation cell is specified by

the average strain in the Martensite calculated at upper scale:

$$\begin{aligned}\varepsilon^{link} &= \frac{\int_\Omega \chi_M(\mathbf{x})\varepsilon^{upper}(\mathbf{x})d\mathbf{x}}{\int_\Omega \chi_M(\mathbf{x})d\mathbf{x}} \\ &= \frac{\int_\Omega (1-\mu_1(\mathbf{x}))\,\varepsilon^{upper}(\mathbf{x})d\mathbf{x}}{\int_\Omega (1-\mu_1(\mathbf{x}))\,d\mathbf{x}},\end{aligned} \tag{3.30}$$

where $\varepsilon^{upper}(\mathbf{x})$ is the strain computed at the upper scale (Eq. 3.23) and ε^{link} will serve as the external strain in the lower scale. As a remark, at the lower scale where the Austenite is not involved, the transformation strain is:

$$\varepsilon^*[\mu] = \mu_2\varepsilon^{(i)} + (1-\mu_2)\varepsilon^{(j)}. \tag{3.31}$$

The simulation starts with random initial conditions for μ_1 and μ_2 at both scales, and iterations between these two scales continue until a stable configuration emerges, as schematically illustrated in figure (3.7). To solve for Eq. 3.29 at either scale, fast Fourier transform is adopted on spatial scale with 128×128 cell size, and semi-implicit finite difference scheme is adopted on temporal scale with a time step of 0.005. The elastic constants of the material are assumed to be $C_{11} = 80 \times 10^9$ Pa, $C_{12} = 20 \times 10^9$ Pa, and $C_{66} = 30 \times 10^9$ Pa. The procedures of the two-scale approach is schematically outlined in figure (3.7).

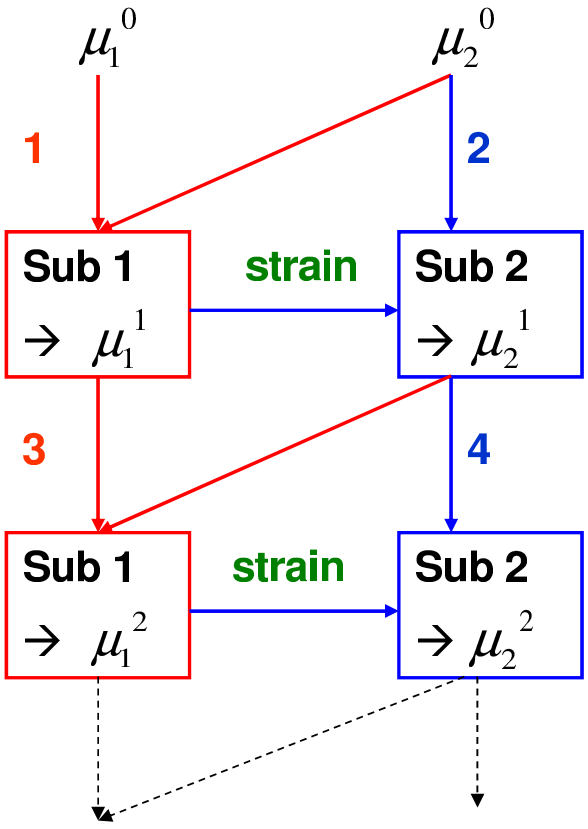

Figure 3.7: Procedures of two scale algorithm. Starting from random initial μ_1^0 and μ_2^0, subprogram 1 is used to iterate μ_1^1 in the upper level. Average total strain is obtained at this level and is passed into the lower level. Subprogram 2 uses μ_1^1 and μ_2^0 to generate μ_2^1. This completes one iteration. The procedures continue until both μ_1^i and μ_2^i meet the convergence criteria.

3.5 Simulation in two dimensions (Plane-Strain Configurations)

The phase field simulation is applied to study Austenite-Martensite interface for a cubic-to-orthorhombic transformation. Two variants of this system (out of a total of 6) are employed in the simulations, which have transformation strains given by $\varepsilon^{(1)}$ and $\varepsilon^{(2)}$:

$$\varepsilon^{(1)} = \begin{pmatrix} \alpha & 0 & \gamma \\ 0 & \beta & 0 \\ \gamma & 0 & \alpha \end{pmatrix}, \varepsilon^{(2)} = \begin{pmatrix} \alpha & 0 & -\gamma \\ 0 & \beta & 0 \\ -\gamma & 0 & \alpha \end{pmatrix}$$

We focus on the volume-preserving transformation, which is a necessary condition for self-accommodating structure. As a result, we have $tr(\varepsilon^{(i)}) = 2\alpha + \beta = 0$, which implies $\beta = -2\alpha$. This constraint reduces the lattice parameters from $\{\alpha, \beta, \gamma\}$ to $\{\alpha, \gamma\}$. The parameters α and γ can be adjusted to simulate a variety of microstructure that involve Austenite-Martensite interfaces.

With these, the three eigenvalues are given by $\{-2\alpha, \alpha - \gamma, \alpha + \gamma\}$.

When $\gamma = \alpha$ is set, the middle eigenvalue is 0. A sharp Austenite-Martensite interface emerges from the simulation, as shown in figure (3.8)(a), and the normal of the interface is indeed what we expect from the geometric linear theory.

When $\gamma = 5\alpha$ is set, the middle eigenvalue is different from 0. Such an exact interface is no longer possible, and a typical Austenite-Martensite structure obtained in the simulation is shown in figure (3.8)(b), where a rough interface between Austenite and Martensitic twin is observed. The Martensitic twin has interface normal and volume fraction expected from Eqs. (3.2) and (3.22), while the Austenite-Martensite interface, though rugged, has an average interface normal that is consistent with Eq. (3.22).

So the simulation we developed can indeed capture the Austenite-Martensite interface, and can reveal the detailed interfacial structure without any prior assumption. There is indeed a transition layer between Austenite and Martensitic twin, as suggested before, due to the incompatibility between Austenite and Martensite phases. The zig-zag type of interface in the transition layer is also consistent with certain experimental observations, and we are working on to capture the fine-scaled branching Martensite twins often observed near the interface.

The incompatible interface is expected to result in higher internal stress, and thus higher elas-

tic energy, and the necessity of Martensitic twin for an averaging compatible interface should also result in higher interfacial energy. This is indeed what we observe in the simulation. The distributions of elastic energy corresponding to the Austenite-Martensite structures in figures (3.8)(a) and (3.8)(b) are shown in figures (3.8)(c) and (3.8)(d). Negligible elastic energy is observed for the exact Austenite-Martensite interface, as expected. On the other hand, stress concentration is observed near the inexact Austenite-Martensite interface due to the incompatibility of the Austenite and Martensite phases, resulting in much higher elastic energy, as shown in figure (3.8)(d). Such stress concentration and higher elastic energy will result in higher energy barrier for AustniteMartensite phase transformation, and consequently higher thermal hysteresis.

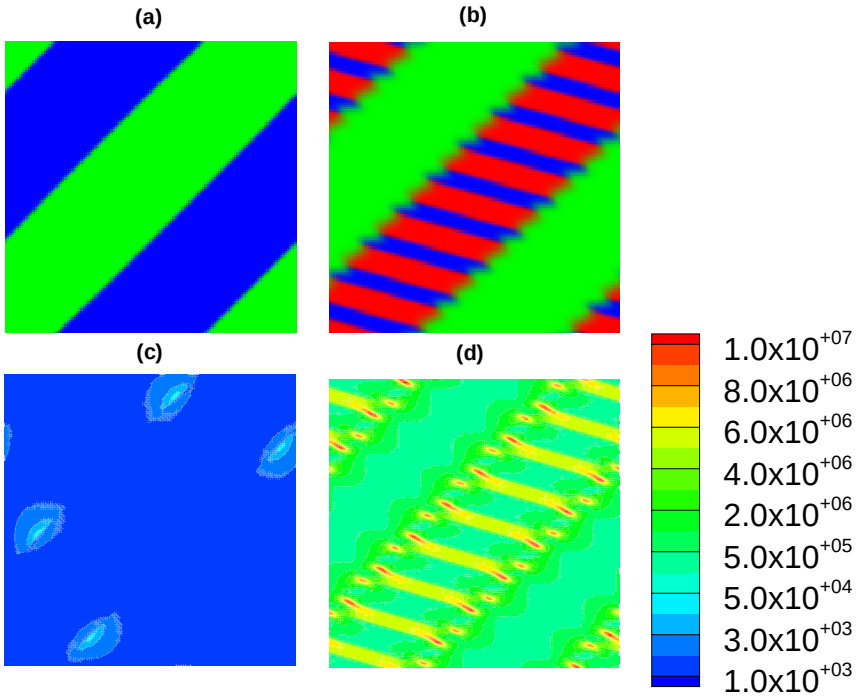

Figure 3.8: AusteniteMartensite interfaces by phase field simulation; (a) compatible interface when the middle eigenvalue of the transformation strain is 0 and (b) inexact interface when the middle eigenvalue of the transformation strain is not 0; (c) and (d) the corresponding distribution of elastic energy in the structure, with the scale bar indicating the elastic energy density.

To appreciate this, we simulate the Austenite-Martensite interfaces for a range of middle eigen-

values of the transformation strains, and calculate the corresponding total elastic energy in the structures, as shown in figure (3.9). Two types of Martensitic twin are considered, one with volume fraction of 60% (when $\gamma = 5\alpha$), and the other 65% (when $\gamma = 3\alpha$). Notice that different volume fractions of Martensitic variants under a fixed middle eigenvalue is possible, since the volume preserving orthorhombic transformation strain has two independent variables α and γ. It is observed that in both structures the elastic energy increases as the middle eigenvalues deviate from 0, suggesting an increased energy barrier and thus higher thermal hysteresis, as observed in recent experiments [54]. The simulation thus is able to explain the thermal hysteresis in shape memory alloys as related to the crystalline symmetry of Austenite and Martensite phases.

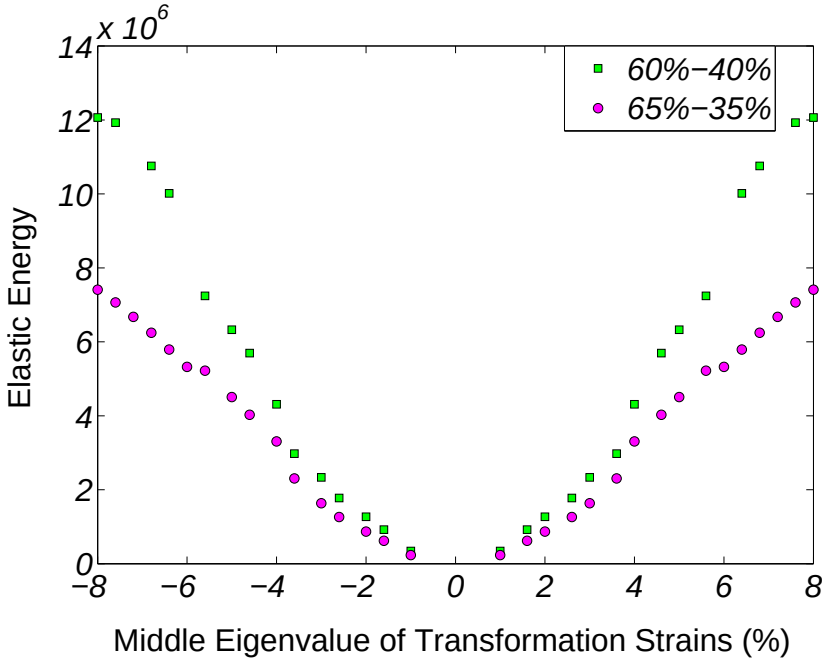

Figure 3.9: The elastic energy as function of middle eigenvalue of the transformation strain for volume-preserving transformation.

3.6 Further exposures to the Austenite-Martensite interfaces in Cubic-to-Orthorhombic system

Motivated by the previous section, in Cubic-to-Orthorhombic system, the relationship between α and γ can possibly be adjusted to generate microstructure with any desired Martensite-Martensite

ratio. It is proposed that as the volume ratio between Martensitic variants is varying, the (zig-zag) pattern of the Austenite-Martensite is also varying. This section is devoted to give a more comprehensive study of the formation of these patterns with respect to the lattice parameter and the resulting Martensitic ratio.

As in previous section, consider two Martensitic variants represented by $\varepsilon^{(1)}$ and $\varepsilon^{(2)}$ given in Eq. **??** and the Austenite represented by $\varepsilon^{(0)} = \mathbf{0}$ are involved in the microstructure. The three eigenvalues of $\varepsilon^{(1)} - \varepsilon^{(2)}$ are $\{-2\gamma, 0, 2\gamma\}$. The condition of forming Martensite-Martensite interfaces is automatically satisfied, since the middle eigenvalue is always zero regardless of the values of the lattice parameters. When Austenite is absent, the ratio of the Martensitic variants can be arbitrarily governed by applying suitable external mechanical condition. However, when Austenite is involved, the lattice parameters and the volume ratio in the twinned Martensite are related through Eq. (3.22).

Denote the volume ratio of the Martensitic variant (1) in the twinned martensite by r and that of the Martensitic variant (2) by $1-r$. The twinned Martensite has an effective transformation strain, given by $r\varepsilon^{(1)} + (1-r)\varepsilon^{(2)}$, whose eigenvalues are $\{\alpha+\gamma-2r\gamma, \alpha-\gamma+2r\gamma, -2\alpha\}$. Non-trivially, we assume that $\alpha > 0$, so that the third eigenvalue (-2α) is always negative. For Austenite-Martensite interface to emerge, one of these eigenvalues must be zero, while the remained one must be positive. There are two possible choices:

$$\begin{cases} \alpha+\gamma-2r\gamma = 0 \\ \alpha-\gamma+2r\gamma > 0 \end{cases} OR \begin{cases} \alpha+\gamma-2r\gamma > 0 \\ \alpha-\gamma+2r\gamma = 0 \end{cases}$$

These two sets of conditions are actually symmetric to each other and are supposed to give the same interpretation. We may focus on either one of them. Without loss of generality, we solve the first set of conditions, which gives:

$$\gamma = \frac{\alpha}{2r-1} \tag{3.32}$$

This establishes a relation between the parameters α and γ with the volume ratio r in the twinned Martensite. Notice that $0 \le r \le 1$ by its definition as volume ratio. However r can not be 0.5 because of the denominator of Eq. (3.32), which means that forming an Austenite-Martenite interface is impossible between Austenite and twinned Martensite with a 50%-50% Martensitic ratio.

Case	volume ratio in twinned Martensite r	$\frac{\gamma}{\alpha}$	eigenvalue of $\varepsilon^{(i)}$ as multiple of α	remark on shape of interface
I	0.6	5	$-4.0 < -\mathbf{2.0} < 6.0$	incompatible
II	0.66	3	$-2.0 < -\mathbf{2.0} < 4.0$	incompatible
II	0.7	2.5	$-2.0 < -\mathbf{1.5} < 3.5$	incompatible
IV	0.75	2	$-2.0 < -\mathbf{1.0} < 3.0$	incompatible
V	0.8	1.6667	$-2.0 < -\mathbf{0.6667} < 2.6667$	incompatible
VI	1	1	$-2.0 < \mathbf{0.0} < 2.0$	compatible

Table 3.1: (Cubic-to-Orthorhombic system) In order to obtain Austenite-Martensite interface between Austenite and twinned Martensites in predicted volume ratio r of Martensitic variants $\varepsilon^{(1)}$ and $\varepsilon^{(2)}$, the lattice parameters α and γ have to be in certain derived ratio. Recall that $\beta = -2\alpha$. The three (common) eigenvalues of the participating Martensitic variants are given. The middle eigenvalue (printed in bold face) is critically related to the appropriate shape of the interface (stereotype). If the middle eigenavlue is 0, a compatible sharp interface is expected. On the other hand, non-zero eigenvalues induce incompatible (rough) interfaces.

We will simulate, in Cubic-to-Orthorhombic system, microstructure involving Austenite-Martensite interfaces for various Martensitic ratios, from $r = 0.6$ to $r = 1.0$, into six cases. The linear relation between the two lattice parameters α and γ will also vary accordingly, as shown in Table 3.1. For each case, the three eigenvalues of the Martensitic variants are listed. We will see that the middle eigenvalue is critically related to the pattern of the Austenite-Martensite interface formed. If the middle eigenavlue is 0, a compatible sharp interface is expected. On the other hand, non-zero eigenvalues induce incompatible (rough) interfaces. We will also explore if there is any other factor for the shape of the rough interface thus generated. While the Martensitic ratios are "fixed" by the the geometric compatibility on the crystal parameters and Martensitc volume fraction as discussed, the volume ratio of autenite to twinned Martensite can be arbitrary. The simulated patterns are shown in figures (3.10), (3.11), (3.12), (3.13), (3.14) and (3.15). For each case (specific Martensitic ratios), simulations are run for increasing Austenite-twinned-Martensite ratio from (a) 0%, (b) 20%, (c) 40%, (d) 50% and (e) 70%. In all the figures that follow, red regions are occupied by Martensitic variant 1, blue regions are occupied by Martensitic variant 2, while green regions are occupied by Austenite. As a remark, for the sake of standardized visualizations and easy convergence, we have re-oriented the transformation strains of the participating Martensitic variants so that the normal of the Austenite-Martensite interface is always parallel to the y-axis the by a suitable rotation (which

we have the procedures outlined in previous section).

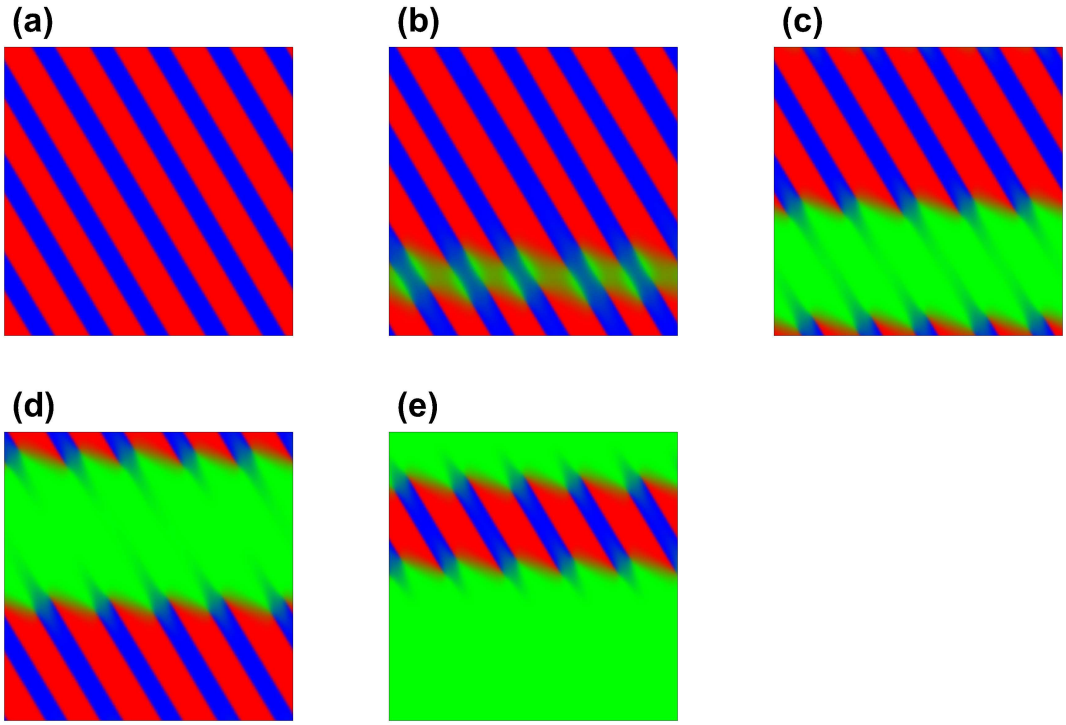

Figure 3.10: Simulation of Austenite-Martensite interface in plane strain configuration when the Martensitic ratio r is 0.6 = 60%. The volume fraction of Austenite in (a), (b), (c), (d) and (e) are respectively 0%, 20%, 40%, 50% and 70%.

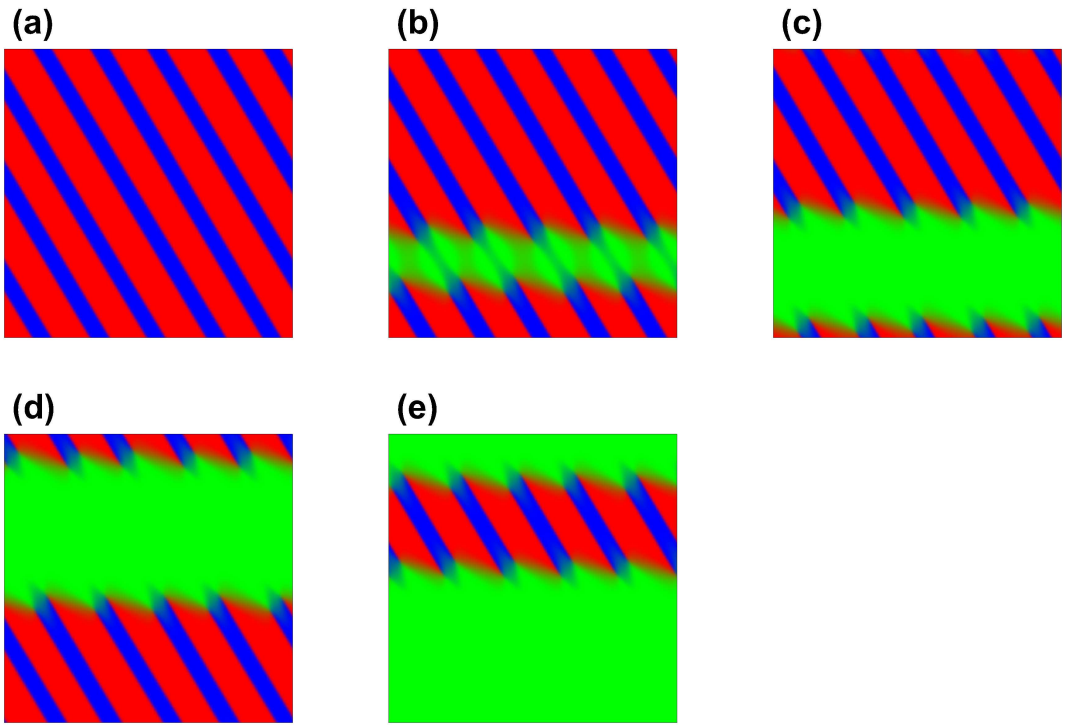

Figure 3.11: Simulation of Austenite-Martensite interface in plane strain configuration when the Martensitic ratio r is 0.66 = 66%. The volume fraction of Austenite in (a), (b), (c), (d) and (e) are respectively 0%, 20%, 40%, 50% and 70%.

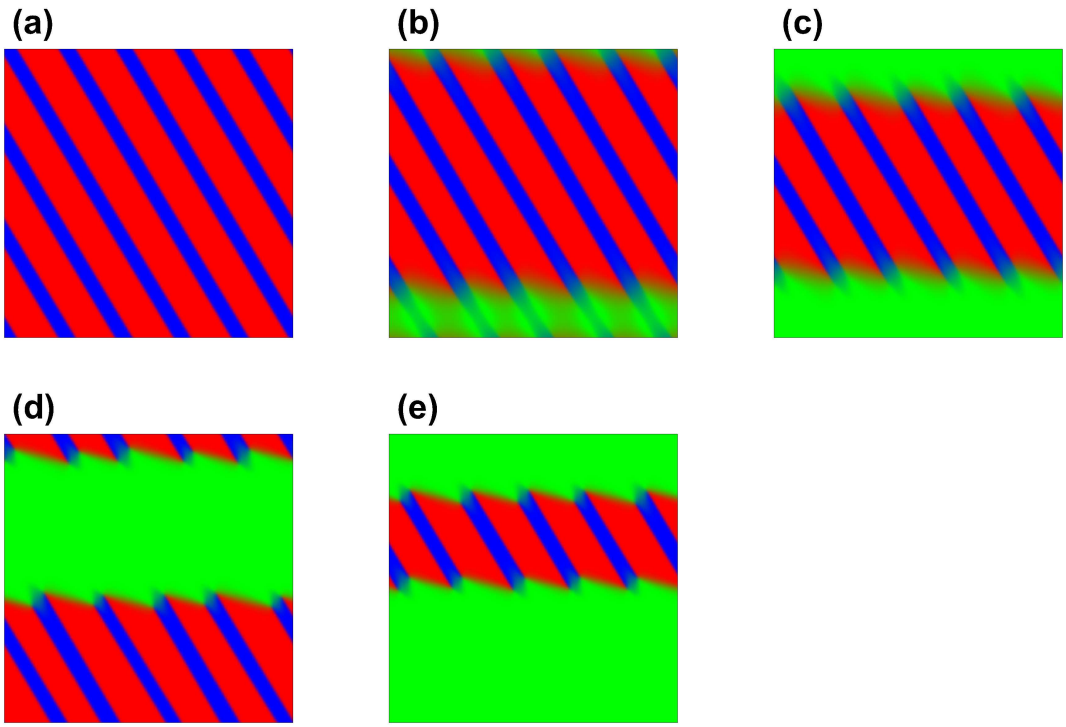

Figure 3.12: Simulation of Austenite-Martensite interface in plane strain configuration when the Martensitic ratio r is 0.7 = 70%. The volume fraction of Austenite in (a), (b), (c), (d) and (e) are respectively 0%, 20%, 40%, 50% and 70%.

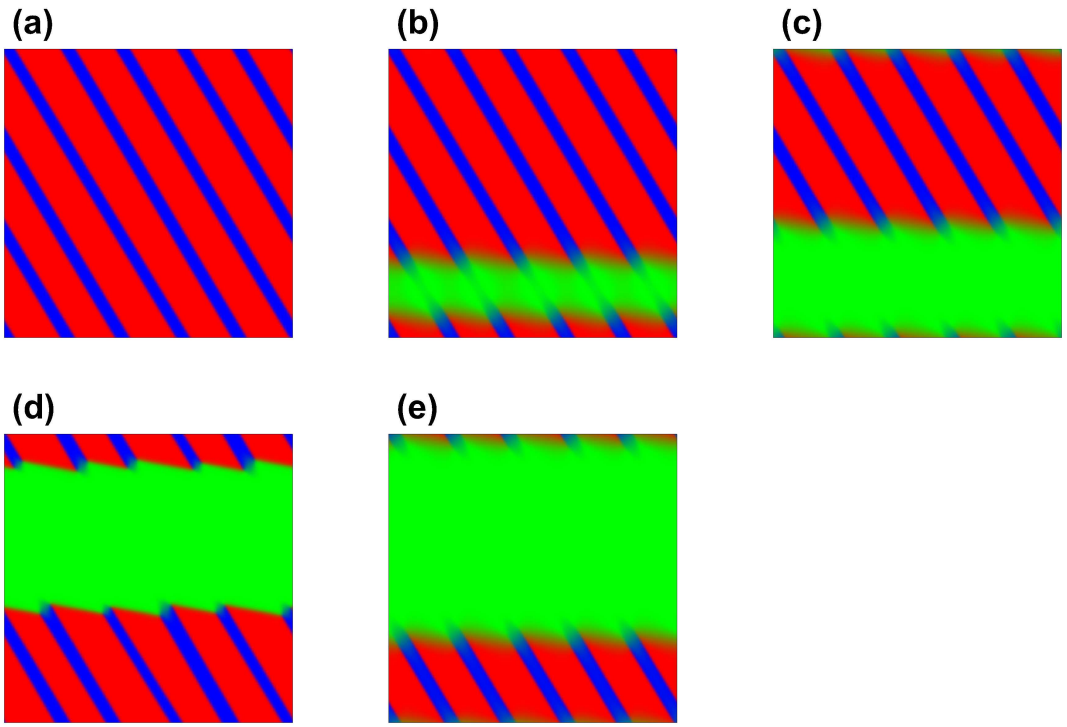

Figure 3.13: Simulation of Austenite-Martensite interface in plane strain configuration when the Martensitic ratio r is 0.75 = 75%. The volume fraction of Austenite in (a), (b), (c), (d) and (e) are respectively 0%, 20%, 40%, 50% and 70%.

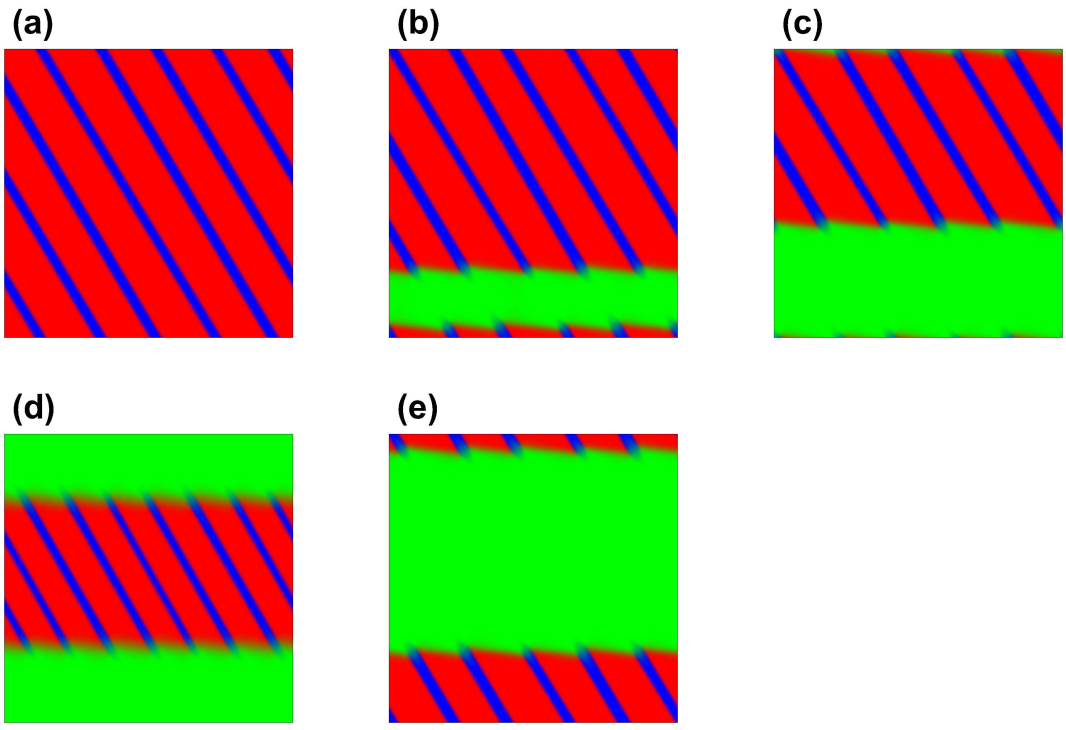

Figure 3.14: Simulation of Austenite-Martensite interface in plane strain configuration when the Martensitic ratio r is 0.8 = 80%. The volume fraction of Austenite in (a), (b), (c), (d) and (e) are respectively 0%, 20%, 40%, 50% and 70%.

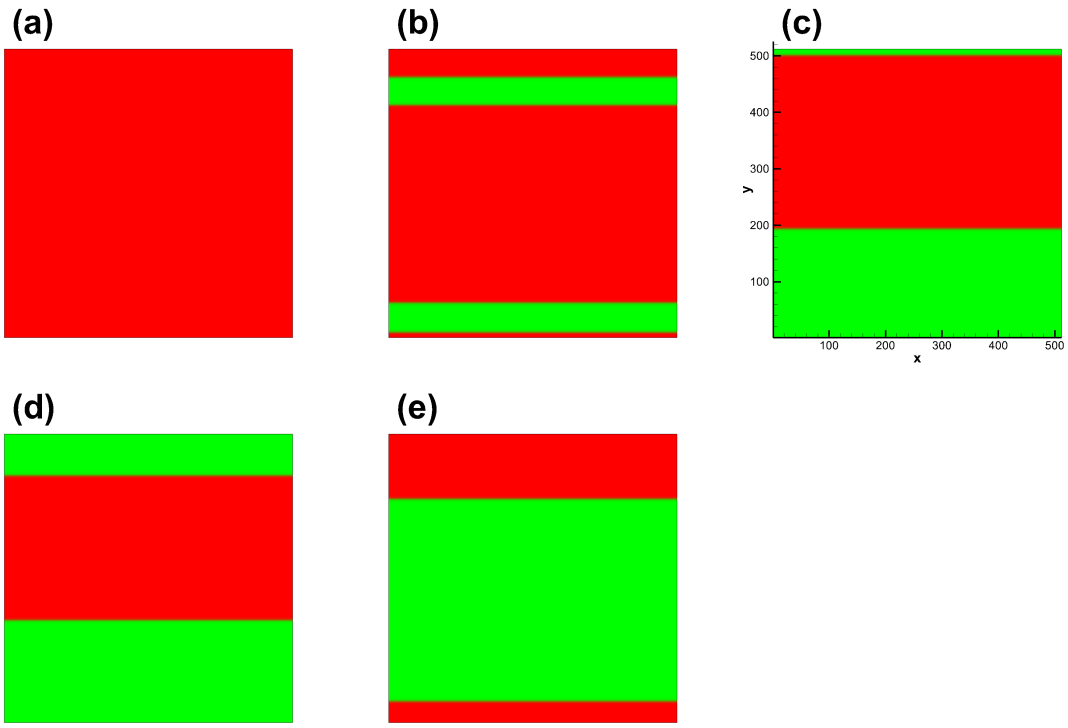

Figure 3.15: Simulation of Austenite-Martensite interface in plane strain configuration when the Martensitic ratio r is 1 = 100%. The volume fraction of Austenite in (a), (b), (c), (d) and (e) are respectively 0%, 20%, 40%, 50% and 70%. Only one martebsitic variant is present and sharp compatible interface is observed. The (common) middle eigenvalue of the Martensitic variant is zero.

3.7 Simulation in three dimensions

We may further extend the phase field simulations in three dimensions. This allows us to explore the more realistic structures of the Austenite-Martensite interfaces. In two dimensions, we did rotate the transformation strains so as to orientate the normal of the Austenite-Martensite interfaces. Simulations without such orientations may not always give the desired patterns due to geometric constraint from requiring that the patterns are periodic in both directions. Extending the simulations in three dimensions may release the strict geometric constraint to make it possible to generate more fanny patterns.

In the following we show the simulated patterns with Martensitic ratios r from 0.6 to 0.8. For each case, we orientate the patterns in four different normal directions of the autenite-Martensite interface through some suitable rotations. The volume ratio of Austenite to twinned Martensites is equal (50%). Of course other ratios can be considered in the simulations.

The simulated patterns are shown in figures (3.16), (3.17), (3.18), (3.19) and (3.20). The orientiated directions of normals to the Austenite-Martensite interfaces being shown on each of these figures are (a) $\mathbf{m} = \begin{pmatrix} 0 \\ 1 \\ 0 \end{pmatrix}$, (b) $\mathbf{m} = \begin{pmatrix} 0 \\ 1 \\ 0 \end{pmatrix}$, (c) $\mathbf{m} = \begin{pmatrix} 0 \\ 1 \\ 0 \end{pmatrix}$, and (d) $\mathbf{m} = \begin{pmatrix} 1 \\ 1 \\ 1 \end{pmatrix}$. Without otherwise stated, red regions are occupied by Martensitic variant 1, blue regions are occupied by Martensitic variant 2 and green regions occupied by Austenite.

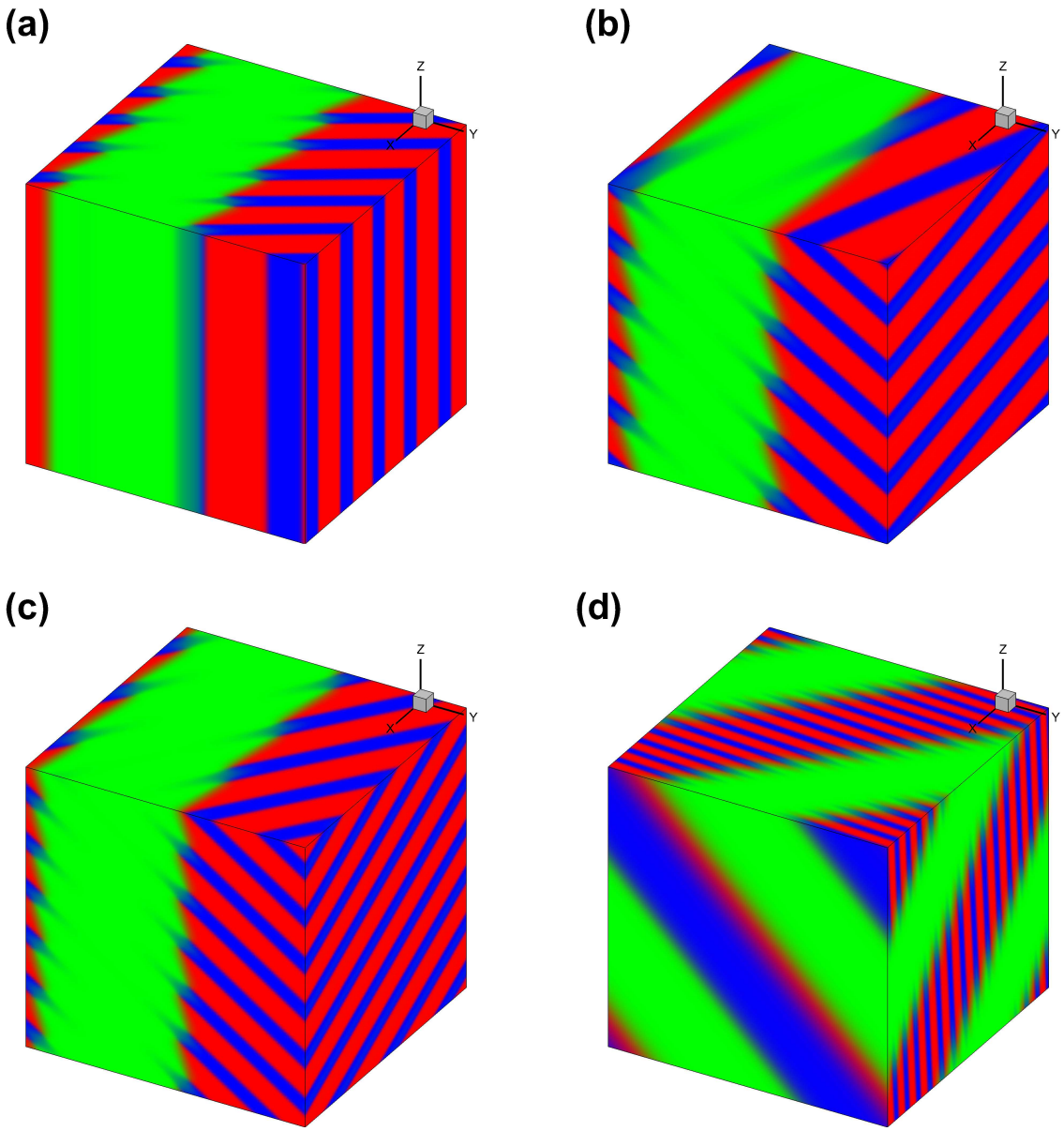

Figure 3.16: Simulation of Austenite-Martensite interface in three dimensions when the Martensitic ratio r is 0.6 = 60%, with various orientations of the Austenite-Martensite interfaces.

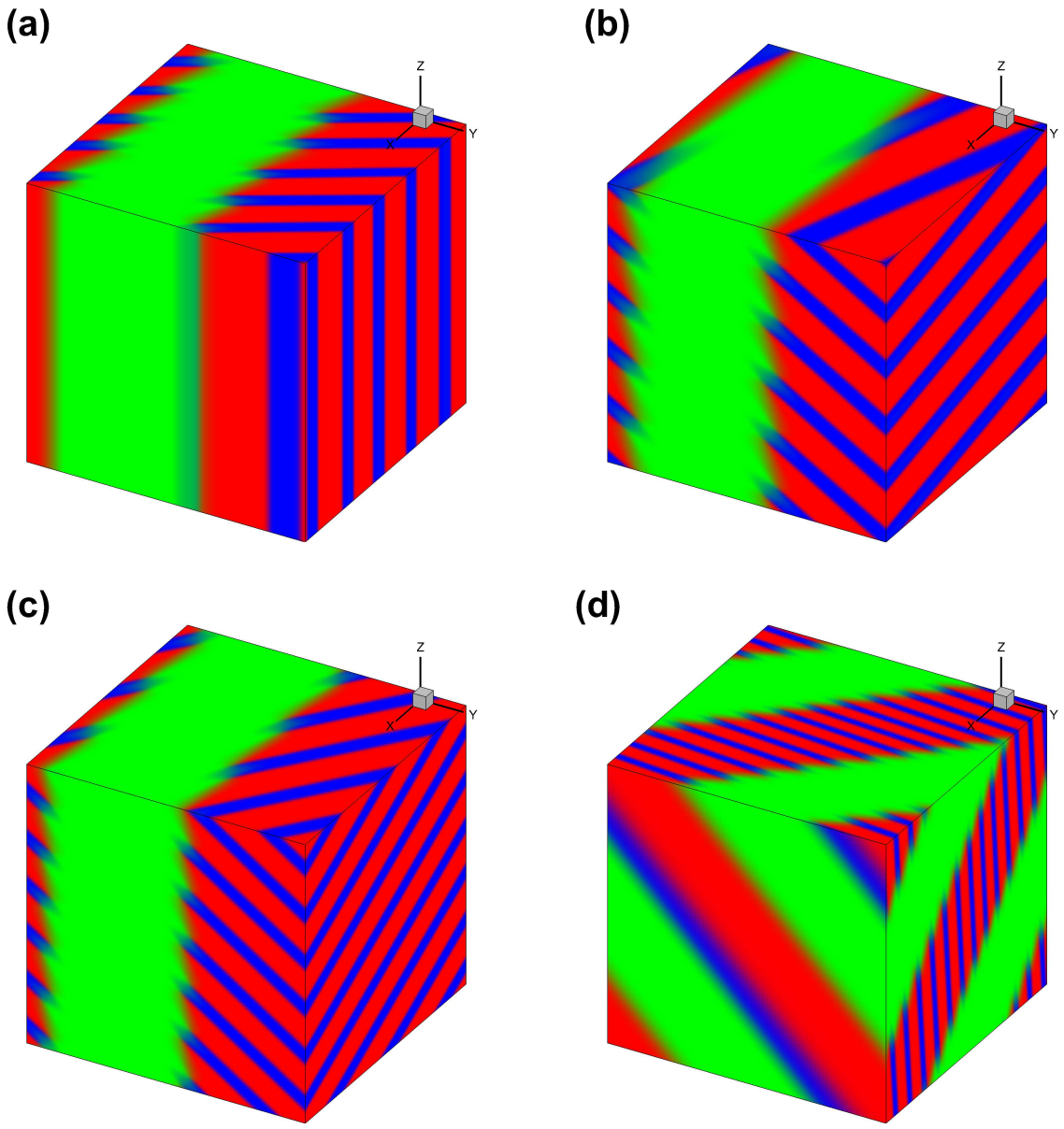

Figure 3.17: Simulation of Austenite-Martensite interface in three dimensions when the Martensitic ratio r is 0.66 = 66%, with various orientations of the Austenite-Martensite interfaces.

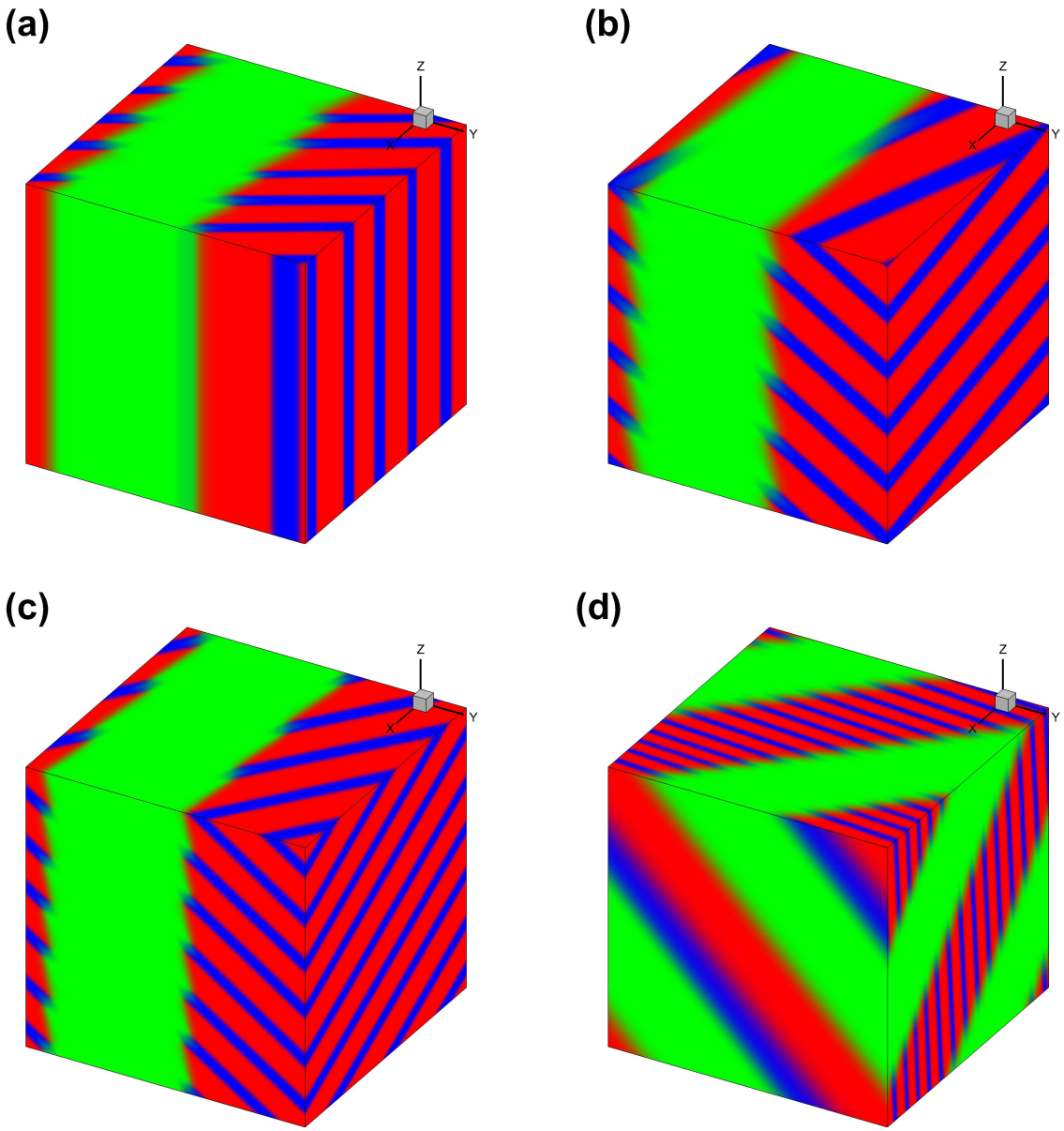

Figure 3.18: Simulation of Austenite-Martensite interface in three dimensions when the Martensitic ratio r is 0.7 = 70%, with various orientations of the Austenite-Martensite interfaces.

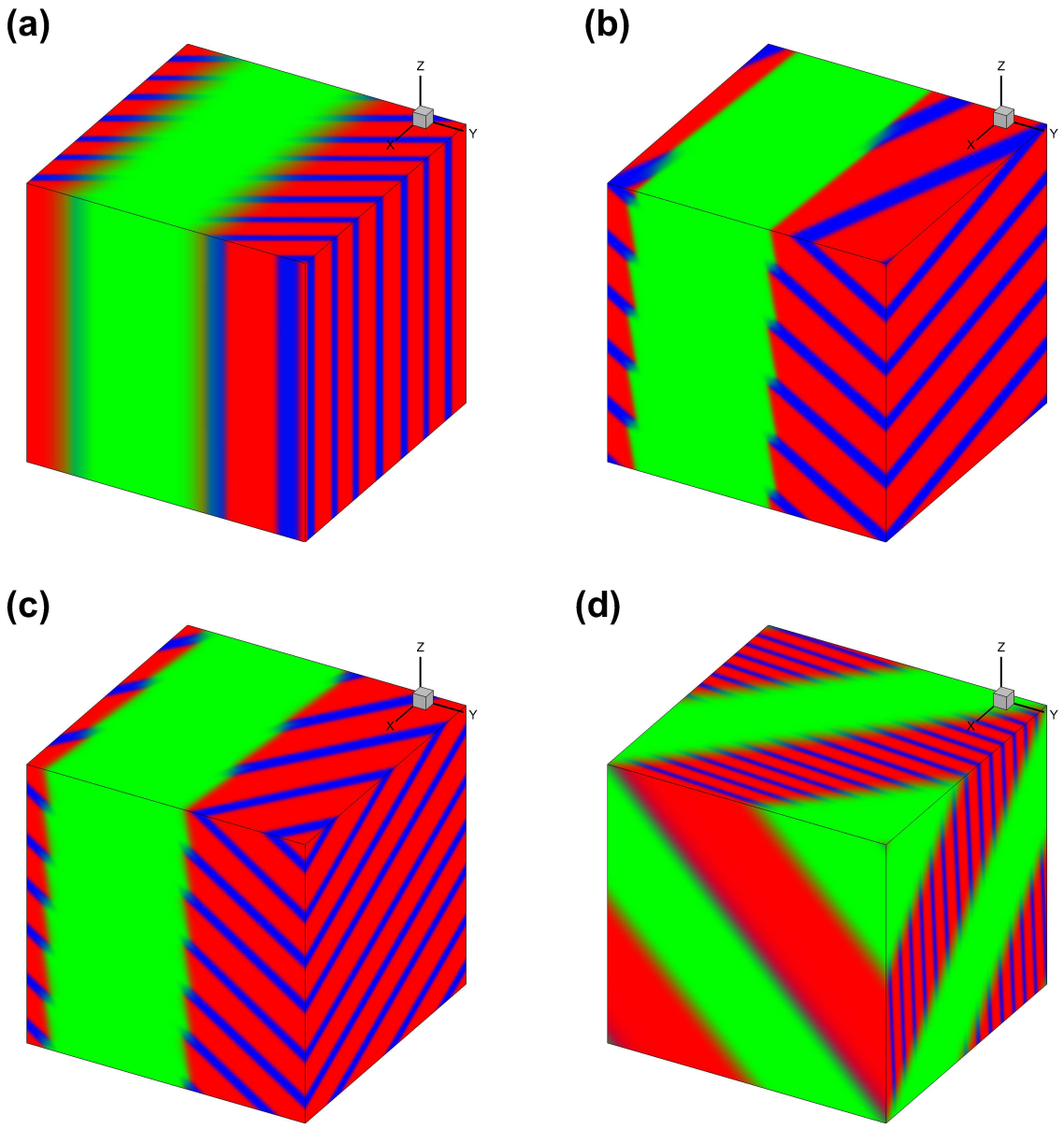

Figure 3.19: Simulation of Austenite-Martensite interface in three dimensions when the Martensitic ratio r is 0.75 = 75%, with various orientations of the Austenite-Martensite interfaces.

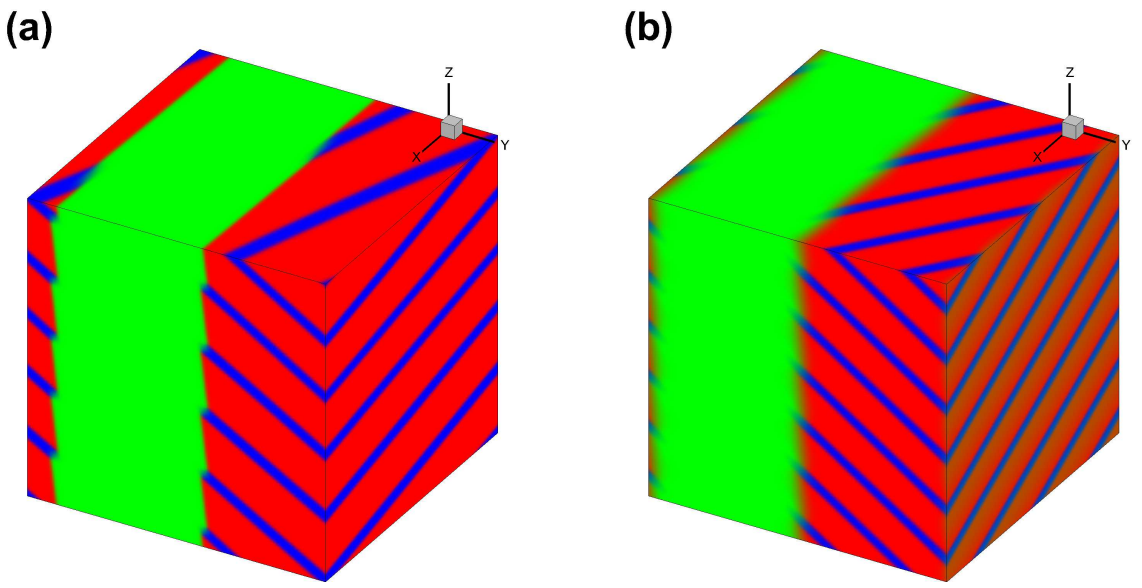

Figure 3.20: Simulation of Austenite-Martensite interface in three dimensions when the Martensitic ratio r is 0.8 = 80%, with various orientations of the Austenite-Martensite interfaces. Unfortunately, simulations with some direction of interface are not successful.

3.8 Hysteresis

Now that the phase field model can work for simulating microstructure below transformation temperature T_c (when Austenite is absent in the simulation) and at the transformation temperature T_c (when Austenite participates in the simulation), we are interested to extend the model to work beyond the current temperature range. For this, we can modify the anisotropy energy, by adding a function that changes with the temperature.

Due to the following facts:

- Above transformation temperature T_c, Austenite becomes more preferable than Martensite. The higher the temperature is over T_c, Austenite gets even more tendency to form.

- Below transformation temperature T_c, Martensite becomes more preferable than Austenite. The lower the temperature is below T_c, Martensite gets even more tendency to form.

- At transformation temperature T_c, both Austenite and Martensite have equal priorities to exist.

They tend to co-exist.

These facts and observations suggest the following form of thermal functional in the upper level where the Austenite is separating from the twinned Martensites:

$$W^{thermal}(\mu) = \begin{cases} |\Delta T|\,\mu_1^2 & T < T_c \\ 0 & T = T_c \\ |\Delta T|\,(1-\mu_1)^2 & T > T_c \end{cases}, \tag{3.33}$$

where $\Delta T = T - T_c$ is the change of temperature from the transformation temperature.

The effect of this thermal functional on the anisotropy energy can be examined by considering the sum of anisotropy energy and thermal energy due to phase change by temperature in Fig. (3.21). At transformation temperature $T = T_c$, the energy is minimized and stable at either Austenite or Martensite, thus both phases have equal priorities to exist. Below transformation temperature $T < T_c$, the energy is minimized at field variable corresponding to Martensites, thus Martensite is more likely to form. Above transformation temperature $T < T_c$, the energy is minimized at field variable corresponding to Austenite, thus Austenite is more likely to form.

With the introduction of thermal energy that modifies the anisotropy energy over a wider temperature range, hysteresis of microstructure in shape memory alloys can be implemented and simulated. The process of hysteresis consists of two stages. In the first stage, the initial pattern consisting entirely Austenite but a layer of Martensites as nucleation is cooled to (twinned) Martensites. In the second stage, the then-formed (twinned) Martensites, now added with a layer of Austenite as nucleation, is heated to Austenite. The temperature applied is sinusoidal, which is explicitly expressed as:

$$\Delta T = \sin\left(\frac{t}{t_{total}} 2\pi\right), \tag{3.34}$$

where t is the iteration or time measure and t_{total} is the total number of iterations for one complete cycle (nucleated Austenite first cooled to Martensites then heated back to Martensite). The resulting hysteresis loop and the snapshots showing simulated patterns are shown in figure (3.22) for $r = 0.6$ and figure (3.23) for $r = 0.7$.

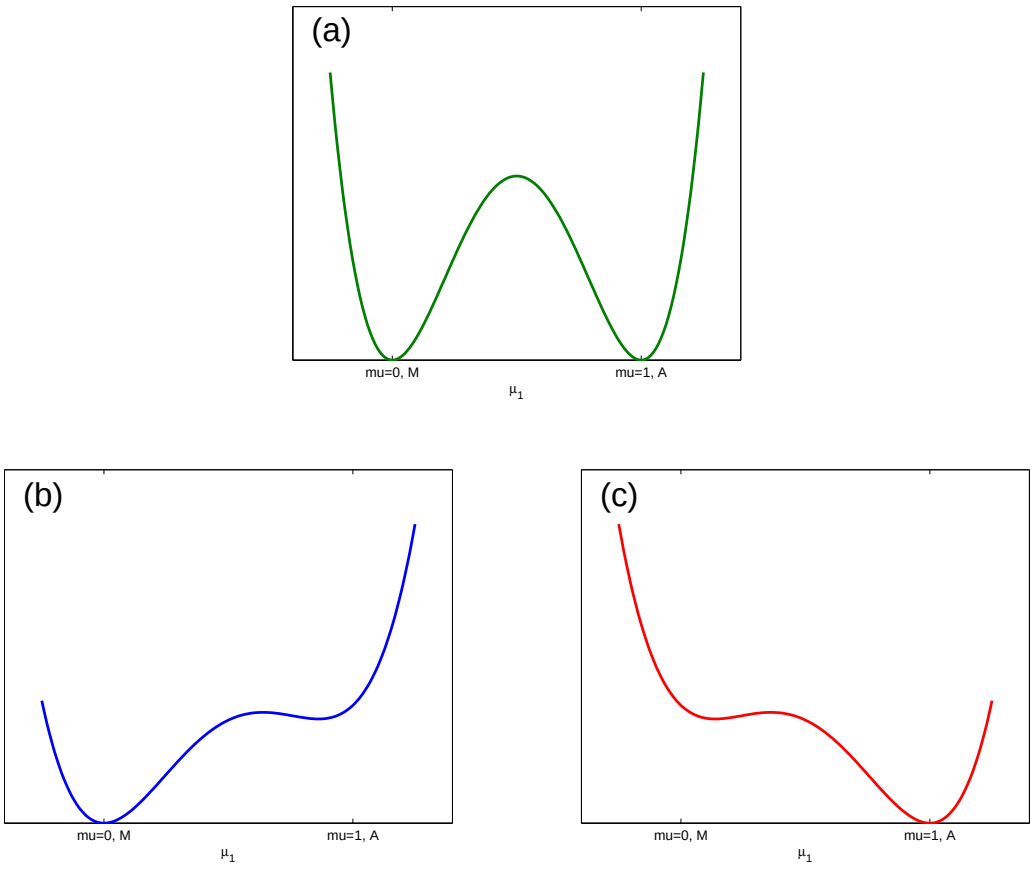

Figure 3.21: Sum of anisotropy energy and thermal energy. (a) At transformation temperature $T = T_c$, the energy is minimized and stable at either Austenite or Martensite, thus both phases have equal priorities to exist. (b) Below transformation temperature $T < T_c$, the energy is minimized at field variable corresponding to Martensites, thus Martensite is more likely to form. (c) Above transformation temperature $T < T_c$, the energy is minimized at field variable corresponding to Austenite, thus Austenite is more likely to form.

As a remark, during the first stage of hysteresis where Austenite is cooled to Martensites, the ratio of the two Martensitic variants are fixed due to constraint from Austenite, based on the geometric compatibility condition. After all Austenite has disappeared, the ratio of these Martensitic variants is longer fixed. In the absence of Austenite, the ratio of Martensites can be arbitrary. Given enough time, the patterns will evolve to one Martensitic variant for stable pattern with minimized total free energy. During the second stage where Martensite is heated to Austenite, whence a layer of Austenite is added. As the content of Austenite is growing, the ratio of Martensitic variants is adjusting to the ratio governed by the geometric compatibility condition with Austenite. These can be observed in the snapshots of figure (3.22) for $r = 0.6$ and figure (3.23) for $r = 0.7$.

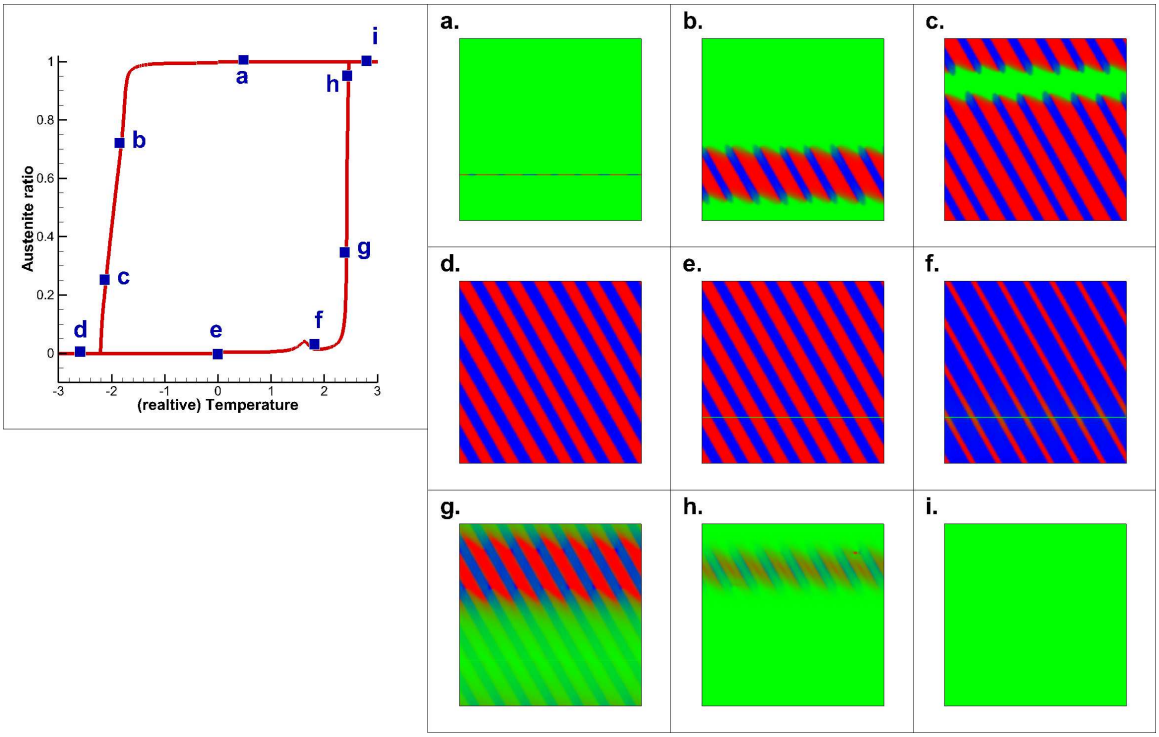

Figure 3.22: Hysteresis loop and snapshots showing the evolution of the microstructure for $r = 0.6$

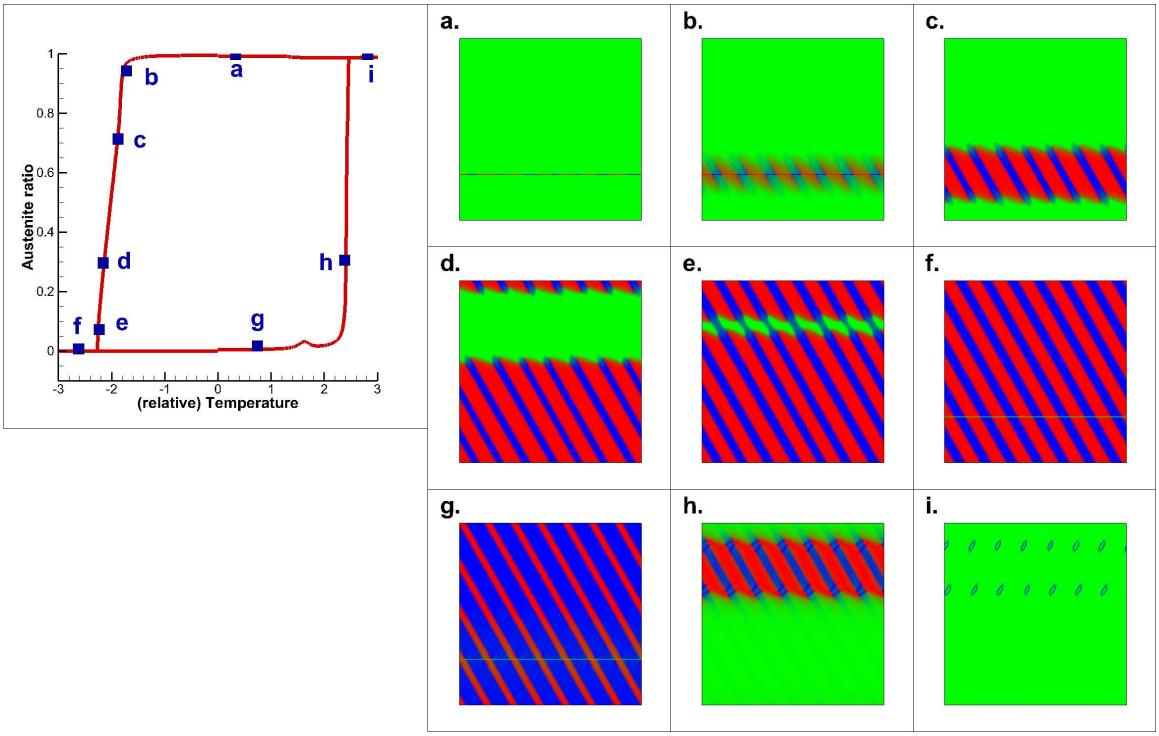

Figure 3.23: Hysteresis loop and snapshots showing the evolution of the microstructure for $r = 0.7$

3.9 Austenite-Martensite interfaces in real crystal systems

We have developed a two-level phase-field simulation to model micro-structures with Auetensite-Martensite interfaces. In this section, we make an attempt to simulate micro-structures in common crystal systems, which include the cubic-to-tetragonal system, cubic-to-orthogonal system and cubic-to-monoclinic-I system. Twinning of different variants in one system can give rise to different micro-structures, of which some can form further Austenite-Martensite interface but some can not [2]. We first outline the criteria to determine if various interface can be generated. These criteria are then applied to different representative pairs in each of the mentioned crystal systems to explore the possible twinned micro-structures, possibly with or without Austenite-Martensite interfaces. These micro-structures are also simulated.

The background theory of Martensite-Martensite and Austenite-Martensite interfaces in shape memory alloys is discussed using the general finite strains. We may identify if these two variants can form interfaces. Consider two variants (which can be two Martensites or one Martensite with one Austenite) quantified by eigen-strains **F** and **G** in finite strain matrix representation. For an interface is formed, the two strains have to satisfy:

$$\mathbf{QF} - \mathbf{G} = \mathbf{a} \otimes \mathbf{n} \tag{3.35}$$

for some rotation matrix **Q**. **a** and **n** are the shear and normal of the interface.

Occasionally the above criterion can not be verified directly. To re-phrase the criterion in a more accessible way, we define $\mathbf{C} \equiv \mathbf{G}^{-T}\mathbf{F}^{T}\mathbf{F}\mathbf{G}^{-1}$. Also define the three eigenvalues of **C** as $\{\lambda_1 \leq \lambda_2 \leq \lambda_3\}$ and the corresponding eigenvectors as $\{\mathbf{n}_1, \mathbf{n}_2, \mathbf{n}_3\}$.

The following criterion is formulated:

- If $\mathbf{C} = \mathbf{I}$, no interface can form.
- If $\mathbf{C} \neq \mathbf{I}$ but if the middle eigenvalue $\lambda_2 \neq 1$, no interface can form.
- If $\mathbf{C} \neq \mathbf{I}$ and the middle eigenvalue $\lambda_2 = 1$, an interface will form.

In case an interface is verified to exist between two variants, the directions of normals **n** and

shears **a** can be computed as:

$$\begin{aligned}\mathbf{a} &= \sqrt{\frac{\lambda_3(1-\lambda_1)}{\lambda_3-\lambda_1}}\mathbf{e}_1 + \kappa_n\sqrt{\frac{\lambda_1(\lambda_3-1)}{\lambda_3-\lambda_1}}\mathbf{e}_3 \\ \mathbf{n} &= \frac{\sqrt{\lambda_3}-\sqrt{\lambda_1}}{\sqrt{\lambda_3-\lambda_1}}\left(-\sqrt{1-\lambda_1}\mathbf{G}^T\mathbf{e}_1 + \kappa_n\sqrt{\lambda_3-1}\mathbf{G}^T\mathbf{e}_3\right),\end{aligned} \tag{3.36}$$

where $\kappa_n = \pm 1$. Thus there are two sets of solutions, denoted by $\{\mathbf{a}^+, \mathbf{n}^+\}$ and $\{\mathbf{a}^-, \mathbf{n}^-\}$.

Notice that if the two variants are Martensite, their ratios in the interfaced microstructure can be arbitrary, which can be practically manipulated by imposing compatible external strains.

For an interface between Austenite and twinned Martensites to form, the transformation strain of the participating Martensite has to satisfy the following equations:

$$\begin{aligned}&\delta \equiv \mathbf{a}\mathbf{G}\left(\mathbf{G}^2-\mathbf{I}\right)^{-1}\mathbf{n} \leq 2 \\ &\eta \equiv tr\left(\mathbf{G}^2\right) - \det\left(\mathbf{G}^2\right) - 2 + \frac{1}{\delta}|\mathbf{a}|^2 \geq 0\end{aligned} \tag{3.37}$$

The existence of autenite-Martensite interface, the participating Martensite variants have to be in fixed ratios $(\lambda{:}1-\lambda)$ or $(1-\lambda{:}\lambda)$, where:

$$\lambda = \frac{1}{2}\left(1 - \sqrt{1+\frac{2}{\delta}}\right) \tag{3.38}$$

With λ, one may further define $\mathbf{D} \equiv (\mathbf{G}+\lambda\mathbf{n}\otimes\mathbf{a})(\mathbf{G}+\lambda\mathbf{a}\otimes\mathbf{n})$. Denote the eigenvalues of **D** be $\{\mu_1 \leq \mu_2 = 1 \leq \mu_3\}$ and and the corresponding eigenvectors as $\{\mathbf{f}_1, \mathbf{f}_2, \mathbf{f}_3\}$. Then the shear (**b**) and normal (**m**) to the interfaces can be computed as:

$$\begin{aligned}\mathbf{b} &= \sqrt{\frac{\mu_3(1-\mu_1)}{\mu_3-\mu_1}}\mathbf{f}_1 + \kappa_m\sqrt{\frac{\mu_1(\mu_3-1)}{\mu_3-\mu_1}}\mathbf{f}_3 \\ \mathbf{m} &= \frac{\sqrt{\mu_3}-\sqrt{\mu_1}}{\sqrt{\mu_3-\mu_1}}\left(-\sqrt{1-\mu_1}\mathbf{f}_1 + \kappa_m\sqrt{\mu_3-1}\mathbf{f}_3\right),\end{aligned} \tag{3.39}$$

where $\kappa_m = \pm 1$. Thus there are two sets of solutions for each of (λ) and $(1-\lambda)$, denoted by $\{\mathbf{b}^+, \mathbf{m}^+\}$ and $\{\mathbf{b}^-, \mathbf{m}^-\}$.

As schematically shown in figure (3.24), for any two variants of the same crystal system, there

can be as many as eight possible configurations of micro-structures.

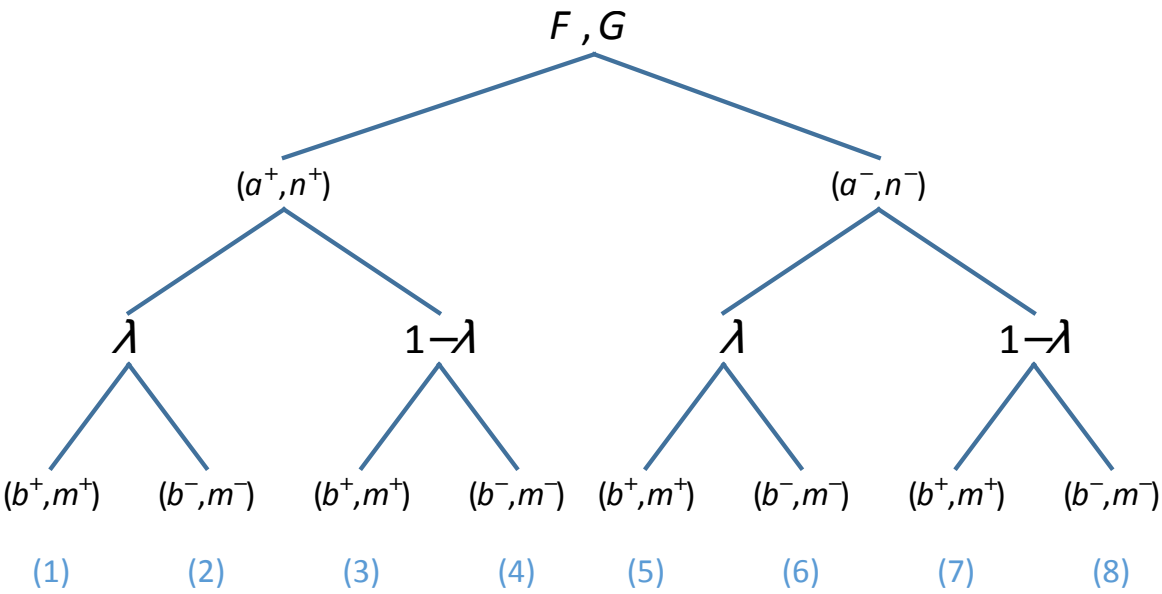

Figure 3.24: Schematic showing how the eight possible of micro-structures are generated.

The occurrences of interfaces in three common crystal systems, namely, Cubic-to-Tetragonal, Cubic-to-Orthorhombic and Cubic-to-Monoclinic-I systems will be presented in appendix (B).

3.10 Discussion and Conclusion

The introductions of the two-scale formulation and the thermal energy functional allow us to simulate patterns over a wide range of temperature that involves twining of Austenite and variants of Martensites based on the geometric compatibility condition for forming interfaces among these variants. These are implemented for thin-film (plane stress) and bulk configuration (plane strain and general three dimension). Hysteresis is also studied.

More efforts are needed to explore the relationship of the length of the hysteresis loops and the (common) middle eigenvalues of the Martensitic phases, which will give us insights on the search of materials that possess quick change of shape and that consume less energy.

There are several directions to extend the current works. One direction is the simulation of the Austenite-Martensite interfaces in other functional materials, such as ferromagnetic shape memory

alloy, ferroelectric materials, which involve coupling of several physical orderings. In the phase field models and simulations, periodicity is assumed so as to facilitate the uses of Fourier transforms. This assumption is valid for nanoscale where the microstructure of the sample (in a unit cell) is simulated. When phase field simulations are applied to real physical system, such as, when the whole sample is adhered to substrate and subjected to various microscopies over the top surface, the condition of periodicity has to be dropped out, thus complicating the analysis and simulation. In a later chapter we are going to resolve this issue.

Chapter 4

MARTENSITIC TENTS AND TUNNELS IN SHAPE MEMORY ALLOY THIN FILMS BY PHASE FIELD SIMULATION

Martensitic tunnels and tents, two common thin film structures grown on substrate, enable extensive studies due to their excellent mechanical performance, efficiency and size. Crystallographical conditions on crystal lattices, using infinitesimal transformation strains, for the formation are derived. A modified phase field simulation with additional energy functional due to substrate constraint was then adopted to investigate pattern formations of tunnels and tents, which corroborate existing experimental results. Thermal hysteresis was also studied to illustrate the evolving patterns under a sinusoidal profile of temperature. This shows that tunnels consume less energy to evolve then tents do. The simulation serves as a guide for the design of thin film structures in various applications.

Micro-actuators capable of delivering a large work output from small volume are highly desirable for microelectromechanical systems (MEMS) [2, 58, 3]. Shape memory alloys (SMAs) whose work outputs per unit volume is largest amongst a variety of active materials are attractive for micro-actuation [2, 58, 3]. Nevertheless, SMA-based actuators usually have poor bandwidth, limited by the rate of heating and cooling, has motivated development of SMA thin films wherein heat transfer is accelerated for their small size [2, 58, 3]. However, conventional SMA thin films are constrained by substrate clamping, which severely reduces their actuation strain and work output [2, 58, 3]. It has been proposed that parts of SMA thin films can be released from the substrate constraint by backing etching, as schematically shown in figure (4.1), making it possible to transform the released portion into Martensite, while keeping the constrained region in austenite [2, 58, 3]. This leads to the formation of Martensite tents and tunnels shown in figure (4.1) that increase the actuation strain and thus the work output in SMA thin films, with the austenite-Martensite (AM) interface functioning as a hinge [2, 58, 3]. Such tent and tunnel structures have indeed been realized in previous experiments, though the transformation is rather difficult [2, 58, 3]. In this letter, we seek to simulate

Martensitic tent and tunnel structures in SMA thin films using our modified phase field method in order to understand the transformation process.

Two types of interfaces are involved in Martensitic tent and tunnel structures shown in figure (4.1). One is the AM interface, and the other is the interface between Martenstic twins. As a result, the following compatibility conditions have to be satisfied [2, 59, 60, 61, 62]:

$$\begin{aligned} \mathbf{f} \cdot cof(\varepsilon^{(i)})\mathbf{f} = 0 \\ tr(\varepsilon^{(i)}) - \mathbf{f} \cdot \varepsilon^{(i)}\mathbf{f} > 0, \end{aligned} \tag{4.1}$$

It is well known that in bulk SMAs, a coherent AM interface is difficult to form, requiring satisfaction of rather restrictive conditions on lattice parameters of austenite and Martensite [2, 59, 60, 61, 62]. In thin films, however, such conditions are relaxed substantially, as compatibility between austenite and Martensite only needs to be satisfied in two-dimensions (2D) instead of three-dimensions (3D) [2, 59, 60, 61, 62, 63]. As a result, only in-plane components of transformation strains need to be considered in compatibility, and out-of-plane components become inconsequential. For cubic-to-orthorhombic transformations we are considering, this implies that:

where $\mathbf{f}$ is the pre-assigned normal to the thin film, $\varepsilon^{(i)}$ is the infinitesimal strain of the Martensitic variant involved in the system, and cof and tr are, respectively, the cofactor and trace operators for 2-tensors.

It is well known that in bulk SMAs, a coherent AM interface is difficult to form, requiring satisfaction of rather restrictive conditions on lattice parameters of austenite and Martensite [2, 59, 60, 61, 62]. In thin films, however, such conditions are relaxed substantially, as compatibility between austenite and Martensite only needs to be satisfied in two-dimensions (2D) instead of three-dimensions (3D) [2, 59, 60, 61, 62, 63]. As a result, only in-plane components of transformation strains need to be considered in compatibility, and out-of-plane components become inconsequential. For cubic-to-orthorhombic transformations we are considering, this implies that:

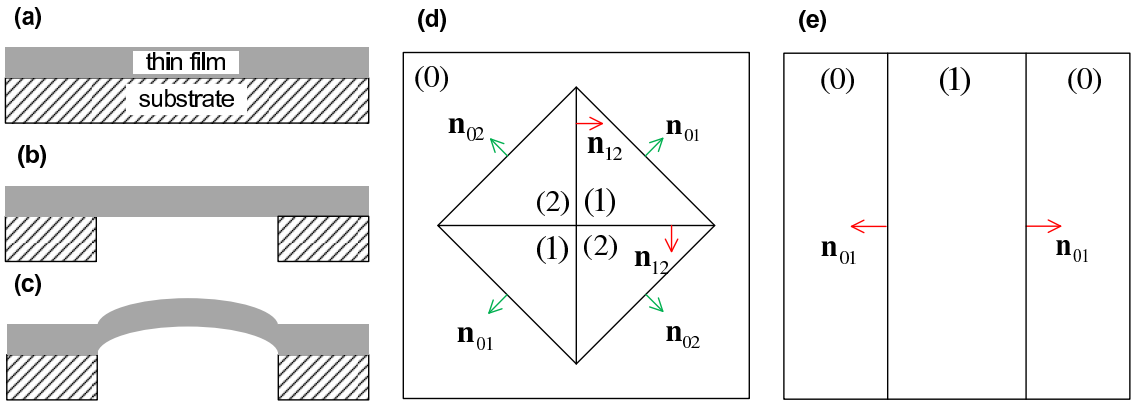

Figure 4.1: Schematic showing (a) shape-memory alloy deposited on a substrate; (b) shape-memory alloy released in a suitable region and remains at in the austenite; (c) bulges out in Martensite below transformation temperature; (d) various interfaces in tent; (e) various interfaces in tunnel. In fig. (d) and (e), the notions (0), (1) and (2) represent the regions occupied by the austenite phase and the two Martensitic phase respectively. Also $\mathbf{n}_{01}$ denotes the interface between austenite and Martensitic variant 1, $\mathbf{n}_{02}$ denotes the interface between austenite and Martensitic variant 2, and $\mathbf{n}_{12}$ denotes the interface between austenite and Martensitic variant 2.

$$\varepsilon^{(0)} = \begin{pmatrix} 0 & 0 \\ 0 & 0 \end{pmatrix}, \varepsilon^{(1)} = \begin{pmatrix} \alpha & \alpha \\ \alpha & \alpha \end{pmatrix}, \quad \varepsilon^{(2)} = \begin{pmatrix} \alpha & -\alpha \\ -\alpha & \alpha \end{pmatrix}, \tag{4.2}$$

which give the AM interfaces for tents $\mathbf{n}_{01} = \pm \begin{pmatrix} \frac{1}{\sqrt{2}} & \frac{1}{\sqrt{2}} \end{pmatrix}^T$, $\mathbf{n}_{02} = \pm \begin{pmatrix} -\frac{1}{\sqrt{2}} & \frac{1}{\sqrt{2}} \end{pmatrix}^T$ and the AM interfaces for tunnels $\mathbf{n}_{01} = \pm \begin{pmatrix} 1 & 0 \end{pmatrix}^T$, $\mathbf{n}_{02} = \pm \begin{pmatrix} 0 & 1 \end{pmatrix}^T$. Within the released region of the tent, the MM-interfaces are $\mathbf{n}_{12} = \pm \begin{pmatrix} 1 & 0 \end{pmatrix}^T, \pm \begin{pmatrix} 0 & 1 \end{pmatrix}^T$. Recall that there is no MM-interface for tunnels due to the existence of only one Martensite [2, 59, 60, 61, 62].

Two Martensite variants and one austenite variant are involved, which are represented by two characteristic functions $\mu_1(\mathbf{x})$ and $\mu_2(\mathbf{x})$ [64, 65, 66, 67, 68, 69]. The austenite region is indicated by $\mu_1(\mathbf{x})$, which takes a value of 1 if $\mathbf{x}$ is occupied by the austenite phase and 0 otherwise, while the particular Martensite variant is indicated by $\mu_2(\mathbf{x})$ in a similar manner. As a result, the transformation

strain at **x** is expressed as:

$$\varepsilon^*[\mu] = (1-\mu_1)\mu_2\varepsilon^{(1)} + (1-\mu_1)(1-\mu_2)\varepsilon^{(2)}, \tag{4.3}$$

where $\varepsilon^{(i)}$ is the transformation strain of Martensite variant, and $\mu = [\mu_1, \mu_2]$. Note that austenite is used as a reference and thus has zero transformation strain. The distribution of transformation strain ε^* may induce elastic strain in the structure, resulting in elastic energy as follows:

$$W^{ela}(\mu) = \frac{1}{2}(\varepsilon - \varepsilon^*[\mu]) \cdot \mathbf{C}(\varepsilon - \varepsilon^*[\mu]), \tag{4.4}$$

where ε is the total strain that can be solved from mechanical equilibrium equation, consisting of both the elastic strain and the transformation strain, and **C** is the elastic stiffness tensor. This allows us to use μ as field variable to simulate the structure. However to ensure that μ_1 and μ_2 take either 1 or 0, an anisotropy energy is introduced that is minimized when μ_i takes either 0 or 1,

$$W^{ani}(\mu) = K_1[\mu_1^2(1-\mu_1)^2 + \mu_2^2(1-\mu_2)^2], \tag{4.5}$$

where K is the anisotropy constant. In addition, interfacial energy is introduced to penalize gradients in the characteristic functions, such that

$$W^{gra}(\mu) = A|\nabla\mu|^2. \tag{4.6}$$

Finally, the constraint on the unrelaxed portion of the film by the substrate is achieved by including an additional penalty for deformation,

$$W^{penalty}(\mu) = B|\varepsilon|^2\chi_s, \tag{4.7}$$

where B is the penalty constant and χ_s is the characteristic function of the region constrained by the substrate. The potential energy of the system is then given by

$$\mathscr{I}(\mu) = \int_\Omega [W^{gra}(\mu) + W^{ani}(\mu) + W^{ela}(\mu) + W^{penalty}(\mu) - \sigma^0 \cdot \varepsilon] d\mathbf{x}, \tag{4.8}$$

where Ω is the domain occupied by the shape memory alloy, and σ^0 is the stress arising from the traction applied at the boundary. The variation of potential energy with respect to μ results in the driving force for the structure evolution,

$$\mathbf{F}(\mu) = -\frac{\delta \mathscr{I}(\mu)}{\delta \mu} = \mathbf{F}^{gra}(\mu) + \mathbf{F}^{ani}(\mu) + \mathbf{F}^{ela}(\mu) + \mathbf{F}^{penalty}(\mu), \tag{4.9}$$

and under a linear kinetic approximation, the evolution equation for μ is derived as

$$\frac{\partial \mu}{\partial t} = M[\mathbf{F}^{gra}(\mu) + \mathbf{F}^{ani}(\mu) + \mathbf{F}^{ela}(\mu) + \mathbf{F}^{penalty}(\mu)], \tag{4.10}$$

where M is the linear evolution coefficient, and $\mathbf{F}^{ani}(\mu) = -\frac{\partial W^{ani}(\mu)}{\partial \mu}$, $\mathbf{F}^{gra}(\mu) = 2A\nabla^2\mu$, $\mathbf{F}^{ela}(\mu) = \sigma \cdot \frac{\partial \varepsilon^*[\mu]}{\partial \mu}$, $\mathbf{F}^{penalty}(\mu) = \frac{\partial W^{penalty}(\mu)}{\partial \mu}$.

This theory is implemented into a numerical simulation on a x_1-x_2 plane, with all the field variables assumed to be independent of x_3 and the normal of the plane set to be $\mathbf{f} = \begin{pmatrix} 0 & 0 & 1 \end{pmatrix}^T$. Thus a two-dimensional simulation will be sufficient, though all the tensorial variables are three-dimensional in nature. To solve Eq. (4.10), fast Fourier transform [70] is adopted on a spatial scale with a 64×64 lattice, and semi-implicit finite difference scheme [71, 72] is adopted on a temporal scale with a time step of 0.001. The elastic constants of the material are assumed to be $C_{11} = 40 \times 10^9$Pa, $C_{12} = 10 \times 10^9$Pa and $C_{33} = 30 \times 10^9$Pa, with $\alpha = 0.045$, $K_1 = 6 \times 10^7$ and $B = 10^7$. Unless otherwise noted, the simulation starts with random initial conditions for μ_1 and μ_2, and iterations continue until a stable configuration emerges.

Phase field simulation is applied to study the pattern formations of the tunnel and the tent for a cubic-to-orthorhombic transformation, which has transformation matrices given by (4.2).

With regard to the mechanical condition, the substrate is subjected to strain-free conditions while the to-be-released region is subjected to the stress-free condition.

In forming the desired structures, AM interfaces are important. The released region should have the correct orientation, and the film should have the correct normal [2]. We seek to arrange the substrate and the to-be-released region in such a way that the Martensite will bulge up like a tunnel or a tent. In particular, we aim to choose the crystallography and the region to be released carefully so that each ridge in the figure is a material interface and the deformations are energy minimizing.

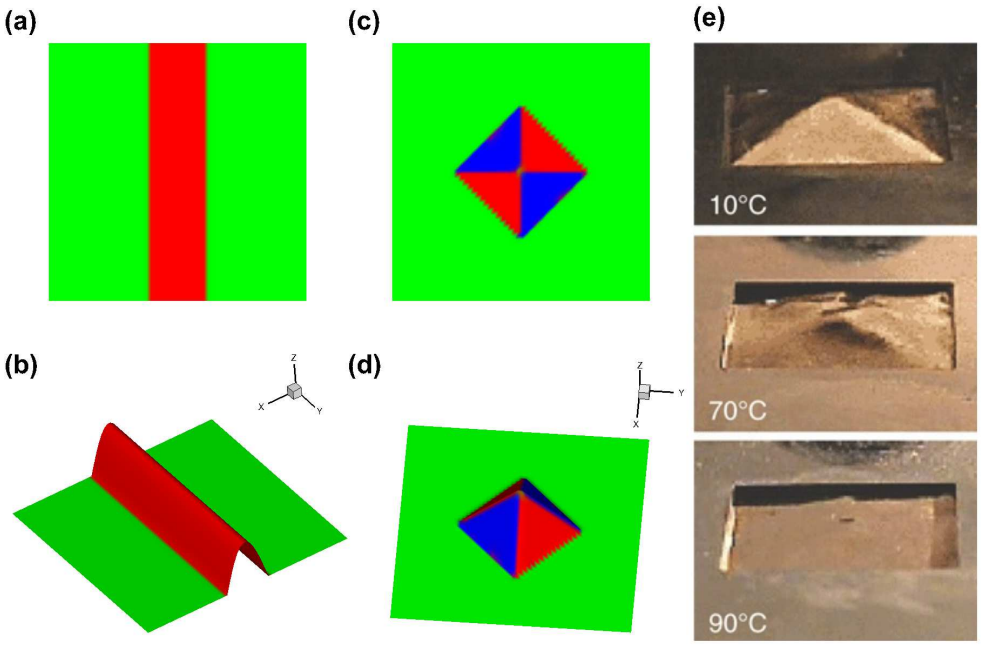

Figure 4.2: Simulation of patterns of tunnel and tent and the corresponding three-dimensional views; (a) Pattern of tunnel; (b) Three-Dimensional view of tunnel; (c) Pattern of tent; (d) Three-Dimensional view of tent; (e) experimentally observed formation of tent (Bhattacharya and James) for comparison.

If this is possible, the films can be exploited to make micro-pumps, micro-valves and other micro-actuators [3, 73, 74].

If the to-be-released region is the middle strip while the remaining region is adhered to the substrate, the middle-released region in the simulated pattern will become Martensite upon cooling and bulge up as a circular arc, as shown in figure (4.2)(a) and (4.2)(b). The two Austenite-Martensite interfaces act as hinges and the resulting structure is the tunnel. The rotation matrix $\mathbf{Q} = \mathbf{Q}(\theta)$ is a one-parameter function.

On the other hand, the to-be-released region is the middle square island, which will become Martensite upon cooling as in figure (4.2)(c) and bulge up as a tent made of four triangular surfaces joined at the center of the film, as in figure (4.2)(d). The rotation matrix $\mathbf{Q}$ is constant over each of

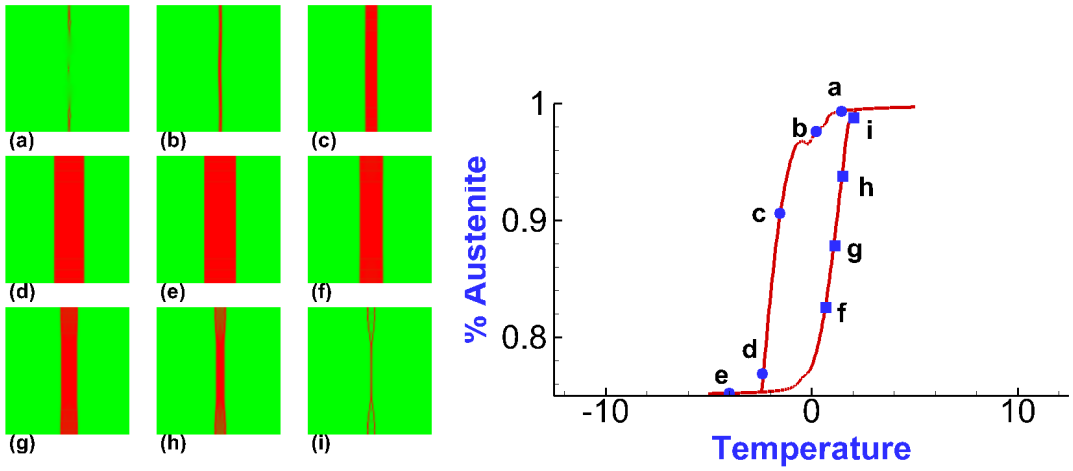

Figure 4.3: Thermal hysteresis of tunnel; (a) $\sim$ (i): patterns of intermediate structures; Patterns along cooling on the curve are marked by circles, patterns along heating are marked by square diamonds.

the four patches.

In all figures showing various patterns, green is designated to Austenite, while red and blue are designated for the two variants of Martensites involved.

We then consider the thermal hysteresis of tunnel and tent [75, 54], subjected to a sinusoidal profile of temperature. Thermal energy is adopted in the form:

$$W^{thermal}(\mu) = \begin{cases} |\Delta T|(1-\mu_1)^2 & : T > T_c \\ |\Delta T|\mu_1^2 & : T < T_c \end{cases}, \tag{4.11}$$

where T_c is the transformation temperature above which austenite becomes more likely to form and below which Martensite becomes more likely, $\Delta T = T - T_c$ is the change of temperature from the transformation temperature. In the simulation, due to the sinusoidal nature of the temperature change, the thermal energy ΔT is a function of time and is expressed explicitly as:

$$\Delta T = sin\left(\frac{t}{L}2\pi\right), \tag{4.12}$$

where t is the iteration or time measure and L is the total number of iterations for one complete cycle

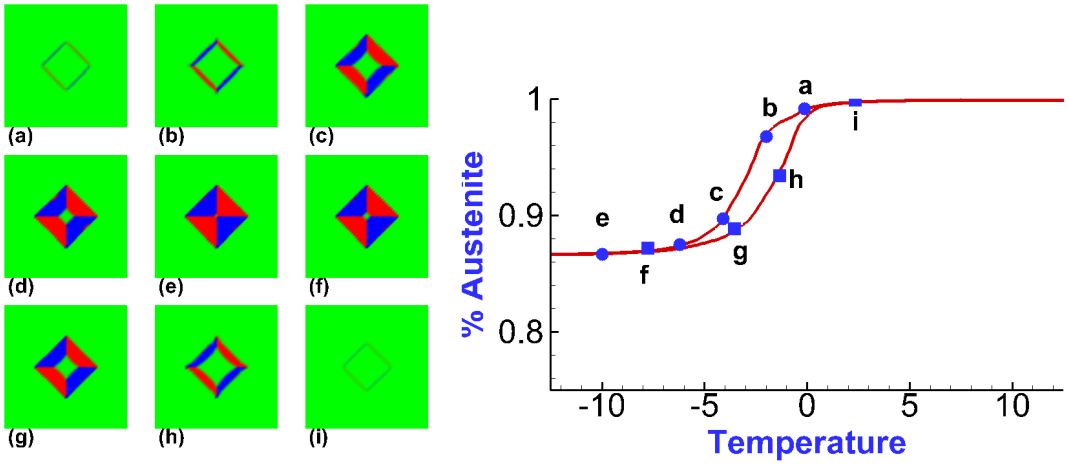

Figure 4.4: Thermal hysteresis of tent; (a) $\sim$ (i): patterns of intermediate structures; Patterns along cooling on the curve are marked by circles, patterns along heating are marked by square diamonds.

(nucleated austenite first cooled to form special thin film structures then heated back to flat sheet of austenite).

Austenite is used as initial condition, with less than 1 percent of Martensite added for nucleation. The resulting curves relating the content of Austenite versus the applied temperature are shown in figure (4.3) for tunnel and figure (4.4) for tent. The released region in the films emerges to Martensite with the formation of tunnel and tent upon cooling, which then degenerates back to Austenite upon re-heating, and a complete thermal cycle is finished.

In summary, for materials whose transformation strains satisfy the crystallography conditions, tunnels and tents may be formed. We have developed an unconventional phase field simulation for these thin film SMA, which is used to simulate the formation of tunnels and tents, and the evolution of the domains under the influence of temperature, using thermal hysteresis loops. The theory and stimulation thus provide a guide to the choice of materials in the design of micro-machines.

Chapter 5

ELECTROMECHANICAL FIELDS IN THIN FILMS (3D-CONFIGURATION)

In our previous work on phase field simulations with periodicities along all directions, we solved the mechanical equilibrium equation (similar for Maxwell's equation) using Fast Fourier Transform (FFT) in all directions [32, 33, 56]. For more realistic configurations, at least one periodicity along the out-of-plane direction is released [76]. We need to resolve the mechanical equilibrium equation (as well as the Maxwell's equation) in this scenario. This chapter is devoted to the numerical solutions of these equations.

5.1 Introduction and Background

So far phase field simulation has been successfully adopted to modal domain patterns in microstructure where periodicity is assumed in all physical dimensions. However, practically, experimental configurations of sample being investigated, such as multi-functional materials under the actions of Scanning Probe Microscopy (SPM), Piezo-response Force Microscopy (PFM), Electrochemical Strain Microscopy (ESM), etc, do not necessarily assume the strong constraint from periodicity. Modified numerical simulations are developed.

From this chapter onwards, we utilize the phase field modal to simulate multi-functional materials in more realistic configurations and with coupling of more than one physical ordering, such as, mechanical with electrical, mechanical with magnetic, etc. As a real physical modal, we release the periodicity condition in the x_3-direction. We outline the numerical schemes to solve the mechanical equilibrium equation (or called elasticity equation) and the Maxwell's equation for three-dimensional samples with periodicities over x_1- and x_2- coordinates only. Two methods for each are derived, which we refer as the **state equation** approach (or **"eigen-expansion"**) and the **finite difference** approach. We apply the simulation to study the electro-mechanical response of a piezoelectric material and the mechanical response of ferroelectric materials under SPM probing.

The configurations for the Maxwell's equation and the mechanical equilibrium equation are

shown in figure (5.1). For the Maxwell's equation, assume that the bottom surface is subjected to some potential through grounding or electrode, while the top surface is subjected to some known potential or electric field. Instantaneous polarization is also pre-assigned. We solve for the electric potential and fields over the entire sample. For the mechanical equilibrium equation, assume that the bottom surface is adhered to a substrate while the top surface is subjected to a traction force. We solve for the displacements (and thus strains and stresses) over the entire sample.

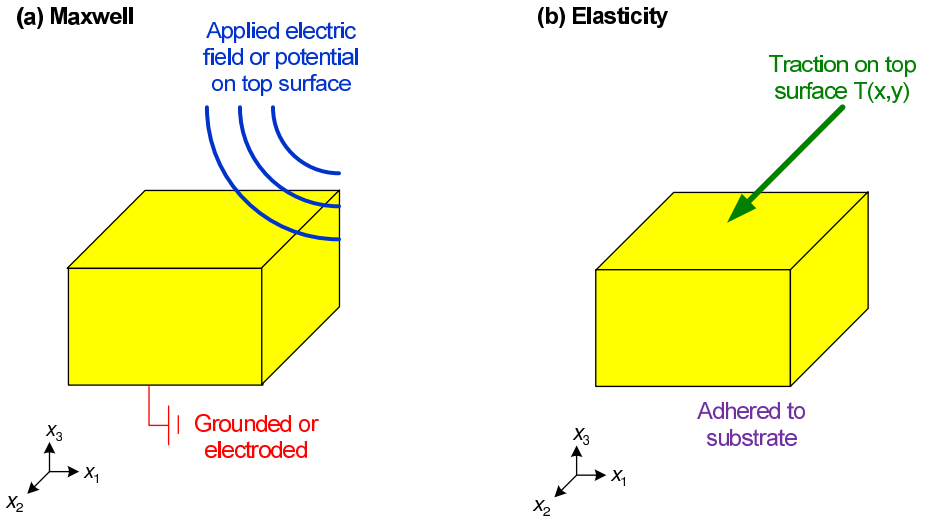

Figure 5.1: Configurations for solving (a) the Maxwell's equation and (b) the mechanical equilibrium equation.

Elasticity and Maxwell's equations in three dimensions are solved numerically and easily by finite element using black-box commercial softwares like ANSYS, Abaqus, COMSOL, etc. It is inconvenient to extract their results and integrate into our phase field simulations that follow. Boundary element method is also used to solve Maxwell's equation, especially for potential and fields outside the sample [67]. For the special case, where periodicity is assumed in all directions, solution using repeated Fourier transforms are developed [22, 66]. If the periodicity in x_3-direction is released, special approach like the Stroh's formulation is adopted and implemented [77, 78, 79], where a lot of mathematical results in linear algebra and complex variables are also quoted. To avoid all these technical difficulties, two approaches for solving these equations are developed, which only use simple mathematics and minimal assumptions based on the physics of the problem. This chapter

serves as a computational prerequisite for all subsequent works.

We will outline the solutions of the Maxwell and elasticity equations using two approaches, namely, eigen-expansions and finite difference. Their central methodologies will be presented briefly. The detailed developments are lengthy and are placed in appendices, for the sake of charity.

We are solving the Maxwell's equation:

$$\begin{cases} -\kappa\nabla\mathbf{E} &= \nabla\cdot\mathbf{P} \\ \mathbf{E} &= -\nabla\phi \end{cases} \tag{5.1}$$

where $\mathbf{P} = (P_1, P_2, P_3)$ is the spontaneous polarization of the sample, $\mathbf{E} = (E_1, E_2, E_3)$ is the electric field and ϕ is the resulting electric potential, and the elasticity equation:

$$\begin{cases} \sigma &= \mathbf{C}(\varepsilon - \varepsilon^*) \\ \nabla\cdot\sigma &= 0 \\ \varepsilon &= \nabla\mathbf{u} \end{cases} \tag{5.2}$$

where ε^* are the stress-free eigen-strains, ε are the total elastic strains, σ are the stresses and $\mathbf{u}$ represent the resulting displacements that describe the deformation of the elastic system.

Since the geometry is imposed with periodic boundary conditions along all in-plane directions, that is, x_1 and x_2, FFT is applied to these equations along these directions subjected to periodicities. These operations will convert the original coupled partial differential equations into system of ordinary differential equations along x_3. In the eigen-expansion method, we decompose and solve each ordinary differential equation into homogeneous part and particular part (also known as the perturbed part). The perturbed part is further solved from two contributions, one due to non-homogeneous eigen-strains with zero out-of-plane boundary conditions and the other one due to out-of-plane boundary conditions only. This is also referred as the semi-classical method.

On the other hand, we may also discretize and solve each ordinary differential equation with finite difference numerical scheme. This approach is known as the finite difference.

The details of how these two methods are adopted to solve the Maxwell's and the elasticity equation are presented in appendices (D.1), (D.2), (D.3) and (D.4). Conventions on quantities (vectors and matrices) related to elasticity equations are outlined in appendix (D.5).

5.2 Simulation in piezoelectric materials and SPM of ferroelectric materials

In this section, we apply the developed numerical methodologies for the Maxwell's equation and the mechanical equilibrium equation to two practical problems, namely, simulation of deformation in piezoelectric material due to applied electric field, and simulation of SPM response of ferroelectric materials.

5.2.1 Deformation in piezoelectric material

Due to the existence of electric dipole moments, piezoelectric materials demonstrate the converse piezoelectric effect, where the application of an electrical field creates mechanical deformation.

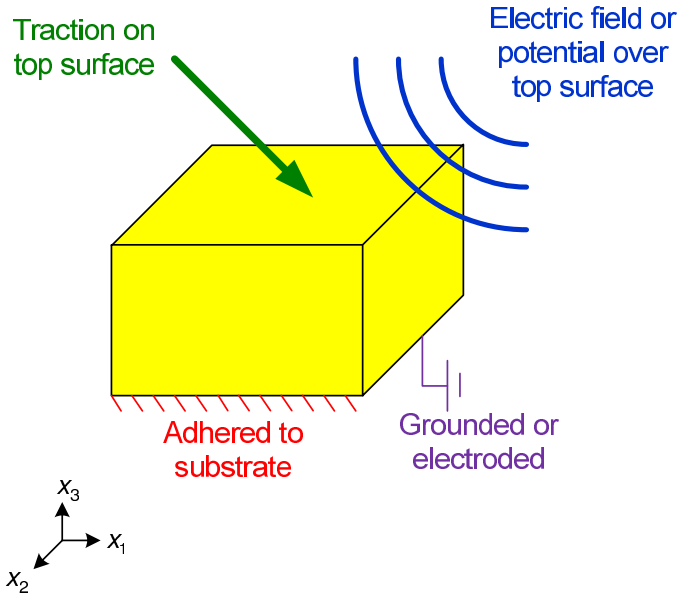

Figure 5.2: Configurations for solving electromechanical responses of piezoelectric materials.

Simulation of piezoelectric response couples two physical orderings: electrical and mechanical. We consider the physical configuration and the associated boundary condition, as demonstrated in figure (5.2). An electric potential $V_0 = V_0(x_1, x_2)$ is applied to the top surface of a slab of piezoelectric material. A force, as traction $\mathbf{T} = \mathbf{T}(x_1, x_2)$, may be applied to the top surface. The base surface is adhered and grounded to an electrode, so that the potential is maintained to be zero and there is no deformation, resulting in zero displacement.

Assume that the applied potential and traction are acted locally on the top surface so that the region far away from the site of application of these loading experience almost no effect from these loadings. We may assume the equations and all physical quantities are periodic in x_1 and x_2 directions. This periodicity is also satisfied if the applied potential and traction are periodic in x_1 and x_2, including the trivial case where these loadings are constant over the top surface.

The simulation consists of three steps: Maxwell's equation, piezoelectric constitutive relation and the mechanical equilibrium equation, with the boundary conditions, as listed as follow:

Step 1: Maxwell's equation:

The distribution of electric potential $\phi = \phi(x_1, x_2)$ is computed from the Maxwell's equation:

$$\kappa \nabla^2 \phi = \nabla \cdot \mathbf{P}, \tag{5.3}$$

subjected to the boundary conditions:

$$\begin{aligned} \phi(x_1, x_2, H) &= V_0 \\ \phi(x_1, x_2, 0) &= 0 \end{aligned} \tag{5.4}$$

Step 2: Piezoelectric constitutive relation:

Electric field $\mathbf{E} = \mathbf{E}(x_1, x_2, x_3)$ is then obtained from the electric potential:

$$\mathbf{E} = -\nabla \phi \tag{5.5}$$

This electric field induces an eigen-strain through the piezoelectric matrix:

$$\varepsilon^s = \mathbf{dE} \tag{5.6}$$

This can be expressed in component form:

$$\begin{pmatrix} \varepsilon^s_{11} \\ \varepsilon^s_{22} \\ \varepsilon^s_{33} \\ \varepsilon^s_{23} \\ \varepsilon^s_{13} \\ \varepsilon^s_{12} \end{pmatrix} = \begin{pmatrix} 0 & 0 & d_{31} \\ 0 & 0 & d_{32} \\ 0 & 0 & d_{33} \\ 0 & d_{24} & 0 \\ d_{15} & 0 & 0 \\ 0 & 0 & 0 \end{pmatrix} \begin{pmatrix} E_1 \\ E_2 \\ E_3 \end{pmatrix} \tag{5.7}$$

Step 3: Mechanical equilibrium equation:

With the eigen-strains identified, deformation strains and stresses can be obtained by the Mechanical equilibrium equation:

$$\begin{aligned} \sigma &= \mathbf{C}\,(\varepsilon - \varepsilon^s) \\ \nabla\sigma &= 0, \end{aligned} \tag{5.8}$$

subjected to the boundary conditions:

$$\begin{aligned} \mathbf{u}(x_1, x_2, 0) &= 0 \\ \sigma(x_1, x_2, H)\mathbf{n}(x_1, x_2, H) &= \mathbf{T}(x_1, x_2, H) \end{aligned} \tag{5.9}$$

To demonstrate the simulation, assume that the rectangular sample of piezo-electric material, with dimensions 4×10^{-6} (m) $\times\ 4\times10^{-6}$ (m) $\times\ 4\times10^{-6}$ (m), is adhered and grounded, so that the displacement and voltage on the bottom surface are zero. The top surface is subjected to a profile of voltage described by:

$$\begin{aligned} \phi(x_1, x_2, H) &= \phi_{top}(x_1, x_2) \\ &= \begin{cases} V_0 \left(\left(\frac{x_1 - x_{10}}{R}\right)^2 + \left(\frac{x_2 - x_{20}}{R}\right)^2 \right) & (x_1 - x_{10})^2 + (x_2 - x_{20})^2 < R \\ 0 & \textit{otherwise} \end{cases}, \end{aligned}$$

where the magnitude of the voltage is decreasing from its peak value V_0 parabolically to zero, away

from the center of the circle of radius R centered at (x_{10}, x_{20}) on the top surface. Also assume that the top surface is subjected to no mechanical loading.

The simulation is implemented in a $100 \times 100 \times 200$ grid. The material parameters are: $c_1 = 80 \times 10^9$, $c_2 = 30 \times 10^9$, $c_3 = 20 \times 10^9$, $d_{13} = -5.43 \times 10^{-12}$, $d_{23} = -5.43 \times 10^{-12}$, $d_{33} = 11.37 \times 10^{-12}$, $d_{42} = -11.34 \times 10^{-12}$, $d_{51} = -11.34 \times 10^{-12}$. In the first trial, assume that there is no internal polarization. The distribution of the resulting physical quantities, including potential, electric fields, displacement (deformation), strains and stresses, are shown in figures (5.3), (5.4), (5.5) and (5.6).

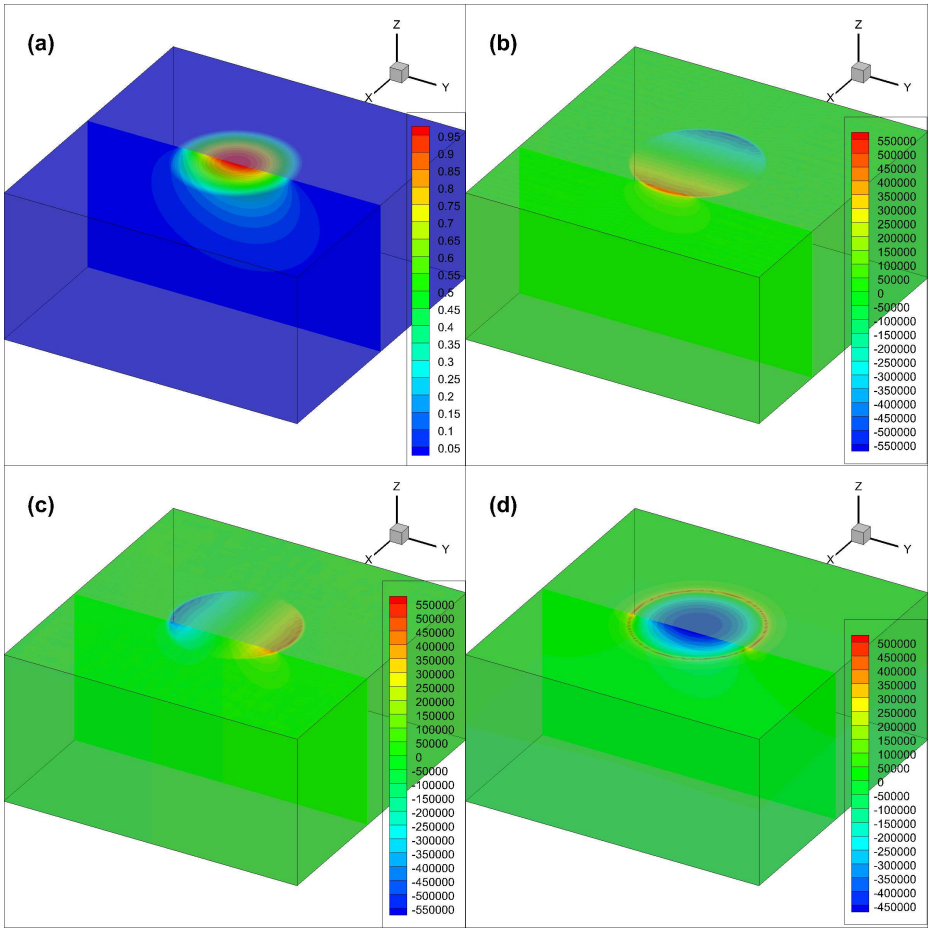

Figure 5.3: (Electromechanical responses of piezoelectric materials) Electric potential and fields: (a) electric potential ϕ, (b) field component E_1, (c) field component E_2 and (d) field component E_3.

We may discuss the effect of instantaneous polarization to the electromechanical responses of

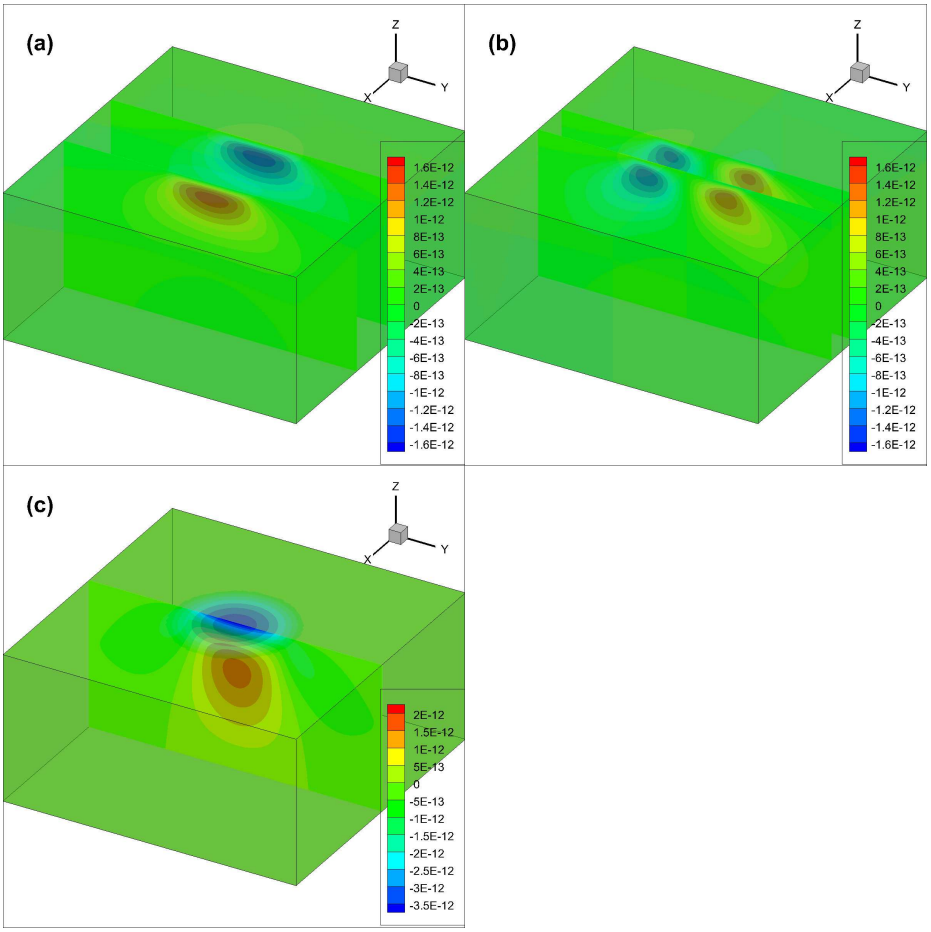

Figure 5.4: (Electromechanical responses of piezoelectric materials) displacement components or deformation: (a) u_1, (b) u_2 and (c) u_3.

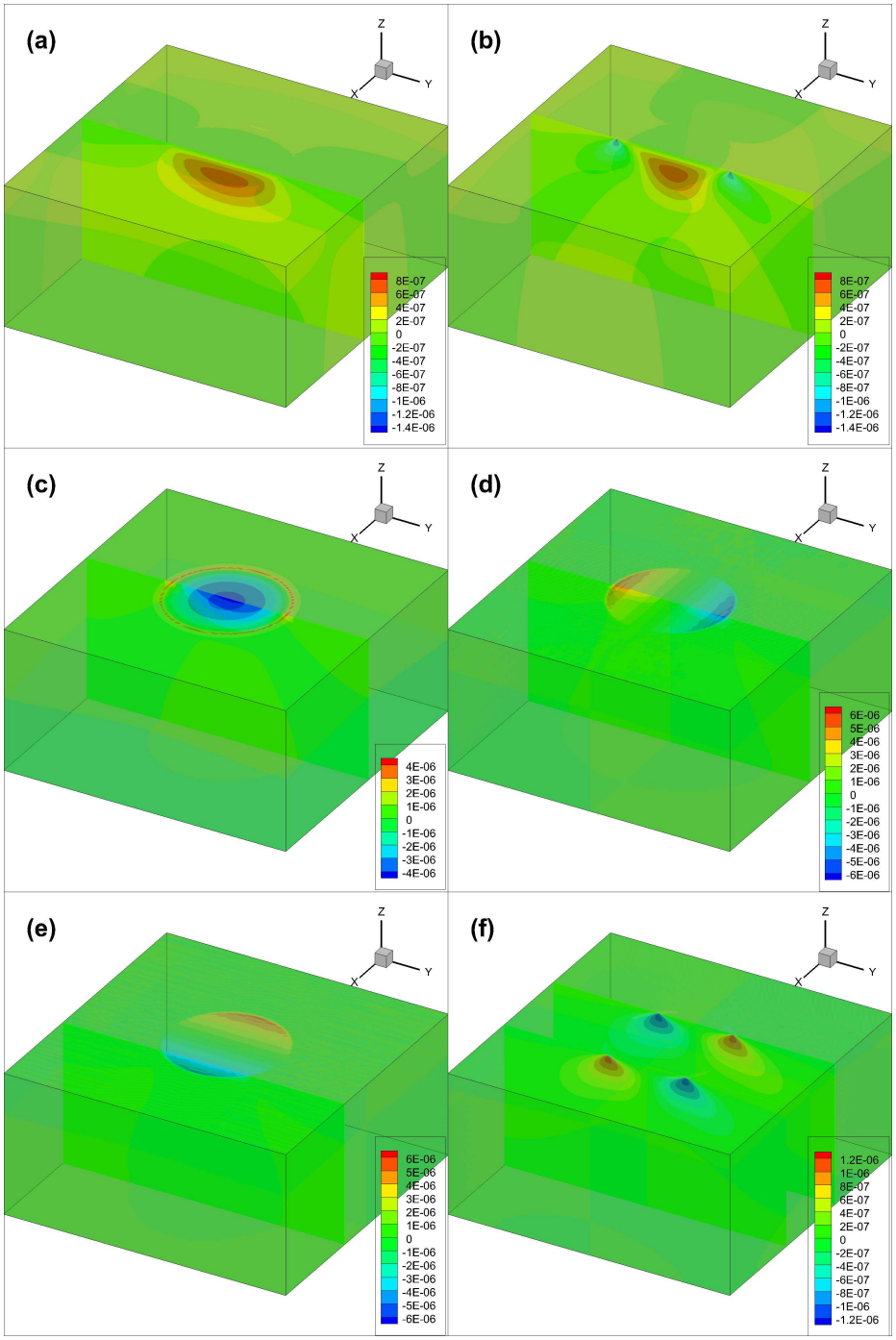

Figure 5.5: (Electromechanical responses of piezoelectric materials) strains: (a) ε_{11}, (b) ε_{22}, (c) ε_{33}, (d) ε_{23}, (e) ε_{13} and (f) ε_{12}.

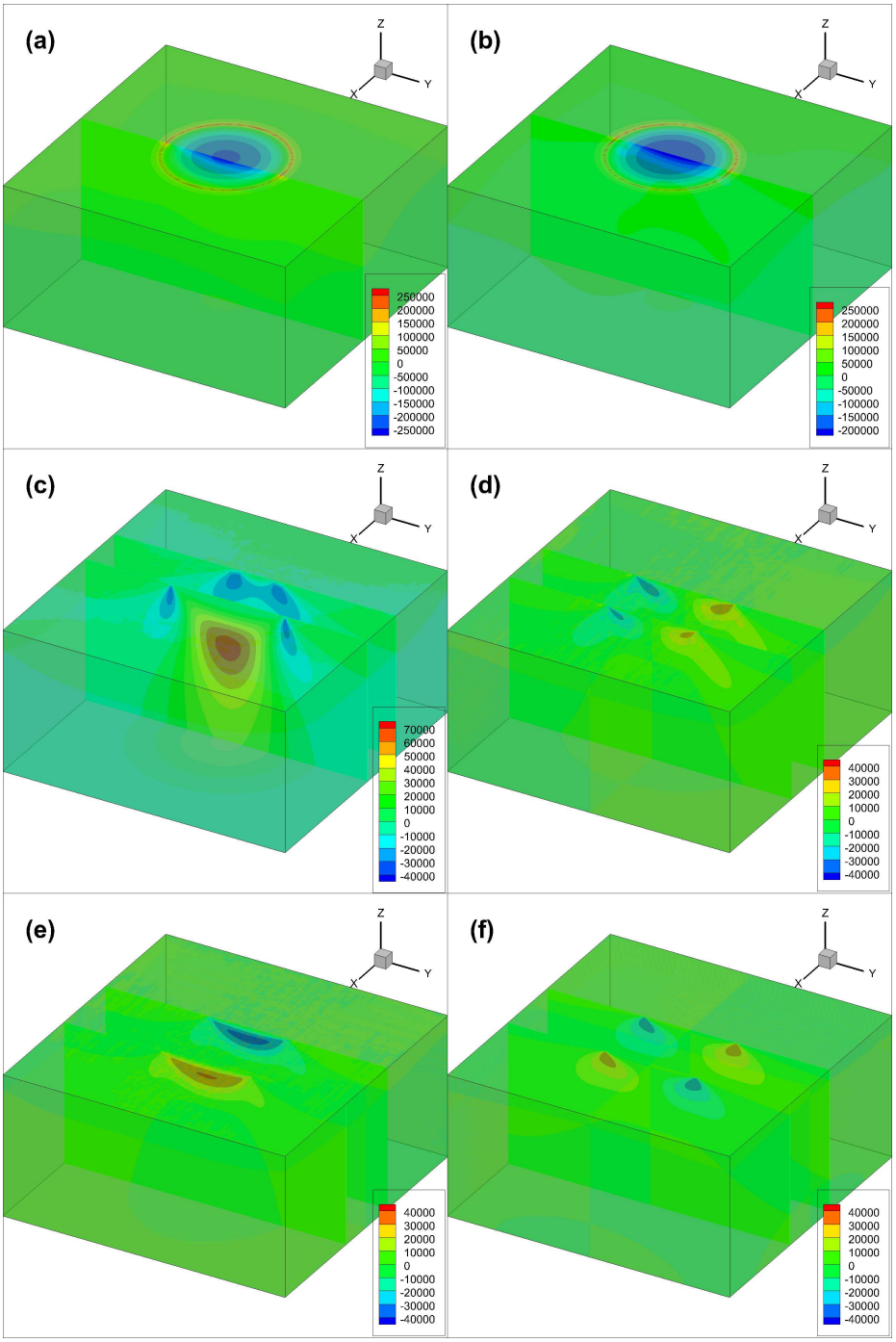

Figure 5.6: (Electromechanical responses of piezoelectric materials) stresses: (a) σ_{11}, (b) σ_{22}, (c) σ_{33}, (d) σ_{23}, (e) σ_{13} and (f) σ_{12}.

piezoelectric materials. Assume that the instantaneous polarization is in a quadratic profile, that is,

$$\mathbf{P}(x_1, x_2, x_3) = P_0 x_3^2 \mathbf{k} \tag{5.10}$$

Numerical simulations are carried out for $P_0 = 10^2$, $P_0 = 10^4$ and $P_0 = 10^6$. For the sake of simplicity, only the resulting distributions of displacements (deformations) for these cases are illustrated in figures (5.7), (5.8) and (5.9).

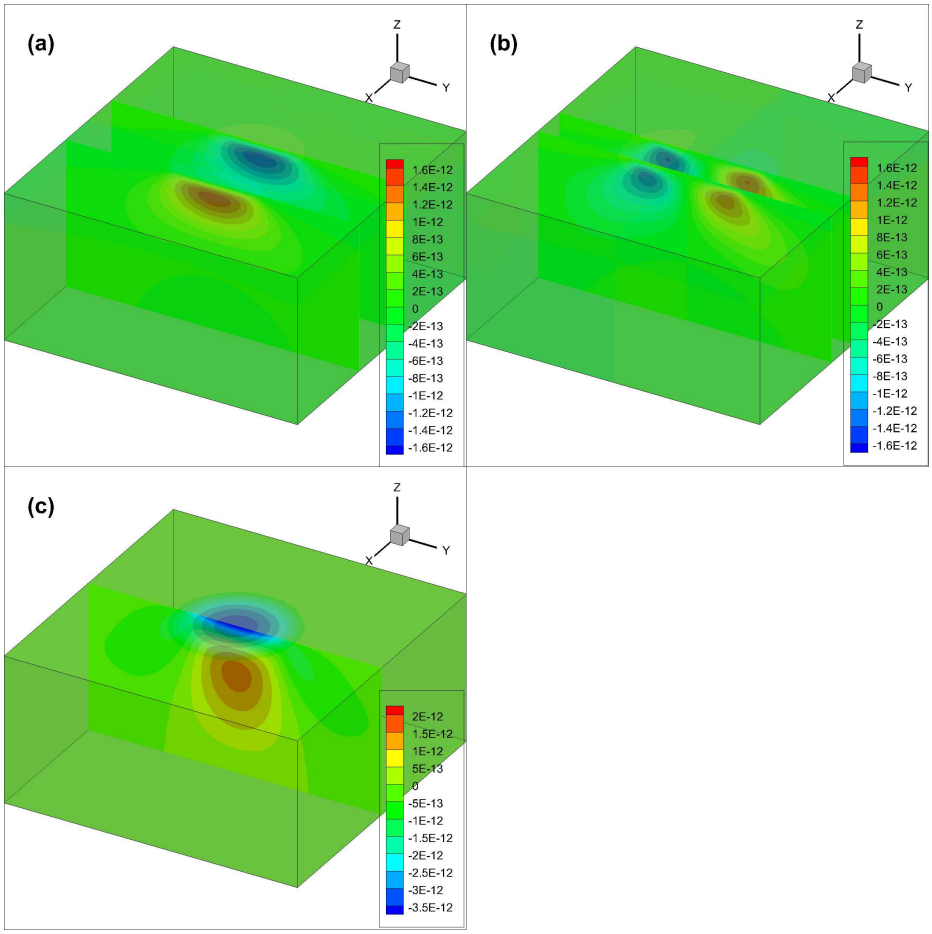

Figure 5.7: (Electromechanical responses of piezoelectric materials) displacement for non-zero polarization with $P_0 = 10^2$: (a) u_1, (b) u_2 and (c) u_3.

It can be seen from the illustrations that as the strength of the polarization increases, its influence on the x_3-displacement is getting more dominant over the influence from the applied electric poten-

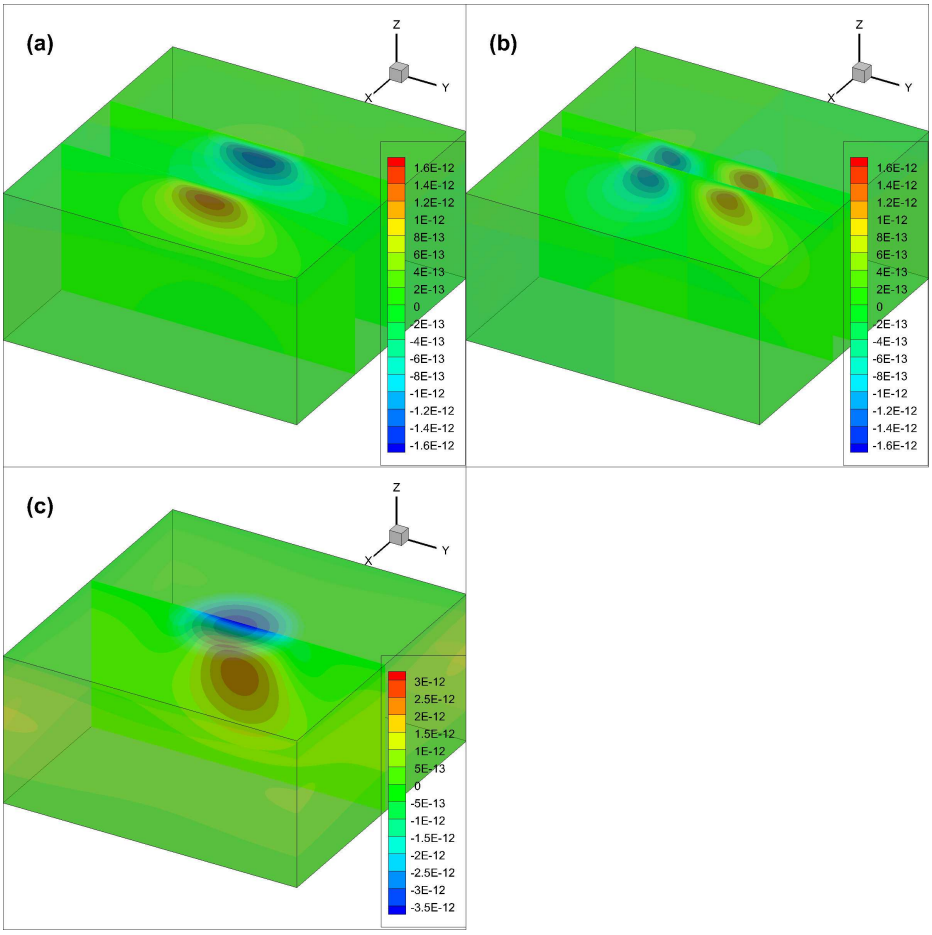

Figure 5.8: (Electromechanical responses of piezoelectric materials) displacement for non-zero polarization with $P_0 = 10^4$: (a) u_1, (b) u_2 and (c) u_3.

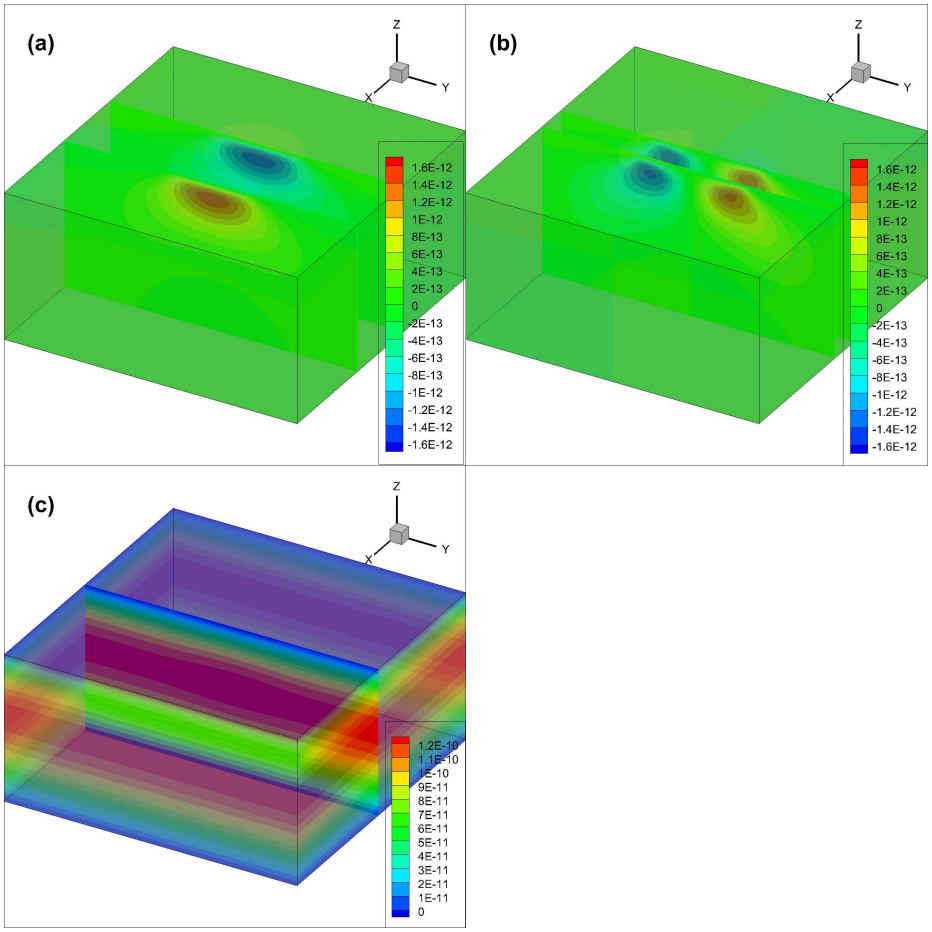

Figure 5.9: (Electromechanical responses of piezoelectric materials) displacement for non-zero polarization with $P_0 = 10^6$: (a) u_1, (b) u_2 and (c) u_3.

tial over the top surface. In Fig. 5.7, the polarization is still weak, thus the displacement in x_3 is similar to the simulated pattern using zero polarization in Fig. 5.4. As the polarization is increasing to $P_0 = 10^4$, its influence is getting significant, the distribution of displacement in x_3 is disturbed, as seen in 5.8. A more delicate examination shows that the magnitude of the displacement in x_3 is decreased, due to the partial compensation of polarization to the applied electric potential. Finally as the polarization is increased to $P_0 = 10^6$, as seen in Fig. 5.9, the influence becomes the greatest of all the cases being studied. The influence of the applied electric potential become negligible, compared to polarization. Thus the displacement in x_3 is mainly due to polarization. Physically speaking, the sample is pulled up by the polarization.

5.2.2 SPM of ferroelectric materials

Ferroelectric materials possess spontaneous electric polarizations that can be reversed by the application of external electric fields. Ferroelectric materials are considered as a sub-class of piezoelectric materials. They can be characterized by their domain at nanoscale using the Piezo-response force microscopy (PFM).

Piezo-response force microscopy (PFM) is a variant of atomic force microscopy (AFM) that allows imaging and manipulation of ferroelectric domains. The mechanism of PFM is similar to that of AFM. A sharp conductive scanning probe is brought into contact with the surface of a ferroelectric (or piezoelectric) material. A voltage V_0 is applied to the specimen through the tip contacting the surface. This voltage will induce or excite a local out-of-plane deformation u_3 and out of plane deformations u_1 and u_2 through the converse piezoelectric effect (CPE). These resulting deflections of the probe cantilever is detected by a split photodiode detector. By scanning the SPM tip over the surface of the probed specimen, distributions of displacement fields can be obtained. The topography and ferroelectric domains can be imaged simultaneously with high resolution. Notice that if the specimen is piezoelectric or ferroelectric, the magnitudes of the displacements can be correlated with the piezoelectic coefficients, while the phase can be correlated with the polarity of the polarization.

While the ferroelectric domain structures can be inferred from the SPM scanning, the correlation between PFM mappings and the underlying ferroelctric structure is often nontrivial. Due to the

fact that the tip induced displacements are governed by long-range electro-elastic interactions, the response is not only affected by the two-dimensional (2D) polarization on the surface, but also influenced by the three-dimensional (3D) polarization distribution.

In this section we aim to simulate the SPM response of a ferroelectric material and further investigate if the domain pattern of the surface can give any insight into the real 3D ferroelectric domain pattern.

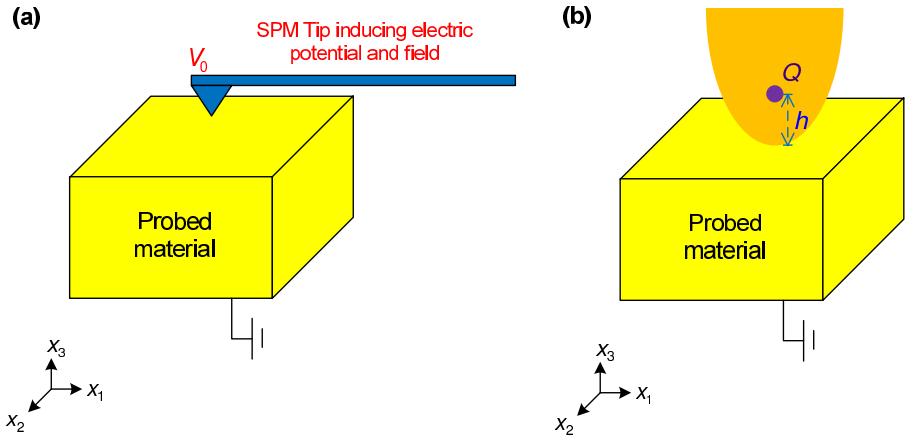

Figure 5.10: Configuration of SPM experiment

We consider a typical SPM experiment, as shown in figure (5.10), where a charged SPM tip is used to induce and probe the piezo-electric vibration of a homogeneous ferroelectric. The potential distribution induced by the charged SPM tip can be determined using the method of image charge. The resulting electric field $\mathbf{E}(\mathbf{x})$ and potential $\phi(\mathbf{x})$ distributions are evaluated as:

$$\begin{aligned} E_i &= -\frac{\partial \phi}{\partial x_i} \\ \phi &= \frac{Q}{2\pi\varepsilon_0(\kappa+1)\sqrt{\rho^2+\left(\frac{x_3}{\gamma}+d\right)}}, \end{aligned} \tag{5.11}$$

where $Q = 2\pi\varepsilon_0 r V_0 \frac{\kappa+1}{\kappa}$ is the equivalent point charge, with V_0 and r being the potential applied and the radius of the SPM tip, ε_0 the permittivity of vacuum, and $\kappa = \sqrt{\varepsilon_{11}\varepsilon_{33}}$ the effective permittivity of the specimen; $\gamma = \sqrt{\frac{\varepsilon_{33}}{\varepsilon_{11}}}$ measures the dielectric anisotropy of the specimen, $d = \frac{r}{k}$ is the

spacing between the effective point charge Q and the probed surface and $\rho = \sqrt{x_1^2 + x_2^2}$ is the polar coordinate of the point of interests.

This electric field induced by the SPM tip will in turn induces a piezoelectic strain field (eigen-strain) denoted by:

$$\varepsilon^s(\mathbf{x}) = \mathbf{d}_{piezo}(\mathbf{x})\mathbf{E}(\mathbf{x}), \tag{5.12}$$

where $\mathbf{d}$ is the piezoelectric tensor. With this eigenstrain, the elasticity problem can be solved for displacements (as deformation), strains and stresses.

The simulation is implemented for BFO in a $100 \times 100 \times 200$ grid. The material parameters are: $c_1 = 80 \times 10^9$, $c_2 = 30 \times 10^9$, $c_3 = 20 \times 10^9$, $d_{13} = -79.0 \times 10^{-12}$, $d_{23} = -79.0 \times 10^{-12}$, $d_{33} = 191.0 \times 10^{-12}$, $d_{42} = 270.0 \times 10^{-12}$, $d_{51} = 270.0 \times 10^{-12}$. The simulated pattern of the resulting SPM response of the top surface of the sample, is shown in figure (5.11).

In fact, our approach also generate the distribution of displacements over the entire domain, as shown in figure (5.12). Since the deformations are localized, the distributions are zoomed near the location of action of the SMP tip to give better and clearer images. The distributions of strains and stresses in principle can also be evaluated but since they are not of particular interest in this study and we skip their graphs.

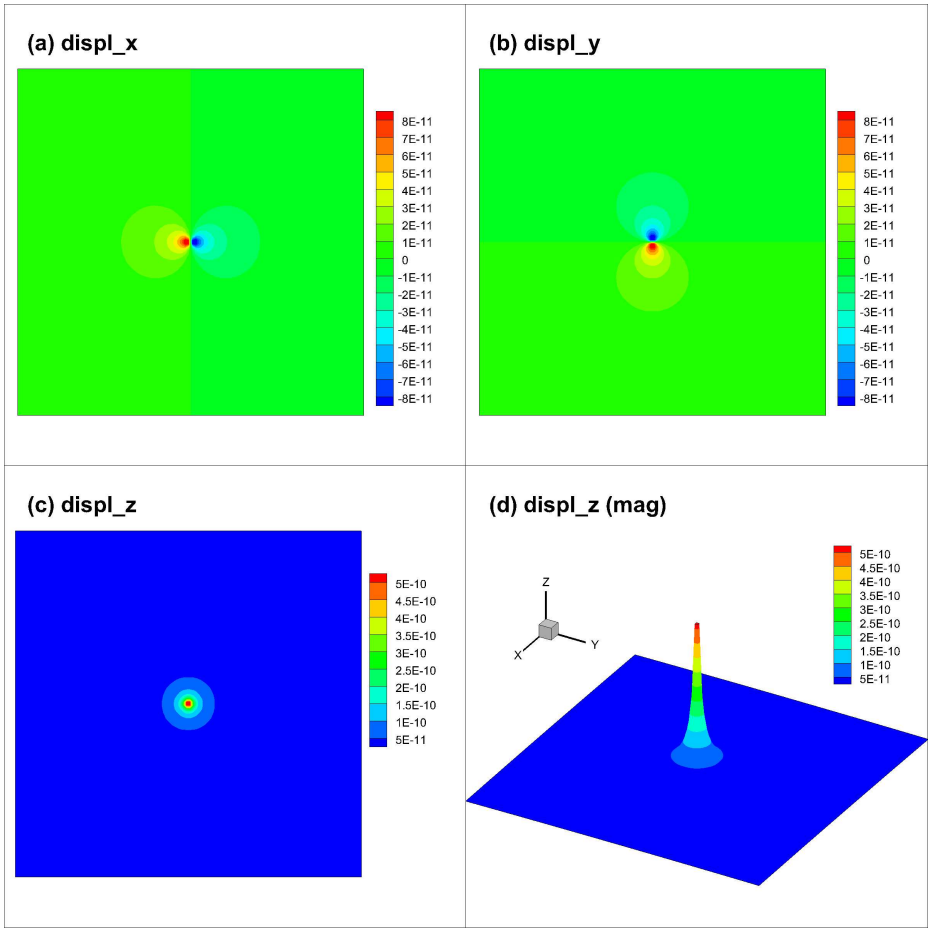

Figure 5.11: (SPM) distribution of displacements on probed surface. (a) u_1; (b) u_2; (c) u_3; (d) magnitude of u_3 as 3D plot

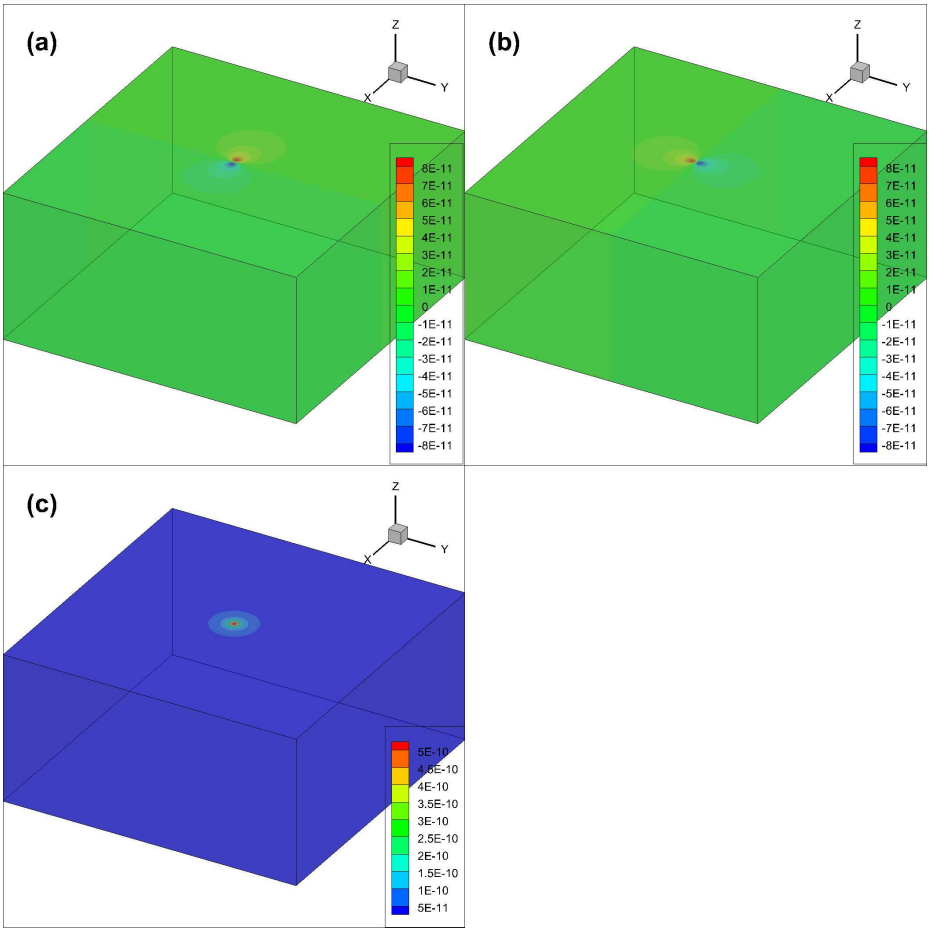

Figure 5.12: (SPM) Distribution of displacements on probed specimen in three-dimensions. (a) u_1; (b) u_2; (c) u_3;

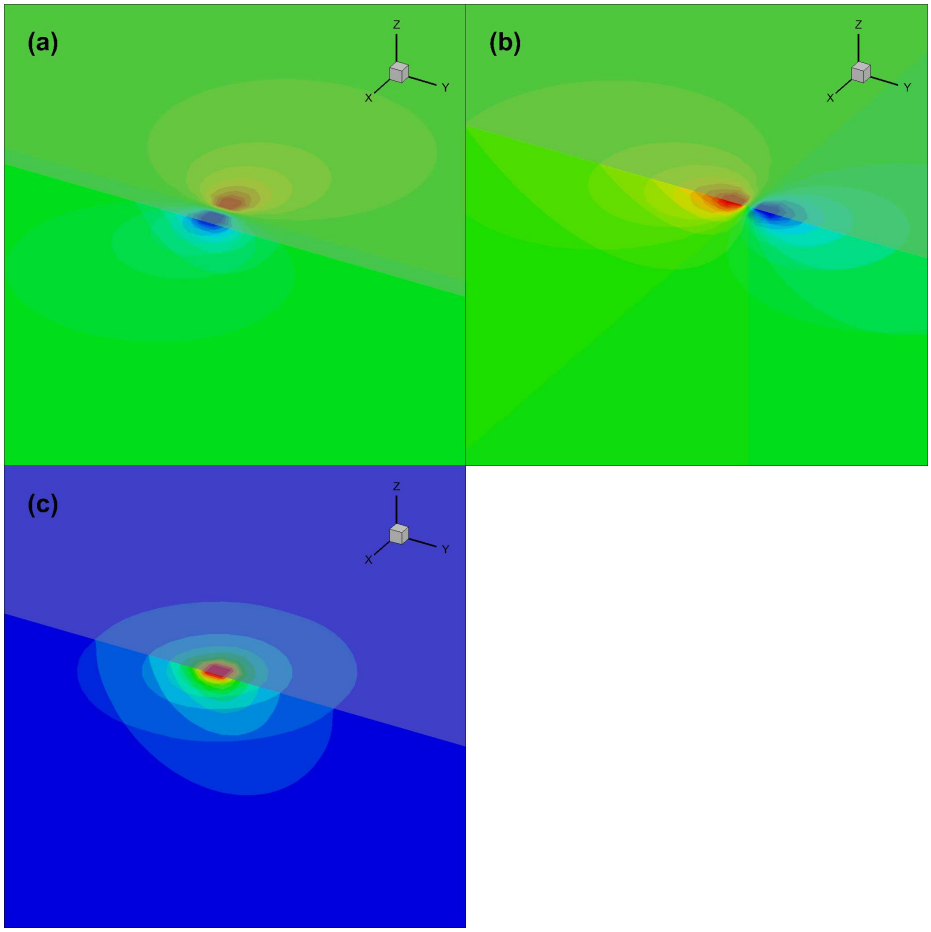

Figure 5.13: (SPM) Distribution of displacements on probed specimen in three-dimensions, zoomed near the SPM tip, to explore the local responses. (a) u_1; (b) u_2; (c) u_3;

5.3 Discussions and Conclusions

In this chapter, we proposed two methods (eigen-expansion and finite-difference) for solving the Maxwell's equation and the mechanical equilibrium equation numerically. We then apply these numerical schemes to solve two problems, namely, the electromechanical response of piezoelectric materials and SPM response of ferroelctric domain.

By incorporating these numerical solution to phase field model, we may develop phase field simulation for macro-scale application, where periodicity is partial released. Some possible projects include: (1) Phase field simulation of shape memory alloys in macroscopic scale. (2) Phase field simulation of polarization switching in piezoelectric materials by probing. (3) SPM scanning for 3D reconstruction of ferroelectric domains. (4) Phase field simulation of electochemical dynamics in Lithion Ion Batterys, and many more unlisted here.

Chapter 6

PHASE FIELD SIMULATION IN FINITE GEOMETRIES

Previous works on phase field simulation have assumed periodic boundary conditions in all directions which makes it hard to simulate domain patterns and capture various physical behaviours in realistic configurations, such as thin film being tested under piezo-response force microscopy. In order to extend the scopes of simulation, phase field simulation for finite geometry will be developed where periodicity along the out-of-plane direction is released [76]. Thus more realistic physical boundary conditions can be considered, which are critical in the role of domain switching. For instance, the variants in the domain may switch to some other variants upon applying force or electric potential or field on the boundaries.

6.1 Unconventional Phase Field Simulation of Shape Memory Alloys in Finite Geometry

Recall that the domain patterns and domain dynamics (evolution) of the participating variants in shape memory alloys (SMA) as well as other multi-functional materials are governed by phase field simulation. If N variants are considered, a set of $(N-1)$ characteristic functions, denoted by $\{\gamma_i, 1 \leq i \leq N\}$, are needed in the formulation. Each variant is associated with a transformation strain, $\varepsilon^{(i)}$. Since each point of the domain can only be occupied by 0 or 1 to denote occurrence of some variant so that $\sum_{i=1}^{N} \gamma_i(\mathbf{x}) = 1$, these N characteristic functions can be reduced to another set of $(N-1)$ laminated characteristic functions $\{\mu_i, 0 \leq i \leq N-1\}$. The effective inhomogeneous transformation strain field (eigen-strain) is given by:

$$\varepsilon^s(\mathbf{x}) = \sum_{i=1}^{N} \gamma_i(\mathbf{x}) \varepsilon^{(i)}, \tag{6.1}$$

where

$$\begin{aligned}
\gamma_1 &= \mu_1 \\
\gamma_2 &= (1-\mu_1)\mu_2 \\
\gamma_3 &= (1-\mu_1)(1-\mu_2)\mu_3 \\
&\cdots \\
\gamma_{N-1} &= (1-\mu_1)(1-\mu_2)\cdot(1-\mu_{N-2})\mu_{N-1} \\
\gamma_N &= (1-\mu_1)(1-\mu_2)\cdot(1-\mu_{N-2})(1-\mu_{N-1})
\end{aligned} \tag{6.2}$$

The set of laminated characteristic functions can be shorthanded as a vector spatial functions:

$$\mu(\mathbf{x}) = \left\{ \begin{array}{c} \mu_1(x_1,x_2) \\ \mu_2(x_1,x_2) \\ \vdots \\ \mu_{N-2}(x_1,x_2) \\ \mu_{N-1}(x_1,x_2) \end{array} \right\} \tag{6.3}$$

The domain pattern is obtained by minimizing the energy functional:

$$\mathscr{I}(\mu) = \int_\Omega \left\{ W^{int}(\mu) + W^{ani}(\mu) + W^{elas}(\mu) \right\} d\mathbf{x}, \tag{6.4}$$

where $W^{int}(\mu) = A|\nabla\mu|^2$ is the interfacial energy that separates different variants, $W^{ani}(\mu) = \sum_{i=1}^{N-1} K_i \mu_i^2 (1-\mu_i)^2$ is the anisotropic energy to make sure that numerical values of the characteristic functions can only be 0 or 1, and $W^{elas} = \frac{1}{2}[\varepsilon - \varepsilon^s] \cdot \mathbf{C}[\varepsilon - \varepsilon^s]$ is the elastic energy. Recall that $A > 0$ is the gradient coefficient and $K_i > 0$ is the anisotropy coefficients. In most simulations, K_i is of the similar order of magnitude as $\mathbf{C}\varepsilon^{(i)} \cdot \varepsilon^{(i)}$.

The evolution equations for the laminated characteristic functions $\mu = \mu(x_1, x_2, t)$ are governed by the evolution equations that results from taking variational derivatives of the total energy func-

tions with respect to μ:

$$\begin{aligned}\frac{\partial \mu}{\partial t} &= M\frac{\delta \mathscr{I}}{\delta \mu} = M\mathbf{F}(\mu)\\ \frac{\partial \mu}{\partial t} &= M\left(\mathbf{F}^{int}(\mu)+\mathbf{F}^{ani}(\mu)+\mathbf{F}^{elas}(\mu)\right),\end{aligned} \tag{6.5}$$

where $\mathbf{F}^{int} = 2A\nabla^2\mu$ is the interfacial driving force, $\mathbf{F}^{ani} = -\frac{\partial W^{ani}}{\partial \mu}$ is the anisotropy driving force, $\mathbf{F}^{elas} = \sigma \cdot \frac{\partial \varepsilon^s(\mu)}{\partial \mu}$ is the elastic driving force, and $M > 0$ is the mobility constant.

Assume that the domain of computation is originally:

$$\{0 \le x_1 \le L_1, 0 \le x_2 \le L_2, 0 \le x_3 \le L_3\} \tag{6.6}$$

Upon normalization with the following variables:

$$\begin{aligned}{x_1}^* &= \frac{x_1}{L_3}\\ {x_2}^* &= \frac{x_2}{L_3}\\ {x_2}^* &= \frac{x_3}{L_3}\\ t^* &= 2MKt\end{aligned} \tag{6.7}$$

the evolution equation becomes:

$$\frac{\partial \mu}{\partial t^*} = D\left(\frac{\partial^2 \mu}{\partial {x_1}^{*2}} + \frac{\partial^2 \mu}{\partial {x_2}^{*2}} + \frac{\partial^2 \mu}{\partial {x_3}^{*2}}\right) + \frac{1}{2K}\left[\mathbf{F}^{ani}(\mu)+\mathbf{F}^{elas}(\mu)\right], \tag{6.8}$$

where $D = \frac{\frac{A}{K}}{L_2^2}$ and the normalized computational domain normalizes to:

$$\left\{0 \le x^* \le \alpha_1 \equiv \frac{L_1}{L_3}, 0 \le x^* \le \alpha_2 \equiv \frac{L_2}{L_3}, 0 \le y^* \le 1\right\} \tag{6.9}$$

From now on, without loss of generality, we will drop the superscript $(*)$ in our proceeding development. To solve the equation numerically, discretization in time domain is implemented as previous works. Recall that periodicity is assumed along in-plane directions (x_1, x_2). FFT is applied along x_1 and x_2, while finite difference is taken along the out-of-plane direction x_3. Also denote for

simplification:

$$\mathbf{F} \equiv \frac{1}{2K}\left[\mathbf{F}^{ani}(\mu) + \mathbf{F}^{elas}(\mu)\right] \tag{6.10}$$

With these, in successive steps, the equation becomes:

$$\begin{aligned}
\frac{\mu^{k+1}-\mu^{k}}{\Delta t} &= D\left(\frac{\partial^2 \mu^k}{\partial {x_1}^2} + \frac{\partial^2 \mu^k}{\partial {x_2}^2} + \frac{\partial^2 \mu^k}{\partial {x_3}^2}\right) + \mathbf{F}(\mu^k) \\
\frac{\overline{\mu}^{k+1}-\overline{\mu}^{k}}{\Delta t} &= D\left(-k_1^2\overline{\mu}^k - k_2^2\overline{\mu}^k + \frac{\partial^2 \overline{\mu}^k}{\partial {x_3}^2}\right) + \overline{\mathbf{F}(\mu^k)}
\end{aligned} \tag{6.11}$$

where k_1 and k_2 are the Fourier coordinates reciprocal to the original coordinates x_1 and x_2, $\overline{f} = \overline{f}(k_1, k_2, x_3$ denotes the FFT of $f = f(x_1, x_2, x_3)$ along the out-of-plane directions.

Along the out-of-plane direction, x_3, the derivative is translated into a matrix of finite difference for second order, denoted by:

$$\frac{\partial^2}{\partial {x_3}^2} = \frac{1}{(\Delta L)^2}\begin{bmatrix}
d_1 & d_2 & & & & & & \\
1 & -2 & 1 & & & & & \\
 & & \ddots & & & & & \\
 & & 1 & -2 & 1 & & & \\
 & & & & \ddots & & & \\
 & & & & 1 & -2 & 1 & \\
 & & & & & d_3 & d_4 &
\end{bmatrix}, \tag{6.12}$$

where ΔL is the size of the subdivision in x_3. The elements, d_1, ..., d_4, in the first and last rows of this matrix depends on the boundary conditions being considered. There are two possible sets of elements, as listed in the following table.

	choice 1	choice 2
d_1	-2	$-\frac{2}{3}$
d_2	2	$\frac{2}{3}$
d_3	2	$\frac{2}{3}$
d_4	-2	$-\frac{2}{3}$

Table 6.1: Two choices of elements on top and bottom rows of the second order differentiation matrix with Neumann boundary conditions at end points

In addition, implicit scheme converges faster and is more stable. This is archived by replacing the μ^k to μ^{k+1}. With these, the current numerical scheme is re-casted into matrix form:

$$\begin{aligned}
\frac{\mathbf{I}\overline{\mu^{k+1}} - \mathbf{I}\overline{\mu^k}}{\Delta t} &= D\left(-k_1^2\mathbf{I}\overline{\mu^{k+1}} - k_2^2\mathbf{I}\overline{\mu^{k+1}} + \frac{\partial^2}{\partial {x_3}^2}\overline{\mu^{k+1}}\right) + \overline{\mathbf{F}(\mu^k)} \\
\mathbf{I}\overline{\mu^{k+1}} - \mathbf{I}\overline{\mu^k} &= -D\left(k_1^2\mathbf{I} + k_2^2\mathbf{I}\right)\overline{\mu^{k+1}}\Delta t + \frac{\partial^2}{\partial {x_3}^2}\overline{\mu^{k+1}}\Delta t + \overline{\mathbf{F}(\mu^k)}\Delta t \\
\left[\mathbf{I} + D\Delta t\left(k_1^2\mathbf{I} + k_2^2\mathbf{I}\right) - \frac{\partial^2}{\partial {x_3}^2}\right]\overline{\mu^{k+1}} &= \mathbf{I}\overline{\mu^k} + \overline{\mathbf{F}(\mu^k)}\Delta t \\
\mathbf{A}\overline{\mu^{k+1}} &= \mathbf{I}\overline{\mu^k} + \mathbf{b}
\end{aligned} \tag{6.13}$$

In the implementation, the term $\mathbf{F}$ need some manipulations with the boundary conditions. Recall that:

$$\mathbf{F} \equiv \frac{1}{2K}\left(\mathbf{F}^{ani} + \mathbf{F}^{elas}\right) \tag{6.14}$$

In component form, we have:

$$\begin{aligned}
F_i &= \frac{1}{2K}\left(F_i^{ani} + F_i^{elas}\right) \\
&= \frac{1}{2K}\left(-\mu_i(1-\mu_i)(1-2\mu_i) + \sigma \cdot \frac{\partial \varepsilon^s}{\partial \mu_i}\right)
\end{aligned} \tag{6.15}$$

All ingredients can be computed directly from μ_i except for σ for which some physical consideration

should be taken into account.

For domain pattern of Shape Memory Alloys in a realistic configuration to form, we may apply traction on top surface and strain constraint from substrate on bottom surface. In addition, thickness of substrate will also affect the domain near the bottom boundary. They are considered when the stress field σ is computed. For instance, according to figure (6.1), the domain is physically subjected to the mentioned boundary conditions (traction on top surface and substrate on bottom surface).

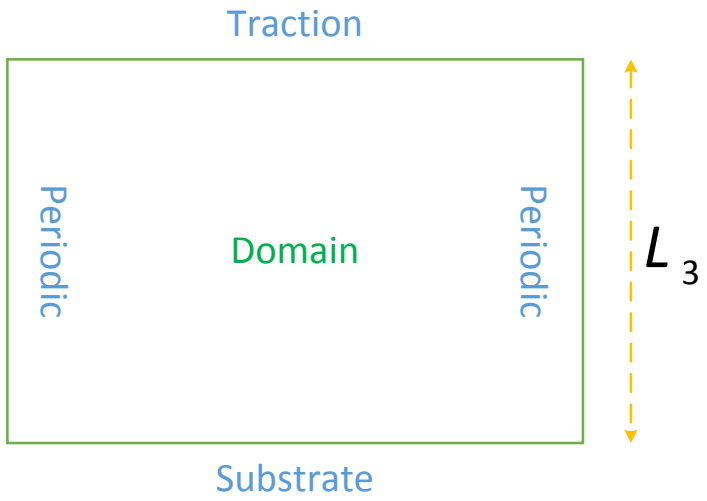

Figure 6.1: Configuration of computational domain for elasticity.

According to the development of non-periodic solution of the elasticity equation in finite geometry discussed in previous chapter, the stress field σ consists of two parts: homogeneous and perturbed solutions, denoted by $\langle\sigma\rangle$ and σ'. The stress field has the decomposition:

$$\sigma = \langle\sigma\rangle + \sigma' \tag{6.16}$$

The homogeneous stress is the macroscopic or average stress which is determined by the misfit strain imposed by the substrate underneath the domain, quantified by $\langle\varepsilon_{11}\rangle \equiv \varepsilon^0_{11}$, $\langle\varepsilon_{12}\rangle \equiv \varepsilon^0_{22}$ and $\langle\varepsilon_{12}\rangle \equiv \varepsilon^0_{12}$. Assume no homogenous traction is applied to the sample, so that, $\langle\sigma_{13}\rangle = \langle\sigma_5\rangle = 0$, $\langle\sigma_{23}\rangle = \langle\sigma_4\rangle = 0$ and $\langle\sigma_{33}\rangle = \langle\sigma_3\rangle = 0$. The homogeneous stress components are computed via the

constitutive equations without eigen-strain:

$$\langle\sigma\rangle = \mathbf{C}\,\langle\varepsilon\rangle$$

$$\begin{Bmatrix} \langle\sigma_1\rangle \\ \langle\sigma_2\rangle \\ \langle\sigma_3\rangle = 0 \\ \langle\sigma_4\rangle = 0 \\ \langle\sigma_5\rangle = 0 \\ \langle\sigma_6\rangle \end{Bmatrix} = \begin{bmatrix} c_1 & c_3 & c_3 & 0 & 0 & 0 \\ c_3 & c_1 & c_3 & 0 & 0 & 0 \\ c_3 & c_3 & c_1 & 0 & 0 & 0 \\ 0 & 0 & 0 & c_2 & 0 & 0 \\ 0 & 0 & 0 & 0 & c_2 & 0 \\ 0 & 0 & 0 & 0 & 0 & c_2 \end{bmatrix} \begin{Bmatrix} \langle\varepsilon_1\rangle = \varepsilon^0_{11} \\ \langle\varepsilon_2\rangle = \varepsilon^0_{22} \\ \langle\varepsilon_3\rangle \\ \langle\varepsilon_4\rangle \\ \langle\varepsilon_5\rangle \\ \langle\varepsilon_6\rangle = \varepsilon^0_{12} \end{Bmatrix} \tag{6.17}$$

The six unknowns of the equation are solved as:

$$\begin{aligned} \langle\varepsilon_3\rangle &= -\frac{c_3\varepsilon^0_{11} + c_3\varepsilon^0_{22}}{c_1} \\ \langle\varepsilon_4\rangle &= 0 \\ \langle\varepsilon_5\rangle &= 0 \\ \langle\sigma_6\rangle &= c_2\varepsilon^0_{12} \\ \langle\sigma_1\rangle &= \frac{c_1^2 - c_3^2}{c_1}\varepsilon^0_{11} + \frac{c_1c_3 - c_3^2}{c_1}\varepsilon^0_{22} \\ \langle\sigma_2\rangle &= \frac{c_1c_3 - c_3^2}{c_1}\varepsilon^0_{11} + \frac{c_1^2 - c_3^2}{c_1}\varepsilon^0_{22} \end{aligned} \tag{6.18}$$

Thus the homogeneous stress field is:

$$\langle\sigma\rangle = \begin{Bmatrix} \langle\sigma_1\rangle \\ \langle\sigma_2\rangle \\ \langle\sigma_3\rangle \\ \langle\sigma_4\rangle \\ \langle\sigma_5\rangle \\ \langle\sigma_6\rangle \end{Bmatrix} = \begin{Bmatrix} \frac{c_1^2 - c_3^2}{c_1}\varepsilon^0_{11} + \frac{c_1c_3 - c_3^2}{c_1}\varepsilon^0_{22} \\ \frac{c_1c_3 - c_3^2}{c_1}\varepsilon^0_{11} + \frac{c_1^2 - c_3^2}{c_1}\varepsilon^0_{22} \\ 0 \\ 0 \\ 0 \\ c_2\varepsilon^0_{12} \end{Bmatrix} \tag{6.19}$$

The second part of the stress field, known as the perturbed stress, is affected by the effective inhomogeneous strains of the participating variants in the domain, $\varepsilon^s(\mathbf{x})$. This stress field is com-

puted by solving a set of partial differential equations that are periodic along the in-plane directions. Along the out-of-plane direction, traction is applied on top surface. The bottom surface is adhered to substrate that impose a misfit strain so that the displacement components may not necessarily be zero. Also, for a differential equation to yield a physically unique solution, a displacement boundary condition is essential. To resolve this issue, we assume that the displacements far away below the bottom surface of the domain are zero. And to implement this numerically, we extend the computational domain below the original domain with a buffer domain that allows the displacement to degenerate to zero. The schematic is shown in figure (6.2).

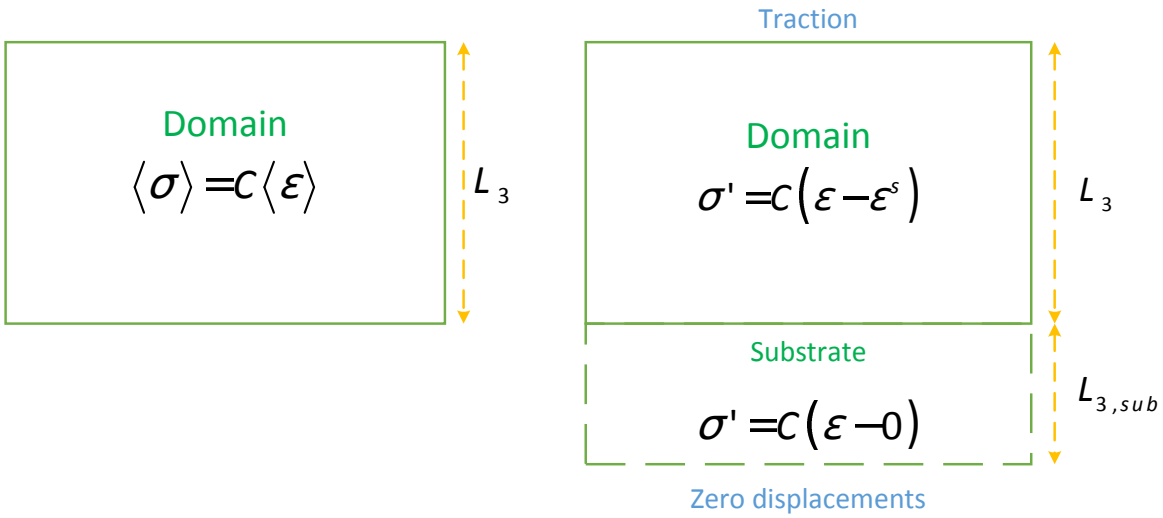

Figure 6.2: Schematic showing how the elasticity equation is solved by decomposing into two parts. The first part represents a macroscopic / homogeneous solution. The second part is a perturbed solution that considers realistic boundary conditions

Recall that the height of the original domain is L_3. We define the imagined substrate has a thickness $L_{3,sub}$. The total height of the computational domain for the perturbed portion of stress is $L_{3,all} = L_3 + L_{3,sub}$. If the computational size associated with the height of the original domain is N_3, the computational size of the added imagined substrate will be approximately $N_{3,sub} = \frac{L_{3,sub}}{L_3} N_3$.

We solve the perturbed stress σ' from the elasticity equation:

$$\begin{cases} \sigma' &= \mathbf{C}\left(\varepsilon - \widehat{\varepsilon^s}\right) \\ \nabla\sigma' &= 0 \end{cases},$$

$$\mathbf{x} \in \{0 \le x_1 \le L_1, 0 \le x_2 \le L_2, -L_{3,sub} \le x_3 \le L_3,\} \tag{6.20}$$

where $\widehat{\varepsilon^s}$ is the modified eigen-strain field of the extended domain (original domain plus added substrate domain). This modified eigen-strain is identical to the same eigen-strain field in the original domain and is zero in the extended substrate domain.

$$\widehat{\varepsilon^s} = \begin{cases} \varepsilon^s & : 0 \le x_3 \le L_3 \\ 0 & : -L_{3,sub} \le x_3 \le 0 \end{cases} \tag{6.21}$$

In the first set of simulations, we will consider shape memory alloys with two variants whose transformation strains are given by:

$$\varepsilon^{(1)} = \alpha \begin{bmatrix} 0 & 0 & 0 \\ 0 & 1 & 0 \\ 0 & 0 & -1 \end{bmatrix}, \varepsilon^{(2)} = \alpha \begin{bmatrix} 0 & 0 & 0 \\ 0 & -1 & 0 \\ 0 & 0 & 1 \end{bmatrix}. \tag{6.22}$$

We will first simulate the domain pattern and analyze the effects of various thicknesses of added substrate, $L_{3,sub}$. We will also study the domain pattern that results from imposing different misfit strains. We will also study the domain dynamics of the domain structure by applying traction over the top surface of the domain.

6.1.1 Simulation 1: Domain pattern formation of SMA and effects of varying substrate thickness

We study the pattern formation of shape memory alloy in finite geometry where the top surface is traction-free and the bottom surface is subjected to substrate with no misfit strain. All four lateral faces are periodic. We investigate the effects of the thickness of the substrate as percentage of the original thickness of the domain. The results are shown in figure (6.3). As we can see from the figure, if there is no substrate, the domain pattern close to the bottom surface is not clear. As the

substrate becomes thicker, the pattern of the two variants become more obvious.

6.1.2 Simulation 2: Domain pattern formation of SMA and effects of misfit strain of substrate

Next we study the effect of the mis-fit strains imposed by the substrate underneath the sample. For all simulations, we assume the thickness to be 50 % of the original thickness of the sample. The magnitude of the mis-fit strain $\langle \varepsilon_{11} \rangle$ is varying linearly from 0.05×0.1 to 0.05×0.6. The resulting domain patterns are shown in figure (6.4). It is seen that as this strain increases, more variant 2 forms.

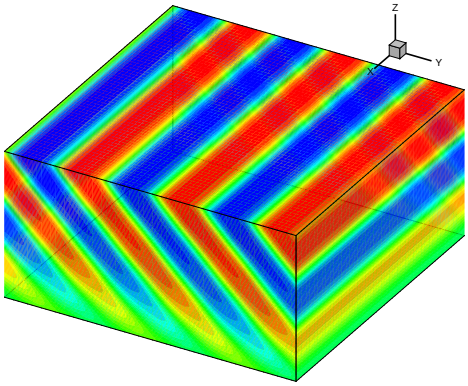

thickness of substrate = 0 (view from top)

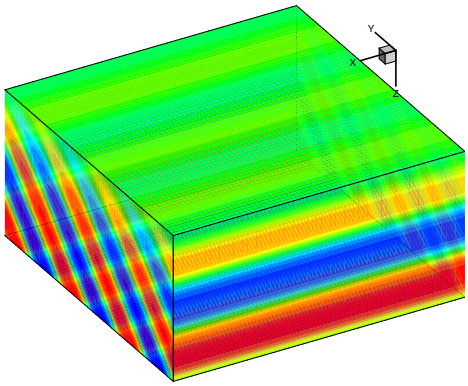

thickness of substrate = 0 (view from bottom)

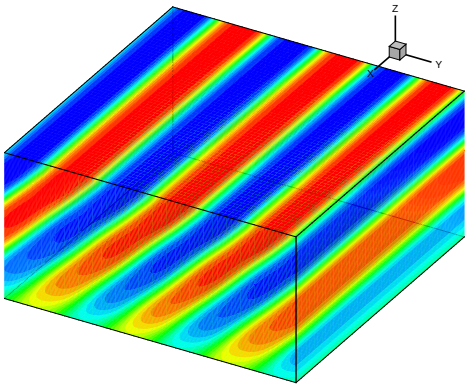

thickness of substrate = 100 (view from top)

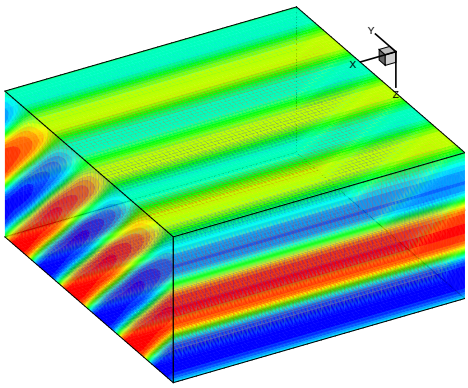

thickness of substrate = 100 (view from bottom)

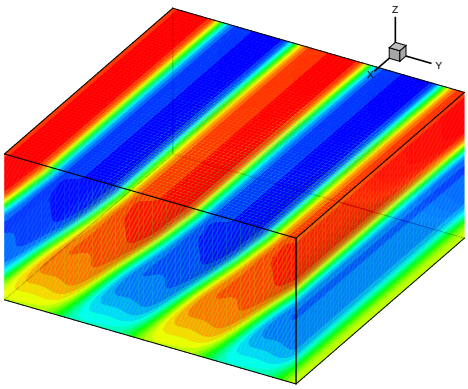

thickness of substrate = 200 (view from top)

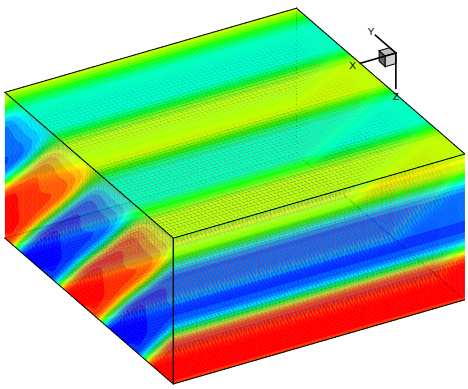

thickness of substrate = 200 (view from bottom)

Figure 6.3: Shape memory alloys with varying thickness of substrate underneath.

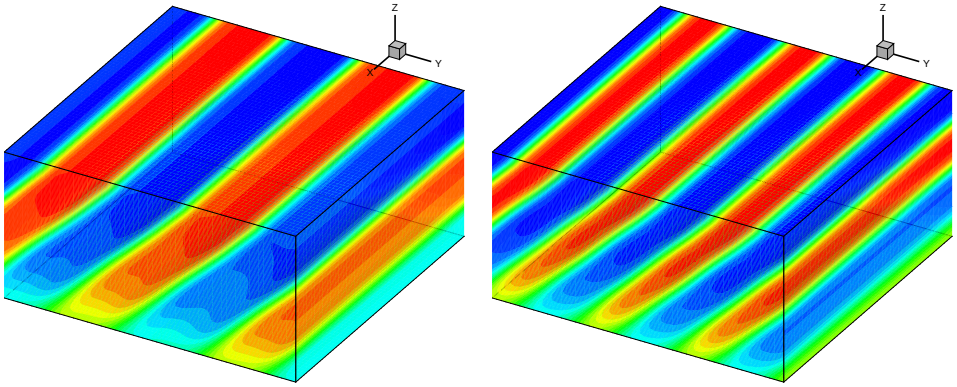

$\langle \varepsilon_{11} \rangle = 0.005 \times 0.1$

$\langle \varepsilon_{11} \rangle = 0.005 \times 0.2$

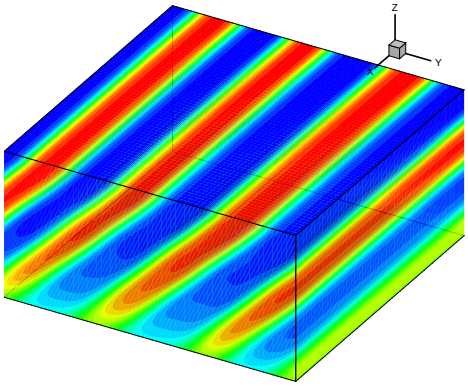

$\langle \varepsilon_{11} \rangle = 0.005 \times 0.3$

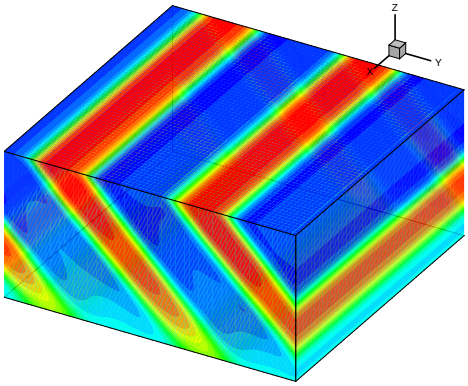

$\langle \varepsilon_{11} \rangle = 0.005 \times 0.4$

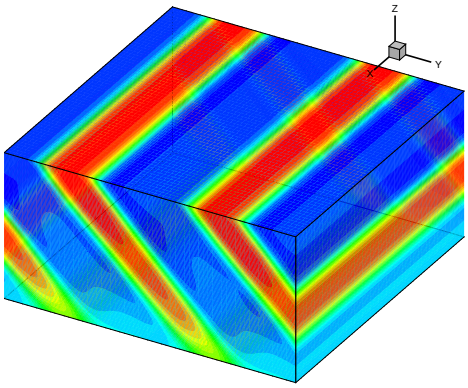

$\langle \varepsilon_{11} \rangle = 0.005 \times 0.5$

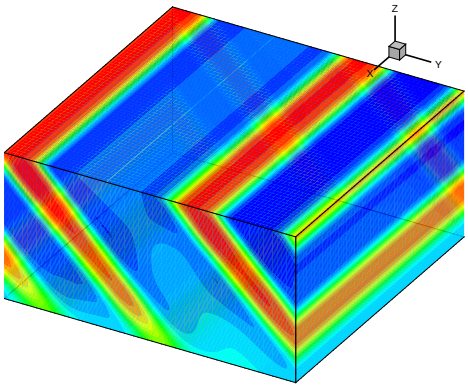

$\langle \varepsilon_{11} \rangle = 0.005 \times 0.6$

Figure 6.4: Shape memory alloys with varying misfit strain of substrate underneath.

6.2 Unconventional Phase Field Simulation of Ferroelectric in Finite Geometry

In this section, we will extend the phase field simulation to include electrostatic components for domains in ferro-electric materials. In brief, the ferroelectricity is a property of certain materials that have a spontaneous electric polarization that can be reversed by the application of an external electric field. This characteristic open a lot of industrial applications as in Varactors for RF / Microwave Circuits, Electro-Optic Modulators, Ferroelectric RAM (FeRAM), Ferroelectric Tunnel Junctions, etc. The formulation of phase field model in ferroelectric will be presented followed by simulations of domain patterns and domain dynamics (or domain switching) by mechanical loading and electrical loading [80, 81, 82].

The unconventional phase field model for ferroelectric materials is simply an extension of that for Shape Memory Alloys in that an addition contribution is invoked to electrostatic effect via spontaneous polarization is considered. The occurrences of N participating variants are quantified by a set of N characteristic functions, denoted by $\{\lambda_i, 1 \le i \le N\}$, or equivalently, a set of $(N-1)$ laminated characteristic functions, denoted by $\{\mu_i, 1 \le i \le N-1\}$. The conversion between these two sets of characteristic functions have been discussed in previous section and is skipped here.

A ferroelectric domain pattern is a mixture of these variants with inhomogeneous distribution of transformation strain and spontaneous polarization given in terms of the characteristic functions and transformation strains, denoted by $\left\{\varepsilon^{(i)}, 1 \le i \le N\right\}$, and instantaneous polarizations, denoted by $\left\{\mathbf{P}^{(i)}, 1 \le i \le N\right\}$, of the participating variants (in the ratios as indicated by their ratios in the mixture):

$$\begin{aligned} \varepsilon^s &= \sum_{i=1}^{N} \lambda_i \varepsilon^{(i)} \\ \mathbf{P}^s &= \sum_{i=1}^{N} \lambda_i \mathbf{P}^{(i)} \end{aligned} \tag{6.23}$$

In other words, these equations establish connection between transformation strain and spontaneous polarization and the set of $(N-1)$ field variable μ_i, and thus it is possible to use $\{\mu_i\}$ as field variables, whose distribution leads to a distribution of transformation strain and spontaneous polarization.

Similar to the unconventional phase field model for Shape Memory Alloys (SMA), anisotropy,

interfacial and elastic energy are included:

$$\begin{aligned} W^{ani} &= \sum_{i=1}^{N-1} K_i \mu_i^2 (1-\mu_i)^2 \\ W^{int} &= \sum_{i=1}^{N-1} A_i \left|\nabla \mu_i\right|^2 \\ W^{elas} &= \frac{1}{2}\left[\varepsilon - \varepsilon^s\right] \cdot \mathbf{C}\left[\varepsilon - \varepsilon^s\right], \end{aligned} \tag{6.24}$$

where the elasticity equation is solved for the strain and stress fields:

$$\begin{cases} \sigma &= \mathbf{C}\left(\varepsilon - \varepsilon^s\right) \\ \nabla\sigma &= 0 \end{cases} \tag{6.25}$$

Recall that in the implementation, the stress field consists of the homogeneous part and the perturbed part. Traction applied over top surface $\mathbf{T} = \{T_x, T_y\}^T$, the thickness $L_{3,sub}$ and the misfit strains $\left\langle \varepsilon_{11}^0 \right\rangle$, $\left\langle \varepsilon_{22}^0 \right\rangle$, $\left\langle \varepsilon_{12}^0 \right\rangle$ of substrate are also considered during the computations.

For ferroelectric with additional electrostatic contribution, we consider the following energy functional:

$$\mathscr{I}(\mu) = \int_\Omega \left(W^{ani}(\mu) + W^{int}(\mu) + W^{elas}(\mu) - \mathbf{E}^0 \cdot \mathbf{P}^s - \sigma^0 \cdot \varepsilon \right) d\mathbf{x} + \frac{1}{2}\int_{R^3} \left|\nabla\phi\right|^2 d\mathbf{x} \tag{6.26}$$

Terms that have not been explained are outlined below:

- $\mathbf{E}^0$ is the external applied electric field, thus $-\int_\Omega \left(\mathbf{E}^0 \cdot \mathbf{P}^s\right) d\mathbf{x}$ refers to the electric loading.
- $\frac{1}{2}\int_{R^3} \left|\nabla\phi\right|^2 d\mathbf{x}$ is the electrostatic energy over the whole space R^3.

Taking variational derivatives of the energy functional with respect to the field variables μ will yield the evolution equation of μ that governs the domain dynamics of the ferroelectric domain:

$$\frac{\partial \mu}{\partial t} = M\left(\mathbf{F}^{int} + \mathbf{F}^{ani} + \mathbf{F}^{elas} + \mathbf{F}^{ele}\right), \tag{6.27}$$

where M is the mobility constant of the material. Notice that this constant will be absorbed upon normalization with respect to time t.

The four driving forces are outlined:

$$\begin{aligned}
\mathbf{F}^{ani} &= -\frac{W^{ani}(\mu)}{\partial \mu} \\
\mathbf{F}^{int} &= A\nabla^2\mu \\
\mathbf{F}^{elas} &= \sigma \cdot \frac{\partial \varepsilon^s}{\partial \mu} \\
\mathbf{F}^{ele} &= \left(\mathbf{E}^0 + \mathbf{E}^d\right) \cdot \frac{\partial \mathbf{P}^s(\mu)}{\partial \mu},
\end{aligned} \tag{6.28}$$

where $\mathbf{E}^0$ is the externally applied electric field over the domain and $\mathbf{E}^d$ is the depolarization field that theoretically results from the Maxwell's equation with spontaneous polarization:

$$\begin{aligned}
\kappa\nabla^2\phi &= \nabla \cdot \mathbf{P}^s \\
\mathbf{E}^d &= -\nabla\phi
\end{aligned} \tag{6.29}$$

For boundary conditions of the electrostatic contribution, potential is usually applied over the bottom surface, while either potential or electric flux (that is, *y*-derivative of electric field) can be applied on the top surface.

In the following we will consider a simulation of ferroelectrics in two dimension. The simulation adopt a material system with the following transformation strains and instantaneous polarizations:

$$\begin{aligned}
\varepsilon^{(1,2)} &= \begin{bmatrix} \alpha & 0 \\ 0 & -\alpha \end{bmatrix} & \mathbf{P}^{(1,2)} &= \pm\frac{P_s}{\sqrt{2}}\begin{Bmatrix} 1 \\ 1 \end{Bmatrix} \\
\varepsilon^{(3,4)} &= \begin{bmatrix} -\alpha & 0 \\ 0 & \alpha \end{bmatrix} & \mathbf{P}^{(3,4)} &= \pm\frac{P_s}{\sqrt{2}}\begin{Bmatrix} 1 \\ -1 \end{Bmatrix}
\end{aligned} \tag{6.30}$$

The computational domain has a normalized height as 1.0 and normalized width as 0.5. The resulting domain pattern is shown in figure (6.5). The arrows in the figure indicate the directions of polarization of the variants. The elastic energy is not strong enough to stretch the variants to more uniformly distributed ratio.

In the simulation, further effort is needed to balance elastic energy and electric energy so as to give rise to desirable micro-structures for ferroelectrics.

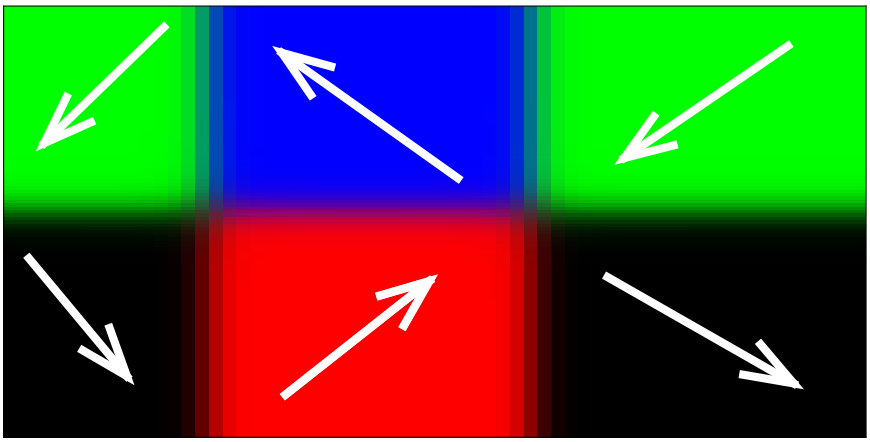

Figure 6.5: Simulated domain pattern of ferroelectric with four variants. Arrows indicate the polarizations.

Chapter 7

LITHIUM ION BATTERY AND ELECTRO-CHEMICAL STRAIN MICROSCOPY

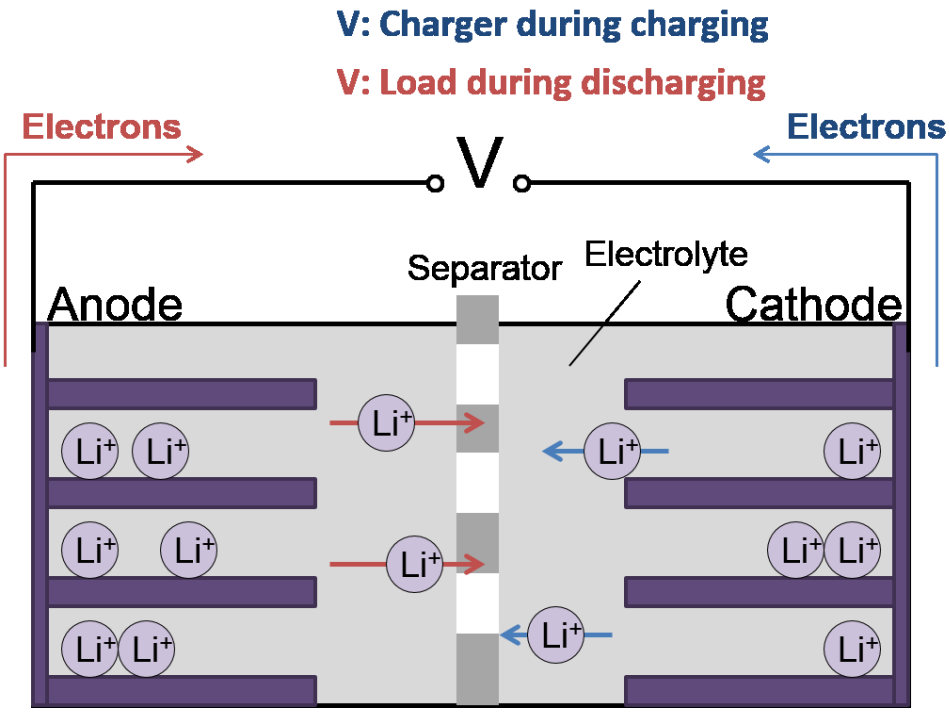

Figure 7.1: Schematic of working principle of lithium ion battery

Lithium ion battery is a family of rechargeable battery types in which lithium ions move from the negative electrode to the positive electrode during discharge, and back when charging, as shown in figure (7.1). It has the advantages of good energy densities (250 - 730 W h /L), light weight, and no memory effect, low self-discharge rate, and is environment-friendly. Nowadays it is extensively employed in portable electronics.

However, repeated charging and discharging induce internal cycling stress that will eventually strain the battery that lead to fatigue of battery material with the build-up of internal resistance. These processes diminish and degrade the ion transport. Moreover, the performance of the cell

also depends on a range of temperature due to the chemical reactions involved. The battery cell irreversibly loses approximately 20% capacity per year.

Researchers have been investigating how these unfavourable mechanisms can be reduced so as to improve overall performance [83, 84, 85, 86, 87, 88, 89].

Failure due to material fatigue from cycling strains is the key to characterize the mechanical property of the battery. Conventional measurement of battery capacity (as ability of ion transport) include AC Impedance Spectroscopy and (other methods). While these methods are indirect, they do not give us information on the local mechanical change at the level of microstructure during the charging / discharge processes and how they affect the performance.

Electrochemical strain microscopy (ESM) is a novel scanning probe microscopy (SPM) that can not only probe Li-ion concentration and diffusivity with nanometer resolution (electrochemical reactivity and ionic flows in solids), but also map local energy dissipation associated with electro-migration of Li-ions. With this technique, the local mechanical characteristics, such as, local crystalline morphologies and defects, can be analyzed experimentally [90]. ESM enables the understanding of the interaction between mechanics and electrochemistry in lithium ion battery and related materials. In this chapter, we study the theoretic foundation of ESM of ion battery, which parallels the experiments.

This chapter is devoted to the analysis and simulation of a simplified model of lithium ion battery with its ESM studies. First we will introduce the simplified model where electrochemical aspect is not considered. We focus on the transport of lithium ion in the sample under the effect to applied electric field (or potential). Second, we will simulate the ESM experiments of the sample which parallels with the experiments carried by [90]. Thirdly, the model is extended to two dimensions that reflects the more realistic physical configuration. Simulation is carried out to study how the distribution of ion will influence the stress / strain distribution in the sample, which evidences the straining of the battery cell that will eventually lead to fatigue over time.

7.1 Model of Lithium Ion Battery

The operating principle of ESM is to probe the tested sample with an electric potential ϕ. The initial uniform concentration of ion will be re-distributed. The deviation of local concentration from the

initial uniform state induces strain in the sample. The resulting deflection (displacement of the top surface) is detected via the tip of the PFM. Various mechanical properties are then analyzed.

As a preliminary study, the system is simplified to consist of only one type of ion. Electrochemistry is not considered. Thus no ion is created or destroyed throughout all processes. We model the ion transport in the solid in one dimension, which consists of diffusion and electro-migration by the applied electric potential.

Denote $c = c(\mathbf{x},t)$ by the concentration of ion at point $\mathbf{x}$ of the sample at time t. The time evolution (motion) of the ion distribution is driven by diffusive flux $\mathbf{J}_{diff}$ due to concentration gradient and advective flux $\mathbf{J}_{adv}$ due to electro-migration under the effect of the electric potential $\phi = \phi(\mathbf{x},t)$. The total flux of ion is thus given as:

$$\begin{aligned} \mathbf{J} &= \mathbf{J}_{diff} + \mathbf{J}_{adv} \\ &= -D\nabla c - D\beta c\nabla\phi, \end{aligned} \tag{7.1}$$

where D is the diffusivity constant, $\beta = \frac{Fn}{RT}$, with F as the Faraday's constant, n as the electric valency, R is the universal gas constant and T as temperature, and ∇ is the gradient operator.

The relation can also be expressed in terms of electric field $\mathbf{E}$, since $\mathbf{E}(\mathbf{x}) = -\nabla\phi$.

$$\mathbf{J} = -D\nabla c + D\beta c\mathbf{E} \tag{7.2}$$

Ion is locally conserved and is driven by flux only. Thus:

$$\frac{\partial c}{\partial t} = -\nabla\cdot\mathbf{J} \tag{7.3}$$

Combining Eq.(7.1) and Eq.(7.3) (as to eliminate $\mathbf{J}$) gives the governing equation of the ion distribution over time by the effect of electric potential.

$$\frac{\partial c}{\partial t} = D\nabla^2 c + D\beta\nabla\cdot(c\nabla\phi), \tag{7.4}$$

This equation is usually referred as the Nernst-Poisson equation. This equation has no analytic solution. Numerical treatment is needed to explore how the distribution of ion is evolved and any

subsequent change in the mechanical properties, such as deformation (as deflection), strains and stresses.

Simulations are carried for static and dynamic (sinusoidal) electric potentials. Steady state (ion in equilibrium) is simulated using static potentials. By simulation with dynamic potentials, effect of various parameters in the system are discussed. Finally, simulation with a DC/AC bias that resembles the charging / discharging processes is studied and compared with the experimental results [90].

7.2 One-dimensional study

The equation is studied for one-dimensional sample whose length is L, which is valid for nanowire and solid whose lateral lengths are much longer than the height. All quantities are functions of the spatial coordinate x. The governing equation becomes:

$$\frac{\partial c}{\partial t} = D\frac{\partial^2 c}{\partial x^2} - D\beta\frac{\partial}{\partial x}(cE), x \in [0, L], \tag{7.5}$$

where $E = E(x) = -\frac{d\phi}{dx}$ is the effective electric field corresponding to the applied electric potential.

Initial and boundary conditions have to be considered for solution.

The initial condition is obviously the initial distribution of ion, given by $c(x,0) = c_0(x)$.

Various kinds of boundary conditions can be proposed: specified ion concentration as in the Dirichlet BC, specified rate of change of ion concentration as in the Neumann BC. However, they are not of practical interest. Indeed, a Robin-type BC is adopted, where the flux J at the two end points are specified as J_a and J_b. In other words,

$$\begin{aligned} -J(0) &= D\frac{\partial c}{\partial x}(0) - D\beta c(0)E(0) = -J_a \\ -J(L) &= D\frac{\partial c}{\partial x}(L) - D\beta c(L)E(L) = -J_b \end{aligned} \tag{7.6}$$

It is interesting to examine what kind of (Ribin-type) boundary conditions can ensure (global) conservation of ion over time. For this, we compute the rate of change of the total amount of ion

over time.

$$\begin{aligned}
\frac{d}{dt}\sum ion &= \frac{d}{dt}\left(\int_0^L c(x,t)dx\right) \\
&= \int_0^L c_t(x,t)dx \\
&= \int_0^L \left(D\frac{\partial^2 c}{\partial x^2} - D\beta\frac{\partial}{\partial x}(cE)\right)dx \\
&= \left[D\frac{\partial c}{\partial x} - D\beta(cE)\right]_0^L \\
&= [-J(x)]_0^L \\
&= J(0) - J(L) \\
&= J_b - J_a
\end{aligned} \tag{7.7}$$

Thus for the conservation of ion over time, one should have $J_b = J_a$, which physically means that the flux of ion going into system at one end must be balanced or compensated by the same flux of ion leaving the system at the other end, or vice versa. For our practical viewpoint, we consider the case when the system is "insulated" at both ends, that is, $J_b = J_a = 0$, prohibiting ion to flow into and out of the system. It is intuitive that when the system is closed, the quantity of ion inside remain the same over time.

The one-dimensional models are used to study two typical configurations: The first configuration is the three dimensional rectangular box whose length and width are much longer than its height, as shown in figure (7.2)(a). The second configuration is the nanotube or nanewire, as shown in figure (7.2)(b). In both configurations, all physical quantities depends on the vertical coordinate.

7.2.1 Deformation due to change of ion distribution

For some materials, as the ones used in lithium ion battery, change of ion distribution can induce an eigen-strain which further implies deformation (as localized change of shape) and stresses. Repeated applications of oscillating external electrical potential, as in the processes of charging and discharging a battery cell, will induce oscillating strains. If this oscillating strain gets too large and too rapid, the material will undergo inelastic deformation and defeats develop due to fracture, thus de-functioning the battery. Understanding how such material deforms as the internal ion evolves

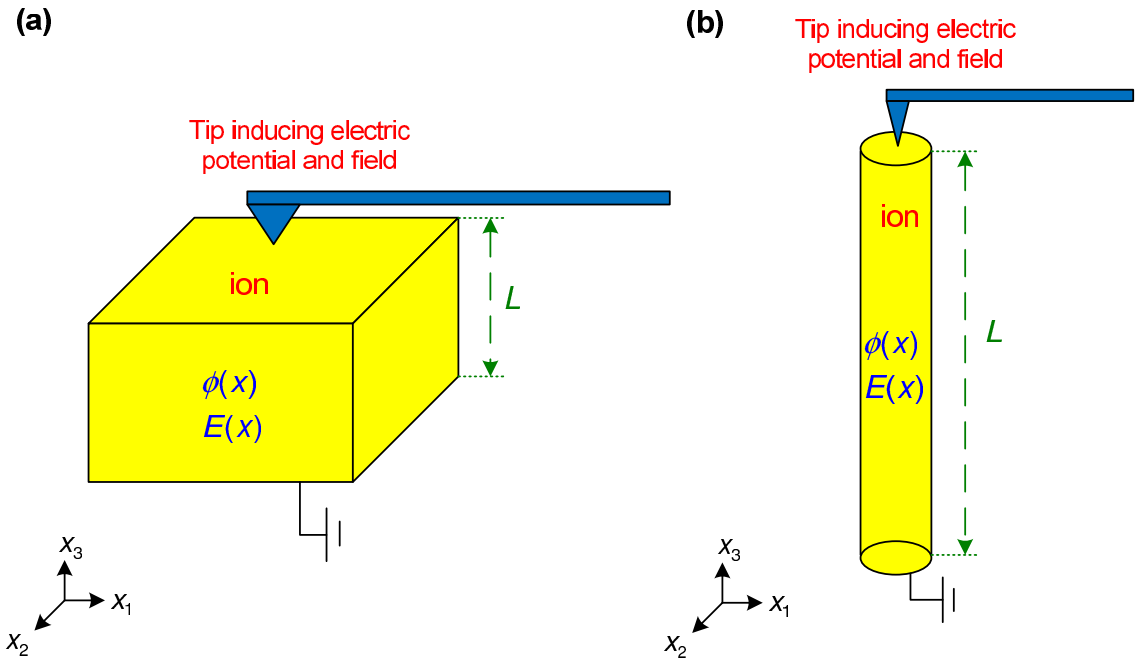

Figure 7.2: Physical configurations for one-dimensional PNP equation: (a) Three dimensional box whose length and width are longer than height. (b) Nanowire or nanotube.

does help to develop materials that can withstand oscillating deformation and avoid fracture.

For the simplest case, the change in ion distribution is related to the induced eigen-strain via:

$$\varepsilon^s(x,t) = s\left(c(x,t) - c(x,0)\right), \tag{7.8}$$

where s is the proportionality constant for the conversion from electro-diffusion to elasticity that depends on individual material.

Knowing the eigen-strain, we are now in a position to solve the elasticity problem for displacement (deformation), strain and stress.

$$\begin{aligned} \sigma &= C\left(\varepsilon - \varepsilon^s\right) \\ \nabla\sigma = \frac{d\sigma}{dx} &= 0 \end{aligned} \tag{7.9}$$

Assume the base surface of the sample is adhered and the top surface is traction-free. The boundary conditions are specified as: $c(x=0)=0$ and $\sigma(x=L)=0$.

Combining the above pair of elasticity equations, we can find the general expression for displacement $u = u(x,t)$:

$$\begin{aligned} 0 = \frac{d\sigma}{dx} &= C\left(\frac{d\varepsilon}{dx} - \frac{d\varepsilon^s}{dx}\right) \\ \frac{d\varepsilon}{dx} &= \frac{d\varepsilon^s}{dx} \\ \frac{d^2u}{dx^2} &= \frac{d\varepsilon^s}{dx} \\ \frac{du}{dx} &= \varepsilon^s + a = s\left(c(x,t) - c(x,0)\right) + a \\ u(x,t) &= s\int_0^x \left(c(\xi,t) - c(\xi,0)\right) d\xi + ax + b, \end{aligned} \tag{7.10}$$

where a and b are unknown constants to be determined from boundary conditions.

Zero displacement at bottom surface forces $b = 0$. To find a, we calculate the stress:

$$\begin{aligned}
u(x,t) &= s\int_0^x (c(x,t) - c(x,0)) + ax \\
\varepsilon(x,t) &= \frac{du(x,t)}{dx} = s\,(c(x,t) - c(x,0)) + a \\
\sigma(x,t) &= C\,(\varepsilon(x,t) - \varepsilon^s(x,t)) \\
&= C\,[s\,(c(x,t) - c(x,0)) + a - s\,(c(x,t) - c(x,0))] \\
&= Ca
\end{aligned} \tag{7.11}$$

The stress is constant all along the length of the sample. Thus traction-free top surface implies $a = 0$.

7.2.2 Steady State Solution

One way to check if the numerical solution for the evolution equation is accurate is to compare its steady state (as t becomes large) and the steady state derived theoretically from the Nernst Poisson equation. Again we are going to derive the closed form in one-dimensional case, subjected to the same set of boundary conditions.

Steady state solution $c_{ss}(x)$ is obtained from the original evolution equation by letting $\frac{\partial c}{\partial t} = 0$. The resulting second order differential equation can be solved with an integration factor.

$$\begin{aligned}
D\frac{d^2 c_{ss}}{dx^2} - D\beta\frac{d}{dx}\,(c_{ss}E(x)) &= 0 \\
\frac{d}{dx}\left[\frac{dc_{ss}}{dx} - \beta c_{ss}E(x)\right] &= 0 \\
\frac{dc_{ss}}{dx} - \beta c_{ss}E(x) &= a \\
e^{\beta\phi(x)}\frac{dc_{ss}}{dx} - e^{\beta\phi(x)}\beta c_{ss}E(x) &= ae^{\beta\phi(x)} \\
\frac{d}{dx}\left(e^{\beta\phi(x)}c_{ss}(x)\right) &= ae^{\beta\phi(x)} \\
e^{\beta\phi(x)}c_{ss}(x) &= a\int_0^x \left(e^{\beta\phi(\xi)}\right)d\xi + b \\
c_{ss}(x) &= \frac{a\int_0^x \left(e^{\beta\phi(\xi)}\right)d\xi + b}{e^{\beta\phi(x)}},
\end{aligned} \tag{7.12}$$

where the integration factor is $\mu(x) = e^{\int -\beta E(x)dx} = e^{\int \beta\phi'(x)dx} = e^{\beta\phi(x)}$, a and b are two unknown

coefficients to be determined from boundary conditions.

To work with the boundary conditions, we need to find $\frac{dc_{ss}}{dx}$.

$$\frac{dc_{ss}}{dx} = a\beta\phi'(x) - \frac{a\beta\phi'(x)\int_0^x \left(e^{\beta\phi(\xi)}\right)d\xi + b\beta\phi'(x)}{e^{\beta\phi(x)}} \tag{7.13}$$

We may now find the constants a and b from the two flux boundary conditions at both ends of the interval.

$$\begin{aligned}
D\frac{dc}{dx}(0) - D\beta u(0)E(0) &= 0 \\
\left[a\beta\phi'(0) - \frac{a\beta\phi'(0)}{e^{\beta\phi(0)}}\right] - \beta\left[\frac{a}{e^{\beta\phi(0)}}\right]E(0) &= 0 \xrightarrow{\phi'(0)=E(0)} \\
\left[-a\beta E(0) + \frac{b\beta E(0)}{e^{\beta\phi(0)}}\right] - \beta\left[\frac{b}{e^{\beta\phi(0)}}\right]E(0) &= 0 \xrightarrow{\text{last 2 terms cancel}} \\
a &= 0
\end{aligned} \tag{7.14}$$

$$\begin{aligned}
D\frac{dc}{dx}(L) - D\beta u(L)E(L) &= 0 \\
\left[-\frac{b\beta\phi'(L)}{e^{\beta\phi(L)}}\right] - \beta\frac{b}{e^{\beta\phi(L)}}E(L) &= 0 \xrightarrow{\phi'(L)=E(L)} \\
\frac{b}{e^{\beta\phi(L)}}E(L) - \beta\frac{b}{e^{\beta\phi(L)}}E(L) &= 0 \\
0 &= 0
\end{aligned} \tag{7.15}$$

This implies that b can be any real number for the found analytic solution to satisfy the differential equation in steady state and boundary conditions. The steady state solution $c_{ss}(x) = be^{-\beta\phi(x)}$ is not unique.

However, since we know that the system is closed and the quantity of ion is conserved at any time, we may find D by equating the quantity of ion in steady state to that at time $t = 0$ (that is, the

initial quantity).

$$\begin{aligned} \int_0^L c_{ss}(x)dx &= \int_0^L c(x,0)dx \\ \int_0^L be^{-\beta\phi(x)}dx &= \int_0^L c(x,0)dx \\ b &= \frac{\int_0^L c(x,0)dx}{\int_0^L e^{-\beta\phi(x)}dx}, \end{aligned} \tag{7.16}$$

Thus the steady state solution is:

$$c_{ss}(x) = \frac{\int_0^L c(x,0)dx}{\int_0^L e^{-\beta\phi(x)}dx} e^{-\beta\phi(x)}, \tag{7.17}$$

which depends on the initial ion distribution $c(x,0)$, the electric potential $\phi(x)$, the electro-diffusion coefficients (D,β) and the length of the sample L.

In the following subsections, we will first outline the numerical algorithm to the evolution equation and apply the approach to solve two simplified problems that originate from experiments. Steady state solution solved analytically is used to compare with the numerical solution when the evolving solution approaches steady state.

7.2.3 Numerical solution

Various numerical methods were proposed, including finite volume, finite element, among others.

Highly accurate scheme is enquired due to the conservative nature of the ion distribution. Canonical finite difference methods may not work.

Here we follow the numerical scheme developed by Perron and Stiles [91, 92], as a tricky modified finite difference method. The one dimensional interval is divided into K sub-intervals of length $\Delta x = \frac{1}{K}$. Denote the $K+1$ subdivision points, as the boundary points of these sub-intervals, by $(x_i)_{i=1}^{K+1}$. Discretized values of the electric field (or potential) and flux are commutated at these points. On the other hand, the discretized values of ion concentration are computed at the mid-points $(y_i)_{i=1}^{K}$ of these sub-intervals. This configuration suggests two sets of grid points related by $y_k = \frac{1}{2}(x_k + x_{k+1}), k = 1,2,..,K$. The sub-division with the two grid points are shown schematically in figure (7.3).

More specifically, at the n-th time step $t \approx t_n = n\Delta t$,

$$
\begin{aligned}
E_j &\approx E(x_j), j = 1,2,..,K+1 \\
J_j^n &\approx J(x_j, t_n), j = 1,2,..,K+1 \\
c_i^n &\approx c(y_i, t_n), i = 1,2,..,K
\end{aligned}
\tag{7.18}
$$

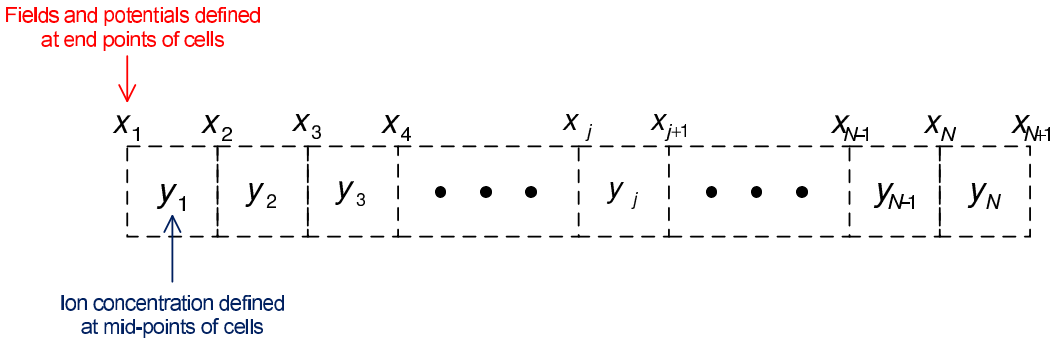

Figure 7.3: Grid for one-dimensional simulation. The length of the sample is divided into N cells with $N+1$ subdivision points denoted by x_i, at which electric fields or potentials are discretized. The midpoints of the cells are denoted by x_j, at which the ion concentrations are discretized.

Under this circumstance, the discretized values of the fluxes at the boundary points $(x_i)_{i=1}^{K+1}$ of sub-intervals in the next time step $t = t_{n+1} = t_n + \Delta t$ are computed from the discretized values of ion concentration at mid-points $(y_i)_{i=1}^{K}$ of sub-intervals in the current time step $t = t_n$ and the preassigned boundary conditions (for instance, zero fluxes at end points x_1 and x_{K+1}).

$$
\begin{aligned}
J_k^{n+1} &= -D\left\{\frac{c_k^n - c_{k-1}^n}{\Delta x} - \beta E_n \frac{c_k^n + c_{k-1}^n}{2}\right\}, k = 2,3,...,K \\
J_1^{n+1} &= J_a = 0 \\
J_{K+1}^{n+1} &= J_b = 0
\end{aligned}
\tag{7.19}
$$

The ion concentration in the next time step $t_{n+1} = t_n + \Delta t$ are then computed from these fluxes

just obtained via the (local) conversation equation.

$$\frac{c_k^{n+1}-c_k^n}{\Delta t}=-\frac{J_{k+1}^{n+1}-J_k^{n+1}}{\Delta x},k=1,2,...,K \tag{7.20}$$

Practically we do not need to know the fluxes explicitly and employ the above two-fold procedures to iteratively compute the ion concentration at successive time steps. Therefore, parallel to the derivation of the Nernst-Poisson equation, we may as well eliminate fluxes to obtain a direct iteration scheme for the evolution of ion concentration. Furthermore, the numerical scheme can be re-casted by the "method of line" (MOL) to a system of ODEs, which are then easily solved by commercialized software like Matlab (using ode solver) [93].

Abusing notations, the ion concentration at the points $(x_i)_{i=1}^K$ are represented by K functions of time:

$$c_i=c_i(t)=c(x_i,t),i=1,2,...,K. \tag{7.21}$$

Adopting the "method of line" (MOL) to the above two-fold numerical scheme generates the following system of ODE for the ion concentration at grid points.

$$\begin{aligned}
\frac{\partial c_1}{\partial t}&=\frac{1}{\Delta x}\left\{D\frac{c_2-c_1}{\Delta x}-\beta E_2\frac{c_2+c_1}{2}\right\}\\
\frac{\partial c_i}{\partial t}&=\frac{1}{\Delta x}\left\{D\frac{c_{i+1}-c_i}{\Delta x}-\beta E_{i+1}\frac{c_{i+1}+c_i}{2}\right\}\\
&\quad-\frac{1}{\Delta x}\left\{D\frac{c_i-u_{i-1}}{\Delta x}-\beta E_i\frac{c_i+c_{i-1}}{2}\right\},i=2,3,...,K-1\\
\frac{\partial c_K}{\partial t}&=-\frac{1}{\Delta x}\left\{D\frac{c_K-c_{K-1}}{\Delta x}-\beta E_K\frac{c_K+c_{K+1}}{2}\right\}
\end{aligned} \tag{7.22}$$

The initial conditions become:

$$c_i(0)=c(x_i,t=0)=c_0(x_i),\forall 1\leq i\leq K \tag{7.23}$$

After the ion distribution is obtained at any time t, the corresponding deformation, strain and stress can be computed. The simulation further results in the steady state solution, which can be checked with the theoretical one.

In the following, we employ the numerical solution of the NP equation for ion distribution and the related elasticity problem to study several experiments, including the ESM study of the lithium ion battery.

7.2.4 Simulation 1 - Block subjected to linear potential

The bottom surface of a three-dimensional sample block initially full of ion (uniformly distributed) is grounded and adhered. A PFM tip with assigned potential is brought to touch the top surface so that the potential over top surface is constant. The potential over the sample is a linear function of z for the simplest case. The potential and field are given by:

$$\begin{aligned}\phi(x_1,x_2,x_3) &= \phi(x_3) = \frac{x_3}{H}V_0 \\ \mathbf{E}(x_1,x_2,x_3) &= -\left(\frac{d\phi}{dx_1},\frac{d\phi}{dx_2},\frac{d\phi}{dx_3}\right) = -\left(0,0,\frac{1}{H}V_0\right),\end{aligned} \tag{7.24}$$

where H is the height of the block and V_0 is the strength of electric potential.

With this field and initial distribution, we may simulate the temporal evolution of the distribution of ion as well as the steady state, from which we solve the elasticity equation and explore how the structure reacts to the applied potential of the tip touching the sample. We may further discuss what happens when we adjust parameters to see their effects. Discussed are the height H of the sample, the strength of the potential on the top surface (V_0), initial distribution of ion concentration $c_0(x_1,x_2,x_3)$, the diffusive and the electro-diffusion coefficients D and β. Since the field produced inside the sample is uniformly pointing, we assume all the associated physical quantities depend on z only. The problem can be solved as if it is one-dimensional.

Figures (7.4) (a) and (b) show the spatial variations of the potential and the associated electric field produced by the ESM tip. Figure (7.4) (c) shows the evolution of total ion in the sample over the whole process. The ion is conserved as predicted and verified by the simulation. Figure (7.4) (d) shows the initial uniform distribution of ion and its distribution in steady state. Figures (7.4) (e) and (f) show the distribution of strain and displacement experienced by the sample. The displacement at the top surface is known to the deflection of the sample which can be measured directly by the ESM tip.

Experimentally, we can not measure the displacement (as deformation) of the sample at any interior points but the deflection of the top surface. From there, the concentration of ion near the top surface can also be predicted. The ion concentration and the deflection of the surface surface, now referred also as the deflection of the ESM tip, from the initial state to the final steady state are temporally illustrated in figures (7.5) (a) and (b).

7.2.5 The normalized equation

The modal has a couple of parameters and variables that may complicate the analysis and parameter study. Normalization can help reducing the number of parameters. With the normalized equation, only several simulations are needed to give the essential insight to the properties of the model. These results are also easily compared with the corresponding experimental data.

Let c_0 be the initial uniform concentration and L be the reference dimension. We may normalize the ion concentration, length and time scale as follow:

$$\begin{aligned} c^* &= \frac{c}{c_0} \\ \mathbf{x}^* &= \frac{\mathbf{x}}{L} \\ t^* &= \frac{t}{L^2/D} \\ \phi^* &= \frac{\phi}{RT/zF} = \frac{\phi}{\beta} \end{aligned} \tag{7.25}$$

The time and spatial derivatives in the normalized scales are expressed as:

$$\begin{aligned} \frac{\partial}{\partial t^*} &= \frac{\partial t}{\partial t^*}\frac{\partial}{\partial t} = \frac{D}{L^2}\frac{\partial}{\partial t} \\ \nabla_{\mathbf{x}^*} &= \nabla_{\mathbf{x}^*}\mathbf{x}\nabla_{\mathbf{x}} = \frac{1}{L}\nabla_{\mathbf{x}} \end{aligned} \tag{7.26}$$

With these normalized quantities, the transport equation is recasted as:

$$\frac{\partial c^*}{\partial t^*} = \nabla_{\mathbf{x}^*}\cdot(\nabla_{\mathbf{x}^*}c^*) + \nabla_{\mathbf{x}^*}\cdot(c^*\nabla_{\mathbf{x}^*}\phi^*) \tag{7.27}$$

This equation applies to arbitrary c_0 and D, and in normalized form, the solution is identical,

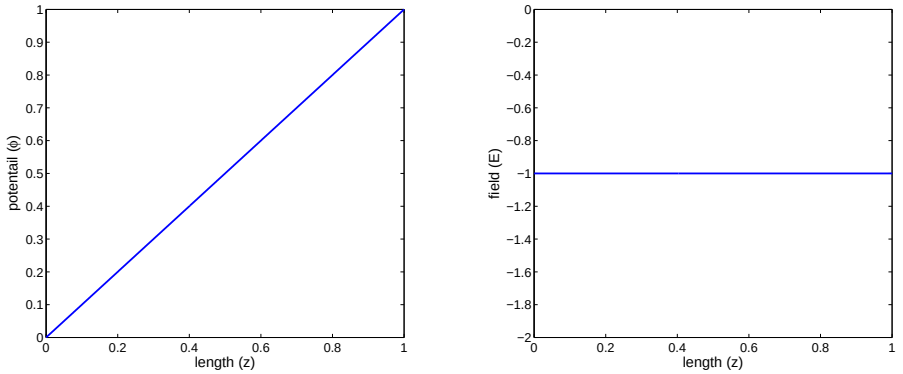

(a) electric potential

(b) electric field

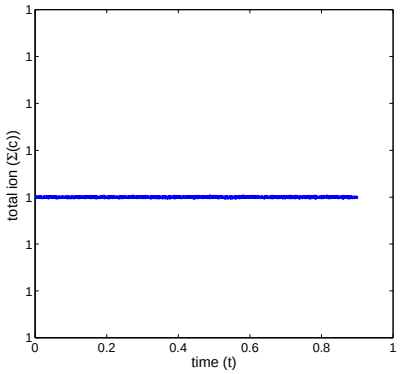

(c) total ion over time

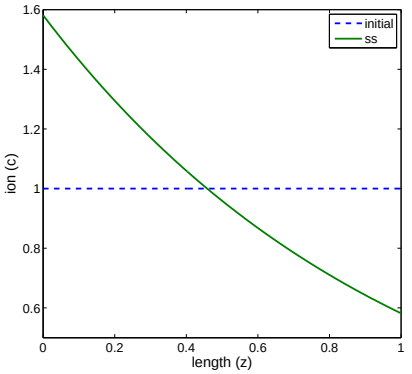

(d) ion distribution

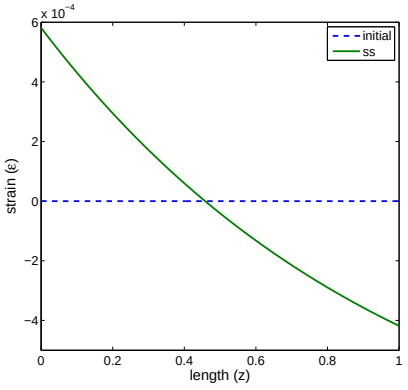

(e) strain

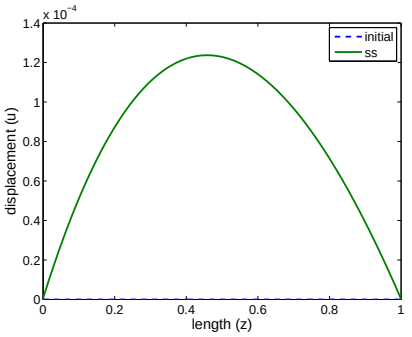

(f) displacement

Figure 7.4: Simulation results for linear applied potential: (a) spatial distribution of electric potential. (b) spatial distribution of electric field. (c) spatial distribution of ion at initial and steady state. (d) spatial distribution of strain at initial and steady state. (e) spatial distribution of displacement at initial and steady state.

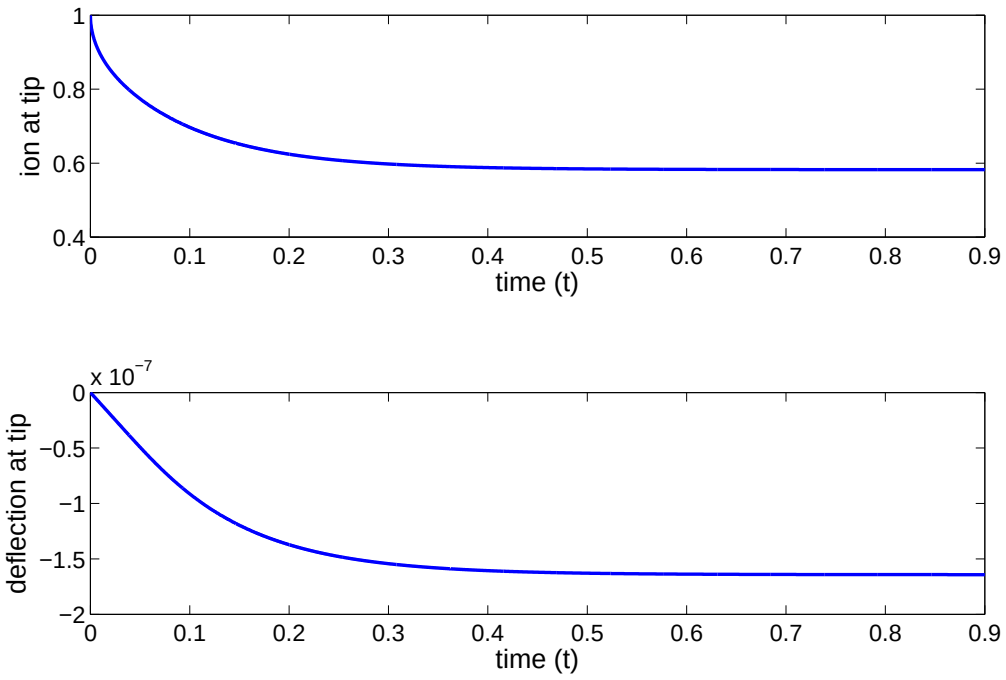

Figure 7.5: Simulation results for linear applied potential: Ion concentration and deflection at the top surface measured from initial to steady states.

regardless of c_0 and D.

The eigenstrain in normalized scale is given by:

$$\begin{aligned}\overline{\varepsilon^s}\varepsilon^{s*}(\mathbf{x}^*,t^*) &= s\left(c_0 c^*(\mathbf{x}^*,t^*) - c_0 1\right)\\ \varepsilon^{s*}(\mathbf{x}^*,t^*) &= c^*(\mathbf{x}^*,t^*) - 1,\end{aligned} \tag{7.28}$$

with $\overline{\varepsilon^s} = sc_0$.

From now on, unless otherwise stated, normalized equation is adopted in the simulations and analysis.

7.2.6 Simulation 2 - Nanowire subjected to ESM tip

Assume an ESM tip with an applied positive voltage (V_0) is brought to the top surface of the sample with initially uniform ion concentration. The configuration of the ESM is illustrated in figure 7.2.

This voltage (V_0) induces a spatial distribution of potential ($\phi = \phi(x)$) over the sample. This potential is stronger towards the top of the sample, while its magnitude is decreasing rapidly away from the top. Notice that the applied voltage does not change with time, so does the induced potential and field. Lithium ions are positive charges. The potential induced by the ESM tip is positive, whence the electric field is positive. As a result, ions are attracted towards the top. The evolution of the distribution of ion concentration from uniform state to steady state is simulated.

To relate the effective potential over the sample from the voltage of the ESM tip, we follow the idea of Y.Y. Liu. The tip of the PFM can be imagined as an equivalent charge Q whose distance from the top of the nanowire is h. We have the following expressions to find the potential ϕ [Y.Y. Liu]:

$$\begin{aligned}h &= \frac{2R_0}{\kappa+1}\ln\frac{1+\kappa}{2} + d\\ Q &= 2\pi\varepsilon_0(\kappa)\phi_0\frac{h^2-d^2}{h+d\kappa}\\ \phi(r,x_3) &= \frac{Q}{2\pi\varepsilon_0(\kappa+1)}\frac{1}{\sqrt{r^2+\left(\frac{x_3}{\gamma}+h\right)^2}},\end{aligned} \tag{7.29}$$

where R_0 is the radius of the tip end, $\kappa = \sqrt{\varepsilon_{11}\varepsilon_{33}}$, d is the distance between the PFM tip and the

top of the nanowire, ε_0 is the permittivity in vacuum, $\gamma = \frac{\varepsilon_{33}}{\varepsilon_{11}}$. $z = \sqrt{x_1^2 + x_2^2}$ is measured downwards from the top of the nanowire sample and r is the radial distance measured from the location of the applied potential.

The following assumptions are made:

1. Since the nanoware is narrow, we may assume that $r = 0$.

2. To simplify the problem, we assume that the tip is touching the nanowire. So we have $d = 0$.

With these, the potential is simplified as:

$$\phi(r, x_3) = \phi(x_3) = \phi_0 h (x_3 + h)^{-1} \tag{7.30}$$

The electric field is thus:

$$\mathbf{E}_3 = -\frac{d\phi}{dx_3} = -\phi_0 h (x_3 + h)^{-2} \tag{7.31}$$

With the normalized equation, assume that the applied voltage of the ESM is $V_0 = 1$, while the distance between the equivalent charge Q and the top surface is $h = 0.01$. The reference length scale L is taken to be the tip radius of the ESM which is typically 50 (nm). The length of the sample being studied is 100 micron, which is equivalent to 20 L. The simulation is started with initial uniform concentration $c_0 = 1$. We want to investigate the influence of the applied voltage of the ESM to the distribution of the ion and any consequence on mechanical properties. As a remark, due to the coordinate system inhered from the equation for the potential induced by the ESM tip, in all the related simulations, $z = 0$ corresponds to top surface.

Figures 7.6(a) and (b) show the spatial variations of the potential and the associated electric field produced by the ESM tip. Figure 7.6(c) shows the evolution of total ion in the sample over the whole process. The ion is conserved as predicted and verified by the simulation. Figure 7.6(d) shows the initial uniform distribution of ion and its distribution in steady state. Figures 7.6(e) and (f) show the distribution of strain and displacement experienced by the sample. The displacement at the top surface is known to the deflection of the sample which can be measured directly by the ESM tip.

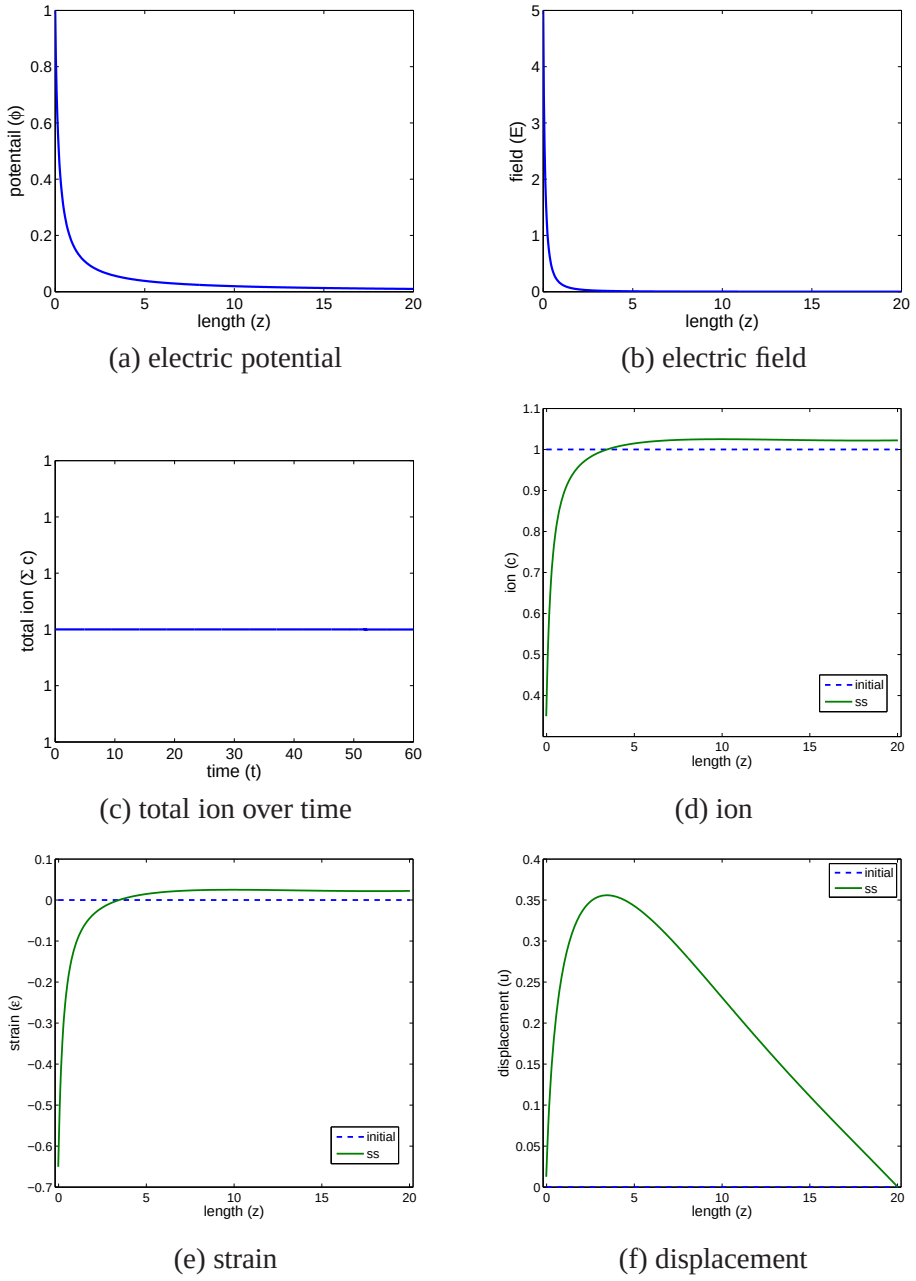

(a) electric potential (b) electric field

(c) total ion over time (d) ion

(e) strain (f) displacement

Figure 7.6: Simulation results for ESM: (a) spatial distribution of electric potential. (b) spatial distribution of electric field. (c) variation of total ion over time, showing that the system is conserved. (d) spatial distribution of ion at initial and steady state. (e) spatial distribution of strain at initial and steady state. (f) spatial distribution of displacement at initial and steady state.

The displacement and the ion concentration of the top surface can be measured by the ESM tip. Their temporal variations from the initial state to the steady state are displayed in figures (7.7) (a) and (b).

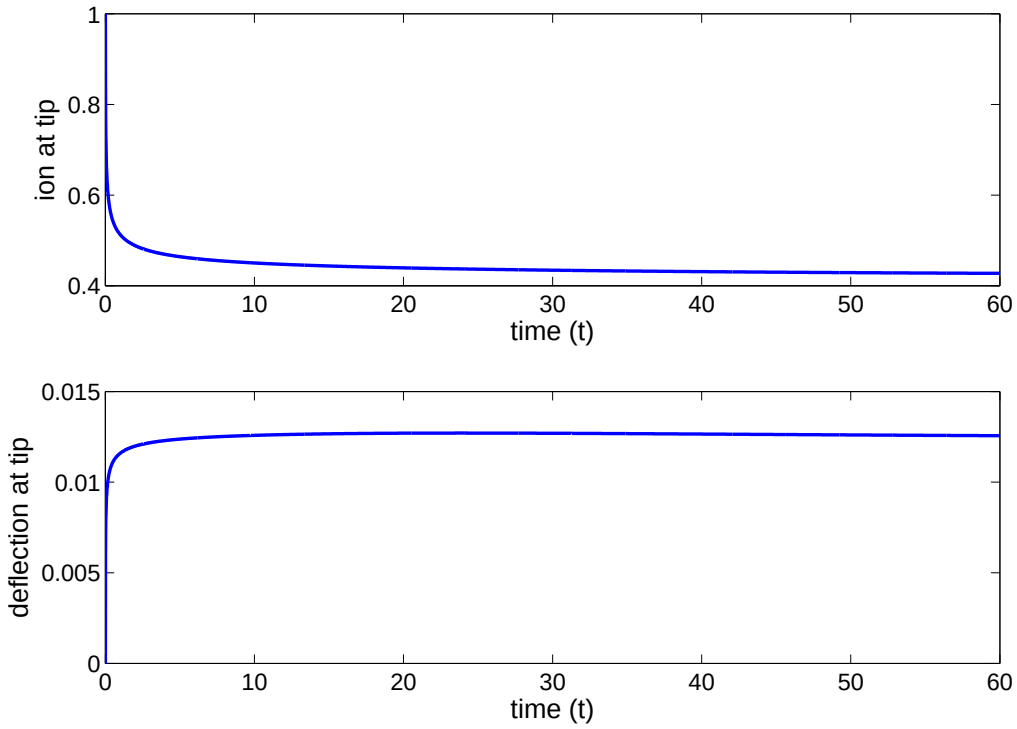

Figure 7.7: Simulation results for ESM: Ion concentration and deflection at the top surface measured from initial to steady states.

7.2.7 Simulation 3 - Nanowire subjected to sinusoidal ESM tip

Assume that that the ESM tip is initiating a sinusoidal profile of voltage $V(t) = V_0 \sin(\omega t)$, where ω is the working frequency of the ESM. In other words, the magnitude of the voltage is oscillating with respect to time. This sinusoidal applied voltage induces a sinusoidal profile of potential over time, expressed as $\Phi(x,t) = \phi(x)\sin(\omega t)$, which is oscillating and switching between positive and negative values. This models the ESM of the sample under an AC bias. Notice that the spatial variation of the potential and fields are identical to the ones employed in the previous simulation.

Lithium ions are alternatively attracted to and repelled from the top surface by the sinusoidal voltage of the ESM tip. The distribution of ion concentration, strain and displacements are similarly changing in a periodic manner over time. As expected in experimental observation, the probed sample undergoes oscillation under the same frequency, which can be seen as the vibrating deflection at the top surface, as detected by the ESM tip.

Simulation is carried for five complete cycles, that is, $0 \leq t \leq 5T = 5 \times \frac{2\pi}{\omega}$, where T denotes the period of the sinusoidal profile. We set $V_0 = 1$. We study the patterns showing the deflection and ion concentration at the top surface that can be measured and probed by the ESM tip in turn.

Figure (7.8)(a) shows the the sinusoidal electric potential. Figures (7.8)(b) and (c) show the resulting oscillating ion concentration and deflection at the top surface of the sample, as detected by the ESM. Snapshots of the displacements at various times are also displayed in figure (7.9). Simulations show that the any point in the sample does experience repeated extension and contraction (indicated as positive and negative displacement) of various magnitude over time, which have not been measured quantitatively in experiments. Moreover, maximum displacement and strain occurs in the interior points.

Deflection VS frequency

We may further study the effect of the operating frequency of the oscillatory applied voltage on the maximum deflection of the top surface, which is measurable by the ESM tip. Notice that the normalized equation has absorbed all the parameters. We do not need to study the effects of these parameters including D and β. Several simulations are run with different operating frequencies ω. The resulting maximum deflections of the tip are recorded. The plot is illustrated in Figure 7.10. It can be seen that increasing frequencies induce decreasing maximum deflections. Lithium ions are attracted and repelled alternatively. They are drifting towards and away from the top surface, thus resulting in alternating upwards and downwards deflections, which are observed as vibration. Also, the deflection is related to the deviation of ion from the initial uniform state. The more concentrated the ion is, the larger the displacement and deflection. Higher frequency refers to shorter time duration for this alteration. In other words, with higher frequency, we do not allow enough time for all lithium ions to concentrate in the top surface, nor to concentrate in the bottom surface, thus decreasing the magnitude of the deflection.

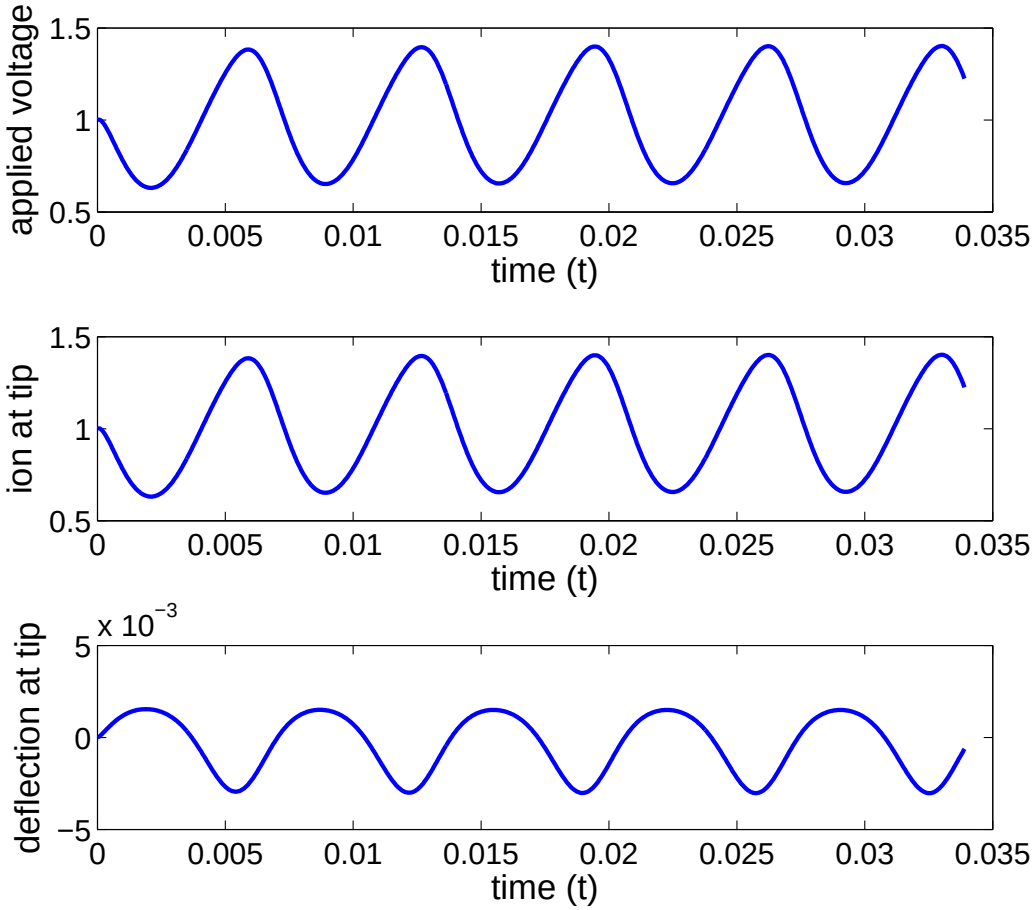

Figure 7.8: Simulation results for ESM due to sinusoidal voltage: (a) Temporal profile of applied voltage of ESM tip. (b) Resulting sinusoidal profile of ion concentration at top surface. (c) Resulting sinusoidal profile of deflection at top surface.

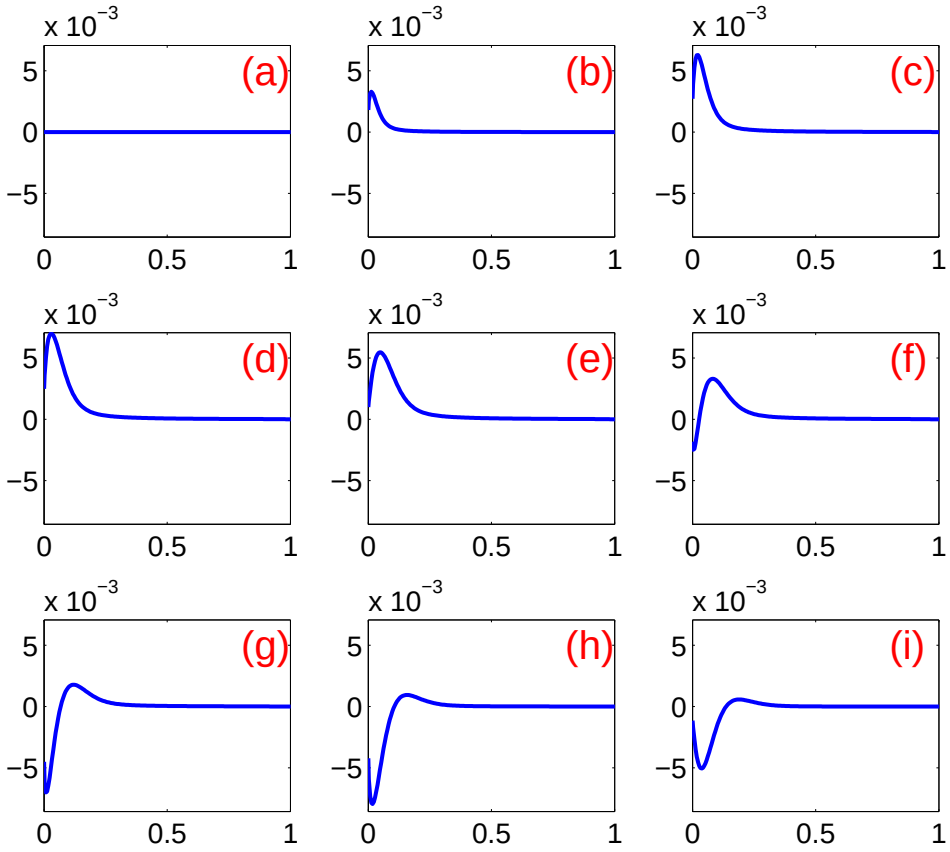

Figure 7.9: Simulation results for ESM due to sinusoidal voltage: Snapshots of displacement of the probed sample over one cycle. x-axis presents the length and y-axis shows the value of the displacement. Notice that x = 0 corresponds to the top surface.

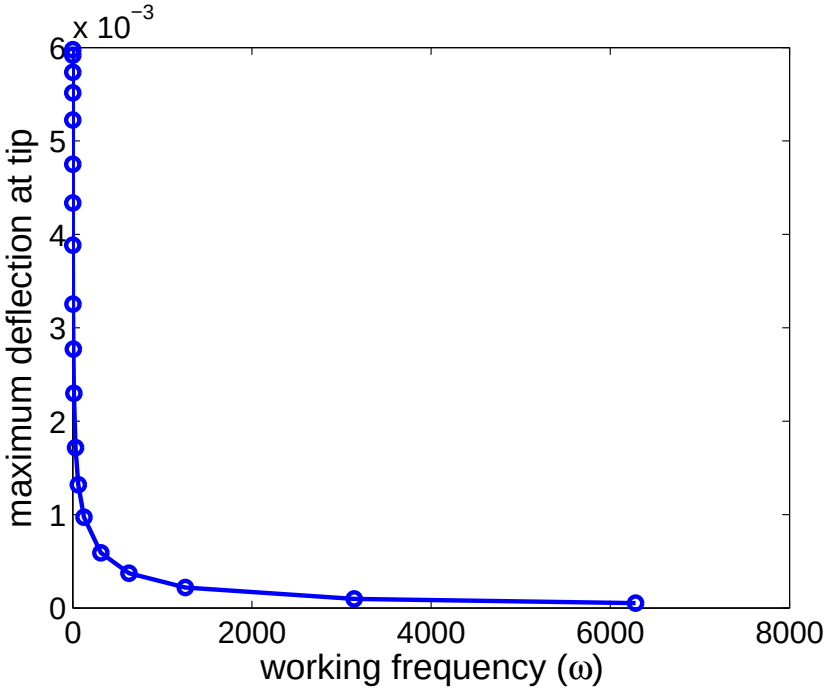

Figure 7.10: Simulation results for ESM due to sinusoidal voltage: Relationship between the operating frequency and the corresponding maximum deflection at the top surface, as measured by the ESM tip.

7.3 Harmonic Analysis in ESM

Recall that the working principle of the Electrochemical strain microcopy (ESM) to probe local concentration: An AC voltage as stimulus applied to the sample surface through the SPM tip redistributes ions in the vicinity near the tip, which in turn induces instantaneous deformation of the electrode (sample). The deflection is then detected by the SPM tip through laser beam and various digital diagnostics. Understanding quantitatively how the applied AC voltage perturbs the instantaneous ion concentration is thus necessary.

This section serves as preparation. We will derive differential equations for first and second harmonics. We will also discuss factors that affect these harmonics. These harmonic responses, together with long-range manipulation of DC voltage, will allow us to track back the diffusivity D and local equilibrium ion concentration n from fitted data in experiments. The methodology to combine simulation and experiment will be presented in next section.

We start with the normalized ESM equation in one dimension:

$$\begin{aligned} c_t &= c_{xx} + (c\phi_x)_x \\ -J(0) = 0 &= c_x(0) + c(0)\phi_x(0) = 0 \\ -J(H) = 0 &= c_x(H) + c(H)\phi_x(H) = 0 \end{aligned} \tag{7.32}$$

where $c = c(x,t)$ is the normalized concentration and $\phi = \phi(x,t)$ is the applied potential. Notice that all variables have been normalized.

Assume that the sample electrode is subjected to an AC modulation given in complex exponential form:

$$V(t) = V_0 e^{j\omega t}, \tag{7.33}$$

where ω is the working frequency of the applied AC voltage.

A distribution of potential over the entire sample is generated, with the same complex exponen-

tial form:

$$\phi(x,t) = \phi(x)e^{j\omega t}, \tag{7.34}$$

This potential field perturbs ion concentration. The ion concentration has the distributions with:

$$c(x,t) = c_0(x) + c_1(x)e^{j\omega t} + c_2(x)e^{j2\omega t}, \tag{7.35}$$

where the first and second exponential terms in the expression are known as the first and second harmonics. We will set up and solve differential equations for these two harmonics and make an attempt to figure their relationships with other variables.

Notice that all the coefficients, c_0, c_1 and c_2 are complex-valued functions of the spatial variable x. Differential equations of these coefficients are complex-valued which make it inconvenient to analyze. To overcome this difficulty, we decompose these complex-valued coefficients into real and purely imaginary parts:

$$\begin{aligned} c_0(x) &\equiv a_0(x) + jb_0(x) \\ c_1(x) &\equiv a_1(x) + jb_1(x) \\ c_2(x) &\equiv a_2(x) + jb_2(x) \end{aligned} \tag{7.36}$$

We substitute the above expressions for induced potential and ion concentration in complex exponential forms into the ESM equations, which eventually yields:

$$\begin{aligned} (j\omega)c_1(x)e^{j\omega t} + (2j\omega)c_1(x)e^{2j\omega t} &= c_0''(x) + c_1''(x)e^{j\omega t} + c_2''(x)e^{2j\omega t} \\ &\quad + \left\{ \left[c_0(x) + c_1(x)e^{j\omega t} + c_2(x)e^{2j\omega t} \right] \phi(x)e^{j\omega t} \right\}_x \\ (j\omega)c_1(x)e^{j\omega t} + (2j\omega)c_1(x)e^{2j\omega t} &= c_0''(x) + c_1''(x)e^{j\omega t} + c_2''(x)e^{2j\omega t} \\ &\quad + c_0'\phi e^{j\omega t} + c_1'\phi e^{2j\omega t} + c_2'\phi e^{3j\omega t} \\ &\quad + c_0\phi' e^{j\omega t} + c_1\phi' e^{2j\omega t} + c_2\phi' e^{3j\omega t} \end{aligned} \tag{7.37}$$

Our strategy is to balance terms without any exponential factor, then with the factors $e^{j\omega t}$ and

$e^{2j\omega t}$ respectively, in order to generate differential equations for first and second harmonics. Before we move on, we formulate the boundary conditions in terms of firstly complex-valued coefficients $c_i(x)$ and secondly the real and imaginary components $a_i(x)$ and $b_i(x)$.

Recall the boundary conditions are zero fluxes at the two boundary points: $x = 0$ and $x = H$.

$$\begin{aligned} -J &= c_x(x,t) + c(x,t)\phi_x(x,t), x = 0, H \\ 0 &= c_0'(x) + c_1'(x)e^{j\omega t} + c_2'(x)e^{2j\omega t} \\ &\quad + c_0(x)\phi'(x)e^{j\omega t} + c_1(x)\phi'(x)e^{2j\omega t} + c_2(x)\phi'(x)e^{3j\omega t} \end{aligned} \tag{7.38}$$

Balancing various exponential factors yield the following boundary conditions:

$$\begin{aligned} c_0'(x) &= 0, \qquad x = 0, H \\ c_1'(x) + c_0(x)\phi'(x) &= 0, \qquad x = 0, H \\ c_2'(x) + c_1(x)\phi'(x) &= 0, \qquad x = 0, H \end{aligned} \tag{7.39}$$

Balancing terms without any exponential factor:

$$\begin{aligned} c_0''(x) &= 0 \\ c_0(x) &= \alpha x + \beta, \end{aligned} \tag{7.40}$$

where α and β are two unknown coefficients to be computed from boundary conditions. Recall that the boundary conditions are $c_0'(x) = 0$ at $x = 0$ and $x = H$. Comparing the solution and the boundary conditions results in $\alpha = 0$ where no restriction is imposed yet to β. Physical insight suggests that the term without complex exponential factor is the constant offset of the concentration. Thus it suffices to assume that β takes the values of the constant initial concentration, or

$$c_0(x) = \beta = n_0 \tag{7.41}$$

As a remark, the explicit expression of this first term of the solution will be included in the equations for the first and second harmonics of the solutions. This solution is separated into real and imaginary

parts:

$$\begin{aligned} a_0(x) &= \beta = n_0 \\ b_0(x) &= 0 \end{aligned} \tag{7.42}$$

7.3.1 First Harmonic

We move on to the deviation of the differential equation for the first harmonic $c_1(x)$.

Balancing terms without exponential factor $e^{j\omega t}$:

Comparing the terms with factor $e^{j\omega t}$ yields the following complex-valued equation:

$$\begin{aligned} (j\omega)c_1(x)e^{j\omega t} &= c_1''(x)e^{j\omega t} + e^{j\omega t}\left(c_0'(x)\phi(x) + c_0(x)\phi'(x)\right) \\ (j\omega)c_1(x) &= c_1''(x) + \left(c_0'(x)\phi(x) + c_0(x)\phi'(x)\right) \\ (j\omega)c_1(x) &= c_1''(x) + \left(0\phi(x) + \beta\phi'(x)\right) \\ (j\omega)c_1(x) &= c_1''(x) + \beta\phi'(x) \end{aligned} \tag{7.43}$$

The differential equations can be separated into two equations for the real and imaginary parts by using $c_1(x) = a_1(x) + b_1(x)$:

$$\begin{aligned} (j\omega)\left(a_1(x) + jb_1(x)\right) &= \left(a_1(x) + jb_1(x)\right)'' + \beta\phi'(x) \\ -b_1(x) + j\omega a_1(x) &= a_1''(x) + \beta\phi'(x) + jb_1''(x) \\ &\begin{cases} a_1''(x) + \omega b_1(x) + \beta\phi'(x) = 0 \\ b_1''(x) - \omega a_1(x) = 0 \end{cases} \end{aligned} \tag{7.44}$$

These coupled real-valued differential equations thus generated are not convenient to solve. They can be combined to give rise to one equation, yet of higher order. Inspecting the form of the second equation suggests that the term $a_1(x) = \frac{1}{\omega}b_1''(x)$ can be substituted into the first equation,

yielding:

$$\begin{aligned} a_1''(x) + \omega b_1(x) + \beta \phi'(x) &= 0 \\ \left(\frac{1}{\omega} b_1''(x)\right)'' + \omega b_1(x) + \beta \phi'(x) &= 0 \\ b_1''''(x) + \omega^2 b_1(x) + \beta \omega \phi'(x) &= 0 \end{aligned} \tag{7.45}$$

Once $b_1(x)$ is solved, $a_1(x)$ as well as the first harmonic can then be computed.

What remains is to set up four conditions for $b_1(x)$, since its differential equation is of fourth order. The process is to replace the complex-valued function in the boundary conditions with real and imaginary parts before separating them into two sets of coupled boundary conditions. They are then re-casted as four boundary conditions, two at each end point, as one of the real-valued functions is eliminated, as previously done.

$$\begin{aligned} c_1'(x) + c_0(x)\phi'(x) &= 0 \\ (a_1(x) + j b_1(x))' + n_0 \phi'(x) &= 0 \\ a_1'(x) + j b_1'(x) + n_0 \phi'(x) &= 0 \end{aligned}$$

$$\begin{cases} a_1'(x) = -n_0 \phi'(x), & x = 0, H \\ b_1'(x) = 0, & x = 0, H \end{cases}$$

$$\begin{cases} a_1'(0) &= -n_0 \phi'(0) \\ a_1'(H) &= -n_0 \phi'(H) \\ b_1'(0) &= 0 \\ b_1'(H) &= 0 \end{cases} \tag{7.46}$$

Using the relationship $a_1(x) = \frac{1}{\omega} b_1''(x)$, we further recast two additional boundary conditions for $b_1(x)$:

$$\begin{aligned} b_1'''(0) &= \omega a_1'(0) = -\omega n_0 \phi'(0) \\ b_1'''(H) &= \omega a_1'(H) = -\omega n_0 \phi'(H) \end{aligned} \tag{7.47}$$

In summary, we have set up a fourth order differential equation for the imaginary part of the first harmonic:

$$b_1''''(x) + \omega^2 b_1(x) + \beta\omega\phi'(x) = 0$$

$$BC: \begin{cases} b_1'(0) &= 0 \\ b_1'(H) &= 0 \\ b_1'''(0) &= -\omega n_0 \phi'(0) \\ b_1'''(H) &= -\omega n_0 \phi'(H) \end{cases} \tag{7.48}$$

The real part is computed by the relation: $a_1(x) = \frac{1}{\omega} b_1''(x)$. The first harmonic is $c_1(x) = a_1(x) + jb_1(x)$. Recall that $\phi = \phi(x)$ is the applied potential over the sample. If SPM tip is used, we adopt $\phi(x) = \frac{hV_0}{x+h}$, where V_0 is the applied voltage and h is the distance between effective charge Q due to SPM and the top surface of the sample.

Redistribution of ion away from initial condition induces eigen-strain:

$$\begin{aligned} \varepsilon^s(x,t,\omega) &= s(c(x,t,\omega) - c_0(x)) \\ &= s(c_1(x,\omega)e^{j\omega t} + \text{higher order terms}) \\ &\approx s c_1(x,\omega)e^{j\omega t} \\ &= (a_1(x,\omega) + jb_1(x,\omega))e^{j\omega t}, \end{aligned} \tag{7.49}$$

where s is the expansion constant taken as 6 % for lithium ions.

The deformation of the sample can be computed by integrating eigen-strain:

$$u(x,t,\omega) = \int_0^x \varepsilon^s(x,t,\omega)dx - \int_0^H \varepsilon^s(x,t,\omega)dx \tag{7.50}$$

Recall that because of the choice of the coordinates, the top surface corresponds to $x = 0$.

Once we obtained the ion concentration, we may evaluate the deflection of the sample as the

displacement of the top surface.

$$\begin{aligned} u_{top}(t,\omega) &= u(0,t,\omega) \\ &= \int_0^{x=0} \varepsilon^s(x,t,\omega)dx - \int_0^H \varepsilon^s(x,t,\omega)dx \\ &= -\int_0^H \varepsilon^s(x,t,\omega)dx \\ &= -s\int_0^H \left[a_1(x,\omega) + jb_1(x,\omega)\right]dxe^{j\omega t} \\ &= -s\underbrace{\int_0^H a_1(x,\omega)dx}_{\approx 0}e^{j\omega t} - js\int_0^H b_1(x,\omega)dxe^{j\omega t} \\ &= e^{j90^0}s\int_0^H b_1(x,\omega)dxe^{j\omega t} \\ &= s\int_0^H b_1(x,\omega)dx\left[e^{j(\omega t-90^0)}\right], \end{aligned} \tag{7.51}$$

where the integral of the real component a_1 is much smaller than that of the imaginary component a_1, as evidenced from numerical simulations that follow, and can thus neglected for simplicity.

For the sake of convenience in data fitting with experiments in proceeding section, we may normalize the governing equation, boundary conditions and deflection.

The differential equations with boundary conditions are linearly with initial concentration c_0 and applied voltage V_0. For instance, the following equations are satisfied:

$$\left(\frac{b_1(x)}{n_0V_0}\right)'''' + \omega^2\left(\frac{b_1(x)}{n_0V_0}\right) + \omega\frac{\phi'(x)}{V_0} = 0$$

$$BC: \begin{cases} \left(\frac{b_1(x)}{n_0V_0}\right)'(0) &= 0 \\ \left(\frac{b_1(x)}{n_0V_0}\right)'(H) &= 0 \\ \left(\frac{b_1(x)}{n_0V_0}\right)'''(0) &= -\omega\frac{\phi'}{V_0}(0) \\ \left(\frac{b_1(x)}{n_0V_0}\right)'''(0) &= -\omega\frac{\phi'}{V_0}(H) \end{cases} \tag{7.52}$$

This motivates us to define a further normalized quantity of the imaginary portion of first harmonic:

$$b_1^* \equiv \frac{b_1}{n_0\beta V_0} \tag{7.53}$$

With the potential supplied by SPM tip, the differential equation and boundary conditions for the normalized first harmonic are given by:

$$b_1^{*''''}(x) + \omega^2 b_1^*(x) = \omega \frac{h}{(x+h)^2}$$
$$BC: \begin{cases} b_1^{*\prime}(0) &= 0 \\ b_1^{*\prime}(H) &= 0 \\ b_1^{*'''}(0) &= \frac{1}{\omega}\frac{1}{h} \\ b_1^{*'''}(H) &= \frac{1}{\omega}\frac{h}{(h+H)^2} \end{cases} \tag{7.54}$$

Thus in the simulations, we may assume the initial concentration as $c(0) = 1$ and applied voltage as $V_0 = 1$.

The normalized deflection on top surface (with respect to the radius tip) is expressed as follow:

$$\begin{aligned} u_{top}(t,\omega) &= s\int_0^H b_1(x,\omega)dx\left[e^{j(\omega t - 90^0)}\right] \\ &= s\int_0^H b_1^*(x,\omega)V_0 n_0 \beta dx\left[e^{j(\omega t - 90^0)}\right] \\ \frac{u_{top}(t,\omega)}{sV_0 n_0 \beta} &= \int_0^H b_1^*(x,\omega)dx\left[e^{j(\omega t - 90^0)}\right], \end{aligned} \tag{7.55}$$

where $u_{top}(t,\omega)$ is the normalized deflection with respect to the length comparable to the tip radius R of the SPM tip, or

$$u_{top}(t,\omega) = \frac{u_{top,real}(t,\omega)}{R}, \tag{7.56}$$

where $u_{top,real}(t,\omega)$ denotes the deflection in real scale.

In addition, since we are interested in the magnitude of the deflection but not the phase delay, we may drop the exponential factor, $e^{j(\omega t - 90^0)}$, whose magnitude is one. Thus, the deflection in real scale can be simplified to:

$$\frac{u_{top,real}(t,\omega)}{sV_0 n_0 \beta R} = \underbrace{\int_0^H b_1^*(x,\omega)dx}_{R=1,n_0=1,\beta=1,V_0=1}, \tag{7.57}$$

Quantities on the left hand side can be obtained via experiments, while the right hand side is computed using simulation with normalized variables $R = 1$, $n_0 = 1$, $\beta = 1$ and $V_0 = 1$. Thus, this equation links experimental data and simulation data, based on which we predict the local ion concentration. More details will be presented in next section.

Several simulations will be presented to explore various properties.

7.3.2 Numerical Solution of First Harmonic and Effect of Domain Thickness

The first harmonic is believed to redistribute ion locally. To verify this, the system of differential equations for first harmonic ($c_1(x) \equiv a_1(x) + jb_i(x)$) is solved for two domains with different thicknesses H. For instance, $H = 20R$ and $H = 200R$ are chosen, where R is the radius of the SPM tip. The sample is subjected to a sinusoidal input, with magnitude $V_{AC} = 0.025(Volts)$, and normalized frequency $\omega^* = 1$. The real and imaginary parts, as well as the magnitude $\sqrt{a_1(x) + b_1(x)}$ of the first harmonic are shown graphically in figure (7.11). It can be seen from figure that the effect of the SPM is localized. Activities of ions appear within approximately $5R$ from the site of the SPM tip for both thicknesses. Thus without loss of generosity, we may adopt domain of shorter thickness since less data points are needed for computation.

We may further verify the localized redistribution of ions by studying the effects of domain thickness on the concentration of ions and the deformation (measured as deflection, as a multiple of radius R of the SPM tip) on the top surface of the domain. In particular, the deflection on top surface is the quantity measurable in ESM experiments. In these two simulations, the thickness ranges from R to $200R$. The results are shown in figure (7.12). It cam be seen that these quantities tend to settle for thickness of the domain is greater than $10R$, as a conservative estimate.

7.3.3 Effect of Operating Frequency on Deflection

Next we consider the effect of operating frequency (ω) on deflection of top surface. An attempt will be made to fit the deflection on top surface (magnitude with respected to the tip radius R) and the operating frequency of the applied AC voltage. Based on previous discussions on the effects of domain thickness H, we simply adopt $H = 20R$ in the simulation. The range of normalized frequencies (ω^*) is from 250 to 15000. The magnitude of the applied voltage V_0 is 0.025 (Volt). The

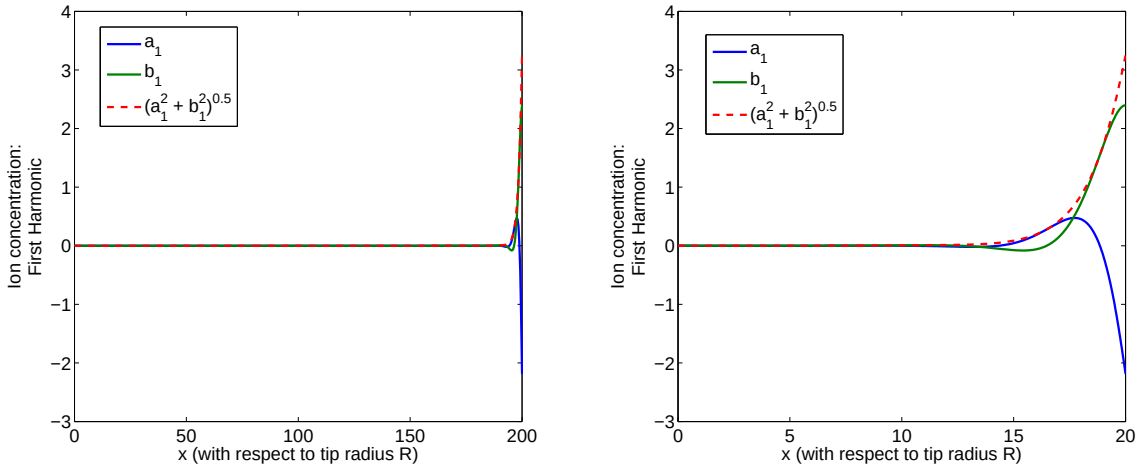

(a) $H = 200R$ (b) $H = 20R$

Figure 7.11: Real and imaginary parts, and magnitude, of first harmonic of ion due to SPM with sinusoidal input voltage.

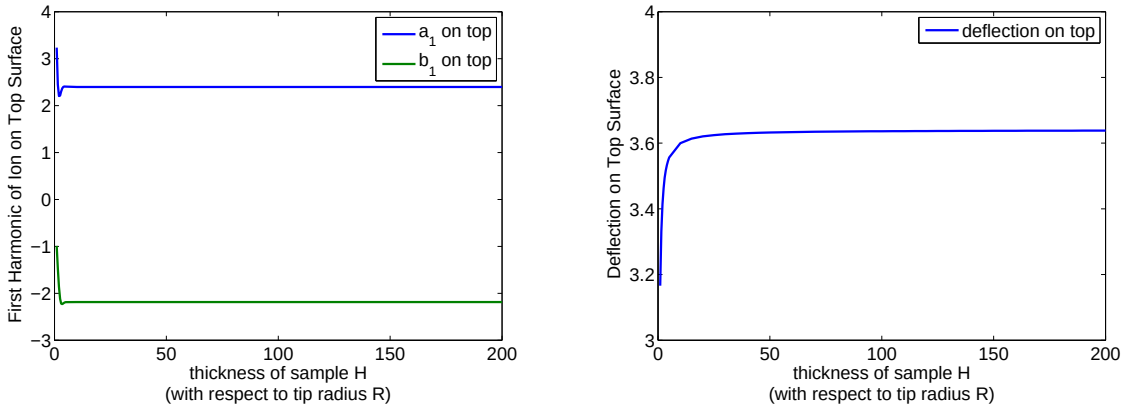

(a) Ion on top (real and imaginary parts) (b) Deflection on top surface

Figure 7.12: Effect of domain thickness on first harmonic of (a) ion concentration and (b) deflection on top surface. Notice that for (b), the magnitude of the deflection is with respect to the tip radius R.

drifting coefficient β takes 1. The initial ion concentration n_0 is 1. The distance between effective charge Q and top surface is take as $0.3788R$. The simulated result is shown in figure (7.13). The fitted equation for normalized deflection and normalized operating frequency is:

$$\frac{u_{top,real}}{sV_0 n_0 \beta R} = \frac{0.36032}{\omega^*} \tag{7.58}$$

This equation will be used, in conjunction with experimental data on ESM, to track back local ion concentration.

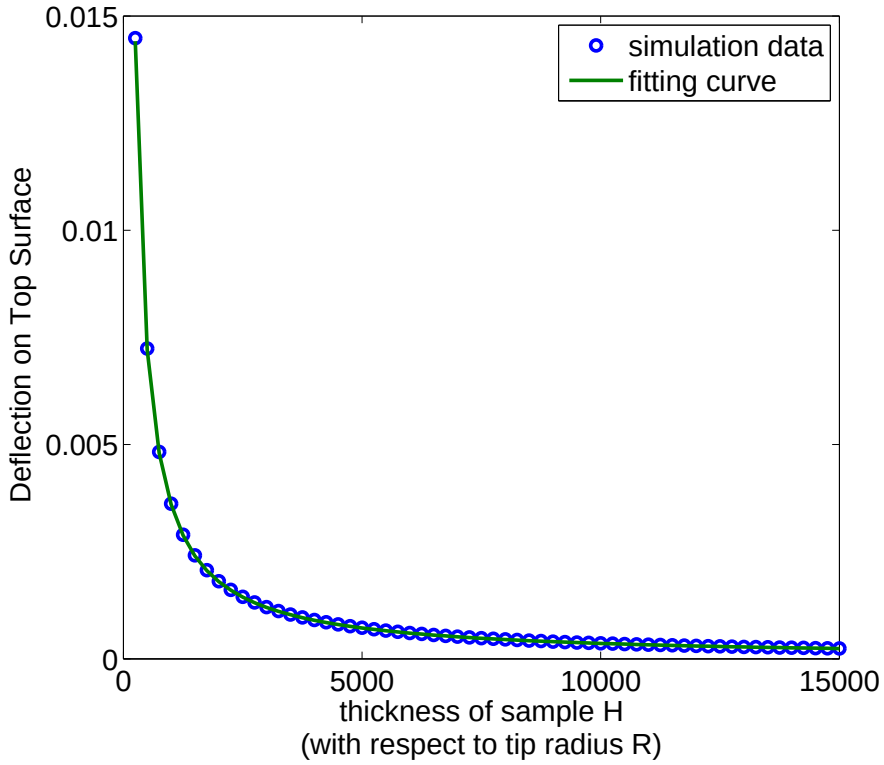

Figure 7.13: Contour showing ion concentration at steady state for domain subjected to SPM tip with positive voltage. Notice that lithium ion are attracted towards the site of SPM tip.

Following the same approach, one may explore the second harmonics by setting and studying the corresponding coupled differential equations. The detail can be found in appendix (E.5)

7.4 Resolving Diffusivity and Local Concentration by Relaxation of ESM

The mechanisms and performance of lithium ion storage are poorly understood, partly due to the lack of reliable tools to measure lithium ion activities at the nanoscale, especially in a quantitative manner. The emergence of electrochemical strain microscopy (ESM) has greatly advanced our capability in probing electrochemistry at nanoscale, enabling imaging of ion diffusion and reaction with nanometer solution. The technique, however, remains largely qualitative in nature, and measuring local ionic diffusivity and concentration at the nanoscale remain to be elusive.

It is possible to measure local ionic diffusivity quantitatively at the nanoscae through ESM relaxation study, enabled by close combination of numerical simulations and SPM experiments. This is accomplished by recognizing a universal time constant in ionic relaxation behaviour driven by the ESM, and further analysis shows that local ionic concentration can also be measured, after the local diffusivity is mapped quantitatively. To this end, we consider an electrode materials probed by a charged SPM tip with radius R and potential V. The potential distribution induced by the charged tip can be approximated by the effective point charge model: In all of our discussion, we assume that the SPM tip is touching the top surface of the sample. In other words, the SPM tip is in contact mode. Thus the distance between the SPM tip and the sample surface is taken as $d_{real} = 0$. The SPM tip is virtually imagined as a point charge Q located at a distance d above the sample surface where:

$$\begin{aligned} Q &= 2\varepsilon_0(1+\kappa)V_0 d \\ d &= \frac{2R}{\kappa-1}\ln\frac{1+\kappa}{2} \\ \phi(x) &= \frac{Q}{2\pi\varepsilon_0(1+\kappa)}\frac{1}{\sqrt{x_1^2+x_2^2+\left(\frac{x_3}{\gamma}+d\right)^2}} \end{aligned} \tag{7.59}$$

where ε_0 is the absolute permittivity of vacuum, κ is the effective permittivity of the specimen, γ measures the dielectric anisotropy of the sample.

The potential distribution would drive perturbation of local lithium ion concentration c in the

electrode underneath the probe, as governed by the classical diffusion and electro-migration:

$$\frac{\partial c}{\partial t} = \nabla \cdot (D\nabla c) + \nabla \cdot \left(D\frac{zF}{RT} c\nabla \phi \right), \tag{7.60}$$

where D and z are the diffusivity and charge number of the considered ion, T is the absolute temperature, and F and R are the Faraday constant and universal time constant, respectively.

For further analysis with numerical analysis, it is revealing to recast the ion transport equation in a normalized or dimensionless version,

$$\frac{\partial c^*}{\partial t^*} = \nabla \cdot (\nabla c^*) + \nabla \cdot (c^* \nabla \phi^*), \tag{7.61}$$

where the length scale is normalized with respect to the tip radius R, $\bar{t} \equiv \frac{R^2}{D}$ measures the time constant involved.

Next we study the kinetic and kinematic of Lithium ions in electrodes. Insights from the ESM equation on balancing diffusion and electro-migration will be explained. Based on these underlying facts, an ESM experiment is designed to probe the deflection of the SPM tip that is in contact with the top surface of the sample during charging / discharging processes, being manipulating by DC-Ac bias. Simulations are then conducted to produce numerical results that exhibits the same pattern of data. After suitable curve fitting and comparison between experiments and simulations, we are able to predict the diffusivity D and local ion concentration (n).

If an AC voltage is applied with relatively high frequencies which are shorter than the typical diffusion time scale, electro-migration dominates over diffusion in the role of redistributing ion concentration through the induced electric potential. The model for this act is simplified as:

$$\frac{\partial c}{\partial t} = c_0 D\beta \nabla^2 \phi. \tag{7.62}$$

As a remark, in the simulation, we deal with its normalized form:

$$\frac{\partial c^*}{\partial t^*} = \nabla^2_{\mathbf{x}^*} \phi^*, \tag{7.63}$$

where the parameter and variable being discussed, D and c_0, are hidden or integrated into the equa-

tion.

Equation (7.62) infers that changes in Li-ion concentration induced by the SPM tip is proportional to the local equilibrium concentration c_0 as well as the diffusion coefficient D. Since this change is directly proportional to molar volume change and thus the ESM response probed, we conclude that ESM amplitude also correlates with the local concentration as well as the diffusion coefficient of Li-ion.

To verify this, a sequence of DC step voltages with AC bias is applied through the SPM tip to the probed sample, as shown in figure (7.14). The profile is basically made up of five regimes. Scenarios from these regimes will be explained. The corresponding ESM responses will also be simulated and compared with experimental data, to predict useful information.

The profile of the applied voltage in the SPM tip is described by:

$$V(t) = V_{AC}\sin(\omega t) + \begin{cases} 0 & : 0 \le t \le T_0 \\ V_0 & : T_0 \le t \le 2T_0 \\ 0 & : 2T_0 \le t \le 4T_0 \\ -V_0 & : 4T_0 \le t \le 5T_0 \\ 0 & : 5T_0 \le t \le 6T_0 \end{cases},$$

where the first term represents the AC bias with ω being the operating frequency much shorter than the relaxation time scale and V_{AC} as the magnitude of the voltage.

The DC voltage is used to manipulate charging so as to redistribute ions towards or away from the site of SPM tip. The AC voltage is used to activate the probing of the deflection locally. The operating frequency of the AC can be as high as 1000 (kHz), which induces small vibrational deflection (known as the AC-deflection). Due to high frequency and small magnitude, this AC voltage does not redistribute ions in the sense of global time scale where relaxation of ions takes place from previously resulted steady state due to DC voltage. The action of the bias voltage and the corresponding response will be outlined with explanation.

Regime ①: Ground State

In this regime, no DC voltage is applied. The AC voltage of high frequency is thus used to probe the ground state of ions, without redistributing these ions much away from the original configuration.

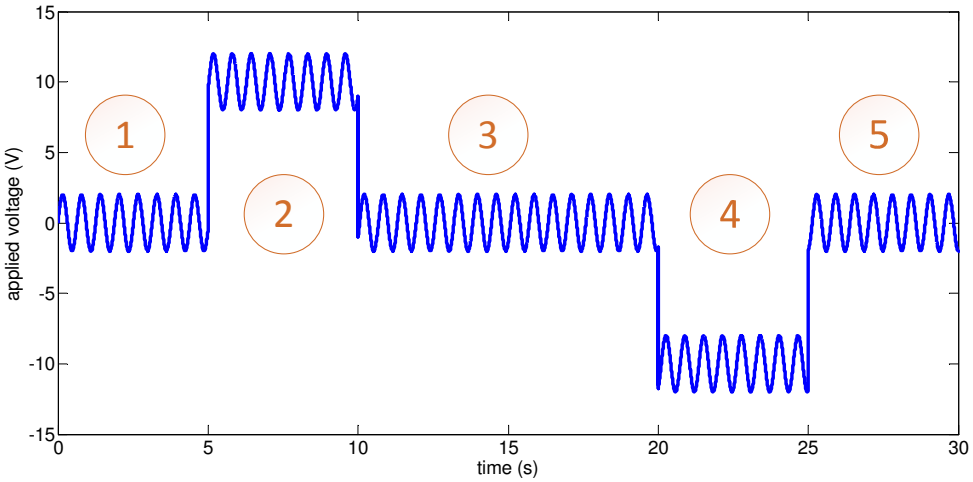

Figure 7.14: Profile of applied voltage $V(t)$ during a charging / relaxation process to probe diffusivity and local ion concentration.

The governing equation of ions in the instantaneous (shorter) time scale for local measurement is:

$$\frac{\partial c}{\partial t} = \underbrace{D\nabla^2 c}_{\text{dominate}} + \underbrace{D\beta c\nabla^2\phi}_{\text{frustrate}}$$
$$c_{init}(x) = c_0(x) = \underbrace{c_0}_{\text{uniform}}, \tag{7.64}$$

while the governing equation of ions in the global (longer) time scale of relaxation:

$$\frac{\partial c}{\partial t} = D\nabla^2 c$$
$$c_{init}(x) = c_0(x) = \underbrace{c_0}_{\text{uniform}}, \tag{7.65}$$

The vibrational deflection will be linked to the simulated AC-deflection with the first harmonic to compute the local ion concentration c, if diffusivity (D) is known.

Regime ②: Charging with Positive Voltage

In this regime, a positive DC voltage is applied so that ions in the vicinity of the SPM tip move away, resulting in deformation. The response is dominated by electrostatic interactions, which leads

to ultrahigh amplitudes, when compared with the responses purely from AC voltage. Thus we do not examine any ESM response during this regime, though simulated deflection can be obtained.

$$\frac{\partial c}{\partial t} = D\beta c\nabla^2\phi$$
$$c_{init}(x) = c_0(x) = c_0, \tag{7.66}$$

The time range is so chosen to allow ions to move to the steady state at the end of this regime. This eventual distribution can be predicted by our previous theoretical calculation.

$$c(x, t_{end}) \equiv c_{ss,p}(x) = \frac{\int_0^H c_0(x)dx}{\int_0^H e^{-\beta\phi(x)}dx} e^{\beta\phi(x)} \tag{7.67}$$

Regime ③: Relaxation from steady state due to previous positive DC charging

In this regime, a large drop in ESM response is observed immediately after the removal of the positive DC voltage, which then gradually increases back to the ground level by the end of this regime. The ions in previous steady state returns to the uniform distribution, up to small frustration due to the high frequency AC. The governing ESM equation in global time scale is:

$$\frac{\partial c}{\partial t} = D\nabla^2 c$$
$$c_{init}(x) = c_{ss,p}(x), \tag{7.68}$$

The distribution of ions by the end of this regime is:

$$c(x, t_{end}) = c_0(x), \tag{7.69}$$

Regime ④: Charging with Negative Voltage

In this regime, a negative DC voltage is applied so that ions in the vicinity of the SPM tip are attracted towards the tip, resulting in deformation. The governing ESM equation in global time scale

is:

$$\frac{\partial c}{\partial t} = D\beta c\nabla^2\phi$$
$$c_{init}(x) = c_0(x) = c_0, \tag{7.70}$$

The time range is so chosen to allow ions to move to the steady state at the end of this regime. This eventual distribution can be predicted by our previous theoretical calculation.

$$c(x,t_{end}) \equiv c_{ss,n}(x) = \frac{\int_0^H c_0(x)dx}{\int_0^H e^{-\beta\phi(x)}dx} e^{\beta\phi(x)} \tag{7.71}$$

Regime ⑤: Relaxation from steady state due to previous negative DC charging

In this regime, a large increase in ESM response is observed immediately after the removal of the positive DC voltage, which then gradually decreases back to the ground level by the end of this regime. The ions in previous steady state returns to the uniform distribution, up to small frustration due to the high frequency AC. The governing ESM equation in global time scale is:

$$\frac{\partial c}{\partial t} = D\nabla^2 c$$
$$c_{init}(x) = c_{ss,n}(x), \tag{7.72}$$

The distribution of ions by the end of this regime is:

$$c(x,t_{end}) = c_0(x), \tag{7.73}$$

The different relaxation characteristics under different DC polarities can be clearly understood from our interpretation of ESM responses - a positive DC voltage by SPM tip reduces the Li-ion concentration underneath the SPM tip, resulting in a smaller response than in the ground state, while a negative DC voltage increases the Li-ion concentration underneath the SPM tip, resulting in a larger ESM response. The relaxation of ESM response to ground state after removal of either positive or negative voltage corresponds to the redistribution of Li-ions to the equilibrium concentration at ground state.

Profile of applied DC voltages and the resulting ion concentration and deformation (referred as deflection) are shown in figure (7.15). Notice that in the figure, ion concentration is normalized to a reference uniform concentration c_0, while the deflection is normalized with respect to the radius of the SPM tip R.

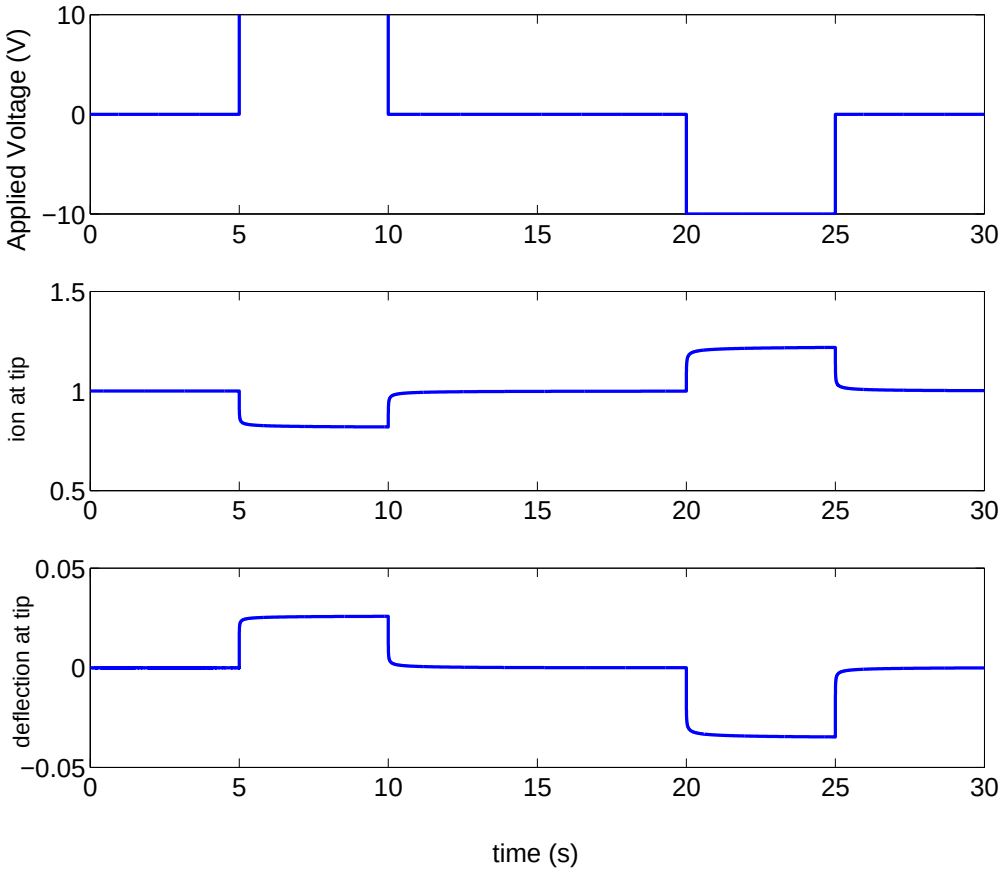

Figure 7.15: Simulation results of relaxation study of lithium ion. The top graph shows the profile of applied voltage $V(t)$. The middle graph shows the resulting ion concentration at the top surface of the electrode, $c(x = H,t)$. The bottom graph shows the deformation, $u(x = H,t)$.

Notice that it is not possible to get direct access of the ion concentration and actual deformation of the electrode, even on the top surface of the electrode that is in direct contact with the SPM tip. As discussed, AC voltage of small magnitude and high frequency, that is biased with the DC voltage, is adopted to obtain vibrational deflection whose magnitude is known as the AC-deflection. Useful

information on diffusivity and local concentrations can be tracked from AC-deflection, together with simulation results. The AC-deflection experimentally obtained in the regime of ground state and the two regions of relaxation are shown in figure (7.16) [90].

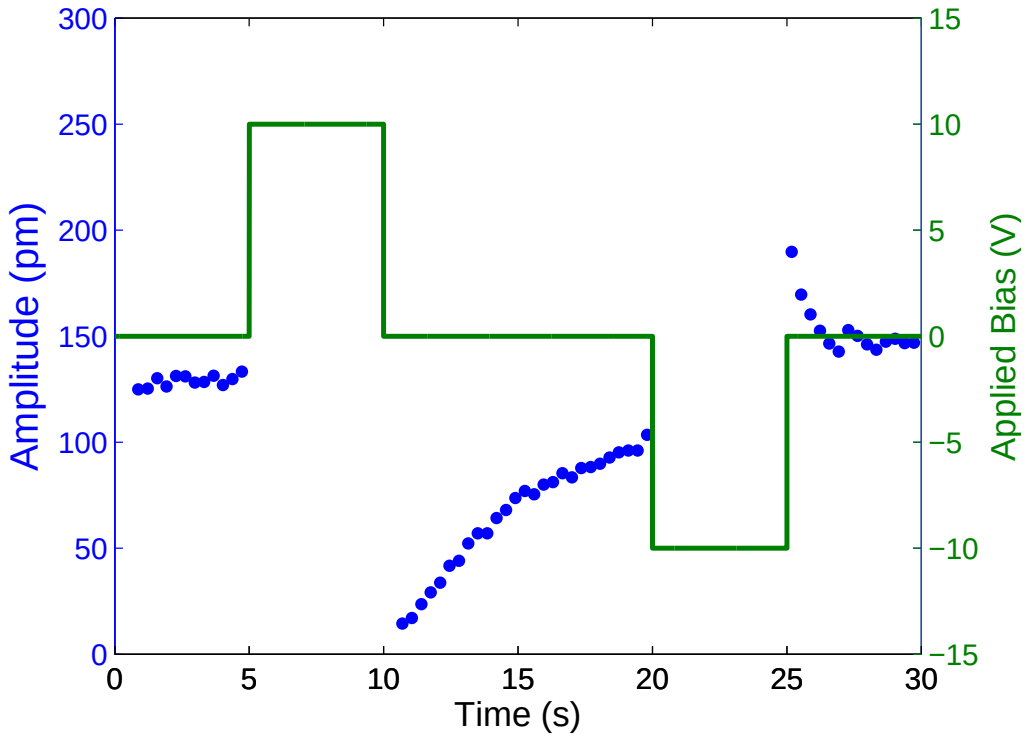

Figure 7.16: Experimental results of relaxation study of lithium ion. Deflection detected by the SPM tip is shown. Profile of DC voltage for manipulating ions is also shown.

The AC-deflection is also numerically simulated. The data on the two regimes of relaxation are also fitted with functions in exponential form:

$$\begin{aligned} u^* &= a\left(1-e^{-bt}\right) = a\left(1-e^{-\frac{t}{\tau}}\right) \quad \text{: first relaxation regime} \\ u^* &= a\left(1+e^{-bt}\right) = a\left(1+e^{-\frac{t}{\tau}}\right) \quad \text{: second relaxation regime,} \end{aligned} \tag{7.74}$$

where τ represents the time constant and a is the value of the function at the end of the regime. The result is shown on figure (7.17).

Next we will link experimental data and simulated data over the two regimes of relaxation to

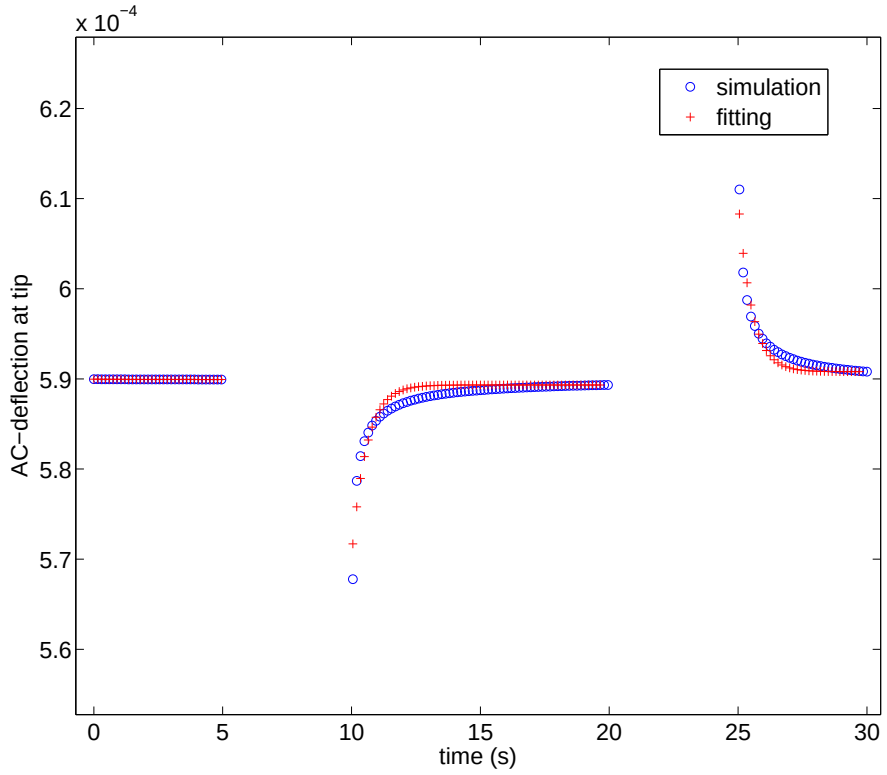

Figure 7.17: Simulation results of relaxation study of lithium ion. Deflection detected by the SPM tip is shown. The data is also fitted with functions in exponential form. The magnitude of the deflection is normalized with respect to the radius of SPM tip.

predict diffusivity (D) and then over the first regime (ground state) to predict local ion concentration (n). During relaxation, without the effect of electro-migration from DC voltage, ions return to the original uniform configuration. The trend is believed to behave exponentially. Our strategy is to estimate the the time constants from experimental data and simulation data. Comparing the time constants with respect to the time scale will enable us to obtain the diffusivity.

Over the first relaxation regime (where the positive voltage was removed), the simulated data is fitted with exponential function:

$$\begin{aligned} u_{simu}(t) &= 0.00001926\left[1-e^{-1.7696t}\right] \\ &= 0.00001926\left[1-e^{-\frac{t}{0.5651}}\right], \end{aligned} \tag{7.75}$$

where the time constant is approximately $\tau_{simu} = 0.5651$.

In the simulation, we have assumed that the diffusivity is $D_{simu} = 5\times 10^{-14}(m^2/s)$. We have also normalized the length scale with respect to the radius of the SPM tip. Thus in the normalized time scale is:

$$\overline{t_{simu}} = \frac{R^2}{D_{simu}} = \frac{\left(10\times 10^{-8}\right)^2}{5\times 10^{-14}} = 0.002(s). \tag{7.76}$$

On the other hand, the experimental data is fitted with the exponential function:

$$\begin{aligned} u_{exp}(t) &= 103 - 115e^{-0.2632t} \\ &= 103 - 115e^{-\frac{t}{0.38}}, \end{aligned} \tag{7.77}$$

where the time constant is approximately $\tau_{exp} = 3.8$.

The normalized time scale for experiment is:

$$\overline{t_{exp}} = \frac{R^2}{D} = \frac{\left(10\times 10^{-8}\right)^2}{D}, \tag{7.78}$$

where D is the actual diffusivity of the ion to be determined.

The dynamic behaviours in experiments and simulations must be consistent. Thus by balancing

the ratio of time constant over the normalized time scale will yield the diffusivity of ions.

$$\frac{\tau_{exp}}{\overline{t_{exp}}} = \frac{\tau_{simu}}{\overline{t_{simu}}}$$
$$\frac{0.38}{\frac{(10\times10^{-8})^2}{D}} = \frac{0.5651}{0.02}$$
$$D \approx 7.4474 \times 10^{-15} (m^2/s) \tag{7.79}$$

Similar procedures can be applied to experimental and simulation data on the second relaxation regime (where the negative voltage was removed) to predict another possible value of diffusivity.

Simulation data: Fitting, time constant and normalized time scale

$$\begin{aligned} u_{simu}(t) &= 0.00001923\left[1+e^{-1.9127t}\right] \\ &= 0.00001923\left[1+e^{-\frac{t}{0.5228}}\right] \\ \tau_{simu} &= 0.5228(s) \\ \overline{t_{simu}} &= \frac{R^2}{D_{simu}} = \frac{\left(10\times10^{-8}\right)^2}{5\times10^{-14}} = 0.002(s). \end{aligned} \tag{7.80}$$

Experimental data: Fitting, time constant and normalized time scale

$$\begin{aligned} u_{exp}(t) &= 142+58.48e^{-1.359t} \\ &= 142+58.48e^{-\frac{t}{0.7358}} \\ \tau_{exp} &= 0.7358 \\ \overline{t_{exp}} &= \frac{R^2}{D} = \frac{\left(10\times10^{-8}\right)^2}{D} \end{aligned} \tag{7.81}$$

Balancing the ratio of time constant over the normalized time scale for both experiment and

simulation will yield the diffusivity of ions.

$$\frac{\tau_{exp}}{t_{exp}} = \frac{\tau_{simu}}{t_{simu}}$$
$$\frac{0.7358}{\frac{(10\times10^{-8})^2}{D}} = \frac{0.5228}{0.02}$$
$$D \approx 3.5526\times10^{-14}(m^2/s) \tag{7.82}$$

Since the experimental data on the second relaxation regime appear to be scattering, the curve fitting of the data suffers inaccuracy and thus the diffusivity predicted may not be fully reliable. From now on, we may assume that the experimental value of diffusivity to be $D \approx 7.4474\times10^{-15}(m^2/s)$, which was obtained on experimental and simulation data on first relaxation regime.

With the estimated value of diffusivity, we may further predict the ion concentration from experimental and simulation data on the regime of ground state where only AC-voltage is applied. Under AC voltage $V(t) = V_0 e^{j\omega t}$, the resulting local ion concentration has the form:

$$c(t) = c_0 + c_1(\omega)e^{j\omega t} + c_2(\omega)e^{j2\omega t} + \cdots, \tag{7.83}$$

where c_1 and c_2 are the first and second harmonics that depends on the operating frequency (ω) of the input voltage. This ion distribution that is oscillating around the initial distribution results in a displacement (which is determined by solving mechanical equilibrium equation accordingly). The deflection at the top surface of the electrode, $u_{top,exp}$, is related to first harmonic:

$$\frac{u_{top,exp}}{sV_0n_0\beta R} = \frac{0.36032}{\omega^*} \tag{7.84}$$

This formula can be re-casted with variables in real scales:

$$\begin{aligned} u_{top,exp} &= sV_0n_0\beta R\times0.36032\frac{1}{\omega^*} \\ &= sV_0n_0\beta R\times0.36032\frac{D}{R^2}\frac{1}{\omega} \\ &= 0.36032sV_0n_0\beta\frac{D}{R}\frac{1}{\omega} \end{aligned} \tag{7.85}$$

The deflection as detected by the SPM tip during ESM experiment is 2 (pm) after integrating with the quality Q-factor. In the simulation, we have assumed electro-chemical constant $s = 1$, applied AC-voltage $\beta V_0 = \frac{3}{40}$, operating frequency $\omega = 1000k$, diffusivity $D = 7.4474 \times 10^{-15}$, radius of SPM tip $R = 10^{-8}$. Substituting these parameters into the formula will yield an estimate value of the ion concentration:

$$\begin{aligned} 2 \times 10^{-12} &= 0.36032 \times 1 \times \frac{3}{40} n_0 \frac{7.4474 \times 10^{-15}}{10^{-8}} \frac{1}{1000 \times 1000} \\ n_0 &= 9.9375(mol/m^3) \end{aligned} \tag{7.86}$$

7.4.1 Summary

We have developed an approach to combine experimental data and simulation for an ESM experiments on relaxation with DC-AC bias to track back useful information on diffusivity (D) and local ion concentration (n). By having experimentally the (AC-)deflection detected by the SPM tip on the top surface, we are able to probe physical quantities of the electrode. On the other hand, we have not yet considered the effect of the second harmonic, which we will focus in future work.

7.5 Formulation in higher dimensions

The preceding one-dimensional simulation and analysis of ion concentration in ESM can be generalized to higher dimensions. For simplicity, most of the effort is placed on two-dimensions. Three-dimensional analogy follows naturally.

We begin our discussion with the general form of the governing equation for ion concentration.

$$\frac{\partial c}{\partial t} = D\nabla^2 c - \beta D \nabla \cdot (c\mathbf{E}), \tag{7.87}$$

where $c = c(x,y)$ is the ion concentration at the spatial coordinates (x,y), $\mathbf{E} = \mathbf{E}(x,y)$ is the applied electric field to the sample, D is the diffusion coefficient and β is the electro-drifting constant.

Following the numerical scheme applied to one-dimensional case, we decompose the equation

into several component equations, which we then discretize.

$$\begin{aligned}\frac{\partial c}{\partial t} &= D\nabla^2 c - \beta D\nabla\cdot(c\mathbf{E}) \\ &= -\nabla\cdot(-D\nabla c + \beta Dc\mathbf{E}) \\ &= -\nabla\cdot(U,V)\,, \end{aligned} \tag{7.88}$$

where $U = U(x,y)$ and $V = V(x,y)$ represent the x- and y- components of the flux of ions.

More specifically, the fluxes are expressed as:

$$\begin{aligned}\begin{pmatrix} U \\ V \end{pmatrix} &= -D\nabla c + \beta Dc\mathbf{E} \\ \begin{pmatrix} U \\ V \end{pmatrix} &= -D\begin{pmatrix} \frac{\partial c}{\partial x} \\ \frac{\partial c}{\partial y} \end{pmatrix} + \beta Dc\begin{pmatrix} E_x \\ E_y \end{pmatrix}, \end{aligned} \tag{7.89}$$

where $E_x = E_x(x,y)$ and $E_y = E_y(x,y)$ are the x- and y- components of the applied electric field.

With these notations, the set of decomposed equations in two dimensions are thus:

$$\begin{aligned}\frac{\partial c}{\partial t} &= -\frac{\partial U}{\partial x} - \frac{\partial V}{\partial y} \\ U(x,y) &= -D\left(\frac{\partial c}{\partial x} - \beta E_x(x,y)c(x,y)\right) \\ V(x,y) &= -D\left(\frac{\partial c}{\partial y} - \beta E_y(x,y)c(x,y)\right) \end{aligned} \tag{7.90}$$

The two-dimensional space occupied by the ESM sample is discretized into $N\times N$ cells as the computational grids. These cells have boundaries denoted by the points X_I and Y_J, where $1 \le I,J \le N+1$. Fluxes and electric fields are defined at these points (X_I, Y_J). The centers of the cells are specified by the coordinates (x_i, y_j), $1 \le i,j \le N$, where the ion concentration is defined. More

specifically,

$$\begin{aligned}
\mathbf{c} \equiv \mathbf{c}(t) \equiv c(x,y,t) &\approx c(x_i,y_j,t) \equiv c_{ij}(t) \\
\mathbf{U} \equiv \mathbf{U}(t) \equiv U(x,y,t) &\approx U(X_I,Y_J,t) \equiv U_{IJ}(t) \\
\mathbf{V} \equiv \mathbf{V}(t) \equiv V(x,y,t) &\approx V(X_I,Y_J,t) \equiv V_{IJ}(t)
\end{aligned} \tag{7.91}$$

These variables may be dependent on time t. Without loss of generality, we will drop this symbol. We also rewrite the components of the applied electrical field as:

$$\begin{aligned}
E &\equiv E_x \\
F &\equiv E_y
\end{aligned} \tag{7.92}$$

The boundary conditions for the problem are the given fluxes along the four boundary lines of the two dimensional sample. Thus:

$$\begin{aligned}
U_{IJ} &= \widehat{U}_{IJ} \\
V_{IJ} &= \widehat{V}_{IJ}
\end{aligned} \tag{7.93}$$

whenever $I = 1, N+1$ and / or $J = 1, N+1$, which corresponds to the points lying on the boundaries.

The set of governing equations for ion transport subjected to zero flux across all boundaries are discretized as:

Numerical scheme for flux components at interior points, $(2 \leq I, J \leq N)$:

$$\begin{aligned}
U_{IJ} &= -D\left(\frac{c_{i,j} - c_{i-1,j}}{h} - E_{IJ}\frac{c_{i,j} + c_{i-1,j}}{2}\right) \\
V_{IJ} &= -D\left(\frac{c_{i,j} - c_{i,j-1}}{h} - F_{IJ}\frac{c_{i,j} + c_{i,j-1}}{2}\right)
\end{aligned} \tag{7.94}$$

Numerical scheme for flux components at boundary points, $I = 0$ or $I = N+1$ or $J = 0$ or

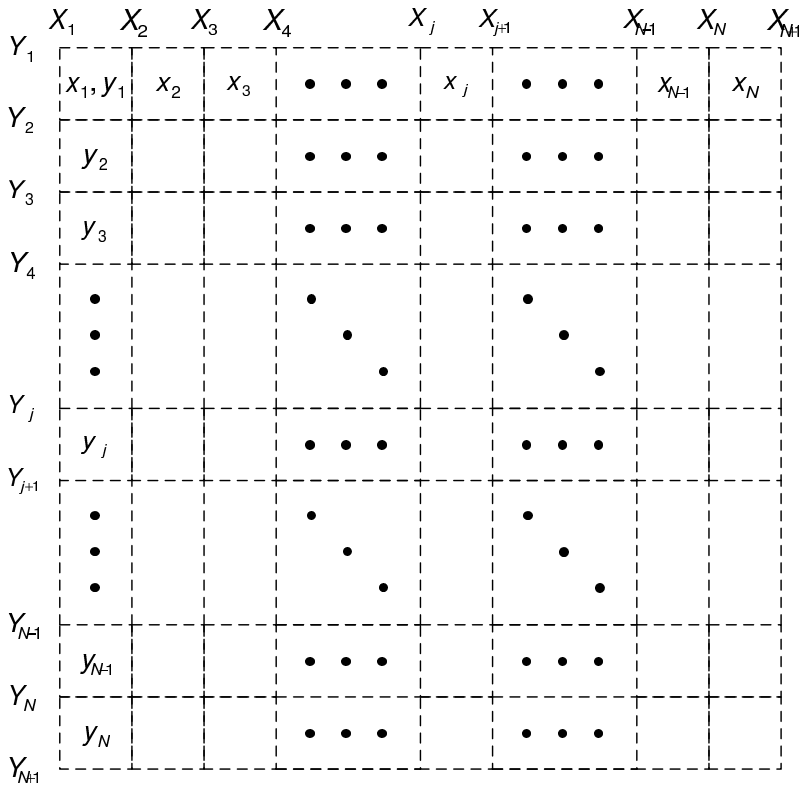

Figure 7.18: Grid for one-dimensional simulation. The length of the sample is divided into N cells with $N+1$ subdivision points denoted by x_i, at which electric fields or potentials are discretized. The midpoints of the cells are denoted by x_j, at which the ion concentrations are discretized.

$J = N + 1$:

$$U_{IJ} = 0$$
$$V_{IJ} = 0 \tag{7.95}$$

Numerical scheme for concentration at all discretized points, $(1 \leq i, j \leq N)$:

$$\frac{\partial c_{ij}}{\partial t} = -\frac{U_{I+1,J} - U_{I,J}}{h} - \frac{V_{I,J+1} - V_{I,J}}{h} \tag{7.96}$$

Combining these three sets of numerical schemes results in a numerical scheme for concentration only. This scheme is formulated at various sections of the grid as outlined in appendix (E.6) and figure (7.19).

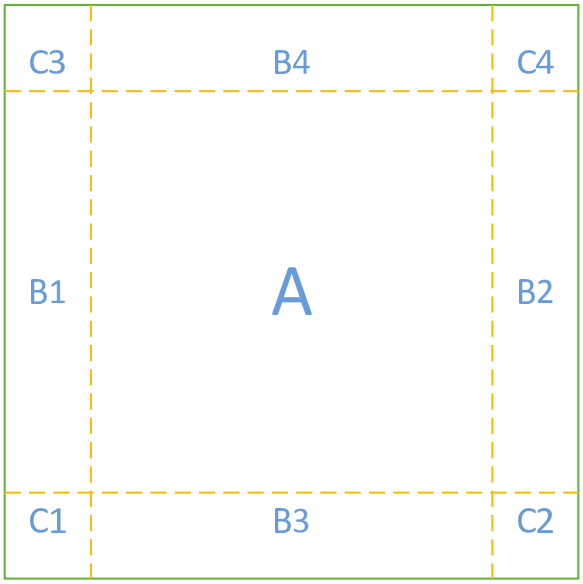

Figure 7.19: The explicit forms of the differential equations for concentration at (x_i, y_j), that is the differential equation for $c_{ij}(t)$, depends on which section of the two-dimensional domain within which (x_i, y_j) lies. There are nine possible cases that refer to interior points (denoted by A), four boundaries (denoted by $B1, B2, B3, B4$) and four corners (denoted by $C1, C2, C3, C4$).

By the method of lines (MOL), these equations are assembled into a nonlinear time-dependent

coefficient ODE system for the concentration c at the grid points (x_i, y_j) as functions of time t:

$$\frac{\partial \mathbf{c}(t)}{\partial t} = \mathbf{M}\left(\mathbf{c}(t), \mathbf{U}(t), \mathbf{V}(t)\right)\mathbf{c}(t), \tag{7.97}$$

where the dimension of $\mathbf{c}$ is $(N^2 \times 1)$ and the dimension of the matrix M is $(N^2 \times N^2)$. The initial conditions of this ODE system is the initial concentration $\mathbf{c}(0) = \mathbf{c}_0 = c_{ij}^0$. Recall that this approach ensures that numerically the total amount concentration at all time t is conserved for zero flux across all boundaries.

In the following, we illustrate two simulations for domain with lithium ions subjected to a SPM tip with positive and negative voltages respectively. The domain, whose thickness is 20 times the tip radius of the tip, is quantified numerically by a (200×200)-grid, so that 40000 differential equations are generated to solve for the ion concentration at $\left\{(x_i, y_j), 1 \le i \le 200, 1 \le j \le 200\right\}$. Assume that the initial ion distribution is unform with the normalized value of one, that is, $c(x_i, y_j)(t = 0) = 1$. The magnitude of both voltages is 0.25 (Volts), small enough so that the distribution of potential from both voltages are moderately symmetric. The distance between the effective charge Q of the SPM tip and the surface of the domain is $0.5R$, where R is the radius of the SPM tip. For simplicity, we take the diffusivity to be $D = 1$. The ESM equation, now expressed as a first order evolution equation, is iterated until steady state is reached. Ion distributions and resulting deformations in steady state will be shown.

As a remark, the first order evolution equation is numerically solved using implicit scheme, as briefly shown below:

$$\begin{aligned} \frac{\mathbf{c}^{k+1} - \mathbf{c}^k}{\Delta t} &= \mathbf{M}\left(\mathbf{C}^k, \mathbf{U}^k, \mathbf{V}^k\right)\mathbf{c}^{k+1} \\ \left[\mathbf{I} - \mathbf{M}\left(\mathbf{C}^k, \mathbf{U}^k, \mathbf{V}^k\right)\Delta t\right]\mathbf{c}^{k+1} &= \mathbf{c}^k \end{aligned} \tag{7.98}$$

The iterative scheme starts with unit initial condition (concentration), or, $\mathbf{c}^0 = \mathbf{c}(0) = 1$. With properly arrangement of entries, the $\mathbf{M}$ can be effectively stored as a banded matrix, so as to accelerate the computation and to allow simulation of large domains that requires more data points for discretization.

After the ion concentration $\mathbf{c}(t) \approx \mathbf{c}(t^k) = \mathbf{c}^k$ has been computed, one may compute the eigen-

strain that results from derivation from the preceding ion concentration $\mathbf{c}(0) \approx \mathbf{c}(t^0) = \mathbf{c}^0$, as follow:

$$\varepsilon^s = s\Delta\mathbf{c} = s\left(\mathbf{c}(t^k) - \mathbf{c}(t^0)\right), \tag{7.99}$$

here s is the expansion coefficient that relates ion redistribution and deformation. With mechanical boundary conditions, elasticity equation is used to solve for the displacements, strains and stresses of the domain when influenced by external voltage. The boundary conditions being considered for both ESM and mechanical equilibrium are shown in figure (7.20).

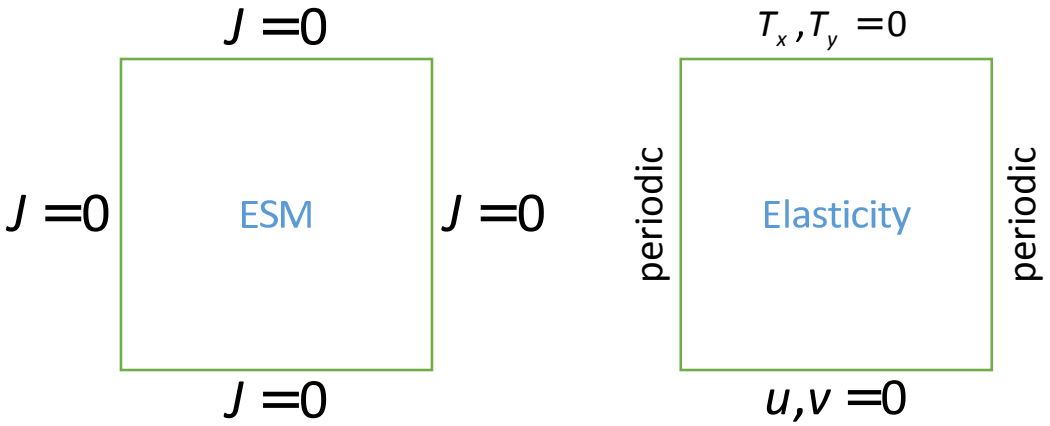

Figure 7.20: Boundary conditions for (a) ESM equation and (b) Elasticity equation. For ESM equation, all four boundaries assume zero flux so as not to allow ion to flow out. For elasticity equation, the top surface is traction-free while the bottom is displacement-free. The left and right boundaries are periodic.

7.5.1 Simulation of Lithium Ions in Two Dimensional Domain Due to SPM tip with Positive Voltage

Using the numerical just developed, assume that a SPM tip with positive voltage ($V_0 > 0$) is brought to the center on the top surface of the domain. Since lithium ions are positive charges, they are attracted by the positive voltage of the SPM tip in the vicinity of the site of the SPM tip, as schematically shown in figure (7.23) (a). Ions are moving away from where the SPM is applied, where the density (or concentration) of ions decreases, eventually resulting in () of the sample, since lithium ions are heavier. In steady state, the ion concentration is shown in figure (7.21). Displacement components due to ion redistribution are shown in figure (7.22). The deformation of the domain is also

exaggeratedly visualized in figure (7.23) (b).

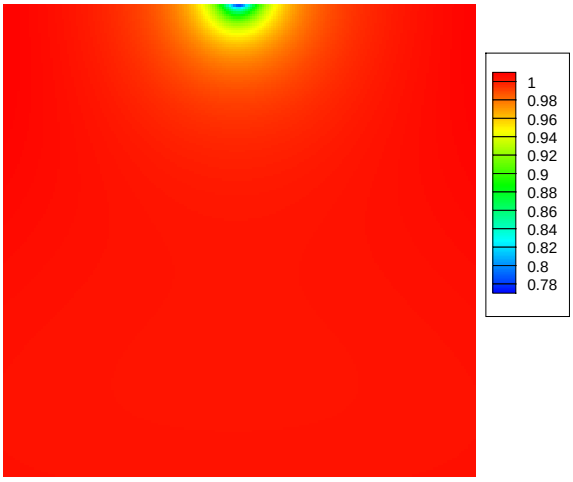

Figure 7.21: Contour showing ion concentration at steady state for domain subjected to SPM tip with positive voltage. Notice that lithium ion are attracted towards the site of SPM tip.

7.5.2 Simulation of Lithium Ions in Two Dimensional Domain Due to SPM tip with Negative Voltage

On the other hand, assume that a SPM tip with positive voltage ($V_0 < 0$) is brought to the center on the top surface of the domain. Since lithium ions are positive charges, they are attracted by the negative voltage of the SPM tip in the vicinity of the site of the SPM tip, as schematically shown in figure (7.26) (a). Ions are moving towards from where the SPM is applied, where the density (or concentration) of ions increases, eventually resulting in () of the sample, since lithium ions are heavier. In steady state, the ion concentration is shown in figure (7.24). Displacement components due to ion redistribution are shown in figure (7.25). The deformation of the domain is also exaggeratedly visualized in figure (7.26) (b).

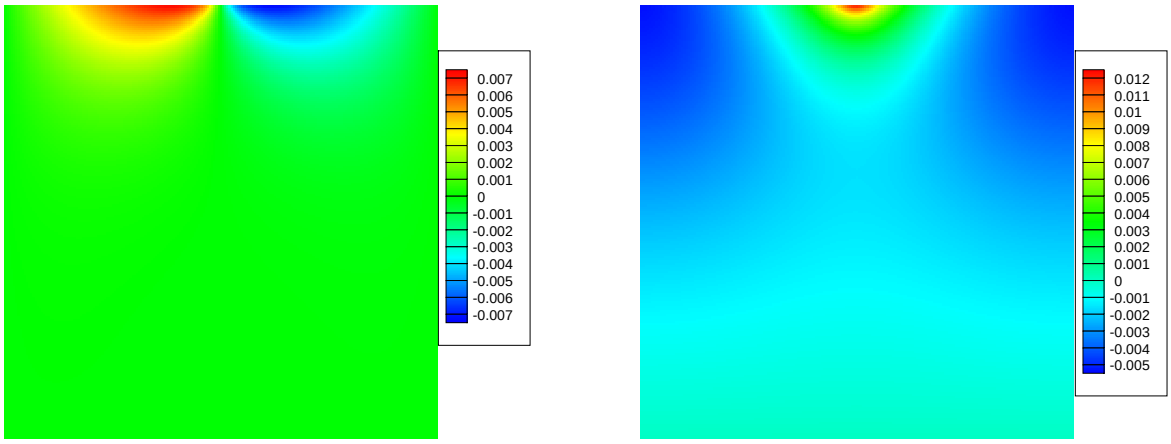

(a) x-displacement u (b) y-displacement v

Figure 7.22: Displacement components of domain of Lithium ions in steady state due to SPM tip with positive voltage.

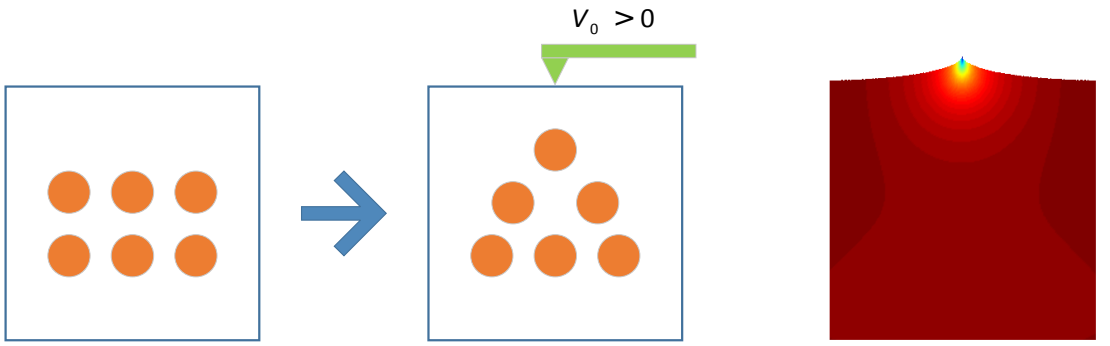

(a) Ions are attracted. (b) Deformation visualized.

Figure 7.23: Schematic showing positive voltage induces attraction of ion towards SPM tip and the resulting deformation.

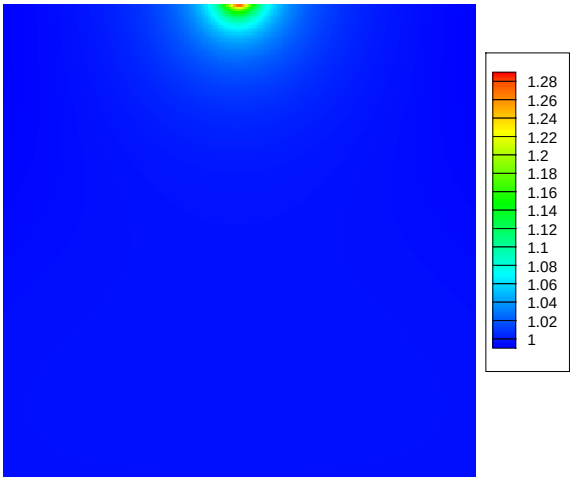

Figure 7.24: Contour showing ion concentration at steady state for domain subjected to SPM tip with negative voltage. Notice that lithium ion are attracted towards the site of SPM tip.

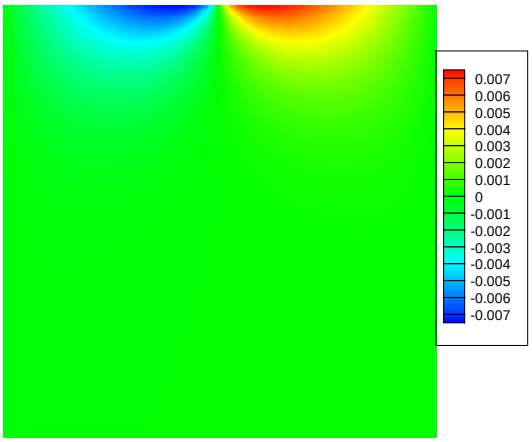

(a) x-displacement u

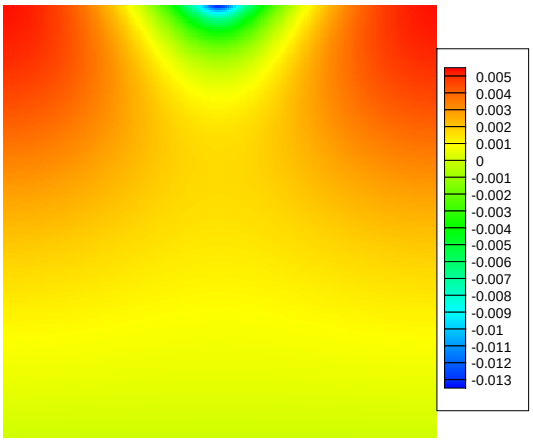

(b) y-displacement v

Figure 7.25: Displacement components of domain of Lithium ions in steady state due to SPM tip with negative voltage.

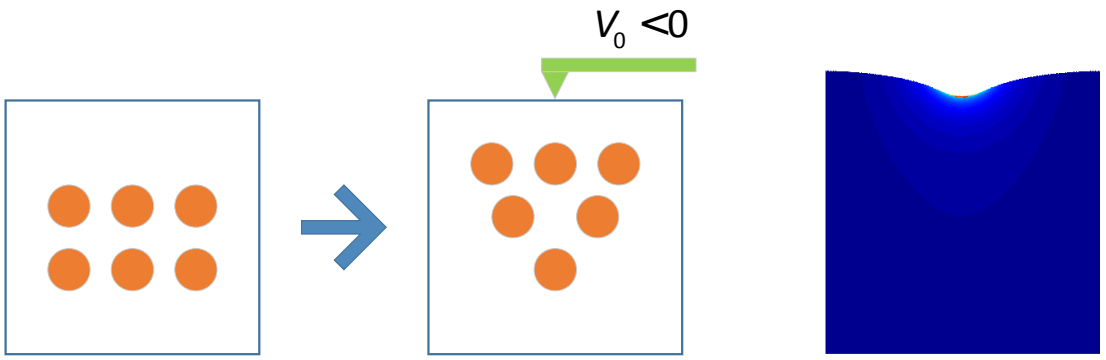

(a) Ions are attracted. (b) Deformation visualized.

Figure 7.26: Schematic showing negative voltage induces attraction of ion towards SPM tip and the resulting deformation.

7.5.3 Region of Influence

From the 2D simulation of ion redistribution, we may identify the region in the vicinity of the SPM tip, which we refer as the region of influence. The trend of ion concentration and deformation (as deflection) over the center line are shown in figure (7.27). Notice that the size of the region of influence is about 7 times of the radius R of the SPM tip, which is consistent with the corresponding results predicted by one-dimensional model. Notice in two dimensions, displacement has two components denoted by u and v. For the sake of convenience, we plot the vector sum of the displacement, that is, $\sqrt{u^2+v^2}$.

7.5.4 Fitting first harmonic deflection for two-dimensional model

With two dimensional model, we may also study the first harmonic deflection that results from applying AC voltage in the SPM tip on the electrode. The simulation data are then curve-fitted to relate normalized deflection and normalized operating frequency:

$$\delta^*_{AC} \approx \frac{0.008732}{\omega^*} \tag{7.100}$$

This formula can be adopted to predict the local concentration with ESM experiments. Simulation data and the fitting curve are shown in figure (7.28).

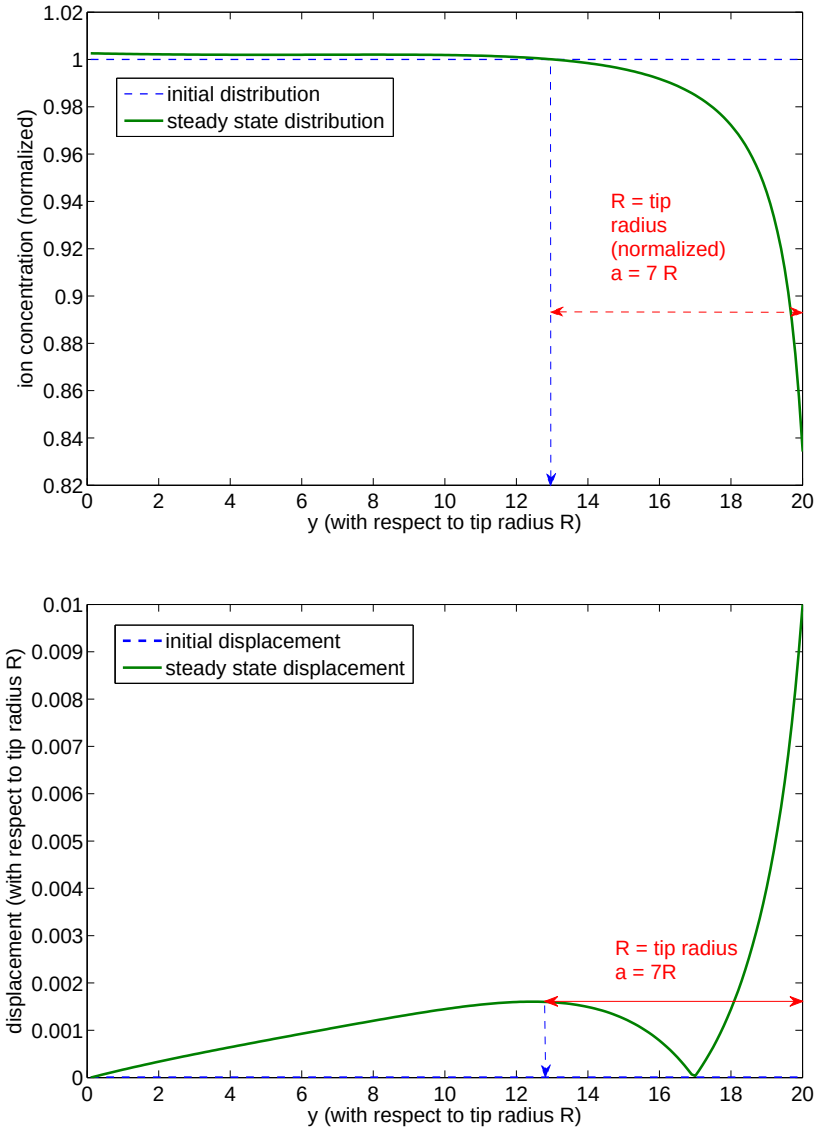

Figure 7.27: Region of influence of ion distribution and displacement on top surface as detected by SPM tip in 2D model. The top graph shows the initial and steady state ion distribution over the center line of the two-dimensional domain. The bottom graph shows the displacements.

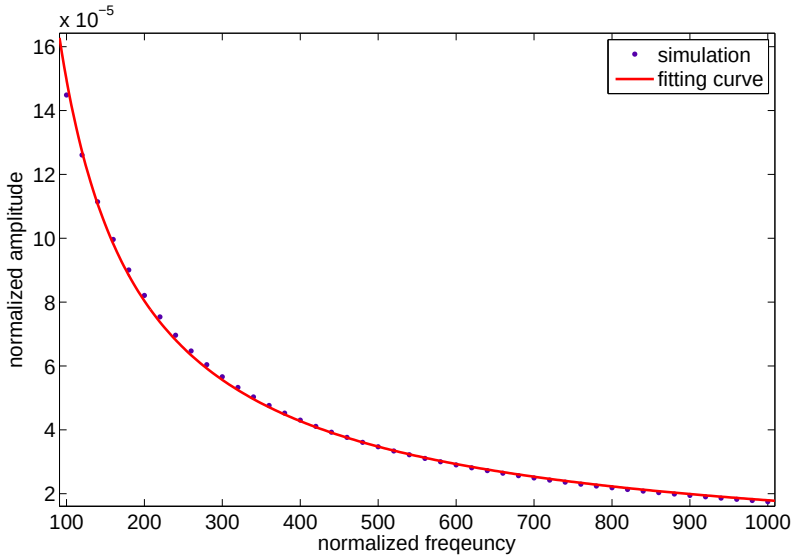

Figure 7.28: First harmonic deflection in two dimensional model.

7.5.5 Sensitivity of SPM tip in probing local concentration in inhomogeneous electrode

In previous one-dimensional model, with known diffusivity (D) (which can be predicted via ion relaxation from manipulating DC voltage), it is possible to probe local ion concentration (n) by linking experimental data of ESM experiments with simulation data for first harmonic deflection on top surface that is due to applied AC voltage with small magnitude and high frequency.

In order to further verify the sensitivity of the SPM tip in the capability to probe local ion concentration at various points over the sample surface, we consider a two dimensional domain with laminating distribution of known ion concentration (1 and 1.5 repeating) across the x-coordinate, as shown in figure (7.29) (a). The ratio of the ion concentration in different layers is 1.5. Two-dimensional model allows us to simulate AC-deflection over each portion, as shown in figure (7.29) (b). The ratio of the magnitude is approximately 1.539. It proves that ESM experiments with simulation based on two-dimensional model allows us to probe local ion concentration using AC voltage.

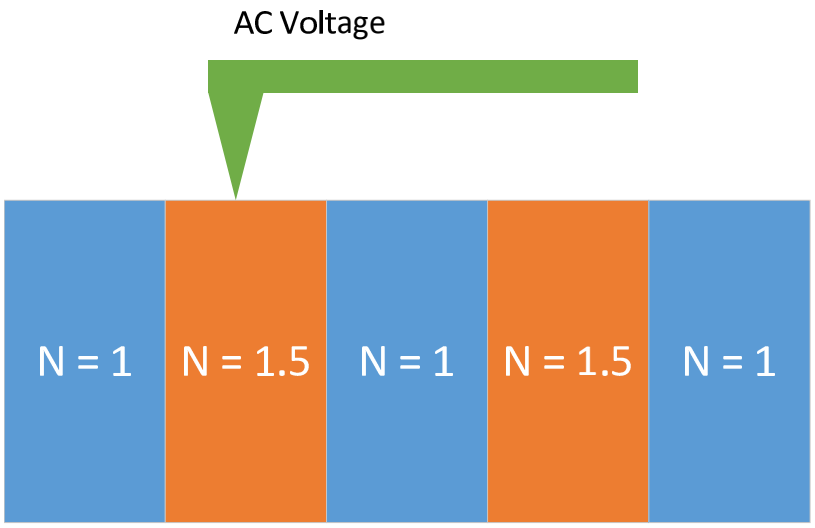

(a) distribution of laminated ion concentration

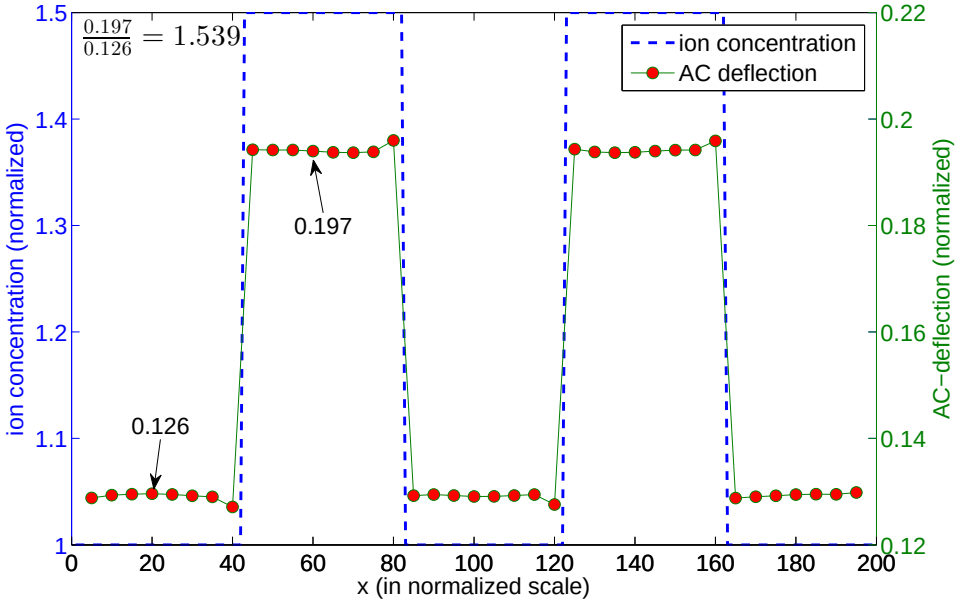

(b) AC-deflection.

Figure 7.29

Chapter 8

SPECTRAL METHODS IN ELECTRO-MECHANICS AND PHASE FIELD SIMULATIONS

In our previous works on solving Maxwell's equations, elasticity equations and phase field simulations, we have assumed periodicity along all directions and then released periodicity along the out-of-plane direction for more realistic configurations. There are three potential reasons for improvement and generalization:

(1) Non-periodicity along out-of-plane direction associates with finite difference whose accuracy is of second order, compared with spectral accuracy of FFT along the two in-plane directions. Effectively the accuracy of the whole numerical scheme is downgraded to second order.

(2) In addition to (1), imposing periodicity along in-plane directions do not take into account the physical boundaries along the four lateral faces of the three-dimensional domain. For mechanical boundary conditions, traction on top surface and displacement constraint on bottom surface are involved, while for electrical boundary conditions, electric fields, charges or potentials on either surfaces are involved.

(3) The constitutive material properties (as in Hooke's law and dielectric equation) being adopted are homogeneous and of isotropic, which do not suffice to study more general configuration, such as non-homogeneous materials.

We would like to extend our current numerical tools to include more general and realistic physical configurations, such as nonhomogeneous and anisotropic materials and physical boundary conditions over lateral surfaces instead of periodicity. For this, we utilize a powerful numerical method known as the spectral method that will enable us to resolve these three issues. We will develop the spectral method to solve Maxwell's equation and elasticity equation for nonhomogeneous materials subjected to arbitrary physical boundary conditions on boundaries without imposing any periodicity, as well as phase field simulation under general configuration. This numerical formulation is of spectral accuracy.

References of spectral methods can be found in works of Trefethen [94, 95, 96]. Application and implementation of the spectral method in heat transfer and related problems can be founded in Guo, Labrosse and Narayanann [97].

8.1 Preparation

Before solving these equations in the general context, we outline the essential building blocks of the spectral method.

We work with simulation in at least micro-scales. As a custom, we normalize the length scale. The in-plane dimensions are scaled to one, $[0,1]$, while the out-of-plane dimension is scaled accordingly, with the same scale factor.

For spectral method, due to various issues with the theory of approximation, we normalize the major dimensions to length of two. For instance, these dimension are scaled to symmetric intervals $[-1,1]$.

Over the normalized intervals, we introduced the coordinate system as the projection of $(n+1)$ points on the upper half of the unit circle in the complex plane. These projected points are known as the Chebyshev points, which can also be mathematically characterized as:

$$x_j = -\cos\left(j\frac{\pi}{n}\right), 0 \le j \le n \tag{8.1}$$

The distribution of these Chebyshev points are illustrated in figure (8.1).

All physical quantities are designated at these points. In other words, all physical quantities (such as displacements and potential) are approximated at the Chebyshev points $\{x_j\}$, through the Chebyshev polynomials $\{T_j\}$, where:

$$\begin{aligned} f(x) &\approx \sum_{k=0}^{n} a_k T_k(x) \\ a_k &= \frac{2}{\pi}\int_{-1}^{1} \frac{f(x)T_k(x)}{\sqrt{1-x^2}}dx \\ T_k(x) &= \cos\left(k\cos^{-1}(x)\right) \end{aligned} \tag{8.2}$$

Over the unevenly distributed Chebyshev points $\{x_j\}$, we may introduce the numerical differ-

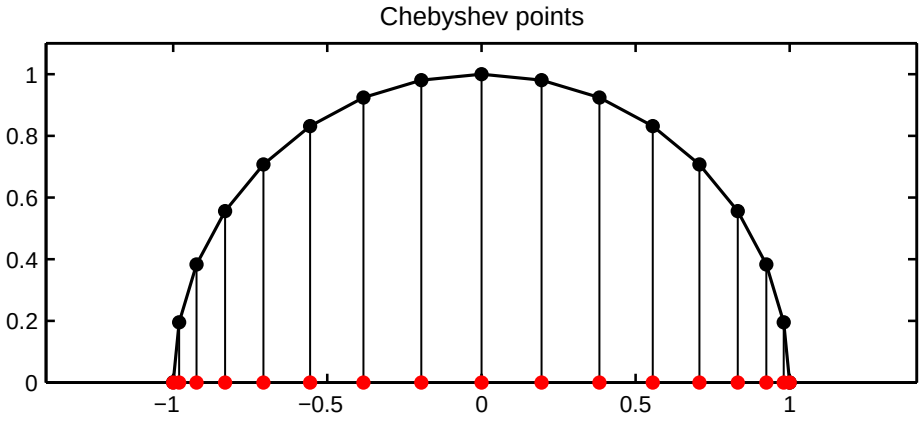

Figure 8.1: Chebyshev points (n = 16)

entiation matrix **D** with high accuracy. The inverse of this matrix, $\mathbf{D}^{-1}$, corresponds to integration.

The elements of the Chebyshev differentiator matrix $\mathbf{D} = [D_{ij}]$ are characterized by the following formula:

$$
\begin{aligned}
D_{00} &= \frac{2N^2+1}{6} \\
D_{NN} &= -\frac{2N^2+1}{6} \\
D_{jj} &= -\frac{x_j}{2\left(1-x_j^2\right)}, j = 1,...,N-1 \\
D_{ij} &= \frac{c_i}{c_j}\frac{(-1)^{i+j}}{x_i - x_j}, i \neq j
\end{aligned}
\tag{8.3}
$$

where we define

$$
c_{ij} = \begin{cases} 2 & for\, i = 0, N \\ 1 & for\, 1 \leq i \leq N-1 \end{cases}
\tag{8.4}
$$

Alternatively, the differentiator matrix has the following structure:

$$\mathbf{D} = \left[\begin{array}{c:cc:c} \frac{2N^2+1}{6} & 2\frac{(-1)^{i+j}}{1-x_j} & & \frac{1}{2}(-1)^N \\ \hdashline -\frac{1}{2}\frac{(-1)^i}{1-x_i} & -\frac{x_j}{2\left(1-x_j^2\right)} & \frac{(-1)^{i+j}}{x_i-x_j} & \frac{1}{2}\frac{(-1)^{N+i}}{1+x_i} \\ & 2\frac{(-1)^{i+j}}{1-x_j} & & \\ \hdashline -\frac{1}{2}(-1)^N & -2\frac{(-1)^{N+j}}{1-x_j} & & -\frac{2N^2+1}{6} \end{array}\right] \tag{8.5}$$

Matrix corresponding to second derivatives **E** is computed by squaring the differentiator matrix **D**. For instance,

$$\mathbf{E} = \mathbf{D}^2 \tag{8.6}$$

If the values of some function $u(x)$ at Chebyshev points $\{x_j\}$ are approximated as $u_i = u(x_i)$, then the approximations of the first and second derivatives, $u'(x)$ and $u''(x)$, at the Chebyshev points $\{x_j\}$, denoted by $v_i = u'(x_i)$ and $w_i = u''(x_i)$ respectively, can be approximated via multiplications with matrices **D** and **E**. Mathematically,

$$\begin{gathered} \left\{u'(x_i)\right\} \approx \mathbf{D}\left\{u(x_i)\right\} \\ \left\{\begin{array}{c} v_0 \\ \vdots \\ v_i \\ \vdots \\ v_N \end{array}\right\} \approx \left[\begin{array}{ccc} & & \\ & \mathbf{D} & \\ & & \end{array}\right] \left\{\begin{array}{c} u_0 \\ \vdots \\ u_i \\ \vdots \\ u_N \end{array}\right\} \end{gathered} \tag{8.7}$$

and

$$\left\{u''(x_i)\right\} \approx \mathbf{E}\left\{u(x_i)\right\}$$

$$\begin{Bmatrix} w_0 \\ \vdots \\ w_i \\ \vdots \\ w_N \end{Bmatrix} \approx \begin{bmatrix} & & \\ & \mathbf{E} & \\ & & \end{bmatrix} \begin{Bmatrix} u_0 \\ \vdots \\ u_i \\ \vdots \\ u_N \end{Bmatrix} \tag{8.8}$$

Without loss of generality, we focus on solving the mentioned problems in two dimensions. We will revisit Maxwell's equation with periodic conditions across x-direction and physical boundary conditions over top and bottom surfaces, for validation against the previous methods using FFT and finite difference. We will then propose a generalization of the spectral method to deal with non-periodicity along both x- and y-directions. Spectral method for elasticity equation and phase field simulation are finally outlined.

8.2 Solving Maxwell's Equation with x-periodicity using Spectral Method

Recall that we are solving the following Maxwell's equation where periodicity is assumed along x-direction:

$$\kappa\nabla^2\phi = \nabla\cdot\mathbf{P}, \tag{8.9}$$

where $\phi = \phi(x,y)$ is the potential over the sample, κ is the permittivity and $\mathbf{P}$ represents the vector for the spontaneous polarization. Various boundary conditions can be considered over the top and bottom boundaries. For Maxwell's equation, potential or electric flux or charge are adopted. (Figure 8.2)

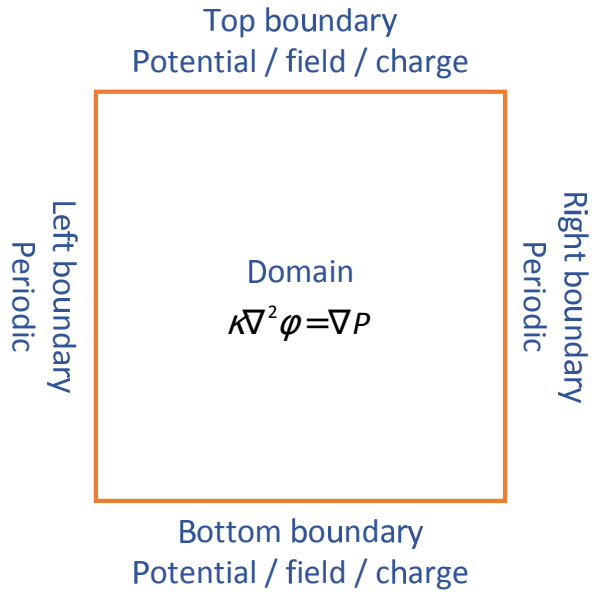

Figure 8.2: Schematic of computational domain for Maxwell's equation with boundary condition. Periodicity is assumed in x-direction.

As what was done before, we take FFT along x-direction:

$$\begin{aligned}
\kappa\nabla^2\phi &= \nabla\cdot\mathbf{P} \\
\kappa\frac{d^2\phi}{dx^2}+\kappa\frac{d^2\phi}{dy^2} &= \frac{dP_x}{dx}+\frac{dP_y}{dy} \xrightarrow{\text{FFT in x}} \\
-\kappa k_x^2\overline{\phi}+\kappa\frac{d^2\overline{\phi}}{dy^2} &= (ik_x)\overline{P_x}+\frac{d\overline{P_y}}{dy},
\end{aligned} \tag{8.10}$$

where k_x are the Fourier coordinates and $\overline{f}=\overline{f}(k_x,y)$ denotes the FFT of $f(x,y)$ in x-direction. This also converts the Maxwell's equation to a decoupled system of ordinary differential equations along y-direction, each of which associates a different k_x.

For the y-direction, we replace the derivative by Chebyshev differentiation matrix $\mathbf{D}$, yielding the following matrix equation for the numerical values of the potential at Chebyshev points $\{y_i\}$:

$$\begin{aligned}
-\kappa k_x^2\mathbf{I}\overline{\phi}+\kappa\mathbf{D}^2\overline{\phi} &= (ik_x)\overline{P_x}+\mathbf{D}\overline{P_y} \\
\left(-\kappa k_x^2\mathbf{I}+\kappa\mathbf{D}^2\right)\overline{\phi} &= (ik_x)\overline{P_x}+\mathbf{D}\overline{P_y}
\end{aligned} \tag{8.11}$$

For each Fourier Coordinate $\{k_x\}$, we solve the matrix equation in the form:

$$\mathbf{A\Phi = b}$$

$$\begin{bmatrix} A(0,0) & A(0,1:n-1) & A(0,n) \\ A(1:n-1,0) & A(1:n-1,1:n-1) & A(1:n-1,n) \\ A(n,0) & A(n,1:n-1) & A(n,n) \end{bmatrix} \begin{Bmatrix} \overline{\phi}_0 \\ \overline{\phi}_i \\ \overline{\phi}_n \end{Bmatrix} = \begin{Bmatrix} b_0 \\ b_i \\ b_n \end{Bmatrix} \tag{8.12}$$

If both surfaces are subjected to given potentials, namely, $\phi_{top}(x)$ and $\phi_{bot}(x)$, we take FFT to obtain:

$$\begin{aligned} \phi_{top}(x) &\xrightarrow{\text{FFT in x}} \overline{\phi}_{top}(k_x) \\ \phi_{bot}(x) &\xrightarrow{\text{FFT in x}} \overline{\phi}_{bot}(k_x) \end{aligned} \tag{8.13}$$

The first and last rows of the matrix equations are then replaced by the FFT of the boundary conditions, which yields:

$$\begin{bmatrix} 1 & 0 & 0 \\ A(1:n-1,0) & A(1:n-1,1:n-1) & A(1:n-1,n) \\ 0 & 0 & 1 \end{bmatrix} \begin{Bmatrix} \overline{\phi}_0 \\ \overline{\phi}_i \\ \overline{\phi}_n \end{Bmatrix} = \begin{Bmatrix} \overline{\phi}_{top}(k_x) \\ b_i \\ \overline{\phi}_{bot}(k_x) \end{Bmatrix} \tag{8.14}$$

The modified matrix equation is inverted to give the numerical values of $\overline{\phi}(k_x,y)$, which further yield the potential in real space $\phi(x,y)$ upon taking inverse FFT.

Neumann boundary condition such as given electric field on top surface, $E_y = -\frac{d\phi}{dy} = f(x)$, can be implemented with the first row of the Chebyshev differentiation matrix and numerical values of

potentials:

$$-\mathbf{D}_0\phi = f(x)$$

$$\left[\begin{array}{c:c:c} D(0,0) & D(0,1:n-1) & D(0,n) \end{array}\right] \left\{\begin{array}{c} \phi_0 \\ \hdashline \\ \phi_i \\ \\ \hdashline \\ \phi_n \end{array}\right\} = -f(x) \tag{8.15}$$

The first row of the matrix equation can then be replaced by this portion of the Chebyshev differentiation matrix:

$$\left[\begin{array}{c:c:c} D(0,0) & D(0,1:n-1) & D(0,n) \\ \hdashline A(1:n-1,0) & A(1:n-1,1:n-1) & A(1:n-1,n) \\ \hdashline 0 & 0 & 1 \end{array}\right] \left\{\begin{array}{c} \overline{\phi}_0 \\ \hdashline \overline{\phi}_i \\ \hdashline \overline{\phi}_n \end{array}\right\} = \left\{\begin{array}{c} -\overline{f}(k_x) \\ \hdashline b_i \\ \hdashline \overline{\phi}_{bot}(k_x) \end{array}\right\} \tag{8.16}$$

The updated matrix equation is then inverted for solution, as previously done.

As a remark, we usually normalize the Maxwell's equation to avoid truncation errors from big and small numbers.

$$\begin{aligned} \varepsilon\nabla^2\phi &= \nabla\mathbf{P} \\ \frac{1}{L^2}\varepsilon\nabla^{*2}\phi &= \frac{1}{L}\nabla^* P_s\mathbf{P}^* \\ \nabla^{*2}\phi &= \frac{LP_s}{\varepsilon}\nabla^*\mathbf{P}^* \\ \nabla^{*2}\phi^* &= \nabla^*\mathbf{P}^*, \end{aligned} \tag{8.17}$$

where the normalized potential has been defined by $\phi^* = \frac{\phi}{\frac{LP_s}{\varepsilon}}$.

Some simulations will be run for validation of the spectral method.

8.2.1 Simulation 1: Periodic Maxwell's equation solved by Spectral Method

For computational convenience, we may choose the domain for simulation to be $\Omega = \{-1 \leq x \leq 1, -1 \leq y \leq 1\}$, the permittivity is unform with value $\varepsilon = 1$. The left and right boundaries are subjected to periodic boundary condition. The bottom surface is grounded (zero potential) while the top surface is subjected to an artificial potential given by $\phi_{top}(x) = \cos(2\pi x)$. This periodic potential is so chosen to make it consistent with the periodicity of the problem. Recall that the simulation results from adopting FFT in x-direction and spectral method in y-direction. The resulting potential is shown in figure (8.3).

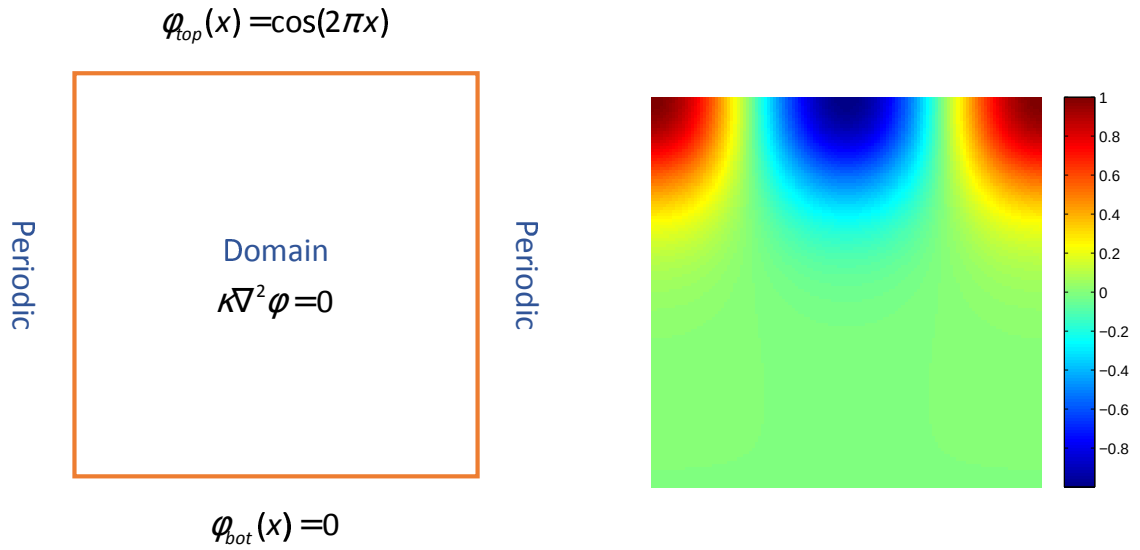

Figure 8.3: Periodic Maxwell's equation; grounded on bottom surface, potential on top surface $\cos(2\pi x)$. (a) Schematic, (b) Simulation: potential.

8.2.2 Simulation 2: Periodic Maxwell's equation solved by Spectral Method

All settings remain unchanged except on the top surface, electric field is applied:

$$E_y = -\frac{\partial \phi}{\partial y} = \sin(\pi x) \tag{8.18}$$

The resulting potential is shown in figure (8.4).

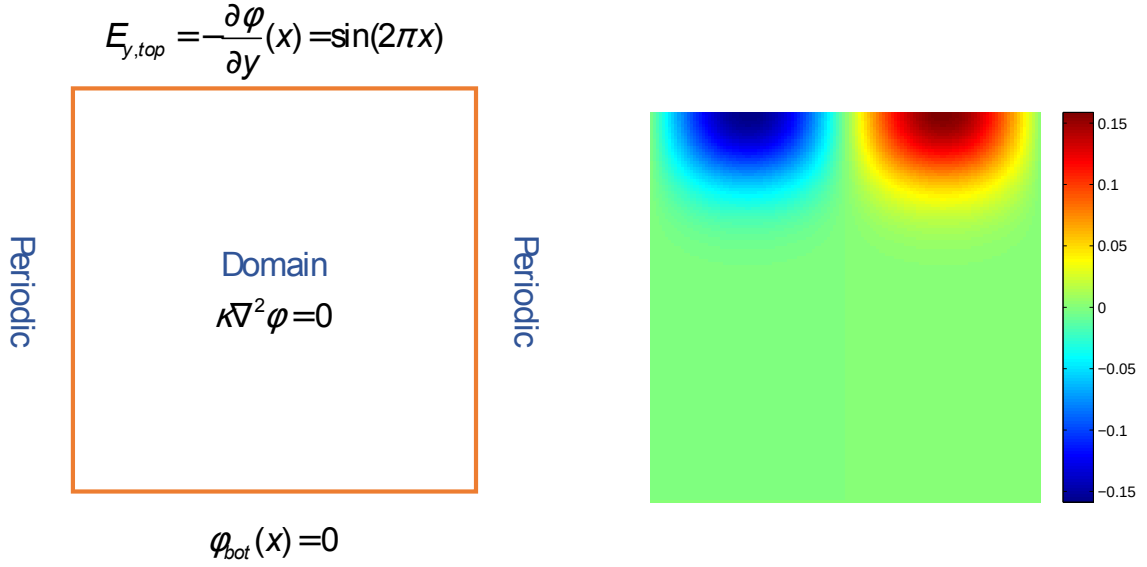

Figure 8.4: Periodic Maxwell's equation; grounded on bottom surface, electric field (y-component) on top surface $E_y = \sin(\pi x)$. (a) Schematic, (b) Simulation: potential.

8.2.3 Simulation 3: Periodic Maxwell's equation solved by Spectral Method

The domain is periodic in x-direction. The bottom surface is grounded while the top surface is subjected to zero electric flux such that $\frac{\partial \phi}{\partial y}(x, y = 1) = 0$. Spontaneous polarization exists and are given by:

$$\mathbf{P} = \left\{ \begin{array}{c} P_x \\ P_y \end{array} \right\} = \left\{ \begin{array}{c} \sin(2\pi x) \\ \sin(2\pi x)(y+1)^2 \end{array} \right\} \tag{8.19}$$

Relative permittivity is needed in the simulation, which is taken as $\kappa = 500$. The resulting potential is shown in figure (8.5).

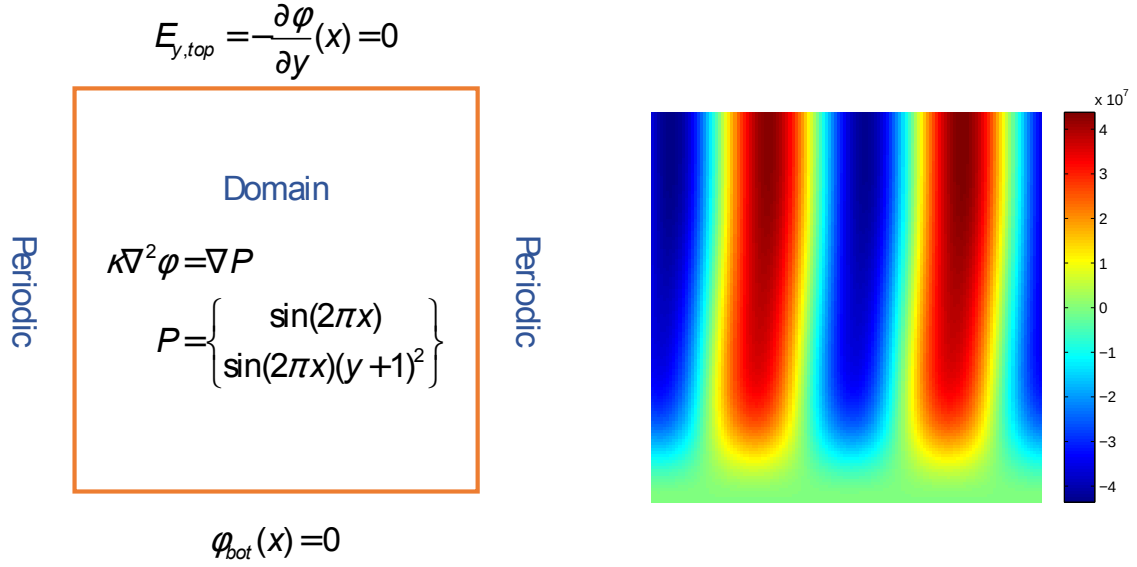

Figure 8.5: Periodic Maxwell's equation; grounded on bottom surface, zero electric flux on top surface. Spontaneous polarization exists. (a) Schematic, (b) Simulation: potential.

8.3 Solving General Maxwell's Equation using Spectral Method

We extend the spectral method to solve the non-periodic Maxwell's equation with general material properties subjected to arbitrary conditions:

$$\begin{aligned} -\nabla \cdot (\kappa(x,y)\nabla\phi(x,y)) &= \nabla \cdot \mathbf{P} \\ -\frac{\partial}{\partial x}\left(\kappa(x,y)\frac{\partial \phi}{\partial x}\right) - \frac{\partial}{\partial y}\left(\kappa(x,y)\frac{\partial \phi}{\partial y}\right) &= \frac{\partial P_x}{\partial x} + \frac{\partial P_y}{\partial y}, \end{aligned} \tag{8.20}$$

where $\kappa = \kappa(x,y)$ is the permittivity, $\mathbf{P} = \begin{Bmatrix} P_x \\ P_y \end{Bmatrix} = \begin{Bmatrix} P_x(x,y) \\ P_y(x,y) \end{Bmatrix}$ is the spontaneous polarization, and $\phi = \phi(x,y)$ is the potential.

We release periodicity in all directions, so that we may now apply realistic boundary conditions, such as potentials on bottom and top boundaries, and electric fields on left and right boundaries. The schematic is shown in figure (8.6).

The normalized domain $\{-1 \le x,y \le 1\}$ is characterized by two set of Chebyshev points de-

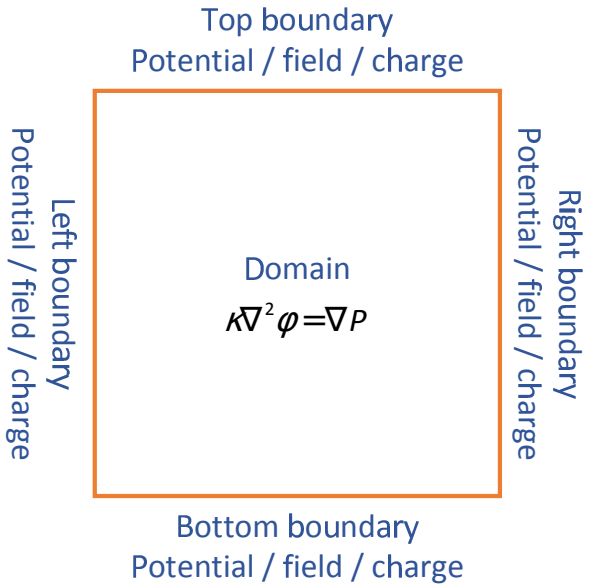

Figure 8.6: Schematic of computational domain for Maxwell's equation with boundary condition. Physical boundary condition can be imposed on each boundary.

noted by (x_i, y_j), where:

$$x_i = -\cos\left(i\frac{\pi}{n_x}\right), 0 \leq i \leq n_x$$
$$y_j = -\cos\left(j\frac{\pi}{n_y}\right), 0 \leq j \leq n_y. \tag{8.21}$$

While FFT decouples the complex equation being studied into a system of independent differential equation whose variables are the FFT of the electric potentials $\overline{\phi}(k_x, y)$, so that a set of (n_x+1) matrix equations, each of size $(n_y+1)\times(n_y+1)$ is generated, spectral method does not. Instead, a single large and dense matrix equation is generated for the electrical potentials at all Chebyshev points (x_i, y_j). For this, we re-express the potentials, which is originally a two-dimensional array, as a one-dimensional vector:

$$\phi(x_i, y_j) \equiv \phi_{ij} \xleftrightarrow{equivalent} \phi_k \tag{8.22}$$

The schematic is also shown in figure (8.7).

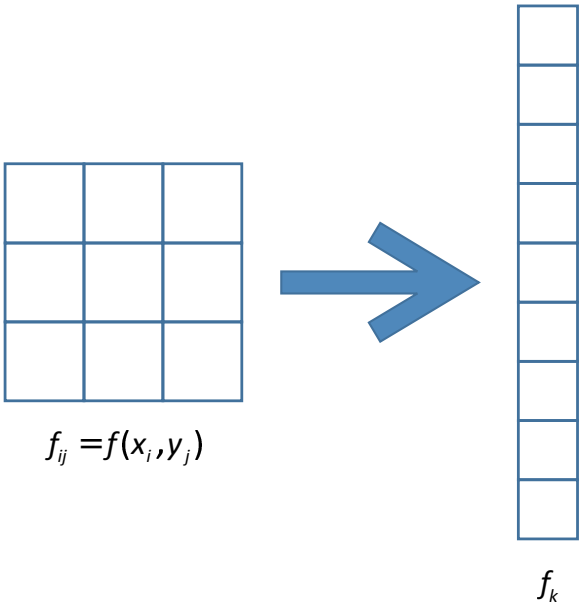

Figure 8.7: Schematic illustrating equivalence between two dimensional data and one dimensional vector

Before we move on to the matrix generated to solve for the electric potentials, we need to modify the Chebyshev differentiators in x and in y so that they can be adopted in two-dimensions. The one-dimensional Chebyshev differentiators, denoted by $\mathbf{D}_x$ and $\mathbf{D}_y$, can be applied repeatedly along all rows and columns of the two-dimensional data to approximate the derivatives in x and in y. If we want to do any derivative utilizing all data points in one single operation, we simply embed the original Chebyshev differentiators to a large matrix which can do numerical differentiation from all data. This can be done by introducing the Kronecker product with the following identity matrices:

$$\mathbf{I}_x = \begin{bmatrix} 1 & & & & \\ & \ddots & & & \\ & & 1 & & \\ & & & \ddots & \\ & & & & 1 \end{bmatrix}_{(n_x+1)\times(n_x+1)} \tag{8.23}$$

and

$$\mathbf{I}_y = \begin{bmatrix} 1 & & & & \\ & \ddots & & & \\ & & 1 & & \\ & & & \ddots & \\ & & & & 1 \end{bmatrix}_{(n_y+1)\times(n_y+1)} \tag{8.24}$$

Differentiators in two-dimension can be obtained by embedding the original differentiators in one-dimension via Kronecker product with $\mathbf{I}_x$ and $\mathbf{I}_y$ as shown below:

$$\begin{aligned} \frac{df}{dx} &\approx \mathbf{D}_x \xrightarrow{embed} \mathbf{I}_y \otimes \mathbf{D}_x f \equiv \mathbf{L}_x \\ \frac{df}{dy} &\approx \mathbf{D}_y \xrightarrow{embed} \mathbf{D}_x \otimes \mathbf{I}_x f \equiv \mathbf{L}_y \\ \frac{d^2f}{dx^2} &\approx \mathbf{E}_x = \mathbf{D}_x^2 \xrightarrow{embed} \mathbf{I}_y \otimes \mathbf{E}_x f \equiv \mathbf{L}_{xx} \\ \frac{d^2f}{dy^2} &\approx \mathbf{E}_y = \mathbf{D}_y^2 \xrightarrow{embed} \mathbf{E}_x \otimes \mathbf{I}_x f \equiv \mathbf{L}_{yy} \end{aligned} \tag{8.25}$$

Mixed derivatives can be obtained by multiplying the individual embedded derivatives:

$$\frac{d^2f}{dxdy} = \mathbf{L}_x\mathbf{L}_y \equiv \mathbf{L}_{xy} \tag{8.26}$$

For example, if $n_x = 4$ and $n_y = 3$, the differentiator matrices for one-dimension and identity

matrices will have the forms:

$$\begin{Bmatrix} f_x(x_0,y_j) \\ f_x(x_1,y_j) \\ f_x(x_2,y_j) \\ f_x(x_3,y_j) \end{Bmatrix} = \mathbf{D}_x \begin{Bmatrix} f(x_0,y_j) \\ f(x_1,y_j) \\ f(x_2,y_j) \\ f(x_3,y_j) \end{Bmatrix} = \begin{bmatrix} X_{00} & X_{01} & X_{02} & X_{03} \\ X_{10} & X_{11} & X_{12} & X_{13} \\ X_{20} & X_{21} & X_{22} & X_{23} \\ X_{30} & X_{31} & X_{32} & X_{33} \end{bmatrix} \begin{Bmatrix} f(x_0,y_j) \\ f(x_1,y_j) \\ f(x_2,y_j) \\ f(x_3,y_j) \end{Bmatrix}$$

$$\begin{Bmatrix} f_y(x_i,y_0) \\ f_y(x_i,y_1) \\ f_y(x_i,y_2) \end{Bmatrix} = \mathbf{D}_y \begin{Bmatrix} f(x_i,y_0) \\ f(x_i,y_1) \\ f(x_i,y_2) \end{Bmatrix} = \begin{bmatrix} Y_{00} & Y_{01} & Y_{02} \\ Y_{10} & Y_{11} & Y_{12} \\ Y_{20} & Y_{21} & Y_{22} \end{bmatrix} \begin{Bmatrix} f(x_i,y_0) \\ f(x_i,y_1) \\ f(x_i,y_2) \end{Bmatrix}$$

$$\mathbf{I}_x = \begin{bmatrix} 1 & 0 & 0 & 0 \\ 0 & 1 & 0 & 0 \\ 0 & 0 & 1 & 0 \\ 0 & 0 & 0 & 1 \end{bmatrix}$$

$$\mathbf{I}_y = \begin{bmatrix} 1 & 0 & 0 \\ 0 & 1 & 0 \\ 0 & 0 & 1 \end{bmatrix} \tag{8.27}$$

The Kronecker product of each differentiator and the identity matrix yields the following differentiators for two-dimension:

$$\frac{\partial f}{\partial x} = \mathbf{I}_y \otimes \mathbf{D}_x f \equiv \mathbf{L}_x f$$

$$\begin{Bmatrix} f_x(x_0,y_0) \\ f_x(x_1,y_0) \\ f_x(x_2,y_0) \\ f_x(x_3,y_0) \\ f_x(x_0,y_1) \\ f_x(x_1,y_1) \\ f_x(x_2,y_1) \\ f_x(x_3,y_1) \\ f_x(x_0,y_2) \\ f_x(x_1,y_2) \\ f_x(x_2,y_2) \\ f_x(x_3,y_2) \end{Bmatrix} = \begin{bmatrix} X_{00} & X_{01} & X_{02} & X_{03} & & & & & & & & \\ X_{10} & X_{11} & X_{12} & X_{13} & & & & & & & & \\ X_{20} & X_{21} & X_{22} & X_{23} & & & & & & & & \\ X_{30} & X_{31} & X_{32} & X_{33} & & & & & & & & \\ & & & & X_{00} & X_{01} & X_{02} & X_{03} & & & & \\ & & & & X_{10} & X_{11} & X_{12} & X_{13} & & & & \\ & & & & X_{20} & X_{21} & X_{22} & X_{23} & & & & \\ & & & & X_{30} & X_{31} & X_{32} & X_{33} & & & & \\ & & & & & & & & X_{00} & X_{01} & X_{02} & X_{03} \\ & & & & & & & & X_{10} & X_{11} & X_{12} & X_{13} \\ & & & & & & & & X_{20} & X_{21} & X_{22} & X_{23} \\ & & & & & & & & X_{30} & X_{31} & X_{32} & X_{33} \end{bmatrix} \begin{Bmatrix} f(x_0,y_0) \\ f(x_1,y_0) \\ f(x_2,y_0) \\ f(x_3,y_0) \\ f(x_0,y_1) \\ f(x_1,y_1) \\ f(x_2,y_1) \\ f(x_3,y_1) \\ f(x_0,y_2) \\ f(x_1,y_2) \\ f(x_2,y_2) \\ f(x_3,y_2) \end{Bmatrix} \tag{8.28}$$

$$\frac{\partial f}{\partial y} = \mathbf{D}_y \otimes \mathbf{I}_x f \equiv \mathbf{L}_y f$$

$$\begin{Bmatrix} f_y(x_0,y_0) \\ f_y(x_1,y_0) \\ f_y(x_2,y_0) \\ f_y(x_3,y_0) \\ f_y(x_0,y_1) \\ f_y(x_1,y_1) \\ f_y(x_2,y_1) \\ f_y(x_3,y_1) \\ f_y(x_0,y_2) \\ f_y(x_1,y_2) \\ f_y(x_2,y_2) \\ f_y(x_3,y_2) \end{Bmatrix} = \begin{bmatrix} Y_{00} & & & & Y_{01} & & & & Y_{02} & & & \\ & Y_{00} & & & & Y_{01} & & & & Y_{02} & & \\ & & Y_{00} & & & & Y_{01} & & & & Y_{02} & \\ & & & Y_{00} & & & & Y_{01} & & & & Y_{02} \\ Y_{10} & & & & Y_{11} & & & & Y_{12} & & & \\ & Y_{10} & & & & Y_{11} & & & & Y_{12} & & \\ & & Y_{10} & & & & Y_{11} & & & & Y_{12} & \\ & & & Y_{10} & & & & Y_{11} & & & & Y_{12} \\ Y_{20} & & & & Y_{21} & & & & Y_{22} & & & \\ & Y_{20} & & & & Y_{21} & & & & Y_{22} & & \\ & & Y_{20} & & & & Y_{21} & & & & Y_{22} & \\ & & & Y_{20} & & & & Y_{21} & & & & Y_{22} \end{bmatrix} \begin{Bmatrix} f(x_0,y_0) \\ f(x_1,y_0) \\ f(x_2,y_0) \\ f(x_3,y_0) \\ f(x_0,y_1) \\ f(x_1,y_1) \\ f(x_2,y_1) \\ f(x_3,y_1) \\ f(x_0,y_2) \\ f(x_1,y_2) \\ f(x_2,y_2) \\ f(x_3,y_2) \end{Bmatrix} \tag{8.29}$$

As a remark, second derivatives $\frac{\partial^2 f}{\partial x^2}$, $\frac{\partial^2 f}{\partial y^2}$ and $\frac{\partial^2 f}{\partial x \partial y} = \frac{\partial^2 f}{\partial y \partial x}$ have the same structures, and are not shown here.

Furthermore, variable coefficient, such as spatial permittivity $\kappa = \kappa(x,y)$ or other material properties can be treated in the following steps:

(1) Compute $\kappa = \kappa(x,y)$ at Chebyshev points (x_i, y_j) as 2D array $\kappa = \kappa_{ij}$.

(2) Re-arrange the 2D array $\kappa = \kappa_{ij}$ to 1D vector $\kappa = \kappa_k$. The length of the vector is $(n_x + 1)(n_y + 1)$.

(3) Set up a diagonal matrix whose diagonal elements are the element of the vector $\kappa = \kappa_k$, in the same order. The size of this diagonal matrix is the same as the differentiator matrices for two dimensions, or, $(n_x + 1)(n_y + 1) \times (n_x + 1)(n_y + 1)$.

The resulting matrix can then be pre-multiplied to the differentiator matrices, in the same order, as what the coefficients appear in the original equations.

In summary, we have:

$$\kappa = \kappa(x,y) \xrightarrow{evaluate} \kappa_{ij} = \kappa(x_i,y_j) \xrightarrow{re-arrange} \{\kappa_k\} \xrightarrow{re-arrange} [\kappa] = diag(\kappa_k) \tag{8.30}$$

The term $\kappa(x,y)\frac{\partial f}{\partial x}$ corresponds to the matrix $[\kappa]\mathbf{L}_x f$ in the formulation of spectral method.

The powerfulness of the spectral method enables us to solve the general Maxwell's equation with variable coefficients (permittivity) by directly translating the given equation into embedded Chebyshev differentiator matrices in the same order, as shown below:

$$\begin{aligned}
-\nabla\cdot(\kappa(x,y)\nabla\phi(x,y)) &= \nabla\cdot\mathbf{P} \\
-\frac{\partial}{\partial x}\left(\kappa(x,y)\frac{\partial\phi}{\partial x}\right) - \frac{\partial}{\partial y}\left(\kappa(x,y)\frac{\partial\phi}{\partial y}\right) &= \frac{\partial P_x}{\partial x} + \frac{\partial P_y}{\partial y} \\
-\kappa\frac{\partial^2\phi}{\partial x^2} - \frac{\partial\kappa}{\partial x}\frac{\partial\phi}{\partial x} - \kappa\frac{\partial^2\phi}{\partial y^2} - \frac{\partial\kappa}{\partial y}\frac{\partial\phi}{\partial y} &= \frac{\partial P_x}{\partial x} + \frac{\partial P_y}{\partial y} \\
\left(-[\kappa]\mathbf{L}_{xx} - \left[\frac{\partial\kappa}{\partial x}\right]\mathbf{L}_x - [\kappa]\mathbf{L}_{yy} - \left[\frac{\partial\kappa}{\partial y}\right]\mathbf{L}_y\right)\{\phi\} &= \mathbf{L}_x\{P_x\} + \mathbf{L}_y\{P_y\} \\
\mathbf{A\Phi} &= \mathbf{b}
\end{aligned} \tag{8.31}$$

Rows of the matrix equation are then replaced by boundary conditions.

If the top surface is subjected to Dirichlet boundary condition, such as given potential,

$$\phi_{i,0} = g(x_i), \forall i = 0,...,n_x, \tag{8.32}$$

which can also be re-labeled as in one-dimensional vector:

$$\phi_k = \phi_{n_x\times i+j} = g(x_i), \forall i = 0,...,n_x, \tag{8.33}$$

then each row of the matrix equation, with $k = n_x \times i + j, \forall i = 0,...,n_x$, is replaced by the following:

$$\begin{aligned}
A(k,k) &= 1 \\
A(k,m\neq k) &= 0 \\
b(k) &= g(x_i)
\end{aligned} \tag{8.34}$$

On the other hand, if the top surface is subjected to Neumann boundary condition, such as electric field,

$$E_y(x_i, y_0) = -\frac{\partial \phi}{\partial x}(x_i, y_0) = g(x_i), \forall i = 0, ..., n_x, \tag{8.35}$$

which can also be re-labeled as in one-dimensional vector:

$$-\frac{\partial \phi_{k=n_x \times i+j}}{\partial x} = g(x_i), \forall i = 0, ..., n_x, \tag{8.36}$$

which can further be expressed in terms of embedded Chebyshev differentiator for two dimensions:

$$(\mathbf{I}_y \otimes \mathbf{D}_x)|_{k=n_x \times i+j} = -g(x_i), \forall i = 0, ..., n_x, \tag{8.37}$$

then each row of the matrix equation, with $k = n_x \times i + j, \forall i = 0, ..., n_x$, is replaced by the following:

$$\begin{aligned} A(k,:) &= (\mathbf{I}_y \otimes \mathbf{D}_x)|_{k=n_x \times i+j} \\ b(k) &= -g(x_i) \end{aligned} \tag{8.38}$$

The updated matrix equation is finally solved for the resulting electric potential. Boundary conditions on other boundaries can be implemented familiarly.

In what follow, we illustrate some simulation for solving general Maxwell's equation using full spectral method.

8.3.1 Simulation 1: General Maxwell's equation solved by Spectral Method

We solve the non-periodic Maxwell's equation with uniform permittivity. The bottom surface is grounded. The left surface is subjected to electrical insulation. The right surface is subjected to the potential $\phi_{right}(y) = \sin(2\pi y)$. The top surface is subjected to the electric field acting in y-direction as $E_{top,y}(x) = (x+1)^2$. The resulting potential is shown in figure (8.8).

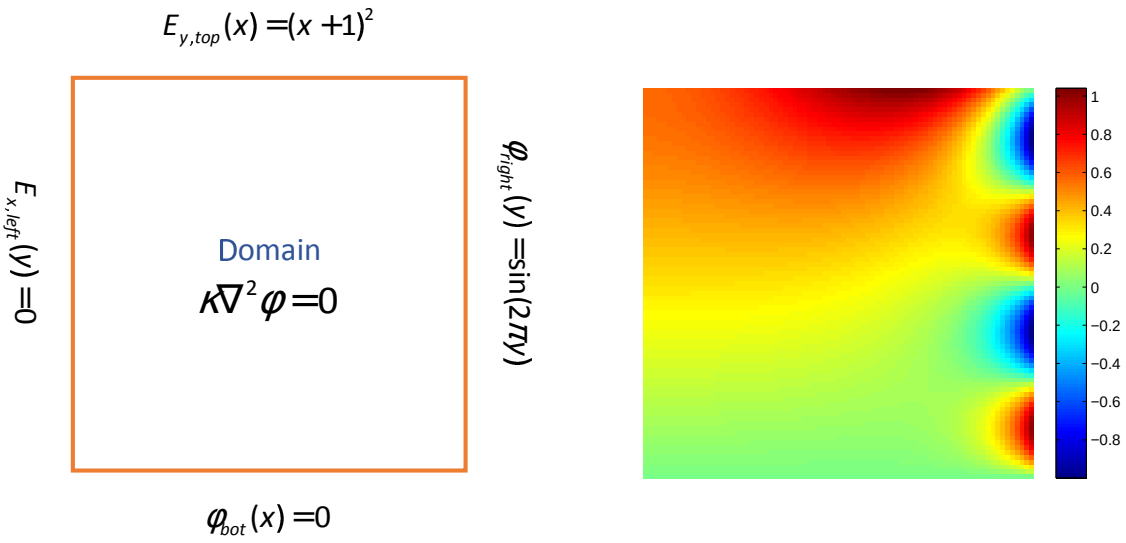

Figure 8.8: Non-periodic Maxwell's equation; four different conditions on four boundaries. (a) Schematic, (b) Simulation: potential.

8.3.2 *Simulation 2: General Maxwell's equation with nonhomogeneous permittivity solved by Spectral Method*

We illustrate how the spectral method can solve general Maxwell's equation with nonhomogeneous permittivity, which makes it distinguishing from the previous method using FFT.

As a control set, we first solve the general Maxwell's equation with homogeneous permittivity, where:

$$\kappa(x,y) = 6 \tag{8.39}$$

For the boundary conditions, we have zero potential on both top and bottom surfaces, while both left and right surfaces are electrically insulated.

Spontaneous polarization exists as:

$$\mathbf{P} = \left\{ \begin{array}{c} P_x(x,y) \\ P_y(x,y) \end{array} \right\} = \left\{ \begin{array}{c} 0 \\ (y+1)^2 \end{array} \right\} \tag{8.40}$$

The mentioned schematic is shown in figure (8.9).

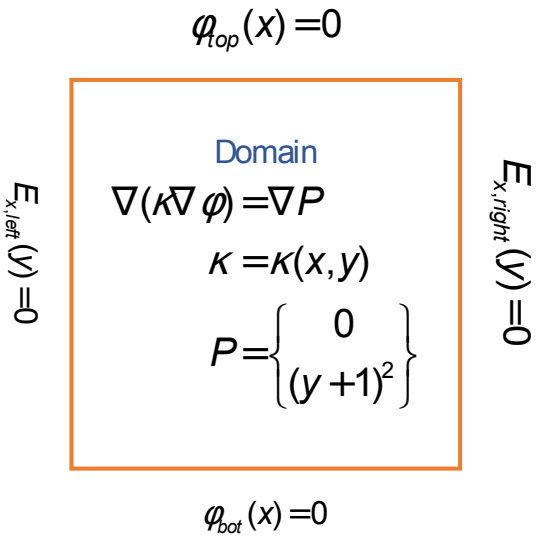

Figure 8.9: Schematic of computational domain for Maxwell's equation with boundary condition. Periodicity is assumed in x-direction.

The spital distribution of permittivity and the resulting potentials are shown in figure (8.10).

We consider the same Maxwell's equation again, now with laminated permittivity, where:

$$\kappa(x,y) = \begin{cases} 10 & : x < 0 \\ 2 & : x > 0 \end{cases}$$

All other conditions (boundary conditions, instantaneous polarization) remain unchanged. The spital distribution of permittivity and the resulting potentials are shown in figure (8.11). Notice that in the latter simulation, different region of permittivity induce different pattern of potential.

8.3.3 Simulation 3: General Maxwell's equation with nonhomogeneous polarization solved by Spectral Method

We may also consider the potential distribution of a sample with alternating instantaneous polarization, such as:

$$P_y(x,y) = \begin{cases} 1 & : x < 0 \\ -1 & : x > 0 \end{cases}$$

The polarization is pointing upwards and downwards as shown in the schematic (8.12).

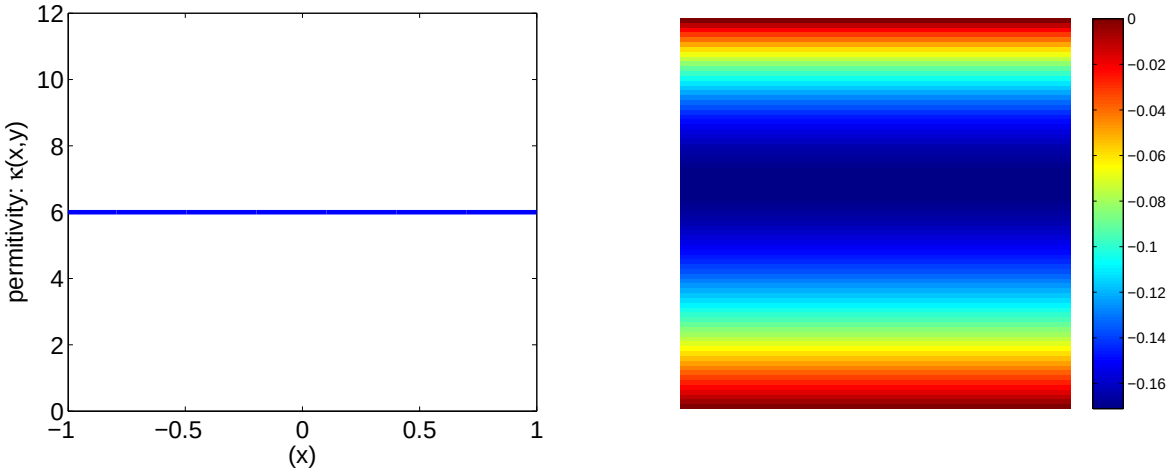

Figure 8.10: Spital distribution of permittivity κ (homogeneous) and resulting potential ϕ. It is used as a control set.

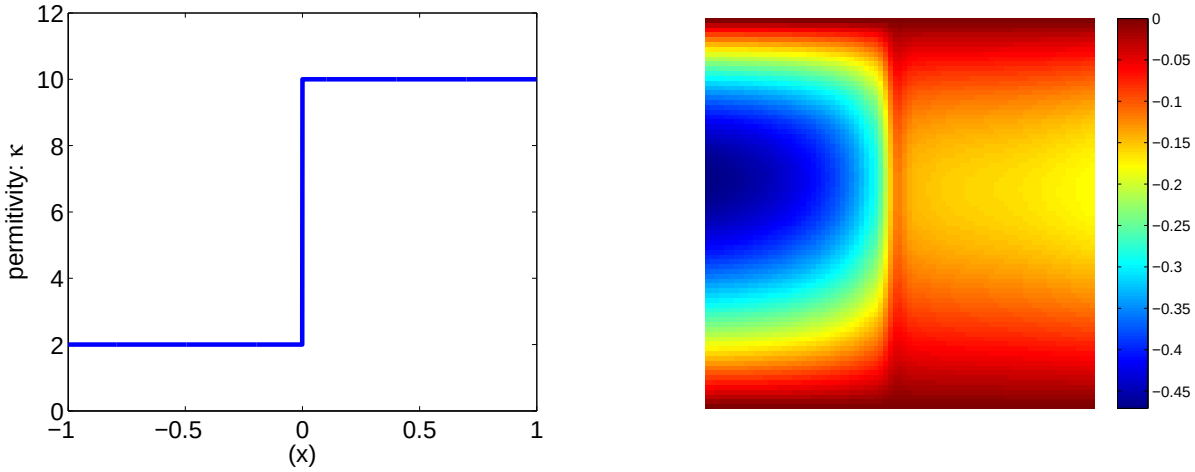

Figure 8.11: Spital distribution of permittivity κ (non-homogeneous) and resulting potential ϕ.

For the boundary conditions, the top and bottom surfaces are grounded while the left and right surfaces are electrically insulated. With constant permittivity, the resulting potential is shown in figure (8.12).

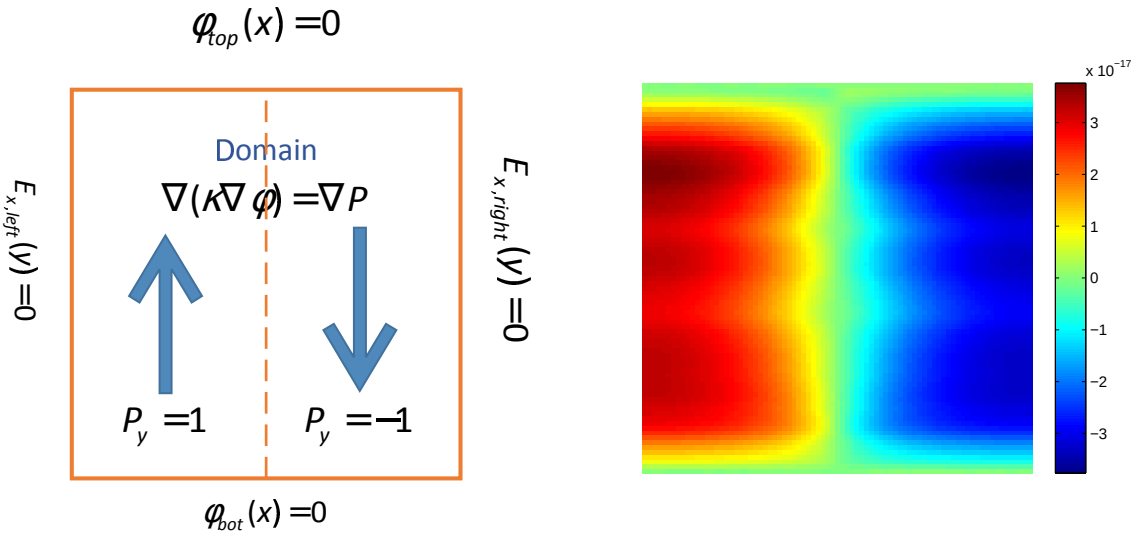

Figure 8.12: Schematic of instantaneous polarization and resulting potential ϕ.

8.4 Solving Elasticity Equation using Spectral Method

Spectral method can be used to solve the general elasticity equation stated as:

$$\sigma_{ij} = C_{ijkl}\left(\varepsilon_{kl} - \varepsilon^*_{kl}\right)$$
$$\sigma_{ij,j} = 0 \tag{8.41}$$

As a preliminary study, we assume the material stiffness to be isotropic yet functions of x and y, so that, with the Vigot notation, the stiffness matrix reduces to the following 3×3-matrix for two-dimension:

$$\mathbf{C}(x,y) = \left[C_{ijkl}(x,y)\right] = \begin{bmatrix} c_{11}(x,y) & c_{12}(x,y) & \\ c_{21}(x,y) & c_{22}(x,y) & \\ & & c_{66}(x,y) \end{bmatrix} \tag{8.42}$$

On each boundary, either displacement constraint or traction can be imposed as boundary conditions. The schematic is shown in figure (8.13).

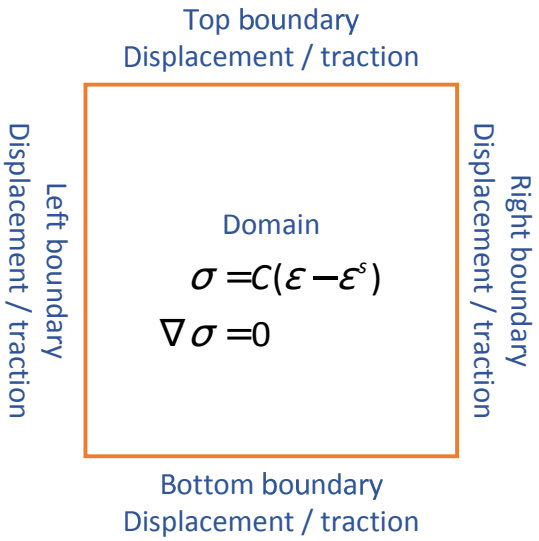

Figure 8.13: Schematic of computational domain for Maxwell's equation with boundary condition. Periodicity is assumed in x-direction.

For two dimension, the elasticity is expressed as a coupled system for the two components of displacement components denoted by u and v:

$$\begin{aligned} & c_{11}\frac{\partial^2 u}{\partial x^2} + c_{12}\frac{\partial^2 v}{\partial x \partial y} + c_{66}\frac{\partial^2 v}{\partial x \partial y} + c_{66}\frac{\partial^2 u}{\partial y^2} + \frac{\partial c_{11}}{\partial x}\frac{\partial u}{\partial x} + \frac{\partial c_{12}}{\partial x}\frac{\partial v}{\partial y} + \frac{\partial c_{66}}{\partial y}\frac{\partial u}{\partial y} + \frac{\partial c_{66}}{\partial y}\frac{\partial v}{\partial x} \\ & = c_{11}\frac{\varepsilon_{11}^*}{\partial x} + c_{12}\frac{\varepsilon_{22}^*}{\partial x} + c_{66}\frac{\varepsilon_{12}^*}{\partial y} + c_{66}\frac{\varepsilon_{21}^*}{\partial y} + \frac{\partial c_{11}}{\partial x}\varepsilon_{11}^* + \frac{\partial c_{12}}{\partial x}\varepsilon_{22}^* + \frac{\partial c_{66}}{\partial y}\varepsilon_{12}^* + \frac{\partial c_{66}}{\partial y}\varepsilon_{21}^* \end{aligned} \tag{8.43}$$

$$\begin{aligned} & c_{66}\frac{\partial^2 u}{\partial x \partial y} + c_{66}\frac{\partial^2 v}{\partial x^2} + c_{21}\frac{\partial^2 u}{\partial x \partial y} + c_{22}\frac{\partial^2 v}{\partial y^2} + \frac{\partial c_{66}}{\partial x}\frac{\partial u}{\partial y} + \frac{\partial c_{66}}{\partial x}\frac{\partial v}{\partial x} + \frac{\partial c_{21}}{\partial y}\frac{\partial u}{\partial x} + \frac{\partial c_{22}}{\partial y}\frac{\partial v}{\partial y} \\ & = c_{66}\frac{\varepsilon_{11}^*}{\partial x} + c_{66}\frac{\varepsilon_{22}^*}{\partial x} + c_{21}\frac{\varepsilon_{12}^*}{\partial y} + c_{22}\frac{\varepsilon_{21}^*}{\partial y} + \frac{\partial c_{66}}{\partial x}\varepsilon_{12}^* + \frac{\partial c_{66}}{\partial x}\varepsilon_{21}^* + \frac{\partial c_{21}}{\partial y}\varepsilon_{11}^* + \frac{\partial c_{22}}{\partial y}\varepsilon_{22}^* \end{aligned} \tag{8.44}$$

Assume that we have re-labeled all the two-dimensional variables (as matrices) into equivalent

one-dimensional vectors, such as:

$$\begin{aligned} u_{ij} = u(x_i, y_j) &\xrightarrow{re-label} u_k \\ v_{ij} = v(x_i, y_j) &\xrightarrow{re-label} v_k \\ \varepsilon^*_{11}|_{ij} = \varepsilon^*_{11}(x_i, y_j) &\xrightarrow{re-label} \varepsilon^*_{11}|_k \end{aligned} \tag{8.45}$$

Stiffness coefficients c_{11}, c_{22}, c_{12}, c_{21} and c_{66} as well as their derivatives, which can be generally functions of x and y, thus expressed numerically as two-dimensional arrays, can be repressed and relabeled as one-dimensional vectors and further as the diagonal elements of diagonal matrices. For example:

$$c_{11}|_{ij} = c_{11}(x_i, y_j) \xrightarrow{re-label} c_{11}|_k \xrightarrow{embed} [c_{11}] = diag\,(c_{11}|_k) \tag{8.46}$$

With this setting, we may translate the coupled elasticity equations into embedded Chebyshev differentiator matrix and variables expressed as one-dimensional vector, in order to generate a matrix equations for the displacement components:

$$\begin{aligned} &[c_{11}]\mathbf{L}_{xx}\{u\} + [c_{12}]\mathbf{L}_{xy}\{v\} + [c_{66}]\mathbf{L}_{xy}\{v\} + [c_{66}]\mathbf{L}_{yy}\{u\} \\ &+ \left[\frac{\partial c_{11}}{\partial x}\right]\mathbf{L}_x\{u\} + \left[\frac{\partial c_{12}}{\partial x}\right]\mathbf{L}_y\{v\} + \left[\frac{\partial c_{66}}{\partial y}\right]\mathbf{L}_y\{u\} + \left[\frac{\partial c_{66}}{\partial y}\right]\mathbf{L}_x\{v\} \\ &= [c_{11}]\mathbf{L}_x\{\varepsilon^*_{11}\} + [c_{12}]\mathbf{L}_x\{\varepsilon^*_{22}\} + [c_{66}]\mathbf{L}_y\{\varepsilon^*_{12}\} + [c_{66}]\mathbf{L}_y\{\varepsilon^*_{21}\} \\ &+ \left[\frac{\partial c_{11}}{\partial x}\right]\{\varepsilon^*_{11}\} + \left[\frac{\partial c_{12}}{\partial x}\right]\{\varepsilon^*_{22}\} + \left[\frac{\partial c_{66}}{\partial y}\right]\{\varepsilon^*_{12}\} + \left[\frac{\partial c_{66}}{\partial y}\right]\{\varepsilon^*_{21}\} \end{aligned} \tag{8.47}$$

$$\begin{aligned} &[c_{66}]\mathbf{L}_{xy}\{u\} + [c_{66}]\mathbf{L}_{xx}\{v\} + [c_{21}]\mathbf{L}_{xy}\{u\} + [c_{22}]\mathbf{L}_{yy}\{v\} \\ &+ \left[\frac{\partial c_{66}}{\partial x}\right]\mathbf{L}_y\{u\} + \left[\frac{\partial c_{66}}{\partial x}\right]\mathbf{L}_x\{v\} + \left[\frac{\partial c_{21}}{\partial y}\right]\mathbf{L}_x\{u\} + \left[\frac{\partial c_{22}}{\partial y}\right]\mathbf{L}_y\{v\} \\ &= [c_{66}]\mathbf{L}_x\{\varepsilon^*_{11}\} + [c_{66}]\mathbf{L}_x\{\varepsilon^*_{22}\} + [c_{21}]\mathbf{L}_y\{\varepsilon^*_{12}\} + [c_{22}]\mathbf{L}_y\{\varepsilon^*_{21}\} \\ &+ \left[\frac{\partial c_{66}}{\partial x}\right]\{\varepsilon^*_{12}\} + \left[\frac{\partial c_{66}}{\partial x}\right]\{\varepsilon^*_{21}\} + \left[\frac{\partial c_{21}}{\partial y}\right]\{\varepsilon^*_{11}\} + \left[\frac{\partial c_{22}}{\partial y}\right]\{\varepsilon^*_{22}\} \end{aligned} \tag{8.48}$$

These two equations are then assembled to yield a large matrix equation in $\{u\}$ and $\{v\}$:

$$\mathbf{A}_{(n_x+1)(n_y+1)\times(n_x+1)(n_y+1)}\mathbf{\Phi}_{(n_x+1)(n_y+1)\times 1} = \mathbf{b}_{(n_x+1)(n_y+1)\times 1}, \tag{8.49}$$

where

$$\mathbf{A} = \left[\begin{array}{c|c} [c_{11}]\mathbf{L}_{xx}+[c_{66}]\mathbf{L}_{yy}+\left[\frac{\partial c_{11}}{\partial x}\right]\mathbf{L}_x+\left[\frac{\partial c_{66}}{\partial y}\right]\mathbf{L}_y & [c_{12}]\mathbf{L}_{xy}+[c_{66}]\mathbf{L}_{xy}+\left[\frac{\partial c_{12}}{\partial x}\right]\mathbf{L}_y+\left[\frac{\partial c_{66}}{\partial y}\right]\mathbf{L}_x \\ \hline [c_{66}]\mathbf{L}_{xy}+[c_{21}]\mathbf{L}_{xy}+\left[\frac{\partial c_{66}}{\partial x}\right]\mathbf{L}_y+\left[\frac{\partial c_{21}}{\partial y}\right]\mathbf{L}_x & [c_{66}]\mathbf{L}_{xx}+[c_{22}]\mathbf{L}_{yy}+\left[\frac{\partial c_{66}}{\partial x}\right]\mathbf{L}_x+\left[\frac{\partial c_{22}}{\partial y}\right]\mathbf{L}_y \end{array}\right] \tag{8.50}$$

and

$$\mathbf{\Phi} = \left\{\begin{array}{c} \{u\} \\ \hline \{v\} \end{array}\right\} \tag{8.51}$$

and

$$\mathbf{b} = \left\{\begin{array}{c} [c_{11}]\mathbf{L}_x\{\varepsilon^*_{11}\}+[c_{12}]\mathbf{L}_x\{\varepsilon^*_{22}\}+[c_{66}]\mathbf{L}_y\{\varepsilon^*_{12}\}+[c_{66}]\mathbf{L}_y\{\varepsilon^*_{21}\} \\ +\left[\frac{\partial c_{11}}{\partial x}\right]\{\varepsilon^*_{11}\}+\left[\frac{\partial c_{12}}{\partial x}\right]\{\varepsilon^*_{22}\}+\left[\frac{\partial c_{66}}{\partial y}\right]\{\varepsilon^*_{12}\}+\left[\frac{\partial c_{66}}{\partial y}\right]\{\varepsilon^*_{21}\} \\ \hline [c_{66}]\mathbf{L}_x\{\varepsilon^*_{11}\}+[c_{66}]\mathbf{L}_x\{\varepsilon^*_{22}\}+[c_{21}]\mathbf{L}_y\{\varepsilon^*_{12}\}+[c_{22}]\mathbf{L}_y\{\varepsilon^*_{21}\} \\ +\left[\frac{\partial c_{66}}{\partial x}\right]\{\varepsilon^*_{12}\}+\left[\frac{\partial c_{66}}{\partial x}\right]\{\varepsilon^*_{21}\}+\left[\frac{\partial c_{21}}{\partial y}\right]\{\varepsilon^*_{11}\}+\left[\frac{\partial c_{22}}{\partial y}\right]\{\varepsilon^*_{22}\} \end{array}\right\} \tag{8.52}$$

The assembled matrix equation is then updated for various boundary conditions.

If the top surface, designated by the points with coordinates $(x_i, y_0)\,\forall i = 0,\ldots,n_x$, is subjected to displacement constraint, $u = v = 0$, or equivalently expressed as one-dimensional vectors,

$$\begin{aligned} u_k &= u_{i,0} = u(x_i, y_0) = 0\,\forall i = 0,..,n_x \\ v_k &= v_{i,0} = v(x_i, y_0) = 0\,\forall i = 0,..,n_x \\ k &= i \times n_x + j, \end{aligned} \tag{8.53}$$

for each of these running indices k, the k-th row and $(k+N)$-th row are replaced by the following:

$$\begin{aligned} A(k,k) &= 1 \\ A(k,m \neq k) &= 0 \\ A(k+N,k+N) &= 1 \\ A(k+N,m \neq k+N) &= 0 \\ b(k) &= 0 \\ b(k+N) &= 0, \end{aligned} \tag{8.54}$$

where we denote $N = (n_x+1)(n_y+1)$.

On the other hand, if the top surface, $(x_i, y_0) \forall i = 0, ..., n_x$,is subjected to a given traction such that

$$\begin{aligned} \mathbf{T} &= \boldsymbol{\sigma}\mathbf{n} \\ \begin{Bmatrix} T_x(x) \\ T_y(x) \end{Bmatrix} &= \begin{bmatrix} \sigma_{11} & \sigma_{12} \\ \sigma_{21} & \sigma_{22} \end{bmatrix} \begin{Bmatrix} 0 \\ 1 \end{Bmatrix} = \begin{Bmatrix} \sigma_{12} \\ \sigma_{22} \end{Bmatrix} \\ &= \begin{Bmatrix} c_{66}(\varepsilon_{12} - \varepsilon_{12}^*) + c_{66}(\varepsilon_{21} - \varepsilon_{21}^*) \\ c_{21}(\varepsilon_{11} - \varepsilon_{11}^*) + c_{22}(\varepsilon_{22} - \varepsilon_{22}^*) \end{Bmatrix} \\ &= \begin{Bmatrix} c_{66}\frac{\partial u}{\partial y} + c_{66}\frac{\partial v}{\partial x} - c_{66}\varepsilon_{12}^* - c_{66}\varepsilon_{21}^* \\ c_{21}\frac{\partial u}{\partial x} + c_{22}\frac{\partial v}{\partial y} - c_{21}\varepsilon_{11}^* - c_{22}\varepsilon_{22}^* \end{Bmatrix} \\ \begin{Bmatrix} c_{66}\frac{\partial u}{\partial y} + c_{66}\frac{\partial v}{\partial x} \\ c_{21}\frac{\partial u}{\partial x} + c_{22}\frac{\partial v}{\partial y} \end{Bmatrix} &= \begin{Bmatrix} T_x(x) + c_{66}\varepsilon_{12}^* + c_{66}\varepsilon_{21}^* \\ T_y(x) + c_{21}\varepsilon_{11}^* + c_{22}\varepsilon_{22}^* \end{Bmatrix} \end{aligned} \tag{8.55}$$

These equations are first re-expressed in terms of the embedded Chebyshev differentiators as:

$$\begin{Bmatrix} c_{66}\mathbf{D}_{y,0} \otimes \mathbf{I}_x \{u\} + c_{66}\mathbf{I}_y \otimes \mathbf{D}_{x,i} \{v\} \\ c_{21}\mathbf{I}_y \otimes \mathbf{D}_{x,i} \{u\} + c_{22}\mathbf{D}_{y,0} \otimes \mathbf{I}_x \{v\} \end{Bmatrix} = \begin{Bmatrix} T_x(x_i) + c_{66}\varepsilon_{12}^*(x_i, y_0) + c_{66}\varepsilon_{21}^*(x_i, y_0) \\ T_y(x_i) + c_{21}\varepsilon_{11}^*(x_i, y_0) + c_{22}\varepsilon_{22}^*(x_i, y_0) \end{Bmatrix} \tag{8.56}$$

where the second lower indices following the Chebyshev differentiators refer to their row indices being considered.

To implement these boundary conditions, for each $0 \leq i \leq n_x$ with $j = 0$, which corresponds to the coordinates (x_i, y_0) of the points on the top surface and which corresponds to the equivalent one-dimensional index $k = in_x + j$, we replace all k-th rows and all $(k+N)$-th rows of the matrix by the left hand side of the above expressions and:

$$\begin{aligned} b(k) &= T_x(x_i) + c_{66}\varepsilon_{12}^*(x_i, y_0) + c_{66}\varepsilon_{21}^*(x_i, y_0) \\ b(k+N) &= T_y(x_i) + c_{21}\varepsilon_{11}^*(x_i, y_0) + c_{22}\varepsilon_{22}^*(x_i, y_0) \end{aligned} \tag{8.57}$$

If traction is applied over the right boundary, whose coordinates are designated by $(x_0, y_j), \forall j = 0, \ldots, n_y$, we may similarly express the traction components into Chebyshev differentiators and replace rows and columns of the assembled matrix $\mathbf{A}$, as shown below:

$$\begin{aligned} \mathbf{T} &= \boldsymbol{\sigma}\mathbf{n} \\ \begin{Bmatrix} T_x(y) \\ T_y(y) \end{Bmatrix} &= \begin{bmatrix} \sigma_{11} & \sigma_{12} \\ \sigma_{21} & \sigma_{22} \end{bmatrix} \begin{Bmatrix} 1 \\ 0 \end{Bmatrix} = \begin{Bmatrix} \sigma_{11} \\ \sigma_{21} \end{Bmatrix} \\ &= \begin{Bmatrix} c_{11}(\varepsilon_{11} - \varepsilon_{11}^*) + c_{12}(\varepsilon_{22} - \varepsilon_{22}^*) \\ c_{66}(\varepsilon_{21} - \varepsilon_{21}^*) + c_{66}(\varepsilon_{12} - \varepsilon_{12}^*) \end{Bmatrix} \\ &= \begin{Bmatrix} c_{11}\frac{\partial u}{\partial x} + c_{12}\frac{\partial v}{\partial y} - c_{11}\varepsilon_{11}^* - c_{12}\varepsilon_{22}^* \\ c_{66}\frac{\partial v}{\partial x} + c_{66}\frac{\partial u}{\partial y} - c_{66}\varepsilon_{21}^* - c_{66}\varepsilon_{12}^* \end{Bmatrix} \\ \begin{Bmatrix} c_{11}\frac{\partial u}{\partial x} + c_{12}\frac{\partial v}{\partial y} \\ c_{66}\frac{\partial v}{\partial x} + c_{66}\frac{\partial u}{\partial y} \end{Bmatrix} &= \begin{Bmatrix} T_x(y) + c_{11}\varepsilon_{11}^* + c_{12}\varepsilon_{22}^* \\ T_y(y) + c_{66}\varepsilon_{21}^* + c_{66}\varepsilon_{12}^* \end{Bmatrix} \end{aligned} \tag{8.58}$$

These two equations are re-written using embedded Chebyshev differentiators:

$$\begin{Bmatrix} c_{11}\mathbf{I}_y \otimes \mathbf{D}_{x,0}\{u\} + c_{12}\mathbf{D}_{y,j} \otimes \mathbf{I}_y\{v\} \\ c_{66}\mathbf{I}_y \otimes \mathbf{D}_{x,i}\{v\} + c_{66}\mathbf{D}_{y,0} \otimes \mathbf{I}_x\{u\} \end{Bmatrix} = \begin{Bmatrix} T_x(y_j) + c_{11}\varepsilon_{11}^*(x_0, y_j) + c_{12}\varepsilon_{22}^*(x_0, y_j) \\ T_y(y_j) + c_{66}\varepsilon_{21}^*(x_0, y_j) + c_{66}\varepsilon_{12}^*(x_0, y_j) \end{Bmatrix} \tag{8.59}$$

For implementation, for each $0 \leq j \leq n_y$ with fixed $j = 0$, which corresponds to the coordinates (x_0, y_j) of the points on the top surface and which corresponds to the equivalent one-dimensional index $k = in_x + j$, we replace all k-th rows and all $(k+N)$-th rows of the matrix by the left hand side

of the above expressions and:

$$b(k) = T_x(y_j) + c_{11}\varepsilon^*_{11}(x_0, y_j) + c_{12}\varepsilon^*_{22}(x_0, y_j)$$
$$b(k+N) = T_y(y_j) + c_{66}\varepsilon^*_{21}(x_0, y_j) + c_{66}\varepsilon^*_{12}(x_0, y_j) \tag{8.60}$$

Other cases of boundary conditions can be treated similarly and are skipped here.

Some example simulations will be shown.

8.4.1 simulation 1: Elasticity solved by Spectral Method

Consider a two-dimensional solid domain that is subjected to zero displacement constraint $u = v = 0$ on bottom, left and right surfaces and a traction over the top surface,

$$\mathbf{T} = \begin{Bmatrix} T_x(x) \\ T_y(x) \end{Bmatrix} = \begin{Bmatrix} 0 \\ 5 \end{Bmatrix} \tag{8.61}$$

Elements of the normalized stiffness stiffness are $c_{11} = c_{22} = 80$, $c_{12} = c_{21} = 30$ and $c_{66} = 20$ respectively. No eigenstrain is included. The schematic and the resulting x- and y-displacements are shown in figure (8.14).

This result is different from the simulation that assumes periodicity along x-direction, which is shown in figure (8.15) for comparison. Recall that the bottom is displacement-free and top is subjected by the same traction. Also the same stiffness matrix is used.

An attempt is also made for the case where the left and right surfaces are traction-free. These surfaces are free to move. The schematic and the corresponding simulation results are shown in figure (8.16).

8.4.2 simulation 2: Elasticity with non-homogeneous eigen-strains solved by Spectral Method

The spectral method can be used to solve for elasticity equation for solid with non-homogeneous eigen-strains such as inclusion in composite materials and micro-mechanics. For instance, we con-

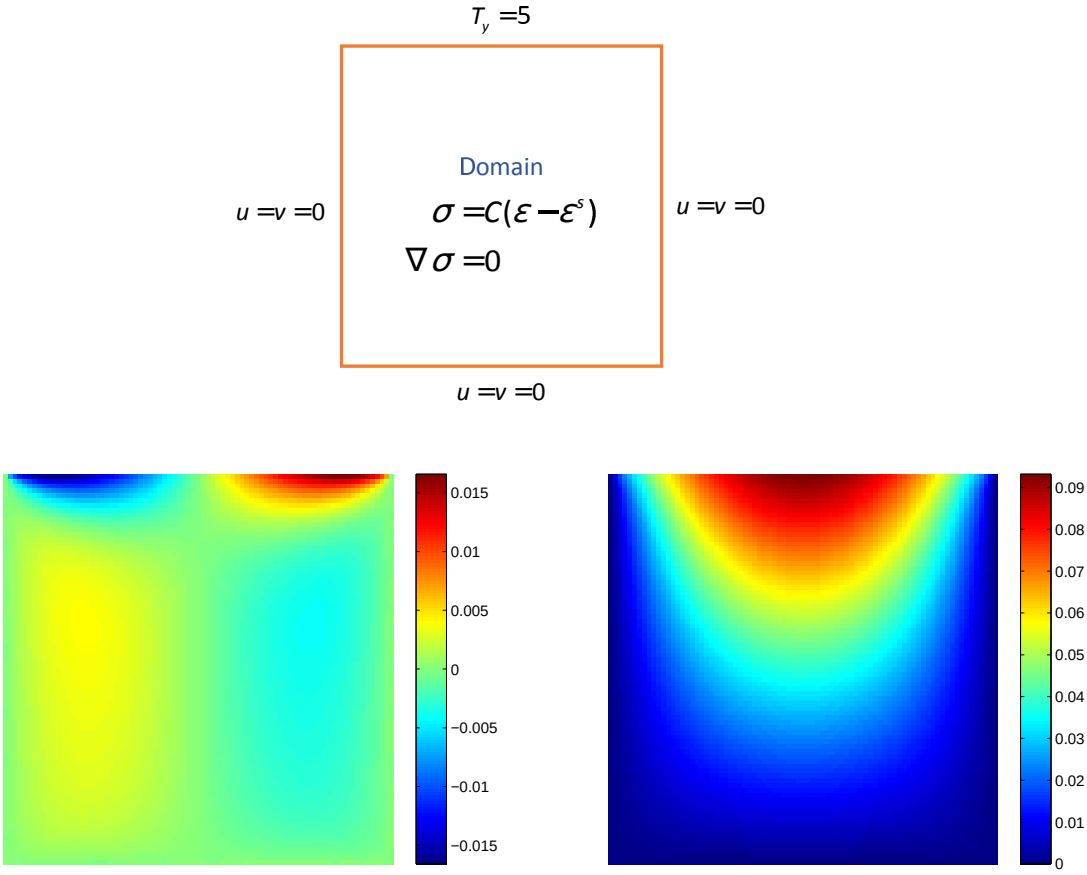

Figure 8.14: Displacement components u and v of solid subjected to traction on top surface and zero displacement on bottom, left and right surface. No periodicity is assumed.

sider the simplest form of laminated eigenstrains with:

$$\varepsilon^*_{12}(x,y) = \begin{cases} -1: & x < 0 \\ 1: & x > 0 \end{cases} \tag{8.62}$$

We adopt the most natural configuration for boundary conditions: top, left and right surfaces are traction-free while the bottom surface is adhered with zero displacements. Stiffness matrix remains unchanged. The resulting displacement components are shown in figure (8.17).

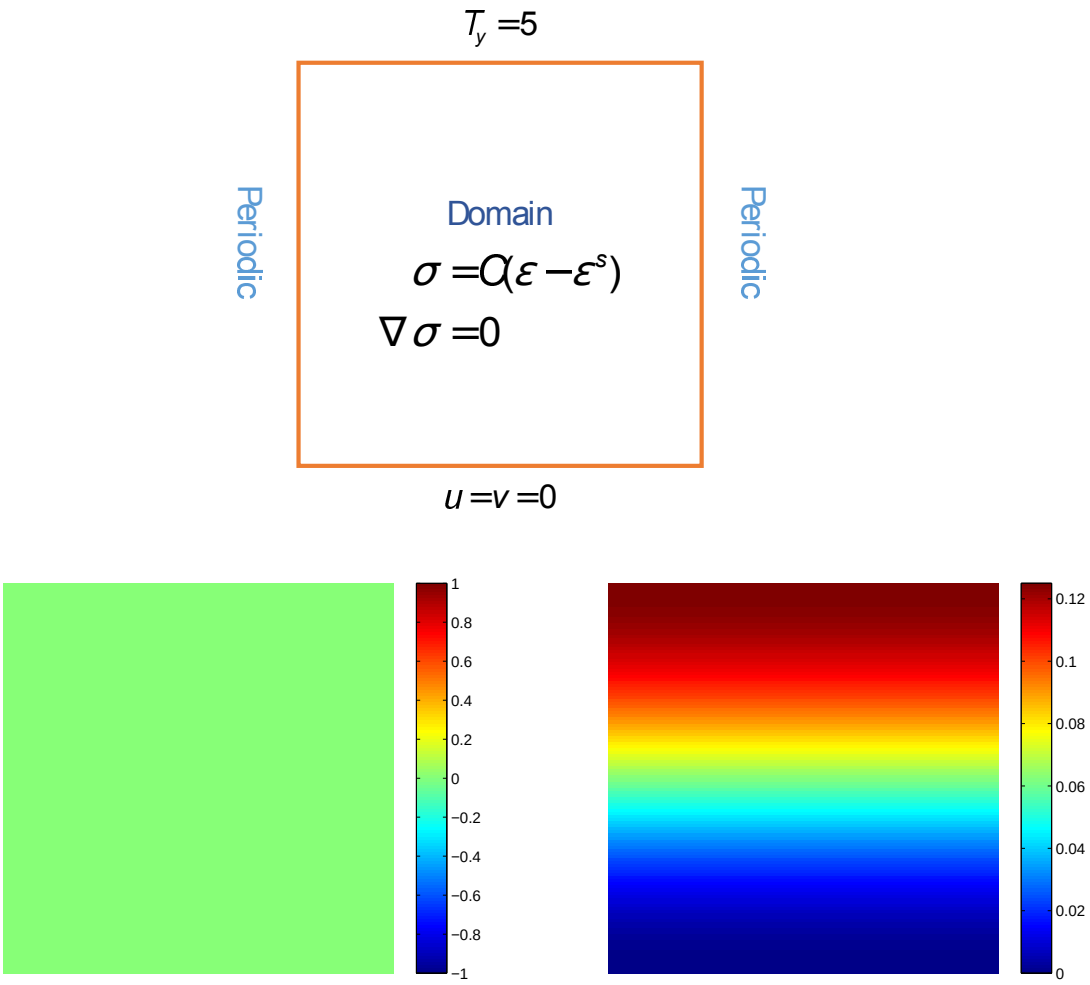

Figure 8.15: Displacement components *u* and *v* of solid subjected to traction on top surface and zero displacement on bottom. Periodicity is assumed in x-direction.

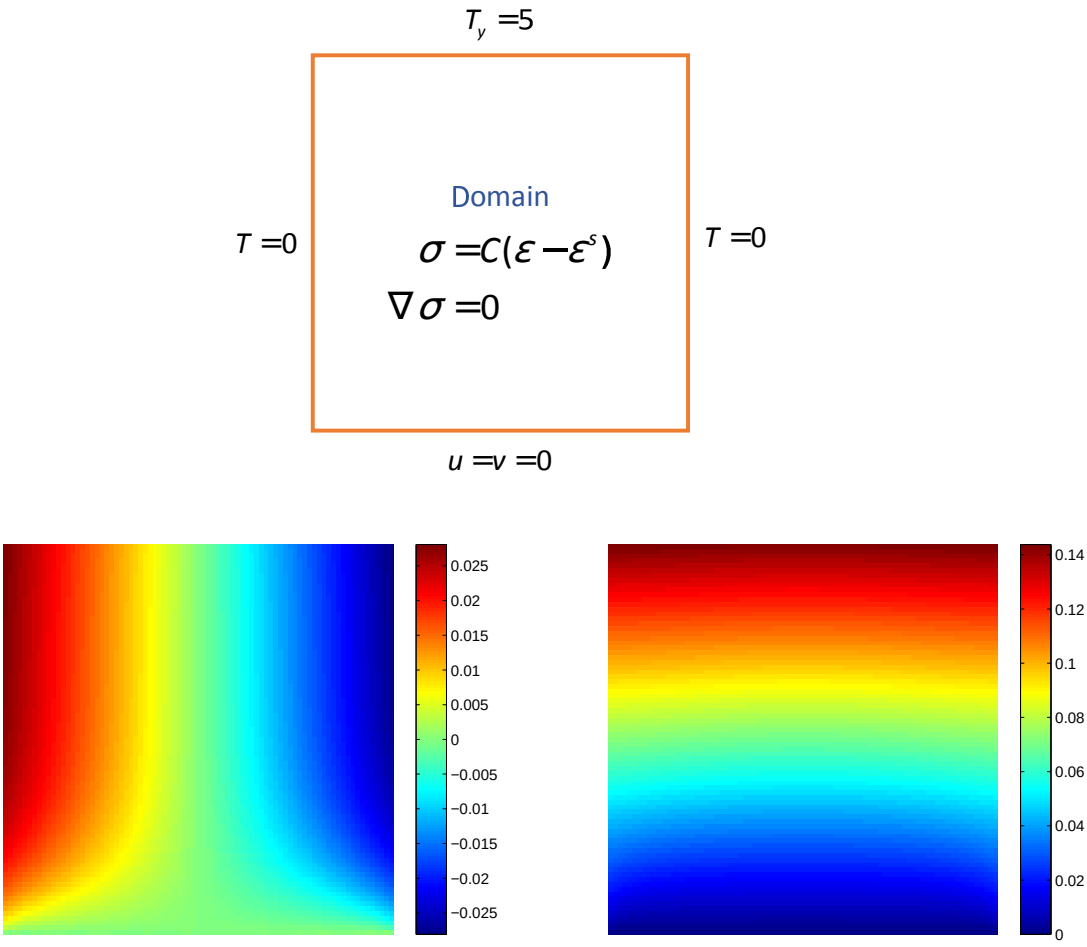

Figure 8.16: Displacement components u and v of solid subjected to traction on top boundary and zero displacement on bottom boundary. The left and right boundaries are traction-free. No periodicity is assumed.

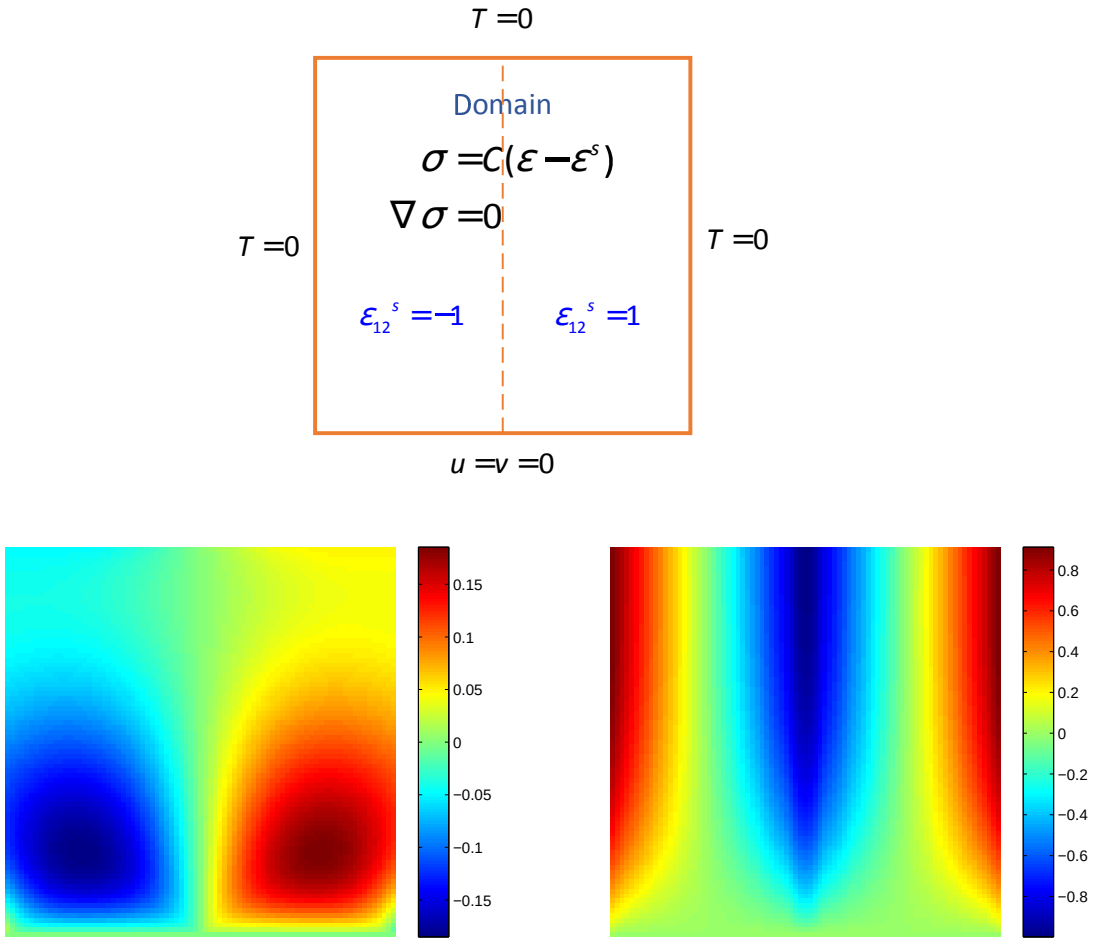

Figure 8.17: Displacement components u and v of solid with laminated eigenstrain ε^*_{12} subjected to traction on top surface and zero displacement on bottom, left and right surface. No periodicity is assumed.

8.5 Fully Coupled Model for Piezoelectric Materials and Solution using Spectral Method

Electromechanical behaviours for piezoelectric material are governed by the matrix equation:

$$\begin{aligned} \sigma &= \mathbf{C}\varepsilon - \mathbf{e}^T\mathbf{E} \\ \mathbf{D} &= \mathbf{e}\varepsilon + \mathbf{k}^T\mathbf{E} \end{aligned} \tag{8.63}$$

where σ is the stress, ε is the strain, $\mathbf{E}$ is the electric field, $\mathbf{D}$ is the electric displacement, $\mathbf{C}$ is the elastic stiffness matrix, $\mathbf{k}$ is the permittivity matrix and $\mathbf{e}$ is the piezoelectric matrix for coupling electrical and elastic contributions for stress-charge form. Notice that Vigot notation is adopted here. The following equations regarding Maxwell's and elasticity equations are also needed:

$$\begin{aligned} \nabla\sigma &= 0 \\ \varepsilon &= \frac{1}{2}\left(\nabla\mathbf{u} + \nabla\mathbf{u}^T\right) \\ \nabla\mathbf{D} &= \rho = 0 \\ \mathbf{E} &= -\nabla\phi \end{aligned} \tag{8.64}$$

where $\mathbf{u}$ is the displacement vector, ρ is the electrical charge, which we assume to be zero in our discussion. We will set up three coupled differential equations in displacement components and electrical potentials.

Expanding these matrix equations for two dimensions, we have:

$$\begin{aligned} \begin{Bmatrix} \sigma_{11} \\ \sigma_{22} \\ \sigma_{12} \end{Bmatrix} &= \begin{bmatrix} c_{11} & c_{12} & \\ c_{12} & c_{22} & \\ & & c_{66} \end{bmatrix} \begin{Bmatrix} \varepsilon_{11} \\ \varepsilon_{22} \\ \varepsilon_{12} \end{Bmatrix} - \begin{bmatrix} e_{11}=0 & e_{31} \\ e_{13}=0 & e_{33} \\ e_{15} & e_{35}=0 \end{bmatrix} \begin{Bmatrix} E_1 \\ E_2 \end{Bmatrix} \\ \begin{Bmatrix} D_1 \\ D_2 \end{Bmatrix} &= \begin{bmatrix} e_{11}=0 & e_{13}=0 & e_{15} \\ e_{31} & e_{33} & e_{35}=0 \end{bmatrix} \begin{Bmatrix} \varepsilon_{11} \\ \varepsilon_{22} \\ \varepsilon_{12} \end{Bmatrix} + \begin{bmatrix} k_{11} & k_{12}=0 \\ k_{21}=0 & k_{22} \end{bmatrix} \begin{Bmatrix} E_1 \\ E_2 \end{Bmatrix} \end{aligned} \tag{8.65}$$

and the following equations:

$$\begin{aligned}
\frac{\partial \sigma_{11}}{\partial x} + \frac{\partial \sigma_{12}}{\partial y} &= 0 \\
\frac{\partial \sigma_{12}}{\partial x} + \frac{\partial \sigma_{22}}{\partial y} &= 0 \\
\frac{\partial D_1}{\partial x} + \frac{\partial D_2}{\partial y} &= 0 \\
\varepsilon_{11} &= \frac{\partial u}{\partial x} \\
\varepsilon_{22} &= \frac{\partial v}{\partial y} \\
\varepsilon_{12} &= \frac{\partial u}{\partial y} + \frac{\partial v}{\partial x} \\
E_1 &= -\frac{\partial \phi}{\partial x} \\
E_2 &= -\frac{\partial \phi}{\partial y}
\end{aligned} \tag{8.66}$$

For convenience, we simplify the piezoelectric constants as $e_{31} = e_{32} = e_a$, $e_{33} = e_b$ and $e_{42} = e_{51} = e_c$.

These equations can be combined to obtain three coupled differential equations in u, v and ϕ as:

First equation:

$$\begin{aligned}
\frac{\partial \sigma_{11}}{\partial x} + \frac{\partial \sigma_{12}}{\partial y} &= 0 \\
\frac{\partial}{\partial x}\left(c_{11}\varepsilon_{11} + c_{12}\varepsilon_{22} - e_a E_2\right) + \frac{\partial}{\partial y}\left(c_{66}\varepsilon_{12} - e_c E_1\right) &= 0 \\
\frac{\partial}{\partial x}\left(c_{11}\frac{\partial u}{\partial x} + c_{12}\frac{\partial v}{\partial y} + e_a\frac{\partial \phi}{\partial y}\right) + \frac{\partial}{\partial y}\left(c_{66}\frac{\partial u}{\partial y} + c_{66}\frac{\partial v}{\partial x} + e_c\frac{\partial \phi}{\partial x}\right) &= 0 \\
\left\{\begin{array}{c} c_{11}\frac{\partial^2 u}{\partial x^2} + c_{12}\frac{\partial^2 v}{\partial x \partial y} + e_a\frac{\partial^2 \phi}{\partial x \partial y} + \frac{\partial c_{11}}{\partial x}\frac{\partial u}{\partial x} + \frac{\partial c_{12}}{\partial x}\frac{\partial v}{\partial y} + \frac{\partial e_a}{\partial x}\frac{\partial \phi}{\partial y} \\ + c_{66}\frac{\partial^2 u}{\partial y^2} + c_{66}\frac{\partial^2 v}{\partial x \partial y} + e_c\frac{\partial^2 \phi}{\partial x \partial y} + \frac{\partial c_{66}}{\partial y}\frac{\partial u}{\partial y} + \frac{\partial c_{66}}{\partial y}\frac{\partial v}{\partial x} + \frac{\partial e_c}{\partial y}\frac{\partial \phi}{\partial x} \end{array}\right\} &= 0
\end{aligned} \tag{8.67}$$

Second equation:

$$\begin{aligned}
\frac{\partial \sigma_{21}}{\partial x}+\frac{\partial \sigma_{22}}{\partial y}&=0\\
\frac{\partial}{\partial x}\left(c_{66}\varepsilon_{12}-e_cE_1\right)+\frac{\partial}{\partial y}\left(c_{21}\varepsilon_{11}+c_{22}\varepsilon_{22}-e_bE_2\right)&=0\\
\frac{\partial}{\partial x}\left(c_{66}\frac{\partial u}{\partial y}+c_{66}\frac{\partial v}{\partial x}+e_c\frac{\partial \phi}{\partial x}\right)+\frac{\partial}{\partial y}\left(c_{21}\frac{\partial u}{\partial x}+c_{22}\frac{\partial v}{\partial y}+e_b\frac{\partial \phi}{\partial y}\right)&=0\\
\left\{\begin{array}{c} c_{66}\frac{\partial^2 u}{\partial x\partial y}+c_{66}\frac{\partial^2 v}{\partial x^2}+e_c\frac{\partial^2 \phi}{\partial x^2}+\frac{\partial c_{66}}{\partial x}\frac{\partial u}{\partial y}+\frac{\partial c_{66}}{\partial x}\frac{\partial v}{\partial x}+\frac{\partial e_c}{\partial x}\frac{\partial \phi}{\partial x}\\ +c_{21}\frac{\partial^2 u}{\partial x\partial y}+c_{22}\frac{\partial^2 v}{\partial y^2}+e_b\frac{\partial^2 \phi}{\partial y^2}+\frac{\partial c_{21}}{\partial y}\frac{\partial u}{\partial x}+\frac{\partial c_{22}}{\partial y}\frac{\partial v}{\partial y}+\frac{\partial e_b}{\partial y}\frac{\partial \phi}{\partial y}\end{array}\right\}&=0
\end{aligned}\tag{8.68}$$

Third equation:

$$\begin{aligned}
\frac{\partial D_1}{\partial x}+\frac{\partial D_2}{\partial y}&=0\\
\frac{\partial}{\partial x}\left(e_c\varepsilon_{12}+k_1E_1\right)+\frac{\partial}{\partial y}\left(e_a\varepsilon_{11}+e_b\varepsilon_{22}+k_2E_2\right)&=0\\
\frac{\partial}{\partial x}\left(e_c\frac{\partial u}{\partial y}+e_c\frac{\partial v}{\partial x}-k_1\frac{\partial \phi}{\partial x}\right)+\frac{\partial}{\partial y}\left(e_a\frac{\partial u}{\partial x}+e_b\frac{\partial v}{\partial y}-k_2\frac{\partial \phi}{\partial y}\right)&=0\\
\left\{\begin{array}{c} e_c\frac{\partial^2 u}{\partial x\partial y}+e_c\frac{\partial^2 v}{\partial x^2}-k_1\frac{\partial^2 \phi}{\partial x^2}+\frac{\partial e_c}{\partial x}\frac{\partial u}{\partial y}+\frac{\partial e_c}{\partial x}\frac{\partial v}{\partial x}-\frac{\partial k_1}{\partial x}\frac{\partial \phi}{\partial x}\\ +e_a\frac{\partial^2 u}{\partial x\partial y}+e_b\frac{\partial^2 v}{\partial y^2}-k_2\frac{\partial^2 \phi}{\partial y^2}+\frac{\partial e_a}{\partial y}\frac{\partial u}{\partial x}+\frac{\partial e_b}{\partial y}\frac{\partial v}{\partial y}-\frac{\partial k_2}{\partial y}\frac{\partial \phi}{\partial y}\end{array}\right\}&=0
\end{aligned}\tag{8.69}$$

These equations are expressed using Chebyshev differentiator matrices and assembled into a single matrix equation as follow.

$$\begin{bmatrix} \mathbf{A}_{11} & \mathbf{A}_{12} & \mathbf{A}_{13}\\ \mathbf{A}_{21} & \mathbf{A}_{22} & \mathbf{A}_{23}\\ \mathbf{A}_{31} & \mathbf{A}_{32} & \mathbf{A}_{33}\end{bmatrix}\begin{Bmatrix} \mathbf{u}\\ \mathbf{v}\\ \phi\end{Bmatrix}=\begin{Bmatrix} \mathbf{0}\\ \mathbf{0}\\ \mathbf{0}\end{Bmatrix}\tag{8.70}$$

where the blocks of matrix are given below:

$$
\begin{aligned}
\mathbf{A}_{11} &= c_{11}\mathbf{L}_{xx} + \frac{\partial c_{11}}{\partial x}\mathbf{L}_x + c_{66}\mathbf{L}_{yy} + \frac{\partial c_{66}}{\partial y}\mathbf{L}_y \\
\mathbf{A}_{12} &= c_{12}\mathbf{L}_{xy} + \frac{\partial c_{12}}{\partial x}\mathbf{L}_y + c_{66}\mathbf{L}_{xy} + \frac{\partial c_{66}}{\partial y}\mathbf{L}_x \\
\mathbf{A}_{13} &= e_a\mathbf{L}_{xy} + \frac{\partial e_a}{\partial x}\mathbf{L}_y + e_c\mathbf{L}_{xy} + \frac{\partial e_c}{\partial y}\mathbf{L}_x \\
\mathbf{A}_{21} &= c_{66}\mathbf{L}_{xy} + \frac{\partial c_{66}}{\partial x}\mathbf{L}_y + c_{21}\mathbf{L}_{xy} + \frac{\partial c_{21}}{\partial y}\mathbf{L}_x \\
\mathbf{A}_{22} &= c_{66}\mathbf{L}_{xx} + \frac{\partial c_{66}}{\partial x}\mathbf{L}_x + c_{22}\mathbf{L}_{yy} + \frac{\partial c_{22}}{\partial y}\mathbf{L}_y \\
\mathbf{A}_{23} &= e_c\mathbf{L}_{xx} + \frac{\partial e_c}{\partial x}\mathbf{L}_x + e_b\mathbf{L}_{yy} + \frac{\partial e_b}{\partial y}\mathbf{L}_y \\
\mathbf{A}_{31} &= e_c\mathbf{L}_{xy} + \frac{\partial e_c}{\partial x}\mathbf{L}_y + e_a\mathbf{L}_{xy} + \frac{\partial e_a}{\partial y}\mathbf{L}_x \\
\mathbf{A}_{32} &= e_c\mathbf{L}_{xx} + \frac{\partial e_c}{\partial x}\mathbf{L}_x + e_b\mathbf{L}_{yy} + \frac{\partial e_b}{\partial y}\mathbf{L}_y \\
\mathbf{A}_{33} &= -k_1\mathbf{L}_{xx} - \frac{\partial k_1}{\partial x}\mathbf{L}_x - k_2\mathbf{L}_{yy} - \frac{\partial k_2}{\partial y}\mathbf{L}_y
\end{aligned}
\tag{8.71}
$$

where each of $\mathbf{A}_{ij}$ is a $(n_x+1)(n_y+1)\times(n_x+1)(n_y+1)$-matrix, $\mathbf{u}$, $\mathbf{v}$, ϕ are one-dimensional equivalent vector for the two-dimensional data representing displacement components and potential.

On each of the four boundaries, three boundary conditions are needed where two are associated with mechanical conditions and the remained one with electrical condition. Examples include two traction components and electric potential on top surface. The schematic is shown in figure (8.18). Boundary conditions are implemented in the same way we treated for the decoupled Maxwell's and elasticity equations. The detail is not presented here.

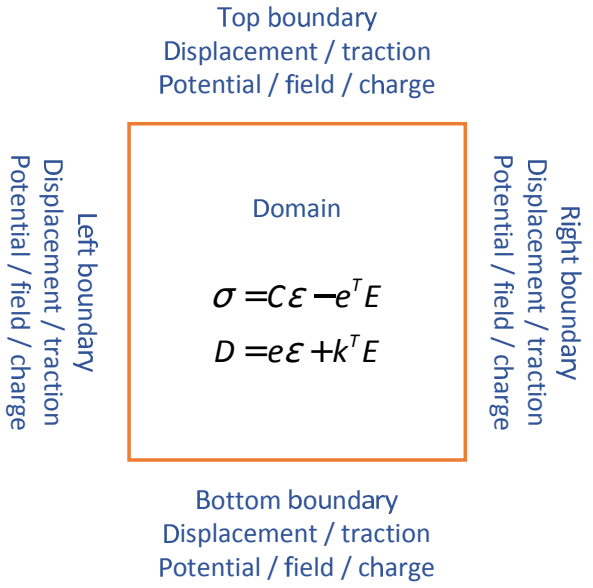

Figure 8.18: Boundary conditions for coupled piezo-electric model.

In each of the following illustrations, PZT-5H is used with the following material properties:

elastic	piezo-electric	dielectric
Pa	C/m^2	ε_0
$c_{11} = 1.27205 \times 10^{11}$	$e_{13} = -6.62281$	$k_1 = 1704.4$
$c_{22} = 1.17436 \times 10^{11}$	$e_{23} = -6.62281$	$k_2 = 1433.6$
$c_{66} = 2.29885 \times 10^{10}$	$e_{33} = 23.2403$	
$c_{12} = 8.46702 \times 10^{10}$	$e_{42} = 17.0345$	
$c_{21} = c_{12}$	$e_{51} = 17.0345$	

(8.72)

8.5.1 Simulation 1: Piezo-electric solved by Spectral Method

The domain of simulation has the length-height ratio as 5:1. An artificial potential, $\phi_{top}(x) = \sin(2\pi x)$, is applied on the top surface. Both left and right boundaries are subjected to natural conditions, that is, traction-free and charge-free. The bottom surface is fixed with no displacement and grounded with zero potential. The schematic and the simulated quantities (potential ϕ, displacements u and v) are shown in figure (8.19).

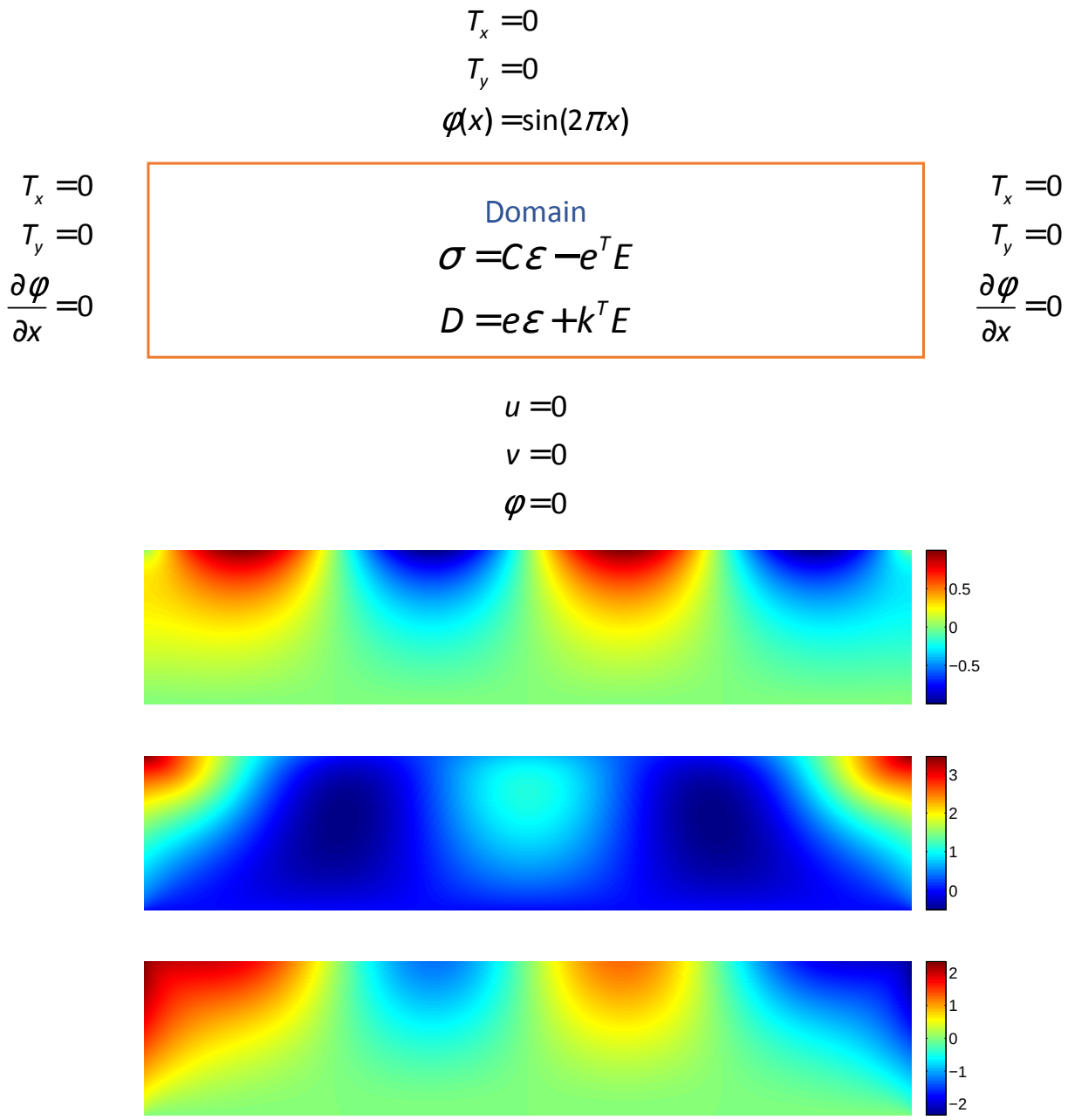

Figure 8.19: Simulation of electromechanical response in piezoelectric material with artificial applied potential on top surface and natural boundary conditions on other boundaries. (a) Potential, (b) x-displacement, (c) y-displacement. Notice that due to normalization, the displacements are in the unit of 10^{10} (m), while the unit of the potential is Volt (V).

8.5.2 Simulation 2: Piezo-electric solved by Spectral Method

The domain of simulation has the length-height ratio as 5:1. An uniform traction acting in the y-direction is exerted on the top surface, $T_y(x) = 5$. The top surface is charge-free, that is, $\frac{\partial \phi}{\partial y} = 0$. Both left and right boundaries are subjected to natural conditions, that is, traction-free and charge-free. The bottom surface is fixed with no displacement and grounded with zero potential. The schematic and the simulated quantities (potential ϕ, displacements u and v) are shown in figure (8.20).

8.5.3 Simulation 3: PFM of Piezo-electric simulated by Spectral Method

The domain of simulation has the length-height ratio as 5:1. We may study the electromechanical response of piezoelectric sample in an experimental setup of piezo-response force microscopy (PFM). The PFM tip is producing a potential over the top surface,

$$\phi_{PFM}(x) = V_0 \frac{\gamma^2}{\gamma^2 + (x - x_0)^2}, \tag{8.73}$$

where V_0 is the applied voltage and γ represents the half width of the PFM tip. In this simulation, the dimension of the sample domain is 500 (nm) $\times$ 100 (nm) while the radius of the PFM tip is 10 (nm). Based on normalization, we take the domain as 10 (unit) by 2 (unit), while the radius of the top γ is 0.1. Assume the PFM tip is located at the center of the top boundary, so $x_0 = 0$. For the boundary conditions, the top surface is fraction-free. Both left and right boundaries are subjected to natural conditions, that is, traction-free and charge-free. The bottom surface is fixed with no displacement and grounded with zero potential. The schematic and the simulated quantities (potential ϕ, displacements u and v) are shown in figure (8.21).

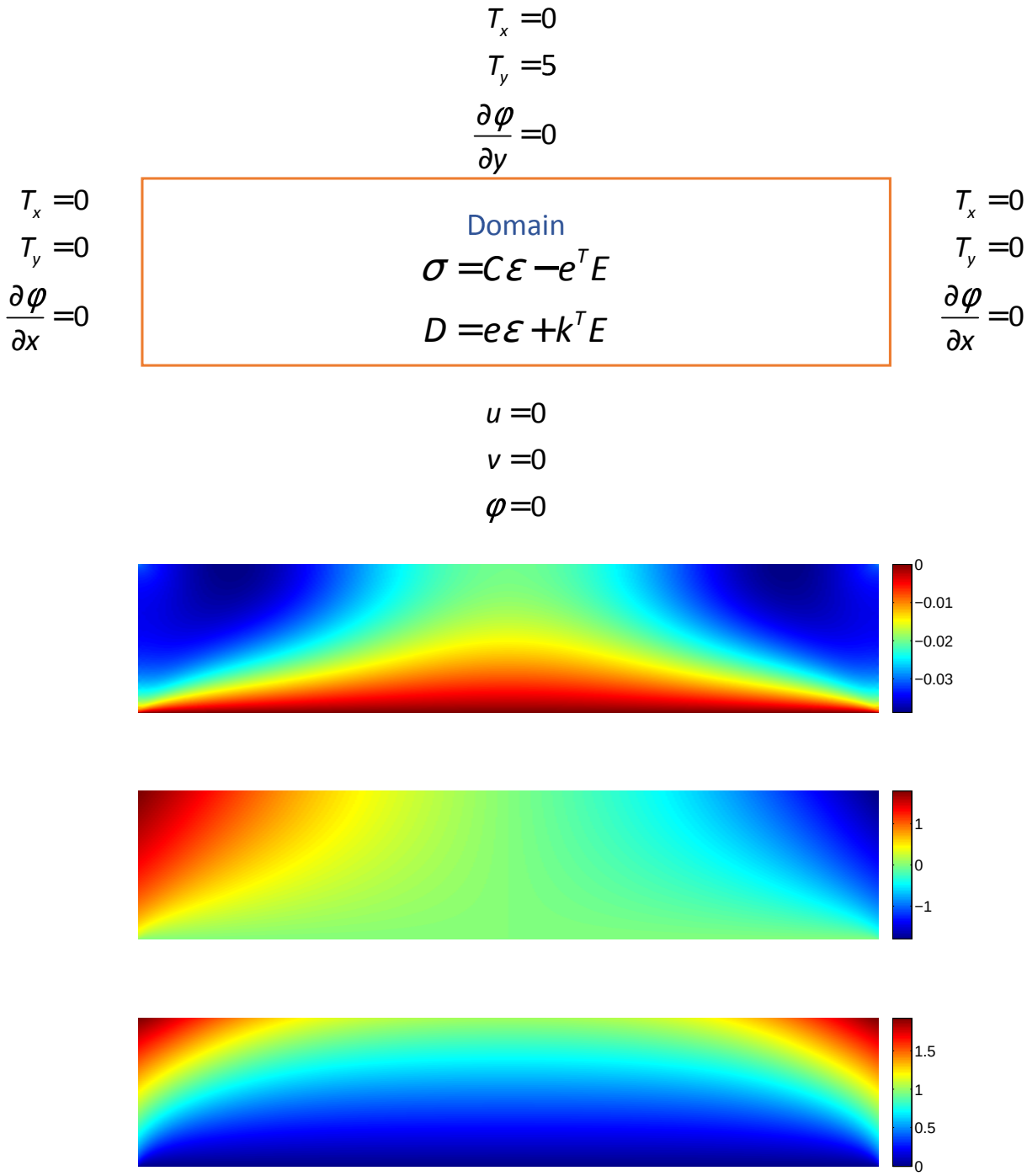

Figure 8.20: Simulation of electromechanical response in piezoelectric material with artificial applied potential on top surface and natural boundary conditions on other boundaries. (a) Potential, (b) x-displacement, (c) y-displacement. Notice that due to normalization, the displacements are in the unit of 10^{10} (m), while the unit of the potential is Volt (V).

$$T_x = 0$$
$$T_y = 0$$
$$\varphi_{PFM}(x) = V_0 \frac{\gamma^2}{\gamma^2 + (x - x_0)^2}$$

$T_x = 0$
$T_y = 0$
$\frac{\partial \varphi}{\partial x} = 0$

Domain

$$\sigma = C\varepsilon - e^T E$$
$$D = e\varepsilon + k^T E$$

$T_x = 0$
$T_y = 0$
$\frac{\partial \varphi}{\partial x} = 0$

$$u = 0$$
$$v = 0$$
$$\varphi = 0$$

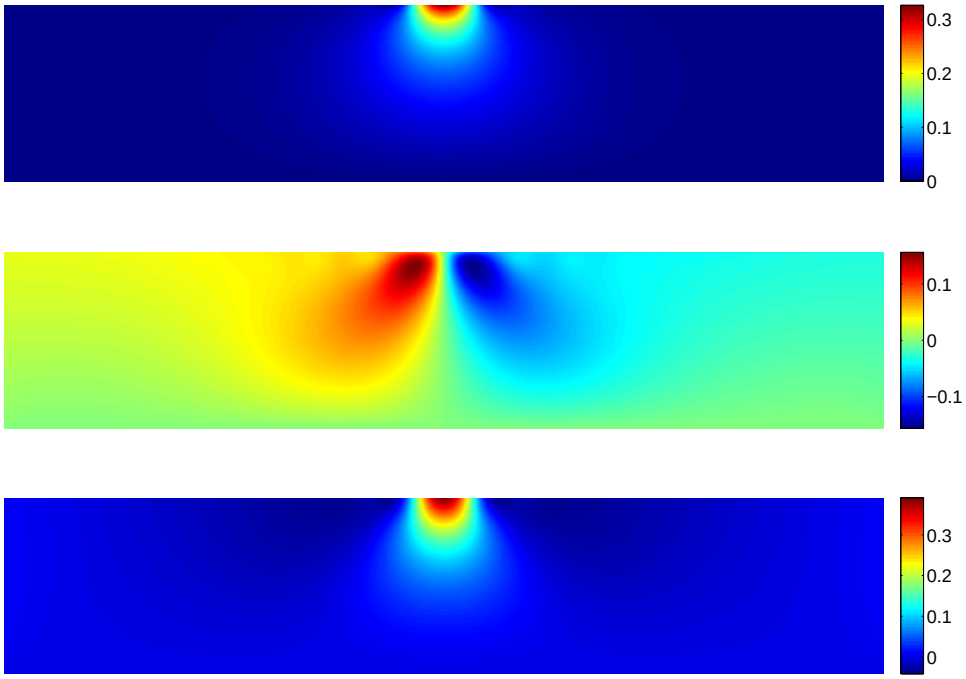

Figure 8.21: Simulation of electromechanical response of piezoelectric material as in PFM. The top surface is subjected to a potential induced by PFM tip. All other boundaries are natural. (a) Potential, (b) x-displacement, (c) y-displacement. Notice that due to normalization, the displacements are in the unit of 10^{10} (m), while the unit of the potential is Volt (V).

8.6 Piezoelectric Response of Ferroelectric with Spectral Method

We use spectral method to study the electromechanical response of ferroelectric material consisting of various instantaneous polarization. Different configurations of polarization induce different vibration amplitudes, thus different readings as detected from the SPM (Scanning Probe Microcopy) tip. Previous works by Pan [98, 99] studied the PFM response of sample of isotropic material with complicated three-dimensional heterogeneity in polarization using green function integrated over semi-infinite half-plane. Yet no boundary condition is considered over lateral and bottom surfaces and the domain is not finite, even though the electrical potential induced by the SPM tip is localized at the site of the tip. Integration over semi-infinite domain also overestimates the resulting displacement field and thus deflection. With the spectral method, we may consider material composed of spatially inhomogeneous material properties (elastic, dielectric, piezo-electric), which gives more realistic analysis of a PFM experiment.

According to the Disk-plane model, during the operation of the PFM, the SPM tip effectively resembles a point charge $Q = 4\varepsilon_0(\kappa+1)R_0V_0$, where ε_0 is the permittivity of free space, R_0 is the radius of the tip, $\kappa = \sqrt{\varepsilon_{11}\varepsilon_{33}}$ is the effective permittivity of the probed sample, $\gamma = \sqrt{\frac{\varepsilon_{33}}{\varepsilon_{11}}}$ is the dielectric anisotropy of the sample and $d = \frac{2R_0}{\pi}$ is the distance between the effective point charge and the probed sample.

The potential $\phi = \phi(x,y)$ and the resulting electric field acting over the sample generated by the effective charge Q from the SPM (Scanning Probe Microcopy) tip are given by:

$$\phi(x,y) = \frac{Q}{2\pi\varepsilon_0(\kappa+1)\sqrt{(x-x_0)^2+\left(\frac{y}{\gamma}+d\right)^2}}$$
$$\mathbf{E} = -\nabla\phi \tag{8.74}$$

where x_0 is the x-coordinate of the tip over the top surface of the sample. The schematic is shown in figure (8.22).

If the size of the sample is 5000 (nm) $\times$ 2000 (nm), the voltage is 1 (Volt) and the radius of the tip is 25 (nm), the resulting potential and electric field components are shown in figures (8.23) (a)(b)(c).

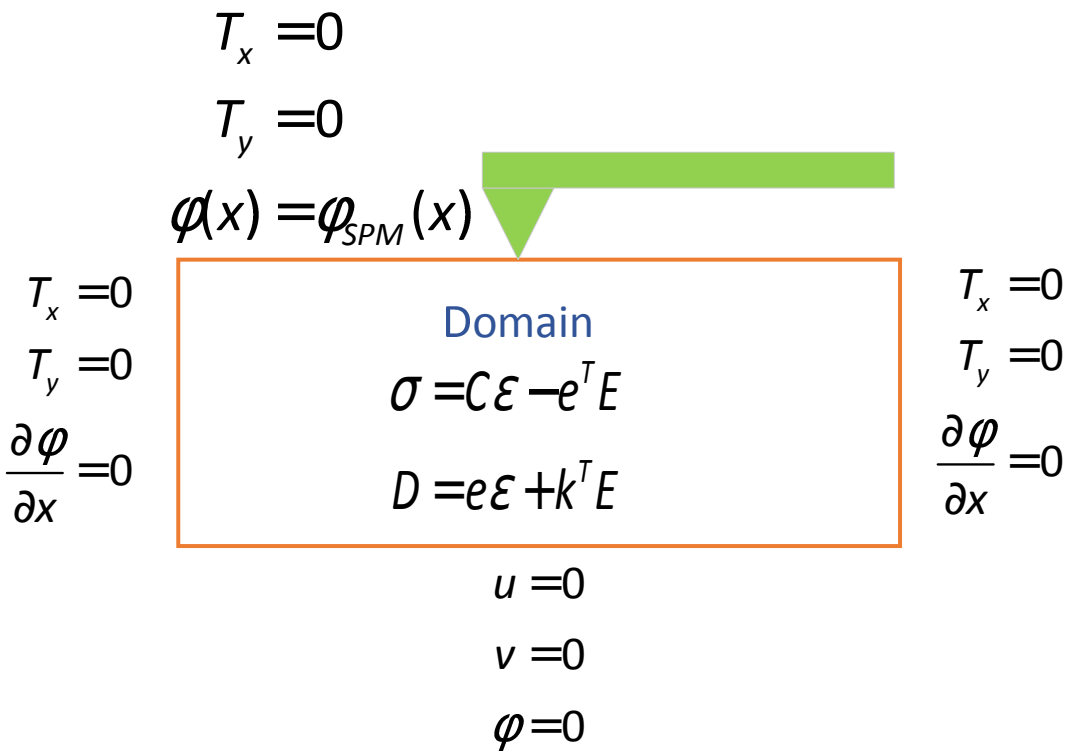

Figure 8.22: SPM of ferroelectric with single domain.

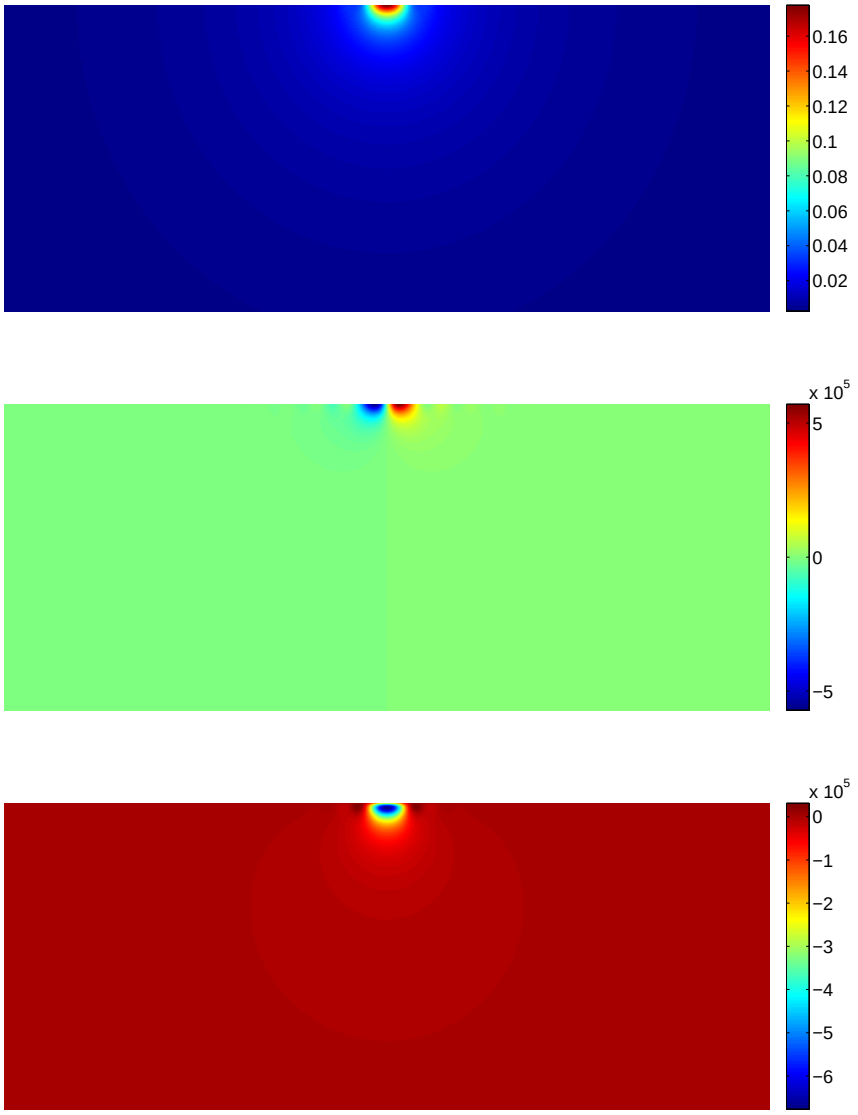

Figure 8.23: Distribution of (a) potential, (b) electric field component E_1 and (c) electric field component E_2 induced by PFM tip whose tip radius is 25 (nm) and applied voltage is 1 (Volt).

This electric field will in turn induces a piezo-electric eigen-strain:

$$\begin{Bmatrix} \varepsilon^s_{11} \\ \varepsilon^s_{22} \\ \varepsilon^s_{12} \end{Bmatrix} = \begin{bmatrix} 0 & d_{31} \\ 0 & d_{33} \\ d_{51} & 0 \end{bmatrix} \begin{Bmatrix} E_1 \\ E_2 \end{Bmatrix} \tag{8.75}$$

With this piezo-electric eigen-strain, deflection can be computed by solving the mechanical equilibrium equation as in:

$$\begin{aligned} \sigma &= \mathbf{C}\left(\varepsilon - \varepsilon^s\right) \\ \nabla\sigma &= 0 \end{aligned} \tag{8.76}$$

We consider natural boundary conditions: the top, left and right boundaries are traction-free and the bottom surface is displacement-free. Figure (8.23) shows the deflections (u and v) over the entire sample. Notice that the deflections on the top surfaces are those being detected by the PFM tip.

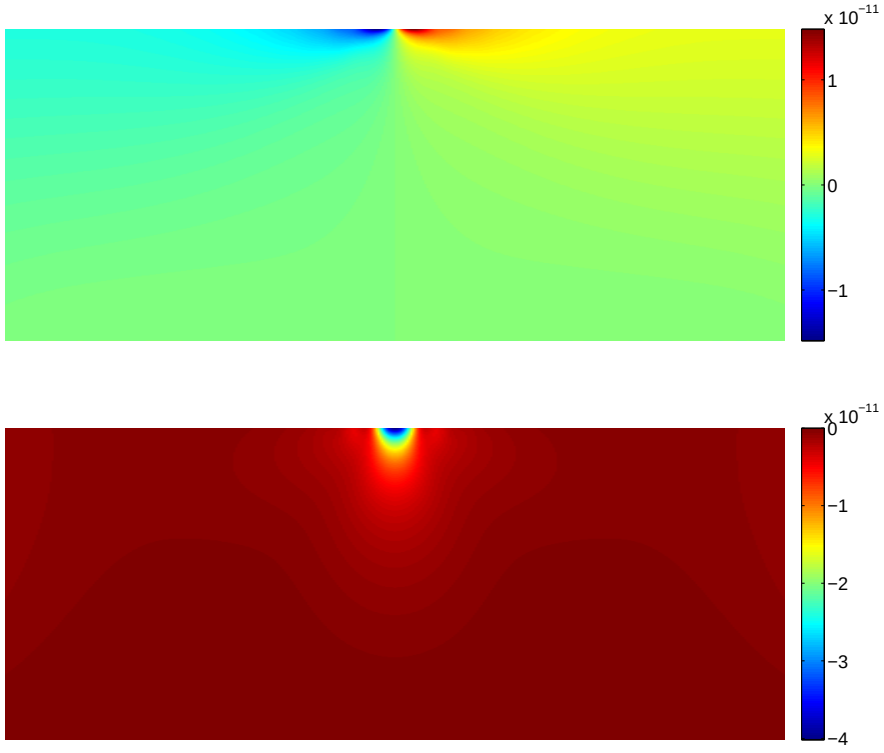

Figure 8.24: Distribution of the displacement components induced from the electric field (a) u, (b) v

Next we consider the domain structure with two domains with a domain wall parallel to the y-axis, as schematically shown in figure (8.25).

The domain wall is assumed to be sharp with no thickness. The polarization orientations are determined by piezoelectric matrix and tensor transformation:

$$d_{ijk}(x,y) = T_{ir}(x,y)T_{js}(x,y)T_{kt}(x,y)d^0_{rst}(x,y), \tag{8.77}$$

where $d^0_{rst}(x,y)$ is the piezoelectric tensor of c-domain in the global coordinate system, $T_{ir}(x,y)$ is the transformation matrix that rotates c-domain to some particular domain at location (x,y), and $d_{ijk}(x,y)$ is the piezoelectric tensor of the rotated domain. For 180 domains, the spontaneous polarization are pointing upward and downward, denoted by $c+$ and $c-$ phases. While the $c+$ phase is quantified by the original piezoelectric matrix, the $c-$ phase is described by the piezo-electric

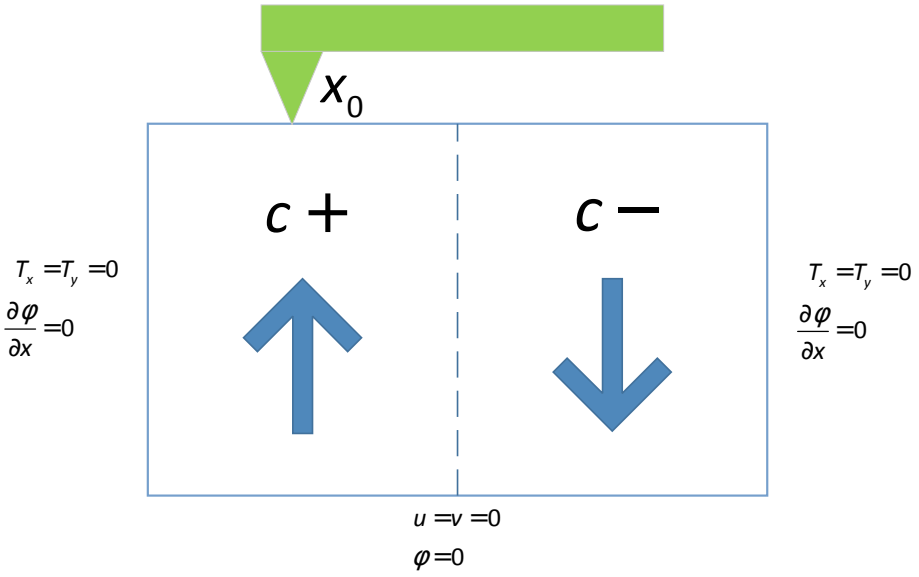

Figure 8.25: SPM of ferroelectric with single domain.

matrix via a 180 degree transformation:

$$\mathbf{d}_{c-} = \begin{bmatrix} & & -d_{31} \\ & & -d_{33} \\ -d_{51} & & \end{bmatrix} \tag{8.78}$$

Scanning and imaging electromechanical response, that is, deflection on surface as detected by PFM tip, of ferroelectric domain with inhomogeneous polarization can be simulated by moving the operating PFM tip over the top surface. The snapshots of the vertical displacement v as the top moves from the left to the right (across the domain wall in the center line) are shown on figure (8.26). The relationship between the vertical deflection versus the distance from the domain wall at the center line is shown on figure (8.27).

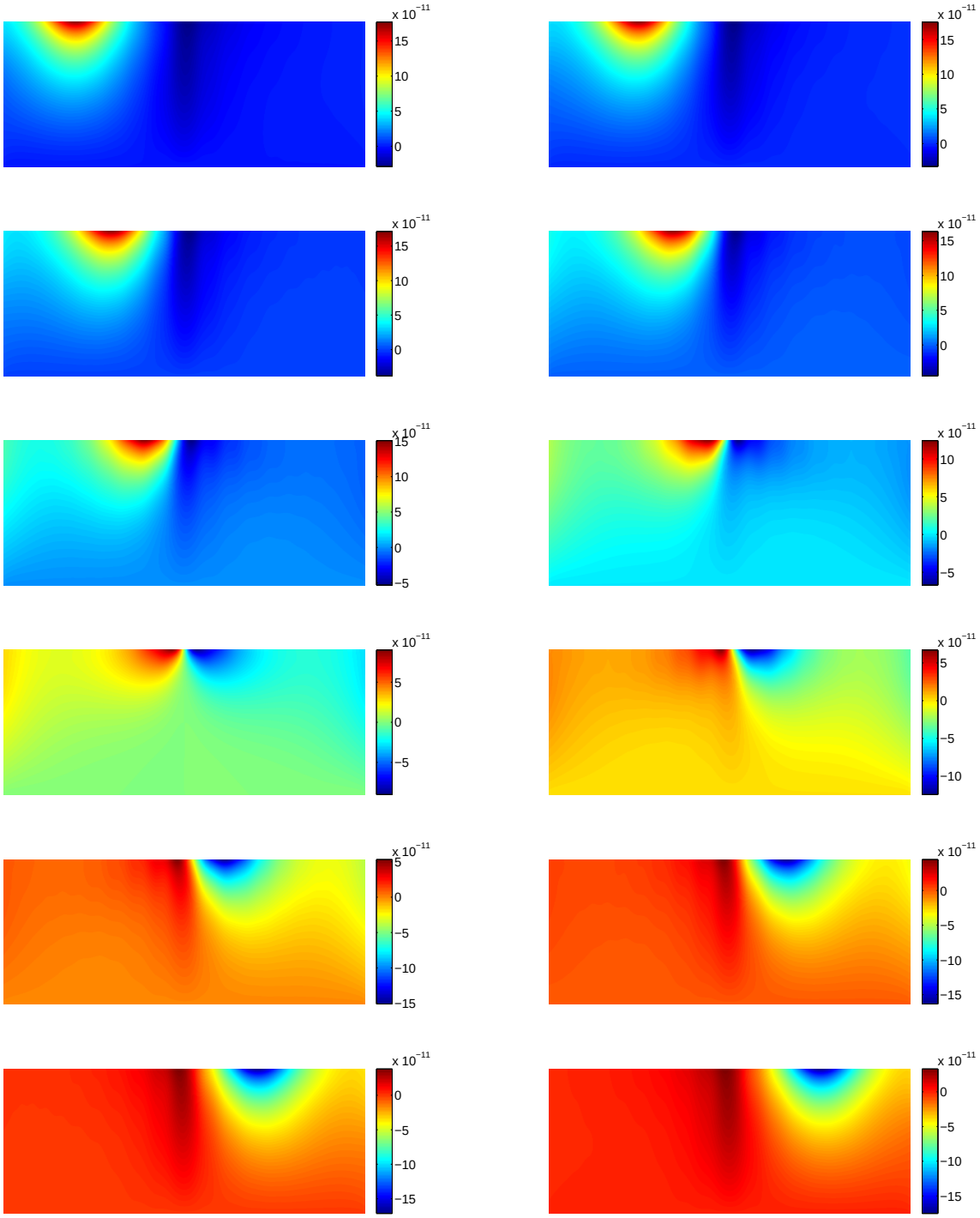

Figure 8.26: Snapshots of vertical displacements for PFM scanning of ferroelectric with two domains

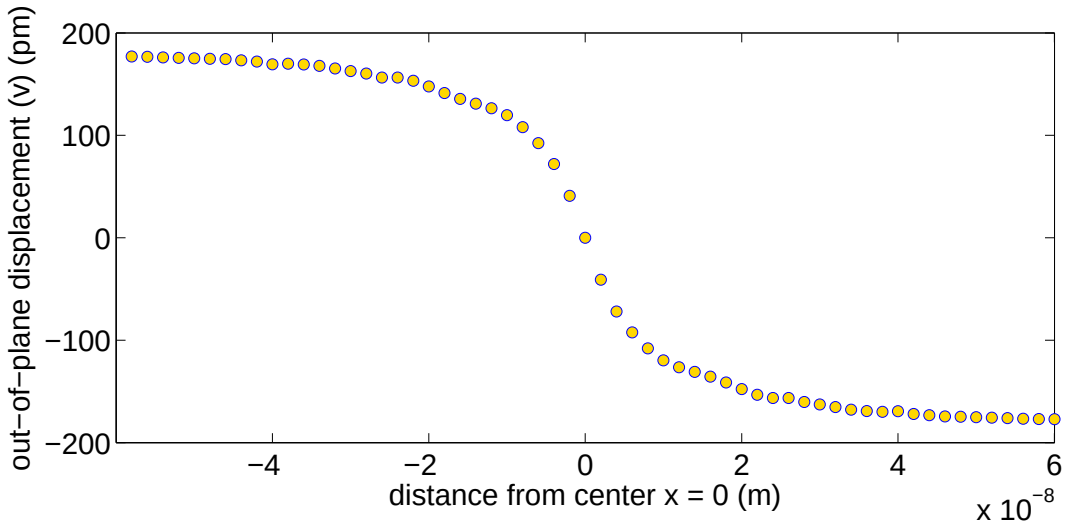

Figure 8.27: Relation between the PFM response as vertical displacement versus distance from the domain wall at center line

8.7 Phase Field Simulations of Multi-variant Multi-functional Materials using Spectral Method

Spectral method can be implemented with phase field simulation. Together with what we have done for Maxwell's equation and elasticity equation with general configuration and conditions, we are able to simulate multi-variant microstructures subjected to general configuration and conditions, such as, inhomogeneity and arbitrary boundary conditions with no restriction from imposing periodicity.

Recall that the microstructural configuration and evolution of multi-functional materials such as shape memory alloys, ferro-electric and ferro-magnetics are mathematically quantified by characteristic functions $\mu_i = \mu_i(x,y,t)$ with a laminating setting. We recall also the evolution equation of characteristic functions with N variants are derived as:

$$\frac{\partial \mu_i}{\partial t} = 2M\left(F_i^{int} + F_i^{ani} + F_i^{elas} + F_i^{ele}\right), \forall i = 1,2,...,N-1 \tag{8.79}$$

Each term in these equations have been discussed in previous chapters and are not explained for chastity. Since all equations for $i = 1,2,...,N$ have the same form, we restrict our discussion to one such equation. We also drop the subscript i.

After normalization, the above equation becomes:

$$\begin{aligned}
\frac{\partial \mu}{\partial t} &= \frac{A}{K}F^{int} + \frac{1}{2K}F^{ani} + \frac{1}{2K}F^{elas} + \frac{1}{2K}F^{ele} \\
\frac{\partial \mu}{\partial t} &= -D\nabla^2\mu + \mu(1-\mu)(1-2\mu) + \frac{1}{2K}\left(\sigma\frac{\partial \varepsilon^*}{\partial \mu} + E\frac{\partial P}{\partial \mu}\right) \\
\frac{\partial \mu}{\partial t} &= -D\left(\frac{\partial^2\mu}{\partial x^2} + \frac{\partial^2\mu}{\partial y^2}\right) + \mu(1-\mu)(1-2\mu) + \frac{1}{2K}\left(\sigma\frac{\partial \varepsilon^*}{\partial \mu} + E\frac{\partial P}{\partial \mu}\right) \\
\frac{\partial \mu}{\partial t} &= -D\left(\frac{\partial^2\mu}{\partial x^2} + \frac{\partial^2\mu}{\partial y^2}\right) + F(\mu),
\end{aligned} \tag{8.80}$$

where ε^* and $\mathbf{P}$ are the effective eigenstrain and the instantaneous polarization respectively of the system, computed as the linear combination of the eigenstrains and polarization of all constituent variants in their volume ratios. σ and $\mathbf{E}$ are the overall stress field and electric field of the system, which are solved from the elasticity (equilibrium) and Maxwell's equations:

$$\begin{aligned}
\sigma &= \mathbf{C}(\varepsilon - \varepsilon^*) \\
\nabla\sigma &= 0 \\
\kappa\nabla^2\phi &= \nabla\cdot\mathbf{P} \\
\mathbf{E} &= -\nabla\phi
\end{aligned} \tag{8.81}$$

Maxwell's equation and elasticity equation are solved using spectral method with Chebyshev approach, which have been outlined in previous sections. To implement spectral method in phase field equation, we re-label or re-arrange all the two-dimensional data such as $\mu_{ij} = \mu(x_i, y_j)$ to equivalent one-dimensional vector μ_k, with the conversion of indices being $k = in_i + j$.

The evolution is also discredited along rime domain t. Denoting $\mu^m = \mu(t_m) = \mu(x_i, y_j, t_m)$, we have the following numerical scheme with Chebyshev differentiator matrices:

$$\begin{aligned}
\frac{\partial \mu}{\partial t} &= -D\left(\frac{\partial^2\mu}{\partial x^2} + \frac{\partial^2\mu}{\partial y^2}\right) + F(\mu) \\
\frac{\mu^{m+1} - \mu^m}{\Delta t} &= -D(\mathbf{L}_{xx} + \mathbf{L}_{yy})(\mu^m) + F(\mu^m),
\end{aligned} \tag{8.82}$$

where $\mathbf{L}_{xx}$ and $\mathbf{L}_{yy}$ are the embedded Chebyshev differentiators in two-dimension for second deriva-

tives.

In the prospective of numerical analysis, one may want to separate μ^m into two portions as:

$$\mu^m \approx \alpha\mu^m + (1-\alpha)\mu^{m+1}, \tag{8.83}$$

where $0 \leq \alpha \leq 1$ is adjusted to generate various semi-implicit and implicit numerical schemes. Previous experience has suggested the choice $\alpha = 0$, or a fully implicit scheme. The discredited evolution equation becomes:

$$\begin{aligned} \mathbf{I}\mu^{m+1} - \mathbf{I}\mu^m &= D\left(\mathbf{L}_{xx} + \mathbf{L}_{yy}\right)\mu^{m+1}\Delta t + F\left(\mu^m\right)\Delta t \\ \left[\mathbf{I} - D\left(\mathbf{L}_{xx} + \mathbf{L}_{yy}\right)\Delta t\right]\mu^{m+1} &= \mu^m + F\left(\mu^m\right)\Delta t \\ \mathbf{A}\mu^{m+1} &= \mathbf{B}\mu^m + F\left(\mu^m\right) = \mathbf{b} \end{aligned} \tag{8.84}$$

Neumann boundary conditions are adopted over all boundaries of the domain, that is,

$$\begin{aligned} \frac{\partial\mu}{\partial y}\left(-1 \leq x \leq 1, y = 1\right) &= 0 \\ \frac{\partial\mu}{\partial y}\left(-1 \leq x \leq 1, y = -1\right) &= 0 \\ \frac{\partial\mu}{\partial x}\left(x = 1, -1 \leq y \leq 1\right) &= 0 \\ \frac{\partial\mu}{\partial x}\left(x = -1, -1 \leq y \leq 1\right) &= 0, \end{aligned} \tag{8.85}$$

which will be translated in Chebsyhev structures as:

$$\begin{aligned} \mathbf{D}_y\mu\left(x_i, y_0\right) &= 0, 0 \leq i \leq n_x \\ \mathbf{D}_y\mu\left(x_i, y_{n_y}\right) &= 0, 0 \leq i \leq n_x \\ \mathbf{D}_x\mu\left(x_0, y_j\right) &= 0, 0 \leq j \leq n_y \\ \mathbf{D}_x\mu\left(x_{n_x}, y_j\right) &= 0, 0 \leq j \leq n_y \end{aligned} \tag{8.86}$$

These boundary conditions are incorporated to update the matrix equation as previously done before in general non-periodic Maxwell's equation. For example, for the boundary condition on top

surface, we replace the row of the matrix equation whose indices are $k = in_x + 0$ by the i-th row of the Chebyshev differentiation matrix:

$$\begin{aligned} A(k,:) &= \mathbf{D}_{y,0} \otimes \mathbf{I}_{x,i} \\ b(k) &= 0, \end{aligned} \tag{8.87}$$

where $\mathbf{D}_{y,0}$ represents the 0-th row of $\mathbf{D}_y$ while $\mathbf{I}_{x,i}$ represents the i-th column of $\mathbf{I}_x$.

After updating the rows of the matrix equations with Chebyshev differentiation matrices due to boundary conditions, these equations are solve to yield the characteristic function μ at a new time step $t = t_{m+1}$. The iteration continues until the convergence criteria are met.

This approach, in practice, does induce computational errors due to its incompleteness to take into account the both derivatives at the four corner points. For instance, at the upper right corner, where $x = x_0$ and $y = y_0$, there associates derivatives with respect to x and y, $\frac{\partial \mu}{\partial x} = 0$ and $\frac{\partial \mu}{\partial y} = 0$. And the approach can only include one of these two derivatives. The schematic is show in figure.

To resolve this issue, we introduce the Alternating Directional Implicit (ADI) method, a special case of the time splitting or fractional step methods. For the sake of simplicity in the explanation, assume that we solve the heat equation:

$$u_t = D\left(\frac{\partial^2 u}{\partial x^2} + \frac{\partial^2 u}{\partial y^2}\right) + f(x,y,t) \tag{8.88}$$

The idea is to use split the original partial differential equation into two equations. Technical in the first equation, we use explicit scheme in one direction and implicit scheme in the other direction to solve for an intermediate solution, denoted by u^* , between the current sub-step u^m and the next sub-step u^{m+1}. In the second equation, we reverse the explicit and implicit schemes to obtain the solution in the next-step u^{m+1}, starting with the intermediate solution u^*. Denote the approximated values of the dependent variable u as $U_{ij}^m \approx u(x_i, y_j, t_m)$. Similarly we denote $F_{ij}^m \approx f(x_i, y_j, t_m)$. These steps are formulated in the numerical schemes for one complete sub-step, from u^m to u^{m+1}:

$$\begin{aligned} U_{ij}^* &= U_{ij}^m + \frac{1}{2}\Delta t \mathbf{D}_{xx} U_{ij}^* + \frac{1}{2}\Delta t \mathbf{D}_{yy} U_{ij}^m + \frac{1}{2}\Delta t F_{ij}^m \\ U_{ij}^{m+1} &= U_{ij}^* + \frac{1}{2}\Delta t \mathbf{D}_{xx} U_{ij}^* + \frac{1}{2}\Delta t \mathbf{D}_{yy} U_{ij}^{m+1} + \frac{1}{2}\Delta t F_{ij}^* \end{aligned} \tag{8.89}$$

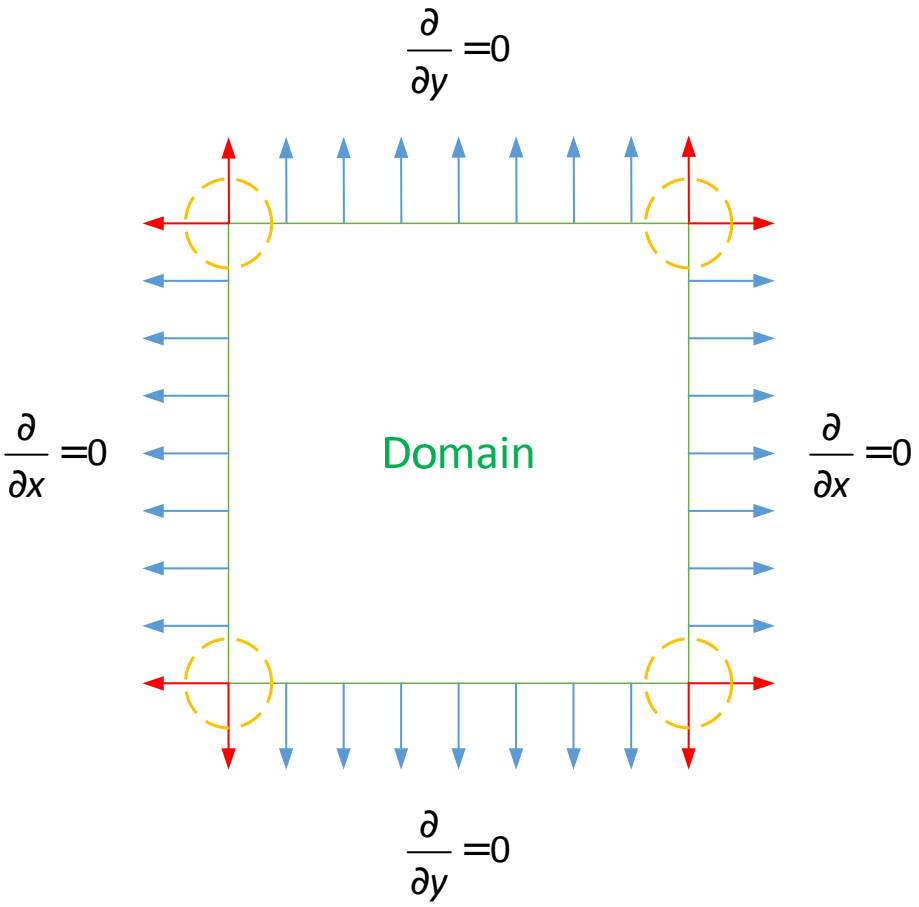

Figure 8.28: Schematic showing how Neumann boundaries are treated in the conventional methods when solving heat equation. Problems occur at the four corners.

This formulation allows us to further corporate spectral method by agreeing the differentiators, $\mathbf{D}_{xx}$ and $\mathbf{D}_{yy}$, to be implemented with the embedded Chebyshev differentiator matrix, $\mathbf{L}_{xx}$ and $\mathbf{L}_{yy}$. With these settings, we may re-construct the ADI schemes into matrix-vector form:

$$\begin{aligned}\left(\mathbf{I}-\frac{1}{2}\Delta t\mathbf{L}_{xx}\right)\mathbf{U}^{*}&=\left(\mathbf{I}+\frac{1}{2}\Delta t\mathbf{L}_{yy}\right)\mathbf{U}^{m}+\frac{1}{2}\Delta t\mathbf{F}^{m}\\ \left(\mathbf{I}-\frac{1}{2}\Delta t\mathbf{L}_{yy}\right)\mathbf{U}^{m+1}&=\left(\mathbf{I}+\frac{1}{2}\Delta t\mathbf{L}_{xx}\right)\mathbf{U}^{*}+\frac{1}{2}\Delta t\mathbf{F}^{*}\end{aligned}\tag{8.90}$$

To deal with the boundary conditions, in the first halve of the ADI, the implicit scheme is taken with respect to x, so that it is treated as a partial differential equation with respect to x only, with y

being fixed, the boundary conditions thus can be taken as Neumann boundary conditions on the left and right boundaries, or,

$$\frac{\partial u^*}{\partial x} = 0 \tag{8.91}$$

In the second halve of the ADI, the implicit scheme is taken with respect to y, so that it is treated as a partial differential equation with respect to y only, with x being fixed, the boundary conditions thus can be taken as Neumann boundary conditions on the top and bottom boundaries, or,

$$\frac{\partial u^{m+1}}{\partial y} = 0 \tag{8.92}$$

The schematic is illustrated in figure (8.29).

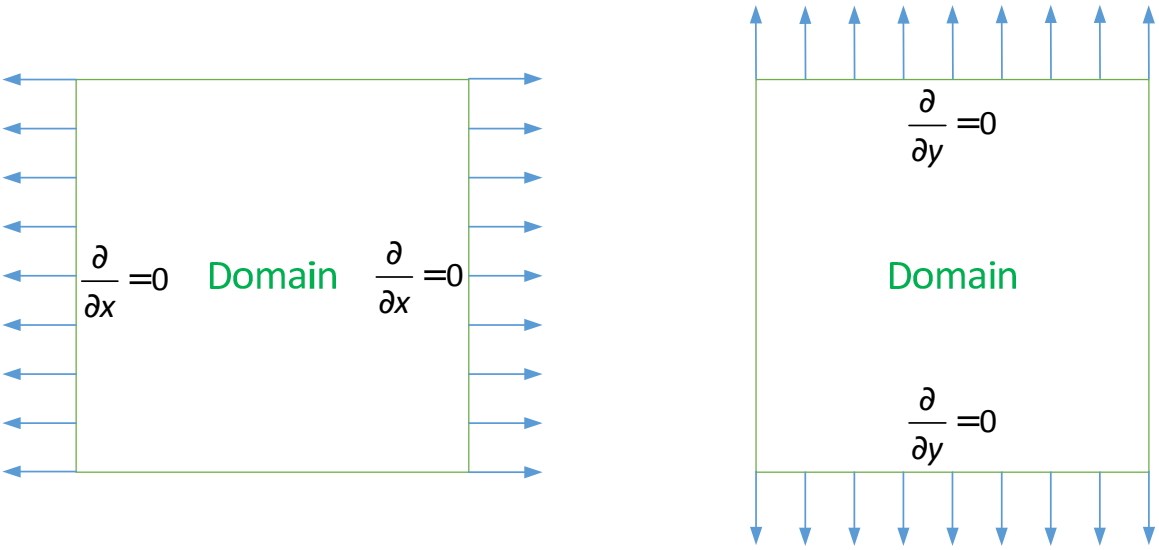

Figure 8.29: Schematic showing how Neumann boundaries are treated during the two stages of the ADI scheme.

As a preliminary study, we make an attempt to simulate the microstructure (domain patterns) in several popular classes of shape memory alloys. We will focus on systems with two martensitic variants, so that one characteristic function suffices to simulate the domain structures. Various physical boundary conditions are considered to generate different domain structures. Since no periodicity

is not involved anymore, we may also consider domain pattern that results from re-orientating the eigen-strains by some angles. This also allows us to keep the original eigen-strains for simulation without previously re-orientating them so as to ensure the interface to be along in certain special angles.

Chapter 9

SUMMARY AND CONCLUSIONS

In summary, we have studied the multi-functional materials such as shape memory alloys, ferro-electric material and piezoelectric materials as well as energy materials such as electrode of lithium ions, in various geometrical configurations which include micro-structures and experimental finite geometry. In the following the main contributions and future works will be outlined.

9.1 Phase Field Simulations in Periodic Geometry

We started from phase field simulation applied to shape memory alloy composing of martensitic variants. One dimensional study shows that the resulting domain patterns do depend on the parameters (anisotropy and interface constants) being chosen in the simulations. The conventional phase field simulation can only model micro-structure below transformation temperature, where there is no autensite phase. We have developed a two-scale methodology that allow us to extend the simulation to include both low-temperature martensites and high-temperature austenite. This helps us to study the formation of the austenite-martensite interface, a special micro-structure found in shape memory alloy, where a twinned martensite (in some special ratio) forms an see-saw shaped interface with austenite, as to minimize the system energy. A further study is focused to explore all possible configurations of micro-structures for any pair of martensitic variants in common crystal systems such as tetragonal, orthorhombic and monoclinic systems. These simulations are adopted to periodic two-dimensional and three-dimensional domains.

There are many cases of configurations and the strict periodic boundary conditions. We are not able to simulate all of them. In this thesis, we mainly concentrate on the methodology and algorithms based on which the simulations are implemented. Future works include to refine the classification of microstructure in other material systems, including ferro-electrics and ferro-magnetics.

9.2 Phase Field Simulation in Thin Film

We also modified the two-scale simulation to study two special micro-structures of shape memory alloys, tunnels and tents. The mechanisms through which these two structures operate are also simulated. They act as a temperature sensor and actuator. We also simulate their thermal hysteresis.

On possible future work will be to simulate these special two-dimensional micro-structures made of other material systems such as ferro-electrics and ferro-magnetics and to explore their possibilities to mechanically behave as electric or magnetic sensor or actuator.

9.3 Phase Field Simulations in Finite Geometry

Requiring periodicity along all directions of the computational domain may restrict the formation of domain pattern. It appears also not a realistic condition. To resolve this issue, we release periodicity along the out-of-plane direction, so that we may study microstates / domain pattern in various material system with a geometric configurations that resemble experimental setups, such as the samples being characterized under piezoelectric-force microscopy (PFM) or electrochemical strain microscopy (ESM).

In these two chapters, we redo Maxwell's equation, elasticity equation and phase field evolution equation without periodicity along the out-of-plane direction. While LQ Chen solved the elasticity by utilizing the Stroh's formulation based on the theory of anisotropic materials. We developed numerical solutions to Maxwell's equation and elasticity equation using two independent approaches. In the first method, the equations are re-structured as a system of state equations which is then solved using eigen-expansion. In the second method, we apply FFT along out-of-plane directions to decompose these equations, which are originally coupled PDE, to systems of coupled ODE, which are then solved numerically using finite difference along the out-of-plane direction. We verify the methods by studying the electro-mechanical response in a piezoelectric material that is being tested in a PFM.

Phase field evolution equation without periodicity along out-of-plane direction is developed to study shape memory alloys and ferroelectric in an experimental setup. We have considered more physical boundary conditions such as applied traction force on top surface, displacement-free boundary, and mis-fit strain imposed by substrate underneath the sample being simulated.

9.4 Lithium Ion Battery and Electrochemical Strain Microscopy

Electrode made of lithium ions is an example of energy materials where ions transported by the effect of external electric potential induces mechanical deformation. This system of ions is conservative since it is is closed system, not allowing ions to pass through the boundaries. We develop numerical solution to solve the model in one dimension and two dimension. We simulated the deformation of the electrode when a SPM tip inducing electrical potential is brought towards the domain. We study the outcomes when different profiles of voltages are applied, such as DC, AC and DC-AC bias. With these simulation results and corresponding experiment data, we are able to predict the diffusivity and local ion concentration of the electrode in the vicinity of the SPM tip.

Future works may consider chemical reactions involving formation and dynamics of lithium ions, and the corresponding probing of the respective electrode behaviours.

9.5 Spectral method

All previous simulations assume periodicity along some directions of the domain, which makes it less practical to model realistic system. Also, these simulations can only work with homogenous material properties. Thus we are motivated to develop spectral method by which we may release all periodicity and include material inhomogeneities. With the spectral method, we may apply any boundary conditions on any boundary. This serves possibly as the universal tool to study simulation of real materials in realistic physical configurations. In this chapter, we discussed spectral method in solving Maxwell's equation, elasticity and phase field equations under general conditions. We also demonstrated how the spectral method can predict the electromechanical responses for materials with alternating internal polarizations as seen in PFM.

The contents in this chapter are preliminary. A lot of works need to be done, especially in the phase field simulations in functional materials.

BIBLIOGRAPHY

[1] Johannes Zimmer. Jog my shape memory: dynamics as a challenge in mathematical materials science. *Philosophical Transactions of the Royal Society A*, 364:3285–3300, 2006.

[2] K. Bhattacharya. *Microstructure of Martensite. Why it Forms and How it Gives Rise to the Shape-Memory Effect.* Oxford University Press, 2003.

[3] K. Bhattacharya and R. D. James. The material is the machine. *Science*, 307:53–54, 2005.

[4] D. C. Lagoudas. *Shape Memory Alloys, Modeling and Engineering Applications*. Springer, New York, 2008.

[5] Christopher T. Nelson, Benjamin Winchester, Yi Zhang, Sung-Joo Kim, Alexander Melville, Carolina Adamo, Chad M. Folkman, Seung-Hyub Baek, Chang-Beom Eom, Darrell G. Schlom, Long-Qing Chen, and Xiaoqing Pan. Spontaneous vortex nanodomain arrays at ferroelectric heterointerfaces. *Nano Letters*, 11:828834, 2011.

[6] S. R. Barman, Aparna Chakrabarti, Sanjay Singh, S. Banik, S. Bhardwaj, P. L. Paulose, B. A. Chalke, A. K. Panda, A. Mitra, and A. M. Awasthi. Theoreticalprediction and experimental study of a ferromagnetic shape memory alloy: Ga2mnni. *Physical Review B*, 78(134406), 2008.

[7] Y. Tani, T. Todaka, and M. Enokizono. Development of an engineering model for ferromagnetic shape memory alloys. *Journal of Magnetism and Magnetic Materials*, 320:e743–e745, 2008.

[8] M.A. Marioni, R.C. OHandley, S.M. Allen, S.R. Hall, D.I. Paul, M.L. Richard, J. Feuchtwanger, B.W. Peterson, J.M. Chambers, and R. Techapiesancharoenkij. The ferromagnetic shape-memory effect in nimnga. *Journal of Magnetism and Magnetic Materials*, 290.

[9] K. Oikawa, L. Wulff, T. Iijima, F. Gejima, T. Ohmori, A. Fujita, K. Fukamichi, R. Kainuma, and K. Ishida. Promising ferromagnetic nicoal shape memory alloy system. *Applied Physics Letters*, 79(3290), 2001.

[10] J. Pons, E. Cesari, C. Segui, F. Masdeu, and R. Santamarta. Ferromagnetic shape memory alloys: Alternatives to nimnga. *Materials Science and Engineering A*, 481.

[11] T. Zhao1, A. Scholl, F. Zavaliche, K. Lee, M. Barry, A. Doran, M. P. Cruz, Y. H. Chu, C. Ederer, N. A. Spaldin, R. R. Das, D. M. Kim, S. H. Baek, C. B. Eom, and R. Ramesh. Electrical

control of antiferromagnetic domains inmultiferroic bifeo3 films at room temperature. *Nature Materials*, 5:823–829, 2006.

[12] Ying-Hao Chu, Lane W. Martin, Mikel B Holcomb, Martin Gajek, Shu-Jen Han, Qing He, Nina Balke, Chan-Ho Yang, Donkoun Lee, Wei Hu, Qian Zhan, Pei-Ling Yang, Arantxa Fraile-Rodriguez, Andreas Scholl, Shan X. Wang, and R. Ramesh. Electric-field control of local ferromagnetism using a magnetoelectric multiferroic. *Nature Materials*, 7:478–482, 2008.

[13] W. Eerenstein, N. D. Mathur, and J. F. Scott. Multiferroic and magnetoelectric materials. *Nature*, 442:759–765, 2006.

[14] Manfred Fiebig. Revival of the magnetoelectric effect. *Journal of Physics D*, 38:R123–R152, 2005.

[15] M. Fiebig, Th. Lottermoser, D. Frhlich, A. V. Goltsev, and R. V. Pisarev. Observation of coupled magnetic and electric domains. *Nature*, 419:818–820, 2002.

[16] Thomas Lottermoser, Thomas Lonkai, Uwe Amann, Dietmar Hohlwein, Jrg Ihringer, and Manfred Fiebig. Magnetic phase control by an electric field. *Nature*, 430:541–544, 2004.

[17] R. Ramesh and Nicola A. Spaldin. Multiferroics: progress and prospects in thin films. *Nature Materials*, 6:21–29, 2007.

[18] J. M. Ball and R. D. James. Fine phase mixtures as minimizers of energy. *Archive for Rational Mechanics and Analysis*, 100(1):13–52, 1987.

[19] Jiangyu Li and Dan Liu. On ferroelectric crystals with engineered domain configurations. *Journal of the Mechanics and Physics of Solids*, 52(8):1719–1742, 2004.

[20] N.T. Tsou and J.E. Huber. Compatible domain structures and the poling of single crystal ferroelectrics. *Mechanics of Materials*, 42(7):740–743, 2010.

[21] N. T. Tsou, P. R. Potnis, and J. E. Huber. Classification of laminate domain patterns in ferroelectrics. *Physical Review B*, 83(184120), 2011.

[22] A. G. Khachaturyan. *Theory of Structural Transformations in Solids*. Wiley, New York, 1983.

[23] R. V. Kohn. The relaxation of a double-well energy. *Continuum Mechanics and Thermodynamics*, 3:193–236, 1991.

[24] J. M. Ball and R. D. James. Proposed experimental tests of a theory of fine microstructure and the two-well problem. *Philosophical Transactions of the Royal Society of London Series A*, 338:389–450, 1992.

[25] A. Braides and A. Defranceschi. *Homogenization of multiple integrals*. Clarendon Press, Oxford, 1998.

[26] P. Ghosez and P. Junquera. *First-principles modeling of ferroelectric oxides nanostructures In: M. Rieth and W. Schommers eds. Handbook Of Theoretical And Computational Nanotechnology,*. American Scientific Publisher USA, 2006.

[27] X. Zhang, J. S. Chen, and S. Osher. A multiple level set method for modeling grain boundary evolution of polycrystalline materials. *Interaction and Multiscale Mechanics*, 1(2):178–191, 2008.

[28] Y. T. Ki, N. Goldenfeld, and J. Dantzig. Computation of dendritic microstructures using a level set method. 62(2), 2000.

[29] Thomas Y Hou, Phoebus Rosakis, and Philippe LeFloch. A level-set approach to the computation of twinning and phase-transition dynamics. *Journal of Computational Physics*, 150(2):302–331, 1999.

[30] Long-Qing. Phase-field models for microstructure evolution. *Annual Review of Materials Research*, 32:113–140, 2002.

[31] Y. C. Shu and J. H. Yen. Pattern formation in martensitic thin films. *Applied Physics Letters*, 91(021908), 2007.

[32] Multivariant model of martensitic microstructure in thin films. *Acta Materialia*, 56:3969–3981, 2008.

[33] C. H. Lei, L. J. Li, Y. C. Shu, and J. Y. Li. Austenite-martensite interface in shape memory alloys. *Applied Physics Letters*, 96(141910), 2010.

[34] Y. C. Shu, J. H. Yen, H. Z. Chen, J. Y. Li, and L. J. Li. Constrained modeling of domain patterns in rhombohedral ferroelectrics. *Applied Physics Letters*, 92(052909), 2009.

[35] L. J. Li, J. Y. Li, Y. C. Shu, H. Z. Chen, and J. H. Yen. Magnetoelastic domains and magnetic field-induced strains in ferromagnetic shape memory alloys by phase-field simulation. *Applied Physics Letters*, 92(172504), 2008.

[36] Y.C. Shu J.Y. Li L.J. Li, C.H. Lei. Phase-field simulation of magnetoelastic couplings in ferromagnetic shape memory alloys. *Acta Materialia*, 59:26482655, 2011.

[37] Y. M. Jin. Domain microstructure evolution in magnetic shape memory alloys: Phase-field model and simulation. *Acta Materialia*, 57:2488–2495, 2009.

[38] L. J. Li, J. Y. Li, Y. C. Shu, and J. H. Yen. The magnetoelectric domains and cross-field switching in multiferroic bifeo3. *Applied Physics Letters*, 93(192506), 2008.

[39] L.J. Li, Y. Yang, Y.C. Shu, and J.Y. Li. Continuum theory and phase-field simulation of magnet oelectric effects in multiferroic bismuth ferrite. *Journal of the Mechanics and Physics of Solids*, 58:16131627, 2010.

[40] Rama K. Vasudevan, Yunya Liu, Jiangyu Li, Wen-I. Liang, Amit Kumar, Stephen Jesse, Yi-Chun Chen, Ying-Hao Chu, Valanoor Nagarajan, and Sergei V. Kalinin. Nanoscale control of phase variants in strain-engineered bifeo3. *Nano Letters*, 11:33463354, 2011.

[41] Y. Y. Liu, R. K. Vasudevan, K. Pan, S. H. Xie, W.-I. Liang, A. Kumar, S. Jesse, Y.-C. Chen, Y.-H. Chu, V. Nagarajan, S. V. Kalinin, and J. Y. Li. Controlling magnetoelectric coupling by nanoscale phase transformation in strain engineered bismuth ferrite. *Nanoscale*, 4:3175–3183, 2012.

[42] D.A. Bonnell, S.V. Kalinin, A.L. Kholkin, and A. Gruverman. Piezoresponse force microscopy: A window into electromechanical behavior at the nanoscale. *MRS Bulletin*, 34(9):648–657, 2009.

[43] S. V. Kalinin and A. Gruverman. *Scanning Probe Microscopy: Electrical and Electromechanical Phenomena at the Nanoscale.* Springer, New York, 2007.

[44] Yuanming Liu, Yanhang Zhang, Ming-Jay Chow, Qian Nataly Chen, and Jiangyu Li. Biological ferroelectricity uncovered in aortic walls by piezoresponse force microscopy. *Physics Review Letters*, 108(078103), 2012.

[45] A. Gruverman and S. V. Kalinin. Piezoresponse force microscopy and recent advances in nanoscale studies of ferroelectrics. *Journal of Materials Science*, 41(1):107–116, 2006.

[46] S. V. Kalinin, A. Gruverman, B. J. Rodriguez, J. Shin, A. P. Baddorf, E. Karapetian, and M. Kachanov. Nanoelectromechanics of polarization switching in piezoresponse force microscopy. *Journal of Applied Physics*, 97(074305), 2005.

[47] A. Gruverman, O. Auciello, and H. Tokumoto. Nanoscale investigation of fatigue effects in pb(zr,ti)o3 films. *Applied Physics Letters*, 69(3191), 1996.

[48] I. K. Bdikin, A. L. Kholkin, A. N. Morozovska, S. V. Svechnikov, S. H. Kim, and S. V. Kalinin. Domain dynamics in piezoresponse force spectroscopy: Quantitative deconvolution and hysteresis loop fine structure. *Applied Physics Letters*, 92(182909), 2008.

[49] L. Q. Chen, Y. Z. Wang, and A. G. Khachaturyan. Transformation-induced elastic strain effect on the precipitation kinetics of ordered intermetallics. *Philosophical Magazine Letters*, 64(5):241–251, 1991.

[50] K. Bhattacharya. Comparison of the geometrically nonlinear and linear theories of martensitic transformation. *Cont. Mech. Thermodyn.*, 5:205–242, 1993.

[51] L. Q. Chen and J. Shen. Applications of semi-implicit fourier-spectral method to phase field equations. *Computer Physics Communications*, 108(2).

[52] R. Abeyaratne, C. Chu, and R.D. James. Kinetics of materials with wiggly energies: theory and application to the evolution of twinning microstructures in a cu-al-ni shape memory alloy. *Phil. Mag.*, (2).

[53] C. Chu and R.D. James. Analysis of microstructures in cu-14.0 % al-3.9 % ni by energy minimization. *J. de Physique III (Colloque C8)*, 5:143–149, 1995.

[54] Z. Zhang, R. D. James, and S. Mueller. Energy barriers and hysteresis in martensitic phase transformations. *Acta Mater.*, 57:4332, 2009.

[55] Yintao Song, Xian Chen, Vivekanand Dabade, T.W. Shield, and R.D. James. Enhanced reversibility and unusual microstructure of a phase-transforming material. *Nature*, 502:85–88, 2013.

[56] Jiang-Yu Li, Chi-Hou Lei, Liang-Jun Li, Yi-Chung Shu, and Yun-Ya Liu. Unconventional phase field simulations of transforming materials with evolving microstructures. *Acta Mechanica Sinica*, 28(4).

[57] Xian Chen, Vijay Srivastava, Vivekanand Dabade, and R.D. James. Study of the cofactor conditions: Conditions of supercompatibility between phases. *J. Mech. Phys. Solids*, 61(12):2566–2587, 2013.

[58] K. Bhattacharya and R. D. James. A theory of thin films of martensitic materials with applications to microactuators. *J. Mech. Phys. Solids*, 47:531–576, 1999.

[59] K. Bhattacharya, A. Desimone, K. Hane, R.D. James, and C.P. Palmstrom. Tents and tunnels on martensitic films. *Mat. Sci. Engng. A*, 273:685–689, 2007.

[60] K.F. Hane and T.W. Shield. Microstructure in a copper-aluminium-nickel shape-memory alloy. *Royal Society of London Proceedings: Mathematical, Physical and Engineering Sciences*, 455(1991):3901–3915, 1999.

[61] K.F. Hane and T.W. Shield. Microstructure in a cubic to orthorhombic transition. *Journal of Elasticity*, 59:267–318, 2000.

[62] K.F. Hane and T.W. Shield. Symmetry and microstructure in martensites. *Philosophical Magazine A*, 78(6):1215–1252, 1998.

[63] K. Bhattacharya. Comparison of the geometrically nonlinear and linear theories of martensitic transformation. *Cont. Mech. Thermodyn.*, 5:203, 1993.

[64] L. J. Li, J. Y. Li, Y. C. Shu, and J. H. Yen. The magnetoelectric domains and cross-field switching in multiferroic $bifeo_3$. *Appl. Phys. Lett.*, 93(192506), 2008.

[65] Y. C. Shu and J. H. Yen. Pattern formation in martensitic thin films. *Appl. Phys. Lett.*, 91(021908).

[66] Y. C. Shu and J. H. Yen. Multivariant model of martensitic microstructure in thin films. *Acta Mater.*, 63:3969, 2008.

[67] L. Yang and K. Dayal. Formulation of phase-field energies for microstructure in complex crystal structures. *Appl. Phys. Lett.*, 96(081916).

[68] L. J. Li, J. Y. Li, Y. C. Shu, H. Z. Chen, and J. H. Yen. Magnetoelastic domains and magnetic field-induced strains in ferromagnetic shape memory alloys by phase-field simulation. *Appl. Phys. Lett.*, 92(172504), 2008.

[69] Y. C. Shu, J. H. Yen, H. Z. Chen, J. Y. Li, and L. J. Li. Constrained modeling of domain patterns in rhombohedral ferroelectrics. *Appl. Phys. Lett.*, 92(052909), 2008.

[70] D. Kopriva. *Implementing Spectral Methods for Partial Differential Equations.* Springer-Verlag, 2009.

[71] L. Q. Chen. Phase-field models for microstructure evolution. *Ann. Rev. Mater.*, 32:113, 2002.

[72] Y.H. Wen, L.Q. Chen, P.M. Hazzledine, and Y. Wang. A three-dimensional phase-field model for computer simulation of lamellar structure formation in gamma tial intermetallic alloys. *Acta Mater.*, 49:2341, 2001.

[73] Y. C. Shu. Theory of sma thin films for microactuators and micropumps (chpater 11). In S. Miyazaki, Y. Q. Fu, and W. M. Huang, editors, *Thin Film Shape Memory Alloys: Fundamental and Device Applications*. Cambridge University Press, 2009.

[74] Y. C. Shu. Shape-memory micropumps. *Materials Transactions*, 43:1037–1044, 2002.

[75] J. Cui, Y. S. Chu, O. O. Famodo, Y. Furuya, J. Hattrick-Simpers, R. D. James amd A. Ludwig, S. Thienhaus, M. Wuttig, Z. Zhang, and I. Takeuchi. Combinatorial search of thermoelastic shape-memory alloys with extremely small hysteresis width. *Nat. Mater.*, 5:286, 2006.

[76] Y.L. Li, S.Y. Hu, Z.K. Liu, and L.Q. Chen. Effect of substrate constraint on the stability and evolution of ferroelectric domain structures in thin films. *Acta Materialia*, 50(2):395–411, 2001.

[77] A. N. Stroh. Dislocations and cracks in anisotropic elasticity. *Philosophical Magazine*, 3:625–646, 1958.

[78] Thomas C. T. Ting. *Anisotropic Elasticity: Theory and Applications (Oxford Engineering Science Series)*. Oxford University Press, 1996.

[79] T.C.T. Ting. Recent developments in anisotropic elasticity. *International Journal of Solids and Structures*, 37:401–409, 2000.

[80] Werner Knzig. *Ferroelectrics and Antiferroelectrics*. Academic Press, 1957.

[81] M. Lines and A. Glass. *Principles and applications of ferroelectrics and related materials*. Clarendon Press, Oxford, 1979.

[82] Karin M. Rabe, Charles H. Ahn, and Jean-Marc Triscone. *Physics of Ferroelectrics, A Modern Perspective*. Springer, 2007.

[83] A. K. Padhi, K. Nanjundaswamy, and J. B. Goodenough. Phospho-olivines as positive-electrode materials for rechargeable lithium batteries. *Journal of the Electrochemical Society*, 144(4):1188–1194, 97.

[84] K. Mizushima, P.C. Jones, P.J. Wiseman, and J.B. Goodenough. Lixcoo2 (0¡x¡-1): A new cathode material for batteries of high energy density. *Materials Research Bulletin*, 15(6):783–789, 1980.

[85] J. Graetz, C. C. Ahn, R. Yazami, and B. Fultz. Highly reversible lithium storage in nanostructured silicon. *Electrochem. Solid-State Lett.*, 6(9):A194–A197, 2003.

[86] Rachid Yazami. Surface chemistry and lithium storage capability of the graphitelithium electrode. *Electrochimica Acta*, 45(1):87–97, 1999.

[87] Rachid Yazami and Yvan F Reynier. Mechanism of self-discharge in graphitelithium anode. *Electrochimica Acta*, 47(8):1217–1223, 2002.

[88] M. Holzapfel, A. Martinent, F. Alloin, B. Le Gorrec, R. Yazami, and C. Montella. First lithiation and charge/discharge cycles of graphite materials, investigated by electrochemical impedance spectroscopy. *Journal of Electroanalytical Chemistry*, 546:41–50, 2003.

[89] R. Edwin Garca, Yet-Ming Chiang, W. Craig Carter, Pimpa Limthongkul, and Catherine M. Bishop. Microstructural modeling and design of rechargeable lithium-ion batteries. *J. Electrochem. Soc.*, 152(1):A255–A263, 2005.

[90] Qian Nataly Chen, Yanyi Liu, Yuanming Liu, Shuhong Xie, Guozhong Cao, and Jiangyu Li. Delineating local electromigration for nanoscale probing of lithium ion intercalation and extraction by electrochemical strain microscopy. *Applied Physics Letters*, 101(063901), 2012.

[91] J. W. Perram and P. J. Stiles. On the nature of liquid junction and membrane potentials. *Physical Chemistry Chemical Physics*, 8(36):42004213, 2006.

[92] J.J. Jasielec, R. Filipek, K. Szyszkiewicz, J. Fausek, M. Danielewski, and A. Lewenstama. Computer simulations of electrodiffusion problems based on nernstplanck and poisson equations. *Computational Materials Science*, 63:75–90, 2012.

[93] William E. Schiesser and Graham W. Griffiths. *A Compendium of Partial Differential Equation Models - Method of Lines Analysis with Matlab*. Cambridge, 2009.

[94] Lloyd N. Trefethen. *Spectral Methods in MATLAB*. SIAM, Philadelphia, 2000.

[95] Lloyd N. Trefethen. *Approximation Theory and Approximation Practice*. SIAM, Philadelphia, 2013.

[96] T. A. Driscoll, N. Hale, and L. N. Trefethen. *Chebfun Guide*. Pafnuty Publications, Oxford, 2014.

[97] Weidong Guo, Grard Labrosse, and Ranga Narayanann. *The Application of the Chebyshev-Spectral Method in Transport Phenomena*. Springer, 2012.

[98] K. Pan, Y. M. Liu, Y. Y. Liu, and J. Y. Li. Analyzing piezoresponse force microscopy for reconstruction of probed ferroelectric structures. *Journal of Applied Physics*, 112(052016).

[99] K. Pan, Y. M. Liu, Y. Y. Liu, and J. Y. Li. Resolving ferroelectric nanostructures via piezoresponse force microscopy - a numerical investigation. *Journal of Applied Physics*, 113(187223).

Appendix A

THEORETICAL DEVELOPMENT IN ONE-DIMENSION

The evolution equation for the volume fraction derived from the previous chapter is highly non-linear and can not be solved analytically. Simulations seem to be the only approach to explore the pattern formation and various related problems, for example, hysteresis. However, in one-dimension, we may carry out several theoretical analyses of the evolution equation to certain extent.

A.1 Microstructure under the effect of External Strain - One dimensional study

In this section, we analyze the modal for the evolution of the microstructure under the effect of external strain in one-dimension. Whether the reasonable simulated patterns can be found depends critically on the anisotropy constant $K = \lambda \varepsilon^{(1)} \cdot \varepsilon^{(1)} = \lambda \varepsilon^{(2)} \cdot \varepsilon^{(2)}$. We investigate how this constant affects the pattern. It is found that if K is too small, no twining of Martensitic variants can be seen. On the other hand, if K is too large, twinning structure can be seen. However the twining patterns appear to repeat too many times that they do not reflect the reality.

Motivated by the two-dimensional simulation shown in Fig.(2.4), we may examine the diagram at a 45^o-view, which resembles an one-dimensional problem. For this, we rotate the transformation strains of the participating Martensitic variants as below:

$$\begin{aligned}
\varepsilon^{(1)} = \begin{pmatrix} \varepsilon_{11}^{(1)} \\ \varepsilon_{22}^{(1)} \\ \varepsilon_{12}^{(1)} \end{pmatrix} = \begin{pmatrix} \delta \\ -\delta \\ 0 \end{pmatrix} \longrightarrow \varepsilon^{(1)\prime} = \begin{pmatrix} \varepsilon_{11}^{(1)} \\ \varepsilon_{22}^{(1)} \\ \varepsilon_{12}^{(1)} \end{pmatrix} = \begin{pmatrix} 0 \\ 0 \\ -2\delta \end{pmatrix} \\
\varepsilon^{(2)} = \begin{pmatrix} \varepsilon_{11}^{(2)} \\ \varepsilon_{22}^{(2)} \\ \varepsilon_{12}^{(2)} \end{pmatrix} = \begin{pmatrix} -\delta \\ \delta \\ 0 \end{pmatrix} \longrightarrow \varepsilon^{(2)\prime} = \begin{pmatrix} \varepsilon_{11}^{(2)} \\ \varepsilon_{22}^{(2)} \\ \varepsilon_{12}^{(2)} \end{pmatrix} = \begin{pmatrix} 0 \\ 0 \\ 2\delta \end{pmatrix}
\end{aligned} \tag{A.1}$$

Without loss of generality, from now on, we may simply drop the prime for the transformation strains.

Now in the new reference frame (by rotation of 45^o anticlockwise),

$$\begin{aligned}\varepsilon^*(\mu) &= \mu(\mathbf{x})\varepsilon^{(1)} + (1-\mu(\mathbf{x}))\varepsilon^{(2)} \\ \frac{\partial \varepsilon^*(\mu)}{\partial \mu} &= \varepsilon^{(1)} - \varepsilon^{(2)} = \begin{pmatrix} 0 \\ 0 \\ -4\delta \end{pmatrix}\end{aligned} \tag{A.2}$$

Recall that the external strain is a linear combination of transformation strains of the participating Martensitic variants in the ratio γ:

$$\varepsilon^0 = \gamma\varepsilon^{(1)} + (1-\gamma)\varepsilon^{(2)} \tag{A.3}$$

The stiffness matrix is given as:

$$\mathbf{C} = \begin{pmatrix} C_{11} & C_{12} & C_{16} \\ C_{21} & C_{22} & C_{26} \\ C_{61} & C_{61} & C_{66} \end{pmatrix} \tag{A.4}$$

We also need the constitutive equation or the stress-strain relationship: $\sigma = \mathbf{C}\left(\varepsilon - \varepsilon^0\right)$. In components,

$$\begin{aligned}\sigma_{11}(\mathbf{x}) &= C_{11}\left[\varepsilon_{11}(\mathbf{x}) - \varepsilon^*_{11}(\mathbf{x})\right] + C_{12}\left[\varepsilon_{22}(\mathbf{x}) - \varepsilon^*_{22}(\mathbf{x})\right] + C_{16}\left[\varepsilon_{12}(\mathbf{x}) - \varepsilon^*_{12}(\mathbf{x})\right] \\ \sigma_{22}(\mathbf{x}) &= C_{21}\left[\varepsilon_{11}(\mathbf{x}) - \varepsilon^*_{11}(\mathbf{x})\right] + C_{22}\left[\varepsilon_{22}(\mathbf{x}) - \varepsilon^*_{22}(\mathbf{x})\right] + C_{26}\left[\varepsilon_{12}(\mathbf{x}) - \varepsilon^*_{12}(\mathbf{x})\right] \\ \sigma_{12}(\mathbf{x}) &= C_{61}\left[\varepsilon_{11}(\mathbf{x}) - \varepsilon^*_{11}(\mathbf{x})\right] + C_{62}\left[\varepsilon_{22}(\mathbf{x}) - \varepsilon^*_{22}(\mathbf{x})\right] + C_{66}\left[\varepsilon_{12}(\mathbf{x}) - \varepsilon^*_{12}(\mathbf{x})\right],\end{aligned}$$

where σ_{12} is the shear stress, ε_{12} is the shear strain and ε^*_{12} is the shear component of the eigen-strain.

We are going to solve the mechanical equilibrium equations (A.5): $\frac{\partial \sigma_{ij}}{\partial x_j} = 0$ for the stress components. Since we are restricting on one dimension, we assume all physical quantities depend on x_1 only.

$$\begin{aligned}
&\frac{\partial \sigma_{11}}{\partial x_1} + \underbrace{\frac{\partial \sigma_{12}}{\partial x_2}}_{0} + \underbrace{\frac{\partial \sigma_{13}}{\partial x_3}}_{0} = 0 \longrightarrow \sigma_{11}(x_1) = constant \\
&\frac{\partial \sigma_{21}}{\partial x_1} + \underbrace{\frac{\partial \sigma_{22}}{\partial x_2}}_{0} + \underbrace{\frac{\partial \sigma_{23}}{\partial x_3}}_{0} = 0 \longrightarrow \sigma_{21}(x_1) = constant \\
&\frac{\partial \sigma_{31}}{\partial x_1} + \underbrace{\frac{\partial \sigma_{32}}{\partial x_2}}_{0} + \underbrace{\frac{\partial \sigma_{33}}{\partial x_3}}_{0} = 0 \longrightarrow \sigma_{31}(x_1) = constant
\end{aligned} \tag{A.5}$$

Taking the average over $x_1 \in [0, L]$ of the first constitutive equation (A.5),

$$\begin{aligned}
\sigma_{11} &= \langle \sigma_{11} \rangle = constant \\
&= C_{11} \left[\langle \varepsilon_{11}(\mathbf{x}) \rangle - \langle \varepsilon^*_{11}(\mathbf{x}) \rangle \right] + C_{12} \left[\langle \varepsilon_{22}(\mathbf{x}) \rangle - \langle \varepsilon^*_{22}(\mathbf{x}) \rangle \right] + C_{16} \left[\langle \varepsilon_{12}(\mathbf{x}) \rangle - \langle \varepsilon^*_{12}(\mathbf{x}) \rangle \right] \\
&= C_{11} \left[\gamma \varepsilon^{(1)}_{11} + (1-\gamma) \varepsilon^{(2)}_{11} - (\langle \mu \rangle \varepsilon^{(1)}_{11} + (1 - \langle \mu \rangle) \varepsilon^{(2)}_{11}) \right] \\
&+ C_{12} \left[\gamma \varepsilon^{(1)}_{22} + (1-\gamma) \varepsilon^{(2)}_{22} - (\langle \mu \rangle \varepsilon^{(1)}_{22} + (1 - \langle \mu \rangle) \varepsilon^{(2)}_{22}) \right] \\
&+ C_{16} \left[\gamma \varepsilon^{(1)}_{12} + (1-\gamma) \varepsilon^{(2)}_{12} - (\langle \mu \rangle \varepsilon^{(1)}_{12} + (1 - \langle \mu \rangle) \varepsilon^{(2)}_{12}) \right] \\
&= (\gamma - \langle \mu \rangle) C_{11} \underbrace{\left(\varepsilon^{(1)}_{11} - \varepsilon^{(2)}_{11} \right)}_{=0} + (\gamma - \langle \mu \rangle) C_{12} \underbrace{\left(\varepsilon^{(1)}_{22} - \varepsilon^{(2)}_{22} \right)}_{=0} + (\gamma - \langle \mu \rangle) C_{16} \left(\varepsilon^{(1)}_{12} - \varepsilon^{(2)}_{12} \right) \\
&= (\gamma - \langle \mu \rangle) C_{16} \cdot -4\delta \\
&= 4 C_{16} \delta \left(\langle \mu \rangle - \gamma \right) \\
&= 4 \cdot 0 \cdot \delta \left(\langle \mu \rangle - \gamma \right) \\
&= 0
\end{aligned}$$

Next we take the average of the second constitutive equation (A.5),

$$
\begin{aligned}
\sigma_{21} &= \langle \sigma_{21} \rangle = constant \\
&= C_{61}\left[\langle \varepsilon_{11}(\mathbf{x})\rangle - \langle \varepsilon^*_{11}(\mathbf{x})\rangle\right] + C_{62}\left[\langle \varepsilon_{22}(\mathbf{x})\rangle - \langle \varepsilon^*_{22}(\mathbf{x})\rangle\right] + C_{66}\left[\langle \varepsilon_{12}(\mathbf{x})\rangle - \langle \varepsilon^*_{12}(\mathbf{x})\rangle\right] \\
&= C_{61}\left[\gamma\varepsilon^{(1)}_{11} + (1-\gamma)\varepsilon^{(2)}_{11} - \left(\langle\mu\rangle\,\varepsilon^{(1)}_{11} + (1-\langle\mu\rangle)\varepsilon^{(2)}_{11}\right)\right] \\
&+ C_{62}\left[\gamma\varepsilon^{(1)}_{22} + (1-\gamma)\varepsilon^{(2)}_{22} - \left(\langle\mu\rangle\,\varepsilon^{(1)}_{22} + (1-\langle\mu\rangle)\varepsilon^{(2)}_{22}\right)\right] \\
&+ C_{66}\left[\gamma\varepsilon^{(1)}_{12} + (1-\gamma)\varepsilon^{(2)}_{12} - \left(\langle\mu\rangle\,\varepsilon^{(1)}_{12} + (1-\langle\mu\rangle)\varepsilon^{(2)}_{12}\right)\right] \\
&= (\gamma - \langle\mu\rangle) C_{61} \underbrace{\left(\varepsilon^{(1)}_{11} - \varepsilon^{(2)}_{12}\right)}_{=0} + (\gamma - \langle\mu\rangle) C_{62} \underbrace{\left(\varepsilon^{(1)}_{22} - \varepsilon^{(2)}_{22}\right)}_{=0} + (\gamma - \langle\mu\rangle) C_{66}\left(\varepsilon^{(1)}_{12} - \varepsilon^{(2)}_{12}\right) \\
&= (\gamma - \langle\mu\rangle) C_{66} \cdot -4\delta \\
&= 4C_{66}\delta(\langle\mu\rangle - \gamma)
\end{aligned}
\tag{A.6}
$$

How about σ_{22} ? σ_{22} is not necessarily a constant. We need to go the other way around by taking into consideration the (geometric) compatibility condition that $\varepsilon_2(\mathbf{x}) = \varepsilon_2(x_1) = 0$:

$$
\begin{aligned}
\varepsilon_{22}(x_1) \equiv 0 = \langle \varepsilon_{22}(x_1)\rangle &= \underbrace{\varepsilon^0_{22}}_{\substack{\text{preassigned} \\ \text{external strain}}} = 0 \\
\sigma_{22}(x_1) &= C_{21}\underbrace{\left[\varepsilon_{11}(x_1) - \varepsilon^*_{11}(x_1)\right]}_{0} + C_{22}\underbrace{\left[\varepsilon_{22}(x_1) - \varepsilon^*_{22}(x_1)\right]}_{0} + \underbrace{C_{26}}_{0}\left[\varepsilon_{12}(x_1) - \varepsilon^*_{12}(x_1)\right] \\
&= 0
\end{aligned}
$$

As a remark, we may extend the above deviation to compute the compatible strain, namely, ε_{ij}. But since this result is not useful in our problem, we will leave them in appendix.

Before we form the governing equation, we study the individual energies and the associated driving forces:

Anisotropy Energy and and its driving Force

$$
\begin{aligned}
W^{ani}(\mu) &= K\mu^2(1-\mu)^2 \\
F^{ani}(\mu) &= -\frac{\partial W^{ani}}{\partial \mu} = -2K(\mu - 3\mu^2 + 2\mu^3)
\end{aligned}
\tag{A.7}
$$

Elastic Energy and and its driving Force

$$
\begin{aligned}
W^{elas}(\mu) &= \frac{1}{2}(\varepsilon - \varepsilon^*)\cdot\mathbf{C}(\varepsilon - \varepsilon^*) \\
F^{elas}(\mu) &= \frac{\partial W^{elas}}{\partial \mu} = \sigma \cdot \frac{\partial \varepsilon^*}{\partial \mu} \\
&= \begin{pmatrix} 0 \\ 0 \\ 4C_{66}\delta(\langle\mu\rangle - \gamma) \end{pmatrix} \cdot \begin{pmatrix} 0 \\ 0 \\ -4\delta \end{pmatrix} \\
&= -16C_{66}\delta^2(\langle\mu\rangle - \gamma)
\end{aligned} \tag{A.8}
$$

Interfacial Energy and and its driving Force

$$
\begin{aligned}
W^{int}(\mu) &= A|\nabla\mu|^2 \\
F^{ani}(\mu) &= -\frac{\partial W^{int}}{\partial \mu} = 2A\nabla^2\mu
\end{aligned} \tag{A.9}
$$

The evolution equation for the evolution of microstructure is given as:

$$
\frac{d\mu}{dt} = M\left(F^{int} + F^{ani} + F^{elas}\right) \tag{A.10}
$$

$$
= M\left(2A\nabla^2\mu - 2K(\mu - 3\mu^2 + 2\mu^3) - 16C_{66}\delta^2(\langle\mu\rangle - \gamma)\right)
$$

$$
= M\left(2A\frac{d^2\mu}{dx^2} - 2K(\mu - 3\mu^2 + 2\mu^3) - 16C_{66}\delta^2(\langle\mu\rangle - \gamma)\right) \tag{A.11}
$$

In the following subsections, we will devote to the **steady state solution** and the **time evolution solution** respectively.

A.1.1 Steady State Solution

Steady state is achieved when $\frac{d\mu}{dt} = 0$. The governing equation is simplified as follow:

$$
\begin{aligned}
\underbrace{\frac{d\mu}{dt}}_{=0} &= M\left(2A\frac{d^2\mu}{dx^2} - 2K(\mu - 3\mu^2 + 2\mu^3) - 16C_{66}\delta^2\left(\langle\mu\rangle - \gamma\right)\right) \\
2A\frac{d^2\mu}{dx^2} &= 2K\left(\mu - 3\mu^2 + 2\mu^3\right) + 16C_{66}\delta^2\left(\langle\mu\rangle - \gamma\right) \\
\frac{d^2\mu}{dx^2} &= \frac{K}{A}\left(\mu - 3\mu^2 + 2\mu^3\right) + 8\frac{C_{66}}{A}\delta^2\left(\langle\mu\rangle - \gamma\right) \\
\frac{d^2\mu}{dx^2} &= \alpha\left(\mu - 3\mu^2 + 2\mu^3\right) + 8\beta\left(\langle\mu\rangle - \gamma\right), \qquad \text{(A.12)}
\end{aligned}
$$

where two parameters are defined for easier book-keeping:

$$
\begin{aligned}
\alpha &\equiv \frac{K}{A} \\
\beta &\equiv \frac{C_{66}}{A}\delta^2
\end{aligned}
$$

This second order nonlinear ODE has no exact solution. We may solve it by numerical method. Notice that we impose periodic boundary conditions to μ at both ends.

Numerical Method - Finite Difference Scheme

Let the values of μ on the x-axis at iteration level 't' be $\mu_n^k = \mu(x_n, t_k)$. The above equation is

discredited as follow:

$$
\begin{aligned}
\frac{d^2\mu^k}{dx^2} &= \alpha\left(\mu^k - 3(\mu^k)^2 + 2(\mu^k)^3\right) + 8\beta\left(\left\langle \mu^k \right\rangle - \gamma\right) \\
\frac{\mu^k_{n+1} - 2\mu^k_n + \mu^k_{n-1}}{(\Delta x)^2} &= \alpha\left(\mu^k_n - 3(\mu^k_n)^2 + 2(\mu^k_n)^3\right) + 8\beta\left(\left\langle \mu^k \right\rangle - \gamma\right) \\
\frac{\mu^k_{n+1} - 2\mu^{k+1}_n + \mu^k_{n-1}}{(\Delta x)^2} &= \alpha\left(\mu^{k+1}_n - 3(\mu^k_n)^2 + 2(\mu^k_n)^3\right) + 8\beta\left(\left\langle \mu^k \right\rangle - \gamma\right) \\
\left(\frac{2}{(\Delta x)^2} + \alpha\right)\mu^{k+1}_n &= \frac{\mu^k_{n+1} + \mu^k_{n-1}}{(\Delta x)^2} + \alpha\left(3(\mu^k_n)^2 - 2(\mu^k_n)^3\right) - 8\beta\left(\left\langle \mu^k \right\rangle - \gamma\right) \\
\mu^{k+1}_n &= \frac{\frac{\mu^k_{n+1} + \mu^k_{n-1}}{(\Delta x)^2} + \alpha\left(3(\mu^k_n)^2 - 2(\mu^k_n)^3\right) - 8\beta\left(\left\langle \mu^k \right\rangle - \gamma\right)}{\frac{2}{(\Delta x)^2} + \alpha} \\
\mu^{k+1}_n &= \frac{\frac{1}{\alpha}\frac{\mu^k_{n+1} + \mu^k_{n-1}}{(\Delta x)^2} + \left(3(\mu^k_n)^2 - 2(\mu^k_n)^3\right) - 8\frac{\beta}{\alpha}\left(\left\langle \mu^k \right\rangle - \gamma\right)}{\frac{2}{\alpha(\Delta x)^2} + 1}
\end{aligned}
\tag{A.13}
$$

Solving the steady state equation with this numerical scheme is not interesting, since we can not predict the intermediate microstructure. We turn our attention to the corresponding evolution equation.

A.1.2 Time Evolution Problem

Recall the governing equation is given by:

$$
\frac{d\mu}{dt} = M\left(2A\frac{d^2\mu}{dx^2} - 2K(\mu - 3\mu^2 + 2\mu^3) - 16C_{66}\delta^2(\langle\mu\rangle - \gamma)\right)
$$

We may want to get rid of the ill-defined parameter M by a change of variable in time t.

$$
\tilde{t} = 2MKt
$$

The equation can now be rewritten with no explicit M:

$$
\begin{aligned}
2MK\frac{d\mu}{d\tilde{t}} &= M\left(2A\frac{d^2\mu}{dx^2} - 2K\left(\mu - 3\mu^2 + 2\mu^3\right) - 16C_{44}\delta^2\left(\langle\mu\rangle - \gamma\right)\right) \\
\frac{d\mu}{d\tilde{t}} &= \frac{A}{K}\frac{d^2\mu}{dx^2} - \left(\mu - 3\mu^2 + 2\mu^3\right) - 8\frac{C_{44}\delta^2}{K}\left(\langle\mu\rangle - \gamma\right) \\
\frac{d\mu}{d\tilde{t}} &= \frac{1}{\alpha}\frac{d^2\mu}{dx^2} - \left(\mu - 3\mu^2 + 2\mu^3\right) - 8\frac{\beta}{\alpha}\left(\langle\mu\rangle - \gamma\right) \qquad \text{(A.14)}
\end{aligned}
$$

Numerical Method - Finite Difference Scheme

Again let the values of μ on the x-axis at iteration level $'t'$ be $\mu_n^k = \mu(x_n, t_k)$. The above equation is discretized as:

$$
\begin{aligned}
\frac{\mu_n^{k+1} - \mu_n^k}{\Delta t} &= \frac{1}{\alpha}\frac{\mu_{n+1}^k - 2\mu_n^k + \mu_{n-1}^k}{(\Delta x)^2} - \left(\mu_n^k - 3(\mu_n^k)^2 + 2(\mu_n^k)^3\right) - 8\frac{\beta}{\alpha}\left(\langle\mu\rangle - \gamma\right) \\
\frac{\mu_n^{k+1} - \mu_n^k}{\Delta t} &= \frac{1}{\alpha}\frac{\mu_{n+1}^k - 2\mu_n^{k+1} + \mu_{n-1}^k}{(\Delta x)^2} - \left(\mu_n^{k+1} - 3(\mu_n^k)^2 + 2(\mu_n^k)^3\right) - 8\frac{\beta}{\alpha}\left(\langle\mu\rangle - \gamma\right) \\
\frac{\mu_n^{k+1}}{\Delta t} + \frac{1}{\alpha}\frac{2}{(\Delta x)^2}\mu_n^{k+1} + \mu_n^{k+1} &= \frac{\mu_n^k}{\Delta t} + \frac{1}{\alpha}\frac{\mu_{n+1}^k + \mu_{n-1}^k}{(\Delta x)^2} + \left(3(\mu_n^k)^2 - 2(\mu_n^k)^3\right) - 8\frac{\beta}{\alpha}\left(\langle\mu\rangle - \gamma\right) \\
\mu_n^{k+1} &= \frac{\frac{\mu_n^k}{\Delta t} + \frac{1}{\alpha}\frac{\mu_{n+1}^k + \mu_{n-1}^k}{(\Delta x)^2} + \left(3(\mu_n^k)^2 - 2(\mu_n^k)^3\right) - 8\frac{\beta}{\alpha}\left(\langle\mu\rangle - \gamma\right)}{1 + \frac{1}{\Delta t} + \frac{1}{\alpha}\frac{2}{(\Delta x)^2}} \qquad \text{(A.15)}
\end{aligned}
$$

A.1.3 Energy

For both the steady state and the time-dependent solutions, we are interested in the energy contents of the microstructure:

$$W^{int} = A|\nabla|^2 \tag{A.16}$$

$$W^{ani} = K\mu^2(1-\mu)^2 \tag{A.17}$$

$$\begin{aligned} W^{elas} &= \frac{1}{2}[\varepsilon - \varepsilon^*] \cdot \mathbf{C}[\varepsilon - \varepsilon^*] \\ &= \frac{1}{2}\mathbf{C}^{-1}\sigma \cdot \underbrace{\mathbf{C}\mathbf{C}^{-1}}_{\mathbf{I}}\sigma \\ &= \frac{1}{2}\mathbf{C}^{-1}\sigma \cdot \sigma \\ &= \frac{1}{2}\mathbf{C}^{-1} \begin{pmatrix} 0 \\ 0 \\ 4C_{66}\delta\left(\langle\mu\rangle - \gamma\right) \end{pmatrix} \cdot \begin{pmatrix} 0 \\ 0 \\ 4C_{66}\delta\left(\langle\mu\rangle - \gamma\right) \end{pmatrix} \\ &= 8C_{66}\delta^2\left(\langle\mu\rangle - \gamma\right)^2 \end{aligned} \tag{A.18}$$

Thus the total energy is:

$$\begin{aligned} W &= W^{int} + W^{ani} + W^{elas} \\ &= A|\nabla\mu|^2 + K\mu^2(1-\mu)^2 + 8C_{66}\delta^2\left(\langle\mu\rangle - \gamma\right)^2 \\ &= A\left[|\nabla\mu|^2 + \frac{K}{A}\mu^2(1-\mu)^2 + 8\frac{C_{66}\delta^2}{A}\left(\langle\mu\rangle - \gamma\right)^2\right] \end{aligned} \tag{A.19}$$

$$\frac{W}{A} = |\nabla\mu|^2 + \alpha\mu^2(1-\mu)^2 + 8\beta\left(\langle\mu\rangle - \gamma\right)^2, \tag{A.20}$$

where the total energy W is normalized with respect to the interfacial parameter.

A.1.4 Simulations and Discussion

We solve the one dimensional phase field model using the two numerical schemes for the steady state and the evolution. We start with initial random configuration $\mu^0(x)$, $x \in [0,1]$. Several cases are run with various ratios γ of the transformation strains of the participating Martensitic variants

in the external strain, $\varepsilon^0 = \gamma\varepsilon^{(1)} + (1-\gamma)\varepsilon^{(2)}$. The plots are shown on Fig. (A.1) for $\gamma = 0.3$, Fig. (A.2) for $\gamma = 0.5$, Fig. (A.3) for $\gamma = 0.8$, Fig. (A.4) for $\gamma = 0$ and Fig. (A.5) for $\gamma = 1$.

As expected, both numerical schemes give consistent patterns in steady states. We see that the forms of the resulting patterns depend on K. If K is too small, the patterns become uniform and homogeneous or the interfaces are not stiff enough. On the other hand, if K is too large, the alternating patterns become too rapid with increased interfacial energy, which are not realistic. Thus there is a range of K over which the simulations give rise to reasonable laminated patterns. For $\gamma = 0$ and $\gamma = 1$, uniform patterns are obtained over the ranges of K.

In conclusion, the one dimensional analysis provides an insight on the range of parameters that can yield reasonable patterns, thus enhancing efficiency for simulation in higher dimensions in the choices of parameters.

A.1.5 Appendix

We make the assumption that in the rotated reference frame (45^0), all quantities depend on x_1 only. Deviation of displacements and strains are outlined for completeness, though not all of them are used in the main work.

Displacement fields

$$\mathbf{u} = (u_1, u_2) = (u_1(x_1), u_2(x_1))$$

Strains

$$\varepsilon_{11} = \frac{\partial u_1(x_1)}{\partial x_1} \tag{A.21}$$

$$\varepsilon_{22} = \frac{\partial u_2(x_1)}{\partial x_2} = 0 \tag{A.22}$$

$$\varepsilon_{12} = \frac{1}{2}\left(\underbrace{\frac{\partial u_1(x_1)}{\partial x_2}}_{=0} + \frac{\partial u_2(x_1)}{\partial x_1}\right) = \frac{1}{2}\frac{\partial u_2(x_1)}{\partial x_1} \tag{A.23}$$

Now we are going to find the exact values of ε_{11} and ε_{12}. Using the stress-strain relation with

the previous result that $\sigma_{12} = 4C_{66}\delta(\langle\mu\rangle - \gamma)$, we obtain ε_{12}:

$$\begin{aligned}
\sigma_{12} &= C_{16}\underbrace{(\varepsilon_{11} - \varepsilon_{11}^*)}_{0} + C_{26}\underbrace{(\varepsilon_{22} - \varepsilon_{22}^*)}_{0} + C_{66}(\varepsilon_{12} - \varepsilon_{12}^*) \\
4C_{66}\delta(\langle\mu\rangle - \gamma) &= C_{44}(\varepsilon_{12} - \varepsilon_{12}^*) \\
\varepsilon_{12} &= 4\delta(\langle\mu\rangle - \gamma) + \varepsilon_{12}^*
\end{aligned} \tag{A.24}$$

Next, with the previous result that $\sigma_{22} = 0$, we have:

$$\begin{aligned}
\sigma_{22} &= C_{21}(\varepsilon_{11} - \varepsilon_{11}^*) + C_{22}(\underbrace{\varepsilon_{22}}_{0} - \varepsilon_{22}^*) + \underbrace{C_{24}}_{0}(\varepsilon_{12} - \varepsilon_{12}^*) \\
0 &= C_{21}(\varepsilon_{11} - \varepsilon_{11}^*) - C_{22}\varepsilon_{22}^* \\
\varepsilon_{11} &= \frac{C_{22}}{C_{21}}\underbrace{\varepsilon_{22}^*}_{0} + \underbrace{\varepsilon_{11}^*}_{0} = 0
\end{aligned} \tag{A.25}$$

Notice that the stress-strain relation for σ_{11} gives us no new information.

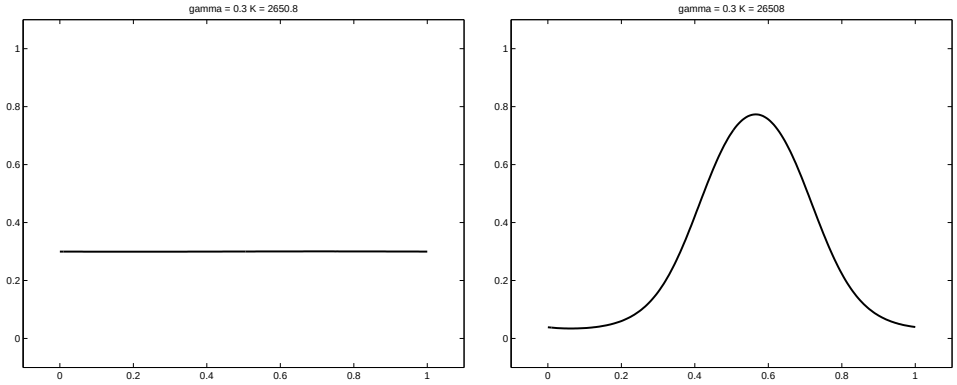

(a) K = 2650.8

(b) K = 26508

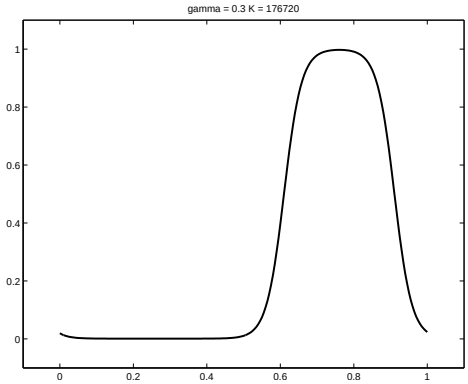

(c) K = 176720

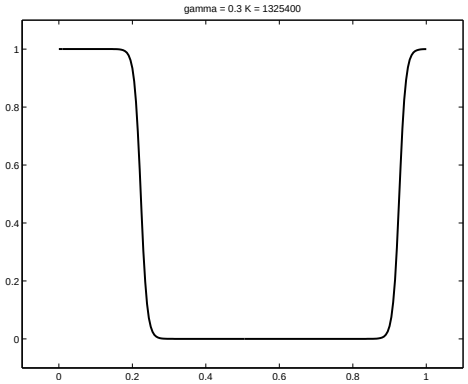

(d) K = 1325400

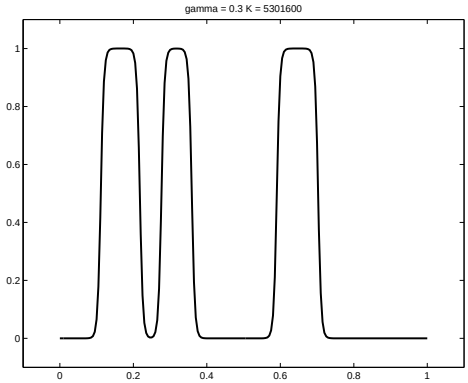

(e) K = 5301600

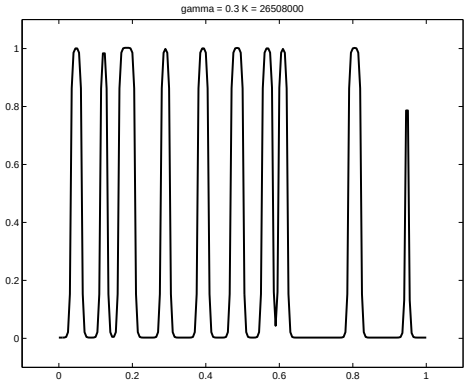

(f) K = 26508000

Figure A.1: One-dimensional simulated patterns for $\gamma = 0.3$. The value of μ is plotted along the x-axis. $\mu = 1$ presents that the domain is occupied by variant 1, while $\mu = 0$ presents that the domain is occupied by variant 2. If K is too small, the pattern is uniform and homogeneous. As K increases, the patterns become laminated. But if K gets too large, the alternating patterns become too rapid and do not reflect the reality. There is a range of K on which the desired patterns can be generated. Notice that the average values of μ is equal to $\gamma = 0.3$.

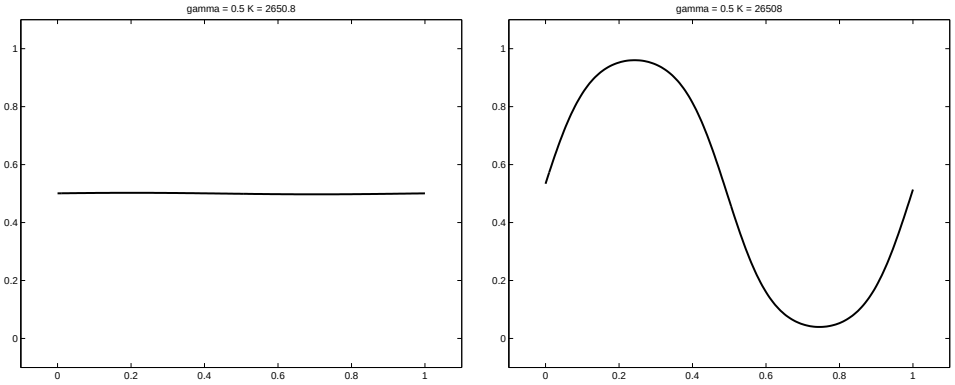

(a) K = 2650.8

(b) K = 26508

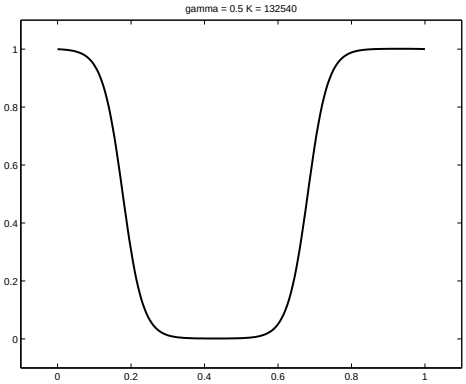

(c) K = 132540

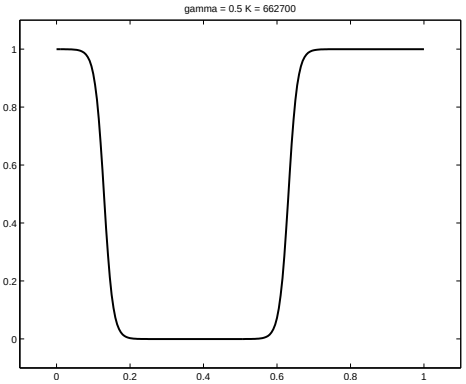

(d) K = 662700

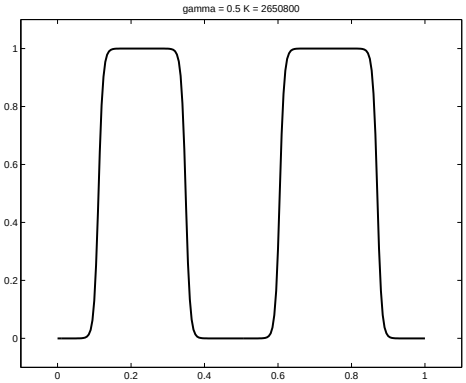

(e) K = 2650800

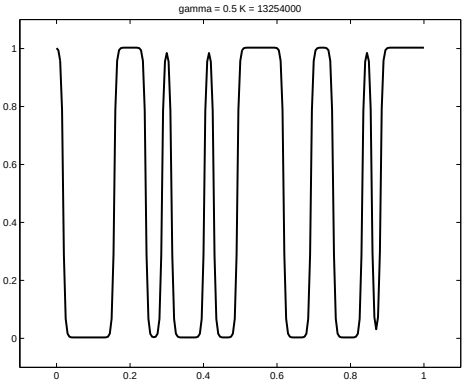

(f) K = 13254000

Figure A.2: One-dimensional simulated patterns for $\gamma = 0.5$. The value of μ is plotted along the x-axis. $\mu = 1$ presents that the domain is occupied by variant 1, while $\mu = 0$ presents that the domain is occupied by variant 2. If K is too small, the pattern is uniform and homogeneous. As K increases, the patterns become laminated. But if K gets too large, the alternating patterns become too rapid and do not reflect the reality. There is a range of K on which the desired patterns can be generated. Notice that the average values of μ is equal to $\gamma = 0.5$.

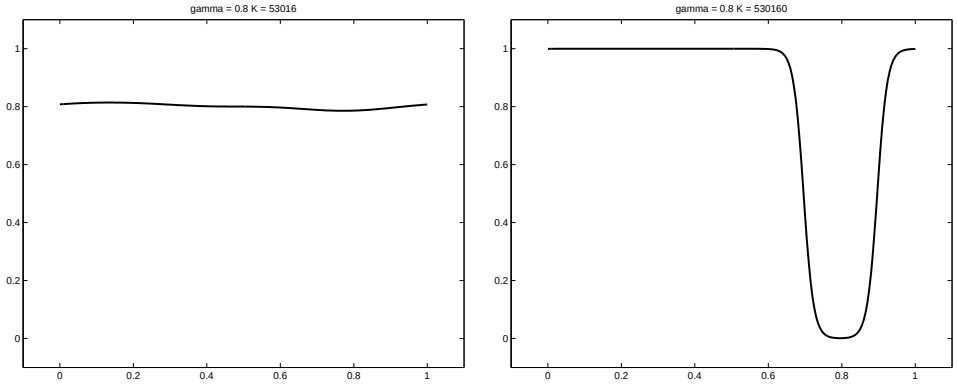

(a) K = 53016

(b) K = 530160

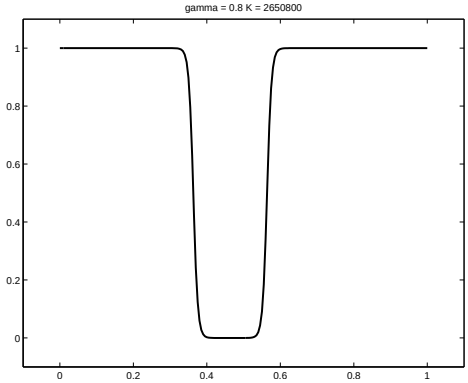

(c) K = 2650800

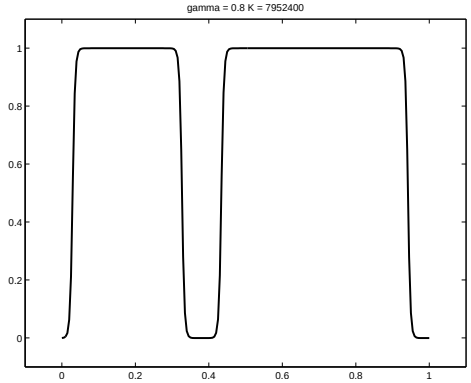

(d) K = 7952400

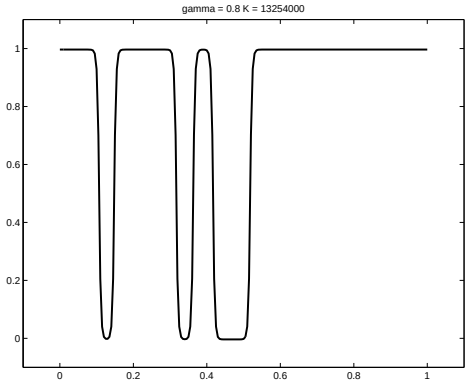

(e) K = 13254000

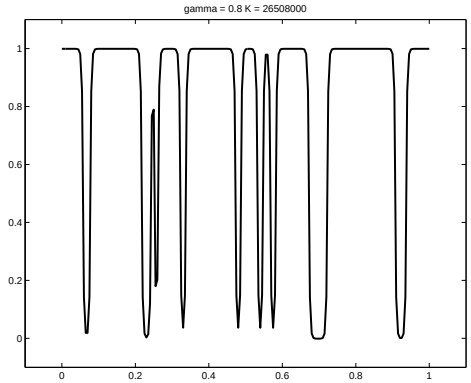

(f) K = 26508000

Figure A.3: One-dimensional simulated patterns for $\gamma = 0.8$. The value of μ is plotted along the x-axis. $\mu = 1$ presents that the domain is occupied by variant 1, while $\mu = 0$ presents that the domain is occupied by variant 2. If K is too small, the pattern is uniform and homogeneous. As K increases, the patterns become laminated. But if K gets too large, the alternating patterns become too rapid and do not reflect the reality. There is a range of K on which the desired patterns can be generated. Notice that the average values of μ is equal to $\gamma = 0.8$.

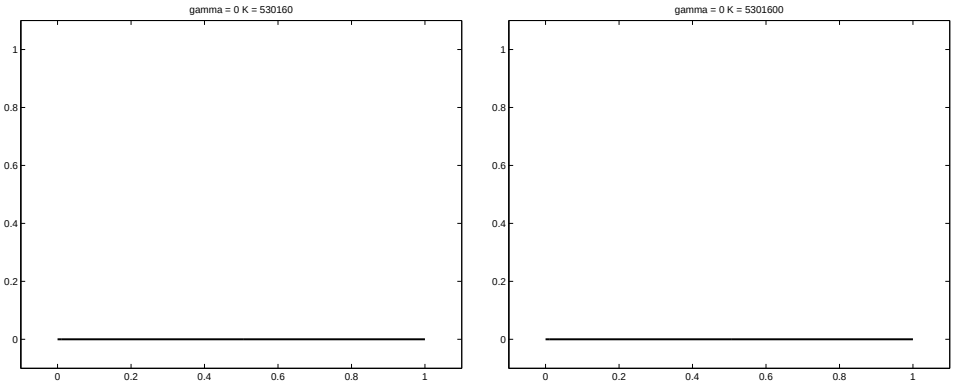

(a) K = 530160 (b) K = 5301600

Figure A.4: One-dimensional simulated patterns for $\gamma = 0$. The value of μ is plotted along the x-axis. $\mu = 1$ presents that the domain is occupied by variant 1, while $\mu = 0$ presents that the domain is occupied by variant 2. Over a wide range of K, the patterns remain uniform as 0.

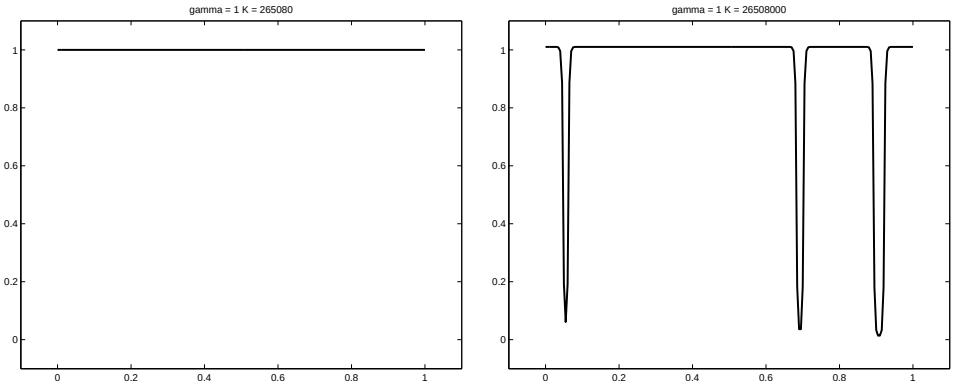

(a) K = 265080 (b) K = 26508000

Figure A.5: One-dimensional simulated patterns for $\gamma = 1$. The value of μ is plotted along the x-axis. $\mu = 1$ presents that the domain is occupied by variant 1, while $\mu = 0$ presents that the domain is occupied by variant 2. Over a wide range of K, the patterns remain uniform as 1. But if K gets too large, at some points of the patterns, there are rapid switching between 0 and 1. The average value of μ is approximately 1.

A.2 Microstructure under the effect of External Stress - One dimensional study

We now consider the outcome if we are given external stress instead of external strain. The theory also lays out the mechanism of Domain Switching under stress.

The same transformation strains as in the previous section are used. Under the effect of mechanical loading as stress σ^0, we solve the mechanical equilibrium equation. We decompose the strain, the eigenstarin (as effective transformation strain) and stress into its average and perturbed (or inhomogeneous) portions.

$$\begin{aligned} \varepsilon &= \langle \varepsilon \rangle + \varepsilon' \\ \varepsilon^* &= \langle \varepsilon^* \rangle + \varepsilon^{*\prime} \\ \sigma &= \langle \sigma \rangle + \sigma' = \underbrace{\sigma^o}_{given} + \sigma' \end{aligned} \tag{A.26}$$

It is straight-forwards to check that these perturbed quantities also satisfy the mechanical equilibrium equation:

$$\begin{cases} \nabla \cdot \sigma' &= 0 \\ \sigma' &= \mathbf{C}\left[\varepsilon' - \varepsilon^{*\prime}\right] \end{cases}, \tag{A.27}$$

while the homogeneous or average quantities satisfy the equation:

$$\langle \sigma \rangle = \sigma^o = \mathbf{C}\left[\langle \varepsilon \rangle - \langle \varepsilon^* \rangle\right] \tag{A.28}$$

A.2.1 Stress that favours specific Martensitic variants

As motivated by the previous simulations in two dimensions that deal with applied stress, if the external stress favours variant one, then variant 1 is likely to form, and vice versa. To simulate a pattern that prefers variant 1, we can find the external stress σ^0 so that the work done by this variant in the total free energy is lower than the other variant, in other words, $-\sigma^o \cdot \varepsilon^{(1)} < -\sigma^o \cdot \varepsilon^{(2)}$. The system is more stable in the state with lower free energy. Given that all transformation strains are equivalent, the anisotropy energy, interfacial energy and elastic energy are equivalent over all

Martensitic variants. Lower work done by one variant corresponds to lower total free energy by that variant, thus the system tends to form pattern with this variant.

$$
\begin{aligned}
-\sigma^0 \cdot \varepsilon^{(1)} &< -\sigma^0 \cdot \varepsilon^{(2)} \\
\sigma^0 \cdot \varepsilon^{(1)} &> \sigma^0 \cdot \varepsilon^{(2)} \\
\sigma^0 \cdot \begin{pmatrix} 0 \\ 0 \\ -2\delta \end{pmatrix} &> \sigma^0 \cdot \begin{pmatrix} 0 \\ 0 \\ 2\delta \end{pmatrix}
\end{aligned}
\tag{A.29}
$$

From here, we may simply take $\sigma^o = \begin{pmatrix} 0 \\ 0 \\ s_1 \end{pmatrix}$, where $s_1 < 0$ is the stress that favors the existence of Martensitic variant 1. Notice that first two components are not effective in the above inequality.

On the other hand, if we want to have variant 2 to appear in the simulated pattern, we set up the inequality $-\sigma^o \cdot \varepsilon^{(2)} < -\sigma^o \cdot \varepsilon^{(1)}$, we should choose $\sigma^0 = \begin{pmatrix} 0 \\ 0 \\ s_2 \end{pmatrix}$, where $s_2 > 0$ is the stress that favors the existence of Martensitic variant 2.

As a final remark, it is important to notice that the preassigned external stress is equivalent to the average stress, that is, $\sigma^0 = \langle \sigma \rangle$.

A.2.2 Perturbed Portions of Stresses

Knowing that the homogeneous stress is equal to the given external stress (so we do not need to calculate it with any effort). We may then go straight to deal with the nonhomogeneous stress. We start from the equilibrium equation $\nabla \cdot \sigma' = 0$ to derive the components of σ' which only depends on possibly x_1.

$$\begin{aligned}
&\frac{\partial \sigma'_{11}}{\partial x_1}+\frac{\partial \sigma'_{12}}{\partial x_2}+\frac{\partial \sigma'_{13}}{\partial x_3}=0 \longrightarrow \sigma'_{11}=constant\\
&\frac{\partial \sigma'_{21}}{\partial x_1}+\frac{\partial \sigma'_{22}}{\partial x_2}+\frac{\partial \sigma'_{23}}{\partial x_3}=0 \longrightarrow \sigma'_{21}=constant\\
&\frac{\partial \sigma'_{31}}{\partial x_1}+\frac{\partial \sigma'_{32}}{\partial x_2}+\frac{\partial \sigma'_{33}}{\partial x_3}=0 \longrightarrow \sigma'_{31}=constant
\end{aligned} \tag{A.30}$$

On the other hand, these components of stresses are perturbed quantities, that is, their averages over the length of domain are 0. These force their constant values to be zero:

$$constant =< \sigma'_{i1} >= 0, \forall i = 1,2,3. \tag{A.31}$$

Thus, $\sigma'_{i1} = 0 \forall i = 1,2,3$.

For the component σ'_{22} , we need to go back to displacement. Displacements are functions of x_1 only. So by definition, the strain component ε_{22} is:

$$\varepsilon_{22} = \frac{\partial u_2}{\partial x_2} = 0 \tag{A.32}$$

Its perturbed portion is 0, since $\varepsilon'_{22} = \varepsilon_{22} - \langle \varepsilon_{22} \rangle = 0$.

With the stress-strain relation in the perturbed quantities in component forms,

$$\begin{aligned}
\underbrace{\sigma'_{11}}_{=0} &= C_{11}(\varepsilon'_{11} - \underbrace{\varepsilon^{*\prime}_{11}}_{=0}) + C_{12}(\underbrace{\varepsilon'_{22}}_{=0} - \underbrace{\varepsilon^{*\prime}_{22}}_{=0}) + \underbrace{C_{16}}_{=0}(\varepsilon'_{12} - \varepsilon^{*\prime}_{12})\\
\sigma'_{22} &= C_{21}(\varepsilon'_{11} - \underbrace{\varepsilon^{*\prime}_{11}}_{=0}) + C_{22}(\underbrace{\varepsilon'_{22}}_{=0} - \underbrace{\varepsilon^{*\prime}_{22}}_{=0}) + \underbrace{C_{26}}_{=0}(\varepsilon'_{12} - \varepsilon^{*\prime}_{12})\\
\underbrace{\sigma'_{12}}_{=0} &= \underbrace{C_{61}}_{=0}(\varepsilon'_{11} - \underbrace{\varepsilon^{*\prime}_{11}}_{=0}) + \underbrace{C_{62}}_{=0}(\underbrace{\varepsilon'_{22}}_{=0} - \underbrace{\varepsilon^{*\prime}_{22}}_{=0}) + C_{66}(\varepsilon'_{12} - \varepsilon^{*\prime}_{12}),
\end{aligned} \tag{A.33}$$

where we have used the facts that **C** is the stiffness matrix for isotropic materials, the first two components of transformation strains are zero, and $\sigma'_{11} = \sigma'_{12} = 0$ from the mechanical equilibrium equation in the perturbed quantities. Also $\varepsilon'_{22} = 0$ was derived from displacement.

Solving the above reduced equations yield:

$$\begin{aligned} \varepsilon'_{11} &= 0 \\ \sigma'_{22} &= 0 \\ \varepsilon'_{12} &= \varepsilon^{*\prime}_{12} = 2\mu'\delta, \end{aligned} \tag{A.34}$$

where μ' is the perturbed portion of μ and δ is the lattice parameters in the transformation strains.

Summing up, we have the following:

$$\sigma' = \begin{pmatrix} \sigma'_{11} \\ \sigma'_{22} \\ \sigma'_{12} \end{pmatrix} = \begin{pmatrix} 0 \\ 0 \\ 0 \end{pmatrix} \tag{A.35}$$

$$\sigma = \langle\sigma\rangle + \sigma' = \sigma^0 + \underbrace{\sigma'}_{0} = \sigma^0 \tag{A.36}$$

Summary

$$\begin{aligned} -\sigma^0 \cdot \varepsilon^{(1)} &< -\sigma^0 \cdot \varepsilon^{(2)} \quad \text{if } s_1 > 0 \\ -\sigma^0 \cdot \varepsilon^{(2)} &< -\sigma^0 \cdot \varepsilon^{(1)} \quad \text{if } s_2 < 0 \end{aligned}$$

A.2.3 Governing Equation

Following the same approach as outlined in previous section, we seek the governing equations (evolution equation) for μ. First we give the three driving forces.

Interfacial Force

$$F^{int} = 2A\nabla^2\mu = 2A\frac{d^2\mu}{dx^2} \tag{A.37}$$

Anisotropic Force

$$F^{ani} = -2K(\mu - 3\mu^2 + 2\mu^3) \tag{A.38}$$

Elastic Force

$$\begin{aligned} F^{elas} &= \sigma \cdot \frac{\partial \varepsilon^*}{\partial \mu} \\ &= \begin{pmatrix} 0 \\ 0 \\ S \end{pmatrix} \cdot \begin{pmatrix} 0 \\ 0 \\ -4\delta \end{pmatrix} \\ &= -4\delta S, \end{aligned} \tag{A.39}$$

where $S = s_1 < 0$ if variant 1 is preferred, while $S = s_2 > 0$ if variant 2 is preferred.

With these, the governing equation is then given by:

$$\begin{aligned} \frac{d\mu}{dt} &= M\left(F^{int} + F^{ani} + F^{elas}\right) \\ \frac{d\mu}{dt} &= M\left(2A\frac{d^2\mu}{dx^2} - 2K\left(\mu - 3\mu^2 + 2\mu^3\right) - 4\delta S\right) \end{aligned} \tag{A.40}$$

The following sub-sections will be devoted to the steady state problem and the time evolution problem of this equation.

A.2.4 Steady State Problem

Recall that the steady state is achieved when $\frac{d\mu}{dt} = 0$. The governing equation is simplified as follow:

$$\begin{aligned} \underbrace{\frac{d\mu}{dt}}_{0} &= M\left(2A\frac{d^2\mu}{dx^2} - 2K\left(\mu - 3\mu^2 + 2\mu^3\right) - 4\delta S\right) \\ 2A\frac{d^2\mu}{dx^2} &= 2K\left(\mu - 3\mu^2 + 2\mu^3\right) + 4\delta S \\ \frac{d^2\mu}{dx^2} &= \frac{K}{A}\left(\mu - 3\mu^2 + 2\mu^3\right) + 2\frac{\delta S}{A} \\ \frac{d^2\mu}{dx^2} &= \alpha\left(\mu - 3\mu^2 + 2\mu^3\right) + 2\eta, \end{aligned} \tag{A.41}$$

where two grouped parameters are defined for easier book-keeping:

$$\alpha \equiv \frac{K}{A}$$
$$\eta \equiv \frac{\delta S}{A}$$

This second order nonlinear ODE has no exact solution. We may solve it by numerical method. Notice that we are imposing periodic boundary conditions to μ at both ends.

Numerical Method - Finite Difference Scheme

Let the values of μ on the x-axis at iteration level '$t = t_k$' be $\mu_n^k = \mu(x_n, t_k)$. Then the above equation can be discretized as:

$$\begin{aligned}
\frac{d^2\mu^k}{dx^2} &= \alpha\left(\mu^k - 3(\mu^k)^2 + 2(\mu^k)^3\right) + 2\eta \\
\frac{\mu_{n+1}^k - 2\mu_n^k + \mu_{n-1}^k}{(\Delta x)^2} &= \alpha\left(\mu_n^k - 3(\mu_n^k)^2 + 2(\mu_n^k)^3\right) + 2\eta \\
\frac{\mu_{n+1}^k - 2\mu_n^{k+1} + \mu_{n-1}^k}{(\Delta x)^2} &= \alpha\left(\mu_n^{k+1} - 3(\mu_n^k)^2 + 2(\mu_n^k)^3\right) + 2\eta \\
\left(\frac{2}{(\Delta x)^2} + \alpha\right)\mu_n^{k+1} &= \frac{\mu_{n+1}^k + \mu_{n-1}^k}{(\Delta x)^2} + \alpha\left(3(\mu_n^k)^2 - 2(\mu_n^k)^3\right) - 2\eta \\
\mu_n^{k+1} &= \frac{\frac{\mu_{n+1}^k + \mu_{n-1}^k}{(\Delta x)^2} + \alpha\left(3(\mu_n^k)^2 - 2(\mu_n^k)^3\right) - 2\eta}{\frac{2}{(\Delta x)^2} + \alpha} \\
&= \frac{\frac{\mu_{n+1}^k + \mu_{n-1}^k}{\alpha(\Delta x)^2} + \left(3(\mu_n^k)^2 - 2(\mu_n^k)^3\right) - 2\frac{\eta}{\alpha}}{\frac{2}{\alpha(\Delta x)^2} + 1}
\end{aligned} \tag{A.42}$$

A.2.5 Time Evolution Problem

Recall the governing equation is given by:

$$\frac{d\mu}{dt} = M\left(2A\frac{d^2\mu}{dx^2} - 2K(\mu - 3\mu^2 + 2\mu^3) - 4\delta S\right)$$

We may want to get rid of the ill-defined parameter M by a change of variable in time t.

$$\tilde{t} = 2MKt$$

With this, the equation can be rewritten with no explicit M:

$$\begin{aligned}
\frac{d\mu}{dt} &= M\left(2A\frac{d^2\mu}{dx^2} - 2K\left(\mu - 3\mu^2 + 2\mu^3\right) - 4\delta S\right) \\
2MK\frac{d\mu}{d\tilde{t}} &= M\left(2A\frac{d^2\mu}{dx^2} - 2K\left(\mu - 3\mu^2 + 2\mu^3\right) - 4\delta S\right) \\
\frac{d\mu}{d\tilde{t}} &= \frac{A}{K}\frac{d^2\mu}{dx^2} - \left(\mu - 3\mu^2 + 2\mu^3\right) - 2\frac{\delta S}{K} \qquad \text{(A.43)} \\
\frac{d\mu}{d\tilde{t}} &= \frac{1}{\alpha}\frac{d^2\mu}{dx^2} - \left(\mu - 3\mu^2 + 2\mu^3\right) - 2\frac{\eta}{\alpha}, \qquad \text{(A.44)}
\end{aligned}$$

where the same grouped parameters are introduced.

Numerical Method - Finite Difference Scheme

Again let the values of μ on the x-axis at iteration level $'t' = t_k$ be $\mu_n^k = \mu(x_n, t_k)$. The evolution equation can be discretized as:

$$\begin{aligned}
\frac{\mu_n^{k+1} - \mu_n^k}{\Delta t} &= \frac{1}{\alpha}\frac{\mu_{n+1}^k - 2\mu_n^k + \mu_{n-1}^k}{(\Delta x)^2} - \left(\mu_n^k - 3(\mu_n^k)^2 + 2(\mu_n^k)^3\right) - 2\frac{\eta}{\alpha} \\
\frac{\mu_n^{k+1} - \mu_n^k}{\Delta t} &= \frac{1}{\alpha}\frac{\mu_{n+1}^k - 2\mu_n^{k+1} + \mu_{n-1}^k}{(\Delta x)^2} - \left(\mu_n^{k+1} - 3(\mu_n^k)^2 + 2(\mu_n^k)^3\right) - 2\frac{\eta}{\alpha} \\
\frac{\mu_n^{k+1}}{\Delta t} + \frac{1}{\alpha}\frac{2}{(\Delta x)^2}\mu_n^{k+1} + \mu_n^{k+1} &= \frac{\mu_n^k}{\Delta t} + \frac{1}{\alpha}\frac{\mu_{n+1}^k + \mu_{n-1}^k}{(\Delta x)^2} + \left(3(\mu_n^k)^2 - 2(\mu_n^k)^3\right) - 2\frac{\eta}{\alpha} \\
\mu_n^{k+1} &= \frac{\frac{\mu_n^k}{\Delta t} + \frac{1}{\alpha}\frac{\mu_{n+1}^k + \mu_{n-1}^k}{(\Delta x)^2} + \left(3(\mu_n^k)^2 - 2(\mu_n^k)^3\right) - 2\frac{\eta}{\alpha}}{1 + \frac{1}{\Delta t} + \frac{1}{\alpha}\frac{2}{(\Delta x)^2}} \qquad \text{(A.45)}
\end{aligned}$$

A.2.6 Energy Density and Energy

In both steady state and time-dependent equations, we may also calculate the energy content of the material as outlined below. Recall the three types of energy constituting the total energy:

The three components of total free energy are:

$$W^{int} = A|\nabla|^2 \tag{A.46}$$

$$W^{ani} = K\mu^2(1-\mu)^2 \tag{A.47}$$

$$\begin{aligned} W^{elas} &= \frac{1}{2}[\varepsilon - \varepsilon^*]\cdot\mathbf{C}[\varepsilon-\varepsilon^*] \\ &= \frac{1}{2}\mathbf{C}^{-1}\sigma\cdot\underbrace{\mathbf{C}\cdot\mathbf{C}^{-1}}_{\mathbf{I}}\sigma \\ &= \frac{1}{2}\mathbf{C}^{-1}\sigma\cdot\sigma \\ &= \frac{1}{2}\mathbf{C}^{-1}\begin{pmatrix}0\\0\\S\end{pmatrix}\cdot\begin{pmatrix}0\\0\\S\end{pmatrix} \\ &= \frac{1}{2}\begin{pmatrix}0\\0\\\frac{S}{C_{66}}\end{pmatrix}\cdot\begin{pmatrix}0\\0\\S\end{pmatrix} \\ &= \frac{1}{2C_{66}}S^2 \end{aligned} \tag{A.48}$$

Thus the total energy (as a fraction of the interfacial constant A) is:

$$\begin{aligned} W &= W^{int} + W^{ani} + W^{elas} \\ &= A|\nabla\mu|^2 + K\mu^2(1-\mu)^2 + \frac{1}{2C_{66}}S^2 \\ &= A\left[|\nabla\mu|^2 + \frac{K}{A}\mu^2(1-\mu)^2 + \frac{1}{2AC_{66}}S^2\right] \end{aligned} \tag{A.49}$$

$$\frac{W}{A} = |\nabla\mu|^2 + \alpha\mu^2(1-\mu)^2 + \frac{1}{2AC_{66}}S^2 \tag{A.50}$$

A.2.7 Simulations and Discussion

Some simulations are run to investigate the effect of applying external stress to the evolution of microstructure. We start from random initial configuration $\mu^0(x)$, as shown on Fig. (A.6) (a),

assume the external stress be $\sigma^0 = \begin{pmatrix} 0 \\ 0 \\ S \end{pmatrix}$, where $S = s_1 < 0$. The resulting entire pattern will evolve to favor variant 1 ($\mu(x) = 1$), as shown on Fig. (A.6) (d). Two intermediate patterns are shown on Figs. (A.6) (b) and (A.6) (c).

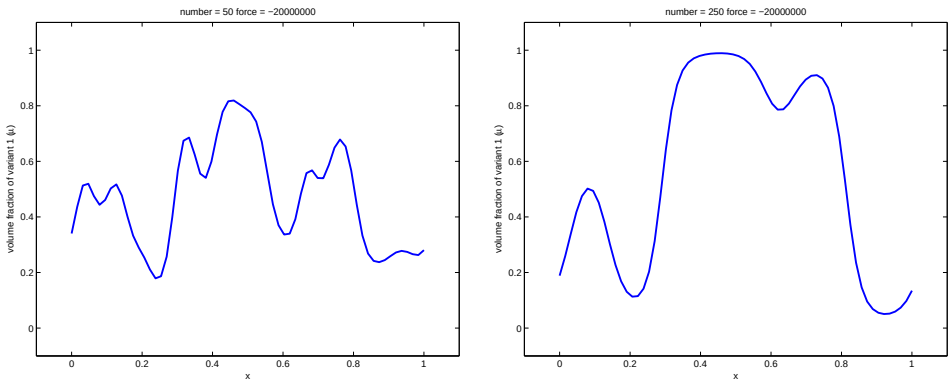

(a) time step = 50 (b) time step = 250

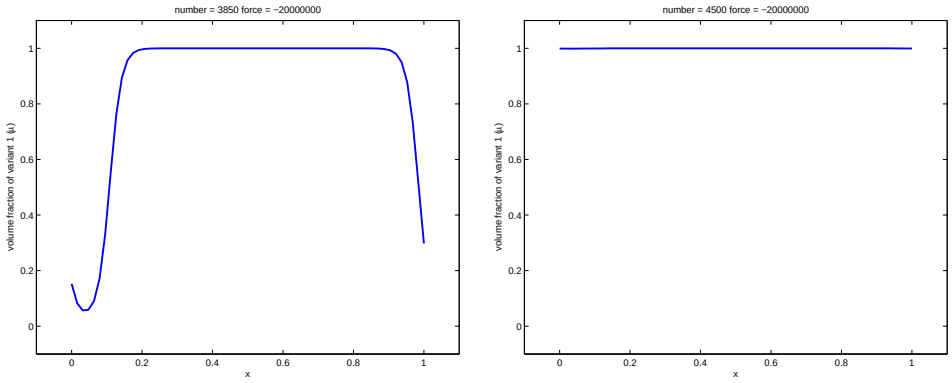

(a) time step = 3850 (b) time step = 4500

Figure A.6: One-dimensional simulated patterns by external stress that favours variant 1 with $S = s_1 < 0$. The value of μ is plotted along the x-axis. $\mu = 1$ presents that the domain is occupied by variant 1, while $\mu = 0$ presents that the domain is occupied by variant 2. (a) Initial random pattern. (b) and (c) Intermediate patterns. (d) Final pattern. The microstructure evolves to variant 1 with $\mu = 1$.

Domain switching by stress is also simulated. The microstructure starts with variant 1 with a nucleation of variant 2, as shown in Fig. (A.8) (a) . External stress that favours variant 2 is applied.

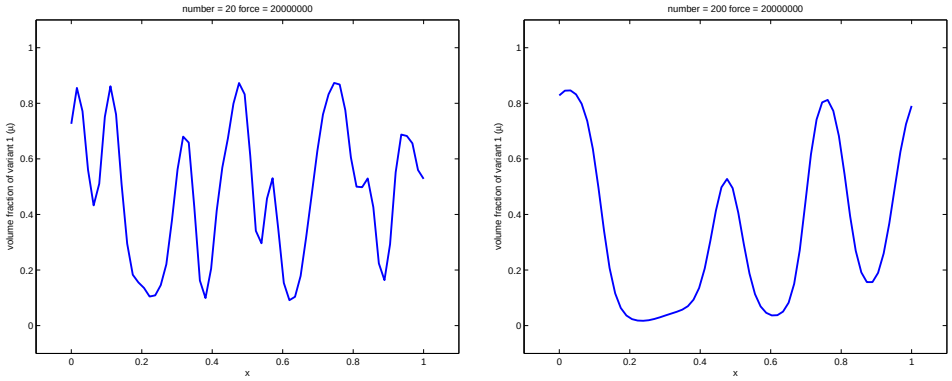

(a) time step = 20 (b) time step = 200

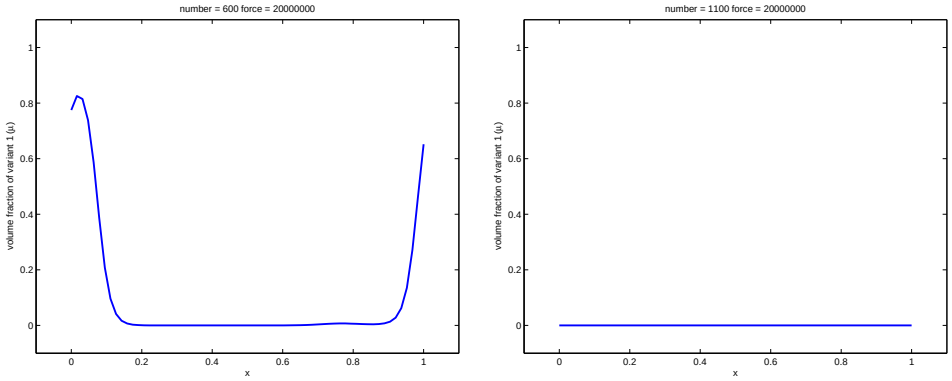

(a) time step = 600 (b) time step = 1100

Figure A.7: One-dimensional simulated patterns by external stress that favours variant 2 with $S = s_2 > 0$. The value of μ is plotted along the x-axis. $\mu = 1$ presents that the domain is occupied by variant 1, while $\mu = 0$ presents that the domain is occupied by variant 2. (a) Initial random pattern. (b) and (c) Intermediate patterns. (d) Final pattern. The microstructure evolves to variant 2 with $\mu = 0$.

It will be seen that the variant 2 will grow from the location of nucleation until the whole domain is occupied by variant 2, as shown in Fig. (A.8) (f). Intermediate patterns showing the snapshots are shown from Figs. (A.8) (b) and (e). Similar result can be shown for the domain switching from variant 2 to variant 1 using stress acting in opposite direction.

A.2.8 Domain switching by Variational analysis

If the stress is not strong enough, domain switching from one variant to another will not take place. We want to find the critical stress to induce this phenomenon, if external effects are accounted. The variational approach thus provides us with more information on how the magnitudes of stresses affect domain switching.

Recall that the total energy of the sample is given by the integral form:

$$\mathscr{I}(\mu) = \int_{\Omega} \left[W^{int} + W^{ani} + W^{elas} - \sigma^{o} \cdot \varepsilon \right] dx \tag{A.51}$$

Given the external stress in the form $\sigma^0 = \begin{pmatrix} 0 \\ 0 \\ S \end{pmatrix}$. We are going to express the energy functional in terms of S and the field variable μ.

The inhomogeneous strain is given by:

$$\varepsilon^* = \mu\varepsilon_1 + (1-\mu)\varepsilon_2 = \begin{pmatrix} 0 \\ 0 \\ 2\delta(1-2\mu) \end{pmatrix} \tag{A.52}$$

Using the stress-strain relation, we obtain the total stress:

$$\begin{aligned} \sigma &= (\varepsilon - \varepsilon^*) \\ \varepsilon &= \varepsilon^* + \mathbf{C}^{-1}\sigma \\ &= \begin{pmatrix} 0 \\ 0 \\ 2\delta(1-2\mu) + \frac{s}{C_{66}} \end{pmatrix} \end{aligned} \tag{A.53}$$

Thus the work done attributed from external stress is given by:

$$\begin{aligned}\sigma^o \cdot \varepsilon &= \begin{pmatrix} 0 \\ 0 \\ s \end{pmatrix} \cdot \begin{pmatrix} 0 \\ 0 \\ 2\delta(1-2\mu)+\frac{s}{C_{66}} \end{pmatrix} \\ &= 2\delta(1-2\mu)s + \frac{s^2}{C_{66}} \end{aligned} \tag{A.54}$$

With these, the energy functional can be expressed in terms of S and μ,

$$\begin{aligned}\mathscr{I}(\mu) &= \int_\Omega \left[W^{int} + W^{ani} + W^{elas} - \sigma^o \cdot \varepsilon \right] dx \\ &= \int_\Omega \left[A\left(\frac{d\mu}{dx}\right)^2 + K\mu^2(1-\mu)^2 + \frac{S^2}{2C_{66}} - 2\delta(1-2\mu)S + \frac{S^2}{C_{66}} \right] dx \\ &= \int_\Omega \left[A\left(\frac{d\mu}{dx}\right)^2 + K\mu^2(1-\mu)^2 - \frac{S^2}{2C_{66}} - 2\delta(1-2\mu)S \right] dx \end{aligned} \tag{A.55}$$

We carry out the variational analysis to this energy functional. Denote $\mu = f + \varepsilon g$. Here $g \in$

$\mathscr{C}_0^\infty(0,1)$ is a smooth perturbed terms with zero boundary conditions at all orders. Thus,

$$\begin{aligned}
\mathscr{I}(f+\varepsilon g) &= \int_0^1 \left[A(f'+\varepsilon g')^2 + K(f+\varepsilon g)^2(1-(f+\varepsilon g))^2 - \frac{S^2}{2C_{66}} - 2\delta(1-2(f+\varepsilon g))S\right] dx \\
&= \int_0^1 \Big[A(f'^2 + 2\varepsilon f'g' + \varepsilon^2 g'^2) \\
&+ Kf^2(1-f)^2 + 2K\varepsilon[f(1-f)^2 g - f^2(1-f)g] + K\varepsilon^2[(1-f)^2 g^2 - 4f(1-f)g^2 + f^2 g^2] \\
&+ -\frac{S^2}{2C_{66}} - 2\delta(1-2f-2\varepsilon g)S\Big] dx \\
&= \int_0^1 \left(Af'^2 + Kf^2(1-f)^2 - \frac{S^2}{2C_{66}} - 2\delta(1-2f)S\right) dx \\
&+ \varepsilon \int_0^1 \left(2Af'g' + 2K[f(1-f)^2 g - f^2(1-f)^2 g] - 2\delta(-2g)S\right) dx \\
&+ \varepsilon^2 \int_0^1 \left(Ag'^2 + K[(1-f)^2 g^2 - 4f(1-f)g^2 + f^2 g^2]\right) dx \\
&= \mathscr{I}(f) + \varepsilon \int_0^1 \left(2A \underbrace{f'g'}_{trick(1)} + 2K \underbrace{[f(1-f)^2 - f^2(1-f)]}_{f-3f^2+2f^3} g + 4\delta S g\right) dx \\
&+ \varepsilon^2 \int_0^1 \left(A \underbrace{g'^2}_{trick(2)} + K[(1-f)^2 g^2 - 4f(1-f)g^2 + f^2 g^2]\right) dx, \qquad \text{(A.56)}
\end{aligned}$$

where we have employed several tricks.

Trick (1): Integration by parts:

$$\begin{aligned}
\int_0^1 f'g'dx &= \int_0^1 f'dg \\
&= \left[f'g\right]_0^1 - \int_0^1 gf''dx \\
&= f'(1)\underbrace{g(1)}_{0} - f'(0)\underbrace{g(0)}_{0} - \int_0^1 gf''dx \\
&= -\int_0^1 gf''dx
\end{aligned}$$

Trick (2): Inequality with periodic BC:

$$\begin{aligned} 0 &\leq \int_0^1 g'^2 dx \\ &= \max_{0\leq x\leq 1} g' \cdot \int_0^1 g' dx \\ &= \max_{0\leq x\leq 1} g' \cdot g|_0^1 \\ &= \max_{0\leq x\leq 1} g' \cdot \underbrace{[g(1)-g(0)]}_{0} = 0 \\ \Rightarrow \int_0^1 g'^2 dx &= 0 \end{aligned}$$

Eventually the energy functional becomes:

$$\begin{aligned} \mathscr{I}(f+\varepsilon g) &= \mathscr{I}(f) + \varepsilon \int_0^1 \left(-2Af''g + 2K(f-3f^2+2f^3)g + 4\delta Sg\right) dx \\ &\quad + \varepsilon^2 \int_0^1 \left(K[(1-f)^2 - 4f(1-f) + f^2]g^2\right) dx \\ &= \mathscr{I}(f) + \delta\mathscr{I} + \delta^2\mathscr{I}, \end{aligned} \tag{A.57}$$

where $\delta\mathscr{I}$ and $\delta^2\mathscr{I}$ are respectively the first and the second variations.

The first variation, as the driving force of the system, should be zero so as to stabilize the microstructure. A second-order differential equation in f is formed.

$$\begin{aligned} 0 &= \delta\mathscr{I} \\ &= \varepsilon \int_0^1 \left(-2Af''g + 2K(f-3f^2+2f^3)g + 4\delta Sg\right) dx \\ &= \varepsilon \int_0^1 2\left(-Af'' + K(f-3f^2+2f^3) + 2\delta S\right) g dx \\ \Rightarrow -Af'' + K(f-3f^2+2f^3) + 2\delta S &= 0 \\ Af'' &= K(f-3f^2+2f^3) + 2\delta S \end{aligned} \tag{A.58}$$

The Second Variation is an indicator of whether the total energy of the microstructure is at

maximum or minimum.

$$\begin{aligned}\delta^2\mathscr{I} &= \varepsilon^2\int_0^1 \left(K[(1-f)^2 - 4f(1-f) + f^2]g^2\right)dx \\ &= \varepsilon^2\int_0^1 K[1-6f+6f^2]g^2dx \end{aligned} \tag{A.59}$$

It can be seen that the first variation is exactly the evolution equation under the effect of external stress. Based on the simulation, the field variable f will converge to either 0 or 1, depending on the direction (or sign) of S. These are the possible critical values. The second variation is used to check if these critical values induce maximum or minimum energy of the system, as to whether it is positive or negative. It is easy to check that, by direct substitution, the second variation is positive at $f = 0$ and $f = 1$, which verifies that the energy is minimized and the system is stable under the effect of external stress, with the outcome that the pattern will either evolve to only one variant.

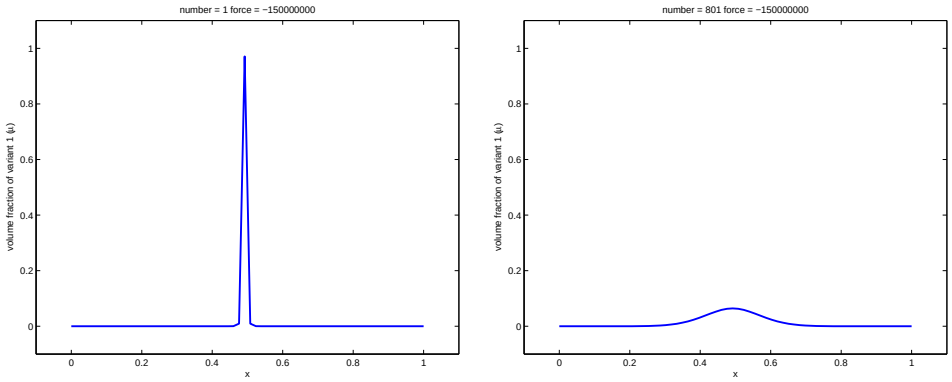

(a) time step = 1 (b) time step = 700

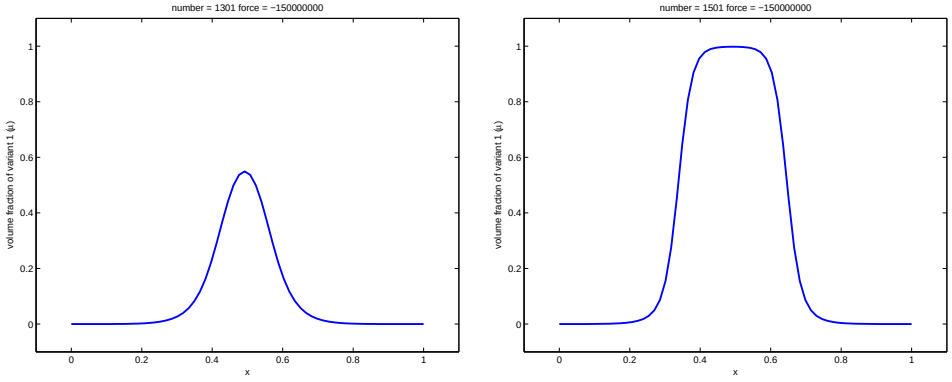

(a) time step = 1300 (b) time step = 1500

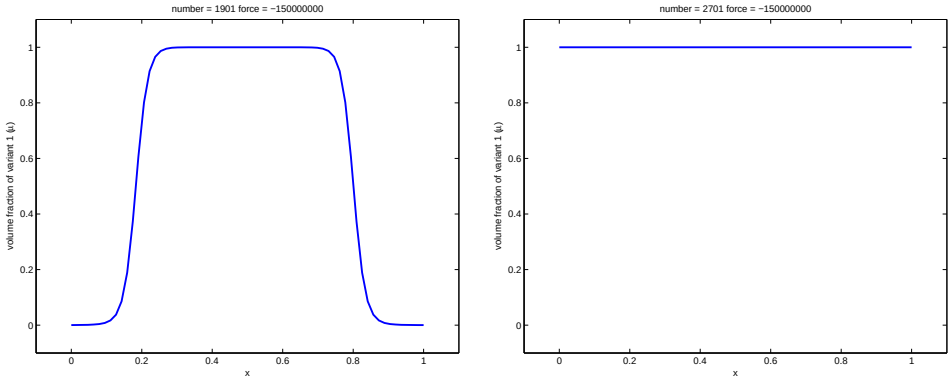

(a) time step = 1900 (b) time step = 2700

Figure A.8: (One dimensional) Illustration of domain switching by stress from variant 1 to variant 2. The value of μ is plotted along the x-axis. $\mu = 1$ presents that the domain is occupied by variant 1, while $\mu = 0$ presents that the domain is occupied by variant 2. (a) Initial pattern: Domain occupied by variant 1 but a narrow nucleation of variant 2. (b) (c) (d) (e) Intermediate patterns. (d) Final pattern. The microstructure evolves to variant 2 with $\mu = 0$, growing from the nucleation.

A.3 Effect of External Strain on 'Uniform' Volume Fraction

Assume we want to analyze the outcomes of microstructure that involves two Martensitic variants given by the transformation strain $\varepsilon^{(1)}$ and $\varepsilon^{(2)}$. The imposed mechanical condition is the external strain which is a linear combination of these two transformation strains, that is, $\varepsilon^{(0)} = \gamma\varepsilon^{(1)} + (1-\gamma)\varepsilon^{(2)}$, where $0 \leq \gamma \leq 1$ is the ratio of contribution from each Martensitic variant. Our goal is to examine the relationship between the external strains (in terms of parameter γ) and the expected stable pattern of microstructure, expressed as volume fraction of the variant one, $\mu = \mu(x), 0 \leq x \leq L$. Note that the final or stable pattern of the microstructure is evolved as a result of minimization of the sum of interfacial, anisotropy and elastic driving forces, $\mathbf{F} = \mathbf{F}^{int} + \mathbf{F}^{ani} + \mathbf{F}^{elas}$, where for stable pattern, the interfacial force is approximated as zero.

The anisotropic energy and its corresponding driving force are:

$$W^{ani} = K\mu^2(1-\mu)^2 \tag{A.60}$$

$$\begin{aligned}\mathbf{F}^{ani} &= -K\frac{\partial W^{ani}}{\partial \mu} \\ &= -2K(\mu - 3\mu^2 + 2\mu^3)\end{aligned} \tag{A.61}$$

For the elastic driving force, we need to find the stress σ and the derivative of the eigen-strain with respect to the volume fraction. Assume that the eigenstrain is given by $\varepsilon^* = \mu(x)\varepsilon^{(1)} + (1-\mu(x))\varepsilon^{(2)}$, where $\mu(x)$ represents the volume fraction of the first variant as a function of x. Its derivative with respect to μ is:

$$\frac{\partial \varepsilon^*}{\partial \mu} = \varepsilon^{(1)} - \varepsilon^{(2)} \tag{A.62}$$

The stress is evaluated from the stress-strain relationship:

$$\begin{aligned}
\sigma &= \mathbf{C}\left(\varepsilon - \varepsilon^{*}\right) \\
&= \mathbf{C}\left[\langle\varepsilon\rangle - \langle\varepsilon^{*}\rangle\right] + \mathbf{C}\left(\varepsilon' - \varepsilon^{*\prime}\right) \\
&= \mathbf{C}\left[\varepsilon^{0} - \langle\varepsilon^{*}\rangle\right] + \underbrace{\sigma'}_{\to 0} \\
&= \mathbf{C}[(\gamma\varepsilon^{(1)} + (1-\gamma)\varepsilon^{(2)}) - (\langle\mu\rangle\,\varepsilon^{(1)} + (1-\langle\mu\rangle)\varepsilon^{(2)})] \\
&= \mathbf{C}[(\gamma\varepsilon^{(1)} + (1-\gamma)\varepsilon^{(2)}) - (\mu\varepsilon^{(1)} + (1-\mu)\varepsilon^{(2)})] \\
&= \mathbf{C}[(\gamma-\mu)\varepsilon^{(1)} - (\gamma-\mu)\varepsilon^{(2)})] \\
&= (\gamma-\mu)\mathbf{C}(\varepsilon^{(1)} - \varepsilon^{(2)})
\end{aligned} \tag{A.63}$$

The elastic driving is thus:

$$\begin{aligned}
\mathbf{F}^{elas} &= \sigma \cdot \frac{\partial\varepsilon^{*}}{\partial\mu} \\
&= (\gamma-\mu)\mathbf{C}(\varepsilon^{(1)} - \varepsilon^{(2)}) \cdot (\varepsilon^{(1)} - \varepsilon^{(2)})
\end{aligned} \tag{A.64}$$

To relate the order of magnitude between the anisotropy and the elastic driving force, based on [32], we consider the anisotropy constant as:

$$K = \lambda\mathbf{C}\varepsilon^{(1)} \cdot \varepsilon^{(1)}1 = \lambda\mathbf{C}\varepsilon^{(2)} \cdot \varepsilon^{(2)}$$

We will see that the value of λ will affect the possible pattern of microstructure thus generated.

We are now in a position to derive an algebraic equation for the resulting volume fraction $\mu = \mu(x)$ that depends on the parameters γ and λ. Minimization of the system energy occurs when the

total driving force is zero, that is,

$$\begin{aligned}
\mathbf{F} &= \mathbf{F}^{int} + \mathbf{F}^{ani} + \mathbf{F}^{elas} \\
0 &= -2K\left(\mu - 3\mu^2 + 2\mu^3\right) + (\gamma - \mu)\mathbf{C}(\varepsilon^{(1)} - \varepsilon^{(2)}) \cdot (\varepsilon^{(1)} - \varepsilon^{(2)}) \\
0 &= -2K\left(\mu - 3\mu^2 + 2\mu^3\right) + (\gamma - \mu)4\frac{K}{\lambda} \\
\lambda\left(2\mu^3 - 3\mu^2 + \mu\right) + 2\mu - 2\gamma &= 0
\end{aligned} \tag{A.65}$$

Notice that γ and λ are given at the beginning, therefore μ is the unknown to be determined from the above equation. We solve this equation numerically by using Matlab with the results visualized graphically.

If we consider the special case $\lambda = 0$, where there is no anisotropic contribution. The equation reduces to $2\mu - 2\gamma = 0$, giving us the linear solution $\mu = \gamma$. The resulting constant value of the volume fraction is identical to the ratio of the transformation strains of the martesbitic variants contributing to the external strain. Say if $\varepsilon^0 = 0.6\varepsilon^{(1)} + 0.4\varepsilon^{(2)}$, the resulting volume fraction will be 0.6 uniformly over the domain. For this, we will reject this case and assume that $\lambda \neq 0$.

We may also study the energy content of the system:

$$\begin{aligned}
W &= W^{ani} + W^{elas} \\
&= K\mu^2(1-\mu)^2 + \frac{1}{2}[\varepsilon - \varepsilon^*(\mu)] \cdot \mathbf{C}[\varepsilon - \varepsilon^*(\mu)] \\
&= K\mu^2(1-\mu)^2 + \frac{1}{2}(\mu - \gamma)\left(\varepsilon^{(1)} - \varepsilon^{(2)}\right) \cdot \mathbf{C}(\mu - \gamma)\left(\varepsilon^{(1)} - \varepsilon^{(2)}\right) \\
&= K\mu^2(1-\mu)^2 + \frac{1}{2}(\mu - \gamma)^2 \underbrace{(\varepsilon^{(1)} - \varepsilon^{(2)}) \cdot \mathbf{C}(\varepsilon^{(1)} - \varepsilon^{(2)})}_{4\frac{K}{\lambda}} \\
&= K\mu^2(1-\mu)^2 + 2\frac{K}{\lambda}(\mu - \gamma)^2 \\
&= K\left[\mu^2(1-\mu)^2 + \frac{2}{\lambda}(\mu - \gamma)^2\right] \\
\frac{W}{K} &= \mu^2(1-\mu)^2 + \frac{2}{\lambda}(\mu - \gamma)^2,
\end{aligned} \tag{A.66}$$

where $\mu = \mu(\gamma)$.

Assume that external strain ratio $0 \leq \gamma \leq 1$ is preassigned, as the ratio of contribution of transfor-

mation strains in external strain, we solve from Eq. A.65 for the so-called optimal volume fraction $0 \leq \mu \leq 1$. The result is then graphed in Fig. (A.9). Here the y-axis stands for the optimal volume fraction μ while the x-axis stands for the preassigned vales of external strain γ.

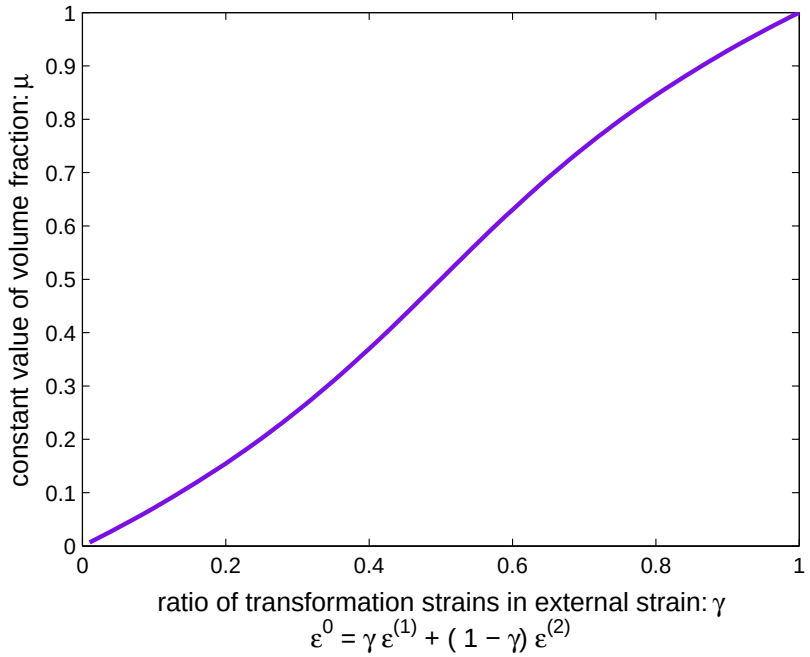

Figure A.9: Relation between the imposed external strains in terms of transformation strains of Martensitc variants in the ratio γ and the resulting volume fraction between the two variants μ. Here $\lambda = 1$

The energy content at each resulting volume fraction μ is plotted in Fig.(A.10)(a). Energy components in anisotropy and elasticity are shown in Fig.(A.10)(b).

Since we do not expect to see uniform (or homogeneous) pattern when twining Martensite is involved, These graphs will help us to filter those badly-simulated patterns, by simply checking the numerical value of the average, maximum and minimum of the volume fraction: $\langle \mu(x) \rangle$, $\max_x \mu(x)$ and $\min_x \mu(x)$, without consuming time and effect to examine the patterns graphically.

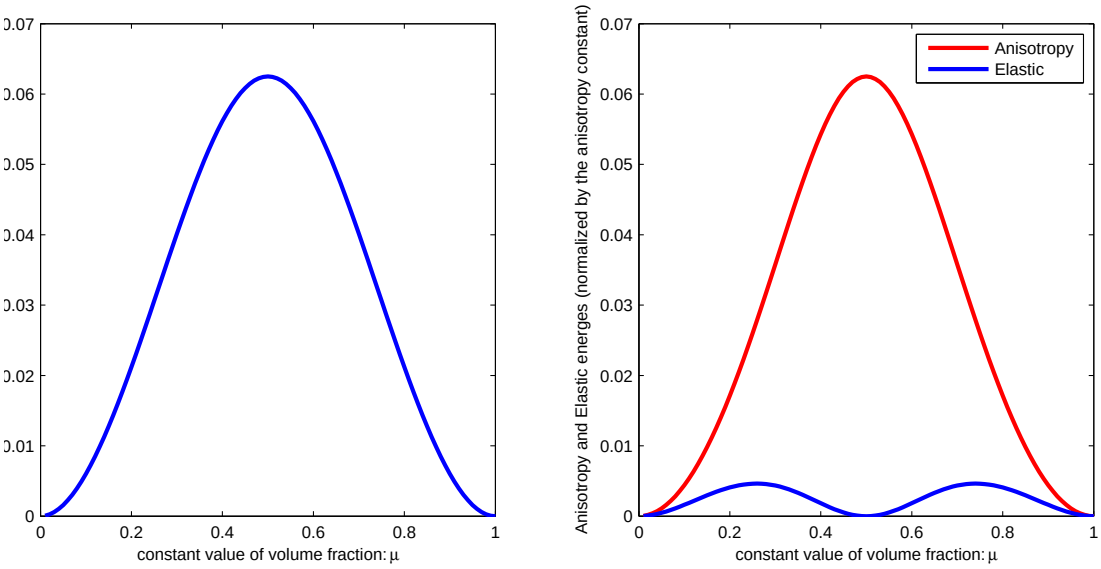

Figure A.10: Relation between the imposed external strains in terms of transformation strains of Martensitc variants in the ratio γ and the resulting volume fraction between the two variants μ. Here $\lambda = 1$

A.4 Summary and Conclusion

The phase field model is analyzed semi-analytically in one-dimensional case, which parallels with the numerical simulations. The analysis is carried out for the system under external strains and external stresses. Phase field simulations depend heavily on the parameters chosen. For this, we also purpose an easy way to filter those parameters that will yield unwanted simulated results.

Appendix B

AUSTENITE-MARTENSITE INTERFACES OF SHAPE MEMORY ALLOYS IN REAL CRYSTAL SYSTEMS

Following the deviations outlined in section (3.9), we will study the occurrences of interfaces in three common crystal systems, namely, Cubic-to-Tetragonal, Cubic-to-Orthorhombic and Cubic-to-Monoclinic-I systems.

B.1 Cubic-to-Tetragonal System

There are three Martensitic variants in this crystal system:

$$\mathbf{U}_1 = \begin{pmatrix} \beta & & \\ & \alpha & \\ & & \alpha \end{pmatrix}, \mathbf{U}_2 = \begin{pmatrix} \alpha & & \\ & \beta & \\ & & \alpha \end{pmatrix}, \mathbf{U}_3 = \begin{pmatrix} \alpha & & \\ & \alpha & \\ & & \beta \end{pmatrix}, \tag{B.1}$$

Due to geometric symmetric, we need to consider the pairs consisting of the two variants: $\mathbf{F} \equiv \mathbf{U}_1$ and $\mathbf{G} \equiv \mathbf{U}_2$.

These two variants can form twinned Martensites with two possible sets of shears and normals that describe the interfaces:

$$\mathbf{a}^+ = \frac{\sqrt{2}(\beta^2 - \alpha^2)}{\beta^2 + \alpha^2} \begin{pmatrix} -\beta \\ \alpha \\ 0 \end{pmatrix}, \mathbf{n}^+ = \frac{1}{\sqrt{2}} \begin{Bmatrix} 1 \\ 1 \\ 0 \end{Bmatrix} \tag{B.2}$$

$$\mathbf{a}^- = \frac{\sqrt{2}(\beta^2 - \alpha^2)}{\beta^2 + \alpha^2} \begin{pmatrix} -\beta \\ \alpha \\ 0 \end{pmatrix}, \mathbf{n}^- = \frac{1}{\sqrt{2}} \begin{Bmatrix} 1 \\ 1 \\ 0 \end{Bmatrix} \tag{B.3}$$

So far the ratio of each variant in the twinned structure can be arbitrary.

For the twinned Martensites make an interface with Austenite, the parameters α and β have to

satisfy one of the following sets of conditions:

$$A: \left\{ \alpha < 1 < \beta, \frac{1}{\alpha^2} + \frac{1}{\beta^2} \leq 2 \right\} \tag{B.4}$$

$$B: \left\{ \beta < 1 < \alpha, \alpha^2 + \beta^2 \leq 2 \right\} \tag{B.5}$$

Also, the volume ratio of the two Martensitic variants in the twinned Martensite is restricted by the choices of lattice parameters α and β:

$$\lambda = \frac{1}{2}\left(1 - \sqrt{1 + \frac{2(\alpha^2-1)(\beta^2-1)(\alpha^2+\beta^2)}{(\beta^2-\alpha^2)^2}}\right) \tag{B.6}$$

Due to symmetry, the ratio can also be $1-\lambda$. More explicitly,

$$1-\lambda = \frac{1}{2}\left(1 + \sqrt{1 + \frac{2(\alpha^2-1)(\beta^2-1)(\alpha^2+\beta^2)}{(\beta^2-\alpha^2)^2}}\right) \tag{B.7}$$

Before we determine the Autenite-Martensite interface, two expressions are defined for the sake of simplicity,

$$\delta \equiv \sqrt{\frac{\alpha^2+\beta^2-2}{1-\alpha^2}} \tag{B.8}$$

$$\tau \equiv \sqrt{\frac{2\alpha^2\beta^2-\alpha^2-\beta^2}{1-\alpha^2}}$$

The eight possible configuration for the AM-interfaces are outline below:

Cases (1) and (2):

MM-interface = $\{\mathbf{a}^+, \mathbf{n}^+\}$

ratio of martensitic variants = $(\lambda : 1-\lambda)$

AM-interface = $\{\mathbf{b}^\pm, \mathbf{n}^\pm\}$, where:

$$\mathbf{b}^{\pm} = \frac{1-\alpha^2}{1+\beta^2}\begin{pmatrix} \mp\frac{\delta+\tau}{2} \\ \pm\frac{\delta-\tau}{2} \\ \beta \end{pmatrix}, \mathbf{m}^{\pm} = \begin{pmatrix} \mp\frac{\delta+\tau}{2} \\ \pm\frac{\delta-\tau}{2} \\ 1 \end{pmatrix}, \tag{B.9}$$

Cases (3) and (4):

MM-interface = $\{\mathbf{a}^{+}, \mathbf{n}^{+}\}$

ratio of martensitic variants = $(1-\lambda : \lambda)$

AM-interface = $\{\mathbf{b}^{\pm}, \mathbf{n}^{\pm}\}$, where:

$$\mathbf{b}^{\pm} = \frac{1-\alpha^2}{1+\beta^2}\begin{pmatrix} \pm\frac{\delta+\tau}{2} \\ \mp\frac{\delta-\tau}{2} \\ \beta \end{pmatrix}, \mathbf{m}^{\pm} = \begin{pmatrix} \pm\frac{\delta+\tau}{2} \\ \mp\frac{\delta-\tau}{2} \\ 1 \end{pmatrix}, \tag{B.10}$$

Cases (5) and (6):

MM-interface = $\{\mathbf{a}^{-}, \mathbf{n}^{-}\}$

ratio of martensitic variants = $(1-\lambda : \lambda)$

AM-interface = $\{\mathbf{b}^{\pm}, \mathbf{n}^{\pm}\}$, where:

$$\mathbf{b}^{\pm} = \frac{1-\alpha^2}{1+\beta^2}\begin{pmatrix} \mp\frac{\delta+\tau}{2} \\ \pm\frac{\delta-\tau}{2} \\ \beta \end{pmatrix}, \mathbf{m}^{\pm} = \begin{pmatrix} \mp\frac{\delta+\tau}{2} \\ \pm\frac{\delta-\tau}{2} \\ 1 \end{pmatrix}, \tag{B.11}$$

Cases (7) and (8):

MM-interface = $\{\mathbf{a}^{-}, \mathbf{n}^{-}\}$

ratio of martensitic variants = $(1-\lambda : \lambda)$

AM-interface = $\{\mathbf{b}^{\pm}, \mathbf{n}^{\pm}\}$, where:

$$\mathbf{b}^{\pm} = \frac{1-\alpha^2}{1+\beta^2}\begin{pmatrix} \pm\frac{\delta+\tau}{2} \\ \mp\frac{\delta-\tau}{2} \\ \beta \end{pmatrix}, \mathbf{m}^{\pm} = \begin{pmatrix} \pm\frac{\delta+\tau}{2} \\ \mp\frac{\delta-\tau}{2} \\ 1 \end{pmatrix}, \tag{B.12}$$

For simulation, we consider $(In-23at.\%Tl)$, where the lattice parameters are $\alpha = 0.9889$ and $\beta = 1.0212$. Twinned Martensite always forms without any restriction. The two possible interfaces are:

$$\mathbf{a}^{+} = 0.0454\begin{pmatrix} -1.0212 \\ 0.9889 \\ 0 \end{pmatrix}, \mathbf{n}^{+} = \frac{1}{\sqrt{2}}\begin{pmatrix} 1 \\ 1 \\ 0 \end{pmatrix}, \tag{B.13}$$

$$\mathbf{a}^{-} = 0.0454\begin{pmatrix} -1.0212 \\ -0.9889 \\ 0 \end{pmatrix}, \mathbf{n}^{-} = \frac{1}{\sqrt{2}}\begin{pmatrix} 1 \\ -1 \\ 0 \end{pmatrix}, \tag{B.14}$$

For AM interface to form, these parameters satisfy condition (B). The volume ratio of the martensitic variants is $\lambda = 0.3475$, or by symmetry, $1-\lambda = 0.6525$. The eight possible configuration of AM-interfaces are outlined below:

case	MM-interface	λ	**b**	**m**
(1)	$\mathbf{a}^{+},\mathbf{n}^{+}$	0.3475	$\left(-0.0102, 2.4439\times10^{-4}, -0.0110\right)^{T}$	$(-0.9474, 0.0226, 1)^{T}$
(2)	$\mathbf{a}^{+},\mathbf{n}^{+}$	0.3475	$\left(0.0102, -2.4439\times10^{-4}, -0.0110\right)^{T}$	$(0.9474, -0.0226, 1)^{T}$
(3)	$\mathbf{a}^{+},\mathbf{n}^{+}$	0.6525	$\left(2.4439\times10^{-4}, -0.0102, -0.0110\right)^{T}$	$(0.0226, -0.9474, 1)^{T}$
(4)	$\mathbf{a}^{+},\mathbf{n}^{+}$	0.6525	$\left(-2.4439\times10^{-4}, 0.0102, -0.0110\right)^{T}$	$(-0.0226, 0.9474, 1)^{T}$
(5)	$\mathbf{a}^{-},\mathbf{n}^{-}$	0.3475	$\left(-0.0102, 2.4439\times10^{-4}, -0.0110\right)^{T}$	$(-0.9474, 0.0226, 1)^{T}$
(6)	$\mathbf{a}^{-},\mathbf{n}^{-}$	0.3475	$\left(0.0102, -2.4439\times10^{-4}, -0.0110\right)^{T}$	$(0.9474, -0.0226, 1)^{T}$
(7)	$\mathbf{a}^{-},\mathbf{n}^{-}$	0.6525	$\left(2.4439\times10^{-4}, -0.0102, -0.0110\right)^{T}$	$(0.0226, -0.9474, 1)^{T}$
(8)	$\mathbf{a}^{-},\mathbf{n}^{-}$	0.6525	$\left(-2.4439\times10^{-4}, 0.0102, -0.0110\right)^{T}$	$(-0.0226, 0.9474, 1)^{T}$

Since we impose strong periodic boundary conditions in all three directions, in order to avoid geometry incompatibility on the boundaries of the simulated domain, the transformation strains have to be re-orientated so that the pre-calculated AM-interface is pointing either in the direction $(0,1,0)^T$ or $(1,1,1)^T$. We adopt the convention, if the transformation strains of the martensitic variants are **F** and **G** respectively, then the transformation strains become $\mathbf{F}_{010}$ and $\mathbf{G}_{010}$ which give rises to AM-interface whose normal is pointing in $(0,1,0)^T$, while they become $\mathbf{F}_{111}$ and $\mathbf{G}_{111}$ which give rises to AM-interface whose normal is pointing in $(1,1,1)^T$.

The transformation strains adopted in the simulations for each case are outlined.

Case (1):

$$\mathbf{F}_{010} = \begin{pmatrix} 1.0102 & 0.0004 & -0.0153 \\ 0.0004 & 0.9889 & -0.0003 \\ -0.0153 & -0.0003 & -0.9999 \end{pmatrix}, \mathbf{G}_{010} = \begin{pmatrix} 0.9949 & -0.0096 & 0.0081 \\ -0.0096 & 1.0042 & -0.0130 \\ 0.0081 & -0.0130 & 0.9999 \end{pmatrix}, \tag{B.15}$$

$$\mathbf{F}_{111} = \begin{pmatrix} 1.0035 & 0.0020 & -0.0160 \\ 0.0020 & 0.9892 & -0.0021 \\ -0.0160 & -0.0021 & -1.0063 \end{pmatrix}, \mathbf{G}_{111} = \begin{pmatrix} 0.9890 & 0.0014 & 0.0002 \\ 0.0014 & 1.0203 & 0.0051 \\ 0.0002 & 0.0051 & 0.9897 \end{pmatrix}, \tag{B.16}$$

Case (2):

$$\mathbf{F}_{010} = \begin{pmatrix} 1.0102 & -0.0004 & -0.0153 \\ -0.0004 & 0.9889 & 0.0003 \\ -0.0153 & 0.0003 & -0.9999 \end{pmatrix}, \mathbf{G}_{010} = \begin{pmatrix} 0.9949 & 0.0096 & 0.0081 \\ 0.0096 & 1.0042 & 0.0130 \\ 0.0081 & 0.0130 & 0.9999 \end{pmatrix}, \tag{B.17}$$

$$\mathbf{F}_{111} = \begin{pmatrix} 1.0027 & 0.0015 & -0.0159 \\ 0.0015 & 0.9891 & -0.0017 \\ -0.0159 & -0.0017 & 1.0072 \end{pmatrix}, \mathbf{G}_{111} = \begin{pmatrix} 1.0071 & -0.0046 & 0.0153 \\ -0.0046 & 0.9901 & -0.0039 \\ 0.0153 & -0.0039 & 1.0018 \end{pmatrix}, \tag{B.18}$$

Case (3):

$$\mathbf{F}_{010} = \begin{pmatrix} 0.9949 & -0.0096 & 0.0081 \\ -0.0096 & 1.0042 & -0.0130 \\ 0.0081 & -0.0130 & 0.9999 \end{pmatrix}, \mathbf{G}_{010} = \begin{pmatrix} 1.0102 & 0.0004 & -0.0153 \\ 0.0004 & 0.9889 & -0.0003 \\ -1.0153 & -0.0003 & 0.9999 \end{pmatrix}, \tag{B.19}$$

$$\mathbf{F}_{111} = \begin{pmatrix} 0.9890 & 0.0014 & 0.0002 \\ 0.0014 & 1.0203 & 0.0051 \\ 0.0002 & 0.0051 & 0.9897 \end{pmatrix}, \mathbf{G}_{111} = \begin{pmatrix} 1.0035 & 0.0020 & -0.0160 \\ 0.0020 & 0.9892 & -0.0021 \\ -0.0160 & -0.0021 & 1.0063 \end{pmatrix}, \tag{B.20}$$

Case (4):

$$\mathbf{F}_{010} = \begin{pmatrix} 0.9949 & 0.0096 & 0.0081 \\ 0.0096 & 1.0042 & 0.0130 \\ 0.0081 & 0.0130 & 0.9999 \end{pmatrix}, \mathbf{G}_{010} = \begin{pmatrix} 1.0102 & -0.0004 & -0.0153 \\ -0.0004 & 0.9889 & 0.0003 \\ -1.0153 & 0.0003 & 0.9999 \end{pmatrix}, \tag{B.21}$$

$$\mathbf{F}_{111} = \begin{pmatrix} 1.0071 & -0.0046 & 0.0153 \\ -0.0046 & 0.9901 & -0.0039 \\ 0.0153 & -0.0039 & 1.0018 \end{pmatrix}, \mathbf{G}_{111} = \begin{pmatrix} 1.0027 & 0.0015 & -0.0159 \\ 0.0015 & 0.9891 & -0.0017 \\ -0.0159 & -0.0017 & 1.0072 \end{pmatrix}, \tag{B.22}$$

Case (5):

$$\mathbf{F}_{010} = \begin{pmatrix} 1.0102 & -0.0004 & -0.0153 \\ -0.0004 & 0.9889 & 0.0003 \\ -0.0153 & 0.0003 & 0.9999 \end{pmatrix}, \mathbf{G}_{010} = \begin{pmatrix} 0.9949 & 0.0096 & 0.0081 \\ 0.0096 & 1.0042 & 0.0130 \\ 0.0081 & 0.0130 & 0.9999 \end{pmatrix}, \tag{B.23}$$

$$\mathbf{F}_{111} = \begin{pmatrix} 1.0027 & 0.0015 & -0.0159 \\ 0.0015 & 0.9891 & -0.0017 \\ -0.0159 & -0.0017 & 1.0072 \end{pmatrix}, \mathbf{G}_{111} = \begin{pmatrix} 1.0071 & -0.0046 & 0.0153 \\ -0.0046 & 0.9901 & -0.0039 \\ 0.0153 & -0.0039 & 1.0018 \end{pmatrix}, \tag{B.24}$$

Case (6):

$$\mathbf{F}_{010} = \begin{pmatrix} 1.0102 & 0.0004 & -0.0153 \\ 0.0004 & 0.9889 & -0.0003 \\ -0.0153 & -0.0003 & 0.9999 \end{pmatrix}, \mathbf{G}_{010} = \begin{pmatrix} 0.9949 & -0.0096 & 0.0081 \\ -0.0096 & 1.0042 & -0.0130 \\ 0.0081 & -0.0130 & 0.9999 \end{pmatrix}, \tag{B.25}$$

$$\mathbf{F}_{111} = \begin{pmatrix} 1.0035 & 0.0020 & -0.0160 \\ 0.0020 & 0.9892 & -0.0021 \\ -0.0160 & -0.0021 & 1.0063 \end{pmatrix}, \mathbf{G}_{111} = \begin{pmatrix} 0.9890 & 0.0014 & 0.0002 \\ 0.0014 & 1.0203 & 0.0051 \\ 0.0002 & 0.0051 & 0.9897 \end{pmatrix}, \tag{B.26}$$

Case (7):

$$\mathbf{F}_{010} = \begin{pmatrix} 0.9949 & 0.0096 & -0.0081 \\ 0.0096 & 1.0042 & -0.0130 \\ -0.0081 & -0.0130 & 0.9999 \end{pmatrix}, \mathbf{G}_{010} = \begin{pmatrix} 1.0102 & -0.0004 & 0.0153 \\ -0.0004 & 0.9889 & -0.0003 \\ 0.0153 & -0.0003 & 0.9999 \end{pmatrix}, \tag{B.27}$$

$$\mathbf{F}_{111} = \begin{pmatrix} 1.0071 & 0.0153 & -0.0046 \\ 0.0153 & 1.0018 & -0.0039 \\ -0.0046 & -0.0039 & 0.9901 \end{pmatrix}, \mathbf{G}_{111} = \begin{pmatrix} 1.0027 & -0.0159 & 0.0015 \\ -0.0159 & 1.0072 & -0.0017 \\ 0.0015 & -0.0017 & 0.9891 \end{pmatrix}, \tag{B.28}$$

Case (8):

$$\mathbf{F}_{010} = \begin{pmatrix} 0.9949 & -0.0096 & -0.0081 \\ -0.0096 & 1.0042 & 0.0130 \\ -0.0081 & 0.0130 & 0.9999 \end{pmatrix}, \mathbf{G}_{010} = \begin{pmatrix} 1.0102 & 0.0004 & 0.0153 \\ 0.0004 & 0.9889 & 0.0003 \\ 0.0153 & 0.0003 & 0.9999 \end{pmatrix}, \tag{B.29}$$

$$\mathbf{F}_{111} = \begin{pmatrix} 0.9890 & 0.0002 & 0.0014 \\ 0.0002 & 0.9897 & 0.0051 \\ 0.0014 & 0.0051 & 1.0203 \end{pmatrix}, \mathbf{G}_{111} = \begin{pmatrix} 1.0035 & -0.0160 & 0.0020 \\ -0.0160 & 1.0063 & -0.0021 \\ 0.0020 & -0.0021 & 0.9892 \end{pmatrix}, \tag{B.30}$$

Furthermore, these outlined transformation strains are expressed in finite strain representation.

In the simulation, these transformation strains are expressed in linearized infinitesimal strain representation. This can be done easily by substraction of 3-by-3 identity matrix. More explicitly,

$$\varepsilon_i = \mathbf{U}_i - \mathbf{I} \tag{B.31}$$

B.1.1 Simulation

We attempt to simulate micro-structures of autenite-Martensite and martenite-Martensite interfaces in each of the eight cases. As previously implemented, all simulations start from random pattern and the iteration continues until convergence is reached. The visualizations are shown in figures (B.1) and (B.1).

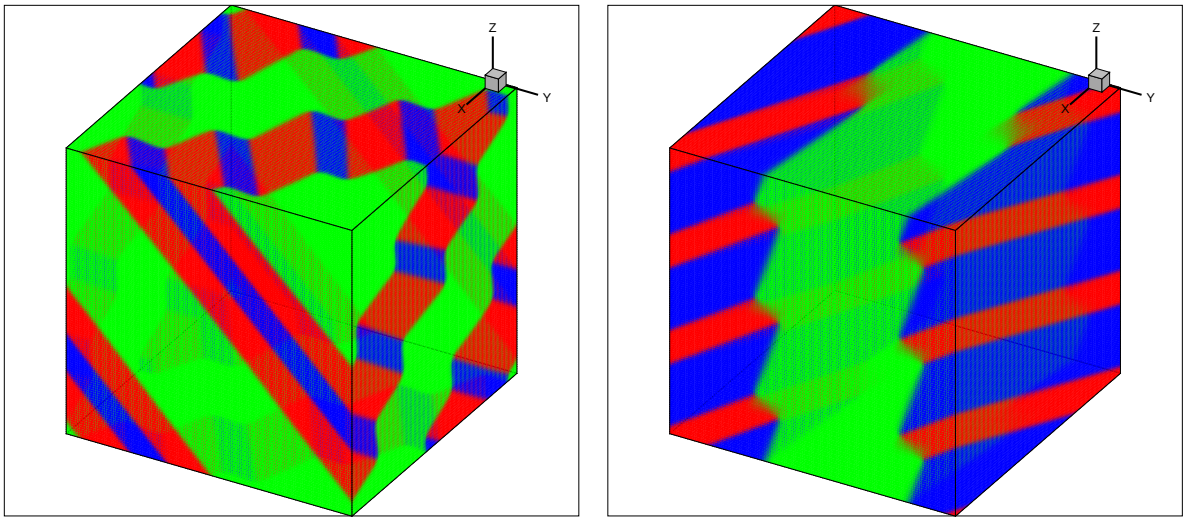

(a) Case (1)

(b) Case (2)

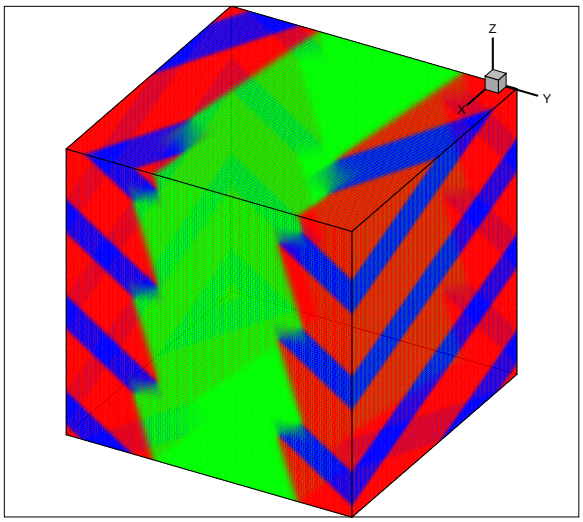

(c) Case (3)

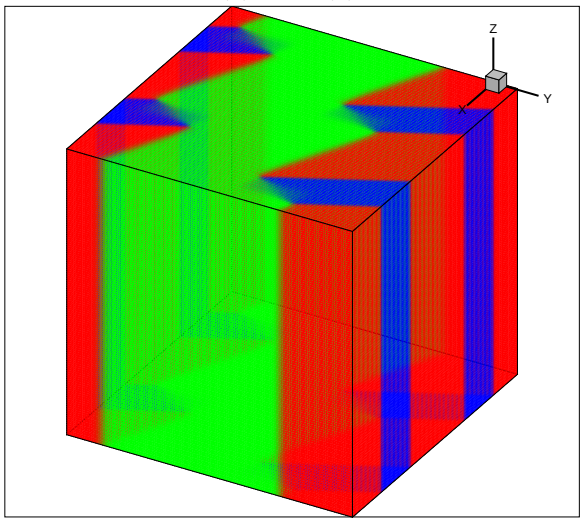

(d) Case (4)

Figure B.1: Simulated micro-structures in tetragonal system: Cases (1) - (4).

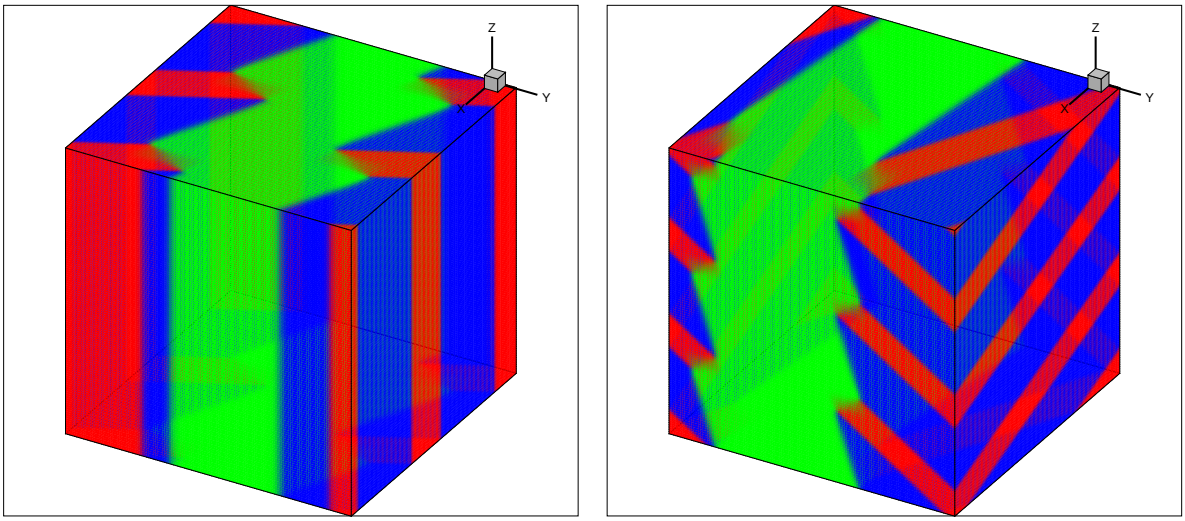

(a) Case (5)

(b) Case (6)

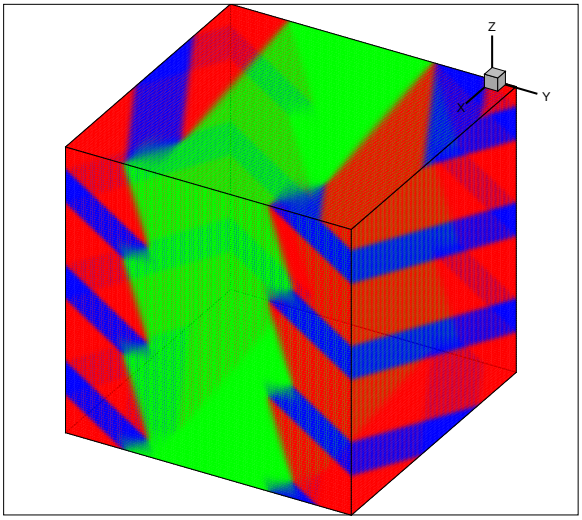

(c) Case (7)

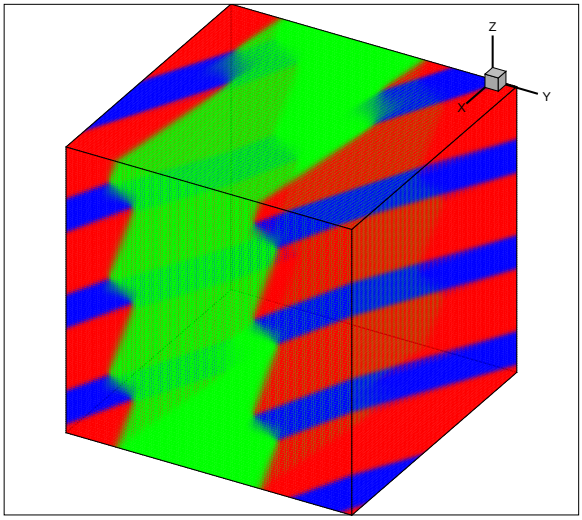

(d) Case (8)

Figure B.2: Simulated micro-structures in tetragonal system: Cases (5) - (8).

B.2 Cubic-to-Orthorhombic System

There are six variants of Martensites for this system:

$$\mathbf{U}_1 = \begin{pmatrix} \frac{\alpha+\gamma}{2} & 0 & \frac{\alpha-\gamma}{2} \\ 0 & \beta & 0 \\ \frac{\alpha-\gamma}{2} & 0 & \frac{\alpha+\gamma}{2} \end{pmatrix}, \mathbf{U}_2 = \begin{pmatrix} \frac{\alpha+\gamma}{2} & 0 & -\frac{\alpha-\gamma}{2} \\ 0 & \beta & 0 \\ -\frac{\alpha-\gamma}{2} & 0 & \frac{\alpha+\gamma}{2} \end{pmatrix}, \mathbf{U}_3 = \begin{pmatrix} \frac{\alpha+\gamma}{2} & \frac{\alpha-\gamma}{2} & 0 \\ \frac{\alpha-\gamma}{2} & \frac{\alpha+\gamma}{2} & 0 \\ 0 & 0 & \beta \end{pmatrix},$$
$$\mathbf{U}_4 = \begin{pmatrix} \frac{\alpha+\gamma}{2} & -\frac{\alpha-\gamma}{2} & 0 \\ -\frac{\alpha-\gamma}{2} & \frac{\alpha+\gamma}{2} & 0 \\ 0 & 0 & \beta \end{pmatrix}, \mathbf{U}_5 = \begin{pmatrix} \beta & 0 & 0 \\ 0 & \frac{\alpha+\gamma}{2} & \frac{\alpha-\gamma}{2} \\ 0 & \frac{\alpha-\gamma}{2} & \frac{\alpha+\gamma}{2} \end{pmatrix}, \mathbf{U}_6 = \begin{pmatrix} \beta & 0 & 0 \\ 0 & \frac{\alpha+\gamma}{2} & -\frac{\alpha-\gamma}{2} \\ 0 & -\frac{\alpha-\gamma}{2} & \frac{\alpha+\gamma}{2} \end{pmatrix}. \tag{B.32}$$

Since there can be many possible pairings of these variants to form interfaces with auteniste.As expected from the symmetry in the matrix representation of these variants, all the pairings of Martensites exhibits similar patterns in interfaces. In the following, we demonstrate two representative pairings, namely compound twin and type-I-type-II twin. The table below shows a summary all possible pairing with type of interfaces they are forming.

	$\mathbf{U}_1$	$\mathbf{U}_2$	$\mathbf{U}_3$	$\mathbf{U}_4$	$\mathbf{U}_5$	$\mathbf{U}_6$
$\mathbf{U}_1$		C	I/II	I/II	I/II	I/II
$\mathbf{U}_2$	C		I/II	I/II	I/II	I/II
$\mathbf{U}_3$	I/II	I/II		C	I/II	I/II
$\mathbf{U}_4$	I/II	I/II	C		I/II	I/II
$\mathbf{U}_5$	I/II	I/II	I/II	I/II		C
$\mathbf{U}_6$	I/II	I/II	I/II	I/II	C	

(B.33)

B.2.1 Compound Twin of Variant 1 and Variant 2

Using equation(3.36), variant 1 and variant 2 form a compound twin with two possible interfaces:

$$\mathbf{a}^{+} = \frac{\gamma^2-\alpha^2}{\gamma^2+\alpha^2}\begin{pmatrix}\alpha-\gamma\\0\\\alpha+\gamma\end{pmatrix}, \mathbf{n}^{+} = \begin{pmatrix}1\\0\\0\end{pmatrix}$$
$$\mathbf{a}^{-} = -\frac{\gamma^2-\alpha^2}{\gamma^2+\alpha^2}\begin{pmatrix}\alpha+\gamma\\0\\\alpha-\gamma\end{pmatrix}, \mathbf{n}^{-} = \begin{pmatrix}0\\0\\1\end{pmatrix} \tag{B.34}$$

Austenite-Martensite interface exists if equation (3.37) is satisfied. The resulting equation is almost impossible to solve for the lattice parameters that yield compatible interfaces. For instance, the first inequality in (3.37) generate the following inequality with high order of polynomials in numerator and denominator.

$$\delta \equiv \frac{\delta_{1,num}}{\delta_{1,den}} \leq 2, \tag{B.35}$$

where $\delta_{1,num}$ and $\delta_{1,den}$ are the numerator and denominator of δ_1:

$$\begin{aligned}\delta_{1,num} &= 3\alpha^4\beta^4 - 4\alpha^4\beta^2\gamma^2 - \alpha^4\beta^2 + 4\alpha^4\gamma^4 - 2\alpha^4\gamma^2 \\ &\quad - 2\alpha^2\beta^4\gamma^2 - 2\alpha^2\beta^4 - 4\alpha^2\beta^2\gamma^4 + 10\alpha^2\beta^2\gamma^2 - 2\alpha^2\gamma^4 \\ &\quad + 3\beta^4\gamma^4 - 2\beta^4\gamma^2 - \beta^2\gamma^4 \\ \delta_{1,den} &= 4(\alpha^2-1)(\beta^2-1)(\gamma^2-1)(\alpha^2\beta^2 + 2\alpha^2\gamma^2 + \beta^2\gamma^2)\end{aligned} \tag{B.36}$$

In fact, according to Bhattacharya [2], no real material will satisfy these conditions. We may still study the interfaces with an artificial sets of parameters that satisfy the conditions (3.37) for

Austenite-Martensite interface.

$$\begin{aligned} \alpha &= 0.99 \\ \beta &= 0.98 \\ \gamma &= 1.02 \end{aligned} \tag{B.37}$$

Using (3.36), two possible Martensite-Martensite interfaces exist:

$$\begin{aligned} \mathbf{n}_1 &= \begin{pmatrix} 0 \\ 0 \\ 1 \end{pmatrix}, \mathbf{a}_1 = \begin{pmatrix} 0.06 \\ 0 \\ -0.0009 \end{pmatrix} \\ \mathbf{n}_2 &= \begin{pmatrix} -1 \\ 0 \\ 0 \end{pmatrix}, \mathbf{a}_2 = \begin{pmatrix} 0.0009 \\ 0 \\ -0.06 \end{pmatrix} \end{aligned} \tag{B.38}$$

For twinned Martensites consisting of these variants to form further interface with Austenite, the martensitic variants have to be in the ratio specified by λ or $1-\lambda$, where $\lambda = 0.3368$ or $\lambda = 0.6632$.

As discussed in previous subsection, there are eight possible sets of Austenite-Martensite interfaces. The combinations of shear and normal vectors of the interfaces will be summarized in the following:

case	MM-interface	λ	**b**	**m**
(1)	$\mathbf{a}^+, \mathbf{n}^+$	0.3368	$(-0.0121, 0.0246, 0.0117)^T$	$(-0.4158, -0.8172, 0.3991)^T$
(2)	$\mathbf{a}^+, \mathbf{n}^+$	0.3368	$(0.0121, 0.0246, -0.0117)^T$	$(0.4158, -0.8172, -0.3991)^T$
(3)	$\mathbf{a}^+, \mathbf{n}^+$	0.6632	$(0.0121, -0.0246, 0.0117)^T$	$(0.4158, 0.8172, 0.3991)^T$
(4)	$\mathbf{a}^+, \mathbf{n}^+$	0.6632	$(-0.0121, -0.0246, -0.0117)^T$	$(-0.4158, 0.8172, -0.3991)^T$
(5)	$\mathbf{a}^-, \mathbf{n}^-$	0.3368	$(-0.0117, 0.0246, 0.0121)^T$	$(-0.3991, -0.8172, 0.4158)^T$
(6)	$\mathbf{a}^-, \mathbf{n}^-$	0.3368	$(0.0117, 0.0246, -0.0121)^T$	$(0.3991, -0.8172, -0.4158)^T$
(7)	$\mathbf{a}^-, \mathbf{n}^-$	0.6632	$(0.0117, -0.0246, 0.0121)^T$	$(0.3991, 0.8172, 0.4158)^T$
(8)	$\mathbf{a}^-, \mathbf{n}^-$	0.6632	$(-0.0117, -0.0246, -0.0121)^T$	$(-0.3991, 0.8172, -0.4158)^T$

Before the transformation strains of the martensitic variants are put to simulation, because of imposed periodic conditions and the resulting geometric compatibility, the matrices representing these transformation strains are re-orientated so that the re-orientated normal vector of the Austenite-Martensite interface is pointing either in $(0,1,0)^T$ or $(1,1,1)^T$. The transformation strains adopted in the simulations for each case are outlined:

Case (1):

$$\mathbf{F}_{010} = \begin{pmatrix} 1.0307 & 0.0307 & 0.0446 \\ 0.0307 & 0.9739 & -0.0426 \\ 0.0446 & -0.0426 & 0.9981 \end{pmatrix}, \mathbf{G}_{010} = \begin{pmatrix} 1.0100 & 0.0411 & 0.0180 \\ 0.0411 & 0.9946 & -0.0590 \\ 0.0180 & -0.0590 & 0.9981 \end{pmatrix}, \quad \text{(B.39)}$$

$$\mathbf{F}_{111} = \begin{pmatrix} 1.0407 & -0.0201 & -0.0033 \\ -0.0201 & 1.0416 & -0.0171 \\ -0.0033 & -0.0171 & 0.9205 \end{pmatrix}, \mathbf{G}_{111} = \begin{pmatrix} 1.0436 & 0.0182 & -0.0091 \\ 0.0182 & 1.0381 & -0.0185 \\ -0.0091 & -0.0185 & 0.9210 \end{pmatrix}, \quad \text{(B.40)}$$

Case (2):

$$\mathbf{F}_{010} = \begin{pmatrix} 1.0307 & -0.0307 & 0.0446 \\ -0.0307 & 0.9739 & 0.0426 \\ 0.0446 & 0.0426 & 0.9981 \end{pmatrix}, \mathbf{G}_{010} = \begin{pmatrix} 1.0100 & -0.0411 & 0.0180 \\ -0.0411 & 0.9946 & 0.0590 \\ 0.0180 & 0.0590 & 0.9981 \end{pmatrix}, \quad \text{(B.41)}$$

$$\mathbf{F}_{111} = \begin{pmatrix} 0.9829 & -0.0693 & 0.0170 \\ -0.0693 & 1.0009 & 0.0118 \\ 0.0170 & 0.0118 & 1.0190 \end{pmatrix}, \mathbf{G}_{111} = \begin{pmatrix} 0.9661 & -0.0493 & 0.0197 \\ -0.0493 & 0.9805 & 0.0202 \\ 0.0197 & 0.0202 & 1.0560 \end{pmatrix}, \quad \text{(B.42)}$$

Case (3):

$$\mathbf{F}_{010} = \begin{pmatrix} 1.0100 & 0.0411 & 0.0180 \\ 0.0411 & 0.9946 & -0.0590 \\ 0.0180 & -0.0590 & 0.9981 \end{pmatrix}, \mathbf{G}_{010} = \begin{pmatrix} 1.0307 & 0.0307 & 0.0446 \\ 0.0307 & 0.9739 & -0.0426 \\ 0.0446 & -0.0426 & 0.9981 \end{pmatrix}, \quad \text{(B.43)}$$

$$\mathbf{F}_{111} = \begin{pmatrix} 1.0436 & 0.0182 & -0.0091 \\ 0.0182 & 1.0381 & -0.0185 \\ -0.0091 & -0.0185 & 0.9210 \end{pmatrix}, \mathbf{G}_{111} = \begin{pmatrix} 1.0407 & -0.0201 & -0.0033 \\ -0.0201 & 1.0416 & -0.0171 \\ -0.0033 & -0.0171 & 0.9205 \end{pmatrix}, \quad \text{(B.44)}$$

Case (4):

$$\mathbf{F}_{010} = \begin{pmatrix} 1.0100 & -0.0411 & 0.0180 \\ -0.0411 & 0.9946 & 0.0590 \\ 0.0180 & 0.0590 & 0.9981 \end{pmatrix}, \mathbf{G}_{010} = \begin{pmatrix} 1.0307 & -0.0307 & 0.0446 \\ -0.0307 & 0.9739 & 0.0426 \\ 0.0446 & 0.0426 & 0.9981 \end{pmatrix}, \quad \text{(B.45)}$$

$$\mathbf{F}_{111} = \begin{pmatrix} 0.9661 & -0.0493 & 0.0197 \\ -0.0493 & 0.9805 & 0.0202 \\ 0.0197 & 0.0202 & 1.0560 \end{pmatrix}, \mathbf{G}_{111} = \begin{pmatrix} 0.9829 & -0.0693 & 0.0170 \\ -0.0693 & 1.0009 & 0.0118 \\ 0.0170 & 0.0118 & 1.0190 \end{pmatrix}, \quad \text{(B.46)}$$

Case (5):

$$\mathbf{F}_{010} = \begin{pmatrix} 1.0307 & 0.0307 & -0.0446 \\ 0.0307 & 0.9739 & 0.0426 \\ -0.0446 & 0.0426 & 0.9981 \end{pmatrix}, \mathbf{G}_{010} = \begin{pmatrix} 1.0100 & 0.0411 & -0.0180 \\ 0.0411 & 0.9946 & 0.0590 \\ -0.0180 & 0.0590 & 0.9981 \end{pmatrix}, \quad \text{(B.47)}$$

$$\mathbf{F}_{111} = \begin{pmatrix} 1.0407 & -0.0033 & -0.0201 \\ -0.0033 & 0.9205 & -0.0171 \\ -0.0201 & -0.0171 & 1.0416 \end{pmatrix}, \mathbf{G}_{111} = \begin{pmatrix} 1.0436 & -0.0091 & 0.0182 \\ -0.0091 & 0.9210 & -0.0185 \\ 0.0182 & -0.0185 & 1.0381 \end{pmatrix}, \quad \text{(B.48)}$$

Case (6):

$$\mathbf{F}_{010} = \begin{pmatrix} 1.0307 & -0.0307 & -0.0446 \\ -0.0307 & 0.9739 & -0.0426 \\ -0.0446 & -0.0426 & 0.9981 \end{pmatrix}, \mathbf{G}_{010} = \begin{pmatrix} 1.0100 & -0.0411 & -0.0180 \\ -0.0411 & 0.9946 & -0.0590 \\ -0.0180 & -0.0590 & 0.9981 \end{pmatrix}, \quad \text{(B.49)}$$

$$\mathbf{F}_{111} = \begin{pmatrix} 0.9829 & 0.0170 & -0.0693 \\ 0.0170 & 1.0190 & 0.0118 \\ -0.0693 & 0.0118 & 1.0009 \end{pmatrix}, \mathbf{G}_{111} = \begin{pmatrix} 0.9661 & 0.0197 & -0.0493 \\ 0.0197 & 1.0560 & 0.0202 \\ -0.0493 & 0.0202 & 0.9805 \end{pmatrix}, \quad \text{(B.50)}$$

Case (7):

$$\mathbf{F}_{010} = \begin{pmatrix} 1.0100 & -0.0411 & -0.0180 \\ -0.0411 & 0.9946 & -0.0590 \\ -0.0180 & -0.0590 & 0.9981 \end{pmatrix}, \mathbf{G}_{010} = \begin{pmatrix} 1.0307 & -0.0307 & -0.0446 \\ -0.0307 & 0.9739 & -0.0426 \\ -0.0446 & -0.0426 & 0.9981 \end{pmatrix}, \quad \text{(B.51)}$$

$$\mathbf{F}_{111} = \begin{pmatrix} 0.9661 & 0.0197 & -0.0493 \\ 0.0197 & 1.0560 & 0.0202 \\ -0.0493 & 0.0202 & 0.9805 \end{pmatrix}, \mathbf{G}_{111} = \begin{pmatrix} 0.9829 & 0.0170 & -0.0693 \\ 0.0170 & 1.0190 & 0.0118 \\ -0.0693 & 0.0118 & 1.0009 \end{pmatrix}, \quad \text{(B.52)}$$

Case (8):

$$\mathbf{F}_{010} = \begin{pmatrix} 1.0100 & 0.0411 & -0.0180 \\ 0.0411 & 0.9946 & 0.0590 \\ -0.0180 & 0.0590 & 0.9981 \end{pmatrix}, \mathbf{G}_{010} = \begin{pmatrix} 1.0307 & 0.0307 & -0.0446 \\ 0.0307 & 0.9739 & 0.0426 \\ -0.0446 & 0.0426 & 0.9981 \end{pmatrix}, \quad \text{(B.53)}$$

$$\mathbf{F}_{111} = \begin{pmatrix} 1.0436 & -0.0091 & 0.0182 \\ -0.0091 & 0.9210 & -0.0185 \\ 0.0182 & -0.0185 & 1.0381 \end{pmatrix}, \mathbf{G}_{111} = \begin{pmatrix} 1.0407 & -0.0033 & -0.0201 \\ -0.0033 & 0.9205 & -0.0171 \\ -0.0201 & -0.0171 & 1.0416 \end{pmatrix}, \quad \text{(B.54)}$$

The simulated micro-structures are shown in figures. (B.3) and (B.4). Unfortunately no desirable micro-structure for case (1) can be simulated.

B.2.2 Type-I / Type-II Twin of Variant 1 and Variant 3

This result is due to Mallard [2]. Variant 1 (denoted by $\mathbf{F} = \mathbf{U}_1$) and variant 3 (denoted by $\mathbf{G} = \mathbf{U}_3$) are related crystallographically by a 180^0-rotation about the axis $\widehat{\mathbf{e}} = \frac{1}{\sqrt{2}} \begin{pmatrix} 0 \\ 1 \\ 1 \end{pmatrix}$, or equivalently, $\mathbf{F}^T\mathbf{F} = \mathbf{R}^T\mathbf{G}^T\mathbf{G}\mathbf{R}$ and $\mathbf{F}^T\mathbf{F} = \mathbf{G}^T\mathbf{G}$, where $\mathbf{R}$ is the rotation matrix about the axis $\widehat{\mathbf{e}}$ about 180^0. These variants form one type-I twin and one type-II twin. The interfaces are computed by:

$$\mathbf{a}^+ = 2\left(\frac{\mathbf{G}^{-T}\widehat{\mathbf{e}}}{|\mathbf{G}^{-T}\widehat{\mathbf{e}}|^2} - \mathbf{G}\widehat{\mathbf{e}}\right), \mathbf{n}^+ = \widehat{\mathbf{e}} \quad \text{(B.55)}$$

$$\mathbf{a}^- = \rho\mathbf{G}\widehat{\mathbf{e}}, \mathbf{n}^- = \frac{2}{\rho}\left(\widehat{\mathbf{e}} - \frac{\mathbf{G}^T\mathbf{G}\widehat{\mathbf{e}}}{|\mathbf{G}\widehat{\mathbf{e}}|^2}\right), \quad \text{(B.56)}$$

where $\rho \neq 0$ is so chosen to make $|\mathbf{n}| = 1$.

More explicitly, these vectors expressed in crystal lattice parameters are:

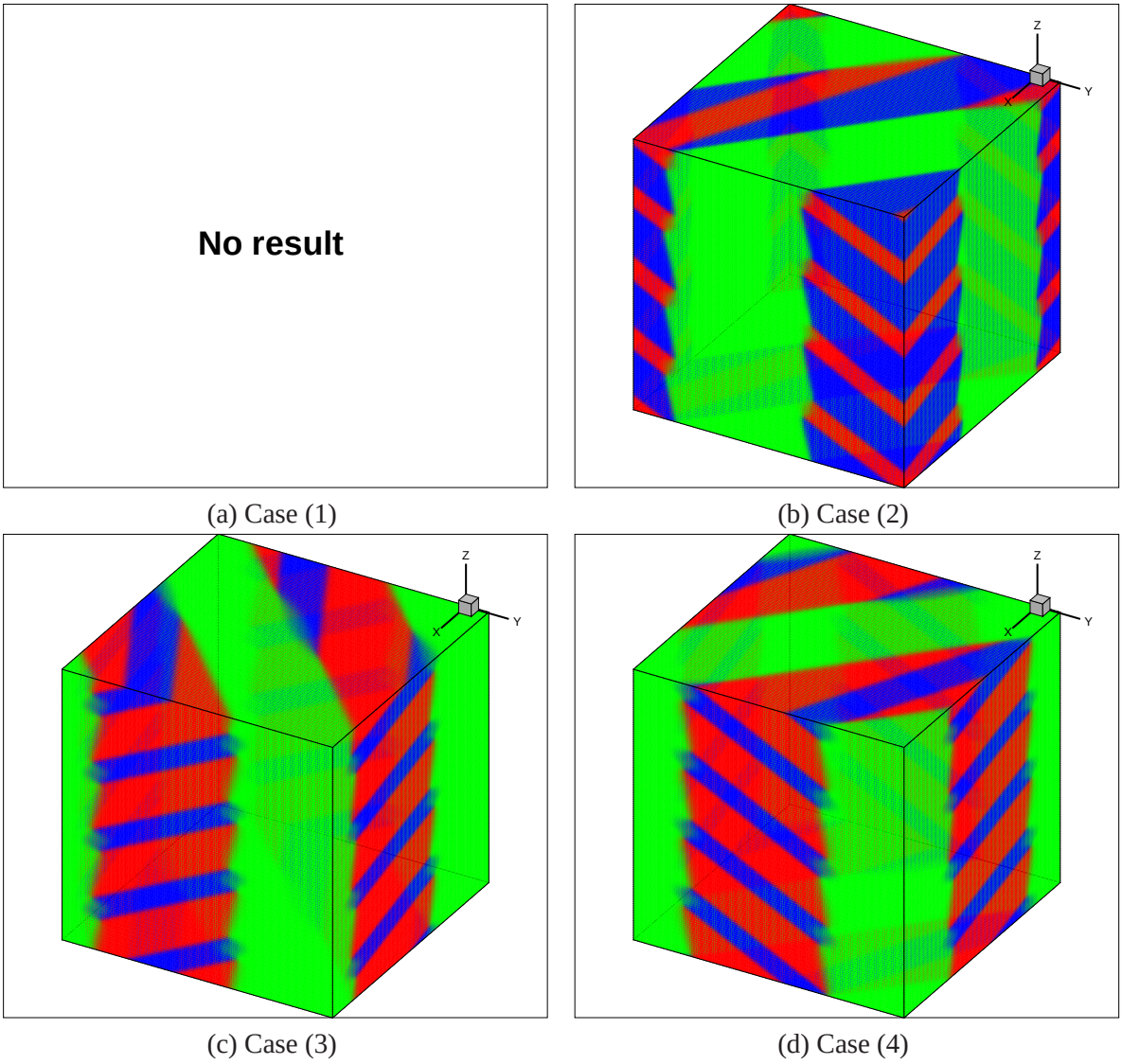

(a) Case (1)

(b) Case (2)

(c) Case (3)

(d) Case (4)

Figure B.3: Simulated micro-structures in orthorhombic system involving variants 1 and 2: Cases (1) - (4).

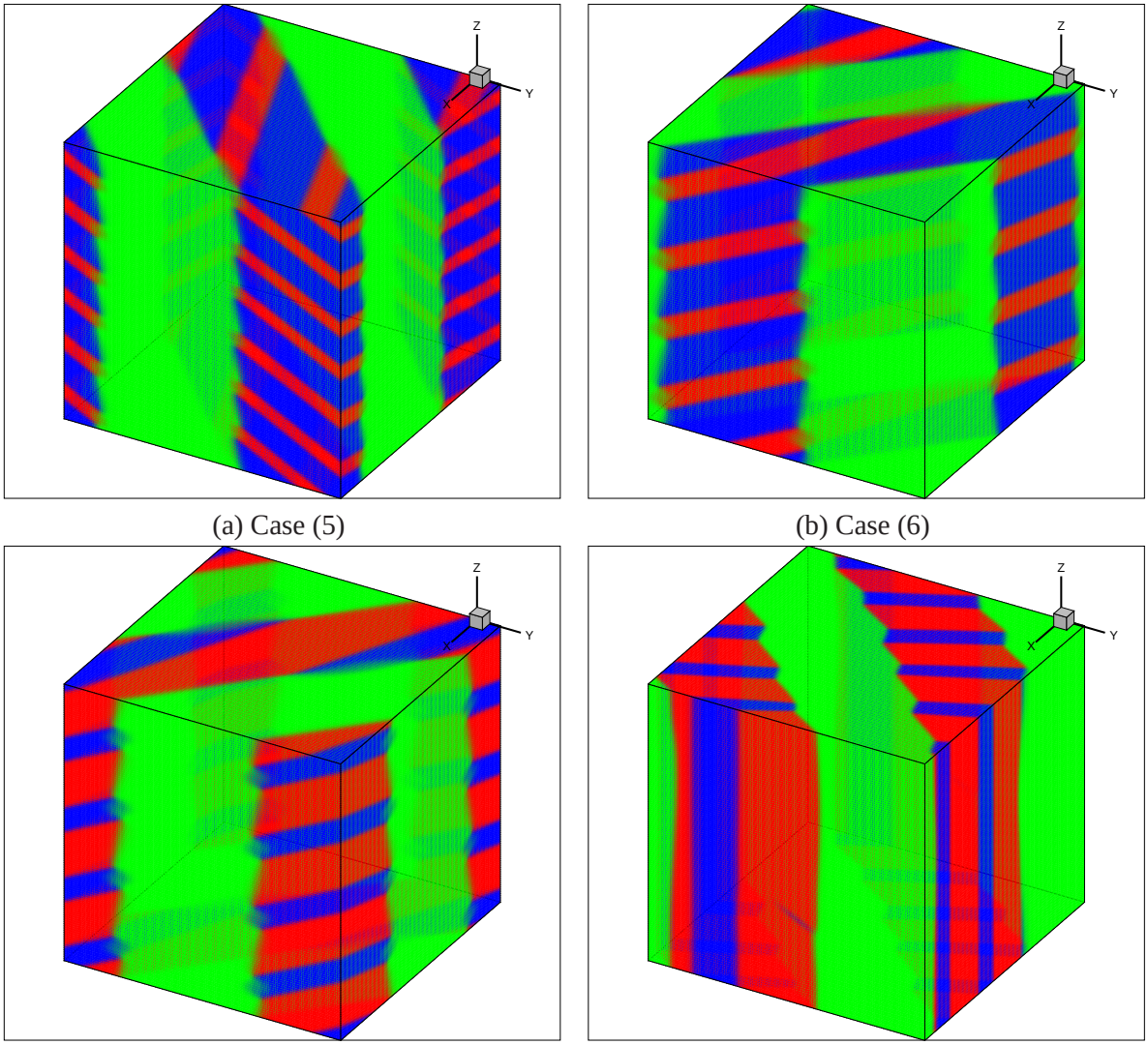

(a) Case (5) (b) Case (6)

(c) Case (7) (d) Case (8)

Figure B.4: Simulated micro-structures in orthorhombic system involving variants 1 and 2: Cases (5) - (8).

$$
\mathbf{a}^{+} = \begin{pmatrix} \frac{-(\alpha-\gamma)\left(\sqrt{2}\alpha\gamma(\alpha+\gamma)^2\beta^2+8\sqrt{2}\alpha^2\beta^2\gamma^2+4\sqrt{2}\alpha\gamma\alpha^2\gamma^2+\sqrt{2}\alpha\gamma\beta^2(\alpha-\gamma)^2\right)}{4\alpha\gamma((\alpha+\gamma)^2\beta^2+4\alpha^2\gamma^2+\beta^2(\alpha-\gamma)^2)} \\ \frac{-(\alpha+\gamma)\left(\sqrt{2}\alpha\gamma(\alpha+\gamma)^2\beta^2-8\sqrt{2}\alpha^2\beta^2\gamma^2+4\sqrt{2}\alpha\gamma\alpha^2\gamma^2+\sqrt{2}\alpha\gamma\beta^2(\alpha-\gamma)^2\right)}{4\alpha\gamma((\alpha+\gamma)^2\beta^2+4\alpha^2\gamma^2+\beta^2(\alpha-\gamma)^2)} \\ \frac{-\left(\sqrt{2}\beta^4(\alpha+\gamma)^2+\sqrt{2}\beta^4(\alpha-\gamma)^2-4\sqrt{2}\alpha^2\beta^2\gamma^2\right)}{2\beta((\alpha+\gamma)^2\beta^2+4\alpha^2\gamma^2+\beta^2(\alpha-\gamma)^2)} \end{pmatrix}
$$

$$
\mathbf{a}^{-} = \rho \begin{pmatrix} \frac{\sqrt{2}}{4}(\alpha-\gamma) \\ \frac{\sqrt{2}}{4}(\alpha+\gamma) \\ \frac{\sqrt{2}}{2}\beta \end{pmatrix}
$$

$$
\mathbf{n}^{-} = \frac{2}{\rho} \begin{pmatrix} \frac{-\sqrt{2}(\alpha^2-\gamma^2)}{\alpha^2+\gamma^2+2\beta^2} \\ -\frac{\sqrt{2}}{2}\frac{\alpha^2+\gamma^2-2\beta^2}{\alpha^2+\gamma^2+2\beta^2} \\ \frac{\sqrt{2}}{2}\frac{\alpha^2+\gamma^2-2\beta^2}{\alpha^2+\gamma^2+2\beta^2} \end{pmatrix}, \tag{B.57}
$$

where we choose ρ so that $|\mathbf{n}^{-}| = 1$, or,

$$
\begin{aligned}
\frac{2}{\rho}\frac{\sqrt{2(\alpha^2-\gamma^2)^2+2\times\frac{1}{2}(\alpha^2+\gamma^2-2\beta^2)^2}}{\alpha^2+\gamma^2+2\beta^2} &= 1 \\
\frac{2}{\rho}\frac{\sqrt{3\alpha^4-4\alpha^2\beta^2-2\alpha^2\gamma^2+4\beta^4-4\beta^2\gamma^2+3\gamma^4}}{\alpha^2+\gamma^2+2\beta^2} &= 1 \\
2\frac{\sqrt{3\alpha^4-4\alpha^2\beta^2-2\alpha^2\gamma^2+4\beta^4-4\beta^2\gamma^2+3\gamma^4}}{\alpha^2+\gamma^2+2\beta^2} &= \rho
\end{aligned} \tag{B.58}
$$

The two Martensite variants will form interface with Austenite if (3.37) holds. For instance, *CuAlNi*, where $\alpha = 1.0619$, $\beta = 0.9178$ and $\gamma = 1.0230$, satisfies the condition. With these numer-

ical crystal parameters, the two possible sets of shear and normal vectors are:

$$\mathbf{a}^{+} = \begin{pmatrix} 0.0515 \\ 0.1637 \\ 0.1869 \end{pmatrix}, \mathbf{n}^{+} = \frac{1}{\sqrt{2}} \begin{pmatrix} 0 \\ 1 \\ -1 \end{pmatrix},$$
$$\mathbf{a}^{-} = \begin{pmatrix} 0.0036 \\ -0.1691 \\ 0.1921 \end{pmatrix}, \mathbf{n}^{-} = \begin{pmatrix} -0.2282 \\ -0.6885 \\ -0.6885 \end{pmatrix}, \tag{B.59}$$

where $\{\mathbf{a}^{+}, \mathbf{n}^{+}\}$ is a Type-I twin and $\{\mathbf{a}^{-}, \mathbf{n}^{-}\}$ is a Type-II twin.

Equation (3.38) applied to each of these twins further confirm the volume ratio of martenitic variants in the twinned structure. For type-I twin, $\lambda = 0.2902$, while for type-II twin, $\lambda = 0.3008$.

With equation (3.39), we may compute the shear and normal vectors of the Austenite-Martensite interface. The eight possible cases are summarized as follow:

case	MM-interface	λ	**b**	**m**
(1)	$\mathbf{a}^{+}, \mathbf{n}^{+}$	0.2902	$(0.0656, -0.0657, 0.0239)^T$	$(0.6350, 0.7486, 0.1908)^T$
(2)	$\mathbf{a}^{+}, \mathbf{n}^{+}$	0.2902	$(-0.0576, -0.0748, -0.0171)^T$	$(-0.7151, 0.6497, -0.2579)^T$
(3)	$\mathbf{a}^{+}, \mathbf{n}^{+}$	0.7098	$(0.0576, 0.0171, 0.0748)^T$	$(0.7151, 0.2579, -0.6497)^T$
(4)	$\mathbf{a}^{+}, \mathbf{n}^{+}$	0.7098	$(-0.0656, -0.0239, 0.0657)^T$	$(-0.6350, -0.1908, -0.7486)^T$
(5)	$\mathbf{a}^{-}, \mathbf{n}^{-}$	0.3008	$(0.0559, 0.0707, 0.0237)^T$	$(0.7304, -0.6679, 0.1430)^T$
(6)	$\mathbf{a}^{-}, \mathbf{n}^{-}$	0.3008	$(-0.0653, 0.0654, -0.0122)^T$	$(-0.6345, -0.7276, -0.2607)^T$
(7)	$\mathbf{a}^{-}, \mathbf{n}^{-}$	0.6992	$(0.0559, 0.0237, 0.0707)^T$	$(0.7304, 0.1430, -0.6679)^T$
(8)	$\mathbf{a}^{-}, \mathbf{n}^{-}$	0.6992	$(-0.0653, -0.0122, 0.0654)^T$	$(-0.6345, -0.2607, -0.7276)^T$

Before the transformation strains of the martensitic variants are put to simulation, because of imposed periodic conditions and the resulting geometric compatibility, the matrices representing these transformation strains are re-orientated so that the re-orientated normal vector of the Austenite-Martensite interface is pointing either in $(0,1,0)^T$ or $(1,1,1)^T$. The transformation strains adopted in the simulations for each case are outlined:

Case (1):

$$\mathbf{F}_{010}=\begin{pmatrix}0.9473 & 0.0218 & -0.0430\\ 0.0218 & 1.0564 & 0.0161\\ -0.0430 & 0.0161 & 0.9989\end{pmatrix},\mathbf{G}_{010}=\begin{pmatrix}1.0264 & -0.0533 & 0.0179\\ -0.0533 & 0.9773 & 0.0422\\ 0.0179 & 0.0422 & 0.9989\end{pmatrix}, \quad \text{(B.60)}$$

$$\mathbf{F}_{111}=\begin{pmatrix}1.0043 & 0.0597 & 0.0233\\ 0.0597 & 0.9613 & 0.0003\\ 0.0233 & 0.0003 & 1.0372\end{pmatrix},\mathbf{G}_{111}=\begin{pmatrix}0.9598 & -0.0565 & -0.0014\\ -0.0565 & 0.9973 & 0.0225\\ -0.0014 & 0.0225 & 1.0456\end{pmatrix}, \quad \text{(B.61)}$$

Case (2):

$$\mathbf{F}_{010}=\begin{pmatrix}0.9891 & -0.0204 & 0.0684\\ -0.0204 & 1.0161 & 0.0166\\ 0.0684 & 0.0166 & 0.9975\end{pmatrix},\mathbf{G}_{010}=\begin{pmatrix}1.0082 & -0.0238 & -0.0284\\ -0.0238 & 0.9970 & -0.0644\\ -0.0284 & -0.0644 & 0.9975\end{pmatrix}, \quad \text{(B.62)}$$

$$\mathbf{F}_{111}=\begin{pmatrix}0.9789 & -0.0421 & 0.0504\\ -0.0421 & 1.0379 & 0.0144\\ 0.0504 & 0.0144 & 0.9860\end{pmatrix},\mathbf{G}_{111}=\begin{pmatrix}0.9820 & 0.0333 & -0.0520\\ 0.0333 & 1.0465 & 0.0128\\ -0.0520 & 0.0128 & 0.9742\end{pmatrix}, \quad \text{(B.63)}$$

Case (3):

$$\mathbf{F}_{010}=\begin{pmatrix}1.0082 & -0.0238 & -0.0284\\ -0.0238 & 0.9970 & -0.0644\\ -0.0284 & -0.0644 & 0.9975\end{pmatrix},\mathbf{G}_{010}=\begin{pmatrix}0.9891 & -0.0204 & 0.0684\\ -0.0204 & 1.0161 & 0.0166\\ 0.0684 & 0.0166 & 0.9975\end{pmatrix}, \quad \text{(B.64)}$$

$$\mathbf{F}_{111}=\begin{pmatrix}0.9820 & 0.0333 & -0.0520\\ 0.0333 & 1.0465 & 0.0128\\ -0.0520 & 0.0128 & 0.9742\end{pmatrix},\mathbf{G}_{111}=\begin{pmatrix}0.9789 & -0.0421 & 0.0504\\ -0.0421 & 1.0379 & 0.0144\\ 0.0504 & 0.0144 & 0.9860\end{pmatrix}, \quad \text{(B.65)}$$

Case (4):

$$\mathbf{F}_{010} = \begin{pmatrix} 1.0264 & -0.0533 & 0.0179 \\ -0.0533 & 0.9773 & 0.0422 \\ 0.0179 & 0.0422 & 0.9989 \end{pmatrix}, \mathbf{G}_{010} = \begin{pmatrix} 0.9473 & 0.0218 & -0.0430 \\ 0.0218 & 1.0564 & 0.0161 \\ -0.0430 & 0.0161 & 0.9989 \end{pmatrix}, \quad \text{(B.66)}$$

$$\mathbf{F}_{111} = \begin{pmatrix} 0.9598 & -0.0565 & -0.0014 \\ -0.0565 & 0.9973 & 0.0225 \\ -0.0014 & 0.0225 & 1.0456 \end{pmatrix}, \mathbf{G}_{111} = \begin{pmatrix} 1.0043 & 0.0597 & 0.0233 \\ 0.0597 & 0.9613 & 0.0003 \\ 0.0233 & 0.0003 & 1.0372 \end{pmatrix}, \quad \text{(B.67)}$$

Case (5):

$$\mathbf{F}_{010} = \begin{pmatrix} 0.9517 & 0.0327 & 0.0416 \\ 0.0327 & 1.0519 & -0.0158 \\ 0.0416 & -0.0158 & 0.9990 \end{pmatrix}, \mathbf{G}_{010} = \begin{pmatrix} 1.0224 & 0.0064 & -0.0174 \\ 0.0064 & 0.9829 & 0.0694 \\ -0.0174 & 0.0694 & 0.9974 \end{pmatrix}, \quad \text{(B.68)}$$

$$\mathbf{F}_{111} = \begin{pmatrix} 1.0160 & 0.0235 & 0.0587 \\ 0.0235 & 1.0302 & -0.0057 \\ 0.0587 & -0.0057 & 0.9565 \end{pmatrix}, \mathbf{G}_{111} = \begin{pmatrix} 1.0153 & -0.0299 & 0.0067 \\ -0.0299 & 0.9270 & -0.0037 \\ 0.0067 & -0.0037 & 1.0604 \end{pmatrix}, \quad \text{(B.69)}$$

Case (6):

$$\mathbf{F}_{010} = \begin{pmatrix} 0.9843 & -0.0098 & -0.0706 \\ -0.0098 & 1.0209 & -0.0113 \\ -0.0706 & -0.0113 & 0.9974 \end{pmatrix}, \mathbf{G}_{010} = \begin{pmatrix} 1.0128 & 0.0588 & 0.0308 \\ 0.0588 & 0.9909 & -0.0320 \\ 0.0308 & -0.0320 & 0.9990 \end{pmatrix}, \quad \text{(B.70)}$$

$$\mathbf{F}_{111} = \begin{pmatrix} 0.9873 & 0.0553 & -0.0355 \\ 0.0553 & 0.9762 & 0.0103 \\ -0.0355 & 0.0103 & 1.0393 \end{pmatrix}, \mathbf{G}_{111} = \begin{pmatrix} 1.0609 & 0.0018 & 0.0113 \\ 0.0018 & 1.0148 & -0.0281 \\ 0.0113 & -0.0281 & 0.9269 \end{pmatrix}, \quad \text{(B.71)}$$

Case (7):

$$\mathbf{F}_{010} = \begin{pmatrix} 1.0128 & -0.0588 & 0.0308 \\ -0.0588 & 0.9909 & 0.0320 \\ 0.0308 & 0.0320 & 0.9990 \end{pmatrix}, \mathbf{G}_{010} = \begin{pmatrix} 0.9843 & 0.0098 & -0.0706 \\ 0.0098 & 1.0209 & 0.0113 \\ -0.0706 & 0.0113 & 0.9974 \end{pmatrix}, \quad \text{(B.72)}$$

$$\mathbf{F}_{111} = \begin{pmatrix} 0.9500 & -0.0520 & 0.0097 \\ -0.0520 & 1.0180 & 0.0273 \\ 0.0097 & 0.0273 & 1.0347 \end{pmatrix}, \mathbf{G}_{111} = \begin{pmatrix} 1.0058 & 0.0507 & -0.0216 \\ 0.0507 & 0.9484 & 0.0010 \\ -0.0216 & 0.0010 & 1.0485 \end{pmatrix}, \quad \text{(B.73)}$$

Case (8):

$$\mathbf{F}_{010} = \begin{pmatrix} 1.0224 & -0.0064 & -0.0174 \\ -0.0064 & 0.9829 & -0.0694 \\ -0.0174 & -0.0694 & 0.9974 \end{pmatrix}, \mathbf{G}_{010} = \begin{pmatrix} 0.9517 & -0.0327 & 0.0416 \\ -0.0327 & 1.0519 & 0.0158 \\ 0.0416 & 0.0158 & 0.9990 \end{pmatrix}, \quad \text{(B.74)}$$

$$\mathbf{F}_{111} = \begin{pmatrix} 1.0031 & 0.0237 & -0.0530 \\ 0.0237 & 1.0464 & 0.0023 \\ -0.0530 & 0.0023 & 0.9532 \end{pmatrix}, \mathbf{G}_{111} = \begin{pmatrix} 0.9543 & -0.0047 & 0.0561 \\ -0.0047 & 1.0353 & 0.0252 \\ 0.0561 & 0.0252 & 1.0131 \end{pmatrix}, \quad \text{(B.75)}$$

The simulated micro-structures are shown in figures. (B.5) and (B.6). Unfortunately no desirable micro-structure for case (2) can be simulated.

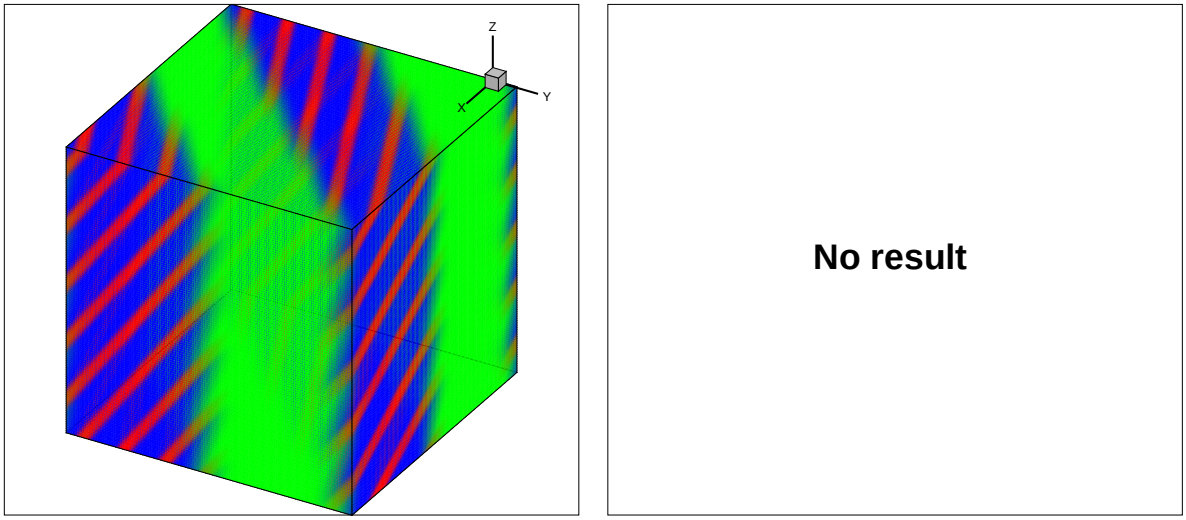

(a) Case (1)

(b) Case (2)

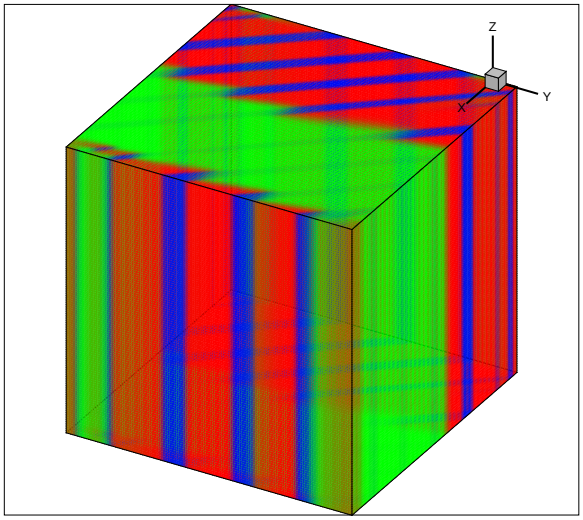

(c) Case (3)

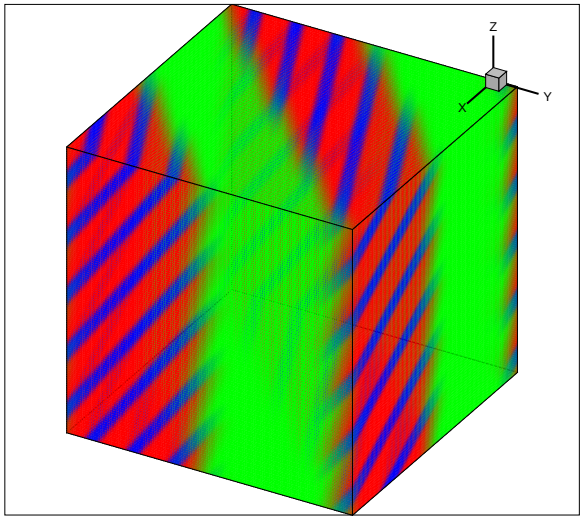

(d) Case (4)

Figure B.5: Simulated micro-structures in orthorhombic system involving variants 1 an 3: Cases (1) - (4).

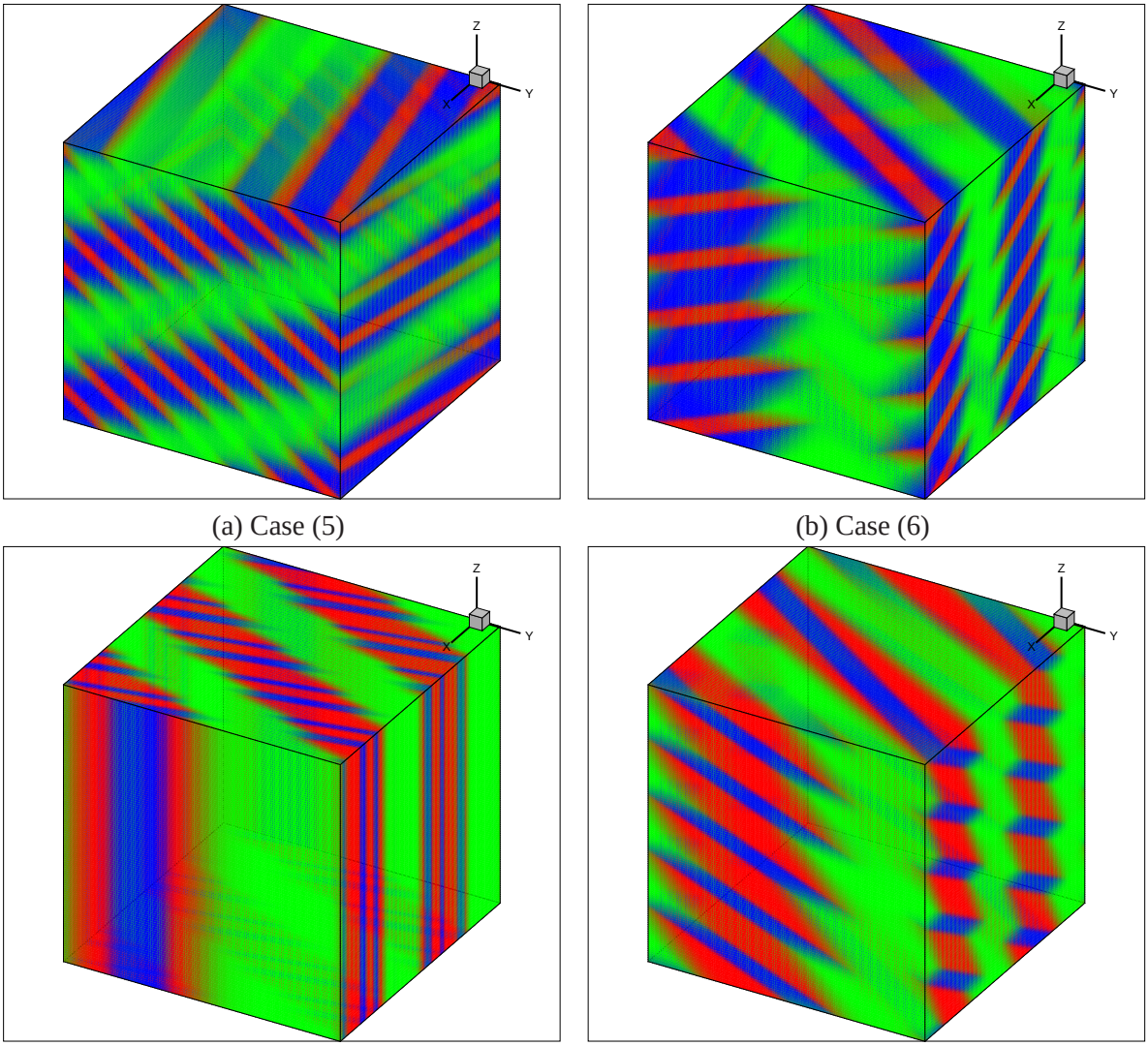

(a) Case (5)

(b) Case (6)

(c) Case (7)

(d) Case (8)

Figure B.6: Simulated micro-structures in orthorhombic system involving variants 1 an 3: Cases (5) - (8).

B.3 Cubic-to-Monoclinic-I System

The twelve Martensite variants are quantified by their transformation strains:

$$\mathbf{U}_1 = \begin{pmatrix} \gamma & \varepsilon & \varepsilon \\ \varepsilon & \alpha & \delta \\ \varepsilon & \delta & \alpha \end{pmatrix}, \mathbf{U}_2 = \begin{pmatrix} \gamma & -\varepsilon & -\varepsilon \\ -\varepsilon & \alpha & \delta \\ -\varepsilon & \delta & \alpha \end{pmatrix},$$

$$\mathbf{U}_3 = \begin{pmatrix} \gamma & -\varepsilon & \varepsilon \\ -\varepsilon & \alpha & -\delta \\ \varepsilon & -\delta & \alpha \end{pmatrix}, \mathbf{U}_4 = \begin{pmatrix} \gamma & -\varepsilon & -\varepsilon \\ \varepsilon & \alpha & -\delta \\ -\varepsilon & -\delta & \alpha \end{pmatrix},$$

$$\mathbf{U}_5 = \begin{pmatrix} \alpha & \varepsilon & \delta \\ \varepsilon & \gamma & \varepsilon \\ \delta & \varepsilon & \alpha \end{pmatrix}, \mathbf{U}_6 = \begin{pmatrix} \alpha & -\varepsilon & \delta \\ -\varepsilon & \gamma & -\varepsilon \\ \delta & -\varepsilon & \alpha \end{pmatrix},$$

$$\mathbf{U}_7 = \begin{pmatrix} \alpha & -\varepsilon & -\delta \\ -\varepsilon & \gamma & \varepsilon \\ -\delta & \varepsilon & \alpha \end{pmatrix}, \mathbf{U}_8 = \begin{pmatrix} \alpha & \varepsilon & -\delta \\ \varepsilon & \gamma & -\varepsilon \\ -\delta & -\varepsilon & \alpha \end{pmatrix},$$

$$\mathbf{U}_9 = \begin{pmatrix} \alpha & \delta & \varepsilon \\ \delta & \alpha & \varepsilon \\ \varepsilon & \varepsilon & \gamma \end{pmatrix}, \mathbf{U}_{10} = \begin{pmatrix} \alpha & \delta & -\varepsilon \\ \delta & \alpha & -\varepsilon \\ -\varepsilon & -\varepsilon & \gamma \end{pmatrix},$$

$$\mathbf{U}_{11} = \begin{pmatrix} \alpha & -\delta & \varepsilon \\ -\delta & \alpha & -\varepsilon \\ \varepsilon & -\varepsilon & \gamma \end{pmatrix}, \mathbf{U}_{12} = \begin{pmatrix} \alpha & -\delta & -\varepsilon \\ -\delta & \alpha & \varepsilon \\ -\varepsilon & \varepsilon & \gamma \end{pmatrix},$$

Two examples of materials in this crystals are *TiNi* and *CuZr*. Their lattice parameters are:

	α	γ	δ	ε
NiTi	1.0243	0.9563	0.058	-0.0427
CuZr	1.0348	1.0229	0.1067	-0.0929

(B.76)

Four classes (referred as modes) of micro-structures can be generated by pairing two of the

martensitic variants. They are named as modes A, B, C and D. Not all of them can form Austenite-Martensite interfaces. Each of these four classes will be studied in the following subsections.

B.3.1 Mode A: Variant 1 and Variant 2

These two variants can twin with two possible martenite-Martensite interfaces. Their shear and normal vectors are computed by (3.36):

$$\begin{aligned}
\mathbf{a}_1 &= \begin{pmatrix} 0.2564 \\ -0.0115 \\ -0.0115 \end{pmatrix}, \mathbf{n}_1 = \begin{pmatrix} 0 \\ \frac{1}{\sqrt{2}} \\ \frac{1}{\sqrt{2}} \end{pmatrix}, \\
\mathbf{a}_2 &= \begin{pmatrix} 0.0127 \\ -0.1604 \\ -0.1604 \end{pmatrix}, \mathbf{n}_2 = \begin{pmatrix} -1 \\ 0 \\ 0 \end{pmatrix},
\end{aligned} \tag{B.77}$$

No (numerical) solution can be found in solving (3.37). Thus no Austenite-Martensite interface can be formed with variants 1 and 2. The transformation strains of these variants can be specified by any volume ratio.

For simulation, we do not need to re-orientate the transformation strains to adjust the normal to point in good direction, as the expected micro-stricture appears to be simpler.

B.3.2 Mode B: Variant 1 and Variant 3

According to equation (3.36), these two martensitic variants form one type-I twin and one type-II twin. The interfaces are quantified by the shear and normal vectors:

$$\begin{aligned}
\mathbf{a}_1 &= \begin{pmatrix} -0.1710 \\ 0.0197 \\ 0.2273 \end{pmatrix}, \mathbf{n}_1 = \begin{pmatrix} 0 \\ -1 \\ 0 \end{pmatrix}, \\
\mathbf{a}_2 &= \begin{pmatrix} -0.0120 \\ 0.2890 \\ 0.0164 \end{pmatrix}, \mathbf{n}_2 = \begin{pmatrix} 0.5851 \\ 0 \\ -0.8109 \end{pmatrix},
\end{aligned} \tag{B.78}$$

Conditions (3.37) are satisfied. So an Austenite-Martensite interface exists. Equation (3.38) gives the ratio of martensitic variants and equation (3.39), the normal and shear vectors of the Austenite-Martensite interfaces are computed. The eight possible sets of micro-structure are summarized below:

case	MM-interface	λ	**b**	**m**
(1)	$\mathbf{a}^+, \mathbf{n}^+$	0.2918	$(-0.1211, 0.0397, 0.0256)^T$	$(0.3462, 0.4335, 0.8320)^T$
(2)	$\mathbf{a}^+, \mathbf{n}^+$	0.2918	$(-0.0527, -0.0536, -0.1061)^T$	$(0.9088, -0.3332, -0.2512)^T$
(3)	$\mathbf{a}^+, \mathbf{n}^+$	0.7082	$(0.0527, -0.0536, 0.1061)^T$	$(-0.9088, -0.3332, 0.2512)^T$
(4)	$\mathbf{a}^+, \mathbf{n}^+$	0.7082	$(0.1211, 0.0397, -0.0256)^T$	$(-0.3462, 0.4335, -0.8320)^T$
(5)	$\mathbf{a}^-, \mathbf{n}^-$	0.2708	$(-0.1196, 0.0485, 0.0216)^T$	$(0.3759, 0.5137, 0.7712)^T$
(6)	$\mathbf{a}^-, \mathbf{n}^-$	0.2708	$(-0.0568, -0.0638, -0.0991)^T$	$(0.8890, -0.4012, -0.2152)^T$
(7)	$\mathbf{a}^-, \mathbf{n}^-$	0.7292	$(0.0568, -0.0638, 0.0991)^T$	$(-0.8890, -0.4012, 0.2152)^T$
(8)	$\mathbf{a}^-, \mathbf{n}^-$	0.7292	$(0.1196, 0.0485, -0.0216)^T$	$(-0.3759, 0.5137, -0.7712)^T$

Before simulation, the transformation strains of the martensitic variants are re-orientated so as to give rise to Austenite-Martensite interface pointing in computationally compatible directions. They are outlined below:

Case (1):

$$\mathbf{F}_{010} = \begin{pmatrix} 1.0457 & 0.0074 & 0.0791 \\ 0.0074 & 0.9625 & 0.0221 \\ 0.0791 & 0.0221 & 0.9966 \end{pmatrix}, \mathbf{G}_{010} = \begin{pmatrix} 0.9877 & -0.0389 & -0.0321 \\ -0.0389 & 1.0206 & 0.0756 \\ -0.0321 & 0.0756 & 0.9966 \end{pmatrix}, \quad \text{(B.79)}$$

$$\mathbf{F}_{111} = \begin{pmatrix} 1.0250 & -0.0807 & 0.0287 \\ -0.0807 & 1.0176 & -0.0067 \\ 0.0287 & -0.0067 & 0.9623 \end{pmatrix}, \mathbf{G}_{111} = \begin{pmatrix} 0.9619 & -0.0105 & 0.0141 \\ -0.0105 & 0.9412 & 0.0249 \\ 0.0141 & 0.0249 & 1.1017 \end{pmatrix}, \quad \text{(B.80)}$$

Case (2):

$$\mathbf{F}_{010} = \begin{pmatrix} 1.0553 & -0.0311 & 0.0600 \\ -0.0311 & 0.9521 & -0.0362 \\ 0.0600 & -0.0362 & 0.9975 \end{pmatrix}, \mathbf{G}_{010} = \begin{pmatrix} 0.9842 & 0.0570 & -0.0240 \\ 0.0570 & 1.0232 & -0.0658 \\ -0.0240 & -0.0658 & 0.9975 \end{pmatrix}, \tag{B.81}$$

$$\mathbf{F}_{111} = \begin{pmatrix} 0.9916 & -0.0616 & -0.0219 \\ -0.0616 & 1.0708 & 0.0091 \\ -0.0219 & 0.0091 & 0.9425 \end{pmatrix}, \mathbf{G}_{111} = \begin{pmatrix} 1.0509 & 0.0672 & -0.0143 \\ 0.0672 & 1.0169 & -0.0205 \\ -0.0143 & -0.0205 & 0.9371 \end{pmatrix}, \tag{B.82}$$

Case (3):

$$\mathbf{F}_{010} = \begin{pmatrix} 0.9842 & 0.0570 & -0.0240 \\ 0.0570 & 1.0232 & -0.0658 \\ -0.0240 & -0.0658 & 0.9975 \end{pmatrix}, \mathbf{G}_{010} = \begin{pmatrix} 1.0553 & -0.0311 & 0.0600 \\ -0.0311 & 0.9521 & -0.0362 \\ 0.0600 & -0.0362 & 0.9975 \end{pmatrix}, \tag{B.83}$$

$$\mathbf{F}_{111} = \begin{pmatrix} 1.0509 & 0.0672 & -0.0143 \\ 0.0672 & 1.0169 & -0.0205 \\ -0.0143 & -0.0205 & 0.9371 \end{pmatrix}, \mathbf{G}_{111} = \begin{pmatrix} 0.9916 & -0.0616 & -0.0219 \\ -0.0616 & 1.0708 & 0.0091 \\ -0.0219 & 0.0091 & 0.9425 \end{pmatrix}, \tag{B.84}$$

Case (4):

$$\mathbf{F}_{010} = \begin{pmatrix} 0.9877 & -0.0389 & -0.0321 \\ -0.0389 & 1.0206 & 0.0756 \\ -0.0321 & 0.0756 & 0.9966 \end{pmatrix}, \mathbf{G}_{010} = \begin{pmatrix} 1.0457 & 0.0074 & 0.0791 \\ 0.0074 & 0.9625 & 0.0221 \\ 0.0791 & 0.0221 & 0.9966 \end{pmatrix}, \quad \text{(B.85)}$$

$$\mathbf{F}_{111} = \begin{pmatrix} 0.9619 & -0.0105 & 0.0141 \\ -0.0105 & 0.9412 & 0.0249 \\ 0.0141 & 0.0249 & 1.1017 \end{pmatrix}, \mathbf{G}_{111} = \begin{pmatrix} 1.0250 & -0.0807 & 0.0287 \\ -0.0807 & 1.0176 & -0.0067 \\ 0.0287 & -0.0067 & 0.9623 \end{pmatrix}, \quad \text{(B.86)}$$

Case (5):

$$\mathbf{F}_{010} = \begin{pmatrix} 1.0477 & -0.0110 & -0.0803 \\ -0.0110 & 0.9605 & -0.0080 \\ -0.0803 & -0.0080 & 0.9967 \end{pmatrix}, \mathbf{G}_{010} = \begin{pmatrix} 0.9875 & -0.0658 & 0.0288 \\ -0.0658 & 1.0194 & -0.0559 \\ 0.0288 & -0.0559 & 0.9980 \end{pmatrix}, \quad \text{(B.87)}$$

$$\mathbf{F}_{111} = \begin{pmatrix} 1.0082 & 0.0179 & -0.0813 \\ 0.0179 & 0.9585 & 0.0016 \\ -0.0813 & 0.0016 & 1.0382 \end{pmatrix}, \mathbf{G}_{111} = \begin{pmatrix} 0.9360 & 0.0013 & -0.0110 \\ 0.0013 & 1.0967 & 0.0364 \\ -0.0110 & 0.0364 & 0.9722 \end{pmatrix}, \quad \text{(B.88)}$$

Case (6):

$$\mathbf{F}_{010} = \begin{pmatrix} 1.0608 & 0.0361 & -0.0626 \\ 0.0361 & 0.9461 & -0.0057 \\ -0.0626 & -0.0057 & 0.9980 \end{pmatrix}, \mathbf{G}_{010} = \begin{pmatrix} 0.9805 & 0.0383 & 0.0227 \\ 0.0383 & 1.0277 & 0.0774 \\ 0.0227 & 0.0774 & 0.9967 \end{pmatrix}, \quad \text{(B.89)}$$

$$\mathbf{F}_{111} = \begin{pmatrix} 1.0566 & 0.0088 & -0.0682 \\ 0.0088 & 0.9427 & -0.0239 \\ -0.0682 & -0.0239 & 1.0056 \end{pmatrix}, \mathbf{G}_{111} = \begin{pmatrix} 1.0323 & -0.0200 & 0.0695 \\ -0.0200 & 0.9362 & -0.0105 \\ 0.0695 & -0.0105 & 1.0364 \end{pmatrix}, \quad \text{(B.90)}$$

Case (7):

$$\mathbf{F}_{010} = \begin{pmatrix} 0.9805 & -0.0383 & 0.0227 \\ -0.0383 & 1.0277 & -0.0774 \\ 0.0227 & -0.0774 & 0.9967 \end{pmatrix}, \mathbf{G}_{010} = \begin{pmatrix} 1.0608 & -0.0361 & -0.0626 \\ -0.0361 & 0.9461 & 0.0057 \\ -0.0626 & 0.0057 & 0.9980 \end{pmatrix}, \tag{B.91}$$

$$\mathbf{F}_{111} = \begin{pmatrix} 0.9601 & 0.0252 & -0.0118 \\ 0.0252 & 1.0987 & 0.0257 \\ -0.0118 & 0.0257 & 0.9461 \end{pmatrix}, \mathbf{G}_{111} = \begin{pmatrix} 0.9885 & -0.0129 & -0.0805 \\ -0.0129 & 0.9674 & 0.0102 \\ -0.0805 & 0.0102 & 1.0490 \end{pmatrix}, \tag{B.92}$$

Case (8):

$$\mathbf{F}_{010} = \begin{pmatrix} 0.9875 & 0.0658 & 0.0288 \\ 0.0658 & 1.0194 & 0.0559 \\ 0.0288 & 0.0559 & 0.9980 \end{pmatrix}, \mathbf{G}_{010} = \begin{pmatrix} 1.0477 & 0.0110 & -0.0803 \\ 0.0110 & 0.9605 & 0.0080 \\ -0.0803 & 0.0080 & 0.9967 \end{pmatrix}, \tag{B.93}$$

$$\mathbf{F}_{111} = \begin{pmatrix} 1.0602 & -0.0133 & 0.0656 \\ -0.0133 & 0.9434 & -0.0257 \\ 0.0656 & -0.0257 & 1.0013 \end{pmatrix}, \mathbf{G}_{111} = \begin{pmatrix} 1.0290 & 0.0166 & -0.0696 \\ 0.0166 & 0.9350 & -0.0088 \\ -0.0696 & -0.0088 & 1.0408 \end{pmatrix}, \tag{B.94}$$

The simulated micro-structures are shown in figure. (B.7). Unfortunately the simulated patterns are desirable. Only three of them are shown.

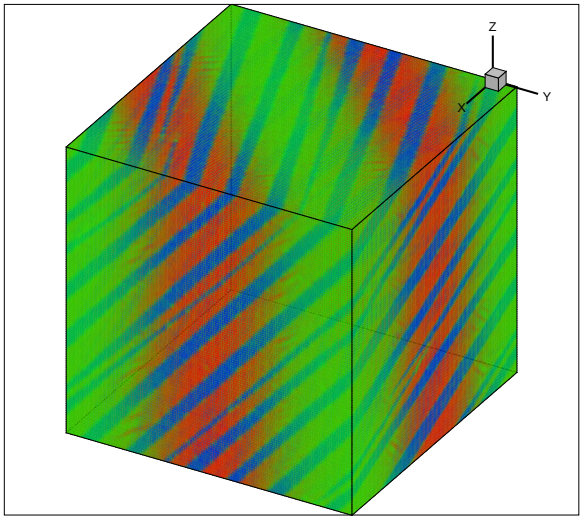

(a) Case (3)

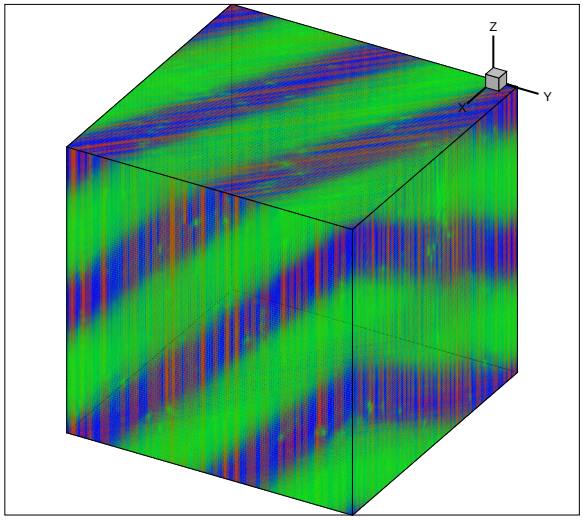

(b) Case (6)

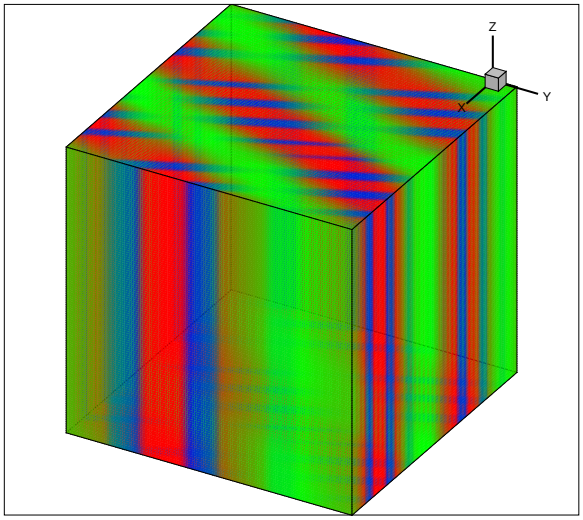

(c) Case (8)

Figure B.7: Simulated micro-structures in monoclinic-I system involving variants 1 an 2: Cases (3) (6) (8).

B.3.3 Mode C: Variant 1 and Variant 5

According to equation (3.36), these two martensitic variants form one type-I twin and one type-II twin. The interfaces are quantified by the shear and normal vectors:

$$\mathbf{a}_1 = \begin{pmatrix} -0.2131 \\ 0.2276 \\ 0.0215 \end{pmatrix}, \mathbf{n}_1 = \begin{pmatrix} -0.2975 \\ -0.2975 \\ -0.9072 \end{pmatrix},$$
$$\mathbf{a}_2 = \begin{pmatrix} 0.0814 \\ 0.1161 \\ 0.2836 \end{pmatrix}, \mathbf{n}_2 = \begin{pmatrix} 0.7071 \\ -0.7071 \\ 0 \end{pmatrix}, \tag{B.95}$$

No (numerical) solution can be found in solving (3.37). Thus no Austenite-Martensite interface can be formed with variants 1 and 2. The transformation strains of these variants can be specified by any volume ratio.

For simulation, we do not need to re-orientate the transformation strains to adjust the normal to point in good direction, as the expected micro-stricture appears to be simpler.

Conditions (3.37) are satisfied. So an Austenite-Martensite interface exists. Equation (3.38) gives the ratio of martensitic variants and equation (3.39), the normal and shear vectors of the Austenite-Martensite interfaces are computed. The eight possible sets of micro-structure are summarized below:

case	MM-interface	λ	**b**	**m**
(1)	$\mathbf{a}^+, \mathbf{n}^+$	0.3231	$(0.0278, 0.1008, 0.0375)^T$	$(-0.8891, 0.0419, 0.4558)^T$
(2)	$\mathbf{a}^+, \mathbf{n}^+$	0.3231	$(0.1000, 0.0010, -0.0484)^T$	$(-0.2010, -0.9097, -0.3633)^T$
(3)	$\mathbf{a}^+, \mathbf{n}^+$	0.6769	$(0.0010, 0.1000, -0.0484)^T$	$(-0.9097, -0.2010, -0.3633)^T$
(4)	$\mathbf{a}^+, \mathbf{n}^+$	0.6769	$(0.1088, 0.0278, 0.0375)^T$	$(0.0419, -0.8891, 0.4558)^T$
(5)	$\mathbf{a}^-, \mathbf{n}^-$	0.3199	$(0.0350, 0.0934, 0.0434)^T$	$(-0.8143, -0.0007, 0.5804)^T$
(6)	$\mathbf{a}^-, \mathbf{n}^-$	0.3199	$(0.0902, 0.0052, -0.0606)^T$	$(-0.2777, -0.8588, -0.4305)^T$
(7)	$\mathbf{a}^-, \mathbf{n}^-$	0.6801	$(0.0052, 0.0902, -0.0606)^T$	$(0.8588, -0.2777, -0.4305)^T$
(8)	$\mathbf{a}^-, \mathbf{n}^-$	0.6801	$(0.0934, 0.0350, 0.0434)^T$	$(-0.0007, -0.8143, 0.5804)^T$

Before simulation, the transformation strains of the martensitic variants are re-orientated so as to give rise to Austenite-Martensite interface pointing in computationally compatible directions. They are outlined below:

Case (1):

$$\mathbf{F}_{010} = \begin{pmatrix} 1.0297 & 0.0294 & 0.0791 \\ 0.0294 & 0.9787 & 0.0275 \\ 0.0791 & 0.0275 & 0.9965 \end{pmatrix}, \mathbf{G}_{010} = \begin{pmatrix} 0.9961 & -0.0706 & -0.0369 \\ -0.0706 & 1.0106 & 0.0463 \\ -0.0369 & 0.0463 & 0.9982 \end{pmatrix}, \quad \text{(B.96)}$$

$$\mathbf{F}_{111} = \begin{pmatrix} 1.0405 & -0.0670 & 0.0468 \\ -0.0670 & 1.0055 & -0.0143 \\ 0.0468 & -0.0143 & 0.9590 \end{pmatrix}, \mathbf{G}_{111} = \begin{pmatrix} 0.9343 & -0.0094 & -0.0143 \\ -0.0094 & 0.9762 & 0.0370 \\ -0.0143 & 0.0370 & 1.0944 \end{pmatrix}, \quad \text{(B.97)}$$

Case (2):

$$\mathbf{F}_{010} = \begin{pmatrix} 1.0740 & 0.0066 & 0.0592 \\ 0.0066 & 0.9327 & -0.0008 \\ 0.0592 & -0.0008 & 0.9982 \end{pmatrix}, \mathbf{G}_{010} = \begin{pmatrix} 0.9704 & 0.0193 & -0.0290 \\ 0.0193 & 1.0380 & -0.0786 \\ -0.0290 & -0.0786 & 0.9965 \end{pmatrix}, \tag{B.98}$$

$$\mathbf{F}_{111} = \begin{pmatrix} 1.0331 & -0.0794 & -0.0117 \\ -0.0794 & 1.0208 & -0.0124 \\ -0.0117 & -0.0124 & 0.9510 \end{pmatrix}, \mathbf{G}_{111} = \begin{pmatrix} 1.0111 & 0.0759 & -0.0217 \\ 0.0759 & 1.0443 & 0.0004 \\ -0.0217 & 0.0004 & 0.9495 \end{pmatrix}, \tag{B.99}$$

Case (3):

$$\mathbf{F}_{010} = \begin{pmatrix} 0.9704 & 0.0193 & 0.0290 \\ 0.0193 & 1.0380 & 0.0786 \\ 0.0290 & 0.0786 & 0.9965 \end{pmatrix}, \mathbf{G}_{010} = \begin{pmatrix} 1.0740 & 0.0066 & -0.0592 \\ 0.0066 & 0.9327 & 0.0008 \\ -0.0592 & 0.0008 & 0.9982 \end{pmatrix}, \tag{B.100}$$

$$\mathbf{F}_{111} = \begin{pmatrix} 1.0111 & -0.0217 & 0.0759 \\ -0.0217 & 0.9495 & 0.0004 \\ 0.0759 & 0.0004 & 1.0443 \end{pmatrix}, \mathbf{G}_{111} = \begin{pmatrix} 1.0331 & -0.0117 & -0.0794 \\ -0.0117 & 0.9510 & -0.0124 \\ -0.0794 & -0.0124 & 1.0208 \end{pmatrix}, \tag{B.101}$$

Case (4):

$$\mathbf{F}_{010} = \begin{pmatrix} 0.9961 & -0.0706 & 0.0369 \\ -0.0706 & 1.0106 & -0.0463 \\ 0.0369 & -0.0463 & 0.9982 \end{pmatrix}, \mathbf{G}_{010} = \begin{pmatrix} 1.0297 & 0.0294 & -0.0791 \\ 0.0294 & 0.9787 & -0.0275 \\ -0.0791 & -0.0275 & 0.9965 \end{pmatrix}, \tag{B.102}$$

$$\mathbf{F}_{111} = \begin{pmatrix} 0.9343 & -0.0143 & -0.0094 \\ -0.0143 & 1.0944 & 0.0370 \\ -0.0094 & 0.0370 & 0.9762 \end{pmatrix}, \mathbf{G}_{111} = \begin{pmatrix} 1.0405 & 0.0468 & -0.0670 \\ 0.0468 & 0.9590 & -0.0143 \\ -0.0670 & -0.0143 & 1.0055 \end{pmatrix}, \tag{B.103}$$

Case (5):

$$\mathbf{F}_{010} = \begin{pmatrix} 1.0389 & -0.0181 & -0.0829 \\ -0.0181 & 0.9695 & 0.0113 \\ -0.0829 & 0.0113 & 0.9965 \end{pmatrix}, \mathbf{G}_{010} = \begin{pmatrix} 0.9889 & -0.0361 & 0.0387 \\ -0.0361 & 1.0195 & -0.0742 \\ 0.0387 & -0.0742 & 0.9965 \end{pmatrix}, \tag{B.104}$$

$$\mathbf{F}_{111} = \begin{pmatrix} 0.9987 & 0.0158 & -0.0707 \\ 0.0158 & 0.9460 & 0.0066 \\ -0.0707 & 0.0066 & 1.0602 \end{pmatrix}, \mathbf{G}_{111} = \begin{pmatrix} 0.9651 & 0.0096 & -0.0063 \\ 0.0096 & 1.1028 & 0.0234 \\ -0.0063 & 0.0234 & 0.9370 \end{pmatrix}, \tag{B.105}$$

Case (6):

$$\mathbf{F}_{010} = \begin{pmatrix} 1.0706 & -0.0199 & -0.0582 \\ -0.0199 & 0.9361 & 0.0154 \\ -0.0582 & 0.0154 & 0.9982 \end{pmatrix}, \mathbf{G}_{010} = \begin{pmatrix} 0.9753 & 0.0643 & 0.0270 \\ 0.0643 & 1.0314 & 0.0538 \\ 0.0270 & 0.0538 & 0.9982 \end{pmatrix}, \quad \text{(B.106)}$$

$$\mathbf{F}_{111} = \begin{pmatrix} 1.0070 & -0.0222 & -0.0769 \\ -0.0222 & 0.9528 & 0.0008 \\ -0.0769 & 0.0008 & 1.0451 \end{pmatrix}, \mathbf{G}_{111} = \begin{pmatrix} 1.0547 & -0.0037 & 0.0714 \\ -0.0037 & 0.9468 & -0.0231 \\ 0.0714 & -0.0231 & 1.0034 \end{pmatrix}, \quad \text{(B.107)}$$

Case (7):

$$\mathbf{F}_{010} = \begin{pmatrix} 0.9753 & -0.0643 & -0.0270 \\ -0.0643 & 1.0314 & 0.0538 \\ -0.0270 & 0.0538 & 0.9982 \end{pmatrix}, \mathbf{G}_{010} = \begin{pmatrix} 1.0706 & 0.0199 & 0.0582 \\ 0.0199 & 0.9361 & 0.0154 \\ 0.0582 & 0.0154 & 0.9982 \end{pmatrix}, \quad \text{(B.108)}$$

$$\mathbf{F}_{111} = \begin{pmatrix} 0.9334 & -0.0028 & 0.0099 \\ -0.0028 & 0.9763 & 0.0376 \\ 0.0099 & 0.0376 & 1.0953 \end{pmatrix}, \mathbf{G}_{111} = \begin{pmatrix} 1.0445 & -0.0800 & -0.0003 \\ -0.0800 & 1.0012 & -0.0180 \\ -0.0003 & -0.0180 & 0.9591 \end{pmatrix}, \quad \text{(B.109)}$$

Case (8):

$$\mathbf{F}_{010} = \begin{pmatrix} 0.9889 & 0.0361 & -0.0387 \\ 0.0361 & 1.0195 & -0.0742 \\ -0.0387 & -0.0742 & 0.9965 \end{pmatrix}, \mathbf{G}_{010} = \begin{pmatrix} 1.0389 & 0.0181 & 0.0829 \\ 0.0181 & 0.9695 & 0.0113 \\ 0.0829 & 0.0113 & 0.9965 \end{pmatrix}, \quad \text{(B.110)}$$

$$\mathbf{F}_{111} = \begin{pmatrix} 1.0331 & 0.0713 & -0.0339 \\ 0.0713 & 1.0241 & -0.0106 \\ -0.0339 & -0.0106 & 0.9476 \end{pmatrix}, \mathbf{G}_{111} = \begin{pmatrix} 1.0329 & -0.0714 & 0.0336 \\ -0.0714 & 1.0246 & -0.0105 \\ 0.0336 & -0.0105 & 0.9474 \end{pmatrix}, \quad \text{(B.111)}$$

The simulated micro-structures are shown in figure. (**??**). Notice that micro-structures in case

(5) and case (8) can not be simulated.

B.3.4 Mode D: Variant 1 and Variant 8

These two variants can twin with two possible Martensite-Martensite interfaces. Their shear and normal vectors are computed by (3.36):

$$\mathbf{a}_1 = \begin{pmatrix} 0.1036 \\ 0.0114 \\ 0.0017 \end{pmatrix}, \mathbf{n}_1 = \begin{pmatrix} 0.6677 \\ -0.6677 \\ -0.3293 \end{pmatrix},$$
$$\mathbf{a}_2 = \begin{pmatrix} -0.0881 \\ 0.0945 \\ 0.0374 \end{pmatrix}, \mathbf{n}_2 = \begin{pmatrix} -0.7071 \\ 0.7071 \\ 0 \end{pmatrix}, \tag{B.112}$$

No (numerical) solution can be found in solving equation (3.37). Thus no Austenite-Martensite interface can be formed with variants 1 and 2. The transformation strains of these variants can be specified by any volume ratio.

For simulation, we do not need to re-orientate the transformation strains to adjust the normal to point in good direction, as the expected micro-stricture appears to be simpler.

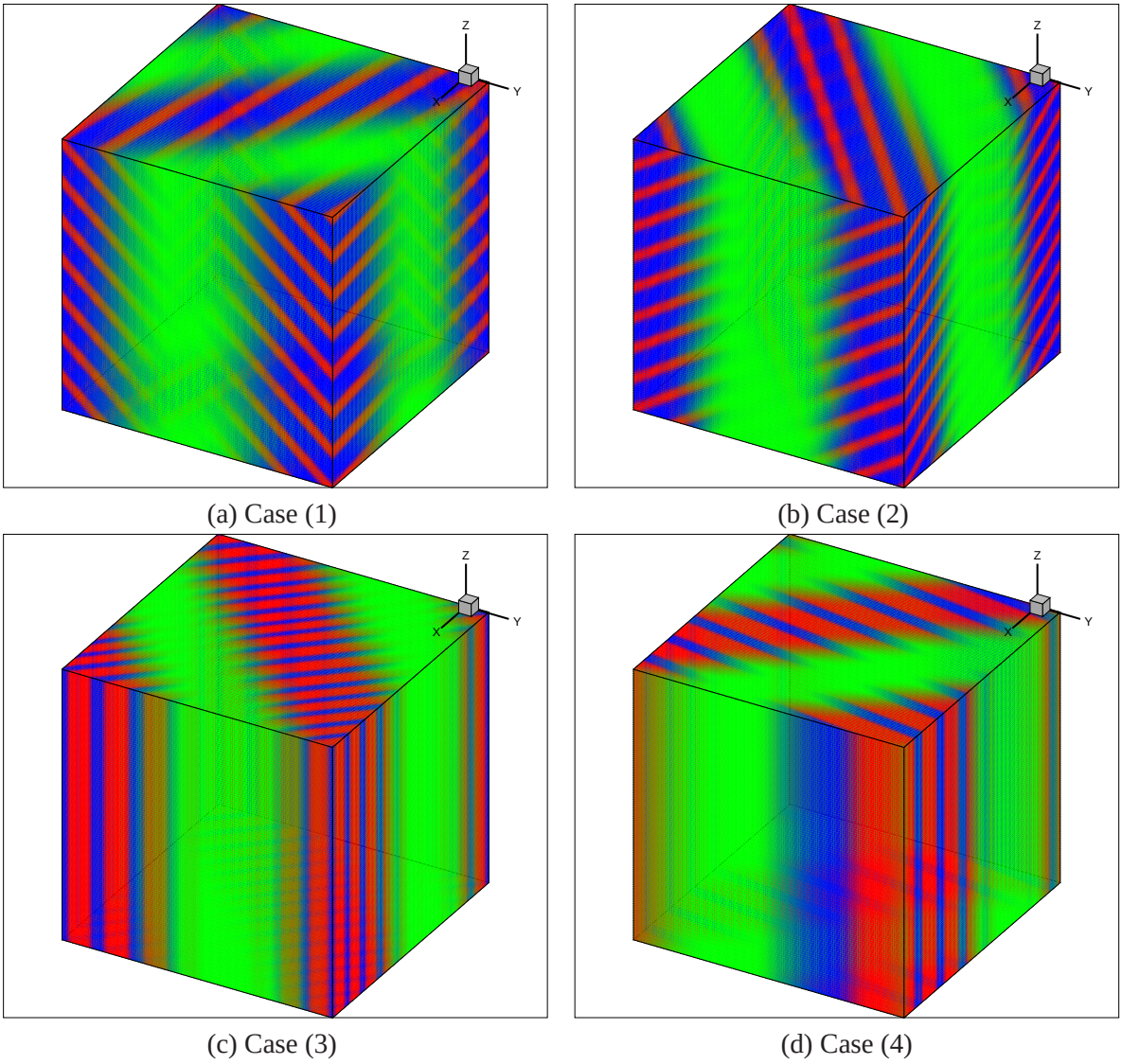

(a) Case (1) (b) Case (2)

(c) Case (3) (d) Case (4)

Figure B.8: Simulated micro-structures in monoclinic-I system involving variants 1 an 5: Cases (1) - (4).

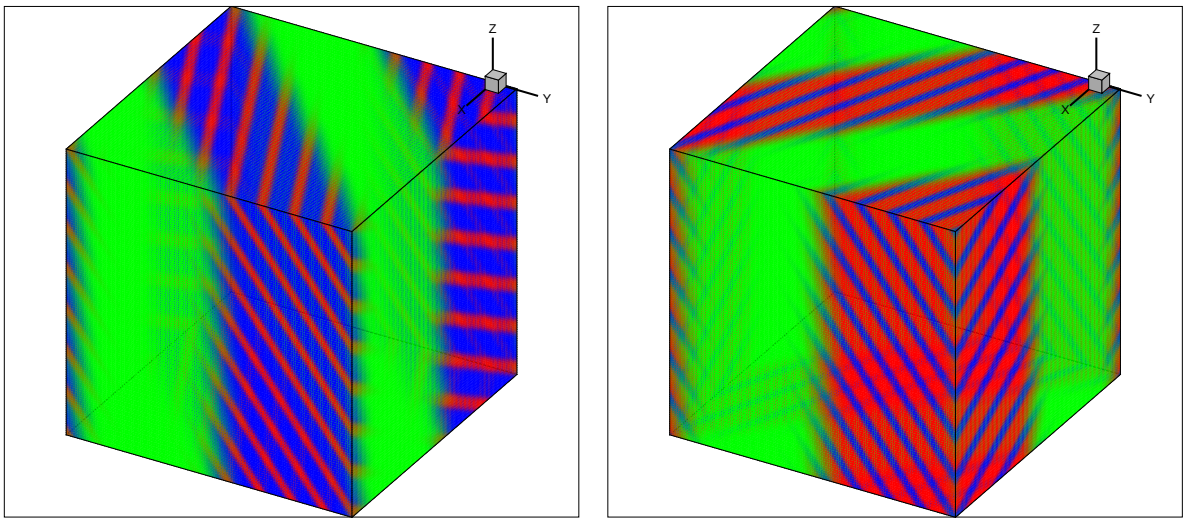

(a) Case (6) (b) Case (7)

Figure B.9: Simulated micro-structures in monoclinic-I system involving variants 1 an 5: Cases (6) and (7).

B.4 Summary and Conclusion

We have studied the micro-structures that result from twinning Martensites and Austenite in common crystal systems. We also simulate many of these micro-structures. The simulations of micro-structure depends on many factors, such as the choices of parameters and the geometrical compatibility with the strongly imposed periodicity over all boundary surfaces.

Appendix C

OTHER FORMS OF CHARACTERISTIC FUNCTIONS IN PHASE FIELD SIMULATION

In phase field simulation, other forms of characteristic functions can be adopted. Conventionally, the numerical values of the characteristic functions are between 0 and 1, where the extreme values (0 and 1) represents the existence or non-existence of the variant. This appendix outlined one other possible set of characteristic functions using trigonometric functions:

$$\begin{aligned}\mu_1 &= \sin^2(\theta_1)\\ \mu_2 &= \sin^2(\theta_2)\\ \mu_3 &= \sin^2(\theta_3)\end{aligned} \tag{C.1}$$

The eigen-strain and spontaneous polarization are given by:

$$\begin{aligned}\boldsymbol{\varepsilon}^s &= \sum_{i=1}^{4} \lambda_i \boldsymbol{\varepsilon}^{(i)}\\ \mathbf{P}^s &= \sum_{i=1}^{4} \lambda_i \mathbf{P}^{(i)},\end{aligned} \tag{C.2}$$

where:

$$\begin{aligned}\lambda_1 &= \mu_1 = \sin^2(\theta_1)\\ \lambda_2 &= (1-\mu_1)\mu_2 = \cos^2(\theta_1)\sin^2(\theta_2)\\ \lambda_3 &= (1-\mu_1)(1-\mu_2)\mu_3 = \cos^2(\theta_1)\cos^2(\theta_2)\sin^2(\theta_3)\\ \lambda_4 &= (1-\mu_1)(1-\mu_2)(1-\mu_3) = \cos^2(\theta_1)\cos^2(\theta_2)\cos^2(\theta_3)\end{aligned} \tag{C.3}$$

In the numerical formulation, the following derivatives with respect to laminated characteristic

functions are computed:

$$\frac{\partial \varepsilon^s}{\partial \theta} = \sum_{i=1}^{4} \frac{\partial \lambda_i}{\partial \theta} \varepsilon^{(i)}$$
$$\frac{\partial \mathbf{P}^s}{\partial \theta} = \sum_{i=1}^{4} \frac{\partial \lambda_i}{\partial \theta} \mathbf{P}^{(i)}, \tag{C.4}$$

where each term in the derivatives are:

$$\begin{aligned}
\frac{\partial \lambda_1}{\partial \theta_1} &= \sin(2\theta_1) \\
\frac{\partial \lambda_1}{\partial \theta_2} &= 0 \\
\frac{\partial \lambda_1}{\partial \theta_3} &= 0 \\
\frac{\partial \lambda_2}{\partial \theta_1} &= -\sin(2\theta_1)\sin^2(\theta_2) \\
\frac{\partial \lambda_2}{\partial \theta_2} &= \cos^2(\theta_1)\sin(2\theta_2) \\
\frac{\partial \lambda_2}{\partial \theta_3} &= 0 \\
\frac{\partial \lambda_3}{\partial \theta_1} &= -\sin(2\theta_1)\cos^2(\theta_2)\sin^2(\theta_3) \\
\frac{\partial \lambda_3}{\partial \theta_2} &= -\cos^2(\theta_1)\sin(2\theta_2)\sin^2(\theta_3) \\
\frac{\partial \lambda_3}{\partial \theta_3} &= \cos^2(\theta_1)\cos^2(\theta_2)\sin(2\theta_3) \\
\frac{\partial \lambda_4}{\partial \theta_1} &= -\sin(2\theta_1)\cos^2(\theta_2)\cos^2(\theta_3) \\
\frac{\partial \lambda_4}{\partial \theta_2} &= -\cos^2(\theta_1)\sin(2\theta_2)\cos^2(\theta_3) \\
\frac{\partial \lambda_4}{\partial \theta_3} &= -\cos^2(\theta_1)\cos^2(\theta_2)\sin(2\theta_3)
\end{aligned} \tag{C.5}$$

The anisotropic energy in terms of trigonometric form is given by:

$$\begin{aligned} W^{ani} &= \sum_{i=1}^{4} \mu_i^2 (1-\mu_i^2) \\ &= \sum_{i=1}^{4} \sin^2\theta_i \cos^2\theta_i \\ &= \sum_{i=1}^{4} \frac{1}{4} \sin^2(2\theta_i) \end{aligned} \tag{C.6}$$

Upon differentiation, the anisotropic driving force is:

$$\begin{aligned} F_i^{ani} &= \frac{\partial W^{ani}}{\partial \theta_i} \\ &= \frac{1}{4} 2\sin(2\theta_i)\cos(2\theta_i)2 \\ &= \frac{1}{4}\sin(4\theta_i) \end{aligned} \tag{C.7}$$

Both sets of characteristic functions have the same form of interfacial energy as it only concerns with transition across the interface:

$$W^{int} = A|\nabla\theta|^2 \tag{C.8}$$

Using these characteristic functions in phase field simulation with periodicity over all direction gives almost the same domain pattern. However, for simulating domain pattern in sample which have released periodicity along the out-of-plane direction, the effects of substrate thickness appear to be negligible as shown in figure. (C.1). Even though there is no substrate underneath the sample, the domain pattern that separates the martensitic variants is obvious. Thus characteristic functions using trigonometric functions θ_i may not be a prefect choice.

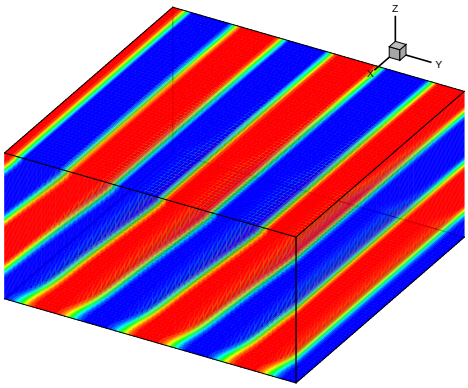

thickness of substrate = 0 (view from top)

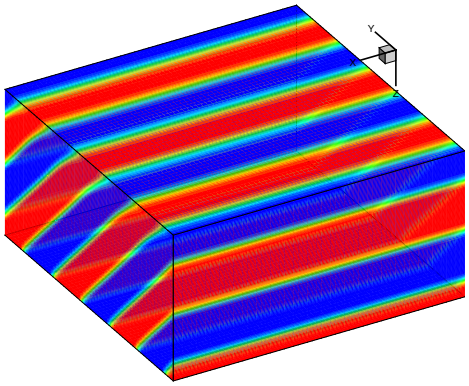

thickness of substrate = 0 (view from bottom)

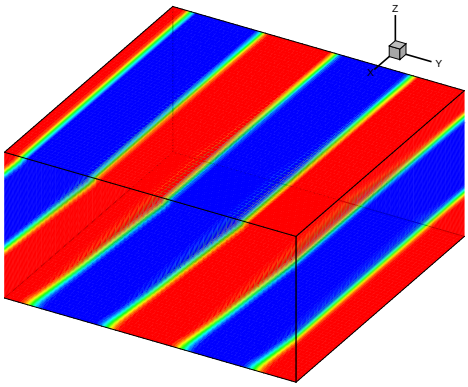

thickness of substrate = 100 (view from top)

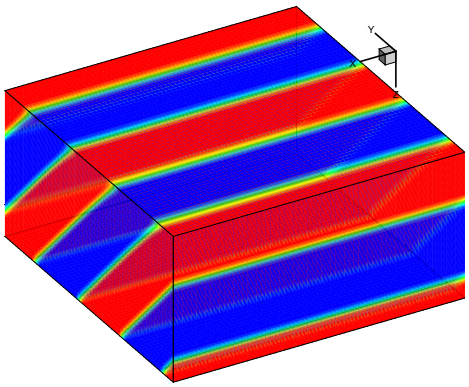

thickness of substrate = 100 (view from bottom)

Figure C.1: Shape memory alloys with varying misfit strain of substrate underneath, using θ as characteristic functions.

Appendix D

NUMERICAL SOLUTIONS OF MAXWELL'S AND ELASTICITY EQUATIONS IN THIN FILMS (3D-CONFIGURATION)

In this appendix the numerical solutions of the Maxwell's and elasticity equations using two approaches are presented in detail. They are:

- Maxwell's equation by eigen-expansion. (D.1)
- Maxwell's equation by finite difference. (D.2)
- Elasticity equation by eigen-expansion. (D.3)
- Elasticity equation by eigen-expansion. (D.4)

D.1 Maxwell's equation by eigen-expansion

Recall the Maxwell equation that relates the electric potential and instantaneous polarization:

$$\kappa \nabla^2 \phi = \nabla \cdot \mathbf{P}, \tag{D.1}$$

where $\mathbf{P} = (P_1, P_2, P_3)$ is the spontaneous polarization of the sample and ϕ is the resulting electric potential.

Assume we can also decompose the electric field into the homogeneous part and two perturbed parts (defined as perturbed part A and perturbed part B) such that:

$$\begin{aligned} \mathbf{E} &= \langle \mathbf{E} \rangle + \mathbf{E}' \\ &= \langle \mathbf{E} \rangle + \mathbf{E}^A + \mathbf{E}^B. \end{aligned} \tag{D.2}$$

We also decompose the spontaneous polarization into the homogeneous part and two perturbed part.

$$\mathbf{P} = \langle \mathbf{P} \rangle + \mathbf{P}' \tag{D.3}$$

The homogeneous part can be obtained from the average value of the instantaneous polarization through the depolarization factor:

$$\langle \mathbf{E} \rangle = \frac{\mathbf{N}_\Omega}{\kappa_0} \langle \mathbf{P} \rangle , \tag{D.4}$$

where $\mathbf{N}_\Omega$ is the standard shape factor for the polarization.

The perturbed parts are to be found indirectly. We need to express the equation in terms of electric potential and set up a differential equation in this variable. Before we move on, we express the total electric field as:

$$\begin{aligned} \mathbf{E} &= \langle \mathbf{E} \rangle + \mathbf{E}' \\ &= \langle \mathbf{E} \rangle + \mathbf{E}^A + \mathbf{E}^B \\ &= \langle \mathbf{E} \rangle - \nabla \phi^A - \nabla \phi^B \\ &= \langle \mathbf{E} \rangle - \nabla \phi . \end{aligned} \tag{D.5}$$

Here we have, by definition, $\phi = \phi^A + \phi^B$ as the portion of potential that contributes to the perturbed parts of the electric field. $\phi = \phi^A + \phi^B$ satisfies the following equation:

$$\begin{aligned} -\kappa \nabla^2 \phi &= \nabla \cdot \mathbf{P}' \\ -\kappa \nabla^2 \left(\phi^A + \phi^B \right) &= \nabla \cdot \mathbf{P}' \\ -\kappa \nabla^2 \phi^A - \kappa \nabla^2 \phi^B &= \nabla \cdot \mathbf{P}' . \end{aligned} \tag{D.6}$$

We solve the above with the following strategy.

- ϕ^A solves the equations: $-\kappa \nabla^2 \phi^A = \nabla \cdot \mathbf{P}'$ subjected to zero boundary conditions.

- ϕ^B solves the equations: $-\kappa\nabla^2\phi^B = 0$ subjected to boundary conditions inhered from the boundary conditions corresponding to the perturbed portion.

We solve each portion of the perturbed electric potential in the following subsections.

D.1.1 Perturbed potential A

Now for (perturbed) potential A, we simply apply 3D FFT to the equation and straight forwards simplification will give the answer.

$$\begin{aligned}
\kappa\nabla^2\phi^A &= \nabla\cdot\mathbf{P}' \\
\kappa\nabla^2\phi^A &= \nabla\cdot P'_{1,1} + P'_{2,2} + P'_{3,3} \xrightarrow{\text{3D-FFT}} \\
\kappa\left(-\xi_1^2-\xi_2^2-\xi_3^2\right)\widetilde{\phi^A} &= i\xi_1\widetilde{P'_1} + i\xi_2\widetilde{P'_2} + i\xi_3\widetilde{P'_3} \\
\widetilde{\phi^A} &= -\frac{i\xi_1\widetilde{P'_1} + i\xi_2\widetilde{P'_2} + ik_z\widetilde{P'_3}}{\kappa\left(\xi_1^2+\xi_2^2+\xi_3^2\right)},
\end{aligned} \tag{D.7}$$

where (ξ_1,ξ_2,ξ_3) are the three Fourier coordinates and $\widetilde{f}(\xi_1,\xi_2,\xi_3)$ is the 3D FFT of the function $f(x_1,x_2,x_3)$. For the special case where $\xi_1=\xi_2=\xi_3=0$, we simply take $\widetilde{f}(0,0,0)=0$ because of the fact that the average of the perturbed quantity is zero.

From there we take the 1D inverse FFT of $\widetilde{\phi^A}(\xi_1,\xi_2,\xi_3)$ to obtain the 2D FFT of ϕ^A, which will then be used to match the boundary conditions with the perturbed potential B. Here we denote the 2D FFT of a function $f(x_1,x_2,x_3)$ to be $\overline{f}(\xi_1,\xi_2,x_3)$. The schematic relating the original function and its Fourier transforms is shown below.

$$\begin{aligned}
f(x_1,x_2,x_3) &\xrightarrow{\text{3D-FFT}} \widetilde{f}(\xi_1,\xi_2,\xi_3) \xrightarrow{\text{inverse 1D-FFT}} \overline{f}(\xi_1,\xi_2,x_3) \\
f(x_1,x_2,x_3) &\xrightarrow{\text{2D-FFT}} \overline{f}(\xi_1,\xi_2,x_3) \xrightarrow{\text{1D-FFT}} \widetilde{f}(\xi_1,\xi_2,\xi_3)
\end{aligned} \tag{D.8}$$

D.1.2 Perturbed potential B

The (perturbed) potential B is assumed to possess periodicities in x- and y- directions. We may take 2D FFT of the associated equation:

$$\begin{aligned}
\kappa\nabla^2\phi^B &= 0 \\
\nabla^2\phi^B &= 0 \\
\frac{\partial^2\phi^B}{\partial x_1^2}+\frac{\partial^2\phi^B}{\partial x_2^2}+\frac{\partial^2\phi^B}{\partial x_3^2} &= 0 \xrightarrow{\text{2D-FFT}} \\
-\xi_1^2\overline{\phi^B}-\xi_2^2\overline{\phi^B}+\frac{\partial^2\overline{\phi^B}}{\partial x_3^2} &= 0 \\
\frac{\partial^2\overline{\phi^B}}{\partial x_3^2} &= \left(\xi_1^2+\xi_2^2\right)\overline{\phi^B} \xrightarrow{\text{solve ODE}} \\
\overline{\phi^B}\left(\xi_1,\xi_2,x_3\right) &= q_1\left(\xi_1,\xi_2\right)e^{x_3\sqrt{\xi_1^2+\xi_2^2}}+q_2\left(\xi_1,\xi_2\right)e^{-x_3\sqrt{\xi_1^2+\xi_2^2}}.
\end{aligned} \tag{D.9}$$

Here at each Fourier coordinate pair (ξ_1,ξ_2), $q_1(\xi_1,\xi_2)$ and $q_2(\xi_1,\xi_2)$ are two unknown constants to be determined, by matching with the boundary conditions.

A special case arises when $\xi_1=\xi_2=0$, where we solve the FFT-transformed equation as:

$$\begin{aligned}
\frac{\partial^2\overline{\phi^B}}{\partial x_3^2} &= \left(\xi_1^2+\xi_2^2\right)\overline{\phi^B} \xrightarrow{\xi_1=\xi_2=0} \\
\frac{\partial^2\overline{\phi^B}}{\partial x_3^2} &= 0 \\
\overline{\phi^B}\left(0,0,x_3\right) &= q_1\left(0,0\right)x_3+q_2\left(0,0\right),
\end{aligned} \tag{D.10}$$

where the solution is a linear function instead of the sum of two exponential functions. $q_1(0,0)$ and $q_2(0,0)$ are two unknown constants to be determined from matching with the boundary conditions.

Next we discuss how to find the unknown constants $q_1(\xi_1,\xi_2)$ and $q_2(\xi_1,\xi_2)$ at each Fourier coordinate pair (ξ_1,ξ_2), from the boundary conditions and the previously found perturbed potential A.

D.1.3 Boundary conditions

We match potential A and potential B with the boundary conditions on the top and the bottom surfaces. Denote the height of the 3D sample is assigned to the x_3-coordinates, so that, $x_3 \in [0, L]$, where L denotes the height of the sample.

In the following we consider two boundary value problems:

- Prescribed electric potentials at the top and the bottom surfaces.
- Prescribed electric field over the top surface and prescribed potential at the bottom surface.

D.1.4 Boundary value problem 1: Prescribed electric potentials at the top and the bottom surfaces

Assume the boundary conditions are given as follow:

- Top surface: an applied potential distribution:
  $\phi\,(x_1, x_2, x_3 = L) = V_{top}(x_1, x_2)$.
- Bottom surface: another applied potential distribution:
  $\phi\,(x_1, x_2, x_3 = 0) = V_{bot}(x_1, x_2)$.

As a remark, for most of our simulations that follow, we usually have the potential distribution on the top surface as a point potential which is described in the form of a delta function:

$$\phi(x_1, x_2, x_3 = L) = V_{top}(x_1, x_2) = V_0 \delta_{(x_{1,0}, x_{2,0})}(x_1, x_2), \tag{D.11}$$

where V_0 is the value of the point potential, $(x_{1,0}, x_{2,0})$ are the coordinates of the applied point charge and $\delta_{(x_0, y_0)}(x, y)$ is the delta or distribution function:

$$\delta_{(x_0, y_0)}(x, y) = \begin{cases} 1 & \text{if } (x, y) = (x_0, y_0) \\ 0 & \text{if } (x, y) \neq (x_0, y_0) \end{cases},$$

while the bottom surface is grounded so that the potential over the bottom surface is zero, with the expression:

$$\phi(x_1,x_2,x_3=0)=V_{bot}(x_1,x_2)=0. \tag{D.12}$$

Thus we have, through the proposed decomposition,

On the top surface,

$$\begin{aligned}
\phi(x_1,x_2,x_3=L)&=V_{top}(x_1,x_2)\\
\phi^A(x_1,x_2,x_3=L)+\phi^B(x_1,x_2,x_3=L)&=V_{top}(x_1,x_2)\\
\phi^B(x_1,x_2,x_3=L)&=-\phi^A(x_1,x_2,x_3=L)+V_{top}(x_1,x_2)\xrightarrow{\text{2D FFT}}\\
\overline{\phi^B}(\xi_1,\xi_2,x_3=L)&=-\overline{\phi^A}(\xi_1,\xi_2,x_3=L)+\overline{V_{top}}(\xi_1,\xi_2),
\end{aligned} \tag{D.13}$$

On the bottom surface,

$$\begin{aligned}
\phi(x_1,x_2,x_3=0)&=V_{bot}(x_1,x_2)\\
\phi^A(x_1,x_2,x_3=0)+\phi^B(x_1,x_2,x_3=0)&=V_{bot}(x_1,x_2)\\
\phi^B(x_1,x_2,x_3=0)&=-\phi^A(x_1,x_2,x_3=0)+V_{bot}(x_1,x_2)\xrightarrow{\text{2D FFT}}\\
\overline{\phi^B}(\xi_1,\xi_2,x_3=0)&=-\overline{\phi^A}(\xi_1,\xi_2,x_3=0)+\overline{V_{bot}}(\xi_1,\xi_2).
\end{aligned} \tag{D.14}$$

With the empirical expressions that we have found for $\overline{\phi^B}$ in the cases $\xi_1^2+\xi_2^2\neq 0$ and $\xi_1=\xi_2=0$, we solve the following matrix equations for the unknowns $q_1(\xi_1,\xi_2)$ and $q_2(\xi_1,\xi_2)$.

Case I: $\xi_1^2+\xi_2^2\neq 0$

Equating the quantities for the top surface,

$$\begin{aligned}
\overline{\phi^B}(\xi_1,\xi_2,x_3=L)&=-\overline{\phi^A}(\xi_1,\xi_2,x_3=L)+\overline{V_{top}}(\xi_1,\xi_2)\\
q_1(\xi_1,\xi_2)e^{L\sqrt{\xi_1^2+\xi_2^2}}+q_2(\xi_1,\xi_2)e^{-L\sqrt{\xi_1^2+\xi_2^2}}&=-\overline{\phi^A}(\xi_1,\xi_2,L)+\overline{V_{top}}(\xi_1,\xi_2)
\end{aligned} \tag{D.15}$$

Equating the quantities for the bottom surface,

$$\begin{aligned}\overline{\phi^B}(\xi_1,\xi_2,x_3=0) &= -\overline{\phi^A}(\xi_1,\xi_2,x_3=0)+\overline{V_{bot}}(\xi_1,\xi_2)\\ q_1(\xi_1,\xi_2)+q_2(\xi_1,\xi_2) &= -\overline{\phi^A}(\xi_1,\xi_2,0)+\overline{V_{bot}}(\xi_1,\xi_2)\end{aligned} \tag{D.16}$$

Combining the above two equations in matrix form, we arrive:

$$\begin{pmatrix} e^{L\sqrt{\xi_1^2+\xi_2^2}} & e^{-L\sqrt{\xi_1^2+\xi_2^2}} \\ 1 & 1 \end{pmatrix} \begin{pmatrix} q_1(\xi_1,\xi_2) \\ q_2(\xi_1,\xi_2) \end{pmatrix} = \begin{pmatrix} -\overline{\phi^A}(\xi_1,\xi_2,L)+\overline{V_{top}}(\xi_1,\xi_2) \\ -\overline{\phi^A}(\xi_1,\xi_2,0)+\overline{V_{bot}}(\xi_1,\xi_2) \end{pmatrix} \tag{D.17}$$

Case II: $\xi_1=\xi_2=0$

Equating the quantities for the top surface,

$$\begin{aligned}\overline{\phi^B}(0,0,x_3=L) &= -\overline{\phi^A}(0,0,L)+\overline{V_{top}}(0,0)\\ q_1(0,0)L+q_2(0,0) &= -\overline{\phi^A}(0,0,L)+\overline{V_{top}}(0,0)\end{aligned} \tag{D.18}$$

Equating the quantities for the bottom surface,

$$\begin{aligned}\overline{\phi^B}(0,0,x_3=0) &= -\overline{\phi^A}(0,0,x_3=0)+\overline{V_{bot}}(0,0)\\ q_1(0,0)0+q_2(0,0) &= -\overline{\phi^A}(0,0,0)+\overline{V_{bot}}(0,0)\\ q_2(0,0) &= -\overline{\phi^A}(0,0,0)+\overline{V_{bot}}(0,0)\end{aligned} \tag{D.19}$$

Combining the above two equations in matrix form, we arrive:

$$\begin{pmatrix} h & 1 \\ 0 & 1 \end{pmatrix} \begin{pmatrix} q_1(0,0) \\ q_2(0,0) \end{pmatrix} = \begin{pmatrix} -\overline{\phi^A}(0,0,L)+\overline{V_{top}}(0,0) \\ -\overline{\phi^A}(0,0,0)+\overline{V_{bot}}(0,0) \end{pmatrix} \tag{D.20}$$

D.1.5 Boundary value problem 2: Prescribed electric field at the top surface and electric potential at the bottom surfaces.

Assume the boundary conditions are given as follow:

- Top surface is subjected to the x_3-component of electric field, or,

$E_3(x_1,x_2,x_3=L)=E_{top}(x_1,x_2)\forall(x_1,x_2)$.

- Bottom surface is given a prescribed a distribution of potential, or,
  $\phi(x_1,x_2,x_3=0)=\phi_{bot}(x_1,x_2)\forall(x_1,x_2)$.

Again through the proposed decomposition,

On the top surface,

$$\begin{aligned} E_3'(x_1,x_2,x_3=L) &= E_{top}(x_1,x_2) \\ E_3^A(x_1,x_2,x_3=L)+E_3^B(x_1,x_2,x_3=L) &= E_{top}(x_1,x_2) \\ E_3^B(x_1,x_2,x_3=L) &= -E_3^A(x_1,x_2,x_3=L)+E_{top}(x_1,x_2) \xrightarrow{\text{2D FFT}} \\ \overline{E_3^B}(\xi_1,\xi_2,x_3=L) &= -\overline{E_3^A}(\xi_1,\xi_2,x_3=L)+\overline{E_{top}}(\xi_1,\xi_2) \end{aligned} \tag{D.21}$$

As a remark, $\overline{E_3^A}$ is obtained from $\widetilde{\phi^A}$ using inverse FFT in x_1-coordinate, as shown in the schematic:

$$\widetilde{\phi^A}(\xi_1,\xi_2,\xi_3) \xrightarrow{E_3^A=-\frac{\partial\phi}{\partial x_3}} \widetilde{E_3^A}(\xi_1,\xi_2,\xi_3)=-i\xi_3\widetilde{\phi^A}(\xi_1,\xi_2,\xi_3) \xrightarrow{\text{inverse 1D FFT}} \overline{E_3^A}(\xi_1,\xi_2,\xi_3) \tag{D.22}$$

On the bottom surface,

$$\begin{aligned} \phi(x_1,x_2,x_3=0) &= \phi_{bot}(x_1,x_2) \\ \phi^A(x_1,x_2,x_3=0)+\phi^B(x_1,x_2,x_3=0) &= \phi_{bot}(x_1,x_2) \\ \phi^B(x_1,x_2,x_3=0) &= -\phi^A(x_1,x_2,x_3=0)+\phi_{bot}(x_1,x_2) \xrightarrow{\text{2D FFT}} \\ \overline{\phi^B}(\xi_1,\xi_2,x_3=0) &= -\phi^A(\xi_1,\xi_2,x_3=0)+\overline{\phi_{bot}}(\xi_1,\xi_2) \end{aligned} \tag{D.23}$$

With the empirical expressions that we have found for $\overline{\phi^B}$ in the cases $\xi_1^2+\xi_2^2\neq 0$ and $\xi_1=\xi_2=0$, we solve the following matrix equations for the unknowns $q_1(\xi_1,\xi_2)$ and $q_2(\xi_1,\xi_2)$.

Case I: $\xi_1^2+\xi_2^2 \neq 0$

Before we deal with the boundary condition on the top surface, we need to derive the x_3-component of the electric field analytically,

$$\begin{aligned}
\overline{\phi^B}(\xi_1,\xi_2,x_3) &= q_1(\xi_1,\xi_2)e^{x_3\sqrt{\xi_1^2+\xi_2^2}} + q_2(\xi_1,\xi_2)e^{-x_3\sqrt{\xi_1^2+\xi_2^2}} \\
\overline{E_3^B}(\xi_1,\xi_2,x_3) &= -\frac{\partial\overline{\phi^B}(\xi_1,\xi_2,x_3)}{\partial x_3} \\
&= -q_1(\xi_1,\xi_2)\sqrt{\xi_1^2+\xi_2^2}e^{x_3\sqrt{\xi_1^2+\xi_2^2}} + q_2(\xi_1,\xi_2)\sqrt{\xi_1^2+\xi_2^2}e^{-x_3\sqrt{\xi_1^2+\xi_2^2}} \qquad \text{(D.24)}
\end{aligned}$$

Equating the quantities for the top surface,

$$\begin{aligned}
\overline{E_3^B}(\xi_1,\xi_2,L) &= -\overline{E_3^A}(\xi_1,\xi_2,L) + \overline{E_{top}}(\xi_1,\xi_2) \\
-q_1(\xi_1,\xi_2)\sqrt{\xi_1^2+\xi_2^2}e^{L\sqrt{\xi_1^2+\xi_2^2}} + q_2(\xi_1,\xi_2)\sqrt{\xi_1^2+\xi_2^2}e^{-L\sqrt{\xi_1^2+\xi_2^2}} &= -\overline{E_3^A} + \overline{E_{top}}(\xi_1,\xi_2)\,(\xi_1,\xi_2) \qquad \text{(D.25)}
\end{aligned}$$

Equating the quantities for the bottom surface,

$$\begin{aligned}
\overline{\phi^B}(\xi_1,\xi_2,0) &= -\overline{\phi^A}(\xi_1,\xi_2,0) + \overline{\phi_{bot}(x_1,x_2)}(\xi_1,\xi_2) \\
q_1(\xi_1,\xi_2)+q_2(\xi_1,\xi_2) &= -\overline{\phi^A}(\xi_1,\xi_2,0) + \overline{\phi_{bot}(x_1,x_2)}(\xi_1,\xi_2) \qquad \text{(D.26)}
\end{aligned}$$

Combining the above two equations in matrix form, we arrive:

$$\begin{pmatrix} -\sqrt{\xi_1^2+\xi_2^2}e^{L\sqrt{\xi_1^2+\xi_2^2}} & \sqrt{\xi_1^2+\xi_2^2}e^{-L\sqrt{\xi_1^2+\xi_2^2}} \\ 1 & 1 \end{pmatrix} \begin{pmatrix} q_1(\xi_1,\xi_2) \\ q_2(\xi_1,\xi_2) \end{pmatrix} = \begin{pmatrix} -\overline{E_3^A}(\xi_1,\xi_2,L) + \overline{E_{top}}(\xi_1,\xi_2) \\ -\overline{\phi^A}(\xi_1,\xi_2,0) + \overline{\phi_{bot}}(\xi_1,\xi_2) \end{pmatrix} \qquad \text{(D.27)}$$

Case II: $\xi_1 = \xi_2 = 0$

Before we deal with the boundary condition on the top surface, we need to derive x_3-component of the electric field analytically,

$$\begin{aligned}\overline{\phi^B}(0,0,x_3) &= q_1(0,0)x_3 + q_2(0,0) \\ \overline{E_z^B}(0,0,x_3) &= -\frac{\partial \overline{\phi^B}(0,0,x_3)}{\partial x_3} = -q_1(0,0)\end{aligned} \tag{D.28}$$

Equating the quantities for the top surface,

$$\begin{aligned}\overline{E_3^B}(0,0,L) &= -\overline{E_3^A}(0,0,L) + \overline{E_{top}}(0,0) \\ -q_1(0,0) &= -\overline{E_3^A}(0,0,L) + \overline{E_{top}}(0,0)\end{aligned} \tag{D.29}$$

Equating the quantities for the bottom surface,

$$\begin{aligned}\overline{\phi^B}(0,0,0) &= -\overline{\phi^A}(0,0,0) + \overline{\phi_{bot}}(0,0) \\ q_2(0,0) &= -\overline{\phi^A}(0,0,0) + \overline{\phi_{bot}}(0,0)\end{aligned} \tag{D.30}$$

Combining the above two equations in matrix form, we arrive:

$$\begin{pmatrix} -1 & 0 \\ 0 & 1 \end{pmatrix} \begin{pmatrix} q_1(0,0) \\ q_2(0,0) \end{pmatrix} = \begin{pmatrix} -\overline{E_3^A}(0,0,L) + \overline{E_{top}}(0,0) \\ -\overline{\phi^A}(0,0,0) + \overline{\phi_{bot}}(0,0) \end{pmatrix} \tag{D.31}$$

More specifically, the 2D FFT of the perturbed potential B at the Fourier coordinates $(\xi_1, \xi_2) = (0,0)$ is:

$$\begin{aligned}\overline{\phi^A}(0,0,x_3) &= q_1(0,0)x_3 + q_2(0,0) \\ &= \left[\overline{E_3^A}(0,0,L) - \overline{E_{top}}(0,0)\right] x_3 + \left[-\overline{\phi^A}(0,0,0) + \overline{\phi_{bot}}(0,0)\right]\end{aligned} \tag{D.32}$$

D.1.6 Post-Processing

After we have obtained $\overline{\phi^A}$ and $\overline{\phi^B}$, we may find the perturbed potential of the entire sample:

$$\overline{\phi} = \overline{\phi^A} + \overline{\phi^B} \xrightarrow{\text{inverse 2D FFT}} \phi \tag{D.33}$$

On the other hand, from the 3D FFT of potential A, we first find the 3D FFT of the (perturbed) electric field A by multiplying the Fourier coordinates. Then we take an inverse FFT to find the 2D FFT of the (perturbed) electric field A.

$$\widetilde{\phi^A} \xrightarrow{\mathbf{E}^A = -\nabla\phi^A} \begin{cases} \widetilde{E_1^A} = -i\xi_1\widetilde{\phi^A} \\ \widetilde{E_2^A} = -i\xi_2\widetilde{\phi^A} \\ \widetilde{E_3^A} = -i\xi_3\widetilde{\phi^A} \end{cases} \xrightarrow{\text{inverse 1D FFT}} \begin{cases} \overline{E_1^A} \\ \overline{E_2^A} \\ \overline{E_3^A} \end{cases} \tag{D.34}$$

For the (perturbed) electric field B, we start from the (perturbed) potential B:

$$\overline{\phi^B}(\xi_1,\xi_2,x_3) = \begin{cases} q_1(\xi_1,\xi_2)e^{x_3\sqrt{\xi_1^2+\xi_2^2}} + q_2(\xi_1,\xi_2)e^{-x_3\sqrt{\xi_1^2+\xi_2^2}} & (\xi_1,\xi_2) \neq (0,0) \\ q_1(0,0)x_3 + q_2(0,0) & (\xi_1,\xi_2) = (0,0) \end{cases} \tag{D.35}$$

Since this part of potential is assumed to be periodic in x_1- and x_2- coordinate, its derivatives in x_1- and x_2- directions can be computed by a similar technique by multiplying by the Fourier coordinates:

$$\begin{aligned} \overline{E_1^B} &= -i\xi_1\phi^B \\ \overline{E_2^B} &= -i\xi_2\phi^B \end{aligned} \tag{D.36}$$

The x_3-derivative of the potential B is obtained simply by direct derivative from the expression

of $\phi^B(\xi_1,\xi_2,x_3)$:

$$\overline{E_3^B}(\xi_1,\xi_2,x_3) = -\frac{\partial\overline{\phi^B}(\xi_1,\xi_2,x_3)}{\partial x_3}$$
$$= \begin{cases} -q_1(\xi_1,\xi_2)\sqrt{\xi_1^2+\xi_2^2}e^{z\sqrt{\xi_1^2+\xi_2^2}} + q_2(\xi_1,\xi_2)\sqrt{\xi_1^2+\xi_2^2}e^{-x_3\sqrt{\xi_1^2+\xi_2^2}} & (\xi_1,\xi_2)\neq(0,0) \\ -q_1(0,0) & (\xi_1,\xi_2)=(0,0) \end{cases} \tag{D.37}$$

Finally we combine the 2D-FFT of both (perturbed) electric field and then transform the result to real-space,

$$\overline{\mathbf{E}}'(\xi_1,\xi_2,z) = \overline{\mathbf{E}}^A(\xi_1,\xi_2,x_3) + \overline{\mathbf{E}}^B(\xi_1,\xi_2,x_3) \xrightarrow{\text{inverse 2D FFT}} \mathbf{E}'(x_1,x_2,x_3) \tag{D.38}$$

The total field is found by adding the homogeneous (average) field and the perturbed field:

$$\mathbf{E}(x_1,x_2,x_3) = \langle\mathbf{E}\rangle + \mathbf{E}'(x_1,x_2,x_3) \tag{D.39}$$

D.1.7 Remark

Despite the fact that the eigen-expansion method is fast due to its semi-analytic formulation, accurate approximation of the potential is questionable. We have adopted FFT in the x_3-direction when we were dealing with the (perturbed) potential A, which somehow violates the beginning assumption that there is no x_3-periodicity of the sample. The 'Runge' phenomenon induces inaccuracy towards the ends of the interval when we are attempting to approximate a non-periodic function with Fourier Transform. Luckily, the resulting electric field, as the derivatives of the potential, are comparably accurate. The derivative suppresses and reduces the discrepancy between the actual and the approximations, to some extent. These are tested and verified by comparing the analytic and simulated results for several spacial cases, such as, uniform external fields, homogeneous material with zero polarization. However, there is no conclusion for general cases. We are not yet certain if the simulated electric fields are correct even though FFT is applied in the x_3-direction.

To this end, we also develope a new approach by considering finite difference along the x_3-directions and FFT in the x_1- and x_2- directions. This method is obviously slower but does give

more reliable results.

D.2 Maxwell's equation by finite differences

Again we are solving the 3D Maxwell's equation given by:

$$\kappa\nabla^2\phi = \nabla\cdot\mathbf{P}, \tag{D.40}$$

where $\phi = \phi(x_1,x_2,x_3)$ is unknown electric potential to be determined and $\mathbf{P} = \mathbf{P}(x_1,x_2,x_3)$ is a known field of spontaneous polarization.

Two kinds of boundary conditions are studied. They are:

1. Prescribed electric potentials at the top and the bottom surfaces.

2. Prescribed electric field over the top surface and prescribed potential at the bottom surface.

Assume periodicity in x_1- and x_2- directions are imposed, we may apply 2D FFT in (x_1,x_2)-coordinates so that:

$$\begin{aligned}
\kappa\nabla^2\phi &= \nabla\cdot\mathbf{P}\\
\kappa\nabla^2\phi &= \frac{\partial P_1}{\partial x_1}+\frac{\partial P_2}{\partial x_2}+\frac{\partial P_3}{\partial x_3} \xrightarrow{\text{2D FFT}}\\
\kappa\left[-\left(\xi_1^2+\xi_2^2\right)\overline{\phi}+\frac{\partial^2\overline{\phi}}{\partial x_3^2}\right] &= i\xi_1\overline{P_1}+i\xi_2\overline{P_2}+\frac{\partial\overline{P_3}}{\partial x_3}\\
\frac{\partial^2\overline{\phi}}{\partial x_3^2}-(\xi_1^2+\xi_2^2)\overline{\phi} &= \frac{1}{\kappa}\left[i\xi_1\overline{P_1}+i\xi_2\overline{P_2}+\frac{\partial\overline{P_3}}{\partial x_3}\right]\\
\frac{\partial^2\overline{\phi}}{\partial x_3^2}-(\xi_1^2+\xi_2^2)\overline{\phi} &\equiv r(\xi_1,\xi_2,x_3),
\end{aligned} \tag{D.41}$$

where we have in notations, $r(x_3)\equiv r(\xi_1,\xi_2,x_3)\equiv\frac{1}{\kappa}\left[i\xi_1\overline{p_1^*}+i\xi_2\overline{p_2^*}+\frac{\partial\overline{p_3^*}}{\partial x_3}\right]$.

Since we are working on a general 3D problem where all fields are functions of (x_1,x_2,x_3) , we cannot obtain the solution (electric potential) in closed form, as outlined in [39]. The problem can only be solved numerically.

Let's set up the formulation. We are in fact solving the 2D FFT of the potential $\overline{\phi} = \overline{\phi}(\xi_1,\xi_2,x_3)$ as a function of x_3, at fixed Fourier coordinates (ξ_1,ξ_2). After that, we may inverse the 2D FFT to

recover the potential $\phi = \phi(\xi_1, \xi_2, x_3)$ in real space.

More specifically, at fixed (ξ_1, ξ_2), the equation of $\overline{\phi}(\xi_1, \xi_2, x_3)$ is rewritten as:

$$\begin{aligned} \frac{\partial^2 \overline{\phi}}{\partial x_3^2} &= (\xi_1^2 + \xi_2^2)\overline{\phi} + r(\xi_1, \xi_2, x_3) \\ \frac{\partial^2 \overline{\phi}}{\partial x_3^2} &= (\xi_1^2 + \xi_2^2)\overline{\phi} + r(x_3) \end{aligned} \tag{D.42}$$

We consider discretization of the above differential equation. The height of the sample, $x_3 \in [a,b] = [0,H]$, is divided into $(N-1)$ segments by N points. The size of the subdivision is then $h = \frac{b-a}{N-1} = \frac{H}{N-1}$ and the coordinates of the subdivision are:

$$x_{3,i} = a + jh = jh, \forall j = 0, 1, 2, ..., N-2, N-1 \tag{D.43}$$

With these, the equation at each of these points z_i is:

$$\frac{\partial^2 \overline{\phi}(\xi_1, \xi_2, x_3)}{\partial x_3^2} = (\xi_1^2 + \xi_2^2)\overline{\phi}(\xi_1, \xi_2, x_3) + r(\xi_1, \xi_2, x_3) \tag{D.44}$$

In the following subsections, two boundary value problems are considered as in discussed using the method of eigen-expansion.

D.2.1 Boundary Value Problem 1: Prescribed electric potentials at the top and the bottom surfaces

Assume that the boundary conditions are the prescribed potentials on the top and bottom surfaces, as distribution of spatial coordinates:

$$\begin{cases} \phi(x_1, x_2, x_3 = a) = \phi_{bot}(x_1, x_2) \\ \phi(x_1, x_2, x_3 = b) = \phi_{top}(x_1, x_2) \end{cases} \tag{D.45}$$

Taking 2D FFT of the above boundary condition yields the following:

$$\begin{cases} \overline{\phi}(\xi_1, \xi_2, x_3 = a) = \overline{\phi_{bot}}(\xi_1, \xi_2) \\ \overline{\phi}(\xi_1, \xi_2, x_3 = b) = \overline{\phi_{top}}(\xi_1, \xi_2) \end{cases} \tag{D.46}$$

These will be incorporated into the matrix equation in the context of finite differences.

Adopting the moral of finite difference as the approximation of derivative, we obtain the following approximation of the equation at $x_{3,i}$:

$$\frac{\overline{\phi}(\xi_1,\xi_2,x_{3,i+1})-2\overline{\phi}(\xi_1,\xi_2,x_{3,i})+\overline{\phi}(\xi_1,\xi_2,x_{3,i-1})}{h^2}=(\xi_1^2+\xi_2^2)\overline{\phi}(\xi_1,\xi_2,x_{3,i})+r(\xi_1,\xi_2,x_{3,i}),\forall i=1,2,...,N-2$$
$$\overline{\phi}(\xi_1,\xi_2,x_{3,0}=a)=\overline{\phi_{bot}}(\xi_1,\xi_2)$$
$$\overline{\phi}(\xi_1,\xi_2,x_{3,N-1}=b)=\overline{\phi_{top}}(\xi_1,\xi_2) \tag{D.47}$$

The above finite difference scheme is carried out at each (ξ_1,ξ_2). We may further define the following variables for the sake of convenience and simplicity.

$$\omega_i\approx\overline{\phi}(\xi_1,\xi_2,x_{3,i}),\forall i=0,1,2,...,N-1 \tag{D.48}$$

Assembly all the equations into matrix equation, we arrive:

$$\mathbf{A}_{(N-2)\times(N-2)}\mathbf{w}_{(N-2)\times1}=\mathbf{b}_{(N-2)\times1}, \tag{D.49}$$

where

$$\mathbf{A}=\begin{pmatrix} 2+h^2\xi & -1 & 0 & 0 & \dots & 0 \\ -1 & 2+h^2\xi & -1 & 0 & \dots & 0 \\ 0 & -1 & 2+h^2\xi & -1 & \dots & 0 \\ \vdots & \ddots & \ddots & \ddots & \ddots & \vdots \\ 0 & \cdots & 0 & -1 & 2+h^2\xi & -1 \\ 0 & \cdots & 0 & 0 & -1 & 2+h^2\xi \end{pmatrix}, \tag{D.50}$$

$$\mathbf{w} = \begin{pmatrix} \omega_1 \\ \omega_2 \\ \omega_3 \\ \vdots \\ \omega_{N-3} \\ \omega_{N-2} \end{pmatrix}, \tag{D.51}$$

and

$$\mathbf{b} = \begin{pmatrix} -h^2 r(x_{3,1}) + \omega_0 \\ -h^2 r(x_{3,2}) \\ -h^2 r(x_{3,3}) \\ \vdots \\ -h^2 r(x_{3,N-3}) \\ -h^2 r(x_{3,N-2}) + \omega_{N-1} \end{pmatrix} = \begin{pmatrix} -h^2 r(x_{3,1}) + \overline{\phi_{bot}}(\xi_1, \xi_2) \\ -h^2 r(x_{3,2}) \\ -h^2 r(x_{3,3}) \\ \vdots \\ -h^2 r(x_{3,N-3}) \\ -h^2 r(x_{3,N-2}) + \overline{\phi_{top}}(\xi_1, \xi_2) \end{pmatrix} \tag{D.52}$$

with $\xi \equiv \xi_1^2 + \xi_2^2$.

In the implementation, matrix **A** is fixed for all iterations, that is, it is independent of the current distribution of instantaneous polarization. Another good thing is that matrix **A** is a banded matrix with three simple constant bands. We may store **A** in a compact form by just two entries. The numerical techniques of LU-decomposition for tri-diagonal matrices can be adopted, for the sakes of speed and storage.

Recall, at each pair (ξ_1, ξ_2), the above matrix equation is solved to obtain the $\omega_i \approx \phi(\xi_1, \xi_2, x_{3,i})$ as an approximation of $\overline{\phi}(\xi_1, \xi_2, x_{3,i})$. Inverse 2D FFT is then applied to recover the potential in real space.

$$\overline{\phi}(\xi_1, \xi_2, x_3) \xrightarrow{\text{inverse 2D FFT}} \phi(x_1, x_2, x_3) \tag{D.53}$$

As a remark, the electric field **E** can be obtained from ϕ by finite differences as approximations of derivatives. Alternatively, FFT can also be used to find the x- and y- components of the electric

field, which is similarly treated in the approach eigen-expansion.

$$\overline{\phi}(\xi_1,\xi_2,x_3) \xrightarrow{\mathbf{E}=-\nabla\phi} \begin{cases} \overline{E_x}(\xi_1,\xi_2,x_3) = i\xi_1\overline{\phi}(\xi_1,\xi_2,x_3) \\ \overline{E_y}(\xi_1,\xi_2,x_3) = i\xi_2\overline{\phi}(\xi_1,\xi_2,x_3) \end{cases} \xrightarrow{\text{inverse 2D FFT}} \begin{cases} E_x(x_1,x_2,x_3) \\ E_y(x_1,x_2,x_3) \end{cases} \tag{D.54}$$

D.2.2 Boundary Value Problem 2: Prescribed electric field at the top surface and electric potential at the bottom surfaces

The numerical scheme can be modified to solve another set boundary conditions. Here the bottom surface is imposed a fixed electric potential $\phi(x_1,x_2,x_3=a)=\phi_{bot}(x_1,x_2)$ and the top surface is subjected to the x_3-component of the electric field $E_3(x_1,x_2,x_3=b)=E_{top}(x_1,x_2)$. In 2D FFT, these conditions are expressed as:

$$\begin{aligned} \overline{E_3}(\xi_1,\xi_2,x_3=b) &= \overline{E_{z,top}}(\xi_1,\xi_2) \\ \overline{\phi}(\xi_1,\xi_2,x_3=a) &= \overline{\phi_{z,top}}(\xi_1,\xi_2) \end{aligned} \tag{D.55}$$

At each Fourier coordinate pair (ξ_1,ξ_2), we are solving for the electric potential $\overline{\phi}(\xi_1,\xi_2,x_3)$ as a function of x_3.

First we express the x_3-component of the electric field in terms of potential at the top surface. Then we we discretize it the quantity at the top end point in x_3-direction, as shown below.

$$\begin{aligned} \mathbf{E} &= -\nabla\phi \\ E_3 &= -\frac{\partial\phi}{\partial x_3} \xrightarrow{\text{at right end point: } x_{3,N-1}} \\ E_{3,N-1} &= -\frac{\phi_N-\phi_{N-2}}{2h} \\ -\phi_{N-2}+\phi_N &= -2hE_{3,N-1} \xrightarrow{\text{2D FFT}} \\ -\overline{\phi_{N-2}}+\overline{\phi_N} &= -2h\underbrace{\overline{E_{3,N-1}}}_{\text{given BC}}, \end{aligned} \tag{D.56}$$

where we have introduced an additional ghost point $x_{3,N}$.

By incorporating the above expression, we modify the associated matric equation as:

$$\mathbf{A}_{N\times N}\mathbf{w}_{N\times 1} = \mathbf{b}_{N\times 1}, \tag{D.57}$$

where

$$\mathbf{A} = \begin{pmatrix} 2+h^2\xi & -1 & 0 & 0 & \dots & \dots & 0 \\ -1 & 2+h^2\xi & -1 & 0 & \dots & \dots & 0 \\ 0 & -1 & 2+h^2\xi & -1 & \dots & \dots & 0 \\ \vdots & \ddots & \ddots & \ddots & \ddots & \ddots & \vdots \\ 0 & \cdots & 0 & -1 & 2+h^2\xi & -1 & 0 \\ 0 & \cdots & 0 & 0 & -1 & 2+h^2\xi & -1 \\ 0 & \cdots & 0 & 0 & -1 & 0 & 1 \end{pmatrix}, \tag{D.58}$$

$$\mathbf{w} = \begin{pmatrix} \omega_1 \\ \omega_2 \\ \omega_3 \\ \vdots \\ \omega_{N-3} \\ \omega_{N-2} \\ \omega_{N-1} \end{pmatrix}, \tag{D.59}$$

and

$$\mathbf{b} = \begin{pmatrix} -h^2 r(x_{3,1}) + \overline{\phi_{bot}}(\xi_1, \xi_2) \\ -h^2 r(x_{3,2}) \\ -h^2 r(x_{3,3}) \\ \vdots \\ -h^2 r(x_{3,N-3}) \\ -h^2 r(x_{3,N-2}) \\ -2h\overline{E_{top}}(\xi_1, \xi_2) \end{pmatrix} \tag{D.60}$$

with $\xi = \xi_1^2 + \xi_2^2$.

Again at each (ξ_1, ξ_2), after the matrix equation is solved for the approximation of $\overline{\phi}(\xi_1, \xi_2, x_3)$, inverse 2D FFT is applied to recover the electric potential $\phi(x_1, x_2, x_3)$ in real space. Electric field **E** can also be found, as described in the previous sub-section.

D.2.3 Remark

The method of using finite difference along the x_3-direction gives more reliable results at the cost of longer computation times. But due to the structure of the formulation and the associated algorithm, the computer program can be effectively parallelized to achieve high speed. In most of our works that follow, unless otherwise stated, finite difference along the x_3-direction is preferably used.

D.3 Elasticity equation by eigen-expansion

D.3.1 Background

The mechanical equilibrium equation involving eigen-strain is given by the equation:

$$\begin{cases} \sigma &= \mathbf{C}(\varepsilon - \varepsilon^*) \\ \nabla \cdot \sigma &= 0, \end{cases} \tag{D.61}$$

where ε^* is the eigen-strain, ε is the total strain, σ is the stress, and $(\varepsilon - \varepsilon^*)$ is the effective elastic strain of the 3D sample. All the physical quantities in the equation are function of the spatial space (x_1, x_2, x_3).

In indicial notation, the equation is rephrased as:

$$\begin{cases} \sigma_{ij} &= \mathbf{C}_{ijkl}(\varepsilon_{kl} - \varepsilon^*_{kl}) \\ \sigma_{ij,j} &= 0, \end{cases} \tag{D.62}$$

In the former chapters, we have successfully solved the above equation with the strong conditions of imposing periodicity in all spatial coordinates. The simulation is useful in the scale of micro-structures; however it might not be useful and meaningful to modal practical phenomena, such as in an experimental set-up. Thus we develop the solution (semi-classical and numerical) to the context of realistic situation, where we drop the periodicity in the vertical / lateral direction (x_3). Periodicities in x_1- and x_2- directions are still imposed. This assumption is valid for the three-dimensional configuration of a thin film, where the vertical dimension (height) is much smaller than the scales over the plane (x_1, x_2).

As in most experiments for small scale thin film, the base surface of the sample is adhered to a substrate such that the displacement of the base surface is zero. The top surface of the sample is subjected by a stress distribution. It is usually the case when we apply a point load (or force) by 'pressing' a cantilever tip on the surface. The lateral sides are free to deform. As long as the location of applying the point load is far away from the boundaries of the top surfaces, the deformations in the x_1-boundaries are equal while the deformations in the x_2-boundaries are equal. Thus periodicities in the x_1- and x_2- directions are valid here. In fact, any stress distribution periodic in x_1- and x_2-directions over the top surface is also workable.

D.3.2 Methodology - Decomposition of strains and stresses

Our goal is to calculate the stress and strain field (or distribution) over the whole body. We separate these quantities into homogeneous and heterogeneous portions based on the following equations proposed by L.Q. Chen [76]:

$$\begin{aligned} \varepsilon_{ij}(\mathbf{x}) &= \langle \varepsilon_{ij} \rangle + \varepsilon'_{ij}(\mathbf{x}) \\ \sigma_{ij}(\mathbf{x}) &= \langle \sigma_{ij} \rangle + \sigma'_{ij}(\mathbf{x}) \end{aligned} \tag{D.63}$$

The resulting homogeneous and perturbed constitutive equations read:

$$\begin{aligned} \left\langle \sigma_{ij} \right\rangle &= \mathbf{C}_{ijkl} \left\langle \varepsilon_{ij} \right\rangle \\ \sigma'_{ij}(\mathbf{x}) &= \mathbf{C}_{ijkl} \left[\varepsilon'_{ij}(\mathbf{x}) - \varepsilon^*_{ij}(\mathbf{x}) \right] \end{aligned} \tag{D.64}$$

In the following sub-sections, we are going to find the homogeneous or macroscopic portions and the perturbed portions of the strains and the stresses.

D.3.3 Homogeneous Strains and Stresses

Assume that the bottom of the 3D sample is constrained by the substrate so that the macroscopic strains of the thin film are:

$$\begin{aligned} \langle \varepsilon_{11} \rangle = \langle \varepsilon_1 \rangle &= a \\ \langle \varepsilon_{22} \rangle = \langle \varepsilon_2 \rangle &= b \\ 2 \langle \varepsilon_{12} \rangle = \langle \varepsilon_6 \rangle &= c, \end{aligned} \tag{D.65}$$

where $\langle f \rangle$ denotes the homogeneous portion of f (as the average of f over the 3D sample), and a, b and c are given constants. In most cases of our works, a, b and c are particularly chosen to zeros, to resemble the case where the base surface is adhered to the substrate, though a general argument is outlined here.

The unknown homogeneous strains are then:

$$\begin{aligned} \langle \varepsilon_{33} \rangle &= \langle \varepsilon_3 \rangle \\ 2 \langle \varepsilon_{23} \rangle &= \langle \varepsilon_4 \rangle \\ 2 \langle \varepsilon_{13} \rangle &= \langle \varepsilon_5 \rangle \end{aligned} \tag{D.66}$$

On the top surface with normal directed by $\mathbf{n} = \begin{pmatrix} n_1 \\ n_2 \\ n_3 \end{pmatrix} = \begin{pmatrix} 0 \\ 0 \\ 1 \end{pmatrix}$, assume we apply the uni-

form traction $\mathbf{T} = \begin{pmatrix} T_1 \\ T_2 \\ T_3 \end{pmatrix}$, so that:

$$
\begin{aligned}
\mathbf{T} &= \sigma \mathbf{n} \\
\begin{pmatrix} T_1 \\ T_2 \\ T_3 \end{pmatrix} &= \begin{pmatrix} \sigma_{11} & \sigma_{12} & \sigma_{13} \\ \sigma_{21} & \sigma_{22} & \sigma_{23} \\ \sigma_{31} & \sigma_{32} & \sigma_{33} \end{pmatrix} \begin{pmatrix} n_1 \\ n_2 \\ n_3 \end{pmatrix} \\
&= \begin{pmatrix} \sigma_{11} & \sigma_{12} & \sigma_{13} \\ \sigma_{21} & \sigma_{22} & \sigma_{23} \\ \sigma_{31} & \sigma_{32} & \sigma_{33} \end{pmatrix} \begin{pmatrix} 0 \\ 0 \\ 1 \end{pmatrix} \\
&= \begin{pmatrix} \sigma_{13} \\ \sigma_{23} \\ \sigma_{33} \end{pmatrix} = \begin{pmatrix} \langle \sigma_5 \rangle \\ \langle \sigma_4 \rangle \\ \langle \sigma_3 \rangle \end{pmatrix}
\end{aligned}
\tag{D.67}
$$

From the equation, we know that the components $\langle \sigma_5 \rangle$, $\langle \sigma_4 \rangle$ and $\langle \sigma_3 \rangle$ of the homogeneous stresses are in fact the components of the tractions acted on the top surface, while the other three components $\langle \sigma_1 \rangle$, $\langle \sigma_2 \rangle$ and $\langle \sigma_6 \rangle$ are still unknowns.

With the constitutive equation between the homogeneous strains and stresses, we may evaluate

the unknown components, as follow:

$$
\begin{pmatrix} \langle\sigma_1\rangle \\ \langle\sigma_2\rangle \\ \langle\sigma_3\rangle \\ \langle\sigma_4\rangle \\ \langle\sigma_5\rangle \\ \langle\sigma_6\rangle \end{pmatrix} = \begin{pmatrix} c_1 & c_3 & c_3 & & & \\ c_3 & c_1 & c_3 & & & \\ c_3 & c_3 & c_1 & & & \\ & & & c_2 & & \\ & & & & c_2 & \\ & & & & & c_2 \end{pmatrix} \begin{pmatrix} \langle\varepsilon_1\rangle \\ \langle\varepsilon_2\rangle \\ \langle\varepsilon_3\rangle \\ \langle\varepsilon_4\rangle \\ \langle\varepsilon_5\rangle \\ \langle\varepsilon_6\rangle \end{pmatrix}
$$

$$
\begin{pmatrix} \langle\sigma_1\rangle \\ \langle\sigma_2\rangle \\ T_3 \\ T_2 \\ T_1 \\ \langle\sigma_6\rangle \end{pmatrix} = \begin{pmatrix} c_1 & c_3 & c_3 & & & \\ c_3 & c_1 & c_3 & & & \\ c_3 & c_3 & c_1 & & & \\ & & & c_2 & & \\ & & & & c_2 & \\ & & & & & c_2 \end{pmatrix} \begin{pmatrix} a \\ b \\ \langle\varepsilon_3\rangle \\ \langle\varepsilon_4\rangle \\ \langle\varepsilon_5\rangle \\ c \end{pmatrix} \tag{D.68}
$$

The equations are solved, yielding the following solution:

$$
\begin{aligned}
\langle\sigma_6\rangle &= c_2 c = c_2 \langle\varepsilon_6\rangle \\
\langle\varepsilon_5\rangle &= \frac{T_1}{c_2} \\
\langle\varepsilon_4\rangle &= \frac{T_2}{c_2} \\
\langle\varepsilon_3\rangle &= \frac{1}{c_1} T_3 - \frac{c_3}{c_1}(a+b) \\
&= \frac{1}{c_1} T_3 - \frac{c_3}{c_1}(\langle\varepsilon_1\rangle + \langle\varepsilon_2\rangle) \\
\langle\sigma_2\rangle &= \frac{c_3}{c_1} T_3 + c_3 a + c_1 b - \frac{c_3^2}{c_1}(a+b) \\
&= \frac{c_3}{c_1} T_3 + c_3 \langle\varepsilon_1\rangle + c_1 \langle\varepsilon_2\rangle - \frac{c_3^2}{c_1}(\langle\varepsilon_1\rangle + \langle\varepsilon_2\rangle) \\
\langle\sigma_1\rangle &= \frac{c_3}{c_1} T_3 + c_1 a + c_3 b - \frac{c_3^2}{c_1}(a+b) \\
&= \frac{c_3}{c_1} T_3 + c_1 \langle\varepsilon_1\rangle + c_3 \langle\varepsilon_2\rangle - \frac{c_3^2}{c_1}(\langle\varepsilon_1\rangle + \langle\varepsilon_2\rangle)
\end{aligned} \tag{D.69}
$$

Remark: As motivated by most experiments on thin film subjected to an AFM-type and a PFM-type tips, the uniform traction is zero and the in-plane strains over the base surface are zeros. Thus in this configuration, the homogeneous strains and stresses are identically zeros.

D.3.4 Perturbed Strains and Stresses

Recall the governing equation for the perturbed part of the problem:

$$\sigma'_{ij}(\mathbf{x}) = \mathbf{C}_{ijkl}\left[\varepsilon'_{kl}(\mathbf{x}) - \varepsilon^*_{kl}(\mathbf{x})\right] \tag{D.70}$$

Since all quantities are not constants, we cannot solve for stresses and strains directly. We rewrite the strains $\varepsilon'_{ij}(\mathbf{x})$ in terms of displacements $u_i(\mathbf{x})$ (and their derivatives).

$$\sigma'_{ij}(\mathbf{x}) = \mathbf{C}_{ijkl}\left[u_{k,l}(\mathbf{x}) - \varepsilon^*_{ij}(\mathbf{x})\right] \tag{D.71}$$

Our goal is to find the displacements as the sum of two solutions, $\mathbf{u}(\mathbf{x}) = \mathbf{u}^A(\mathbf{x}) + \mathbf{u}^B(\mathbf{x})$. The decomposition is shown below.

By incorporating the equilibrium equations,

$$\begin{aligned}
\sigma_{ij,j} = 0 &\xrightarrow{\text{take perturbed portion}} \\
\sigma'_{ij,j} &= 0 \\
C_{ijkl}(\varepsilon'_{kl,j} - \varepsilon^*_{kl,j}) &= 0 \\
C_{ijkl}(u_{k,lj} - \varepsilon^*_{kl,j}) &= 0 \\
C_{ijkl}(u^A_{k,lj} + u^B_{k,lj} - \varepsilon^*_{kl,j}) &= 0 \\
C_{ijkl}(u^A_{k,lj} - \varepsilon^*_{kl,j}) + C_{ijkl}u^B_{k,lj} &= 0 \\
&\rightarrow \begin{cases} C_{ijkl}(u^A_{k,lj} - \varepsilon^*_{kl,j}) = 0 \\ C_{ijkl}u^B_{k,lj} = 0 \end{cases}
\end{aligned} \tag{D.72}$$

Thus we have formulated two sub-problems, namely A and B, with solutions denoted by displacement A and displacement B, $\mathbf{u}^A(\mathbf{x})$ and $\mathbf{u}^B(\mathbf{x})$.

Actually the equation, before the decomposition, $C_{ijkl}u_{k,lj} = C_{ijkl}\varepsilon^0_{kl,j}$ can be thought of to be a

nonhomogeneous second order differential equation. Corresponding to the nonhomogeneous term $C_{ijkl}\varepsilon^0_{kl,j}$, we find the particular solution. Secondly, we solve the general solution $C_{ijkl}u_{k,lj} = 0$. We add the general solution and the particular solution which then require the boundary conditions for the undetermined coefficients. This serves as another reason for the decomposition into solutions A and B.

This is also commonly used in computational mechanics: We solve for the field concerning inclusion (in this case, transformation strains) which usually does not involve any boundary condition. Then we solve the elasticity problem without inclusion which satisfies the boundary conditions of the overall (original) problem. The two solutions are then added whose sum solves the overall (original) elasticity problem with inclusion (described as eigen-strains) and satisfies all the BC.

Before we deal with these two solutions in detail, we visualize the decomposition of the elasticity equation in the following schematic.

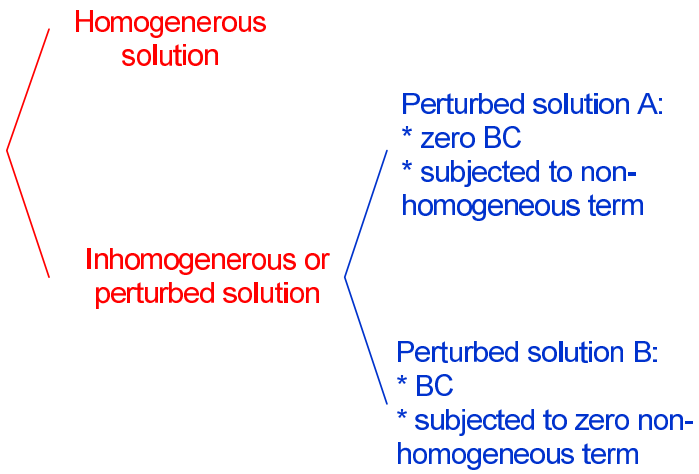

Figure D.1: Configurations for solving (a) the Maxwell's equation and (b) the mechanical equilibrium equation.

D.3.5 Perturbed Displacement A

Solution for displacement A is solved by adopting 3-dimensional FFT. No boundary conditions are needed due to periodicities.

Recall in Vigot's notation, displacements, strains and stresses are expressed as:

$$\mathbf{u} = \begin{pmatrix} u_1 \\ u_2 \\ u_3 \end{pmatrix}, \varepsilon = \begin{pmatrix} \varepsilon_1 \\ \varepsilon_2 \\ \varepsilon_3 \\ \varepsilon_4 \\ \varepsilon_5 \\ \varepsilon_6 \end{pmatrix} = \begin{pmatrix} \varepsilon_{11} \\ \varepsilon_{22} \\ \varepsilon_{33} \\ \varepsilon_{23} + \varepsilon_{32} \\ \varepsilon_{13} + \varepsilon_{31} \\ \varepsilon_{12} + \varepsilon_{21} \end{pmatrix}, \sigma = \begin{pmatrix} \sigma_1 \\ \sigma_2 \\ \sigma_3 \\ \sigma_4 \\ \sigma_5 \\ \sigma_6 \end{pmatrix} = \begin{pmatrix} \sigma_{11} \\ \sigma_{22} \\ \sigma_{33} \\ \sigma_{23} \\ \sigma_{13} \\ \sigma_{12} \end{pmatrix}. \tag{D.73}$$

Define the differentiator matrix for 3D elasticity,

$$\mathbf{B} = 2\pi I \begin{pmatrix} \xi_1 & 0 & 0 \\ 0 & \xi_2 & 0 \\ 0 & 0 & \xi_3 \\ 0 & \xi_3 & \xi_2 \\ \xi_3 & 0 & \xi_1 \\ \xi_2 & \xi_1 & 0 \end{pmatrix}, \tag{D.74}$$

so that the FFTs of displacements and strains are related via:

$$\widetilde{\varepsilon} = \mathbf{B}\widetilde{\mathbf{u}} \tag{D.75}$$

With this context, upon applying 3D FFT, the equilibrium equations become:

$$\begin{aligned} \widetilde{\sigma} &= \mathbf{C}(\widetilde{\varepsilon} - \widetilde{\varepsilon^*}) \\ \mathbf{B}\widetilde{\sigma} &= 0 \end{aligned} \tag{D.76}$$

It is straight forwards to combine the two expressions above (so as to eliminate σ) and to express

the FFT of displacement in terms of other quantities, as shown below.

$$\begin{aligned}
\mathbf{BC}(\widetilde{\varepsilon} - \widetilde{\varepsilon^*}) &= 0 \\
\mathbf{BC}(\mathbf{B}\widetilde{\mathbf{u}^A} - \widetilde{\varepsilon^*}) &= 0 \\
\mathbf{BCB}\widetilde{\mathbf{u}^A} &= \mathbf{BC}\widetilde{\varepsilon^*} \\
\widetilde{\mathbf{u}^A} &= (\mathbf{BCB})^{-1}\mathbf{BC}\widetilde{\varepsilon^*}
\end{aligned} \tag{D.77}$$

Inverse FFT can then be applied to recover the displacement in real space. Thus, without any specified boundary conditions, displacement A is obtained from the eigen-strains.

D.3.6 Perturbed Displacement B

For solution B, we solve the following (second order) homogeneous differential equation,

$$C_{ijkl}u^B_{k,lj} = 0, \tag{D.78}$$

subjected to the boundary conditions:

$$\begin{aligned}
\sigma_{i3}|_{top} &= T_i'(x_1, x_2) \\
u_i|_{bot} &= 0,
\end{aligned} \tag{D.79}$$

Recall that from the physical configuration that the three components of perturbed stresses on the top surface are equal to the perturbed portion of the traction, $T_i' = T_i - \langle T_i \rangle, i = 1,2,3$, while the three components of displacements on the base are zero.

By our proposed decomposition into displacements A and B, we may rewrite the boundary conditions as:

$$\begin{aligned}
C_{i3kl}u^B_{k,l}\big|_{top} &= -C_{i3kl}\left(u^A_{k,l} - \varepsilon^*_{kl}\right)\big|_{top} + T_i'(x_1, x_2) \\
u^B_i\big|_{bot} &= -u^A_i\big|_{bot}, i = 1,2,3.
\end{aligned} \tag{D.80}$$

These BC come from the BC imposed to the whole problem (homogeneous and perturbed portions).

Thus in order to find the displacement B, we need to incorporate displacement A and the uniform perturbed stress distribution on the top surface as the boundary conditions. Thus we need to compute solution A before we can find solution B.

We apply 2D FFT in x_1- and x_2- directions (where the indices are 1 or 2) to the governing equation, that is, $C_{ijkl}u^B_{k,lj}=0$. We group terms so that $l=(1,2,3)=(\alpha,3)$ and $j=(1,2,3)=(\beta,3)$.

$$\begin{aligned} C_{i\alpha k\beta}u^B_{k,\alpha\beta}+C_{i\alpha k3}u^B_{k,3\alpha}+C_{i3k\beta}u^B_{k,\beta 3}+C_{i3k3}u^B_{k,33}=0 \xrightarrow{\text{2D FFT}} \\ C_{i\alpha k\beta}(I\xi_\alpha)(I\xi_\beta)\widetilde{u^B_k}+(C_{i\alpha k3}+C_{i3k\alpha})\widetilde{u^B_{k,3}}+C_{i3k3}\widetilde{u^B_{k,33}}=0 \end{aligned} \tag{D.81}$$

This defines a set of second order differential equations whose derivatives are in the third coordinate at each Fourier coordinate pair (ξ_1,ξ_2). Due to the complexity of system of equation in relation to the Fourier coordinate pair (ξ_1,ξ_2), we need to separately discuss four cases, as illustrated in the following schematic.

Case 1: $\xi_1\neq 0,\xi_2\neq 0$

For the general case where both Fourier coordinates are non-zero, we take the 2D FFT on the these equilibrium equations,

$$C_{i\alpha k\beta}(I\xi_\alpha)(I\xi_\beta)\widetilde{u^B_k}+(C_{i\alpha k3}+C_{i3k\alpha})\widetilde{u^B_{k,3}}+C_{i3k3}\widetilde{u^B_{k,33}}=0,\forall i=1,2,3. \tag{D.82}$$

A coupled system of three second order differential equations in the three components of displacements will result.

Without loss of generality, we simplify the notations by setting $U_i\equiv\widetilde{u^B_i}$, $U_i'\equiv\widetilde{u^B_i}_{,3}$ and $U_i''\equiv\widetilde{u^B_i}_{,33}$, $\forall i=1,2,3$. Thus:

$$C_{i\alpha k\beta}(I\xi_\alpha)(I\xi_\beta)U_k+(C_{i\alpha k3}+C_{i3k\alpha})U_k'+C_{i3k3}U_k''=0,\forall i=1,2,3. \tag{D.83}$$

We will express the three equations explicitly by writing down all the terms as follow. Recall that we are working with isotropic materials so that all components of the material stiffness matrix degenerate to c_1, c_2 and c_3.

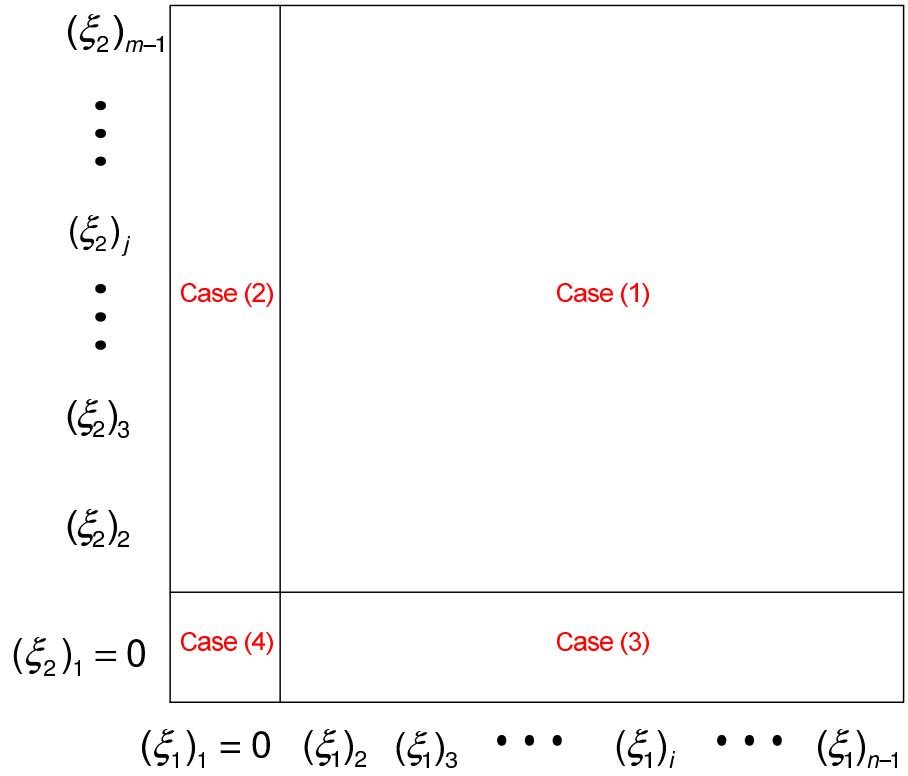

Figure D.2: Configurations for solving (a) the Maxwell's equation and (b) the mechanical equilibrium equation.

$$
\begin{aligned}
&i=1\\
&C_{1\alpha k\beta}(I\xi_\alpha)(I\xi_\beta)U_k+(C_{1\alpha k3}+C_{13k\alpha})U_k'+C_{13k3}U_k''=0\\
&\left.\begin{array}{l}c_{11k1}(I\xi_1)(I\xi_1)U_k\\ c_{11k2}(I\xi_1)(I\xi_2)U_k\\ c_{12k1}(I\xi_2)(I\xi_1)U_k\\ c_{12k2}(I\xi_2)(I\xi_2)U_k\end{array}\right|+\left|\begin{array}{l}(c_{11k3}+c_{13k1})(I\xi_1)U_k'\\ (c_{12k3}+c_{13k2})(I\xi_2)U_k'\end{array}\right|+\left|c_{13k3}U_k''\right|=0\\
&\underline{\left|\begin{array}{l}c_{1111}(I\xi_1)(I\xi_1)U_1+c_{1121}(I\xi_1)(I\xi_1)U_2+c_{1131}(I\xi_1)(I\xi_1)U_3\\ c_{1112}(I\xi_1)(I\xi_2)U_1+c_{1122}(I\xi_1)(I\xi_2)U_2+c_{1132}(I\xi_1)(I\xi_2)U_3\\ c_{1211}(I\xi_2)(I\xi_1)U_1+c_{1221}(I\xi_2)(I\xi_1)U_2+c_{1231}(I\xi_2)(I\xi_1)U_3\\ c_{1212}(I\xi_2)(I\xi_2)U_1+c_{1222}(I\xi_2)(I\xi_2)U_2+c_{1232}(I\xi_2)(I\xi_2)U_3\end{array}\right|}+\left|\begin{array}{l}(c_{1113}+c_{1311})(I\xi_1)U_1'\\ (c_{1123}+c_{1321})(I\xi_1)U_2'\\ (c_{1133}+c_{1331})(I\xi_1)U_3'\\ (c_{1213}+c_{1312})(I\xi_2)U_1'\\ (c_{1223}+c_{1322})(I\xi_2)U_2'\\ (c_{1233}+c_{1332})(I\xi_2)U_3'\end{array}\right|+\left|\begin{array}{l}c_{1313}U_1''\\ c_{1323}U_2''\\ c_{1333}U_3''\end{array}\right|=0\\
&\left|\begin{array}{l}c_{11}(I\xi_1)(I\xi_1)U_1+c_{16}(I\xi_1)(I\xi_1)U_2+c_{15}(I\xi_1)(I\xi_1)U_3\\ c_{16}(I\xi_1)(I\xi_2)U_1+c_{12}(I\xi_1)(I\xi_2)U_2+c_{14}(I\xi_1)(I\xi_2)U_3\\ c_{61}(I\xi_2)(I\xi_1)U_1+c_{66}(I\xi_2)(I\xi_1)U_2+c_{65}(I\xi_2)(I\xi_1)U_3\\ c_{66}(I\xi_2)(I\xi_2)U_1+c_{62}(I\xi_2)(I\xi_2)U_2+c_{64}(I\xi_2)(I\xi_2)U_3\end{array}\right|+\left|\begin{array}{l}(c_{15}+c_{51})(I\xi_1)U_1'\\ (c_{14}+c_{41})(I\xi_1)U_2'\\ (c_{13}+c_{55})(I\xi_1)U_3'\\ (c_{65}+c_{56})(I\xi_2)U_1'\\ (c_{64}+c_{52})(I\xi_2)U_2'\\ (c_{63}+c_{54})(I\xi_2)U_3'\end{array}\right|+\left|\begin{array}{l}c_{55}U_1''\\ c_{54}U_2''\\ c_{53}U_3''\end{array}\right|=0\\
&\left|\begin{array}{l}c_{11}(I\xi_1)(I\xi_1)U_1\\ c_{12}(I\xi_1)(I\xi_2)U_2\\ c_{66}(I\xi_2)(I\xi_1)U_2\\ c_{66}(I\xi_2)(I\xi_2)U_1\end{array}\right|+\left|(c_{13}+c_{55})(I\xi_1)U_3'\right|+\left|c_{55}U_1''\right|=0\\
&-c_1\xi_1^2U_1-c_3\xi_1\xi_2U_2-c_2\xi_2\xi_1U_2-c_2\xi_2^2U_1+(c_3+c_2)(I\xi_1)U_3'+c_2U_1''=0
\end{aligned}
$$

(D.84)

$$
\begin{aligned}
&i=2\\
&C_{2\alpha k\beta}(I\xi_\alpha)(I\xi_\beta)U_k+(C_{2\alpha k3}+C_{23k\alpha})U'_k+C_{23k3}U''_k=0\\
&\left.\begin{array}{l}c_{21k1}(I\xi_1)(I\xi_1)U_k\\ c_{21k2}(I\xi_1)(I\xi_2)U_k\\ c_{22k1}(I\xi_2)(I\xi_1)U_k\\ c_{22k2}(I\xi_2)(I\xi_2)U_k\end{array}\right|+\left|\begin{array}{l}(c_{21k3}+c_{23k1})(I\xi_1)U'_k\\ (c_{22k3}+c_{23k2})(I\xi_2)U'_k\end{array}\right|+\left|c_{23k3}U''_k\right|=0\\
&\left.\begin{array}{l}c_{2111}(I\xi_1)(I\xi_1)U_1+c_{2121}(I\xi_1)(I\xi_1)U_2+c_{2131}(I\xi_1)(I\xi_1)U_3\\ c_{2112}(I\xi_1)(I\xi_2)U_1+c_{2122}(I\xi_1)(I\xi_2)U_2+c_{2132}(I\xi_1)(I\xi_2)U_3\\ c_{2211}(I\xi_2)(I\xi_1)U_1+c_{2221}(I\xi_2)(I\xi_1)U_2+c_{2231}(I\xi_2)(I\xi_1)U_3\\ c_{2212}(I\xi_2)(I\xi_2)U_1+c_{2222}(I\xi_2)(I\xi_2)U_2+c_{2232}(I\xi_2)(I\xi_2)U_3\end{array}\right|+\left|\begin{array}{l}(c_{2113}+c_{2311})(I\xi_1)U'_1\\ (c_{2123}+c_{2321})(I\xi_1)U'_2\\ (c_{2133}+c_{2331})(I\xi_1)U'_3\\ (c_{2213}+c_{2312})(I\xi_2)U'_1\\ (c_{2223}+c_{2322})(I\xi_2)U'_2\\ (c_{2233}+c_{2332})(I\xi_2)U'_3\end{array}\right|+\left|\begin{array}{l}c_{2313}U''_1\\ c_{2323}U''_2\\ c_{2333}U''_3\end{array}\right|=0\\
&\left.\begin{array}{l}c_{61}(I\xi_1)(I\xi_1)U_1+c_{66}(I\xi_1)(I\xi_1)U_2+c_{65}(I\xi_1)(I\xi_1)U_3\\ c_{66}(I\xi_1)(I\xi_2)U_1+c_{62}(I\xi_1)(I\xi_2)U_2+c_{64}(I\xi_1)(I\xi_2)U_3\\ c_{21}(I\xi_2)(I\xi_1)U_1+c_{26}(I\xi_2)(I\xi_1)U_2+c_{25}(I\xi_2)(I\xi_1)U_3\\ c_{26}(I\xi_2)(I\xi_2)U_1+c_{22}(I\xi_2)(I\xi_2)U_2+c_{24}(I\xi_2)(I\xi_2)U_3\end{array}\right|+\left|\begin{array}{l}(c_{65}+c_{41})(I\xi_1)U'_1\\ (c_{64}+c_{41})(I\xi_1)U'_2\\ (c_{63}+c_{45})(I\xi_1)U'_3\\ (c_{25}+c_{46})(I\xi_2)U'_1\\ (c_{24}+c_{42})(I\xi_2)U'_2\\ (c_{23}+c_{44})(I\xi_2)U'_3\end{array}\right|+\left|\begin{array}{l}c_{45}U''_1\\ c_{44}U''_2\\ c_{43}U''_3\end{array}\right|=0\\
&\left.\begin{array}{l}c_{66}(I\xi_1)(I\xi_1)U_2\\ c_{66}(I\xi_1)(I\xi_2)U_1\\ c_{21}(I\xi_2)(I\xi_1)U_1\\ c_{22}(I\xi_2)(I\xi_2)U_2\end{array}\right|+\left|(c_{23}+c_{44})(I\xi_2)U'_3\right|+\left|c_{44}U''_2\right|=0\\
&-c_2\xi_1^2U_2-c_2\xi_1\xi_2U_1-c_3\xi_2\xi_1U_1-c_1\xi_2^2U_2+(c_3+c_2)(I\xi_2)U'_3+c_2U''_2=0
\end{aligned}
$$

(D.85)

$$
\begin{aligned}
&i=3\\
&C_{3\alpha k\beta}(I\xi_\alpha)(I\xi_\beta)U_k+(C_{3\alpha k3}+C_{33k\alpha})U_k'+C_{33k3}U_k''=0\\
&\left.\begin{matrix}c_{31k1}(I\xi_1)(I\xi_1)U_k\\ c_{31k2}(I\xi_1)(I\xi_2)U_k\\ c_{32k1}(I\xi_2)(I\xi_1)U_k\\ c_{32k2}(I\xi_2)(I\xi_2)U_k\end{matrix}\right\}+\left\{\begin{matrix}(c_{31k3}+c_{33k1})(I\xi_1)U_k'\\ (c_{32k3}+c_{33k2})(I\xi_2)U_k'\end{matrix}\right\}+\left\{c_{33k3}u_k''\right\}=0\\
&\left.\begin{matrix}c_{3111}(I\xi_1)(I\xi_1)U_1+c_{3121}(I\xi_1)(I\xi_1)U_2+c_{3131}(I\xi_1)(I\xi_1)U_3\\ c_{3112}(I\xi_1)(I\xi_2)U_1+c_{3122}(I\xi_1)(I\xi_2)U_2+c_{3132}(I\xi_1)(I\xi_2)U_3\\ c_{3211}(I\xi_2)(I\xi_1)U_1+c_{3221}(I\xi_2)(I\xi_1)U_2+c_{3231}(I\xi_2)(I\xi_1)U_3\\ c_{3212}(I\xi_2)(I\xi_2)U_1+c_{3222}(I\xi_2)(I\xi_2)U_2+c_{3232}(I\xi_2)(I\xi_2)U_3\end{matrix}\right\}+\left\{\begin{matrix}(c_{3113}+c_{3311})(I\xi_1)U_1'\\ (c_{3123}+c_{3321})(I\xi_1)U_2'\\ (c_{3133}+c_{3331})(I\xi_1)U_3'\\ (c_{3213}+c_{3312})(I\xi_2)U_1'\\ (c_{3223}+c_{3322})(I\xi_2)U_2'\\ (c_{3233}+c_{3332})(I\xi_2)U_3'\end{matrix}\right\}+\left\{\begin{matrix}c_{3313}U_1''\\ c_{3323}U_2''\\ c_{3333}U_3''\end{matrix}\right\}=0\\
&\left.\begin{matrix}c_{51}(I\xi_1)(I\xi_1)U_1+c_{56}(I\xi_1)(I\xi_1)U_2+c_{55}(I\xi_1)(I\xi_1)U_3\\ c_{56}(I\xi_1)(I\xi_2)U_1+c_{52}(I\xi_1)(I\xi_2)U_2+c_{54}(I\xi_1)(I\xi_2)U_3\\ c_{41}(I\xi_2)(I\xi_1)U_1+c_{46}(I\xi_2)(I\xi_1)U_2+c_{45}(I\xi_2)(I\xi_1)U_3\\ c_{46}(I\xi_2)(I\xi_2)U_1+c_{42}(I\xi_2)(I\xi_2)U_2+c_{44}(I\xi_2)(I\xi_2)U_3\end{matrix}\right\}+\left\{\begin{matrix}(c_{55}+c_{31})(I\xi_1)U_1'\\ (c_{54}+c_{36})(I\xi_1)U_2'\\ (c_{53}+c_{35})(I\xi_1)U_3'\\ (c_{45}+c_{36})(I\xi_2)U_1'\\ (c_{44}+c_{32})(I\xi_2)U_2'\\ (c_{43}+c_{34})(I\xi_2)U_3'\end{matrix}\right\}+\left\{\begin{matrix}c_{35}U_1''\\ c_{34}U_2''\\ c_{33}U_3''\end{matrix}\right\}=0\\
&\left.\begin{matrix}c_{55}(I\xi_1)(I\xi_1)U_3\\ c_{44}(I\xi_2)(I\xi_2)U_3\end{matrix}\right\}+\left\{\begin{matrix}(c_{55}+c_{31})(I\xi_1)U_1'\\ (c_{44}+c_{32})(I\xi_2)U_2'\end{matrix}\right\}+\left\{c_{33}U_3''\right\}=0\\
&-c_2\xi_1^2U_3-c_2\xi_2^2U_3+(c_2+c_3)(I\xi_1)U_1'+(c_2+c_3)(I\xi_2)U_2'+c_1U_3''=0
\end{aligned}
\tag{D.86}
$$

In summary, the coupled system of three DE's are:

$$
\begin{aligned}
-c_1\xi_1^2U_1-c_3\xi_1\xi_2U_2-c_2\xi_2\xi_1U_2-c_2\xi_2^2U_1+(c_3+c_2)(I\xi_1)U_3'+c_2U_1''=0\\
-c_2\xi_1^2U_2-c_2\xi_1\xi_2U_1-c_3\xi_2\xi_1U_1-c_1\xi_2^2U_2+(c_3+c_2)(I\xi_2)U_3'+c_2U_2''=0\\
-c_2\xi_1^2U_3-c_2\xi_2^2U_3+(c_2+c_3)(I\xi_1)U_1'+(c_2+c_3)(I\xi_2)U_2'+c_1U_3''=0
\end{aligned}
\tag{D.87}
$$

Motivated by the formulation of the state equations, we define three new variables (as the deriva-

tives of the three variables U_i) so as to generate a larger system of first order, which can then be solved by the method in linear algebra.

$$\begin{aligned} V_1 &\equiv U_1' = \widetilde{u_i^B}_{,3}, \\ V_2 &\equiv U_2' = \widetilde{u_i^B}_{,3}, \\ V_3 &\equiv U_3' = \widetilde{u_i^B}_{,3}. \end{aligned} \tag{D.88}$$

With this setting, the three second order differential equations are re-casted into a first order system of six differential equations. First, we rewrite the three second order differential equations in terms of U_i and V_i and their first derivatives only.

$$\begin{aligned} -c_1\xi_1^2U_1 - c_3\xi_1\xi_2U_2 - c_2\xi_2\xi_1U_2 - c_2\xi_2^2U_1 + (c_3+c_2)(I\xi_1)U_3' + c_2U_1'' &= 0 \\ -c_1\xi_1^2U_1 - c_3\xi_1\xi_2U_2 - c_2\xi_2\xi_1U_2 - c_2\xi_2^2U_1 + (c_3+c_2)(I\xi_1)V_3 + c_2V_1' &= 0 \\ c_1\xi_1^2U_1 + c_3\xi_1\xi_2U_2 + c_2\xi_2\xi_1U_2 + c_2\xi_2^2U_1 - (c_3+c_2)(I\xi_1)V_3 &= c_2V_1' \\ \left(\frac{c_1}{c_2}\xi_1^2 + \xi^2\right)U_1 + \left(\frac{c_3}{c_2}+1\right)\xi_1\xi_2U_2 - \frac{c_3+c_2}{c_2}(I\xi_1)V_3 &= V_1' \end{aligned} \tag{D.89}$$

$$\begin{aligned} -c_2\xi_1^2U_2 - c_2\xi_1\xi_2U_1 - c_3\xi_2\xi_1U_1 - c_1\xi_2^2U_2 + (c_3+c_2)(I\xi_2)U_3' + c_2U_2'' &= 0 \\ -c_2\xi_1^2U_2 - c_2\xi_1\xi_2U_1 - c_3\xi_2\xi_1U_1 - c_1\xi_2^2U_2 + (c_3+c_2)(I\xi_2)V_3 + c_2V_2' &= 0 \\ c_2\xi_1^2U_2 + c_2\xi_1\xi_2U_1 + c_3\xi_2\xi_1U_1 + c_1\xi_2^2U_2 - (c_3+c_2)(I\xi_2)V_3 &= c_2V_2' \\ \left(1+\frac{c_3}{c_2}\right)\xi_1\xi_2U_1 + \left(\xi_1^2 + \frac{c_1}{c_2}\xi_2^2\right)U_2 - \frac{c_3+c_2}{c_2}(I\xi_2)V_3 &= V_2' \end{aligned} \tag{D.90}$$

$$
\begin{aligned}
-c_2\xi_1^2U_3 - c_2\xi_2^2U_3 + (c_2+c_3)(I\xi_1)U_1' + (c_2+c_3)(I\xi_2)U_2' + c_1U_3'' &= 0\\
-c_2\xi_1^2U_3 - c_2\xi_2^2U_3 + (c_2+c_3)(I\xi_1)V_1 + (c_2+c_3)(I\xi_2)V_2 + c_1V_3' &= 0\\
c_2\xi_1^2U_3 + c_2\xi_2^2U_3 - (c_2+c_3)(I\xi_1)V_1 - (c_2+c_3)(I\xi_2)V_2 &= c_1V_3'\\
\frac{c_2}{c_1}\xi_1^2U_3 + \frac{c_2}{c_1}\xi_2^2U_3 - \frac{c_2+c_3}{c_1}(I\xi_1)V_1 - \frac{c_2+c_3}{c_1}(I\xi_2)V_2 &= V_3'
\end{aligned}
\tag{D.91}
$$

We may then assembly all the six equations (whose highest order of derivative ia one) above to matrix form:

$$
\frac{d}{dx_3}\begin{pmatrix} U_1\\ U_2\\ U_3\\ V_1\\ V_2\\ V_3 \end{pmatrix} = \begin{pmatrix}
0 & 0 & 0 & 1 & 0 & 0\\
0 & 0 & 0 & 0 & 1 & 0\\
0 & 0 & 0 & 0 & 0 & 1\\
\frac{c_1}{c_2}\xi_1^2+\xi_2^2 & \frac{c_3+c_2}{c_2}\xi_1\xi_2 & 0 & 0 & 0 & -\frac{c_3+c_2}{c_2}(I\xi_1)\\
\frac{c_3+c_2}{c_2}\xi_1\xi_2 & \xi_1^2+\frac{c_1}{c_2}\xi_2^2 & 0 & 0 & 0 & -\frac{c_3+c_2}{c_2}(I\xi_2)\\
0 & 0 & \frac{c_2}{c_1}(\xi_1^2+\xi_2^2) & -\frac{c_2+c_3}{c_1}(I\xi_1) & -\frac{c_2+c_3}{c_1}(I\xi_2) & 0
\end{pmatrix}\begin{pmatrix} U_1\\ U_2\\ U_3\\ V_1\\ V_2\\ V_3 \end{pmatrix}
\tag{D.92}
$$

Symbolically, we have:

$$
\mathbf{W}' = \mathbf{A}\mathbf{W} \tag{D.93}
$$

Since the material is isotropic, we may simplify all material constants further to the Young modulus (E) and the Poisson ratio (ν).

$$
\mathbf{A} = \begin{pmatrix}
0 & 0 & 0 & 1 & 0 & 0\\
0 & 0 & 0 & 0 & 1 & 0\\
0 & 0 & 0 & 0 & 0 & 1\\
\frac{2(1-\nu)}{1-2\nu}\xi_1^2+\xi_2^2 & \frac{1}{1-2\nu}\xi_1\xi_2 & 0 & 0 & 0 & -\frac{1}{1-2\nu}(I\xi_1)\\
\frac{1}{1-2\nu}\xi_1\xi_2 & \xi_1^2+\frac{2(1-\nu)}{1-2\nu}\xi_2^2 & 0 & 0 & 0 & -\frac{1}{1-2\nu}(I\xi_2)\\
0 & 0 & \frac{1-2\nu}{2(1-\nu)}(\xi_1^2+\xi_2^2) & -\frac{1}{2(1-\nu)}(I\xi_1) & -\frac{1}{2(1-\nu)}(I\xi_2) & 0
\end{pmatrix}
\tag{D.94}
$$

In fact, only Poisson ratio (ν) suffices to describe the matrix.

We need to find the eigenvalues and eigenvectors of matrix $\mathbf{W}$. The results are a Jordan Form and the modal matrix ■ consisting of eigenvectors and generalized eignevectors. The decomposition

takes the form:

$$\mathbf{WV} = \mathbf{VJ}, \tag{D.95}$$

where

$$\mathbf{J} = \left(\begin{array}{c|cc|c|cc} \sqrt{\xi_1^2+\xi_2^2} & 0 & 0 & 0 & 0 & 0 \\ \hline 0 & \sqrt{\xi_1^2+\xi_2^2} & 1 & 0 & 0 & 0 \\ 0 & 0 & \sqrt{\xi_1^2+\xi_2^2} & 0 & 0 & 0 \\ \hline 0 & 0 & 0 & -\sqrt{\xi_1^2+\xi_2^2} & 0 & 0 \\ \hline 0 & 0 & 0 & 0 & -\sqrt{\xi_1^2+\xi_2^2} & 1 \\ 0 & 0 & 0 & 0 & 0 & -\sqrt{\xi_1^2+\xi_2^2} \end{array}\right), \tag{D.96}$$

and

$$\blacksquare = \left(\begin{array}{c|cc|c|cc} \psi_1 & \psi_2 & \psi_3 & \psi_4 & \psi_5 & \psi_6 \end{array}\right), \tag{D.97}$$

with

$$\psi_1 = \begin{pmatrix} -\frac{\xi_2^3-2\xi_2(\xi_1^2+\xi_2^2)+2\xi_2^2\nu(\xi_1^2+\xi_2^2)}{\xi_1(4\nu-1)(\xi_1^2+\xi_2^2)^{\frac{3}{2}}} \\ -\frac{2\xi_1^2-2\nu(\xi_1^2+\xi_2^2)+\xi_2^2}{(4\nu-1)(\xi_1^2+\xi_2^2)^{\frac{3}{2}}} \\ 0 \\ -\frac{\xi_1^2\left(\frac{1}{2}\xi_2-\frac{1}{2}\xi_2\nu\right)-\frac{1}{2}\xi_2^3\nu+\frac{1}{4}\xi_2^3}{\xi_1\xi_2^2-\xi_1^3\nu+\xi_1^3-\xi_1\xi_2^2\nu} \\ \frac{2\xi_1^2\nu+2\xi_2^2\nu-2\xi_1^2-\xi_2^2}{4(\nu-1)(\xi_1^2+\xi_2^2)} \\ 0 \end{pmatrix}, \psi_2 = \begin{pmatrix} -\frac{\xi_1^2}{(8\nu-4)\sqrt{\xi_1^2+\xi_2^2}} \\ -\frac{\xi_1\xi_2}{(8\nu-4)\sqrt{\xi_1^2+\xi_2^2}} \\ I\frac{\xi_1}{8\nu-4} \\ \frac{\xi_1^2}{8\nu-4} \\ -\frac{\xi_1\xi_2}{8\nu-4} \\ I\frac{\xi_1(\xi_1^2+\xi_2^2)}{(8\nu-4)\sqrt{\xi_1^2+\xi_2^2}} \end{pmatrix}, \psi_3 = \begin{pmatrix} \frac{1}{2} \\ 0 \\ -I\frac{\xi_1}{(8\nu-4)\sqrt{\xi_1^2+\xi_2^2}} \\ -\frac{3\xi_1^2-4\nu(\xi_1^2+\xi_2^2)+2\xi_2^2}{4(2\nu-1)\sqrt{\xi_1^2+\xi_2^2}} \\ -\frac{\xi_1\xi_2}{4(2\nu-1)\sqrt{\xi_1^2+\xi_2^2}} \\ 0 \end{pmatrix},$$

$$\psi_4 = \begin{pmatrix} \frac{\xi_2^3-2\xi_2(\xi_1^2+\xi_2^2)+2\xi_2^2\nu(\xi_1^2+\xi_2^2)}{\xi_1(4\nu-1)(\xi_1^2+\xi_2^2)^{\frac{3}{2}}} \\ \frac{2\xi_1^2-2\nu(\xi_1^2+\xi_2^2)+\xi_2^2}{(4\nu-1)(\xi_1^2+\xi_2^2)^{\frac{3}{2}}} \\ 0 \\ -\frac{\xi_1^2\left(\frac{1}{2}\xi_2-\frac{1}{2}\xi_2\nu\right)-\frac{1}{2}\xi_2^3\nu+\frac{1}{4}\xi_2^3}{\xi_1\xi_2^2-\xi_1^3\nu+\xi_1^3-\xi_1\xi_2^2\nu} \\ \frac{2\xi_1^2\nu+2\xi_2^2\nu-2\xi_1^2-\xi_2^2}{4(\nu-1)(\xi_1^2+\xi_2^2)} \\ 0 \end{pmatrix}, \psi_5 = \begin{pmatrix} \frac{\xi_1^2}{(8\nu-4)\sqrt{\xi_1^2+\xi_2^2}} \\ \frac{\xi_1\xi_2}{(8\nu-4)\sqrt{\xi_1^2+\xi_2^2}} \\ I\frac{\xi_1}{8\nu-4} \\ -\frac{\xi_1^2}{8\nu-4} \\ -\frac{\xi_1\xi_2}{8\nu-4} \\ -I\frac{\xi_1(\xi_1^2+\xi_2^2)}{(8\nu-4)\sqrt{\xi_1^2+\xi_2^2}} \end{pmatrix}, \psi_6 = \begin{pmatrix} \frac{1}{2} \\ 0 \\ I\frac{\xi_1}{(8\nu-4)\sqrt{\xi_1^2+\xi_2^2}} \\ \frac{3\xi_1^2-4\nu(\xi_1^2+\xi_2^2)+2\xi_2^2}{4(2\nu-1)\sqrt{\xi_1^2+\xi_2^2}} \\ \frac{\xi_1\xi_2}{4(2\nu-1)\sqrt{\xi_1^2+\xi_2^2}} \\ 0 \end{pmatrix}. \quad \text{(D.98)}$$

From the Jordan Form **J**, we denote the eigenvalues of the system as $\lambda_1 = \lambda_2 = \lambda_3 = \sqrt{\xi_1^2+\xi_2^2} \equiv \xi$ and $\lambda_4 = \lambda_5 = \lambda_6 = -\sqrt{\xi_1^2+\xi_2^2} \equiv -\xi$.

For the sake of convenience, we express the structures of the six eigenvectors as $\psi_i = \begin{pmatrix} \mathbf{a}_i \\ \mathbf{b}_i \end{pmatrix}$, where $\mathbf{a}_i$ contains the first three components of the original eigenvector ψ_i, which corresponds to the three components of the displacement. Being the solution to a second-order system, each component of the displacement is of the form $\left\{\mathbf{a}_i e^{\lambda_i x_3}\right\}_{i=1..6}$. Notice that the last three entries of ψ_i, that is, $\mathbf{a}_i$, are not counted towards the solution. They were generated mathematically for finding and they are discarded and unused.

Thus the general solution takes the form:

$$\begin{aligned}\begin{pmatrix}\widetilde{u}_1^B(\xi_1,\xi_2,x_3)\\ \widetilde{u}_2^B(\xi_1,\xi_2,x_3)\\ \widetilde{u}_3^B(\xi_1,\xi_2,x_3)\end{pmatrix} &= q_1(\xi_1,\xi_2)\mathbf{a}_1 e^{\lambda_1 x_3}+q_2(\xi_1,\xi_2)\mathbf{a}_2 e^{\lambda_2 x_3}+q_3(\xi_1,\xi_2)\left[\mathbf{a}_3+x_3\mathbf{a}_2\right]e^{\lambda_3 x_3}\\ &+q_4(\xi_1,\xi_2)\mathbf{a}_4 e^{\lambda_4 x_3}+q_5(\xi_1,\xi_2)\mathbf{a}_5 e^{-\lambda_5 x_3}+q_6(\xi_1,\xi_2)\left[\mathbf{a}_6+x_3\mathbf{a}_5\right]e^{\lambda_6 x_3}\\ &= q_1(\xi_1,\xi_2)\mathbf{a}_1 e^{\xi x_3}+q_2(\xi_1,\xi_2)\mathbf{a}_2 e^{\xi x_3}+q_3(\xi_1,\xi_2)\left[\mathbf{a}_3+x_3\mathbf{a}_2\right]e^{\xi x_3}\\ &+q_4(\xi_1,\xi_2)\mathbf{a}_4 e^{-\xi x_3}+q_5(\xi_1,\xi_2)\mathbf{a}_5 e^{-\xi x_3}+q_6(\xi_1,\xi_2)\left[\mathbf{a}_6+x_3\mathbf{a}_5\right]e^{-\xi x_3},\end{aligned} \tag{D.99}$$

where $\{q_i(\xi_1,\xi_2)\}_{i=1..6}$ are unknown constants to be evaluated from the six boundary conditions (three from BC on the top surface while the other three from BC on the bottom surface).

Case 2: $\xi_1=0,\xi_2\neq 0$

The condition $\xi_1=0$ simplifies the above second order ODE system into:

$$\begin{aligned}&\xrightarrow{\xi_1=0} C_{i\alpha k\beta}(I\xi_\alpha)(I\xi_\beta)\widetilde{u}_k^B+(C_{i\alpha k3}+C_{i3k\alpha})\widetilde{u}_{k,3}^B+C_{i3k3}\widetilde{u}_{k,33}^B=0,\forall i=1,2,3\\ &\begin{cases}\widetilde{u}_{1,33}^B-\xi^2\widetilde{u}_1^B=0\\ c_{22}(I\xi_2)^2\widetilde{u}_2^B+(c_{23}+c_{44})(I\xi_2)\widetilde{u}_{3,3}^B+c_{44}\widetilde{u}_{2,33}^B=0\\ c_{44}(I\xi_2)^2\widetilde{u}_3^B+(c_{44}+c_{32})(I\xi_2)\widetilde{u}_{2,3}^B+c_{33}\widetilde{u}_{3,33}^B=0\end{cases}\end{aligned} \tag{D.100}$$

Here contracted notation for the stiffness matrix is adopted.

The first equation is a second order differential equation in $\widetilde{u}_1^B$, whose solution is straight forwards:

$$\widetilde{u}_1^B(\xi_1,\xi_2,x_3)=\widetilde{u}_1^B(0,\xi_2,x_3)=q_1(0,\xi_2)e^{\xi x_3}+q_2(0,\xi_2)e^{-\xi x_3}, \tag{D.101}$$

where $\xi=\sqrt{\xi_1^2+\xi_2^2}=\sqrt{\xi_2^2}=|\xi_2|$.

The second and third equations are two coupled differential equations of $\widetilde{u}_2^B$ and $\widetilde{u}_3^B$. Similar to the state-space formulation, we introduce new variables to replace the first-order derivatives to

ensure that the resulting systems of equations are of first-order, despite the fact that the system gets larger.

Without loss of generality, we simplify the notations:

$$\begin{aligned} U_2 &\equiv \widetilde{u_2^B} \\ U_3 &\equiv \widetilde{u_3^B}, \end{aligned} \tag{D.102}$$

so that the derivative of these variables in the third coordinate x_3 are:

$$\begin{aligned} V_2 = U_2' &= \widetilde{u_{2,3}^B} \\ V_3 = U_3' &= \widetilde{u_{3,3}^B} \end{aligned} \tag{D.103}$$

and the second derivatives of $\widetilde{u_2^B}$ and $\widetilde{u_3^B}$ are expressed as:

$$\begin{aligned} \widetilde{u_{2,33}^B} = U_2'' &= V_2' \\ \widetilde{u_{3,33}^B} = U_3'' &= V_3' \end{aligned} \tag{D.104}$$

Under this circumstance, the two equations above can be re-casted as:

$$\begin{aligned} c_{22}(I\xi_2)^2\widetilde{u_2^B} + (c_{23}+c_{44})(I\xi_2)\widetilde{u_{3,3}^B} + c_{44}\widetilde{u_{2,33}^B} = 0 &\xrightarrow{\text{contracted indices}} \\ c_1(I\xi_2)^2 U_2 + (c_3+c_2)(I\xi_2)V_3 + c_2 U_2'' = 0 & \\ -c_1\xi_2^2 U_2 + (c_3+c_2)(I\xi_2)V_3 + c_2 V_2' = 0 & \\ V_2' = \frac{c_1}{c_2}\xi_2^2 U_2 - \frac{c_3+c_2}{c_2}(I\xi_2)V_3 & \end{aligned} \tag{D.105}$$

$$\begin{aligned} c_{44}(I\xi_2)^2\widetilde{u_3^B} + (c_{44}+c_{32})(I\xi_2)\widetilde{u_{2,3}^B} + c_{44}\widetilde{u_{3,33}^B} = 0 &\xrightarrow{\text{contracted indices}} \\ c_2(I\xi_2)^2 U_3 + (c_2+c_3)(I\xi_2)V_2 + c_2 U_3'' = 0 & \\ -c_2\xi_2^2 U_2 + (c_2+c_3)(I\xi_2)V_2 + c_2 V_3' = 0 & \\ V_3' = \frac{c_2}{c_1}\xi_2^2 U_3 - \frac{c_3+c_2}{c_2}(I\xi_2)V_2 & \end{aligned} \tag{D.106}$$

Reassembly into a system of differential equations, a matrix differential equation is formed.

$$\frac{d}{dx_3}\begin{pmatrix} U_2 \\ U_3 \\ V_2 \\ V_3 \end{pmatrix} = \begin{pmatrix} 0 & 0 & 1 & 0 \\ 0 & 0 & 0 & 1 \\ \frac{c_1}{c_2}\xi_2^2 & 0 & 0 & -\frac{c_2+c_3}{c_2}I\xi_2 \\ 0 & \frac{c_2}{c_1}\xi_2^2 & -\frac{c_2+c_3}{c_1}I\xi_2 & 0 \end{pmatrix}\begin{pmatrix} U_2 \\ U_3 \\ V_2 \\ V_3 \end{pmatrix} \tag{D.107}$$

For isotropic material, we may further express the contacted stiffness constants in terms of the Young modulus (E) and the Poisson ratio (ν). Thus, we have:

$$\frac{d}{dx_3}\begin{pmatrix} U_2 \\ U_3 \\ V_2 \\ V_3 \end{pmatrix} = \begin{pmatrix} 0 & 0 & 1 & 0 \\ 0 & 0 & 0 & 1 \\ \frac{2(1-\nu)}{1-2\nu}\xi_2^2 & 0 & 0 & -\frac{1}{1-2\nu}I\xi_2 \\ 0 & \frac{1-2\nu}{2(1-\nu)}\xi_2^2 & -\frac{1}{2(1-\nu)}I\xi_2 & 0 \end{pmatrix}\begin{pmatrix} U_2 \\ U_3 \\ V_2 \\ V_3 \end{pmatrix} \tag{D.108}$$

Symbolically and compactly, the matrix equation is presented by:

$$\mathbf{W}' = \mathbf{A}\mathbf{W} \tag{D.109}$$

In order to solve this matrix differential equation, we find the eigenvalues and eigenvectors of $\mathbf{W}$:

$$\mathbf{W}\blacksquare = \blacksquare\mathbf{J}, \tag{D.110}$$

where Jordan Form $\mathbf{J}$ is utilized due to the existence of repeated eigenvalues and $\blacksquare$ is the modal matrix consisting of all the eigenvectors and the generalized eigenvectors:

$$\mathbf{J}=\begin{pmatrix} \xi_2 & 1 & & \\ & \xi_2 & & \\ & & -\xi_2 & 1 \\ & & & -\xi_2 \end{pmatrix}, \blacksquare = \left(\begin{array}{c|c|c|c} \psi_1 & \psi_2 & \psi_3 & \psi_4 \end{array} \right) = \left(\begin{array}{c|c|c|c} -\frac{\xi_2}{8\nu-4} & \frac{1}{2} & \frac{\xi_2}{8\nu-4} & \frac{1}{2} \\ I\frac{\xi_2}{8\nu-4} & -I\frac{1}{8\nu-4} & I\frac{\xi_2}{8\nu-4} & I\frac{1}{8\nu-4} \\ -\frac{\xi_2^2}{8\nu-4} & -\frac{(3-4\nu)\xi_2}{8\nu-4} & \frac{\xi_2^2}{8\nu-4} & \frac{(3-4\nu)\xi_2}{8\nu-4} \\ I\frac{\xi_2^2}{8\nu-4} & 0 & -I\frac{\xi_2^2}{8\nu-4} & 0 \end{array} \right) \tag{D.111}$$

Following the methodology developed in the general case, the expressions for the displacements:

$$\begin{aligned} \widetilde{u_1^B}(0,\xi_2,x_3) &= q_1(0,\xi_2)e^{\xi_2 x_3} + q_4(0,\xi_2)e^{-\xi_2 x_3} \\ \begin{pmatrix} \widetilde{u_2^B}(0,\xi_2,x_3) \\ \widetilde{u_3^B}(0,\xi_2,x_3) \end{pmatrix} &= q_2(0,\xi_2)\mathbf{a}_1 e^{\xi_2 x_3} + q_3(0,\xi_2)\left[\mathbf{a}_2 + x_3\mathbf{a}_1\right]e^{\xi_2 x_3} \\ &\quad + q_5(0,\xi_2)\mathbf{a}_3 e^{-\xi_2 x_3} + q_6(0,\xi_2)\left[\mathbf{a}_4 + x_3\mathbf{a}_3\right]e^{-\xi_2 x_3} \\ &= q_2(0,\xi_2)\begin{pmatrix} -\frac{\xi_2}{8\nu-4} \\ I\frac{\xi_2}{8\nu-4} \end{pmatrix} e^{\xi_2 x_3} + q_3(0,\xi_2)\left[\begin{pmatrix} \frac{1}{2} \\ -I\frac{1}{8\nu-4} \end{pmatrix} + x_3\begin{pmatrix} -\frac{\xi_2}{8\nu-4} \\ I\frac{\xi_2}{8\nu-4} \end{pmatrix}\right] e^{\xi_2 x_3} \\ &\quad + q_5(0,\xi_2)\begin{pmatrix} \frac{\xi_2}{8\nu-4} \\ I\frac{\xi_2}{8\nu-4} \end{pmatrix} e^{-\xi_2 x_3} + q_6(0,\xi_2)\left[\begin{pmatrix} \frac{1}{2} \\ I\frac{1}{8\nu-4} \end{pmatrix} + x_3\begin{pmatrix} \frac{\xi_2}{8\nu-4} \\ I\frac{\xi_2}{8\nu-4} \end{pmatrix}\right] e^{-\xi_2 x_3}, \end{aligned} \tag{D.112}$$

where $\mathbf{a}_i$ consists of the first two components of $\left\{ \psi_i = \begin{pmatrix} \mathbf{a}_i \\ \mathbf{b}_i \end{pmatrix} \right\}_{i=1..4}$.

Now we have six unknown constants to be determined, $\{q_i\}_{i=1..6}$, at each Fourier coordinate pair $(0,\xi_2)$. We may further combine the above solutions in a single matrix expression for the sake of computation:

$$
\begin{aligned}
\begin{pmatrix} \widetilde{u_1^B}(0,\xi_2,x_3) \\ \widetilde{u_2^B}(0,\xi_2,x_3) \\ \widetilde{u_3^B}(0,\xi_2,x_3) \end{pmatrix} &= q_1(0,\xi_2)\begin{pmatrix} 1 \\ 0 \\ 0 \end{pmatrix} e^{\xi_2 x_3} + q_2(0,\xi_2)\begin{pmatrix} 0 \\ -\frac{\xi_2}{8\nu-4} \\ I\frac{\xi_2}{8\nu-4} \end{pmatrix} e^{\xi_2 x_3} \\
&+ q_3(0,\xi_2)\left[\begin{pmatrix} 0 \\ \frac{1}{2} \\ -I\frac{1}{8\nu-4} \end{pmatrix} + x_3\begin{pmatrix} 0 \\ -\frac{\xi_2}{8\nu-4} \\ I\frac{\xi_2}{8\nu-4} \end{pmatrix}\right] e^{\xi_2 x_3} \\
&+ q_4(0,\xi_2)\begin{pmatrix} 1 \\ 0 \\ 0 \end{pmatrix} e^{-\xi_2 x_3} + q_5(0,\xi_2)\begin{pmatrix} 0 \\ \frac{\xi_2}{8\nu-4} \\ I\frac{\xi_2}{8\nu-4} \end{pmatrix} e^{-\xi_2 x_3} \\
&+ q_6(0,\xi_2)\left[\begin{pmatrix} 0 \\ \frac{1}{2} \\ I\frac{1}{8\nu-4} \end{pmatrix} + x_3\begin{pmatrix} 0 \\ \frac{\xi_2}{8\nu-4} \\ I\frac{\xi_2}{8\nu-4} \end{pmatrix}\right] e^{-\xi_2 x_3}
\end{aligned} \tag{D.113}
$$

Case 3: $\xi_1 \neq 0, \xi_2 = 0$

The condition $\xi_2 = 0$ simplifies the above second order ODE system into:

$$
\begin{aligned}
& C_{i\alpha k\beta}(I\xi_\alpha)(I\xi_\beta)\widetilde{u_k^B} + (C_{i\alpha k3} + C_{i3k\alpha})\,\widetilde{u_{k,3}^B} + C_{i3k3}\widetilde{u_{k,33}^B} = 0, \forall i = 1,2,3 \\
\xrightarrow{\xi_2=0} & \begin{cases} c_1(I\xi_1)^2\widetilde{u^B}_1 + (c_3+c_2)(I\xi_1)\widetilde{u_{3,3}^B} + c_2\widetilde{u_{1,33}^B} = 0 \\ \widetilde{u_{2,33}^B} - \xi^2\widetilde{u_2^B} = 0 \\ c_2(I\xi_1)^2\widetilde{u^B}_3 + (c_2+c_3)(I\xi_1)\widetilde{u_{1,3}^B} + c_1\widetilde{u_{3,33}^B} = 0 \end{cases}
\end{aligned} \tag{D.114}
$$

Here contracted notation for the stiffness matrix is adopted.

The second equation is a second order differential equation in $\widetilde{u_2^B}$, whose solution is straight forwards:

$$
\widetilde{u_2^B}(\xi_1,\xi_2,x_3) = \widetilde{u_2^B}(\xi_1,0,x_3) = q_2(\xi_1,0)e^{\xi_1 x_3} + q_5(\xi_1,0)e^{-\xi_1 x_3}. \tag{D.115}
$$

The first and third equations are two coupled differential equations of $\widetilde{u_1^B}$ and $\widetilde{u_3^B}$. Similar to the

state-space formulation, we introduce new variables to replace the first-order derivatives to ensure that the resulting systems of equations are of first-order, despite the fact that the system gets larger.

Without loss of generality, we simplify the notations:

$$\begin{aligned} U_1 &\equiv \widetilde{u_1^B} \\ U_3 &\equiv \widetilde{u_3^B}, \end{aligned} \tag{D.116}$$

so that the derivative of these variables in the third coordinate x_3 are:

$$\begin{aligned} V_1 = U_1' &= \widetilde{u_{1,3}^B} \\ V_3 = U_3' &= \widetilde{u_{3,3}^B} \end{aligned} \tag{D.117}$$

and the second derivatives of $\widetilde{u_2^B}$ and $\widetilde{u_3^B}$ are expressed as:

$$\begin{aligned} \widetilde{u_{1,33}^B} = U_1'' &= V_1' \\ \widetilde{u_{3,33}^B} = U_3'' &= V_3' \end{aligned} \tag{D.118}$$

Under this circumstance, the two equations above can be re-casted as:

$$\begin{aligned} c_1(I\xi_1)^2\widetilde{u_1^B} + (c_3+c_2)(I\xi_1)\widetilde{u_{3,3}^B} + c_2\widetilde{u_{1,33}^B} = 0 &\xrightarrow{\text{contracted indices}} \\ c_1(I\xi_1)^2 U_1 + (c_3+c_2)(I\xi_1)V_3 + c_2 U_1'' = 0 & \\ -c_1\xi_1^2 U_1 + (c_3+c_2)(I\xi_1)V_3 + c_2 V_1' = 0 & \\ V_1' = \frac{c_1}{c_2}\xi_1^2 U_1 - \frac{c_3+c_2}{c_2}(I\xi_1)V_3 & \end{aligned} \tag{D.119}$$

$$\begin{aligned} c_2(I\xi_1)^2\widetilde{u_3^B} + (c_2+c_3)(I\xi_1)\widetilde{u_{2,3}^B} + c_1\widetilde{u_{3,33}^B} = 0 &\xrightarrow{\text{contracted indices}} \\ c_2(I\xi_1)^2 U_3 + (c_2+c_3)(I\xi_1)V_1 + c_1 U_3'' = 0 & \\ -c_2\xi_1^2 U_3 + (c_2+c_3)(I\xi_1)V_1 + c_1 V_3' = 0 & \\ V_3' = \frac{c_2}{c_1}\xi_1^2 U_3 - \frac{c_3+c_2}{c_1}(I\xi_1)V_1 & \end{aligned} \tag{D.120}$$

Reassembly into a system of differential equations, a matrix differential equation is formed.

$$\frac{d}{dx_3}\begin{pmatrix} U_1 \\ U_3 \\ V_1 \\ V_3 \end{pmatrix} = \begin{pmatrix} 0 & 0 & 1 & 0 \\ 0 & 0 & 0 & 1 \\ \frac{c_1}{c_2}\xi_1^2 & 0 & 0 & -\frac{c_2+c_3}{c_2}I\xi_1 \\ 0 & \frac{c_2}{c_1}\xi_1^2 & -\frac{c_2+c_3}{c_1}I\xi_1 & 0 \end{pmatrix}\begin{pmatrix} U_1 \\ U_3 \\ V_1 \\ V_3 \end{pmatrix} \tag{D.121}$$

For isotropic material, we may further express the contacted stiffness constants in terms of the Young modulus (E) and the Poisson ratio (ν). Thus, we have:

$$\frac{d}{dx_3}\begin{pmatrix} U_1 \\ U_3 \\ V_1 \\ V_3 \end{pmatrix} = \begin{pmatrix} 0 & 0 & 1 & 0 \\ 0 & 0 & 0 & 1 \\ \frac{2(1-\nu)}{1-2\nu}\xi_1^2 & 0 & 0 & -\frac{1}{1-2\nu}I\xi_1 \\ 0 & \frac{1-2\nu}{2(1-\nu)}\xi_1^2 & -\frac{1}{2(1-\nu)}I\xi_1 & 0 \end{pmatrix}\begin{pmatrix} U_1 \\ U_3 \\ V_1 \\ V_3 \end{pmatrix} \tag{D.122}$$

Symbolically and compactly, the matrix equation is presented by:

$$\mathbf{W}' = \mathbf{A}\mathbf{W} \tag{D.123}$$

In order to solve this matrix differential equation, we find the eigenvalues and eigenvectors of $\mathbf{W}$:

$$\mathbf{W}\blacksquare = \blacksquare\mathbf{J}, \tag{D.124}$$

where Jordan Form $\mathbf{J}$ is utilized due to the existence of repeated eigenvalues and $\blacksquare$ is the modal matrix consisting of all the eigenvectors and the generalized eigenvectors:

$$\mathbf{J}=\begin{pmatrix} \xi_1 & 1 & & \\ & \xi_1 & & \\ & & -\xi_1 & 1 \\ & & & -\xi_1 \end{pmatrix}, \blacksquare = \left(\begin{array}{c|c|c|c} \psi_1 & \psi_2 & \psi_3 & \psi_4 \end{array} \right) = \left(\begin{array}{c|c|c|c} -\frac{\xi_1}{8\nu-4} & \frac{1}{2} & \frac{\xi_1}{8\nu-4} & \frac{1}{2} \\ I\frac{\xi_1}{8\nu-4} & -I\frac{1}{8\nu-4} & I\frac{\xi_1}{8\nu-4} & I\frac{1}{8\nu-4} \\ -\frac{\xi_1^2}{8\nu-4} & -\frac{(3-4\nu)\xi_1}{8\nu-4} & \frac{\xi_1^2}{8\nu-4} & \frac{(3-4\nu)\xi_1}{8\nu-4} \\ I\frac{\xi_1^2}{8\nu-4} & 0 & -I\frac{\xi_1^2}{8\nu-4} & 0 \end{array} \right) \tag{D.125}$$

Following the methodology developed in the general case, the expressions for the displacements:

$$\begin{aligned} \widetilde{u_2^B}(\xi_1,0,x_3) &= q_2(\xi_1,0)e^{\xi_1 x_3} + q_5(\xi_1,0)e^{-\xi_1 x_3} \\ \begin{pmatrix} \widetilde{u_1^B}(\xi_1,0,x_3) \\ \widetilde{u_3^B}(\xi_1,0,x_3) \end{pmatrix} &= q_1(\xi_1,0)\mathbf{a}_1 e^{\xi_1 x_3} + q_3(\xi_1,0)\left[\mathbf{a}_2 + x_3\mathbf{a}_1\right]e^{\xi_1 x_3} \\ &\quad + q_4(\xi_1,0)\mathbf{a}_3 e^{-\xi_1 x_3} + q_6(\xi_1,0)\left[\mathbf{a}_4 + x_3\mathbf{a}_3\right]e^{-\xi_1 x_3} \\ &= q_1(\xi_1,0)\begin{pmatrix} -\frac{\xi_1}{8\nu-4} \\ I\frac{\xi_1}{8\nu-4} \end{pmatrix} e^{\xi_1 x_3} + q_3(\xi_1,0)\left[\begin{pmatrix} \frac{1}{2} \\ -I\frac{1}{8\nu-4} \end{pmatrix} + x_3\begin{pmatrix} -\frac{\xi_1}{8\nu-4} \\ I\frac{\xi_1}{8\nu-4} \end{pmatrix}\right] e^{\xi_1 x_3} \\ &\quad + q_4(\xi_1,0)\begin{pmatrix} \frac{\xi_1}{8\nu-4} \\ I\frac{\xi_1}{8\nu-4} \end{pmatrix} e^{-\xi_1 x_3} + q_6(\xi_1,0)\left[\begin{pmatrix} \frac{1}{2} \\ I\frac{1}{8\nu-4} \end{pmatrix} + x_3\begin{pmatrix} \frac{\xi_1}{8\nu-4} \\ I\frac{\xi_1}{8\nu-4} \end{pmatrix}\right] e^{-\xi_1 x_3}, \end{aligned} \tag{D.126}$$

where $\mathbf{a}_i$ consists of the first two components of $\left\{ \psi_i = \begin{pmatrix} \mathbf{a}_i \\ \mathbf{b}_i \end{pmatrix} \right\}_{i=1..4}$.

Here we have six unknown constants to be determined, $q_i = \{q_i(\xi_1,0)\}_{i=1..6}$, at each Fourier coordinate pair $(\xi_1,0)$. We may further combine the above solutions in a single matrix expression for the sake of computation:

$$\begin{aligned}
\begin{pmatrix} \widetilde{u_1^B}(\xi_1,0,x_3) \\ \widetilde{u_2^B}(\xi_1,0,x_3) \\ \widetilde{u_3^B}(\xi_1,0,x_3) \end{pmatrix} &= q_1(\xi_1,0)\begin{pmatrix} -\frac{\xi_1}{8\nu-4} \\ 0 \\ I\frac{\xi_1}{8\nu-4} \end{pmatrix} e^{\xi_1 x_3} + q_2(\xi_2,0)\begin{pmatrix} 0 \\ 1 \\ 0 \end{pmatrix} e^{\xi_1 x_3} \\
&+ q_3(\xi_2,0)\left[\begin{pmatrix} \frac{1}{2} \\ 0 \\ -I\frac{1}{8\nu-4} \end{pmatrix} + x_3\begin{pmatrix} -\frac{\xi_1}{8\nu-4} \\ 0 \\ I\frac{\xi_1}{8\nu-4} \end{pmatrix}\right] e^{\xi_1 x_3} \\
&+ q_4(\xi_1,0)\begin{pmatrix} \frac{\xi_2}{8\nu-4} \\ 0 \\ I\frac{\xi_2}{8\nu-4} \end{pmatrix} e^{-\xi_1 x_3} + q_5(\xi_1,0)\begin{pmatrix} 0 \\ 1 \\ 0 \end{pmatrix} e^{-\xi_1 x_3} \\
&+ q_6(\xi_1,0)\left[\begin{pmatrix} \frac{1}{2} \\ 0 \\ I\frac{1}{8\nu-4} \end{pmatrix} + x_3\begin{pmatrix} \frac{\xi_1}{8\nu-4} \\ 0 \\ I\frac{\xi_1}{8\nu-4} \end{pmatrix}\right] e^{-\xi_1 x_3}
\end{aligned} \tag{D.127}$$

Case 4: $\xi_1 = \xi_2 = 0$

The condition $\xi_1 = \xi_2 = 0$ simplify the above second order ODE system into:

$$\begin{aligned}
C_{i\alpha k\beta}(I\xi_\alpha)(I\xi_\beta)\widetilde{u_k^B} + (C_{i\alpha k3} + C_{i3k\alpha})\widetilde{u_{k,3}^B} + C_{i3k3}\widetilde{u_{k,33}^B} &= 0, \forall i = 1,2,3 \\
C_{i3k3}\widetilde{u_{k,33}^B} &= 0, \forall i = 1,2,3 \\
C_{i3k3}\widetilde{u_{k,33}^B} &= 0, \forall i = 1,2,3
\end{aligned} \tag{D.128}$$

Writing out all the equations, we have:

$$\begin{cases}
\widetilde{u_{1,33}^B} = 0 \\
\widetilde{u_{2,33}^B} = 0 \\
\widetilde{u_{3,33}^B} = 0
\end{cases} \tag{D.129}$$

The solutions of these equations are straight forwards, that is,

$$\begin{cases} \widetilde{u_1^B}(\xi_1,\xi_2,x_3) = \widetilde{u_1^B}(0,0,x_3) = q_1(0,0)x_3 + q_4(0,0) \\ \widetilde{u_2^B}(\xi_1,\xi_2,x_3) = \widetilde{u_2^B}(0,0,x_3) = q_2(0,0)x_3 + q_5(0,0) \\ \widetilde{u_3^B}(\xi_1,\xi_2,x_3) = \widetilde{u_3^B}(0,0,x_3) = q_3(0,0)x_3 + q_6(0,0) \end{cases}, \tag{D.130}$$

where $\{q_i = q_i(0,0)\}|_{i=1..6}$ are the unknown coefficients to be determined from BC.

D.3.7 Solving the Boundary Value Problems from $q_i(\xi_1,\xi_2)$

Regardless of the differences in the technical details in the four cases above, we end up with the procedure to evaluate the six unknown coefficients $\{q_i(\xi_1,\xi_2)\}_{i=1..6}$ using the six boundary conditions imposed on the top and bottom surface of the sample. Solving for q_i is the same as solving the system of algebraic equations at each Fourier coordinate (ξ_1,ξ_2):

$$\mathbf{A}_{6\times6}\mathbf{q}_{6\times1} = \mathbf{b}_{6\times1}, \tag{D.131}$$

where $\mathbf{A} = \mathbf{A}(\xi_1,\xi_2)$ is the same for all iterations and is computed at the beginning of the program.

The vector **b** comes from the boundary conditions that are also related to the displacement A, as in the BC equations:

$$\begin{aligned} c_{i3kl}u^B_{k,l}\big|_{top} &= -\,c_{i3kl}\left(u^A_{k,l} - \varepsilon^*_{kl}\right)\big|_{top} + T_i', \forall i = 1,2,3 \\ u^B_i\big|_{bot} &= -\,u^A_i\big|_{bot}, \forall i = 1,2,3 \end{aligned} \tag{D.132}$$

This vector should be generated and renewed in every iteration.

More specifically, the six boundary conditions are explicitly given:

$$
\begin{aligned}
u^B_{1,3}(:,:,L)+u^B_{3,1}(:,:,L) &= -\left(u^A_{1,3}(:,:,h)+u^A_{3,1}(:,:,L)\right)+\varepsilon^*_{13}(:,:,L)+\frac{T_1'(:,:)}{c_3}\\
u^B_{2,3}(:,:,L)+u^B_{3,2}(:,:,L) &= -\left(u^A_{2,3}(:,:,h)+u^A_{3,2}(:,:,L)\right)+\varepsilon^*_{23}(:,:,L)+\frac{T_2'(:,:)}{c_3}\\
c_3u^B_{1,1}(:,:,L)+c_3u^B_{2,2}(:,:,L)+c_1u^B_{3,3}(:,:,L) &= -c_3\left(u^B_{1,1}(:,:,L)-\varepsilon^*_{11}(:,:,L)\right)\\
&\quad -c_3\left(u^B_{2,2}(:,:,L)-\varepsilon^*_{22}(:,:,L)\right)\\
&\quad -c_1\left(u^B_{3,3}(:,:,L)-\varepsilon^*_{33}(:,:,L)\right)+T_3'(:,:)\\
u^B_1(:,:,0) &= -u^A_1(:,:,0)\\
u^B_2(:,:,0) &= -u^A_2(:,:,0)\\
u^B_3(:,:,0) &= -u^A_3(:,:,0)
\end{aligned}
\tag{D.133}
$$

Transforming these boundary conditions in their 2D FFT, and substituting the general solutions A and B and comparing with coefficients will yield the unknown constants $\{q_i = q_i(\xi_1,\xi_2)\}_{i=1..6}$ at each Fourier coordinate pair (ξ_1,ξ_2).

After we have found $q_i(\xi_1,\xi_2)$, displacements B in 2D FFT are also known. We may then assembly the displacements A and B for perturbed portion of strains and stresses. Homogeneous and heterogeneous fields give the total fields.

D.4 Elasticity equation by finite differences

The ”state equation” approach is elegant in the sense of theoretic development and fast in the corresponding numerical algorithm. However call that in the process of finding the perturbed displacement A, we adopted FFT in the x_3-direction, which violates our first physical assumption that the sample may not be necessarily periodic in the x_3-direction. This is related to the ”Runge's phenomenon” in the field of numerical analysis, where numerical approximation of functions by polynomials near the edges of the interval induces oscillation from the expected values.

In our simulation using the state space approach, the displacements computed commit the mentioned oscillating behaviors towards the very ends of the interval along the x_3-direction. To give a

feeling on how bad the numerical approximation is to the solution (displacement), say, if the number of subdivision points is 64, then probably the first 4 and the last 4 data are oscillating away from the expected valves.

Luckily, the strains, which we compute from the displacements, are accurate numerically. This might be due to the fact that taking derivatives of the displacements kill the oscillation towards the two ends of the interval. Thus if the simulations do not require the explicit processing of the displacement fields, the "state equation" approach is workable. In most cases, the more important physical quantities are the strains and the stresses. However if the simulations do require the explicit uses of the displacements, as in the case of displaying the surface tomography (the shape of deformation), we may want to develop a more accurate numerical method. A good alternative is the finite difference approach along the x_3-direction, despite the fact that it is slower than the former numerical scheme.

D.4.1 Discretization of differential equations

We start with the three mechanical equilibrium equations after taking 2D FFT (Recall that we have obtained these in last subsection):

$$\begin{aligned} C_{ijkl}\left(u_{k,lj}-\varepsilon^{*}_{kl,j}\right)=0, i=1,2,3 \\ C_{ijkl}u_{k,lj}=C_{ijkl}\varepsilon^{*}_{kl,j}, i=1,2,3 \end{aligned} \tag{D.134}$$

For the sake of simplifying the expressions, we assume that the non-homogeneous terms of the three differential equations to be f, g and h. They are computed as follow:

Non-homogeneous term of the first equation ($i = 1$):

$$
\begin{aligned}
& i = 1 \\
f(x_1, x_2, x_3) &= C_{1jkl}\varepsilon^*_{kl,j} \\
&= C_{11kl}\varepsilon^*_{kl,1} + C_{12kl}\varepsilon^*_{kl,2} + C_{13kl}\varepsilon^*_{kl,3} \\
&= C_{1111}\varepsilon^*_{11,1} + C_{1122}\varepsilon^*_{22,1} + C_{1133}\varepsilon^*_{33,1} \\
&+ C_{1212}\varepsilon^*_{12,2} + C_{1221}\varepsilon^*_{21,2} + C_{1313}\varepsilon^*_{13,3} + C_{1331}\varepsilon^*_{31,3} \\
&= C_{11}\varepsilon^*_{11,1} + C_{12}\varepsilon^*_{22,1} + C_{13}\varepsilon^*_{33,1} \\
&+ C_{66}\varepsilon^*_{12,2} + C_{66}\varepsilon^*_{21,2} + C_{55}\varepsilon^*_{13,3} + C_{55}\varepsilon^*_{31,3} \\
&= c_1\varepsilon^*_{11,1} + c_3\varepsilon^*_{22,1} + c_3\varepsilon^*_{33,1} \\
&+ c_2\varepsilon^*_{12,2} + c_2\varepsilon^*_{21,2} + c_2\varepsilon^*_{13,3} + c_2\varepsilon^*_{31,3} \\
&= c_1\varepsilon^*_{1,1} + c_3\varepsilon^*_{2,1} + c_3\varepsilon^*_{3,1} + c_2\varepsilon^*_{6,2} + c_2\varepsilon^*_{5,3}
\end{aligned}
\tag{D.135}
$$

Non-homogeneous term of the second equation ($i = 2$):

$$
\begin{aligned}
& i = 2 \\
g(x_1, x_2, x_3) &= C_{2jkl}\varepsilon^*_{kl,j} \\
&= C_{21kl}\varepsilon^*_{kl,1} + C_{22kl}\varepsilon^*_{kl,2} + C_{23kl}\varepsilon^*_{kl,3} \\
&= C_{2121}\varepsilon^*_{21,1} + C_{2112}\varepsilon^*_{12,1} \\
&+ C_{2211}\varepsilon^*_{11,2} + C_{2222}\varepsilon^*_{22,2} + C_{2233}\varepsilon^*_{33,2} \\
&+ C_{2323}\varepsilon^*_{23,3} + C_{2332}\varepsilon^*_{32,3} \\
&= C_{66}\varepsilon^*_{21,1} + C_{66}\varepsilon^*_{12,1} \\
&+ C_{21}\varepsilon^*_{11,2} + C_{22}\varepsilon^*_{22,2} + C_{23}\varepsilon^*_{33,2} \\
&+ C_{44}\varepsilon^*_{23,3} + C_{44}\varepsilon^*_{32,3} \\
&= c_2\varepsilon^*_{21,1} + c_2\varepsilon^*_{12,1} \\
&+ c_3\varepsilon^*_{11,2} + c_1\varepsilon^*_{22,2} + c_3\varepsilon^*_{33,2} \\
&+ c_2\varepsilon^*_{23,3} + c_2\varepsilon^*_{32,3} \\
&= c_2\varepsilon^*_{6,1} + c_3\varepsilon^*_{1,2} + c_1\varepsilon^*_{2,2} + c_3\varepsilon^*_{3,2} + c_2\varepsilon^*_{4,3}
\end{aligned}
\tag{D.136}
$$

Non-homogeneous term of the third equation ($i = 3$):

$$
\begin{aligned}
& i = 3 \\
k(x_1, x_2, x_3) &= C_{3jkl}\varepsilon^*_{kl,j} \\
&= C_{31kl}\varepsilon^*_{kl,1} + C_{32kl}\varepsilon^*_{kl,2} + C_{33kl}\varepsilon^*_{kl,3} \\
&= C_{3131}\varepsilon^*_{31,1} + C_{3113}\varepsilon^*_{13,1} \\
&+ C_{3232}\varepsilon^*_{32,2} + C_{3223}\varepsilon^*_{23,2} \\
&+ C_{3311}\varepsilon^*_{11,3} + C_{3322}\varepsilon^*_{22,3} + C_{3333}\varepsilon^*_{33,3} \\
&= C_{55}\varepsilon^*_{31,1} + C_{55}\varepsilon^*_{13,1} \\
&+ C_{44}\varepsilon^*_{32,2} + C_{44}\varepsilon^*_{23,2} \\
&+ C_{31}\varepsilon^*_{11,3} + C_{32}\varepsilon^*_{22,3} + C_{33}\varepsilon^*_{33,3} \\
&= c_2\varepsilon^*_{31,1} + c_2\varepsilon^*_{13,1} \\
&+ c_2\varepsilon^*_{32,2} + c_2\varepsilon^*_{23,2} \\
&+ c_3\varepsilon^*_{11,3} + c_3\varepsilon^*_{22,3} + c_1\varepsilon^*_{33,3} \\
&= c_2\varepsilon^*_{5,1} + c_2\varepsilon^*_{4,2} + c_3\varepsilon^*_{1,3} + c_3\varepsilon^*_{2,3} + c_1\varepsilon^*_{3,3}
\end{aligned}
\tag{D.137}
$$

The left hand sides ($C_{ijkl}u_{k,lj}$) of the three differential equations are in fact identical to those derived in the last section and are listed below.

$$
\begin{aligned}
-c_1\xi_1^2\overline{u_1} - c_3\xi_1\xi_2\overline{u_2} - c2\xi_2\xi_1\overline{u_2} - c_2\xi_1^2\overline{u_1} + (c_2+c_3)(I\xi_1)\overline{u_1}' + c_2\overline{u_1}'' &= \overline{f} \\
-c_2\xi_1^2\overline{u_2} - c_2\xi_1\xi_2\overline{u_1} - c3\xi_2\xi_1\overline{u_1} - c_1\xi_2^2\overline{u_2} + (c_2+c_3)(I\xi_2)\overline{u_3}' + c_2\overline{u_3}'' &= \overline{g} \\
-c_2\xi_1^2\overline{u_3} - c_2\xi_2^2\overline{u_3} + (c_2+c_3)(I\xi_1)\overline{u_1}' + (c_2+c_3)(I\xi_2)\overline{u_2}' + c_1\overline{u_3}'' &= \overline{k},
\end{aligned}
\tag{D.138}
$$

where we have adopted the notation:

$$
\begin{aligned}
u_i &\equiv u_i(x_1, x_2, x_3), i = 1,2,3 \\
\overline{u_i} &\equiv \overline{u_i}(\xi_1, \xi_2, x_3), i = 1,2,3 \\
\overline{u_i}' &\equiv \frac{\partial \overline{u_i}(\xi_1, \xi_2, x_3)}{\partial x_3}, i = 1,2,3 \\
\overline{u_i}'' &\equiv \frac{\partial^2 \overline{u_i}(\xi_1, \xi_2, x_3)}{\partial x_3^2}, i = 1,2,3
\end{aligned}
\tag{D.139}
$$

In the following we discretize each of these three equations using finite differences at each interior points. At each Fourier pair (ξ_1, ξ_2), we denote the following variables to approximate the 2D FFT of the displacements along the z-coordinate.

$$
\begin{aligned}
U_i &\approx \overline{u_1}(\xi_1, \xi_2, x_{3,i}), i = 1,2,...,N \\
V_i &\approx \overline{u_2}(\xi_1, \xi_2, x_{3,i}), i = 1,2,...,N \\
W_i &\approx \overline{u_3}(\xi_1, \xi_2, x_{3,i}), i = 1,2,...,N \\
F_i &\approx \overline{f}(\xi_1, \xi_2, x_{3,i}), i = 1,2,...,N \\
G_i &\approx \overline{g}(\xi_1, \xi_2, x_{3,i}), i = 1,2,...,N \\
H_i &\approx \overline{h}(\xi_1, \xi_2, x_{3,i}), i = 1,2,...,N
\end{aligned}
\tag{D.140}
$$

Discretization of the first equation at at $x_{3,i}, i = 1,2,..,N$***:***

$$
\begin{aligned}
-c_1\xi_1^2\overline{u_1} - c_3\xi_1\xi_2\overline{u_2} - c2\xi_2\xi_1\overline{u_2} - c_2\xi_1^2\overline{u_1} + (c_2+c_3)(I\xi_1)\overline{u_3}' + c_2\overline{u_1}'' &= \overline{f} \xrightarrow{\text{discretize at } x_{3,i}} \\
-c_1\xi_1^2 U_i - c_3\xi_1\xi_2 V_i - c2\xi_2\xi_1 V_i - c_2\xi_1^2 U_i + (c_2+c_3)(I\xi_1)W_i' + c_2 U_i'' &= F_i \\
\begin{aligned}
&-c_1\xi_1^2 U_i - c_3\xi_1\xi_2 V_i - c2\xi_2\xi_1 V_i - c_2\xi_1^2 U_i \\
&+(c_2+c_3)(I\xi_1)\tfrac{W_{i+1}-W_{i-1}}{2h} + c_2\tfrac{U_{i+1}-2U_i+U_{i-1}}{h^2}
\end{aligned} &= F_i \\
\begin{aligned}
&2c_2U_{i-1} - h(c_2+c_3)(I\xi_1)W_{i-1} \\
&-4c_2U_i - 2h^2(c_1\xi_1^2 + c_2\xi_2^2)U_i - 2h^2(c_2+c_3)\xi_1\xi_2 V_i \\
&+2c_2U_{i+1} + h(c_2+c_3)(I\xi_1)W_{i+1}
\end{aligned} &= 2h^2F_i \\
A_1U_{i-1} + A_3W_{i-1} + A_4U_i + A_5V_i + A_7U_{i+1} + A_9W_{i+1} &= 2h^2F_i, \qquad \text{(D.141)}
\end{aligned}
$$

where $A_j = A_j(\xi_1,\xi_2)$ are the coefficients introduced for the set-up of the matrices in the finite difference scheme.

Discretization of the second equation at $z_i, i = 1,2,..,N$***:***

$$
\begin{aligned}
-c_2\xi_1^2\overline{u_2} - c_2\xi_1\xi_2\overline{u_1} - c3\xi_2\xi_1\overline{u_1} - c_1\xi_2^2\overline{u_2} + (c_2+c_3)(I\xi_2)\overline{u_3}' + c_2\overline{u_2}'' &= \overline{g} \xrightarrow{\text{discretize at } x_{3,i}} \\
-c_2\xi_1^2 V_i - c_2\xi_1\xi_2 U_i - c3\xi_2\xi_1 U_i - c_1\xi_2^2 V_i + (c_2+c_3)(I\xi_2)W_i' + c_2 V_i'' &= G_i \\
\begin{aligned}
&-c_2\xi_1^2 V_i - c_2\xi_1\xi_2 U_i - c3\xi_2\xi_1 U_i - c_1\xi_2^2 V_i \\
&+(c_2+c_3)(I\xi_2)\tfrac{W_{i+1}-W_{i-1}}{2h} + c_2\tfrac{V_{i+1}-2V_i+V_{i-1}}{h^2}
\end{aligned} &= G_i \\
\begin{aligned}
&2c_2V_{i-1} - h(c_2+c_3)(I\xi_2)W_{i-1} \\
&-2h^2(c_2+c_3)\xi_1\xi_2 U_i - 2h^2(c_2\xi_1^2 + c_1\xi_2^2)V_i - 4c_2V_i \\
&+2c_2V_{i+1} + h(c_2+c_3)(I\xi_2)W_{i+1}
\end{aligned} &= 2h^2G_i \\
B_2V_{i-1} + B_3W_{i-1} + B_4U_i + B_5V_i + B_8V_{i+1} + B_9W_{i+1} &= 2h^2G_i, \qquad \text{(D.142)}
\end{aligned}
$$

where $B_j = B_j(\xi_1,\xi_2)$ are the coefficients introduced for the set-up of matrices in the finite difference scheme.

Discretization of the third equation at $z_i, i = 1,2,..,N$**:**

$$
\begin{aligned}
-c_2\xi_1^2\overline{u_3} - c_2\xi_2^2\overline{u_3} + (c_2+c_3)(I\xi_1)\overline{u_1}' + (c_2+c_3)(I\xi_2)\overline{u_2}' + c_1\overline{u_3}'' &= \overline{k} \xrightarrow{\text{discretize at } x_{3,i}} \\
-c_2\xi_1^2 W_i - c_2\xi_2^2 W_i + (c_2+c_3)(I\xi_1)U_i' + (c_2+c_3)(I\xi_2)V_i' + c_1 W_i'' &= K_i \\
-c_2\xi_1^2 W_i - c_2\xi_2^2 W_i + (c_2+c_3)(I\xi_1)\tfrac{U_{i+1}-U_{i-1}}{2h} & \\
+(c_2+c_3)(I\xi_2)\tfrac{V_{i+1}-V_{i-1}}{2h} + c_1\tfrac{W_{i+1}-2W_i+W_{i-1}}{h^2} &= K_i \\
-h(c_2+c_3)(I\xi_1)U_{i-1} - h(c_2+c_3)(I\xi_2)V_{i-1} + 2c_1 W_{i-1} & \\
-2h^2 c_2(\xi_1^2+\xi_2^2)W_i - 4c_1 W_i &= 2h^2 K_i \\
+h(c_2+c_3)(I\xi_1)U_{i+1} + h(c_2+c_3)(I\xi_2)V_{i+1} + 2c_1 W_{i+1} & \\
C_1U_{i-1} + C_2V_{i-1} + C_3W_{i-1} + C_6W_i + C_7U_{i+1} + C_8V_{i+1} + C_9W_{i+1} &= 2h^2K_i, \qquad \text{(D.143)}
\end{aligned}
$$

where $C_j = C_j(\xi_1, \xi_2)$ are the coefficients introduced for the set-up of matrices in the finite difference scheme.

These pairs of three equations will be assembled into the matrix for $i = 2$ to $i = n-1$, that is, all rows except the top three and the bottom three rows, which we will deal with using the the boundary conditions imposed over the top and bottom surfaces, as will be discussed in the next section.

D.4.2 Boundary conditions

Recall that the boundary conditions are:

1. Tractions on the top surface.

2. Displacements on the bottom surface.

Assume that the height $x_3 \in [0, L]$ of the sample is discretized into N subdivision points such that the size of subdivision is $h = dz = \frac{L}{N-1}$. Since the boundary conditions on the top surface are expressed in terms of displacements, we introduce a ghost-point beyond the right end point in the x_3-coordinate ($x_{3,n+1} = x_{3,n} + h$) and incorporate the resulting discretizated equations into the last three rows of the matrix.

BC:* x_1*-component of traction on top surface

$$
\begin{aligned}
\sigma_{31}(x_1,x_2,x_3) &= \sigma_5(x_1,x_2,x_3)\\
&= c_2\left[\varepsilon_5(x_1,x_2,x_3) - \varepsilon_5^*(x_1,x_2,x_3)\right]\\
&= c_2\left[u_{1,3}(x_1,x_2,x_3) + u_{3,1}(x_1,x_2,x_3) - \varepsilon_5^*(x_1,x_2,x_3)\right] \xrightarrow{\text{2D FFT}}\\
\overline{\sigma_{31}}(\xi_1,\xi_2,x_3) &= c_2\left[\frac{\partial \overline{u_1}}{\partial x_3}(\xi_1,\xi_2,x_3) + \overline{u_3}(\xi_1,\xi_2,x_3)I\xi_1 - \overline{\varepsilon_5^*}(\xi_1,\xi_2,x_3)\right] \xrightarrow{\text{discretization @ } x_{3,n}}\\
\overline{\sigma_{31}}(\xi_1,\xi_2,x_{3,n}) &= c_2\left[\frac{\partial \overline{u_1}}{\partial x_3}(\xi_1,\xi_2,x_{3,n}) + \overline{u_3}(\xi_1,\xi_2,x_{3,n})I\xi_1 - \overline{\varepsilon_5^*}(\xi_1,\xi_2,x_{3,n})\right]\\
\frac{\overline{\sigma_{31}}(\xi_1,\xi_2,x_{3,n})}{c_2} &= \frac{\partial U_n}{\partial x_3} + W_n I\xi_1 - \overline{\varepsilon_5^*}(\xi_1,\xi_2,x_{3,n})\\
\frac{\overline{T_1'}(\xi_1,\xi_2)}{c_2} &= \frac{U_{n+1}-U_{n-1}}{2h} + W_n I\xi_1 - \overline{\varepsilon_5^*}(\xi_1,\xi_2,x_{3,n})\\
-U_{n-1} + 2hI\xi_1 W_n + U_{n+1} &= \frac{2h}{c_2}\overline{T_1'}(\xi_1,\xi_2) + 2h\overline{\varepsilon_5^*}(\xi_1,\xi_2,z_n) \equiv \widetilde{F}\\
-U_{n-1} + D_1 W_n + U_{n+1} &= \widetilde{F}
\end{aligned}
\tag{D.144}
$$

BC:* x_2*-component of traction on top surface

$$
\begin{aligned}
\sigma_{32}(x_1,x_2,x_3) &= \sigma_4(x_1,x_2,x_3)\\
&= c_2\left[\varepsilon_4(x_1,x_2,x_3) - \varepsilon_4^*(x_1,x_2,x_3)\right]\\
&= c_2\left[u_{2,3}(x_1,x_2,x_3) + u_{3,2}(x_1,x_2,x_3) - \varepsilon_4^*(x_1,x_2,x_3)\right] \xrightarrow{\text{2D FFT}}\\
\overline{\sigma_{32}}(\xi_1,\xi_2,x_3) &= c_2\left[\frac{\partial \overline{u_2}}{\partial x_3}(\xi_1,\xi_2,x_3) + \overline{u_3}(\xi_1,\xi_2,x_3)I\xi_2 - \overline{\varepsilon_4^*}(\xi_1,\xi_2,x_3)\right] \xrightarrow{\text{discretization @ } x_{3,n}}\\
\overline{\sigma_{32}}(\xi_1,\xi_2,x_{3,n}) &= c_2\left[\frac{\partial \overline{u_2}}{\partial x_3}(\xi_1,\xi_2,x_{3,n}) + \overline{u_3}(\xi_1,\xi_2,x_{3,n})I\xi_2 - \overline{\varepsilon_4^*}(\xi_1,\xi_2,x_{3,n})\right]\\
\frac{\overline{\sigma_{32}}(\xi_1,\xi_2,x_{3,n})}{c_2} &= \frac{\partial V_n}{\partial x_3} + W_n I\xi_2 - \overline{\varepsilon_4^*}(\xi_1,\xi_2,x_{3,n})\\
\frac{\overline{T_2'}(\xi_1,\xi_2)}{c_2} &= \frac{V_{n+1}-V_{n-1}}{2h} + W_n I\xi_2 - \overline{\varepsilon_4^*}(\xi_1,\xi_2,x_{3,n})\\
-V_{n-1} + 2hI\xi_1 W_n + V_{n+1} &= \frac{2h}{c_2}\overline{T_2'}(\xi_1,\xi_2) + 2h\overline{\varepsilon_4^*}(\xi_1,\xi_2,x_{3,n}) \equiv \widetilde{G}\\
-V_{n-1} + D_2 W_n + V_{n+1} &= \widetilde{G}
\end{aligned}
\tag{D.145}
$$

BC:* x_3*-component of traction on top surface

$$
\begin{aligned}
\sigma_{33}(x_1,x_2,x_3) &= \sigma_3(x_1,x_2,x_3) \\
&= c_3\left[\varepsilon_1(x_1,x_2,x_3) - \varepsilon_1^*(x_1,x_2,x_3)\right] \\
&+ c_3\left[\varepsilon_2(x_1,x_2,x_3) - \varepsilon_2^*(x_1,x_2,x_3)\right] \\
&+ c_1\left[\varepsilon_3(x_1,x_2,x_3) - \varepsilon_3^*(x_1,x_2,x_3)\right] \\
&= c_3\left[u_{1,1}(x_1,x_2,x_3) - \varepsilon_1^*(x_1,x_2,x_3)\right] \\
&+ c_3\left[u_{2,2}(x_1,x_2,x_3) - \varepsilon_2^*(x_1,x_2,x_3)\right] \\
&+ c_1\left[u_{2,3}(x_1,x_2,x_3) - \varepsilon_3^*(x_1,x_2,x_3)\right] \xrightarrow{\text{2D FFT}} \\
\overline{\sigma_{33}}(\xi_1,\xi_2,x_3) &= c_3\left[\overline{u_1}(\xi_1,\xi_2,x_3)I\xi_1 - \overline{\varepsilon_1^*}(\xi_1,\xi_2,x_3)\right] \\
&+ c_3\left[\overline{u_2}(\xi_1,\xi_2,x_3)I\xi_2 - \overline{\varepsilon_2^*}(\xi_1,\xi_2,x_3)\right] \\
&+ c_1\left[\frac{\overline{u_3}}{\partial z}(\xi_1,\xi_2,x_3) - \overline{\varepsilon_3^*}(\xi_1,\xi_2,x_3)\right] \xrightarrow{\text{discretization @ } x_{3,n}} \\
\overline{\sigma_{33}}(\xi_1,\xi_2,x_{3,n}) &= c_3\left[\overline{u_1}(\xi_1,\xi_2,x_{3,n})I\xi_1 - \overline{\varepsilon_1^*}(\xi_1,\xi_2,x_{3,n})\right] \\
&+ c_3\left[\overline{u_2}(\xi_1,\xi_2,x_{3,n})I\xi_2 - \overline{\varepsilon_2^*}(\xi_1,\xi_2,x_{3,n})\right] \\
&+ c_1\left[\frac{\overline{u_3}}{\partial x_3}(\xi_1,\xi_2,x_{3,n}) - \overline{\varepsilon_3^*}(\xi_1,\xi_2,x_{3,n})\right] \\
\frac{\overline{\sigma_{33}}(\xi_1,\xi_2,x_{3,n})}{c_3} &= U_nI\xi_1 - \overline{\varepsilon_1^*}(\xi_1,\xi_2,x_{3,n}) + V_nI\xi_2 - \overline{\varepsilon_2^*}(\xi_1,\xi_2,x_{3,n}) \\
&+ \frac{c_1}{c_3}\left[\frac{\partial W_n}{\partial x_3} - \overline{\varepsilon_3^*}(\xi_1,\xi_2,x_{3,n})\right] \\
\frac{\overline{T_3'}(\xi_1,\xi_2)}{c_3} &= U_nI\xi_1 + V_nI\xi_2 + \frac{c_1}{c_3}\frac{W_{n+1}-W_{n-1}}{2h} \\
&- \overline{\varepsilon_1^*}(\xi_1,\xi_2,x_{3,n}) - \overline{\varepsilon_2^*}(\xi_1,\xi_2,x_{3,n}) - \frac{c_1}{c_3}\overline{\varepsilon_3^*}(\xi_1,\xi_2,x_{3,n})
\end{aligned}
$$

$$
\begin{aligned}
-W_{n-1} + 2h\frac{c_3}{c_1}I\xi_1U_n + 2h\frac{c_3}{c_1}I\xi_2V_n + W_{n+1} &= \frac{2h}{c_1}T_3' + 2h\frac{c_3}{c_1}\overline{\varepsilon_1^*}(x_{3,n}) + 2h\frac{c_3}{c_1}\overline{\varepsilon_2^*}(x_{3,n}) + 2h\overline{\varepsilon_3^*}(x_{3,n}) \\
-W_{n-1} + D_3U_n + D_4V_n + W_{n+1} &= \widetilde{H}
\end{aligned}
\tag{D.146}
$$

The resulting expressions corresponding to the three boundary conditions on the top surface will be meshed to the top three rows of the matrix for finite difference.

BC: displacements on bottom surface

Assume that the three components of the displacements are given as $u_i(x,y,x_3=0), i=1,2,3$, whose 2D FFTs are computed as $U_1(\xi_1,\xi_2) \approx \overline{u_1}(\xi_1,\xi_2,x_3=0)$, $V_1(\xi_1,\xi_2) \approx \overline{u_2}(\xi_1,\xi_2,x_3=0)$ and $W_1(\xi_1,\xi_2) \approx \overline{u_3}(\xi_1,\xi_2,x_3=0)$.

As a remark, for practical consideration, the 3D sample is adhered to a substrate so that the three components are zero, so that $U_1(\xi_1,\xi_2) = V_1(\xi_1,\xi_2) = W_1(\xi_1,\xi_2) = 0$. But here we give the BC in the general scenario.

In the context of discretization, at each Fourier pair (ξ_1,ξ_2),

$$\begin{cases} A_1U_1 + A_3W_1 + A_4U_2 + A_5V_2 + A_7U_3 + A_9W_3 &= 2h^2F_2 \\ B_2V_1 + B_3W_1 + B_4U_2 + B_5V_2 + B_8V_3 + B_9W_3 &= 2h^2G_2 \\ C_1U_1 + C_2V_1 + C_3W_1 + C_6W_2 + C_7U_3 + C_8V_3 + C_9W_3 &= 2h^2K_2 \end{cases} \tag{D.147}$$

Since U_1, V_1 and W_1 are give numerical values, we rearrange the expressions above:

$$\begin{cases} A_4U_2 + A_5V_2 + A_7U_3 + A_9W_3 &= 2h^2F_2 - A_1U_1 - A_3W_1 \\ B_4U_2 + B_5V_2 + B_8V_3 + B_9W_3 &= 2h^2G_2 - B_2V_1 - B_3W_1 \\ C_6W_2 + C_7U_3 + C_8V_3 + C_9W_3 &= 2h^2K_2 - C_1U_1 - C_2V_1 - C_3W_1 \end{cases} \tag{D.148}$$

These three expressions will then be meshed into the matrix for finite difference.

D.4.3 Assembly of matrices for the finite difference scheme

With the numerical schemes developed in the interior points and the boundary points, we end up with the following matrix equation for solving for the 2D FFTs of the three components of displacements, at each Fourier pair (ξ_1,ξ_2).

$$
\left(\begin{array}{ccc:ccc:ccc:ccc:ccc:ccc:c}
A_4 & A_5 & & A_7 & & A_9 & & & & & & & & & & & & & U_2 \\
B_4 & B_5 & & & B_8 & B_9 & & & & & & & & & & & & & V_2 \\
 & & C_6 & C_7 & C_8 & C_9 & & & & & & & & & & & & & W_2 \\
\hdashline
A_1 & & A_3 & A_4 & A_5 & & A_7 & & A_9 & & & & & & & & & & U_3 \\
 & B_2 & B_3 & B_4 & B_5 & & & B_8 & B_9 & & & & & & & & & & V_3 \\
C_1 & C_2 & C_3 & & & C_6 & C_7 & C_8 & C_9 & & & & & & & & & & W_3 \\
\hdashline
 & & & A_1 & & A_3 & A_4 & A_5 & & A_7 & & A_9 & & & & & & & U_4 \\
 & & & & B_2 & B_3 & B_4 & B_5 & & & B_8 & B_9 & & & & & & & V_4 \\
 & & & C_1 & C_2 & C_3 & & & C_6 & C_7 & C_8 & C_9 & & & & & & & W_4 \\
\hdashline
 & & & & & & \ddots & \ddots & \ddots & \ddots & \ddots & \ddots & \ddots & & & & & & \vdots \\
 & & & & & & & \ddots & \ddots & \ddots & \ddots & \ddots & \ddots & \ddots & & & & & \vdots \\
 & & & & & & & & \ddots & \ddots & \ddots & \ddots & \ddots & \ddots & \ddots & & & & \vdots \\
\hdashline
 & & & & & & & & & A_1 & & A_3 & A_4 & A_5 & & A_7 & & A_9 & U_n \\
 & & & & & & & & & & B_2 & B_3 & B_4 & B_5 & & & B_8 & B_9 & V_n \\
 & & & & & & & & & C_1 & C_2 & C_3 & & & C_6 & C_7 & C_8 & C_9 & W_n \\
\hdashline
 & & & & & & & & & -1 & & & & & D_1 & 1 & & & U_{n+1} \\
 & & & & & & & & & & -1 & & & & D_2 & & 1 & & V_{n+1} \\
 & & & & & & & & & & & -1 & D_3 & D_4 & & & & 1 & W_{n+1}
\end{array}\right)
$$

$$
= \left(\begin{array}{c}
F_2 - A_1U_1 - A_2V_1 - A_3W_1 \\
G_2 - B_1U_1 - B_2V_1 - B_3W_1 \\
H_2 - C_1U_1 - C_2V_1 - C_3W_1 \\
\hdashline
F_3 \\ G_3 \\ H_3 \\
\hdashline
F_4 \\ G_4 \\ H_4 \\
\hdashline
\vdots \\ \vdots \\ \vdots \\
\hdashline
F_n \\ G_n \\ H_n \\
\hdashline
\widetilde{F} \\ \widetilde{G} \\ \widetilde{H}
\end{array}\right)
\tag{D.149}
$$

We notice that the matrix is a basically block tri-diagonal matrix except for the last three rows. We need to modify the block LU decomposition for tri-diagonal matrix for the inverse matrix.

D.4.4 Modified block LU decomposition

We now decompose the "modified" block tri-diagonal square matrix **A** by the approach similar to the LU-decomposition. For the purpose of illustration and for the sake of simplified formulation, assume we are working with a system with 7 blocks. Generalization can then be carried out.

The method is as follow: With the proposed structures of the two decomposed matrices **L** and **U**, we multiply them and compare the original matrix **A**. Comparison with the appropriate entries give the formulae for the decomposition.

$$\mathbf{A} = \mathbf{LU}$$

$$\begin{pmatrix} b & c & & & & \\ a & b & c & & & \\ & a & b & c & & \\ & & a & b & c & \\ & & & a & b & c \\ & & & d & e & f \end{pmatrix} = \begin{pmatrix} I & & & & & \\ L_2 & I & & & & \\ M_3 & L_3 & I & & & \\ & M_4 & L_4 & I & & \\ & & M_5 & L_5 & I & \\ & & & M_6 & L_6 & I \end{pmatrix} \begin{pmatrix} U_1 & N_1 & & & & \\ & U_2 & N_2 & & & \\ & & U_3 & N_3 & & \\ & & & U_4 & U_4 & \\ & & & & U_5 & U_5 \\ & & & & & U_6 \end{pmatrix}$$

$$= \begin{pmatrix} U_1 & N_1 & & & & \\ L_2U_1 & L_2N_1+U_2 & N_2 & & & \\ M_3U_1 & M_3N_1+L_3U_2 & L_3N_2+U_3 & N_3 & & \\ & M_4U_2 & M_4N_2+L_4U_3 & L_4N_3+U_4 & N_4 & \\ & & M_5U_3 & M_5N_3+L_5U_4 & L_5N_4+U_5 & U_5 \\ & & & M_6U_4 & M_6N_4+L_6U_5 & L_6N_5+U_6 \end{pmatrix} \tag{D.150}$$

In the above, all the entries involved, a, b, c, d, e, f, L_i, M_i, U_i, N_i, are all 3×3-matrices. I is the 3×3 identity matrix.

Comparison along the upper diagonal entries gives $N_i = c$. Comparison in all other entries generate the formula, as summarized in the following table.

i	M_i	L_i	U_i	U_i^{-1}
1			$U_1 = b$	U_1^{-1}
2		$L_2 = aU_1^{-1}$	$U_2 = b - L_2 c$	U_2^{-1}
3	0	$L_3 = aU_2^{-1}$	$U_3 = b - L_3 c$	U_3^{-1}
4	0	$L_4 = aU_3^{-1}$	$U_4 = b - L_4 c$	U_4^{-1}
5	0	$L_5 = aU_4^{-1}$	$U_5 = b - L_5 c$	U_5^{-1}
6	$M_6 = dU_4$	$L_6 = (e - M_6 c)U_5^{-1}$	$U_6 = f - L_6 c$	U_6^{-1}

Our goal is to solve the algebraic equations with this kind of matrices, $\mathbf{Au} = \mathbf{f}$. This involves two processes, namely, the forwards substitution and the backwards substitution.

$$\begin{aligned} \mathbf{Au} &= \mathbf{f} \\ \mathbf{LUu} &= \mathbf{f} \\ \mathbf{Lv} &= \mathbf{f} \end{aligned} \tag{D.151}$$

The LU decomposition suggests us to solve the following sub-systems.

Forwards substitution

$$\begin{pmatrix} I & & & & & \\ L_2 & I & & & & \\ M_3 & L_3 & I & & & \\ & M_4 & L_4 & I & & \\ & & M_5 & L_5 & I & \\ & & & M_6 & L_6 & I \end{pmatrix} \begin{pmatrix} v_1 \\ v_2 \\ v_3 \\ v_4 \\ v_5 \\ v_6 \end{pmatrix} = \begin{pmatrix} f_1 \\ f_2 \\ f_3 \\ f_4 \\ f_5 \\ f_6 \end{pmatrix}$$

$$\begin{cases} v_1 = f_1 & \to v_1 = f_1 \\ L_2 v_1 + v_2 = f_2 & \to v_2 = f_2 - L_2 v_1 \\ L_3 v_2 + v_3 = f_2 & \to v_3 = f_3 - L_3 v_2 \\ L_4 v_3 + v_4 = f_2 & \to v_4 = f_4 - L_4 v_3 \\ L_5 v_4 + v_5 = f_2 & \to v_5 = f_5 - L_5 v_4 \\ M_6 v_4 + L_6 v_5 + v_6 = f_2 & \to v_6 = f_6 - L_6 v_5 - M_6 v_4 \end{cases} \tag{D.152}$$

Backwards substitution

$$\begin{pmatrix} U_1 & N_1 & & & & \\ & U_2 & N_2 & & & \\ & & U_3 & N_3 & & \\ & & & U_4 & U_4 & \\ & & & & U_5 & U_5 \\ & & & & & U_6 \end{pmatrix} \begin{pmatrix} u_1 \\ u_2 \\ u_3 \\ u_4 \\ u_5 \\ u_6 \end{pmatrix} = \begin{pmatrix} v_1 \\ v_2 \\ v_3 \\ v_4 \\ v_5 \\ v_6 \end{pmatrix}$$

$$\begin{pmatrix} U_1 & c & & & & \\ & U_2 & c & & & \\ & & U_3 & c & & \\ & & & U_4 & c & \\ & & & & U_5 & c \\ & & & & & U_6 \end{pmatrix} \begin{pmatrix} u_1 \\ u_2 \\ u_3 \\ u_4 \\ u_5 \\ u_6 \end{pmatrix} = \begin{pmatrix} v_1 \\ v_2 \\ v_3 \\ v_4 \\ v_5 \\ v_6 \end{pmatrix}$$

$$\begin{cases} U_6 u_6 = v_6 & \rightarrow u_6 = U_6^{-1} v_6 \\ U_5 u_5 + c u_6 = v_5 & \rightarrow u_5 = U_5^{-1}(v_5 - c u_6) \\ U_4 u_4 + c u_5 = v_4 & \rightarrow u_4 = U_4^{-1}(v_4 - c u_5) \\ U_3 u_3 + c u_4 = v_3 & \rightarrow u_3 = U_3^{-1}(v_3 - c u_4) \\ U_2 u_2 + c u_3 = v_2 & \rightarrow u_2 = U_2^{-1}(v_2 - c u_3) \\ U_1 u_1 + c u_2 = v_1 & \rightarrow u_1 = U_1^{-1}(v_1 - c u_2) \end{cases} \tag{D.153}$$

The general algorithm for the decomposition and the linear equation solvers are summarized:

$\mathbf{A}=\mathbf{LU}$	Inputs: component blocks a,b,c,d,e,f of matrix $\mathbf{A}$
$i=1$	$L_1=0$ $U_1=b$
$i=2...n-1$	$N_i=c$ $L_i=aU_{i-1}^{-1}$ $U_i=b-L_ic$
$i=n$	$M_n=dU_{n-2}^{-1}$ $L_n=(e-M_nc)U_{n-1}^{-1}$ $U_n=f-L_nc$

forwards	$\mathbf{Lv}=\mathbf{f}$
$i=1$	$v_1=f_1$
$i=2...n-1$	$v_i=f_i-L_iv_{i-1}$
$i=n$	$v_n=f_n-L_nv_{n-1}-M_nv_{n-2}$

backwards	$\mathbf{Uu}=\mathbf{v}$
$i=n$	$u_n=U_n^{-1}v_n$
$i=n-1...1$	$u_i=U_i^{-1}(v_i-cu_{i+1})$

D.4.5 Remark on alterative approach to deal with BC with derivative

Following the method of introducing 'ghost point' beyond the right end point in the z-coordinate, we may express the displacements at these ghost points by other existing quantities so as to eliminate them, by considering solving the following six equations:

$$\xrightarrow[\text{difference}\\ \text{at } i=n]{\text{finite}} \begin{cases} A_1U_{n-1}+A_3W_{n-1}+A_4U_n+A_5V_n+A_7U_{n+1}+A_9W_{n+1} &= 2h^2F_n \\ B_2V_{n-1}+B_3W_{n-1}+B_4U_n+B_5V_n+B_8V_{n+1}+B_9W_{n+1} &= 2h^2G_n \\ C_1U_{n-1}+C_2V_{n-1}+C_3W_{n-1}+C_6W_n+C_7U_{n+1}+C_8V_{n+1}+C_9W_{n+1} &= 2h^2K_n \end{cases} \tag{D.154}$$

$$\xrightarrow[\text{at } i=n]{\text{boundary condition}} \begin{cases} -U_{n-1}+D_1W_n+U_{n+1} &= \widetilde{F} \\ -V_{n-1}+D_2W_n+V_{n+1} &= \widetilde{G} \\ -W_{n-1}+D_3U_n+D_4V_n+W_{n+1} &= \widetilde{H} \end{cases} \tag{D.155}$$

From the six equations listed above, we may express U_n, V_n, W_n, U_{n+1}, V_{n+1} and W_{n+1} in terms of other quantities, which is equivalent to eliminating the uses of the quantities at ghost points. This act also reduces the size of the matrix for finite difference from N blocks down to $N-2$ blocks. However the drawback is that the calculations are tough and the resulting expressions of the variables are complicated.

D.5 Convention of elastic stiffness

$$\mathbf{C} = \begin{pmatrix} C_{11} & C_{12} & C_{13} & C_{14} & C_{15} & C_{16} \\ C_{21} & C_{22} & C_{23} & C_{24} & C_{25} & C_{26} \\ C_{31} & C_{32} & C_{33} & C_{34} & C_{35} & C_{36} \\ C_{41} & C_{42} & C_{43} & C_{44} & C_{45} & C_{46} \\ C_{51} & C_{52} & C_{53} & C_{54} & C_{55} & C_{56} \\ C_{61} & C_{62} & C_{63} & C_{64} & C_{65} & C_{66} \end{pmatrix} = \begin{pmatrix} c_1 & c_3 & c_3 & & & \\ c_3 & c_1 & c_3 & & & \\ c_3 & c_3 & c_1 & & & \\ & & & c_2 & & \\ & & & & c_2 & \\ & & & & & c_2 \end{pmatrix} \tag{D.156}$$

D.5.1 Hooke's Law

In Vigot's notation,

$$\begin{pmatrix} \varepsilon_1 \\ \varepsilon_2 \\ \varepsilon_3 \\ \varepsilon_4 \\ \varepsilon_5 \\ \varepsilon_6 \end{pmatrix} = \begin{pmatrix} \varepsilon_{11} \\ \varepsilon_{22} \\ \varepsilon_{33} \\ 2\varepsilon_{23} \\ 2\varepsilon_{13} \\ 2\varepsilon_{12} \end{pmatrix} = \begin{pmatrix} u_{1,1} \\ u_{2,2} \\ u_{3,3} \\ u_{2,3}+u_{3,2} \\ u_{1,3}+u_{3,1} \\ u_{1,2}+u_{2,1} \end{pmatrix} \tag{D.157}$$

The stress-strain relation is:

$$\begin{pmatrix} \sigma_{11} \\ \sigma_{22} \\ \sigma_{33} \\ \sigma_{23} \\ \sigma_{13} \\ \sigma_{12} \end{pmatrix} = \frac{E}{(1+\nu)(1-2\nu)} \begin{pmatrix} 1-\nu & \nu & \nu & & & \\ \nu & 1-\nu & \nu & & & \\ \nu & \nu & 1-\nu & & & \\ & & & 1-2\nu & & \\ & & & & 1-2\nu & \\ & & & & & 1-2\nu \end{pmatrix} \begin{pmatrix} \varepsilon_{11} \\ \varepsilon_{22} \\ \varepsilon_{33} \\ \varepsilon_{23} \\ \varepsilon_{13} \\ \varepsilon_{12} \end{pmatrix}$$

$$\begin{pmatrix} \sigma_{1} \\ \sigma_{2} \\ \sigma_{3} \\ \sigma_{4} \\ \sigma_{5} \\ \sigma_{6} \end{pmatrix} = \frac{E}{(1+\nu)(1-2\nu)} \begin{pmatrix} 1-\nu & \nu & \nu & & & \\ \nu & 1-\nu & \nu & & & \\ \nu & \nu & 1-\nu & & & \\ & & & \frac{1-2\nu}{2} & & \\ & & & & \frac{1-2\nu}{2} & \\ & & & & & \frac{1-2\nu}{2} \end{pmatrix} \begin{pmatrix} \varepsilon_{1} \\ \varepsilon_{2} \\ \varepsilon_{3} \\ \varepsilon_{4} \\ \varepsilon_{5} \\ \varepsilon_{6} \end{pmatrix} \quad \text{(D.158)}$$

D.5.2 Matlab code to find the eigenvalue decomposition of the matrix

```
% general case
% v = 0.2;

k1 = 0;
syms v k2
% syms v k1 k2

G = [ 0, 0, 0, 1, 0, 0;
    0, 0, 0, 0, 1, 0;
    0, 0, 0, 0, 0, 1;
    2*(1-v)/(1-2*v)*k1^2+k2^2, k1*k2/(1-2*v), 0, 0, 0, -I*k1/(1-2*v);
    k1*k2/(1-2*v), k1^2 + 2*(1-v)/(1-2*v)*k2^2, 0, 0, 0, -I*k2/(1-2*v);
    0, 0, (1-2*v)/2/(1-v)*(k1^2+k2^2), -I*k1/2/(1-v), -I*k2/2/(1-v), 0 ];
```

```
[V,J] = jordan(G)
V = simplify(factor(expand(V)))
check3 = simplify( G*V – V*J )
```

Appendix E

SOME BACKGROUND OF ESM

This appendix outlines some background on the models related to the evolution equation for lithium ions and the electrochemical strain microscopy.

E.1 Normalization of the ESM equation

Since we study sample of lithium ions and associated dynamics under SPM tip in small scale, it is reasonable to normal the equation in both length scale (with respect to the radius of the SPm tip R) and time scale (with respect to dynamics of ions). The original governing evolution equations for ions, also known as the PNP equation, is given by:

$$\frac{\partial c}{\partial t} = D\frac{\partial^2 c}{\partial x^2} + D\beta\frac{\partial}{\partial x}\left(c\frac{\partial \phi}{\partial x}\right), \tag{E.1}$$

where c is the concentration of ions in the unit of mole of number of particles, D is the diffusivity of the ion in the unit of m^2/s, ϕ is the induced potential over the entire sample due to SPM in the unit of J/C, β is the drifting coefficient of the ion in the unit of C/J. It is noted that the units of ϕ and β are reciprocal to each other, which will suggest a possible normalized quantity for potential.

The length scale is normalized with respect to the tip radius R:

$$x^* \equiv \frac{x}{R} \tag{E.2}$$

The partial derivatives in spatial coordinate can be written as:

$$\begin{aligned} \frac{\partial}{\partial x} &= \frac{\partial x^*}{\partial x}\frac{\partial}{\partial x^*} = \frac{1}{R}\frac{\partial}{\partial x^*} \\ \frac{\partial^2}{\partial x^2} &= \frac{1}{R^2}\frac{\partial^2}{\partial x^{*2}} \end{aligned} \tag{E.3}$$

The equation is rewritten as:

$$\frac{\partial c}{\partial t} = D\frac{1}{R^2}\frac{\partial^2 c}{\partial x^{*2}} + D\frac{1}{R^2}\frac{\partial}{\partial x^*}\left(c\frac{\partial(\beta\phi)}{\partial x^*}\right) \tag{E.4}$$

The common factor $\frac{D}{R^2}$ on the right hand side suggests us to introduce the following normalization in time scale:

$$t^* \equiv \frac{t}{\frac{R^2}{D}} \tag{E.5}$$

Also the product of β and ϕ is a unit-less quantity, which suggests us to define:

$$\phi^* \equiv \beta\phi \tag{E.6}$$

With these, the ESM is normalized as:

$$\frac{\partial c}{\partial t^*} = \frac{\partial^2 c}{\partial x^{*2}} + \frac{\partial}{\partial x^*}\left(c\frac{\partial \phi^*}{\partial x^*}\right) \tag{E.7}$$

E.2 SPM tip

The following is the list of variables involved in the study of SPM tip for ESM of ion:

variables	names	units
R	tip radius	Meters (m)
V_0	applied voltage	Volts (V)
ε_{ii}	permittivity	Farad/meter (F/m)
$\kappa = \sqrt{\varepsilon_{33}\varepsilon_{11}}$	effective permittivity	NA
$\gamma = \sqrt{\frac{\varepsilon_{33}}{\varepsilon_{11}}}$	dielectric anisotropy	NA
Q	effective charge of the SPM tip	Coulomb (C)
d_{real}	distance between tip and sample surface	Meters (m)
d	distance between effective charge Q due to SPM tip and sample surface	Meters (m)
ϕ	potential developed in sample	Volt (V)
E	electric field developed in sample	Volt/meters (V/m)

E.3 Plane-Sphere Model

In all of our discussion, we assume that the SPM tip is touching the top surface of the sample. In other words, the SPM tip is in contact mode. Thus the distance between the SPM tip and the sample surface is taken as $d_{real} = 0$. The SPM tip is virtually imagined as a point charge Q located at a distance d above the sample surface where:

$$\begin{aligned} Q &= 2\varepsilon_0(1+\kappa)V_0\frac{d^2 - d_{real}^2}{d + d_{real}} = 2\varepsilon_0(1+\kappa)V_0 d \\ d &= \frac{2R}{\kappa - 1} ln\frac{1+\kappa}{2} + d_{real} = \frac{2R}{\kappa - 1} ln\frac{1+\kappa}{2}, \end{aligned} \tag{E.8}$$

where ε_0 is the absolute permittivity of vacuum. This charge Q induces a potential ϕ over the domain of the sample:

$$\begin{aligned} \phi(x) &= \frac{Q}{2\pi\varepsilon_0(1+\kappa)}\frac{1}{\frac{x}{\gamma} + d} \\ &= V_0 d\left(\frac{x}{\gamma} + d\right)^{-1} \end{aligned} \tag{E.9}$$

Equivalently, an electric field E, acting in x-direction, is generated over the sample:

$$\begin{aligned} E(x) &= -\frac{\partial \phi}{\partial x} \\ &= \frac{V_0 d}{\gamma}\left(\frac{x}{\gamma}+d\right)^{-2} \end{aligned} \tag{E.10}$$

For Lithium Iron Phosphate ($LiFeO_4$), we assume the permittivities in all directions to be identically. Under this assumption, we have the following simplified expressions of various quantities being discussed:

$$\begin{aligned} \varepsilon_{11} &= \varepsilon_{33} = \varepsilon \\ \kappa &= \varepsilon \\ \gamma &= 1 \\ d &= \frac{2R}{\varepsilon - 1}\ln\frac{1+\varepsilon}{2} \\ \phi &= V_0 d(x+d)^{-1} \\ E &= V_0 d(x+d)^{-2} \end{aligned} \tag{E.11}$$

In some analyses and simulations, we also need to normalize these quantities. For instance,

$$\begin{aligned} x^* &\equiv \frac{x}{R} \\ d^* &\equiv \frac{d}{R} \\ H^* &\equiv \frac{H}{R} \\ \phi^*(x^*) &= \underbrace{\beta V_0}_{\text{dimension-less}}\ d^*(x^*+d^*)^{-1} \\ E^*(x^*) &= \underbrace{\beta V_0}_{\text{dimension-less}}\ d^*(x^*+d^*)^{-2} \end{aligned} \tag{E.12}$$

E.4 Parameters used in simulations

The parameters used in the simulation depends on the real system and experimental data. The radius of the SPM tip is usually 10 (nm), or, 10×10^{-9} (m). The thickness of the sample is 1 (micron),

or, 10^{-6} (m). According to literatures, the diffusivity D is in the range of 10^{-22} to 10^{-14} (m^2/s). Experience suggests that we may normalize it with $D = 10^{-18}$. For study in relaxation with bias DC-AC voltage, the experiment takes about 30 (s). The AC voltage is operating at a frequency of 1000 (kHz), or, 1000×1000 (Hz). The voltages of DC and AC are respectively 10 Volts and 3 Volts.

The time and spatial scales are normalized with respect to:

$$\begin{aligned} \overline{x} &= R = 10 \times 10^{-9}(m) \\ \overline{t} &= \frac{R^2}{D} = \frac{(10 \times 10^{-9})}{10^{-14}} = 0.01(s) \\ \overline{\omega} &= \frac{1}{\overline{t}} = 100(Hz) \end{aligned} \tag{E.13}$$

Thus the quantities in real and normalized scales are summarized in the table:

Quantities	in real scale	in normalized scale
Radius of SPM tip	$R = 10(nm) = 10 \times 10^{-9}(m)$	$R^* = 1$
Distance between Q and sample surface	$d = 0.3788R$	$d^* = 0.3788$
Thickness of sample	$H = 2 \times 10^{-6}(m)$	$H^* = 200$
time range	$t = 30(s)$	$t^* = 3000$
frequency range	$\omega = 1000 \times 1000(Hz)$	$\omega^* = 10000$
DC Voltage	$V_{DC} = 10(V)$	$V_{DC}^* = 10 \times 40$
AC Voltage	$V_{AC} = 3(V)$	$V_{AC}^* = 3 \times 40$

E.5 Second Harmonic

Following the same methodology that we developed the first harmonic, we may derive further a set of differential equations with boundary conditions for the second harmonic $c_2(x)$. We balance terms with the exponential factor $e^{2j\omega t}$ and substitute the resulting expression into real and imaginary parts using $c_i(x) = a_i(x) + jb_i(x)$:

$$
\begin{aligned}
(2j\omega)c_2(x) &= c_2''(x) + c_1'(x)\phi(x) + c_1(x)\phi'(x) \\
(2j\omega)(a_2(x) + jb_2(x)) &= (a_2(x) + jb_2(x))'' + (a_1(x) + jb_1(x))'\phi(x) + (a_1(x) + jb_1(x))\phi'(x) \\
-2\omega b_2(x) + j2\omega a_2(x) &= a_2''(x) + jb_2''(x) + a_1'(x)\phi(x) + jb_1'(x)\phi(x) + a_1(x)\phi'(x) + jb_1(x)\phi'(x) \\
&\begin{cases} -2\omega b_2(x) &= a_2''(x) + a_1'(x)\phi(x) + a_1(x)\phi'(x) \\ 2\omega a_2(x) &= b_2''(x) + b_1'(x)\phi(x) + b_1(x)\phi'(x) \end{cases} \\
&\begin{cases} a_2''(x) + 2\omega b_2(x) &= -a_1'(x)\phi(x) - a_1(x)\phi'(x) \\ b_2''(x) - 2\omega a_2(x) &= -b_1'(x)\phi(x) - b_1(x)\phi'(x) \end{cases}
\end{aligned} \tag{E.14}
$$

These two equations can be combined into a single equation of higher order. The second equation is rewritten as:

$$
\begin{aligned}
a_2(x) &= b_2''(x) + b_1'(x)\phi(x) + b_1(x)\phi'(x) \\
&= \frac{1}{2\omega} b_2''(x) + \frac{1}{2\omega}(b_1(x)\phi(x))'
\end{aligned} \tag{E.15}
$$

This is then substituted into the first equation:

$$
\begin{aligned}
a_2''(x) + 2\omega b_2(x) &= -a_1'(x)\phi(x) - a_1(x)\phi'(x) \\
\left(\frac{1}{2\omega} b_2''(x) + \frac{1}{2\omega}(b_1(x)\phi(x))'\right)'' + 2\omega b_2(x) &= -(a_1(x)\phi(x))' \\
b_2''''(x) + (b_1(x)\phi(x))''' + 4\omega^2 b_2(x) &= -2\omega(a_1(x)\phi(x))' \\
b_2''''(x) + 4\omega^2 b_2(x) &= -2\omega(a_1(x)\phi(x))' - (b_1(x)\phi(x))'''
\end{aligned} \tag{E.16}
$$

We also separate the boundary conditions into two sets of boundary conditions for the real and

imaginary parts.

$$
\begin{aligned}
c_2'(x) + c_1(x)\phi'(x) &= 0 \\
(a_2(x) + jb_2(x))' + (a_1(x) + jb_1(x))\phi'(x) &= 0 \\
a_2'(x) + jb_2'(x) + a_1(x)\phi'(x) + jb_1(x)\phi'(x) &= 0
\end{aligned}
$$

$$
\begin{cases} a_2'(x) &= -a_1(x)\phi'(x), \quad x = 0, H \\ b_2'(x) &= -b_1(x)\phi'(x), \quad x = 0, H \end{cases}
$$

$$
\begin{cases} a_2'(0) &= -a_1(0)\phi'(0) \\ a_2'(H) &= -a_1(H)\phi'(H) \\ b_2'(0) &= -b_1(0)\phi'(0) \\ b_2'(H) &= -b_1(H)\phi'(H) \end{cases} \tag{E.17}
$$

From the second differential equation, we express $b_2(x)$ in terms of $a_2(x)$:

$$
b_2''(x) = 2\omega a_2(x) - 2\omega(b_1(x)\phi(x))' \tag{E.18}
$$

The additional boundary conditions for $b_2(x)$ are obtained by differentiating the above expression and substituting x by the coordinates of the boundary:

$$
\begin{aligned}
b_2'''(0) &= 2\omega a_2'(0) - 2\omega(b_1\phi)''(0) \\
&= -2\omega a_1(0)\phi'(0) - 2\omega(b_1\phi)''(0) \\
b_2'''(H) &= 2\omega a_2'(H) - 2\omega(b_1\phi)''(H) \\
&= -2\omega a_1(H)\phi'(H) - 2\omega(b_1\phi)''(H)
\end{aligned} \tag{E.19}
$$

In summary, the differential equation of the imaginary part of the second harmonic is:

$$b_2''''(x)+4\omega^2 b_2(x) = -2\omega(a_1(x)\phi(x))' - (b_1(x)\phi(x))'''$$

$$BC: \begin{cases} b_2'(0) &= -b_1(0)\phi'(0) \\ b_2'(H) &= -b_1(H)\phi'(H) \\ b_2'''(0) &= -2\omega a_1(0)\phi'(0) - 2\omega(b_1\phi)''(0) \\ b_2'''(H) &= -2\omega a_1(H)\phi'(H) - 2\omega(b_1\phi)''(H) \end{cases} \tag{E.20}$$

With b_2, one may compute a_2 by the relation: $a_2(x) = \frac{1}{2\omega}b_2''(x) + (b_1(x)\phi(x))'$ and the second harmonic is $c_2(x) = a_2(x) + jb_2(x)$.

E.6 Numerical scheme for ESM equation in 2D

(A) Interior points: $i, j \in \{2,3,...,N-2,N-1\}$

$$\begin{aligned} \frac{\partial c_{ij}}{\partial t} &= -\frac{U_{I+1,J}-U_{I,J}}{h} - \frac{V_{I,J+1}-V_{I,J}}{h} \\ &= \frac{D}{h}\left[\left(\frac{c_{i+1,j}-c_{i,j}}{h} - E_{i+1,j}\frac{c_{i+1,j}+c_{i,j}}{2}\right) - \left(\frac{c_{i,j}-c_{i-1,j}}{h} - E_{i,j}\frac{c_{i,j}+c_{i-1,j}}{2}\right)\right] \\ &+ \frac{D}{h}\left[\left(\frac{c_{i,j+1}-c_{i,j}}{h} - F_{i,j+1}\frac{c_{i,j+1}+c_{i,j}}{2}\right) - \left(\frac{c_{i,j}-c_{i,j-1}}{h} - F_{i,j}\frac{c_{i,j}+c_{i,j-1}}{2}\right)\right] \end{aligned} \tag{E.21}$$

(B1): Left boundary: $i = 1, j \in \{2,3,...,N-2,N-1\}$

$$\begin{aligned} \frac{\partial c_{1j}}{\partial t} &= -\frac{U_{2,J}-U_{1,J}}{h} - \frac{V_{1,J+1}-V_{1,J}}{h} \\ &= -\frac{U_{2,J}-0}{h} - \frac{0-0}{h} \\ &= \frac{D}{h}\left(\frac{c_{2,j}-c_{1,j}}{h} - E_{2,j}\frac{c_{2,j}+c_{1,j-1}}{2}\right) \end{aligned} \tag{E.22}$$

(B2): Right boundary: $i = N, j \in \{2,3,...,N-2,N-1\}$

$$\begin{aligned}\frac{\partial c_{Nj}}{\partial t} &= -\frac{U_{N+1,J}-U_{N,J}}{h} - \frac{V_{N,J+1}-V_{N,J}}{h} \\ &= -\frac{0-U_{N,J}}{h} - \frac{V_{N,J+1}-V_{N,J}}{h} \\ &= \frac{D}{h}\left[-\left(\frac{c_{N,j}-c_{N-1,j}}{h} - E_{i,j}\frac{c_{N,j}+c_{N-1,j}}{2}\right)\right] \\ &+ \frac{D}{h}\left[\left(\frac{c_{N,j+1}-c_{i,j}}{h} - F_{N,j+1}\frac{c_{N,j+1}+c_{N,j}}{2}\right) - \left(\frac{c_{N,j}-c_{N,j-1}}{h} - F_{N,j}\frac{c_{N,j}+c_{N,j-1}}{2}\right)\right]\end{aligned} \tag{E.23}$$

(B3): Lower boundary: $i \in \{2,3,...,N-2,N-1\}, j = 1$

$$\begin{aligned}\frac{\partial c_{i1}}{\partial t} &= -\frac{U_{i+1,1}-U_{i,1}}{h} - \frac{V_{i,2}-V_{i,1}}{h} \\ &= -\frac{0-0}{h} - \frac{V_{i,2}-0}{h} \\ &= \frac{D}{h}\left(\frac{c_{i,2}-c_{i,1}}{h} - F_{i,2}\frac{c_{i,2}+c_{i,1}}{2}\right)\end{aligned} \tag{E.24}$$

(B4): Upper boundary: $i \in \{2,3,...,N-2,N-1\}, j = N$

$$\begin{aligned}\frac{\partial c_{iN}}{\partial t} &= -\frac{U_{i+1,N}-U_{i,N}}{h} - \frac{V_{i,N+1}-V_{i,N}}{h} \\ &= -\frac{U_{i+1,N}-U_{i,N}}{h} - \frac{0-V_{i,N}}{h} \\ &= \frac{D}{h}\left[\left(\frac{c_{i+1,N}-c_{i,N}}{h} - E_{i+1,N}\frac{c_{i+1,N}+c_{i,N}}{2}\right) - \left(\frac{c_{i,N}-c_{i-1,N}}{h} - E_{i,N}\frac{c_{i,N}+c_{i-1,N}}{2}\right)\right] \\ &+ \frac{D}{h}\left[-\left(\frac{c_{i,N}-c_{i,N-1}}{h} - F_{i,N}\frac{c_{i,N}+c_{i,N-1}}{2}\right)\right]\end{aligned} \tag{E.25}$$

(C1): At lower left corner: $i = 1, j = 1$

$$\begin{aligned}\frac{\partial c_{11}}{\partial t} &= -\frac{U_{2,1}-U_{1,1}}{h} - \frac{V_{1,2}-V_{1,1}}{h} \\ &= -\frac{0-0}{h} - \frac{0-0}{h} \\ &= 0\end{aligned} \tag{E.26}$$

(C2): At lower right corner: $i = N, j = 1$

$$\begin{aligned}\frac{\partial c_{N1}}{\partial t} &= -\frac{U_{N+1,1} - U_{N,1}}{h} - \frac{V_{N,2} - V_{N,1}}{h} \\ &= -\frac{0-0}{h} - \frac{V_{N,2} - 0}{h} \\ &= \frac{D}{h}\left(\frac{c_{1,2} - c_{1,1}}{h} - F_{1,2}\frac{c_{1,2} + c_{1,1}}{2}\right)\end{aligned} \tag{E.27}$$

(C3): At upper left corner: $i = 1, j = N$

$$\begin{aligned}\frac{\partial c_{1N}}{\partial t} &= -\frac{U_{2,N} - U_{1,N}}{h} - \frac{V_{1,N+1} - V_{1,N}}{h} \\ &= -\frac{U_{2,N} - 0}{h} - \frac{0-0}{h} \\ &= \frac{D}{h}\left(\frac{c_{2,N} - c_{1,N}}{h} - E_{2,N}\frac{c_{2,N} + c_{1,N}}{2}\right)\end{aligned} \tag{E.28}$$

(C4): At upper right corner: $i = N, j = N$

$$\begin{aligned}\frac{\partial c_{NN}}{\partial t} &= -\frac{U_{N+1,N} - U_{N,N}}{h} - \frac{V_{N,N+1} - V_{N,N}}{h} \\ &= -\frac{0 - U_{N,N}}{h} - \frac{0 - V_{N,N}}{h} \\ &= -\frac{D}{h}\left(\frac{c_{N,N} - c_{N-1,N}}{h} - E_{N,N}\frac{c_{N,N} + c_{N-1,N}}{2}\right) - \frac{D}{h}\left(\frac{c_{N,N} - c_{N,N-1}}{h} - F_{N,N}\frac{c_{N,N} + c_{N,N-1}}{2}\right)\end{aligned} \tag{E.29}$$

VITA

Chi Hou Lei was born and raised in Macau (an ex-colony of Portugal), China. He earned a Bachelor of Science degree in Mathematics (BS) and a Bachelor of Science degree in Mechanical Engineering (BSME) at National Taiwan University in 2006. He earned a Master of Science degree in Mathematics in 2008 at the Michigan State University and a Doctor of Philosophy in Mechanical Engineering in 2015 at the University of Washington.